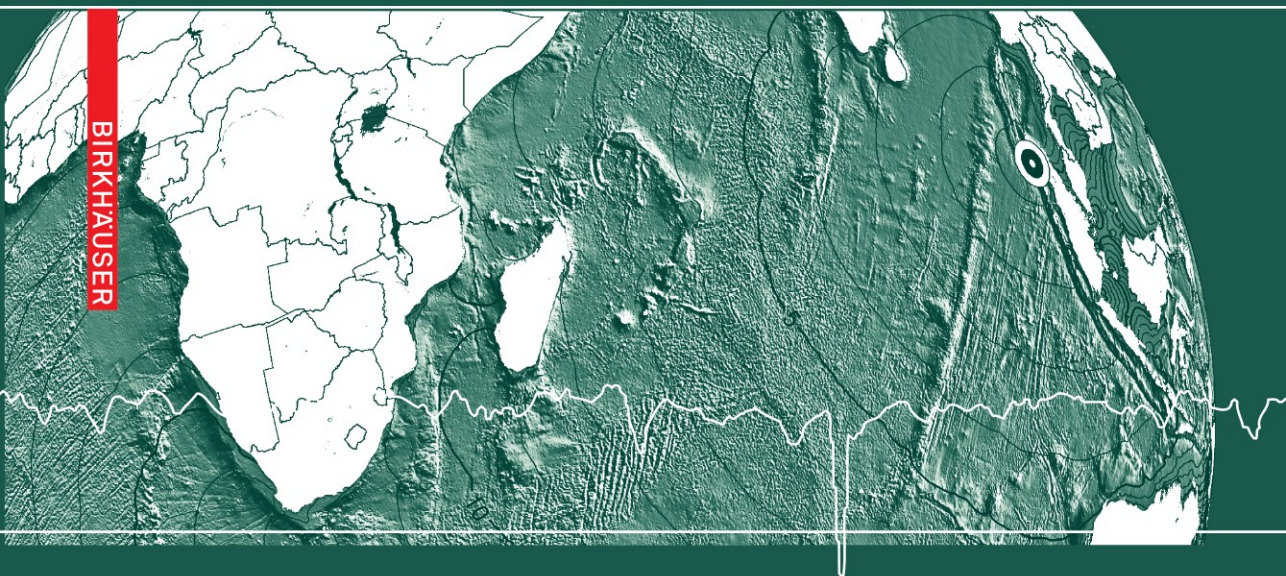# Tsunami Science
Four Years after the **2004** Indian Ocean Tsunami

Part I: Modelling and Hazard Assessment

Edited by
Phil R. Cummins
Laura S. L. Kong
Kenji Satake

BIRKHÄUSER

Tsunami Science
Four Years after the **2004 Indian Ocean Tsunami**

Part I: Modelling and Hazard Assessment

Edited by
Phil R. Cummins
Laura S. L. Kong
Kenji Satake

Phil R. Cummins
Geoscience Australia
P.O. Box 378
Canberra, ACT 2601
Australia
Email: phil.cummins@ga.gov.au

Kenji Satake
Earthquake Research Institute
University of Tokyo
1-1-1 Yayoi
Bunkyo-ku
Tokyo 113-0032
Japan
Email: satake@eri.u-tokyo.ac.jp

Laura S. L. Kong
UNESCO Intergovernmental Oceanographic
Commission (IOC)
International Tsunami Information Centre
737 Bishop Street
Suite 2200
Honolulu, HI, 96813
USA
Email: l.kong@unesco.org

Contents

Introduction to "Tsunami Science Four Years After the 2004 Indian Ocean Tsunami, Part I: Modelling and Hazard Assessment"

Phil R. Cummins,[1] Laura S. L. Kong,[2] and Kenji Satake[3]

Abstract—In this introduction we briefly summarize the 14 contributions to Part I of this special issue on Tsunami Science Four Years after the 2004 Indian Ocean Tsunami. These papers are representative of the new tsunami science being conducted since the occurrence of that tragic event. Most of these were presented at the session: Tsunami Generation and Hazard, of the International Union of Geodesy and Geophysics XXIV General Assembly held at Perugia, Italy, in July of 2007. That session included over one hundred presentations on a wide range of topics in tsunami research. The papers grouped into Part I, and introduced here, cover topics directly related to tsunami mitigation such as numerical modelling, hazard assessment and databases. Part II of this special issue, Observations and Data Analysis, will be published in a subsequent volume of Pure and Applied Geophysics.

Key words: Tsunami, seiche, harbor resonance, numerical modeling, hazard assessment, inundation, tsunami mitigation, tsunami warning system, runup, tsunami database, rissaga.

1. Introduction

Four years after the 2004 Indian Ocean Tsunami, the most lethal tsunami disaster in human history, tsunami science continued to move forward rapidly. The research and disaster management community that supports tsunami mitigation has expanded greatly. Observation platforms, especially in the Indian Ocean, have far surpassed their pre-2004 capacity for detecting and measuring tsunamis and the earthquakes that most frequently cause them. A remarkable crosssection of this research was presented in the session Tsunami Generation and Hazard, at the International Union of Geodesy and Geophysics (IUGG) XXIV General Assembly in Perugia, Italy, held in July of 2007. Over one hundred presentations were made at this session, spanning topics ranging from paleotsunami research, to nonlinear shallow-water theory, to tsunami hazard and risk

[1] Geoscience Australia, GPO, Box 378, Canberra, ACT 2601, Australia.
E-mail: Phil.Cummins@ga.gov.au
[2] UNESCO IOC International Tsunami Information Centre, 737 Bishop St. Ste. 2200, Honolulu, Hawaii 96813, USA. E-mail: l.kong@unesco.org
[3] Earthquake Research Institute, University of Tokyo, 1-1-1 Yayoi, Bunkyo-ku, Tokyo 113-0032, Japan. E-mail: satake@eri.u-tokyo.ac.jp

assessment. The IUGG's Tsunami Commission arranged for a selection of this work, along with other papers on similar topics, to be published in detail in the 28 papers of this 2-part special issue of Pure and Applied Geophysics.

In this introductory paper, we briefly discuss the papers in Part I of "Tsunami Science Four Years After the 2004 Indian Ocean Tsunami". In Section 2 we discuss new advances in the fundamental numerical techniques used to model tsunamis and Section 3 reviews several contributions that apply such techniques to improve our understanding of how near-coast processes affect tsunami propagation. Sections 4 and 5 discuss the application of tsunami modeling to tsunami hazard assessment, in a deterministic and a probabilistic sense, respectively. Section 6 describes two database efforts that are supporting researchers and warning system operators to access the most current and accurate information on tsunami events.

2. Advances in Analytical and Numerical Modeling of Tsunamis

The increased focus on tsunami science since the 2004 Sumatra-Andaman Earthquake and subsequent Indian Ocean Tsunami has seen a rapid expansion in the tsunami modeling community. Prior to 2004, this community consisted of a handful of research groups that utilized a few well-tested codes for numerical modeling of tsunamis. Since 2004, many more research groups have taken an interest in tsunami modeling, and these groups have in some cases either developed new codes for tsunami modeling, or adapted hydrodynamic codes that had originally been developed for other purposes. Tsunami forecasting via numerical modeling is also seeing increased use as an operational part of tsunami warning systems.

In response to this recent proliferation of tsunami modeling codes, SYNOLAKIS *et al.* (2008) pointed out the importance of validation and verification of codes used in tsunami hazard assessment or forecasting systems. They reviewed several methods by which this can be accomplished. These included analytical and laboratory validation benchmarks, as well as examples of field observations against which numerical models can be verified. A summary of the theoretical development for formulae used as analytical benchmarks was given, and details of the laboratory experiments and field observations were reviewed. In addition to the use of these benchmarks for inundation modeling in tsunami hazard studies, operational requirements for forecasting tsunamis in real-time were discussed.

ZHANG and BATISTA (2008) presented an example of the adaptation of a multi-purpose baroclinic circulation model (SELFE) to tsunami inundation and propagation. The model has several interesting features that make it a useful addition to the suite of tools already available: Release as open source, facilitating further development by a community of users; use of an unstructured grid, allowing for variable resolution to accommodate complex geometry only where necessary; an implicit time-stepping algorithm that avoids the stringent Courant–Friedrichs–Lewy stability condition, and a simple wetting/drying

algorithm that implements inundation. Along the lines suggested by SYNOLAKIS *et al.* (2008), the authors presented validation results against scenarios from the 3rd International Workshop in Long-Wave Runup Models (http://www.cee.cornell.edu/longwave).

GREENSLADE and TITOV (2008), on the other hand, use a tried and tested tsunami code (MOST – see TITOV and GOZAREZ, 1997) to compare two tsunami forecasting systems used by the U.S. National Oceanic and Atmospheric Administration (NOAA), and the Australian Bureau of Meteorology. The tsunamis caused by the 2006 Tonga and 2007 Sumatra earthquakes were used as test cases. Both systems use results of tsunami computations made prior to earthquakes and stored in a database. While the specifications of numerical simulation of tsunami propagation are very similar, the scenario sources distributed around the Pacific Basins are slightly different. The Australian system assumes different faults depending on the earthquake magnitude, while the U.S. system scales the slip amount by assimilation of tsunameter (a.k.a. DART) data. Because different sources are used to approximate the Tonga and Sumatra earthquakes, the forecasted waveforms at offshore tsunameter locations are slightly different. However, the differences in waveforms computed at coastal tide gauges are considerably smaller, indicating insensitivity of coastal tsunamis to the details of the tsunami source.

Despite substantial recent progress in numerical tsunami modeling, the rapid forecast of runup values remains a difficult problem, due to its nonlinearity and sensitivity to input data such as bathymetry and initial waveform. The paper by DIDENKULOVA *et al.* (2008) demonstrated that analytical results still have an important role to play in estimating runup. They discussed results from nonlinear shallow-water wave theory for runup of solitary tsunami waves, and showed that appropriate definitions of significant wave height and length (based on 2/3 of maximum wave height) result in formulae for computing runup characteristics that are relatively independent of incident wave shape (for symmetric incident waves). Such formulae may be used in rapidly estimating potential inundation once the tsunami height, wavelength and period in the open ocean are known.

3. Modeling of Near-Coast Effects on Tsunami Propagation

One of the most challenging aspects of tsunami modeling is accurate representation of propagation effects near the coast, including reflection and refraction by shallow bathymetry, and resonances in semi-enclosed bays and inlets. Several papers in this issue address these topics.

BABA *et al.* (2008) examined the effects of Great Barrier Reef, the world's largest coral reef located offshore Australia, on the tsunami generated by the April 1, 2007 Solomon Islands earthquake. They carried out tsunami numerical simulation from a source model based on their seismic waveform inversion. The simulated waveforms show good agreement with tide gauge data in northeast Australia. In order to examine the effect of the coral reef, they also made tsunami simulations with artificial bathymetry data

without the coral reef; the reef was replaced with deep ocean in one dataset and shallow ocean in the other. Simulations with these models indicate that the tsunami energy was reduced by direct reflection outside the reef and by refraction when the tsunami passed through the reef. As a result, the tsunami was delayed by 10–15 minutes, the amplitude became about a half or less, and the period became longer.

Semi-enclosed bays and inlets present another challenge to tsunami modeling in the form of potential resonant enhancement of tsunamis. Alberni inlet is a long (~ 40 km) and narrow (1–2 km) fjord in Vancouver Island, Canada. The tsunami caused by the 1964 Alaskan earthquake had a height of about 8 m above mean sea level at Port Alberni, located at the head of the inlet and about 65 km from the Pacific Ocean. FINE *et al.* (2008) examined resonance characteristics of the Alberni inlet by using numerical calculations. Their results indicated that strong amplification occurred at a period of 112 min with an amplification factor of more than 10.

VILIBIĆ *et al.* (2008) presented a comprehensive analysis of a destructive meteotsunami (*rissaga)* that occurred in the Balearic Islands in 2006. This event was not associated with an earthquake source and excited destructive harbor oscillations of several meters amplitude, resulting in an economic loss estimated at tens of millions of euros. VILIBIĆ *et al.* used a numerical model, verified using a series of measurements made during smaller *rissaga* events in 1997, and microbarograph measurement to show how the 2006 *rissaga* resulted from ocean-atmosphere resonance excited by a travelling atmospheric disturbance, which in turn induced the hazardous harbor oscillations observed. The potential for developing a *rissaga* warning system based on this model was also discussed.

4. Scenario Modeling for Tsunami Hazard Assessment

In addition to rapid tsunami forecasts that may form part of a tsunami warning, emergency managers and planners in coastal communities need information about how large tsunamis affecting their communities might be. Such questions can be answered by scenario modeling, which forms the basis of a deterministic hazard assessment. Such assessments are normally designed to encompass the worst credible, as well as the most likely, scenarios.

TIBERTI *et al.* (2008) numerically modeled potential tsunamis in the Adriatic Sea. Maximum credible earthquakes were assumed along the six source zones. They classified the computed maximum tsunami heights into three levels: marine, land and severe land for 0.05 m, 0.5 m and 1.0 m, respectively. The results indicate that the largest tsunamis are expected on the Apulia and Gargano coasts of southern Italy. They found that focusing of energy due to bathymetric features enhances the tsunami heights.

At Stromboli volcano, southern Italy, on December 30, 2002, a moderate-sized landslide (with a volume of 0.02–0.03 km^3) generated a tsunami, with a maximum runup height of about 10 m. Because it occurred in the winter, there was no loss of human life,

nonetheless damage was caused on the coast. This slide occurred at Sciara del Fuoco (SdF), a steep scar of the island which can potentially produce a landslide with a volume of 1 km^3. TINTI *et al.* (2008) numerically simulated tsunamis from three other potential sources of landslides around the island. The expected landslide volume is similar to that of the 2002 slide. They showed that a landslide at Punta Lena, south of the island, can produce a tsunami even larger than the 2002 tsunami.

The paper by HEIDARZADEH *et al.* (2008) presented a deterministic assessment of tsunami hazard in the northwestern Indian Ocean by considering a series of six large (M$_w$ 8.3) tsunamigenic earthquake scenarios along the Makran subduction zone. They used the tsunami model TUNAMI-2 (GOTO *et al.*, 1997), along with the GEBCO bathymetry grid, to calculate tsunami heights at the coastline for these scenarios. The calculated tsunami heights and arrival times were verified against observations of the tsunami caused by a Makran subduction zone earthquake that occurred in 1945. The scenario modeling demonstrated that earthquakes along the Makran subduction zone pose a substantial tsunami threat to the Arabian Sea coasts of Iran, Pakistan, Oman and India.

5. *Probabilistic Tsunami Hazard Assessment*

A further level of refinement in tsunami hazard assessment considers not only how large a tsunami affecting a particular community may be, but also how likely is the occurrence of a tsunami of a given magnitude. This is known as probabilistic tsunami hazard assessment, and its implementation is similar in concept to that of Probabilistic Seismic Hazard Assessment (CORNELL, 1968).

The paper by PARSONS and GEIST (2008) presents a probabilistic tsunami hazard assessment for the Caribbean region. This assessment involves consideration of both historical events, based on the impressive 500-year-long catalog of Caribbean tsunami observations, and also earthquake sources based on numerically-modelled seismic moment release along the convergent margins of the Caribbean plate. While the former potentially accounts for non-earthquake tsunami sources (e.g., submarine landslides), the latter accounts for earthquakes with long return periods that may not be represented in the catalog. The authors developed a Bayesian method for combining these to produce a tsunami hazard map that made optimal use of the information available from both the catalog and modeling results.

BURBIDGE *et al.* (2008) calculated probabilistic tsunami hazard for the coast of western Australia. Tsunamis from great earthquakes along the Sumbawa, Java and Sunda trenches have affected the western coasts of Australia. Probabilistic tsunami hazard was used to estimate offshore wave heights as a function of return period. While the tsunami heights along the Australian coasts from a magnitude 8 earthquake with the return period of about 100 years were not very high, those from a magnitude 9 earthquake, similar to the 2004 Sumatra-Andaman earthquake, with a return period of about 1,000 years, would be very large and potentially cause damage.

6. Tsunami Databases

Databases are essential for the support of tsunami hazard and risk assessments and warning systems. The task of collating information of varying quality from many different sources is a formidable one, and unless validated information about tsunami observations and observation platforms is made available in a consistent form, this information cannot be used effectively. Two papers in this issue discuss databases that are designed to provide effective support to hazard/risk assessment and warning systems.

MARRA *et al.* (2008) introduce readers to the concept of web services as a means to efficiently describe, collect, integrate, and publish sea-level station metadata that are contributed by many countries and organizations, and used by station operators, tsunami and other coastal hazard warning systems, disaster management officials, and coastal inundation researchers. The service incorporates an agreed-upon sea-level station XML schema for automatic and continuous station reporting, thus facilitating the implementation of always up-to-date data mining client applications. One example that is described is Tide Tool, which was developed by the Pacific Tsunami Warning Center to continuously download and decode sea-level data globally and to monitor tsunamis in real-time.

DUNBAR *et al.* (2008) describe the enhancements to the National Geophysical Data Center World Data Center for Geophysics and Marine Geology (WDC-GMG) national and international long-term tsunami data archive since 2004. The archive has expanded from the original global historical event databases and damage photo collection, to include tsunami deposits, coastal water-level data, DART buoy data, and high-resolution coastal Digital Elevation Model datasets for supporting model validation, guidance to warning centers, tsunami hazard assessment, and education of the public. The data are available in the public domain, and tools have been provided for interactive on-line and off-line data discovery and download in multiple formats to facilitate further integration and re-use by everyone.

Acknowledgments

REFERENCES

BABA, T., MLECZKO, R., BURBIDGE, D., CUMMINS, P.R., and THIO, H. K. (2008), *The effect of the Great Barrier Reef on the propagation of the 2007 Solomon Islands tsunami recorded in northeastern Australia*, Pure Appl. Geophys. *165*, 2003-2018.

BURBIDGE, D., CUMMINS, P.R., MLECZKO, R., and THIO, H. K. (2008), *A Probabilistic Tsunami Hazard Assessment for Western Australia*, Pure Appl. Geophys. *165*, 2059–2088.

CORNELL, C.A. (1968), *Engineering seismic risk analysis*, Bull. Seismol. Soc. Am. *58*, 1583–1606.

DIDENKULOVA, I., PELINOVSKY, E., and SOMERE, T. (2008), *Runup characteristics of symmetrical solitary tsunami waves of "unknown" shapes*, Pure Appl. Geophys., *165*, 2249–2264.

DUNBAR, P.K., STROKER, K.J., BROCKO, V.R., VARNER, J.D., McLEAN, S.J., TAYLOR, L.A., EAKINS, B.W., CARIGNAN, K.S., and WARNKEN, R.R. (2008), *Long-term tsunami data archive supports tsunami forecast, warning, research, and mitigation*, Pure Appl. Geophys. *165*, 2275–2291.

FINE, I. V., CHERNIAWSKY, J. Y., RABINOVICH, A. B., and STEPHENSON, F. (2008), *Numerical modeling and observations of tsunami waves in Alberni Inlet and Barkley Sound, British Columbia*, Pure Appl. Geophys. *165*, 2019–2044.

GOTO, C., OGAWA, Y., SHUTO, N., and IMAMURA, F. (1997), *Numerical Method of Tsunami Simulation with the Leap-Frog Scheme (IUGG/IOC Time Project)*, IOC Manual, UNESCO, No. 35.

GREENSLADE, D.J.M. and TITOV, V. V. (2008), *Comparison study of two numerical tsunami forecasting systems*, Pure Appl. Geophys. *165*, 1991–2001.

HEIDARZADEH, M., PIROOZ, M.D., ZAKER, N.H., and SYNOLAKIS, C.E. (2008), *Evaluating tsunami hazard in the northwestern Indian Ocean*, Pure Appl. Geophys. *165*, 2045–2058.

MARRA, J., KARI, U.S., and WEINSTEIN, S.A. (2008), *A tsunami detection and warning-focused sea-level station metadata web service*, Pure Appl. Geophys. *165*, 2265–2273.

PARSONS, T. and GEIST, E.L. (2008), *Tsunami probability in the Caribbean region*, Pure Appl. Geophys., *165*, 2089–2116.

SYNOLAKIS, C., BERNARD, E.N., TITOV, V.V., KANOGLU, U., and GONZALEZ, F.I. (2008), *Validation and verification of tsunami numerical models*, Pure Appl. Geophys. *165*, 2197–2228.

TIBERTI, M. M., LORITO, S., BASILI, R., KASTELIC, V., PIATANESI, A., and VALENSISE, G. (2008), *Scenarios of earthquake-generated tsunamis for the Italian coast of the Adriatic Sea*, Pure Appl. Geophys. *165*, 2117–2142.

TINTI, S., ZANIBONI, F., PAGNONI, G., and MANUCCI, A. (2008), *Stromboli Island (Italy): Scenarios of tsunamis generated by submarine landslides*, Pure Appl. Geophys. *165*, 2143–2167.

TITOV, V.V. and GONZALEZ, F.I. (1997), *Implementation and testing of the Method of Splitting Tsunami (MOST) model*, NOAA Technical Memorandum ERL PMEL-112, 11 pp.

VILIBIĆ, I., MONSERRAT, S., RABINOVICH, A., and MIHANOVIĆ, H. (2008), *Numerical modelling of the destructive meteotsunami of 15 June 2006 on the coast of the Balearic Islands*, Pure Appl. Geophys. *165*, 2169–2195.

ZHANG, Y.J. and BATISTA, A. M. (2008), *An efficient and robust tsunami model on unstructured grids. Part I: Inundation benchmarks*, Pure Appl. Geophys. *165*, 2229–2247.

To access this journal online:
www.birkhauser.ch/pageoph

A Comparison Study of Two Numerical Tsunami Forecasting Systems

DIANA J. M. GREENSLADE[1] and VASILY V. TITOV[2]

Abstract—This paper presents a comparison of two tsunami forecasting systems: the NOAA/PMEL system (SIFT) and the Australian Bureau of Meteorology system (T1). Both of these systems are based on a tsunami scenario database and both use the same numerical model. However, there are some major differences in the way in which the scenarios are constructed and in the implementation of the systems. Two tsunami events are considered here: Tonga 2006 and Sumatra 2007. The results show that there are some differences in the distribution of maximum wave amplitude, particularly for the Tonga event, however both systems compare well to the available tsunameter observations. To assess differences in the forecasts for coastal amplitude predictions, the offshore forecast results from both systems were used as boundary conditions for a high-resolution model for Hilo, Hawaii. The minor differences seen between the two systems in deep water become considerably smaller at the tide gauge and both systems compare very well with the observations.

Key words: Tsunami, tsunami forecast.

1. Introduction

Recent tsunami events (e.g., Sumatra 2004, Java 2006, Solomon Islands 2007) have demonstrated the need for providing accurate and timely tsunami warnings for all the world's ocean basins. Improvements in the availability of sea-level observations and advances in numerical modelling techniques are increasing the potential for tsunami warnings to be based on numerical model forecasts. Numerical tsunami propagation and inundation models are well developed, but they present a challenge to run in real-time; partly due to computational limitations and also due to a lack of detailed knowledge on the earthquake rupture details (TITOV *et al.,* 2005). For these reasons, current tsunami forecast systems are based on pre-computed tsunami scenarios. A tsunami scenario is a single model run that is calculated ahead of time with the initial conditions carefully selected so that they are likely to represent an actual tsunamigenic earthquake.

This paper will present a comparison of two tsunami scenario databases: the NOAA/PMEL system (a.k.a. Short-term Inundation Forecast for Tsunamis – SIFT), currently

[1] Centre for Australian Weather and Climate Research, Bureau of Meteorology, GPO Box 1289, Melbourne, Victoria 3001, Australia. E-mail: d.greenslade@bom.gov.au

[2] NOAA Center for Tsunami Research, NOAA/PMEL/OERD, 7600 Sand Point Way NE, Bldg. 3, Seattle, WA 98115-0070, U.S.A.

being implemented at NOAA Tsunami Warning Centers and the Bureau of Meteorology system (T1), which has been developed for the Joint Australian Tsunami Warning Centre. Both scenario databases are based on the Method Of Splitting Tsunamis (MOST) model (TITOV and SYNOLAKIS, 1998), but there are some differences in the way the scenarios are constructed. These will be described in Section 2. A comparison of model forecasts for some recent events is presented in Section 3. The events chosen are the only two tsunamis that occur within the domains of both systems and for which a good set of deep ocean observations exists. Section 4 contains a discussion of the results.

2. Description of the Scenario Databases

2.1. T1 (Joint Australian Tsunami Warning Centre)

T1 is described in detail in GREENSLADE *et al.* (2007). It consists of a total of 741 scenarios calculated using the MOST model. The bathymetry data set used in the construction of the scenarios was extracted from a data set developed for the Bureau of Meteorology's ocean forecasting system (Mansbridge, unpublished document). The underlying bathymetry used in this data set is the Naval Research Laboratory Digital Bathymetry Data Base 2 arc minute resolution (NRL DBDB2). This has the GEBCO Digital Atlas merged into it south of 68°S, and the bathymetry used in the Australian region is the 2002 issue of Geoscience Australia's bathymetry and topography data set, with some manual adjustments incorporated. This merged 2 arc minute data set was sub-sampled at 4 arc minutes for T1.

The scenarios are distributed over 230 source locations in the Australian region. They are located 100 km apart along subduction zones (BIRD, 2003). Each source location has four scenarios associated with it, with magnitudes of 7.5, 8, 8.4 and 9. The defined rupture details for each scenario are listed in Table 1. Other details of the ruptures are fixed for each scenario. These are the depth (10 km), dip (25°) and rake (90°). TITOV *et al*. (1999) demonstrated that details of the first few tsunami waves are relatively insensitive to variations in the dip and the rake, so the impact of setting these parameters to be fixed for all scenarios is minimal. The current recommendation for using the scenarios operationally is that if the magnitude of an event is not one of the 4 magnitudes existing in the database, then the closest upper magnitude scenario should be used for forecast guidance. It is acknowledged that this could result in over-warning, which is a serious issue: The production of false alarms should be kept to a minimum within a tsunami warning system. However, over-warning is preferable to under-warning, which can result in direct catastrophic impacts. It should be noted that this "upper scenario" strategy is a temporary measure only and an enhanced scenario database with a scaling technique is currently being developed that will provide more appropriate guidance for intermediate magnitude earthquakes (SIMAN-JUNTAK and GREENSLADE, 2008).

Table 1

Rupture details for T1 scenarios

Magnitude (M_w)	Width (W) (km)	Length (L) (km)	Slip (u_0) (m)
7.5	50	100	1
8.0	65	200	2.2
8.4	80	400	3
9.0	100	1000	8.8

Specific details of the model configurations for the scenarios are: spatial resolution: 4 arc minutes, minimum offshore depth: 20 m, time step: 8 seconds, sea level (and depth-averaged currents) at every grid-point saved every 15 time steps (i.e., 2 minutes) and the model is run for 10 hours of model time.

2.2. NOAA's Short-term Inundation Forecast (SIFT)

The NOAA propagation database is described in detail in GICA *et al.* (2008). The forecast strategy is based on a unit source function methodology, whereby the model runs are individually scaled and combined to produce arbitrary tsunami scenarios. Each unit source function is equivalent to a tsunami generated by a M_w 7.5 earthquake with a rectangular fault 100 km by 50 km in size and 1 m slip. These are similar to the T1 M_w 7.5 events (see Table 1). The faults of the unit functions are placed adjacent to each other. When the functions are linearly combined, the resultant source function is equivalent to a tsunami generated by a combined fault rupture with assigned slip at each subfault.

The MOST model is used to generate the scenarios and the bathymetry for the Pacific Ocean is based on the SMITH and SANDWELL (1994) 2 arc minute data set. The model utilizes the bathymetry data in the original Mercator projection format of the Smith and Sandwell data, where the grid cells become smaller for locations farther away from the equator. The data are subsampled to twice coarser resolution (4 arc minutes at the equator) of the original dataset.

There are currently a total of 1400 unit sources distributed throughout the Pacific, Atlantic and Indian Oceans. These are arranged in several rows along known fault zones, to cover areas of potential tsunami sources. The rake is set at 90°, as in T1. The main differences with the T1 scenarios are that the dip and depth vary according to known assessments of the fault geometries (KIRBY *et al.*, 2006). Where depth estimates are not available, the depth of the top row of sources is set at 5 km and the depth of the lower rows of sources depends on the dip of the top rows.

Other relevant specific details of the model configuration are: Spatial resolution: 4 arc minutes, minimum offshore depth: 20 m, time step: 15 seconds, sea level (and depth-averaged currents) at every fourth grid-point are saved every 4 time steps (i.e., 1 minute) and the model is run for 24 hours of model time.

For the model forecasts considered here, the NOAA system uses inversion techniques to select the best combination of unit source functions in order to match observations of sea level from the tsunameters (GICA *et al.*, 2008; TITOV *et al.*, 2005). The inversion is done by performing a positively-constrained combined least-squares fit of model-data comparisons for all DART locations for a given combination of unit sources. The inversion defines the scaling coefficients for each unit source in the combination.

3. Event Forecasts

Two different tsunami events are considered here. These particular events are chosen because they are in either the Indian or Southwest Pacific Oceans, and therefore occur within the domains of both systems (recall that the domain of T1 is limited to the Australian region). In addition, there are observations of sea level from deep-ocean buoys available for each event which can be used for inversion and/or verification. At the time of writing these were in fact the only events for which both these criteria were true, i.e., the events occurred within the domain of both systems and observations from deep-ocean buoys were available. With the current rapid expansion of the global tsunameter network, and the future expansion of the domain of T1, further tsunami events will provide more opportunities for comparison of the two forecasting systems.

3.1. Tonga 2006

The Tonga event occurred on May 3, 2006 at 15:26:39 (UTC) about 160 km northeast of Nuku'Alofa, Tonga. The first Pacific Tsunami Warning Center (PTWC) bulletin issued had the earthquake details as M_w 8.1 at (174.2°W, 19.9°S), with subsequent bulletins lowering the magnitude to 7.8. The United States Geological Survey (USGS) has analyzed the event as M_w 7.9 at 55-km depth and located at (174.164°W, 20.13°S). There were some minor impacts seen but no major injuries. Tide gauges in the region observed a tsunami with peak-to-trough wave heights of up to 50 cm.

The maps of maximum tsunami amplitude (H_{max}) from each system are shown in Figure 1. For the T1 database, this is the closest scenario to the actual event—in this case, the M_w 8.0 scenario with epicenter located at (173.4°W, 20.64°S). For the NOAA system, the best combination of unit sources to match the available tsunameter observations (see later) was a scaling factor of 6.6 applied to the time series of surface elevation associated with a single unit source located at (173.83°W, 20.43°S), which, in fact, is equivalent to a M_w 8.0 event. The distribution of H_{max} differs between the two systems predominantly because of the different source lengths: 200 km for T1 and 100 km for SIFT. The longer source results in a distribution of energy that is more focussed perpendicular to the fault
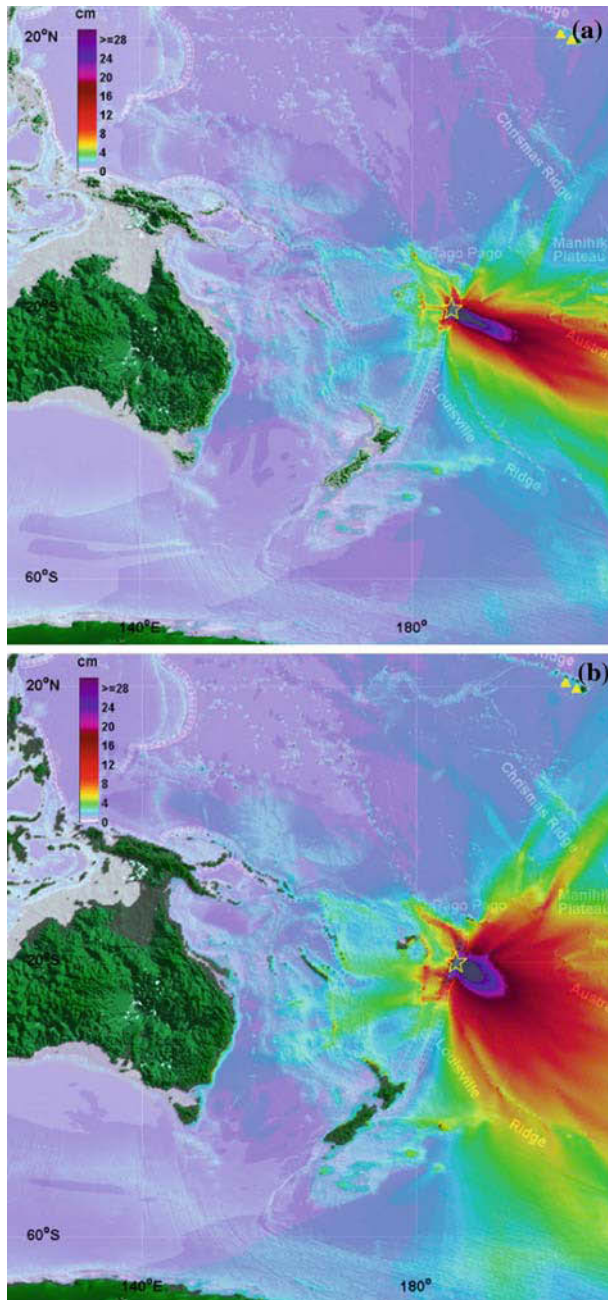
Figure 1
(a) Maximum tsunami amplitude from closest T1 scenario and (b) maximum tsunami amplitude from the SIFT system.

line while the shorter source acts more as a point source with energy distributed over a wider range of directions.

Observations of sea level in the deep ocean were available for this event from a Deep Ocean Assessment and Reporting of Tsunamis (DART) buoy (51407) at (203.493°E, 19.634°N) and an Easy-To-Deploy (ETD) DART buoy at (201.887°E, 20.5095°N) both near Hawaii. The locations of these buoys are shown by the yellow triangles in Figure 1. For each of the two systems, time series of sea level were extracted from the model output at the closest model grid point to the observation location. These time series are shown in Figure 2.

It can be seen that both systems compare well to the observations. For the DART (Fig. 2a), the time of arrival of the first crest from both systems matches the observed arrival time very well. In addition, the frequency of the wave appears very good, at least
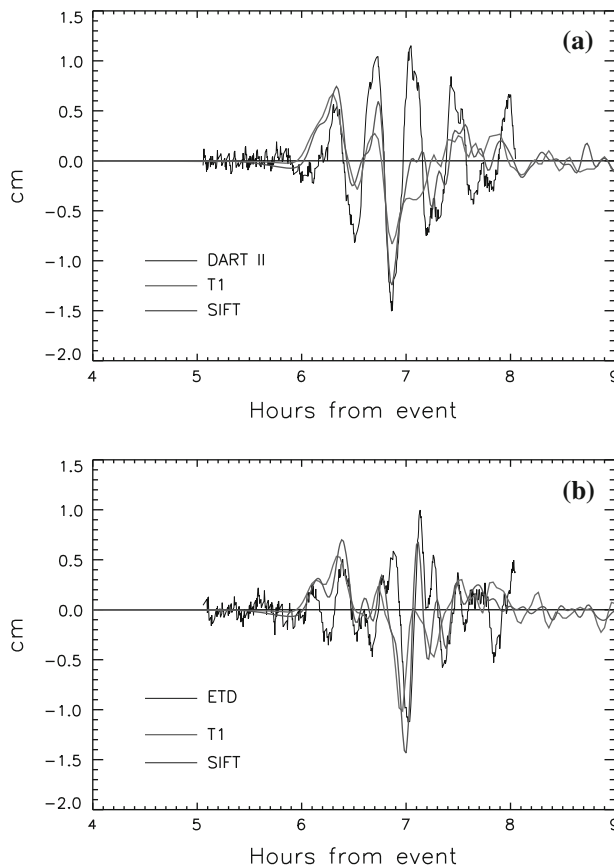
Figure 2
Time series of sea level elevation from tsunameters and scenario forecasts. (a) DART at (203.493°E, 19.634°N) and (b) ETD at (201.887°E, 20.5095°N) for the Tonga event.

for the first three waves. Both models miss the third crest and the overall decay in the amplitude of the waves from the models is more rapid than observed.

There are only minor differences between the two model time series—the SIFT results match the observed peak amplitudes slightly better—this is most likely a reflection of the fact that SIFT is scaled to match the observations, while the T1 result is raw model output that is not qualified by any data.

Comparisons at the ETD (Fig. 2b) are qualitatively similar. However, this time, the T1 scenario compares better in amplitude to a few of the peaks.

To investigate how the differences in the offshore forecasts would appear at the coast, a high-resolution model was run for Hilo, using both forecast results as boundary conditions. A high-resolution 2-D inundation simulation is run with the MOST model to obtain a local inundation forecast as part of the SIFT forecast procedures. The data input for the inundation computations is the result of the offshore forecast—tsunami parameters along the perimeter of the inundation computation area. The forecast inundation models (Stand-by Inundation Model—SIM) are optimized in order to obtain local forecasts in real time. Three levels of telescoping grids with increasing spatial resolution (down to 30 m for the finest grid) are employed to model local tsunami dynamics and inundation onto dry land. Each SIM is implemented and optimized for speed and accuracy, and validated thoroughly with historical tsunamis (TANG et al., 2008). To date, over 30 SIMs have already been developed and are now available for forecasting.

The SIM for Hilo, Hawaii was used in this study to compare how differences between the two deep-water propagation forecasts manifest themselves at the tide gauge in Hilo harbor. Figure 3 shows that the small differences between the two scenarios observed in deep water have become even smaller for the tide gauge predictions. This, plus the good comparison with the observed gauge data, indicates that the nearshore dynamics of a tsunami may be only sensitive to the amplitude and period of the first few waves and is mostly driven by the local geometry of the harbor around the gauge. This is good news for database-driven forecast systems, since it suggests that uncertainties in the model tsunami source definition may not be crucial for accurate coastal forecasts, provided that the amplitude and period of the approaching tsunami are captured correctly. More comparisons at different coastal locations relative to the source may show alternate differences between the methods. While this test at an individual location cannot be conclusive, the results are encouraging, showing, at least, that small differences offshore, result in small (or even smaller) differences at the coast.

3.2. Sumatra 2007

On September 12, 2007 at 11:10:26 (UTC) an earthquake occurred off southern Sumatra. This event had some significant impacts with 25 fatalities and numerous people injured. PTWC's initial Tsunami Bulletin had the magnitude of the earthquake set at M_w
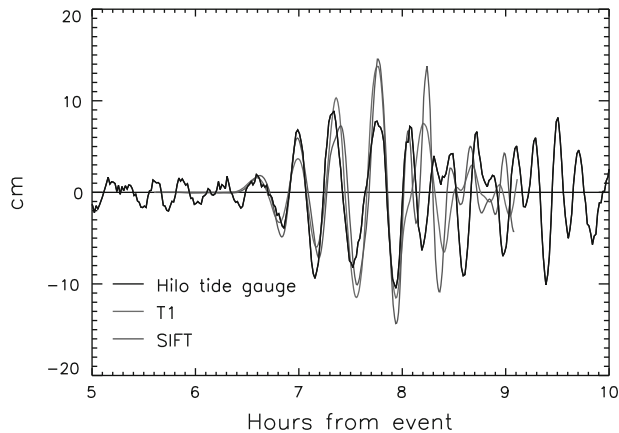
Figure 3

Time series of surface elevation at the Hilo tide gauge and from the inundation model fed by the two scenario databases.

7.9. This was subsequently raised to M_w 8.2 for the second and all subsequent bulletins. USGS has analyzed the event to be M_w 8.4 at (101.374°E, 4.520°S) and depth 55 km. The event was recorded at DART buoy 23401, to the west-northwest of Phuket at (88.54°E, 8.9°N) (see Fig. 4). A tsunami wave of 2 cm amplitude was observed by the instrument.

For the T1 database, the closest scenario to the event is the M_w 8.4 scenario with epicenter located at (100.53°E, 4.9°S). The distribution of H_{max} from T1 is shown in Figure 4. Data recorded by the DART and transmitted in real time were used to constrain the SIFT propagation forecast for the associated tsunami via a process of selecting the combination of unit sources that provided the best fit to the observed signal at the DART. The DART-inverted source used three database segments with scaling factors of 8.7, 5.6 and 3.9 on the three unit fault segments which correspond to an M_w 8.3 model tsunami source (Fig. 4).

The time series of surface elevation from the two databases at the location of the DART is shown in Figure 5. Both systems capture the arrival time of the tsunami at the DART very well. The SIFT database marginally overestimates the first peak, while the T1 forecast of the peak is too broad. SIFT also captures the first trough very well, while the T1 forecast misses it. Both systems miss the second peak but fit the third peak quite well, with T1 being slightly closer in amplitude.

At the time of the tsunami, the SIFT database for the Indian Ocean had not been completed and only the two shallowest rows of unit sources had been precomputed. This event might therefore be better described with additional deeper fault segments. Despite this potential limitation, the comparison of the modelled SIFT time series with observations at the DART shows a fairly good fit.

Figure 4

Maximum computed offshore amplitudes for the September 12, 2007 Sumatra tsunami from T1 (left panel) and SIFT (right panel).
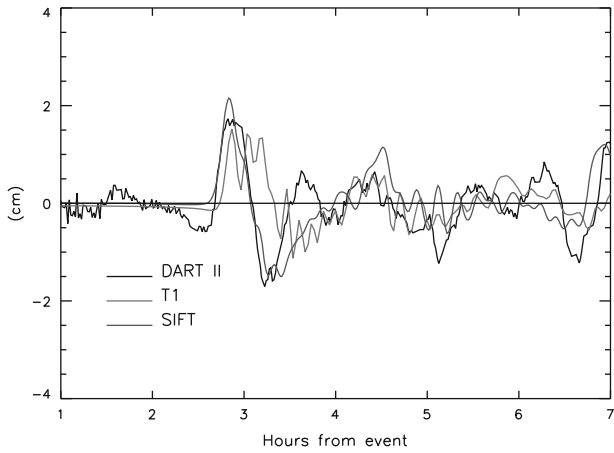
Figure 5

Time series of sea level elevation from scenario forecasts for the Sumatra event compared to the DART.

4. Discussion

The two forecast systems considered in this study employ a similar modelling strategy that is based on a precomputed database of propagation runs. Use of the same model and a similar database structure allows for potential interconnection between the two databases in many differen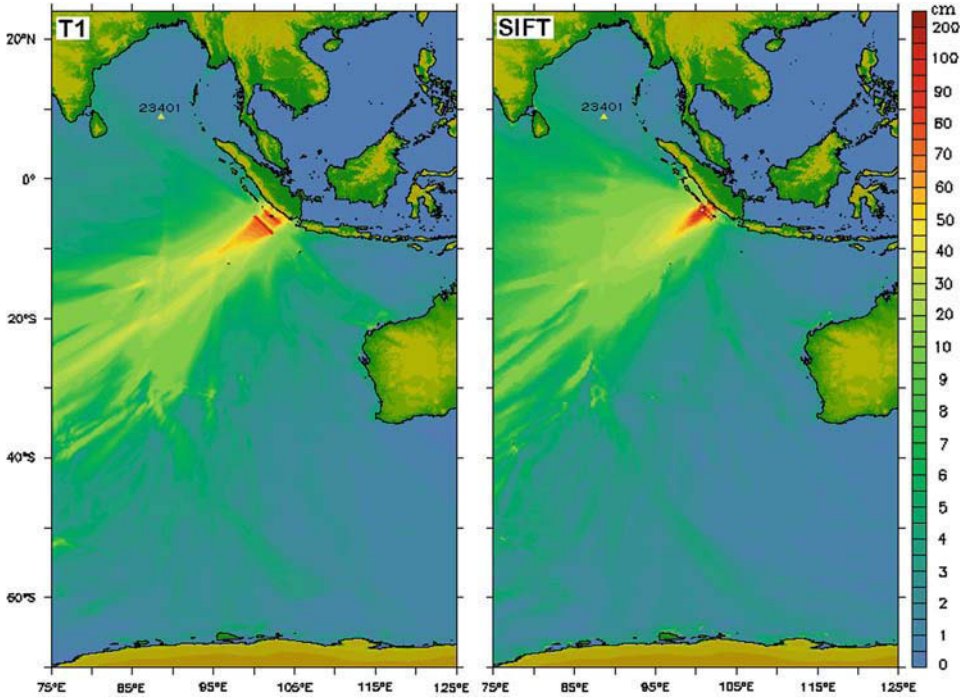t ways. Each system can potentially use the other system's scenarios for an event assessment to complement, double-check or extend forecasts to larger or different regions.

This comparison study is the first attempt to investigate potential similarities, differences, benefits and limitations of two forecast systems.

The obvious advantage of the T1 approach is the simplicity and speed of use, which may lead to fast and robust forecast procedures. The individual precomputed scenarios can be linked to precomputed warning structures which can then be rapidly disseminated (ALLEN and GREENSLADE, 2008). In fact, once the magnitude of the earthquake is known, the relevant warnings can be produced almost instantaneously. Considering that the T1 forecasts are "blind runs" and completely independent of the tsunameter data, the system compares very well to the observations. The SIFT method assimilates real-time tsunami measurements into the forecast, in addition to seismic estimates. The method comes with the price of a complex data inversion process and multi-step forecast procedure. While the seismic-based forecast can be obtained as soon as the magnitude is known, the final SIFT forecast is based on real-time tsunami measurements and can be done only after receiving data from tsunameters. The SIFT method is more flexible, can potentially reproduce complex tsunami sources and provide high accuracy. It also includes high-resolution coastal forecasts to reproduce coastal dynamics.

The different implementations of the model tsunami sources lead to differences in the forecast results. However, the differences in the offshore forecasts are surprisingly small, at least where validation observations were available. The test comparison of the coastal forecast at one location (Hilo) showed even smaller differences for the Tonga event. These results are encouraging, since they demonstrate consistency in the forecast results. This is important for establishing a common ground for warning procedures for this inherently international phenomenon that requires an international response.

Acknowledgements

REFERENCES

ALLEN, S.C.R. and GREENSLADE, D.J.M. (2008), *Developing Tsunami warnings from numerical model output*, Nat. Hazards, doi:10.1007/s11069-007-9180-8.

BIRD, P. (2003), *An updated digital model of plate boundaries*, Geochem. Geophys. Geosys. *4*(3), 1027, doi:10.1029/2001GC000252.

GICA, E., SPILLANE, M.C., TITOV, V.V., CHAMBERLIN, C.D., and NEWMAN, J.C. (2008), *Development of the forecast propagation database for NOAA's Short-Term Inundation Forecast for Tsunamis (SIFT)*, NOAA Tech. Memo. OAR PMEL-139, 89 pp.

GREENSLADE, D.J.M, SIMANJUNTAK, M.A., CHITTLEBOROUGH, J., and BURBIDGE, D. (2007), *A first-generation real-time tsunami forecasting system for the Australian region*, BMRC Research Report No. 126, Bur. Met., Australia.

KIRBY, S., GEIST, E.L., LEE, W.H.K., SCHOLL, D., and BLAKELY, R. (2006), *Tsunami source characterization for western Pacific subduction zones: A preliminary report*, Tsunami Sources Workshop, 2006, http://walrus.wr.usgs.gov/tsunami/workshop/.

MANSBRIDGE, J., *Bathymetry comparisons*, unpublished document, CSIRO.

SIMANJUNTAK, M.A. and GREENSLADE, D.J.M. (2008), *Towards a scaling method for a tsunami scenario database: The effect of wave dispersion*, EGU General Assembly 2008, Vienna, Austria.

SMITH, W.H.F. and SANDWELL, D.T. (1994), *Bathymetric prediction from dense satellite altimetry and sparse shipboard bathymetry*, J. Geophys. Res. *99*, 21,803–21,824.

TANG, L., TITOV, V.V., WEI, Y., MOFJELD, H.O., SPILLANE, M., ARCAS, D., CHAMBERLIN, C., BERNARD, E.N., GICA, E., and NEWMAN, J. (2008), *Tsunami Forecast Analysis for the May 2006 Tonga Tsunami*, J. Geophys. Res., accepted.

TITOV, V.V., MOFJELD, H.O., GONZALEZ, F.I., and NEWMAN, J.C. (1999), *Offshore forecasting of Alaska-Aleutian Subduction Zone tsunamis in Hawaii*, NOAA Technical Memorandum ERL PMEL-114, 22 pp.

TITOV, V.V., GONZÁLEZ, F.I., BERNARD, E.N., EBLE, M.C., MOFJELD, H.O., NEWMAN, J.C., and VENTURATO, A.J. (2005), *Real-time tsunami forecasting: Challenges and solutions*, Nat. Hazards *35*(1), 41–58.

TITOV, V.V. and SYNOLAKIS, C.E. (1998), *Numerical Modeling of Tidal Wave Runup*, J. Waterw. Port Coast. Ocean Eng. *124*(4), 157–171.

To access this journal online:
www.birkhauser.ch/pageoph

The Effect of the Great Barrier Reef on the Propagation of the 2007 Solomon Islands Tsunami Recorded in Northeastern Australia

Toshitaka Baba,[1,2] Richard Mleczko,[2] David Burbidge,[2] Phil R. Cummins,[2]
and Hong Kie Thio[3]

Abstract—The effect of offshore coral reefs on the impact from a tsunami remains controversial. For example, field surveys after the 2004 Indian Ocean tsunami indicate that the energy of the tsunami was reduced by natural coral reef barriers in Sri Lanka, but there was no indication that coral reefs off Banda Aceh, Indonesia had any effect on the tsunami. In this paper, we investigate whether the Great Barrier Reef (GBR) offshore Queensland, Australia, may have weakened the tsunami impact from the 2007 Solomon Islands earthquake. The fault slip distribution of the 2007 Solomon Islands earthquake was firstly obtained by teleseismic inversion. The tsunami was then propagated to shallow water just offshore the coast by solving the linear shallow water equations using a staggered grid finite-difference method. We used a relatively high resolution (approximately 250 m) bathymetric grid for the region just off the coast containing the reef. The tsunami waveforms recorded at tide gauge stations along the Australian coast were then compared to the results from the tsunami simulation when using both the realistic 250 m resolution bathymetry and with two grids having fictitious bathymetry: One in which the the GBR has been replaced by a smooth interpolation from depths outside the GBR to the coast (the "No GBR" grid), and one in which the GBR has been replaced by a flat plane at a depth equal to the mean water depth of the GBR (the "Average GBR" grid). From the comparison between the synthetic waveforms both with and without the Great Barrier Reef, we found that the Great Barrier Reef significantly weakened the tsunami impact. According to our model, the coral reefs delayed the tsunami arrival time by 5–10 minutes, decreased the amplitude of the first tsunami pulse to half or less, and lengthened the period of the tsunami.

Key words: Tsunami, the Great Barrier Reef, the 2007 Solomon Islands earthquake.

1. Introduction

The coral reefs offshore Sri Lanka reportedly reduced the impact of the 2004 Indian Ocean tsunami (Fernando *et al.*, 2005). Where there were gaps in the reef the tsunami was able to inundate up to 1.5 km inland. Yet, a few kilometers away where coral reefs

---

[1] Department of Oceanfloor Network System Development for Earthquakes and Tsunamis, Japan Agency for Marine - Earth Science and Technology, 2–15 Natsushima - cho, Yokosuka-city, Kanazawa 2370061, Japan. E-mail: babat@jamstec.go.jp
[2] Geoscience Australia, GPO Box 378, Canberra ACT 2601, Australia.
[3] URS Group Inc., 556 El Dorado Street, Pasadena, California 91101, U.S.A.

did not have gaps, the wave only travelled 50 m inland. A numerical study indicated that the healthy reefs off the coast produced at least twice as much protection as dead reefs by using an idealized model of tsunami impact on a reef-bounded shoreline (KUNKEL *et al.*, 2006). By contrast, in Banda Aceh, Indonesia, the presence or absence and condition of coral reefs made no difference in the impact of the giant Indian Ocean tsunami that penetrated kilometers inland (ADGER *et al.*, 2005; BAIRD *et al.*, 2005). To our knowledge, there has been no quantitative comparison between observed and calculated wave runup heights or inundation distance due to the presence or absence of reefs for this region. This is probably due to lack of publicly available, accurate bathymetric data which is essential for accurate numerical simulation of a tsunami. Accordingly, more work is needed to confidently conclude that coral reefs can mitigate tsunami damage along the coast.

A great earthquake occurred on 1 April, 2007 at the southern New Britain-San Cristobal trench off the Solomon Islands (the 2007 Solomon Islands earthquake). This earthquake ruptured the plate boundary of the Pacific plate with, respectively, the Australia, Woodlark, and the Solomon Sea plates. The magnitude of the earthquake was estimated to be 8.1 by the U.S. Geological Survey (USGS). Because it was a large submarine earthquake, it generated a large tsunami which left 52 people dead and more than 7,000 people homeless in the Solomon Islands. The tsunami also propagated into the Coral Sea and reached the Australian coast over the Great Barrier Reef (GBR), the world's largest coral reef system. The Great Barrier Reef was approximately 1,500 km from the source of the tsunami. Clear (but small) tsunami waveforms were recorded by tide gauges in northeastern Australia at communities behind the Great Barrier Reef. Geoscience Australia's 250 m gridded bathymetric dataset (GA250, see Fig. 1) was fortunately available to calculate the tsunami from this event. This dataset was compiled from 20 years accumulation of bathymetric survey data acquired by various organisations in the waters offshore Australia.. We believe that the data density is generally sufficient to represent the configuration of the coral reefs in the numerical simulation reasonably well, although there are noticeable gaps in parts of the data coverage. The tsunami observation and bathymetric dataset, therefore, provided a good opportunity to model the effect of the GBR on tsunami propagation.

We investigate the 2007 Solomon Islands tsunami in this paper. Since the tsunami was caused by the sea-floor deformation due to an underwater earthquake, initially an earthquake rupture model is required. We calculate this by inverting the teleseismic waves observed worldwide from this event. This is then used to calculate the initial sea-floor deformation based on a linear elastic dislocation model. Propagation of the 2007 Solomon Islands tsunami is modelled by solving the linear shallow water equations using the GA250 bathymetry dataset for the region near the coast. Furthermore, two tsunami simulations are performed in which the GBR in GA250 is replaced with fictitious bathymetry for purposes of comparison. We focus here on the bathymetric effects of the GBR on the tsunami propagation rather than other potential effects on the wave such as its sensitivity to the earthquake rupture model.
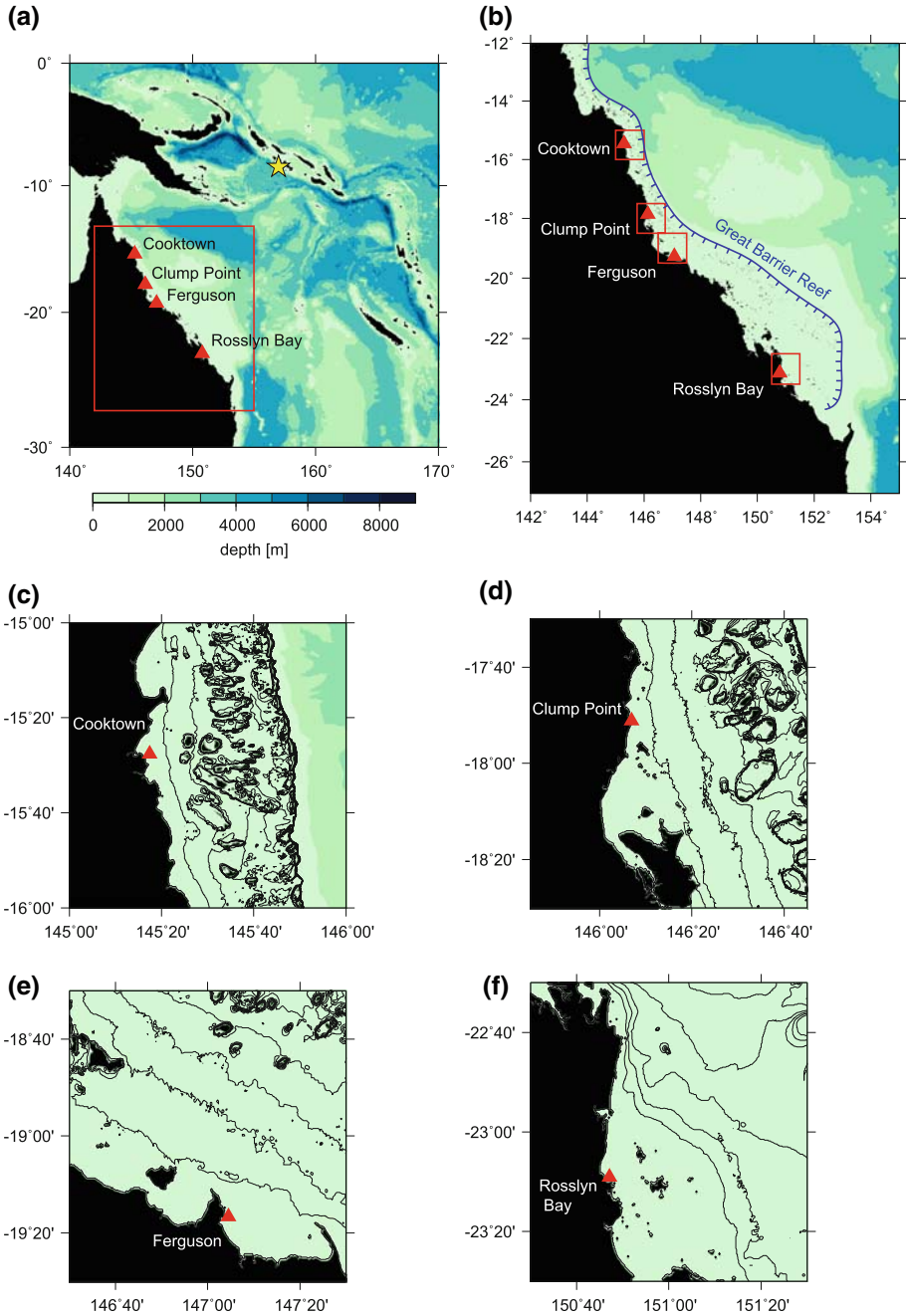
Figure 1

Bathymetric maps for: (a) the entire computational domain (90" grid spacing, a combination of the GA250 and DBDB2 bathymetry grids)), (b) GBR area (30" grid spacing) and (c-f) areas near tide gauges (10" grid spacing), both based on the GA250 bathymetry grid. Red squares show the areas of finer bathymetry used in the tsunami computation. Star and triangles indicate the epicenter of the 2007 Solomon Islands earthquake and tide gauges, respectively.

2. *Initial Sea-Surface Deformation of the 2007 Solomon Islands Tsunami*

To estimate the rupture model of the 2007 Solomon Islands earthquake, we applied the multiple time window method described in THIO *et al.* (2004). GSN (Global Seismological Network) data were downloaded from the IRIS DMC (http://www.iris.washington.edu/). We selected 19 teleseismic P and 17 SH waveforms based on the quality of the data and the station distribution (Fig. 2a). The waveforms were then converted to displacement and bandpass-filtered between 4 mHz and 4 Hz. The first 100 seconds after the arrival times of P and S waves were included in the inversion. Rayleigh and Love waves recorded at 21 sites were also used in order to stabilize the inversion. These surface waves were bandpassed-filtered between 3 mHz and 6 mHz.

The strike of the fault plane used in the inversion was adjusted from the approximately 330° azimuth obtained in the Global (formerly Harvard) CMT inversion to 307°, so as to better match the strike of the trench as expressed by water depth contours in this area. We experimented with a range of fault-dip angles between 10° and 50° and found that a dip angle of 35° produces the smallest misfit between the observed and synthetic SH waves (Fig. 3). This dip angle was consistent with the fault mechanism of this event obtained by the Global CMT Project and with the subduction angle of the plate shown by marine seismic surveys of this area (MIURA *et al.*, 2004; YONESHIMA *et al.*, 2005). The rake angle was determined from the inversion but was constrained to be 90° ± 45°. The total maximum dimensions of the fault plane were assumed to be 300 km × 100 km. This was divided into 20 km × 20 km subfaults and the slip and rake was determined for each subfault. The hypocenter location determined by the USGS was used as the rupture starting point, that is latitude −8.481°, longitude 156.978°, and depth 10.0 km.

Figure 2b shows the cumulative slip distribution of the 2007 Solomon Islands earthquake obtained by the seismic inversion. The earthquake rupture propagated unilaterally along the strike direction to the northwest. The dimension of the area of significant fault slip was about 180 km × 80 km. There was a large slip patch about 140 km to the northwest of the hypocenter and a moderate slip patch near the hypocenter. The maximum amount of slip was estimated to be about 5.2 m. The estimated moment magnitude was 8.1, consistent with the NEIC and the Global CMT solutions. The variance reduction (VR) of the seismic waveforms (determined by $1 - \Sigma(d_{obs} - d_{cal})^2 / \Sigma d_{obs}^2$) was 66%, where d_{obs} and d_{cal} indicate normalized observed and calculated waveforms, respectively. Figure 4 shows the calculated and observed seismic waves used in the inversion.

The vertical deformation at the seafloor was calculated using the equations of OKADA (1992) for a dislocation in an elastic half-space, and the seafloor deformation we obtained is shown in Figure 2c. A Poisson's ratio of 0.25 was used in the calculation. Most of the area over the earthquake source region was uplifted and all the area of significant uplift (over 1 m of uplift) was beneath the sea. Thus this event would be very effective in generating a tsunami. The maximum amount of uplift was about 2.1 m. We assumed that the seafloor deformation was the same as the initial wave height of the tsunami.

(a)

(b)

(c)
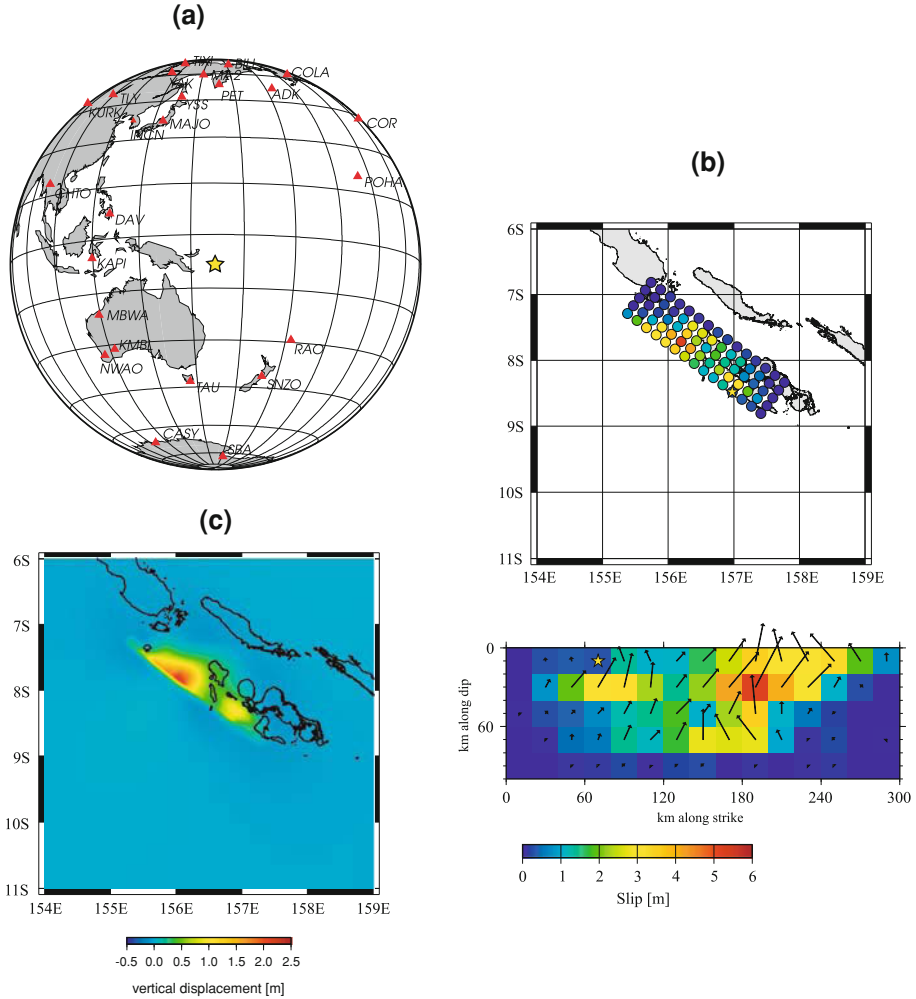
Figure 2

(a) Seismic station distribution (triangles) used in the inversion. Star shows the epicenter of the 2007 Solomon Islands earthquake. (b) Cumulative slip distribution on the fault plane during the event. The color shows the slip amount and arrows represent the motion of the hanging wall relative to the footwall. The star shows the rupture starting point (hypocenter). (c) Coseismic seafloor vertical displacements derived from the obtained slip distribution.

3. Numerical Simulation of the 2007 Solomon Islands Tsunami

The 2007 Solomon Islands tsunami, after passing over the GBR, was observed by the network of storm tide gauges operated by the Environment Protection Agency of Queensland, Australia. The storm tide network was adjusted so as to record changes in water-levels each minute immediately after the earthquake. Normally, these gauges record water-level changes every 10 minutes, however, this sampling period would not

Figure 3
(a) Variance reductions as a function of fault-dip angle calculated for observed vs. synthetic P, S, surface wave, and a combination of all of these. The curves are deviations from the value obtained from assuming a dip angle of 15 degrees. A clear peak was found around a dip angle of 35 degrees by the S-wave curve. (b) Variance reductions as a function of dip for S-waves recorded at TLY, MAJ, INC and KUR (see Fig. 2a).

Figure 4
Comparison between the calculated (black) and observed teleseismic waveforms (red) of the 2007 Solomon Islands earthquake. Station names and components (P: vertical component P wave, S: SH wave, R: Rayleigh wave, L: Love wave) are shown. Zero level of the calculated body waves was shifted downward for ease of comparison.

have provided sufficient resolution to accurately detect the tsunami event. They provided 21 tsunami waveforms recorded by the network in a report (ENVIRONMENT PROTECTION AGENCY, 2007). While most tide gauges recorded a tsunami wave height in crest to trough of less than 0.3 m, the gauges at Clump Point and Rosslyn Bay both recorded a wave of about 0.5 m crest to trough. We used the data recorded at the 4 stations shown in Figure 1, based on quality and station distribution.

In the present study, the propagation of the 2007 Solomon Islands tsunami was modelled by solving the equations of linear shallow-water wave theory. We used the method of ICHINOSE *et al*. (2007) which was modified from the uniform finite-difference scheme described in SATAKE (2002) to include a variable nested grid scheme. Three grids were used in the tsunami computation. The coarsest grid was used to represent the entire computational domain, including the tsunami source and the tide gauge stations, stretching from 140°E to 170°E and 30°S to 0°S (Fig. 1a). The bathymetry used for this grid was defined using a combination of GA250 in that part of the computational domain that it covers, i.e., south of 10°S and west of 155°E, and the global bathymetry grid DBDB2 for the rest of the domain. DBDB2 is a global 2 arc-minute bathymetry grid assembled by the U.S. Naval Research Laboratory (www7320.nrlssc.navy. mil/DBDB2_WWW). These bathymetry grids were subsampled and interpolated, respectively, to 90 arc-sec spacing. Nested within this coarse grid is a medium-resolution grid of 30 arc-second spacing defined over the area indicated in Figure 1b by subsampling GA250. Finally, nested within the medium-resolution grid is a series of high-resolution grids covering the areas near the tide gauges indicated in Figures 1c–1f, whose 10 arc-second spacing is almost equal with the original grid spacing of GA250 (250 m). It is important to note that points of the high-resolution grid near the Australian coast that had a water depth less than 10 m were reset to be exactly 10 m deep (i.e., no point had a depth between 0 and 10 m). This helped to ensure the stability and validity of our numerical model, which uses the linear shallow water wave equations to calculate the tsunami waveforms. The linear shallow water equations assume that the wave amplitude is much smaller than the water depth, which may not be true in shallow waters (less than 10 m). The rise time of the initial wave height was assumed to be 60 seconds, based on the source duration of the 2007 Solomon Islands earthquake. The time step used in the computation was 0.5 seconds in order to satisfy the stability condition of the finite-difference calculation in the finest grid.

Figure 5 shows comparisons between the observed and the computed tsunami waveforms derived from the teleseismic source model of the 2007 Solomon Islands earthquake. In the previous report by the Environment Protection Agency (2007), the numerical simulation of the Solomon Islands tsunami did not match the observations well. Arrival times of the tsunami wave were noticeably later by about 30 minutes than those they had predicted. Our model indicated misfits of arrival time less than 5 minutes at Cooktown, Clump Point and Ferguson and about 10 minutes at Rosslyn Bay. This improvement was a consequence of the use of good bathymetric data near the coastline and the GBR. However, the computed wave heights were still slightly smaller than the observations.
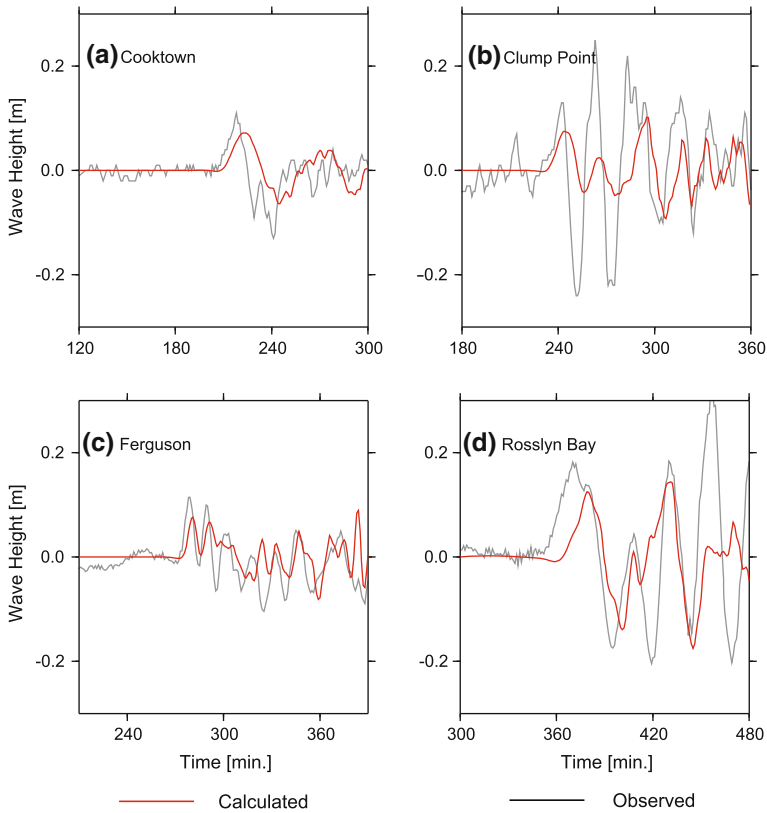
Figure 5

Comparison between the calculated and observed tsunami waveforms at tide gauges along the coast of northeastern Australia (tide gauge locations are illustrated in Fig. 1). Black and red waveforms indicate observed and calculated tsunami waveforms, respectively.

Cooktown was a suitable site to investigate the effect of the local GBR on the tsunami propagation because our model provided a better match to the observed tsunami wave (Fig. 5a) and there were coral reefs near the coast (Fig. 1c). Fictitious bathymetry near the gauge excluding the GBR in the innermost grid (10 arc seconds) was created for the purpose of comparison. We deleted the bathymetric data points within the area of the GBR from the original dataset and replaced them with bathymetry that was smoothly interpolated across the resulting gap. The resulting "No GBR" bathymetry of the innermost grid is shown in Figure 6b. We then conducted a tsunami calculation by using this bathymetry and with the same method we applied above. Figure 6c indicates three tsunami waveforms for the point of Cooktown: The recorded wave and the two waves calculated using the original and "No GBR" bathymetry grids. We furthermore plotted computed waveforms at imaginary tide gauge sites along the coastline numbered from 1 to 7 just to the north and south of Cooktown
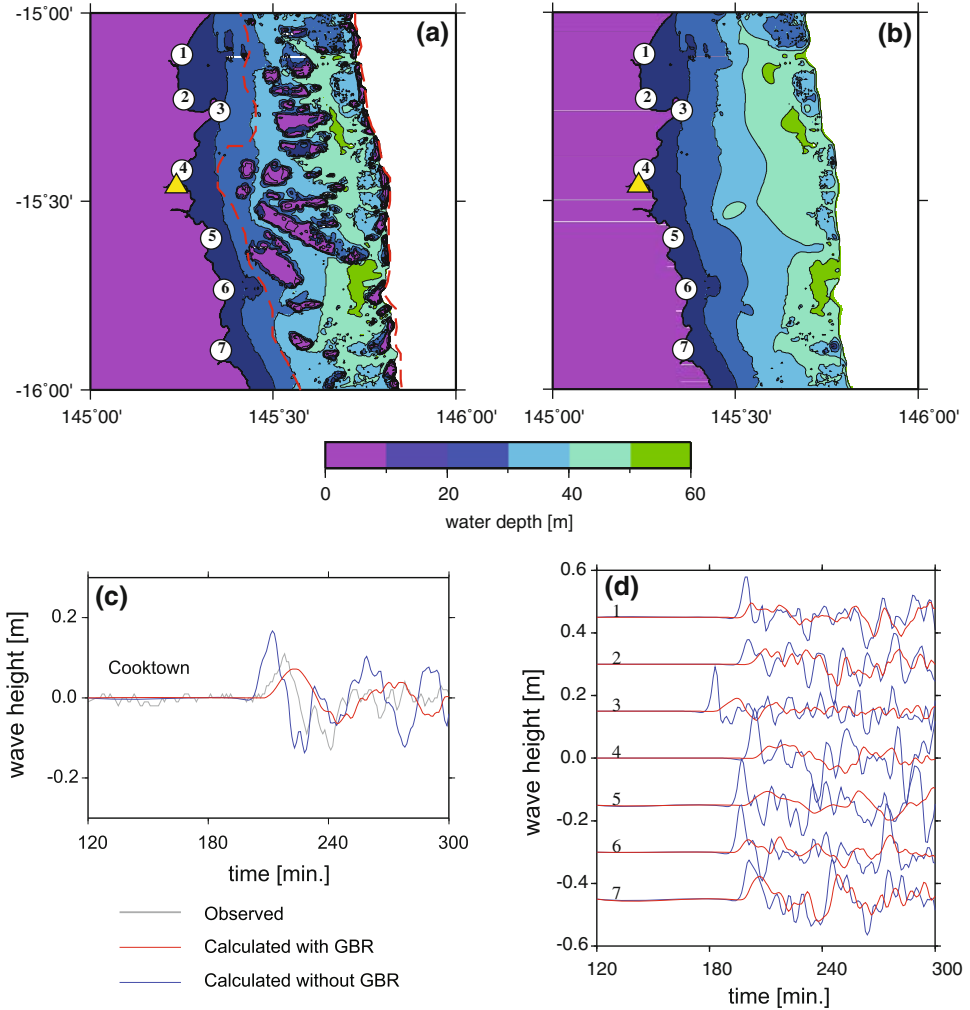
Figure 6

(a) Actual bathymetry. Triangle shows location of Cooktown tide gauge. The dashed red line indicates the boundaries of the polygon used to calculate the "Average GBR" bathymetry model (b) The "No GBR" bathymetry model, where an irregular region of high relief was removed from the grid in (a) and smoothly interpolated across. (c) Comparison of tsunami waveforms at Cooktown. Black waveform is the observed one. (d) Calculated tsunami waveforms at imaginary tide gauges from 1 to 7 shown in (a) and (b). Red and blue ones are derived from the simulations with the actual bathymetry (a) and the "No GBR" bathymetry (b), respectively.

(Fig. 6d). For the "No GBR" bathymetry grid the tsunami arrived 5 to 10 minutes earlier, and the amplitude was larger by a factor of two or more than the wave produced by the model which did include the GBR. It is also worth mentioning that the period of the tsunami computed with the dataset that excluded the GBR was shorter than for the wave obtained using the actual bathymetry.
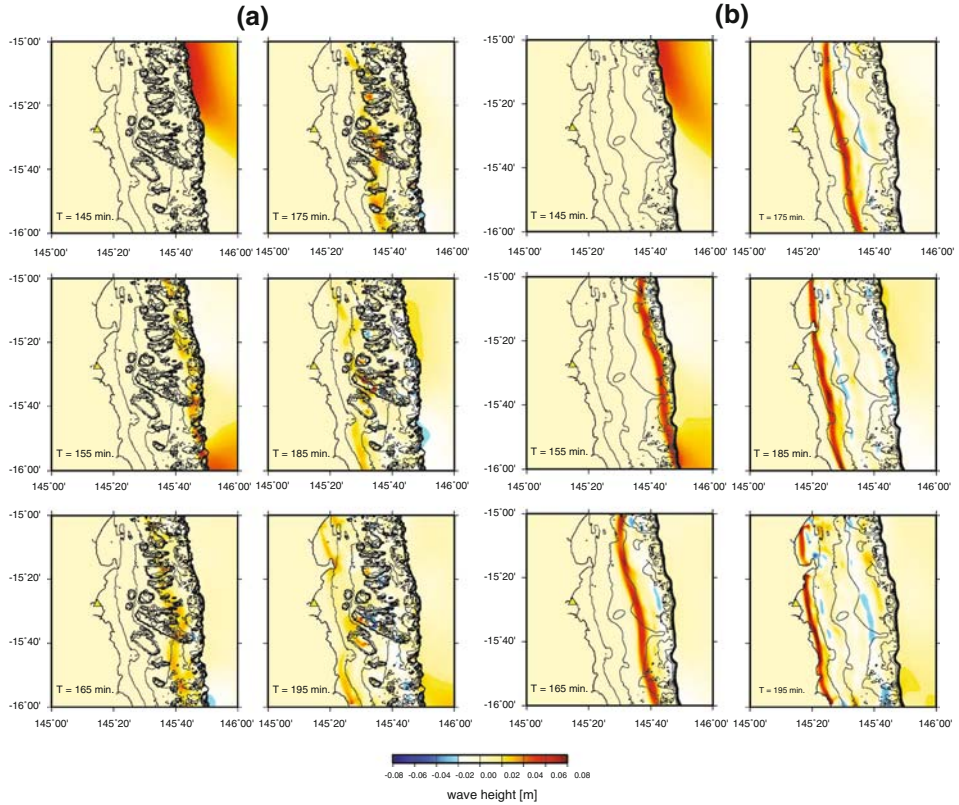
Figure 7
Snapshots showing the tsunami generated by the 2007 Solomon Islands earthquake approaching the northeast Australian coast. (a) and (b) were modelled with the actual and "No GBR" bathymetric grids, respectively. Color shows the wave height following the color scale bar. The contours were drawn for the bathymetry with an interval of 10 m within a range of 10 to 100 m depths.

Figure 7 shows the simulated tsunami approaching Cooktown in time sequences taken every 10 minutes. The tsunami wave amplitude is shown by the color scale at the bottom of the figure (red for above initial sea level and blue for below initial sea level). The contours indicate the bathymetry and have a spacing of 10 m. The depth contours deeper than 100 m unrelated to the GBR were not shown, to avoid complicating the figure. The water depth rapidly deepens outside the contoured area. The tsunami arrived at the coral reef region about 145 minutes after the earthquake's origin time. At 155 min, the tsunami's wavelength shrank substantially and its amplitude increased rapidly as the tsunami traversed the transition from the deep ocean to shallow water. This is a well-known bathymetric effect on tsunami propagation called 'shoaling'. The shoaling effect is not as clear in the model with the realistic bathymetry (Fig. 7a) as it is in the one without the GBR (Fig. 7b) due to the frontal

reefs protecting the GBR region from the tsunami impact. However, some tsunami energy was able to pass through the frontal reefs, beyond which it was largely disrupted by the reefs lying in the middle section of the reef. By contrast, the tsunami arrived smoothly right along the coast in the simulation which used the No GBR bathymetry grid (Fig. 7b).

Figure 8 shows the tsunami waveforms for four locations along the coast (Cooktown, Clump Point, Ferguson and Rosslyn Bay) where the GBR was removed from all the grids (waveforms labelled "No GBR"), and also where it was replaced by a constant water depth equal to the average depth in the GBR (waveforms labelled "Average GBR"). Instead of interpolating the bathymetry across the GBR as was done for the "No GBR" grid, the grid produced for the "Average GBR" run forced the water depth within a polygon containing the GBR to be equal to the average water depth in the polygon. The polygon taken as representative of the GBR was in of 96,000 square km area with an average width of 57 km. The average water depth within this polygon was 41 m with a standard deviation of 24 m. Figure 6a shows the polygon boundary near Cooktown. Also shown are the tide gauge observations ("OBS") and the model which contained the GBR in all grids ("GBR") in Figure 8.

Figure 8 shows that completely removing the GBR results in larger amplitude waves at all the points near the coast. The arrival time of the first wave was also consistently earlier than the arrival time in the model with the GBR. The waves at Cooktown and Clump Point also contained a signal with a much higher frequency than the model with the GBR. Therefore the presence of the GBR appears to have suppressed the higher frequency components of the incoming wave at these locations.

In the computations that used the "Average GBR" bathymetry grid, the amplitudes at the Clump Point and Cape Ferguson points were quite similar to the amplitudes in the model containing the GBR. However the amplitude was considerably larger at the Rosslyn Bay point in the model with the GBR than it was in the model with the average water depth. This suggests the gaps in the reef may have focussed the wave at that location. Arrival times were similar in both the "Average GBR" and "GBR" models. Again, there was a larger high-frequency component in the Cooktown and Clump Point models in the "Average GBR" model than there was in the "GBR" model.

4. Discussion

4.1. Differences in Maximum Amplitude

There could be several reasons why we obtained a consistently smaller wave height in the "GBR" model than was observed on the gauges. One reason could be that the spatial resolution of the bathymetry data may be insufficient. We used the
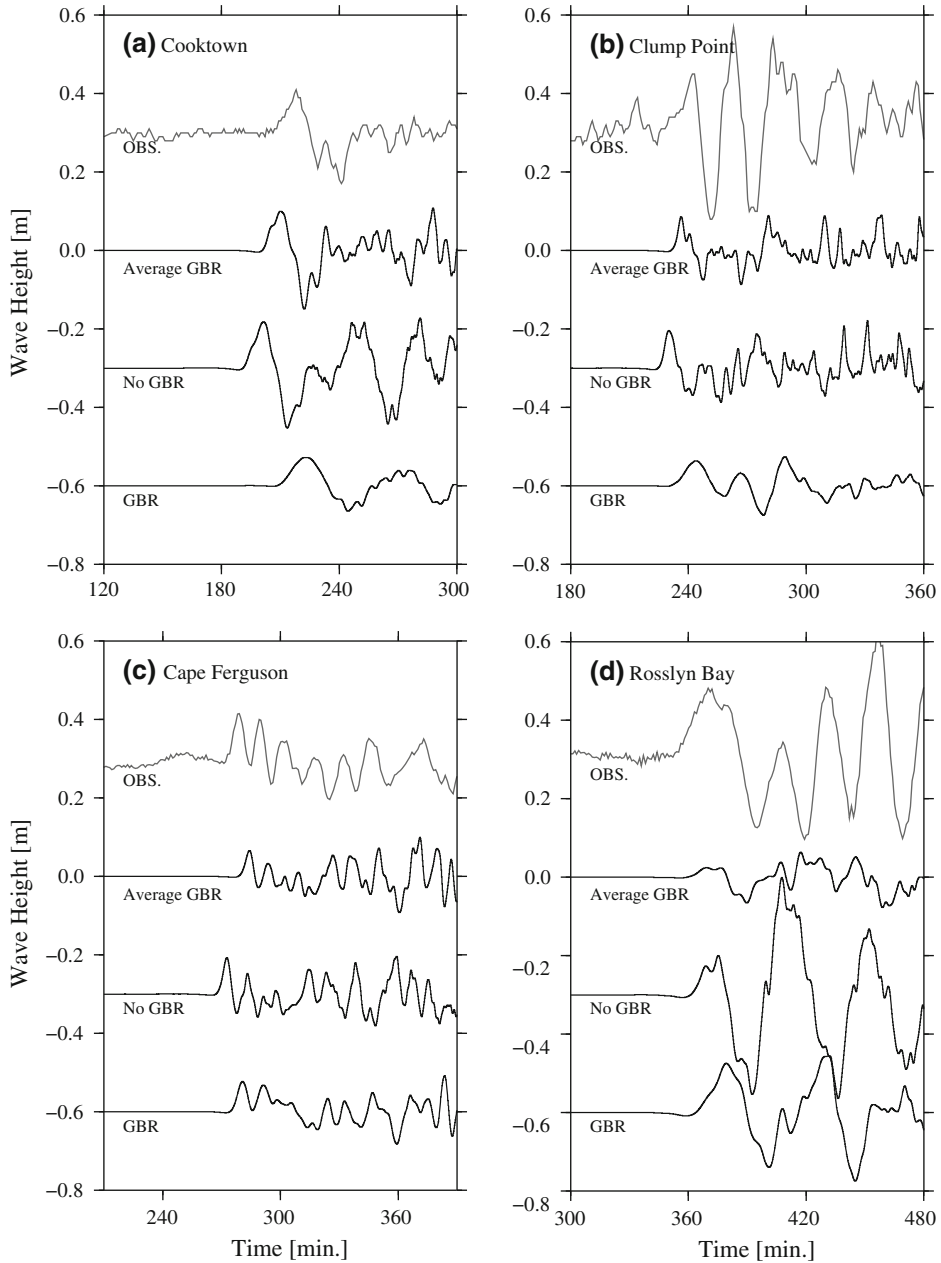
Figure 8
Observed and modelled tsunami waveforms for (a) Cooktown, (b) Clump Point, (c) Cape Ferguson and (d) Rosslyn Bay. The waveform labelled "OBS" is the observed wave at tide gauges at these locations. The waveform labelled "Average GBR" uses a fictitious bathymetry where the Great Barrier Reef was replaced by a flat plane at a depth equal to the average depth of water of the Reef. The "No GBR" waveform is the model result from a run with the Great Barrier Reef removed from the grid and the water depth in that area was interpolated across the gap. The "GBR" waveform derives from the model which uses our best possible bathymetric data for the Great Barrier Reef.

GA250 bathymetric grid, which is certainly the best bathymetric dataset for this part of Australia. We have previously modelled this tsunami with 2 arc-minute data using a variety of global bathymetry datasets, and the GA250 produced a significantly smaller misfit than all the others for Queensland tide gauges (BABA *et al.*, 2007). However, some previous tsunami studies have used a much finer bathymetric spacing around tide gauges than we have used in either study. For example, SÁNCHEZ *et al.* (2007) used a bathymetric grid at 3 seconds of arc resolution (about 90 m) of Oahu Island, Hawaii, for the highest resolution of nested grid system to compute far-field tsunamis. The Rosslyn Bay gauge was actually within a marina, thus to accurately model the tsunami to the gauge would require a bathymetric model with a spatial resolution that was small enough to resolve the marina. However, bathymetry with this level of resolution was not available at the time of this study.

A second reason which may cause the amplitude difference is errors in the rupture model. For example, if the slip was significantly over or underestimated then this could cause a change in the amplitude of the tsunami waveform. Similarly, if the actual slip was underneath dry land, instead of the open ocean, that could also cause a substantial change in the tsunami amplitude, even on the coast of Queensland. However, we believe that the teleseismic rupture model we obtained here should have been enough to simulate the tsunami, based on the results from a previous study of the 2006 Kuril Islands earthquake (BABA *et al.*, 2008).

Finally, the third and probably most important reason for the difference in amplitude was that the minimum water depth in the models is 10 m, while the gauges are usually in water less than a few meters deep. Since the wave amplitude increases with decreasing water depth, this means that the wave amplitude at the model output point could be expected to be on average less than the observed wave amplitude at a gauge in shallower water. For example, according to Green's law, a wave could grow in amplitude by about 18% as it goes from 10 m to 5 m. This could account for much of the difference in amplitude seen in Figure 5. A higher resolution model centered on the gauge, would not only allow us to better model the details of the bathymetry but would also allow us to select a closer model output point to the gauge, and therefore select a point with a water depth considerably closer to the gauge's true depth. Similarly, changes in water depth due to the tide could also help reduce the misfit to observations (we assumed the water was at mean sea level in these computations).

4.2. *Effect of the GBR*

From the numerical results shown in Figures 6 and 7, we suggest two mechanisms for how the GBR weakened the tsunami impact. The first one is a barrier effect deduced from the image showing that the tsunami was attenuated by the front line of the reefs (T = 155 min. in Fig. 7a). The frontal reefs are relatively small, and run almost parallel to the coastline. Some parts of this frontal reef system appear to be above the sea level.

We believe that this reef barrier worked to reflect much of the tsunami energy from the 2007 Solomon Islands earthquake.

The second effect mitigating the tsunami impact was caused by the refraction of the tsunami wavefront as it moved through the reef. In linear shallow water theory, the tsunami speed is defined by the square root of the product of gravity and water depth. This means that the tsunami will slow down in shallow bathymetry of the reefs, but goes quickly through the gaps between the reefs, thus causing refraction of the tsunami wavefront (e.g. T = 175 min. in Fig. 7a). Even though the tsunami quickly propagated between the reefs, the path was curved by the reef configuration. This increases the distance the leading wave must travel to reach parts of the coast. Hence the arrival time of the tsunami is delayed. The fast tsunami wave that has travelled between the reefs was followed by the slower tsunami which went over the reefs. Consequently, the tsunami energy was split. The length and amplitude of the first tsunami wave became longer and smaller, respectively, in comparison with the wave which was unaffected by the GBR. We can certainly see this effect on the tsunami waveforms shown in Figures 6c and 6d.

Refracted and reflected tsunami waves due to the complicated bathymetry of the GBR occasionally constructively interfere, which would result in waves with a much higher amplitude in isolated areas. Such focusing of the tsunami could be seen in our simulation (e.g. T = 185 min. in Fig. 7a). However, in this particular bathymetric setting, the distance between the coast and the reef system was such that tide gauges were not at any of the focal points of the tsunami refracted by the GBR.

The contributions we discussed thus far are all related to the bathymetry of the GBR. In addition to the bathymetric effects, the bottom friction of the coral reefs may also influence the tsunami. Experimental and theoretical studies indicated that reefs have a strong bottom drag coefficient which is about an order of magnitude larger than that for sand (see, e.g. BAPTISTA *et al.*, 1989; KARINS *et al.*, 1998). Based on that, KUNKEL *et al.* (2006) performed a simple numerical simulation with idealized topography to experiment on the effect of bottom friction due to a reef on tsunami runup. The tsunami runup was decreased to roughly 50% by changing the bottom drag coefficient of an order of magnitude as the bathymetry remained constant. If their result is correct, the contribution of the GBR reducing the tsunami impact would be even more impressive. However, it should be noted that the 2007 Solomon Islands tsunami was overall fairly well modelled without the bottom friction in this study. Since it is likely to reduce the amplitude, rather than raise it, adding bottom friction to the model will tend to increase the misfit.

5. Conclusion

Through the tsunami simulation, we found two bathymetric mechanisms by which the GBR reduced the energy of the 2007 Solomon Islands tsunami. The first one was the effect of the reef barrier, which directly reflected the tsunami back to the deep ocean.

The second mechanism was due to the effect of refraction of the tsunami as it passed through the reef due to the wide range of water depths within the reef system. The reef delayed the arrival time and increased the period of the tsunami as well as decreasing the tsunami amplitude of the first wave. Although we may need further simulations using more realistic physics (e.g., including bottom friction and dispersion) before we can reach a definitive conclusion, we suggest that coral reefs should normally play the role of natural barriers to a tsunami approaching the coast.

However, this conclusion applies only to a tsunami whose wave height is small compared to the average depth of the coral reef. In the case considered here, the tsunami incident on the outer reef had a maximum wave height of 10 cm, much less than the typical depth to the top of the reef (Fig. 6). This height might be typical of a tsunami experienced along the eastern Australian coast due to large earthquakes in the Southwest Pacific. Nonetheless our conclusion that the coral reef acts as an effective barrier to tsunamis for this situation does not necessarily extend to that of a large local tsunami, whose height may exceed the average depth to the top of the reef. The latter case would involve considerably more extensive nonlinear hydrodynamic modelling, using very high-resolution bathymetry data, to understand the interaction of the tsunami with the coral reef.

Acknowledgments

REFERENCES

ADGER, W.N., HUGHES, T.P., FOLKE, C., CARPENTER, S.R., and ROCKSTROM, J. (2005), *Social-ecological resilience to coastal disasters*, Science *309*, 1036–1039.

BABA, T., CUMMINS, P.R., THIO, H.K., and TSUSHIMA, H. (2008), *Validation and joint inversion of teleseismic waveforms for earthquake source models using deep ocean bottom pressure records: A case study of the 2006 Kuril megathrust earthquake*, Pure Appl. Geophys. *this issue*.

BABA, T., MLECZKO, R., CUMMINS, P.R., THIO, H.K., and BURBIDGE, D. (2007), *Accurate tsunami modelling due to the 2007 Solomon earthquake by using the seismic rupture model and the GA-DBDB2 bathymetric dataset*, HYDRO2007 Proceedings, pp. 47–53.

BAIRD, A.H., CAMPBELL, S., ANGGORO, A., ARDIWIJAYA, R., FADLI, N., HERDIANA, Y., KARTAWIJAYA, T., MAHYIDDIN, D., MUKMININ, A., and PARDEDE, S. (2005), *Acehnese reefs in the wake of the Asian tsunami*, Curr. Biol. *15*, 1926–1930.

BAPTISTA, A.M., WESTERINK, J.J., and TURNER, P.J. (1989), *Tides in the English Channel and Southern North Sea. A Frequency-Domain Analysis Using Model TEA-NL.* Advances in Water Resources *12*, 166–183.

Environmental Protection Agency, Queensland Government (2007), Fact Sheet Solomon Islands tsunami, online at http://www.epa.qld.gov.au/publications/p02118aa.pdf/Solomon_Islands_tsunami.pdf.

FERNANDO, H.J.S., McCULLEY, J.S., MENDIS, S.G., and PERERA, K. (2005), *Coral poaching worsens tsunami destruction in Sri Lanka*, EOS Trans., AGU *86*, 301–304.

ICHINOSE, G., SOMERVILLE, P., THIO, H.K., GRAVES, R., and O'CONNELL, H. (2007), *Rupture process of the 1964 Prince William Sound, Alaska, earthquake from the combined inversion of seismic, tsunami and geodetic data*, J. Geophys. Res. *112*, doi:10.1029/2006JB004728.

KRAINES, S.B., YANAGI, T., ISOBE, M., and KOMIYAMA, H. (1998), *Wind-wave driven circulation on the coral reef at Bora Bay, Miyako Island*, Coral Reefs *17*, 133–143.

KUNKEL, C.M., HALLBERG, R.W., HALLBERG, W., and OPPENHEIMER, M. (2006), *Coral reefs reduce tsunami impact in model simulations*, Geophys. Res. Lett. *33*, L23612, doi:10.1029/2006GL027892.

MIURA, S., SUYEHIRO, K., SHINOHARA, M., TAKAHASHI, N., ARAKI, E., and TAIRA, A. (2004), *Seismological structure and implications of collision between the Ontong Java Plateau and Solomon Island Arc from ocean bottom seismometer-airgun data*, Tectonophysics *389*, 191–220.

OKADA, Y. (1992), *Internal deformation due to shear and tensile faults in a half space*, Bull. Seismol. Soc. Am. *82*, 1018–1040.

SÁNCHEZ, A. and CHEUNG, K.F. (2007), *Tsunami forecast using an adaptive inverse algorithm for the Peru-Chile source region*, Geophys. Res. Lett. *34*, L13605, doi:10.1029/2007GL030158.

SATAKE, K. *Tsunamis, in International Handbook of Earthquake and Engineering Seismology*, (eds. Lee, W.H.K., Kanamori, H., Jennings, P.C., and Kisslinger, C.) (Academic Press 2002) 81A, pp. 437–451.

THIO, H.K., GRAVES, R.W., SOMERVILLE, P.G., SATO, T., and ISHII, T. (2004), *A multiple time window rupture model for the 1999 Chi-Chi earthquake from a combined inversion of teleseismic, surface wave, strong motion and GPS data*, J. Geophys. Res. *109*, doi:10.1029/2002JB002381.

WESSEL, P., SMITH, W.H.F. (1998), New, improved version of generic mapping tools released, EOS Trans., AGU *79*, 579.

YONESHIMA, S., MOCHIZUKI, K., ARAKI, E., HINO, R., SHINOHARA, M., and SUYEHIRO, K. (2005), *Subduction of the Woodlark Basin at New Britain Trench, Solomon Islands region*, Tectonophysics *397*, 225–239.

To access this journal online:
www.birkhauser.ch/pageoph

Numerical Modeling and Observations of Tsunami Waves in Alberni Inlet and Barkley Sound, British Columbia

Isaac V. Fine,[1] Josef Y. Cherniawsky,[1] Alexander B. Rabinovich,[1,2]
Fred Stephenson[1]

Abstract—Alberni Inlet is a long and narrow fjord adjacent to Barkley Sound on the Pacific Coast of Vancouver Island, Canada. Port Alberni, at the head of the inlet, was affected in 1964 by the largest Pacific tsunami waves in Canadian history. We use observations and results from two numerical models to investigate the resonant characteristics of the region and amplification of tsunami waves in Barkley Sound and Alberni Inlet. The first model (A) was forced at its open boundary with a stationary autoregressive signal, similar to the observed background noise. The second model (B) used an initial sea-level deformation from a potential earthquake off California in the southern segment of the Cascadia Subduction Zone, producing transient tsunami waves. Spectral, cross-spectral and frequency-time (*f-t*) analyses of the observations were used to examine the resonant properties and topographic response of the local area. The respective results show large admittance functions over a wide 0.5–0.9 cph frequency band, implying a low Q factor but high amplification of arriving waves. This unusual behavior is a result of two effects: A quarter-wave resonance of the system for its fundamental Helmholtz mode and amplification due to the narrowing of the channel cross section from Barkley Sound to Alberni Inlet. The model A numerical results agree favorably with the observations, indicating an energetic resonant mode at frequency of ∼0.53 cph (112 min), with its nodal line located near the entrance to Barkley Sound and amplification factor value close to 12. The results from the tsunami propagation model (B) yield spectral characteristics similar to those from the model A and from the observations. The maximum tsunami current speed for this scenario is 2.4 ms^{-1} in Sproat Narrows, which divides Alberni Inlet into two parts, while the largest computed wave height is 1.6 m in the northern Alberni Inlet, in the area of Port Alberni.

Key words: Port Alberni, 1964 Alaska tsunami, tsunami modeling, tide gauge records, resonant oscillations, seiches, cross-spectral analysis.

1. Introduction

Alberni Inlet is a long (∼40 km) and narrow (1–2 km) fjord located on the west coast of Vancouver Island on the Pacific Coast of Canada (Fig. 1). This fjord is the longest on the island and is characterized by a deep (>250 m) southern part of the channel but

[1] Institute of Ocean Sciences, Fisheries and Oceans Canada, 9860 West Saanich Rd., Sidney, BC V8L 4B2, Canada. E-mail: Josef.Cherniawsky@dfo-mpo.gc.ca

[2] Russian Academy of Sciences, P.P. Shirshov Institute of Oceanology, 36 Nakhimovsky Prosp., Moscow 117997, Russia.
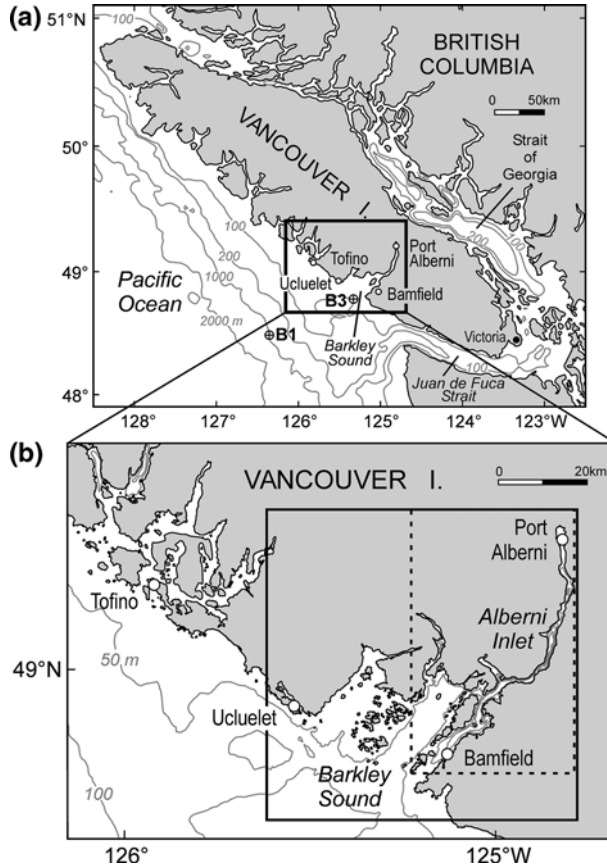
Figure 1

(a) Map of the area of Vancouver Island (British Columbia) shown with depth contours and locations of tide gauges in Tofino, Bamfield, Port Alberni and Victoria. The symbols ⊕ mark locations of sea-level timeseries at B1 (1000 m depth) and B3 (85 m). (b) Map of Barkley Sound and Alberni Inlet showing domains of the two numerical models: Model A (solid frame), which was used to examine characteristic wave properties of the Barkley Sound–Alberni Inlet system, and the innermost grid of model B (dashed frame), used for modeling tsunami waves.

relatively shallow (∼ 100 m) approaches in the relatively wide Barkley Sound located between the inlet and the continental shelf. On March 28, 1964, the town of Port Alberni, at the head of the inlet and about 65 km from the open Pacific Ocean, experienced the largest tsunami waves on the coast of Vancouver Island, generated by the 1964 ("Good Friday") Alaska Earthquake (M_w = 9.2). These waves caused wide-spread flooding and property damage estimated to be about 10 million (1964) dollars (WHITE, 1966; CLAGUE, 2001; CLAGUE et al., 2003; ANDERSON and GOW, 2004). However, alarms were sounded, people were rescued from flooded homes and there was no loss of life in Port Alberni. Notably, this Pacific-wide tsunami was responsible for close to 130 deaths and about 125

million dollars in damage in Alaska, Washington, California and Hawaii (Spaeth and Berkman, 1967; Lander, 1996; Stephenson *et al.*, 2007). This tsunami was recorded by twelve tide gauges on the Pacific Coast of Canada (cf. Wigen and White, 1964; Wigen, 1983; Stephenson *et al.*, 2007), including the tide gauges at Tofino, located northwest of Barkley Sound, at Port Alberni in Alberni Inlet, and at Victoria, inside Juan de Fuca Strait (Fig.1).

The 1964 tsunami was destructive at several locations on the coast of Vancouver Island (Clague *et al.,* 2003; Anderson and Gow, 2004; Stephenson *et al.,* 2007), with the highest wave in Canada occurring at Shields Bay, on the west coast of Graham Island (Queen Charlotte Islands), where a wave crest was reported to be 5.2 m above spring high water, or 9.8 m above tidal datum (Spaeth and Berkman, 1967; Stephenson *et al.,* 2007). However, most of the damage occurred in Port Alberni, where wave heights exceeded 8 m. The Port Alberni tide gauge was disabled temporarily and stopped working several times before the wave height maxima were reached (Fig. 2a), but according to witness reports, the second wave was the highest in the series, reaching 6.4 m above tidal datum, as was determined from water marks on buildings and harbor structures. This can be compared to a maximum wave height of 2.4 m in Tofino (Stephenson *et al.,* 2007). The resulting flooding and property damage in Port Alberni
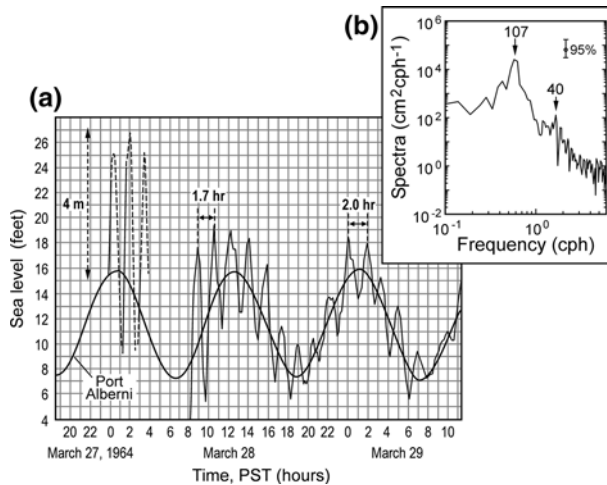
Figure 2

(a) A restored copy of Port Alberni tide gauge record of the Alaska tsunami of March 28, 1964 (from Wigen and White, 1964). Predicted tide is shown by a thick line. The tide gauge stopped working on March 28 after 04:00 PST, and resumed operation four hours later. The highest recorded sea level, about 4 m above high tide at 02:00 PST, was due to a second incoming tsunami wave, while the corresponding maximum (peak-to-through) wave height at Port Alberni was about 6 m, or larger, and occurred during the third, or a later wave. The exact count and the maximum wave height of the largest tsunami wave are uncertain because of the 4-hour data gap. Oscillations in Alberni Inlet persisted for at least 48 hours, with wave periods from 1.7 to 2 hours. (b) Computed spectrum of the tsunami record at Port Alberni shown in (a) for the time period between 08:00 28 March and 10:00 29 March. Periods (in min) of two main spectral peaks are indicated.

were made worse by the fact that the first two waves arrived around the time of high water tide (Fig. 2a).

A number of questions arose from this catastrophic event. What is the physical mechanism responsible for the destructive tsunami oscillations observed in Port Alberni? Why did such strong oscillations occur specifically in this inlet? Which tsunami waves (local or distant) are likely to cause significant future damage in this area?

Significant tsunami oscillations in Port Alberni (as well as at other B.C. stations) continued for several days, being highly regular and almost monochromatic, with wave periods between 1.7 and 2 hours (Fig. 2a). It was therefore naturally assumed that the 1964 event in Alberni Inlet had a resonant character (cf. MURTY and BOILARD, 1970; MURTY, 1992; HENRY and MURTY, 1995). The averaged wave spectrum at Port Alberni (Fig. 2b) shows a dominant peak with a period of approximately 1.8 hours ($\sim$107 min). Such a strong response was likely due to the fact that this spectral peak is near the fundamental period of the inlet.

Several numerical models were constructed to simulate tsunami wave propagation in the northeastern Pacific Ocean and wave transformation on the continental shelf, including the shelf of Vancouver Island (cf. HEBENSTREIT and MURTY, 1989; DUNBAR et al., 1991; WHITMORE, 1993; MYERS and BAPTISTA, 2001; CHERNIAWSKY et al., 2007). A number of studies (MURTY and BOILARD, 1970; HENRY and MURTY, 1972; 1995; KOWALIK and MURTY, 1993) were focused specifically on explaining the observed 1964 tsunami oscillations in the Alberni Inlet. However, the spatial resolution of these models and the accuracy of the bathymetry were insufficient for the region with such complicated topography. These models also did not allow to resolve the detailed frequency spectrum and relative amplification of the long-wave oscillations in the inlet. Finally, the lack of high-quality digital records of tsunamis and background oscillations was a key factor limiting the ability to estimate the frequency characteristics of the wave field in the region and to verify the numerical tsunami models in this area.

The destructive tsunamis of the 1990s in the Pacific Ocean initiated a major upgrade of the existing Tsunami Warning system and of the Permanent Water Level Network (PWLN) on the coast of British Columbia. New digital instruments were introduced to continuously measure sea-level variations with 1-min sampling. During the period 1999–2007, long time series of such high quality sea-level data were collected at a number of stations, including Tofino and Bamfield, and several weak tsunamis were recorded by these instruments (RABINOVICH and STEPHENSON, 2004; STEPHENSON et al., 2007; STEPHENSON and RABINOVICH, 2008). At the outset of 2006, a digital tide gauge was installed at Port Alberni, replacing an older analogue tide gauge used at this site during 1961–1997. This new and precise instrument provided us with reliable two-year long time series of the background oscillations at the head of Alberni Inlet, and measured a weak tsunami from the Kuril Islands earthquake (M_w = 8.3) of 15 November, 2006 (STEPHENSON et al., 2007). In addition, we re-examined historical analogue recordings of tide gauges on the BC coast and identified four tsunamis during 1994–1996 that were observed at several sites, including Port Alberni (STEPHENSON and RABINOVICH, 2008).

These new tsunami and sea-level background data are used here to estimate the spectral properties of oscillations in the inlet and to verify the numerical model results.

We used two numerical models to investigate the resonant characteristics of the Barkley Sound and Alberni Inlet system and to examine transformation and amplification of tsunami waves arriving from the open ocean. The first model (A) was forced at its open boundary with a stationary autoregressive (AR) signal, similar to the observed background wave noise. This was an updated and improved version of the model that was used to investigate the resonant oscillations in the bays and inlets of the Kuril and Balearic Islands (DJUMAGALIEV et al., 1994; RABINOVICH et al., 1999). The second model (B) used an initial sea-level deformation from a potential earthquake off California, in the southern segment of the Cascadia Subduction Zone, to produce transient tsunami waves arriving at the shelf of Vancouver Island and then propagating inside Barkley Sound and Alberni Inlet. A similar model was used successfully to estimate sea-level variations and associated currents in bays and harbors of the southern and southwestern coast of Vancouver Island (CHERNIAWSKY et al., 2007). Results from these models are compared with actual observational data.

2. Observations of Tsunamis

The 1964 Alaska tsunami was the strongest tsunami ever recorded in Port Alberni and on the Pacific Coast of Canada. However, there were also records of other tsunamis in Alberni Inlet; although all of them were relatively small (other major Pacific Ocean tsunami events, such as Aleutian 1946, Kamchatka 1952 and Chile 1960, were not recorded due to the absence of a tide gauge in Port Alberni). The most complete information on tsunamis at Port Alberni, as well as at other locations on the BC coast, can be found in the catalogue by STEPHENSON et al. (2007).

Four tsunamis were identified in the analogue records of the BC tide gauges for the period of 1994–1996 (STEPHENSON et al., 2007; STEPHENSON and RABINOVICH, 2008), with the corresponding earthquakes listed in Table 1.

All four tsunamis were recorded at Port Alberni, as well as at several other BC stations, including Tofino and Bamfield (see Figs. 30–33 in STEPHENSON et al., 2007).

Table 1

Earthquakes in the Pacific Ocean (1994–1996) which generated tsunamis recorded on the BC coast

Date	Region	M_w
04 October 1994	Kuril Islands, Russia	8.3
30 July 1995	Northern Chile	8.0
03 December 1995	Kuril Islands, Russia	7.9
17 February 1996	Irian Jaya Region, Indonesia	8.2

Tide gauge records at these three sites for the Kuril Islands 1994 and 1995 events are shown in Figure 3. Tsunami waves are evident in Figure 3 and the arrival times of these waves are relatively clear. Other important features of these observations are:
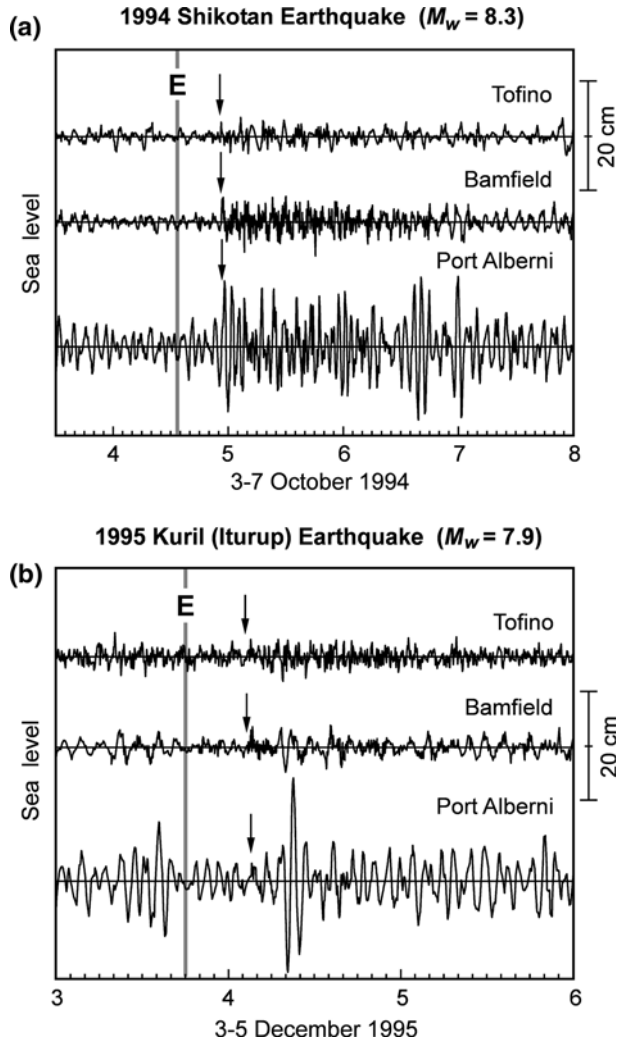

Figure 3

Tsunami records from three tide gauges (Tofino, Bamfield and Port Alberni) located on the west coast of Vancouver Island for two trans-Pacific tsunamis: (a) From a 1994 Shikotan earthquake ($M_w = 8.3$) and (b) from the 1995 Kuril (Iturup) earthquake ($M_w = 7.9$). "E" denotes the time of the main earthquake shocks, while arrows depict the tsunami arrival time.

(a) Tsunami ringing is relatively long, longer than 2–3 days, and their energy decay is slow.
(b) The maximum wave heights at Port Alberni are 3–4 times larger than at Tofino or Bamfield and are more often in a third (e.g., in 1964), or a later wave.
(c) The dominant oscillations at Port Alberni are more regular and have lower frequencies than at the other stations.

It is likely that these features and the differences between various sites are determined by local topographic effects.

To examine transient behavior at frequencies of the observed tsunami waves, we used the multiple-filter technique (EMERY and THOMSON, 2001). This method is similar to wavelet analysis and was developed to study nonstationary signals whose time series exhibit temporal changes in amplitude and/or phase. It uses narrow-band filters and a Gaussian window which isolates a specific center frequency $\omega_n = 2\pi f_n$. Demodulation of a sea-level time series $\zeta(\omega_n; t)$ yields a matrix of amplitudes and phases of wave signals, with columns representing the time and rows the frequency (the so-called f-t diagrams). This method is used effectively to examine tsunami records and to analyze tsunami wave energy $E(f, t)$ as a function of frequency and time (cf. RABINOVICH et al., 2006).

Figure 4 presents f-t diagrams for the 1994 Shikotan and the 1995 Kuril Islands (Iturup) tsunami records at Bamfield and Port Alberni. Most of the energy in these plots is at low frequencies (periods of 60–180 min). The arrival of tsunami waves from the 1994 earthquake is clearly seen as an increase in the energy level at all frequencies at Bamfield and for periods exceeding about 20 min at Port Alberni. For this event, there were no pronounced oscillations prior to the tsunami arrival. Specifically, the incoming tsunami wave energy induced significant seiche oscillations observed at these two sites.

In contrast, the 1995 Kuril (Iturup) tsunami wave was weaker (Fig. 3b) and its arrival was masked by existing background ocean wave noise, as noticeable background oscillations were observed before the tsunami arrival. Tsunami waves introduce additional energy and are further amplified at discrete frequencies that correspond to the natural oscillations, or standing wave modes of an inlet or a harbor. Such resonant modes are usually numbered in the order of frequency, starting from the gravest ($n = 0$) fundamental mode. In particular, an increase in the energy at tsunami arrival time is apparent in Figure 4 for a period of ~ 110 min. Except for this minor difference, the f-t diagrams for these two events are very similar.

The diagrams in Figure 4 demonstrate that the tsunami wave energy is concentrated mostly in the same frequency bands as the energy for the background long-wave oscillations. This feature of tsunami waves plays a key role in the coastal water response to the arriving tsunami waves (cf. MILLER, 1972). Specifically, there is resonant generation and amplification of local seiches when the periods of the incoming waves match the characteristic (natural) periods of the site. Conversely, a non-resonant response is observed when there is a pronounced mismatch in these periods. Three distinct
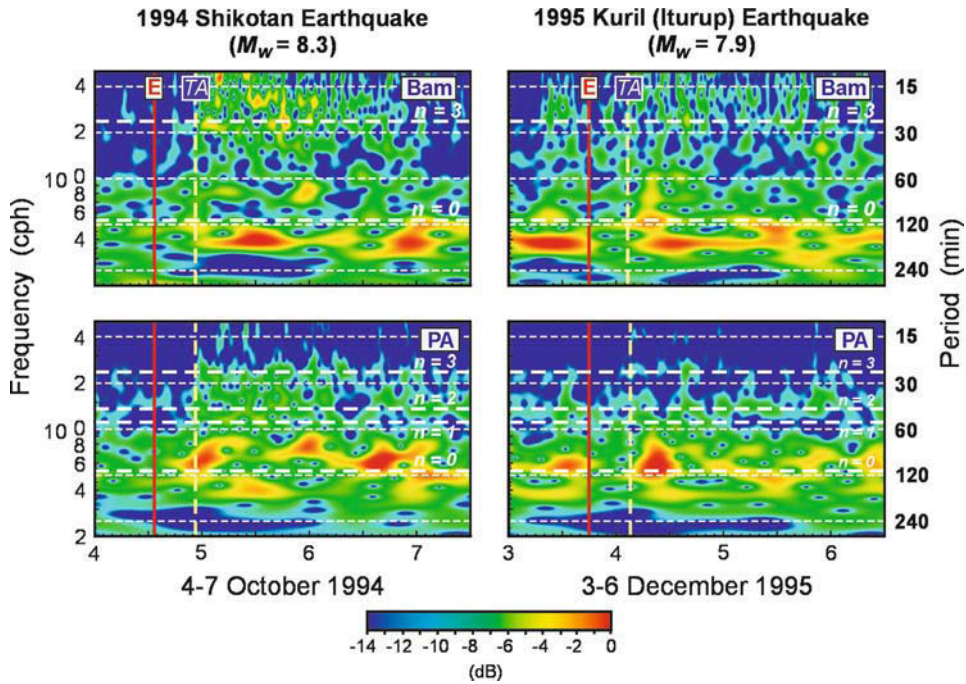
Figure 4

Frequency-time plots (*f-t* diagrams) for the 1994 Shikotan and the 1995 Kuril (Iturup) tsunamis from tide gauge records at Bamfield (Bam) and Port Alberni (PA). The vertical red line labelled "E" denotes the time of the main earthquake shock, while the dashed vertical yellow line labelled "*TA*" marks the estimated tsunami arrival time. Thick dashed horizontal lines mark the frequencies and periods of characteristic modes; two ($n = 0, 3$) modes were marked for Bamfield and four ($n = 0, 1, 2, 3$) for Port Alberni (these modes were computed by the model A, as is explained below).

frequency bands, with peak periods of approximately 110, 43 and 23 min, are evident in the *f-t* diagrams for Port Alberni (Fig. 4). As shown in the next two sections, these bands are related to the characteristic modes of the Alberni Inlet – Barkley Sound system. Two of the frequency bands, with periods of 110 min and 23 min, are also apparent in the *f-t* diagram for Bamfield. These plots reveal an obvious tsunami wave-train (packet) structure; the duration of each wave train is 12 to 18 hours.

3. Observations of Background Noise

To determine the spectral properties of longwave oscillations in the Barkley Sound – Alberni Inlet system and to compare these properties at various sites, we analyzed 2-month-long records of background oscillations (with 1-min sampling) at Port Alberni, Bamfield and Tofino. The spectral procedure used is similar to that described in EMERY and THOMSON (2003). To improve our spectral estimates, we used a Kaiser-Bessel spectral
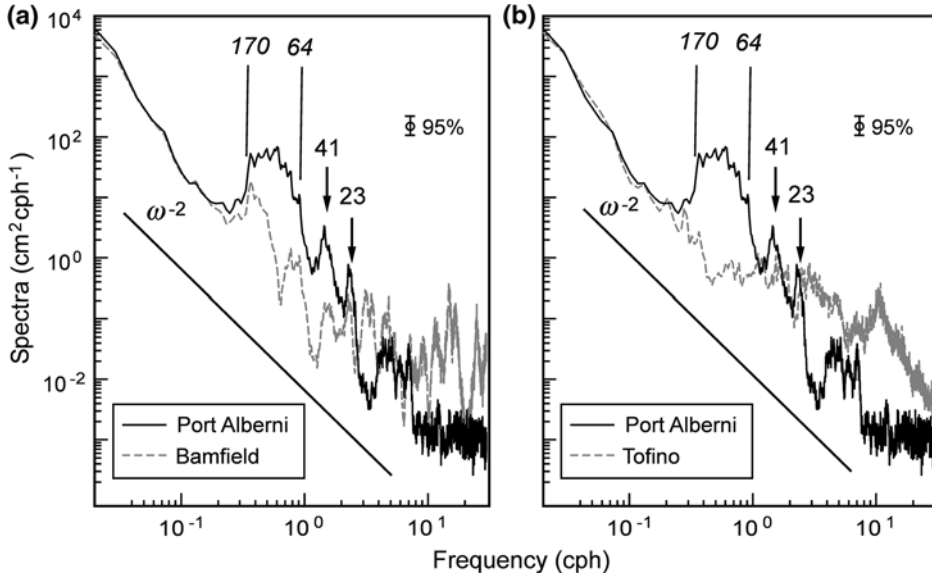
Figure 5
Comparison between the spectra of background sea-level oscillations: (a) at Bamfield and Port Alberni, (b) at Tofino and Port Alberni. Periods (in min) of the main peaks are indicated.

window, with half-window overlaps, prior to applying the Fourier transform. The width of the window was chosen to be 4096 min ($\sim$68.3 h), yielding about 80 degrees of freedom per spectral estimate. The results are shown in Figure 5. For comparison, we present in Figure 5a the spectrum for Port Alberni together with that for Bamfield, while in Figure 5b we show the spectra for Port Alberni and for Tofino.

The general forms of the background spectra for Port Alberni, Bamfield and Tofino are similar and for wave periods longer than 3 hours, the three spectra are almost identical. These spectra are "red," as their spectral energy decreases with increasing frequency, with their slope proportional to ω^{-2}, which is typical for long-wave sea-level spectra in the open ocean (cf. KULIKOV *et al.*, 1983; FILLOUX *et al.*, 1991; RABINOVICH, 1997). The long ocean waves are transformed as they propagate from the open ocean onto the shelf and along the shore. Their spectra become more energetic and "jagged" with decreasing depth and when approaching the coast (cf. Fig. 1 in RABINOVICH, 1997).

The spectrum of background atmosphere-induced waves near the coast can be described as (RABINOVICH, 1997):

$$S_b(\omega) = S_0(\omega)\, Q_b(\omega)\, P_b(\omega), \tag{1}$$

Where Q_b is the admittance function for a shelf (which can also include a bay, or a gulf, similar to Barkley Sound), P_b is the inlet/harbor admittance function and S_0 is the open ocean background spectrum. The remarkable feature of $S_0(\omega)$ is that it is usually smooth

and monotonic and has no distinct spectral peaks. Thus, individual peaks and troughs in the observed spectra $S_b(\omega)$ are related to topographic features.

While tsunami waves have larger amplitudes than the background waves, their transformation on the shelf and in bays and harbors is mostly linear, except in very shallow bays and during on-shore run-up (e.g., TITOV and SYNOLAKIS, 1993; SATAKE, 1995). Thus, admittance functions and other spectral characteristics of the tsunami waves can be studied by comparison with the spectra of background noise.

The spectral characteristics of Alberni Inlet are of primary interest for the present study. In general, the background spectrum at Port Alberni (Fig. 5) looks similar to the spectrum of the 1964 tsunami wave at this site (Fig. 2b). However, the background spectrum has considerably better resolution (~ 0.015 cph) and thus contains far more detail.

The most interesting and important feature of this spectrum is the wide spectral rise in the frequency range of 0.35–0.94 cph (periods of 64–170 min). It is worth emphasizing that the high resolution of this spectrum ensures that this rise is the physical property of the system and not related to insufficient spectral resolution. The corresponding rise is mostly absent in the spectra for Tofino and Bamfield. It is therefore likely that this rise is mainly due to the influence of Alberni Inlet. At the same time, this spectral feature is significantly different from typical spectra of long-wave oscillations in long and narrow inlets, or in bays and harbors with narrow entrance, which normally have a strong and narrow spectral peak associated with the fundamental Helmholtz mode of the basin, as was observed, for example, in Malokuriskaya Bay, Kuril Islands (DJUMAGALIEV et al., 1994; RABINOVICH, 2008), or in Citadella Inlet, Balearic Islands (RABINOVICH et al., 1999; RABINOVICH, 2008; VILIBIĆ et al., 2008).

The strong broadening of the spectral peak at Port Alberni may be partly due to the influence of Barkley Sound (Fig. 1). This is supported by a particular feature of the spectrum at Bamfield (located near the entrance to Barkley Sound), which has a peak with a period near 170 min, matching the frequency of spectral energy increase at Port Alberni (Fig. 5a). In contrast, the spectrum at Tofino (located to the north of Barkley Sound) has no such peak (Fig. 5b).

Other noteworthy features of the Port Alberni spectrum (Fig. 5) are the peaks at 1.45 cph (41.5 min) and 2.61 cph (23 min). The Bamfield spectrum peaks (Fig. 5a) are similar to those at Port Alberni, although with less energy. The similarity of the background spectra at Port Alberni and Bamfield indicates that these two sites are part of a common system, influenced by similar basin modes. In contrast, the Tofino spectrum (Fig. 5b) is very different from those at Bamfield and Port Alberni. Therefore, sea-level oscillations at Tofino are essentially independent from those in Barkley Sound and in Alberni Inlet.

At higher frequencies (periods less than 23 min), the Port Alberni spectrum decreases more rapidly than the Bamfield and Tofino spectra. Oscillations at Bamfield and Tofino at these frequencies appear to be related to local seiches. Several high-frequency peaks (with periods of 2.4, 3.5, 5 and 18 min at Bamfield and 5.6 and 12 min at Tofino) are observed in these spectra (Fig. 5). Similar peaks were also observed at these sites during

the 2001 Peru, 2001 Queen Charlotte and 2004 Sumatra tsunami events (RABINOVICH and STEPHENSON, 2004; RABINOVICH et al., 2006).

4. Numerical Model A: Background Waves in Barkley Sound and Alberni Inlet

To examine long-wave background oscillations in the Barkley Sound–Alberni Inlet system, we used a linear shallow-water equations numerical model (so-called "model A"). Its finite-difference formulation is similar to that in the TUNAMI N2 model (IMAMURA, 1996).

The model was forced by prescribed incident waves at its open boundaries, which have "red noise" spectra, similar to the observed background noise. A stationary autoregressive (AR) model of the first order was used for this purpose:

$$\zeta_0^j = a\zeta_0^{j-1} + \varepsilon, \tag{2}$$

where $\zeta_0^1, \zeta_0^2, \ldots, \zeta_0^{j-1}$ are the input wave elevations, a is the regression coefficient ($0 < a < 1$), and ε is a random process of the "white noise" type. The normalized spectrum of (2) has the form

$$S_\zeta(\omega) = [1 - 2a\cos(\omega\Delta t) + a^2]^{-1}, \tag{3}$$

where Δt is the sampling interval of the input time series. The spectrum (3) is a monotonic function of ω, which for $\omega\Delta t \ll 1$, decreases according to a ω^{-2} power law, similar to the observed background spectra in the open ocean (KULIKOV et al., 1983; FILLOUX et al., 1991; RABINOVICH, 1997). The original version of this model was used to examine the resonant oscillations in the bays and inlets of Shikotan Island (Kuril Islands) (DJUMAGALIEV et al., 1994) and Menorca Island (Balearic Islands) (RABINOVICH et al., 1999).

There are two main advantages in applying such a model. First, and in contrast to a common method based on numerical simulation of monochromatic waves with select frequencies (cf. HENRY and MURTY, 1995), the present model is forced at its open boundary using waves with a continuous spectrum. This allows us to calculate the system response over a complete frequency range. Second, this model time series of simulated sea levels can be examined using the same spectral and cross-spectral analyses as for the observed time series. The simulated and observed time series and their spectra can then be compared in great detail and also used for the verification of the model.

The computational domain for this model is shown in Figure 1b. Its grid dimensions are 1213×1223 and (x, y) grid size is 50 m. The time step used was 0.53 s.

Model sea-level time series were computed and stored for Port Alberni and Bamfield. These time series were used in cross-spectral analysis, for estimation of coherence, phase differences and admittance functions between the two sites. Similar analyses were also performed on the two-month long time series of observed sea levels at these two locations.

Figure 6

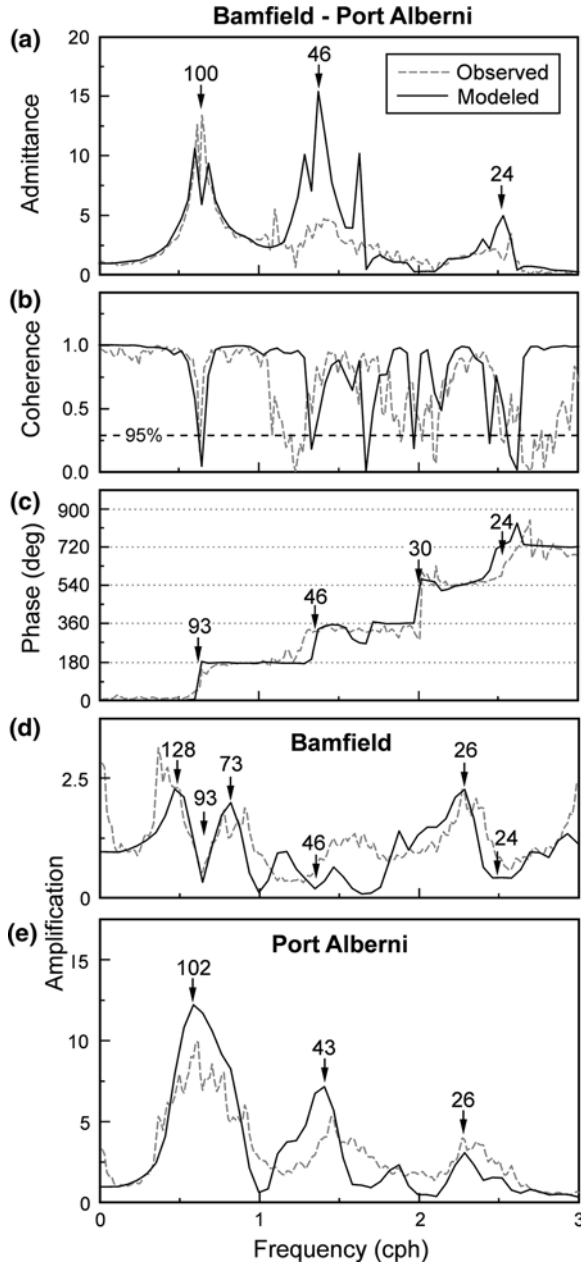Characteristics of the cross-spectra between Bamfield and Port Alberni for the observed and the model A simulated sea-level oscillations: (a) admittance, (b) coherence and (c) phase difference. Periods (in min) of the main peaks are indicated. Observed and the model A simulated amplification factors: (d) at Bamfield, (e) at Port Alberni. Periods (in min) of the main peaks and troughs are indicated.

The model was integrated for 10 days using above random forcing at its open boundary, providing sufficiently long quasi-stationary time series for standard spectral analyses. To verify the model performance, we compared between the observed and the modeled Bamfield – Port Alberni cross spectra (Fig. 6).

In general, admittance, coherence and phase spectra show a very good agreement with the observations in the frequency range of up to 2.5 cph. This is especially true for the model phase spectrum, which is nearly identical to the observed (Fig. 6c). The modeled admittance is close to the observed up to 1 cph. However, the level of the modeled peak at 46 min (1.3 cph) is much higher than observed (Fig. 6a), which is likely due to a standing wave node being located near Bamfield at this frequency in the model. This peak is not as prominent in the observations at Bamfield, as it is masked by additional non-coherent noise.

The remarkable agreement in Figure 6 between the simulated and the observed spectra for Bamfield and Port Alberni suggest that this model is sufficiently reliable and can provide realistic results not just for these two stations but for the entire area.

Cross-spectral analysis of the observed sea-level variations at Port Alberni and Bamfield (Fig. 6) provides additional insight, beyond the features shown by the autospectra in Figure 5a. The admittance function in Figure 6a has prominent peaks at approximately the same frequencies as in the Port Alberni spectrum (Fig. 5a), however the admittance peaks are sharper and more pronounced than the spectral peaks. The coherence is high over the entire frequency range of 0.0–3.0 cph (i.e., at periods longer than 20 min), except for some narrow and abrupt troughs (Fig. 6b).

Phase differences between the two sites are step-like, with phase shifts near $0°$ or $180°$ (Fig. 6c). These shifts correspond exactly to the frequencies of the coherence minima. The cross-spectral coherence and phase plots indicate that oscillations in Alberni Inlet and in the adjacent Barkley Sound are due to standing waves in the system. Therefore, phase shifts and coherence minima are related to the nodes moving past Bamfield and into the inlet with increasing frequency. Indeed, the Bamfield spectrum (Fig. 5a) shows minima at these transition frequencies.

The cross-spectral characteristics between Bamfield and Port Alberni sea-level records (Fig. 6) confirm the general features of the Port Alberni spectrum (Fig. 5), with additional peaks corresponding to the minima observed at the Bamfield spectrum. The first node is near Bamfield at 0.63 cph (95 min), inside the 0.5–1 cph frequency band of the broad Port Alberni spectral peak. This means that a maximum amplitude response in Alberni Inlet (near 0.6 cph) corresponds to the first ($n = 0$) fundamental mode, with node location further offshore from Bamfield, probably close to the mouth of Barkley Sound.

From (1), we calculate the observed wave amplification $A(\omega)$ at Port Alberni and Bamfield:

$$A(\omega) = \sqrt{Q_b(\omega)\,P_b(\omega)} = \sqrt{S_b(\omega)/S_0(\omega)}, \tag{4}$$

where $S_0(\omega) = (\omega_0^2/\omega^2)\, S(\omega_0) = C/\omega^2$. ω_0 is a reference frequency (chosen here $\omega_0 = 0.25$ cph) and C is a constant related to the open ocean spectra, computed from Figure 5 as $C = 0.125$ cm^2 h^{-1} = 3.5×10^{-9} m^2 s^{-1}.

For the model simulated records, we calculate the amplification function as:

$$A_M(\omega) = 0.5\sqrt{S_M(\omega)/S_{0M}(\omega)}, \tag{5}$$

where $S_M(\omega)$ is sea-level spectrum at a particular location and $S_{0M}(\omega)$ is the spectrum of the prescribed incident (forcing) waves. The coefficient 0.5 in equation (5) ensures that the modeled amplification factor is equal to unity at low frequencies, as is the case for the observed waves.

The modeled amplification functions show a good agreement with the observations both for Bamfield and for Port Alberni (Figs. 6d, e). The main features of these functions are similar for both locations, as was also indicated by the high coherence between Bamfield and Port Alberni (Fig. 6b). Amplification at Port Alberni (Fig. 6e) is relatively high for periods from 70 to 120 min. Another maximum in amplification, though smaller in value, is near the 43-min period.

Amplification at Bamfield (Fig. 6d) shows similar, though much smaller peaks. The main peak at 0.5–1 cph is split into two peaks due to a spectral minimum near 0.6 cph (see Fig. 5a). As was explained above, this minimum corresponds to the position near Bamfield of the first node at this frequency (Figs. 6a-c). Amplification at Bamfield also shows additional (in comparison to Port Alberni) minima at wave frequencies higher than 1 cph, when the nodes of these waves are located near Bamfield.

The first minimum (at 93 min) in Figure 6d is the same for both the observed and the modeled spectra. However, the minimum at a 46-min period appears only in the modeled function, with the observed function showing a broad minimum from about 55 to 45 min. These differences in amplification are consistent with the differences between the modeled and the observed admittance functions (Fig. 6a).

Spatial distribution of the response is shown in Figure 7 for six selected frequencies. At 0.4 cph, the Barkley Sound–Alberni Inlet system shows relatively weak amplification, with no nodes (lines of zero amplitude) present in Figure 7a. As the frequency increases, amplification sharply increases inside Alberni Inlet and Barkley Sound, reaching a maximum at 0.53 cph (113 min). This maximum in amplification corresponds to a nodal line near the entrance to Barkley Sound (Fig. 7b). With further frequency increase, this first node moves into the inlet and amplification in Alberni Inlet remains high up to 0.73 cph (Figs. 7c to 7e). As this node moves past Bamfield and inside Alberni Inlet, the oscillations in Alberni Inlet and in Barkley Sound have an opposite phase. When frequency reaches 0.93 cph, the amplitudes decrease sharply and the oscillations are weak everywhere (Fig. 7f).

Figure 8 provides yet another description of the model frequency response, showing the spatial structure of the three main modes (Fig. 8a) and relative sea levels (amplification) for frequencies up to 2 cph (Fig. 8b) along a transect from Barkley
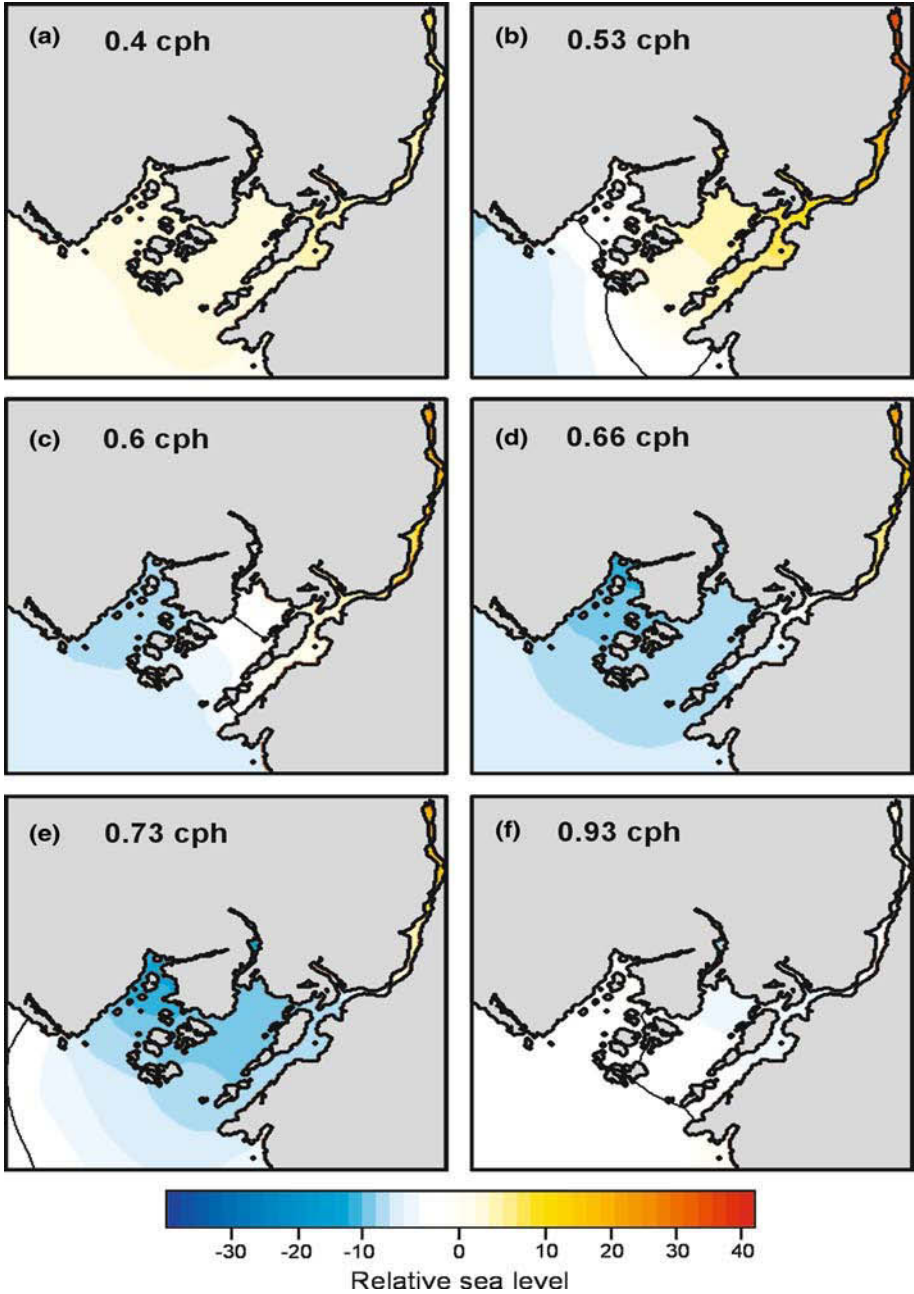
Figure 7
Computed (model A) relative sea-level oscillations in the Barkley Sound and Alberni Inlet system, shown for six
select frequencies (marked in each panel).
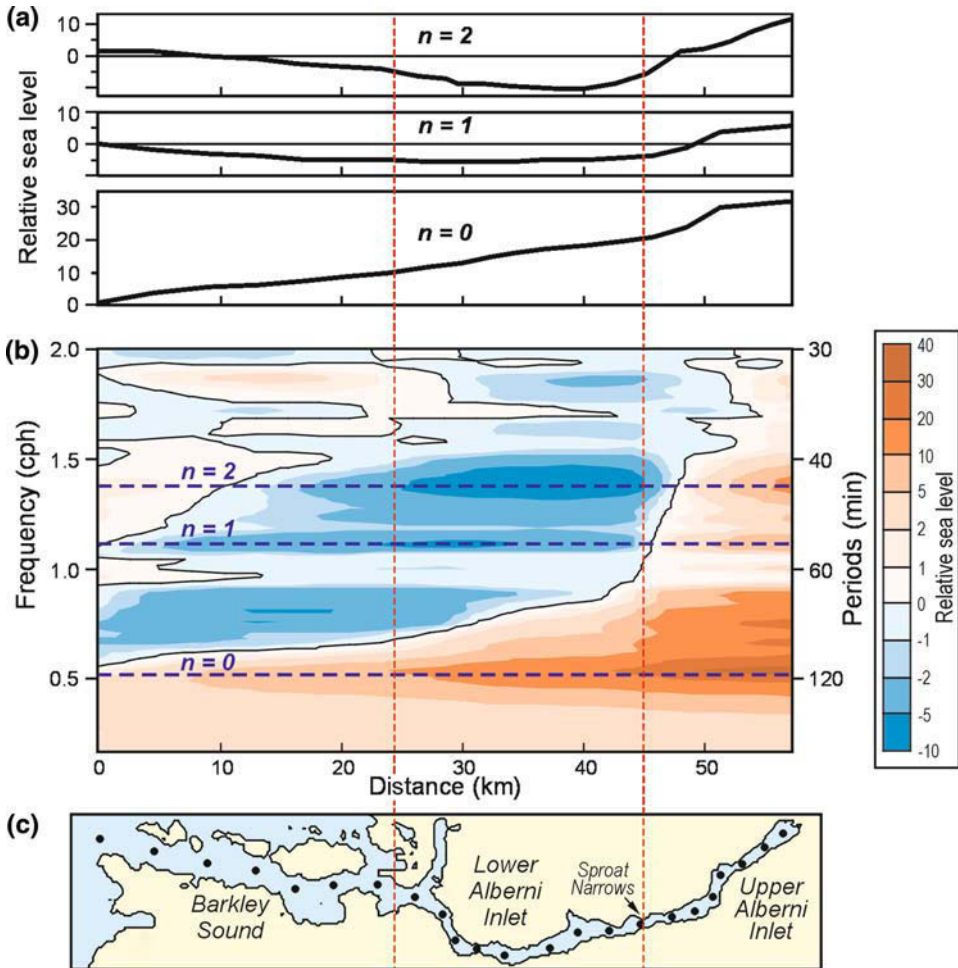
Figure 8
Along-channel computed (model A) structure of sea-level oscillations in Barkley Sound and Alberni Inlet. (a) Computed forms of three first modes ($n = 0$, 1 and 2). (b) Relative sea-level along-channel heights as a function of frequency with frequencies of the first three modes indicated by horizontal dashed lines. (c) Location of the along-channel transect in Barkley Sound and Alberni Inlet (marked by black solid circles). The red dashed lines separate the three regions: Barkley Sound, lower Alberni Inlet and upper Alberni Inlet.

Sound entrance to Port Alberni (Fig. 8c). This area can be divided into 3 parts: Barkley Sound, the lower Alberni Inlet (up to the Sproat Narrows) and the upper Alberni Inlet.

For low frequencies, up to the 0.9 cph, all three parts show the fundamental mode ($n = 0$) maximum at 112 min (Fig. 8b). As the frequency increases from about 0.55 to 0.8 cph there is still high amplification in much of the area, despite the fact that the nodal line moves inside Barkley Sound. When this line moves past the middle of the lower

Alberni Inlet and the frequency increases beyond 0.9 cph, the oscillations in all three parts decrease in amplitude.

A weak amplification maximum occurs at about 54 min, when another nodal line is located near the entrance of Barkley Sound. However, more significant amplification occurs at 43 min. It is confined mainly to Alberni Inlet, behaving as a classical first-mode asymmetrical pendulum and oscillating between the upper and lower Alberni Inlet, with its nodal line located in the "bottleneck" of Sproat Narrows (Fig. 8c). From the point of view of the complete system, this oscillation can be described as the $n = 2$ mode.

For frequencies beyond 1.5 cph (40 min), Alberni Inlet and Barkley Sound oscillations become decoupled, as the upper Alberni Inlet is almost "blocked" by Sproat Narrows. The lower part of the inlet and Barkley Sound show only weak amplification for these higher frequencies.

5. Numerical Model B: Tsunami Waves in Alberni Inlet from a Remote Subduction Zone Earthquake

In the previous two sections we discussed amplification of tsunami waves and excitation of characteristic modes in Alberni Inlet using existing observations of background waves and of tsunami waves from remote earthquakes, as well as from a numerical model (A) forced by stationary auto-regressive spectra. To complete the analysis, we present here results from another model, which uses a scenario of a partial rupture of the Cascadia Subduction Zone (CSZ), the so-called *short-south* scenario of SATAKE *et al.* (2003; see also WANG *et al.*, 2003).

The main purpose of the present study is to examine the resonant characteristics of the Alberni Inlet–Barkley Sound system rather than attempt to reproduce exactly the 1964 tsunami waves observed in this system. That is why, and also because we would like to continue the previous study (CHERNIAWSKY *et al.*, 2007; thereafter C07), we used in our computations one of the Cascadia Subduction Zone (CSZ) scenarios instead of the 1964 Alaska scenario.

C07 used three CSZ scenarios to simulate tsunami waves and currents in harbors of Ucluelet, Victoria and Esquimalt, located on the southern Vancouver Island Coast (Fig. 1): (1) *long-narrow* (which represents a full rupture of CSZ); (2) *short-north*; and (3) *short-south*. The last two are also plausible scenarios because some megathrust earthquakes involve the rupture of limited segments of a subduction zone. We chose the *short-south* scenario because it also represents a realistic case of a relatively strong earthquake that is likely to generate a well-defined response in Alberni Inlet. At the same time, it is a remote earthquake, allowing us to study relative amplification of distantly-arriving waves in this inlet system.

The *short-south* scenario source region extends about 440 km north to south along the California coast (Fig. 9a). Earthquake magnitude (M_w), equivalent uniform rupture width
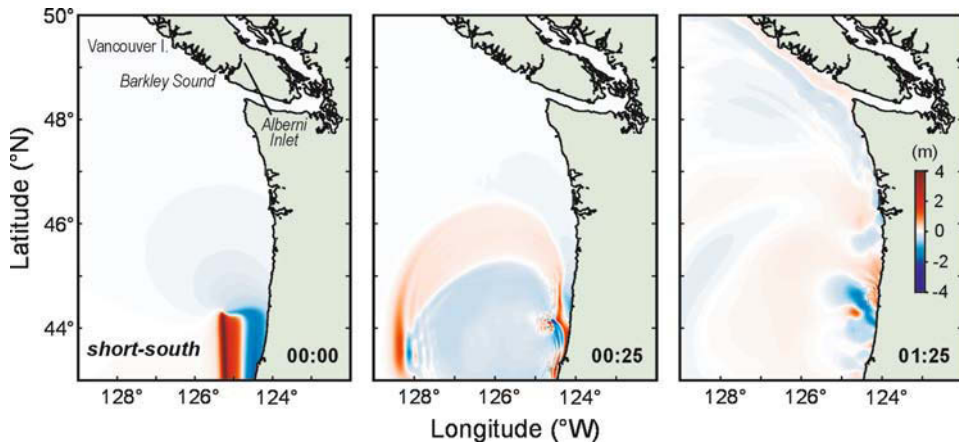
Figure 9
Propagation of the model B simulated tsunami waves from a remote tsunami source off California, generated by
the so-called *short-south* CSZ earthquake scenario (M$_w$ = 8.8) (SATAKE *et al.*, 2003). The three panels show the
wave heights (a) at initial time, (b) at 25 min and (c) at 85 min after the earthquake.

and full-slip zone width for this scenario are 8.8, 56 km, and 37 km, respectively (SATAKE
et al., 2003). The resulting tsunami wave energy flux is mostly in a zonal direction,
perpendicular to the coast. These waves are expected to produce significant damage in
California, Oregon and possibly in Hawaii, but not at coastal locations that are much
farther north, such as British Columbia (C07).

The MOST numerical model (TITOV and SYNOLAKIS, 1997), used here and also
described in more detail in C07, has three nested grids. The model coarse grid (its grid
size $\Delta x \times \Delta y$ = 1500 × 1100 m) extends from 43°N to 50°N, covering the coastlines of
Northern California, Oregon, Washington and the southern Vancouver Island (Fig. 9).
The coarse and medium (245 × 185 m) grids are the same as in C07, while the fine grid
(outlined with a dashed frame in Fig. 1b) has a horizontal grid size of about 50 m
(compared to about 10 m used in C07) and includes Alberni Inlet and a large part of
Barkley Sound. This model was integrated for 26 hours using a 0.3-sec time step in its
fine grid.

Figure 9 shows initial sea-surface deformation and two snapshots of sea level, after
25 and 85 minutes. The first tsunami waves arrive on southern Vancouver Island coast
about 1.5 hours after the earthquake (Fig. 9c). The resulting sea-level maxima at a deep
ocean station B1 (at ∼1000 m depth; Fig. 1a) and at a station B3 on the shelf off Barkley
Sound (∼85 m depth; Fig. 1a) are about 0.15 m and 0.3 m, respectively. As the waves
pass through Barkley Sound and into Alberni Inlet, they are amplified. Figure 10 shows
nine snapshots on the model fine grid at 10-minute intervals, from 01:40 until 03:00,
covering an almost complete wave period after the arrival of the first tsunami wave in
Barkley Sound. The minimum and maximum simulated sea-level values during this
80-min period are about ±1.1 m.
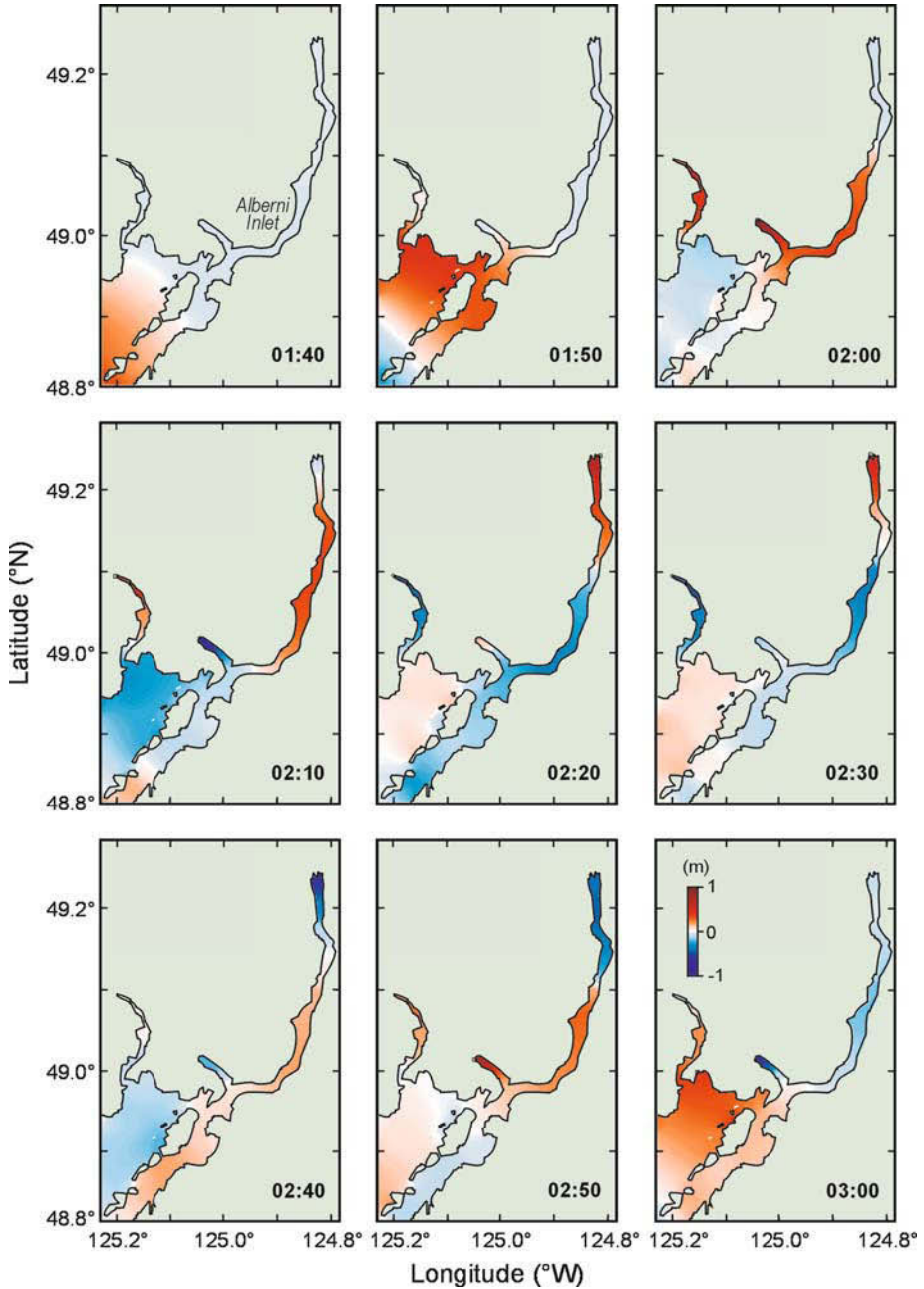
Figure 10
Propagation of tsunami waves inside the model B innermost fine-resolution (50 m) grid in Barkley Sound and Alberni Inlet, shown at 10-minute intervals after the arrival of the first tsunami wave. Time in hours and minutes after the earthquake is marked in each panel (ordered left to right, top to bottom).
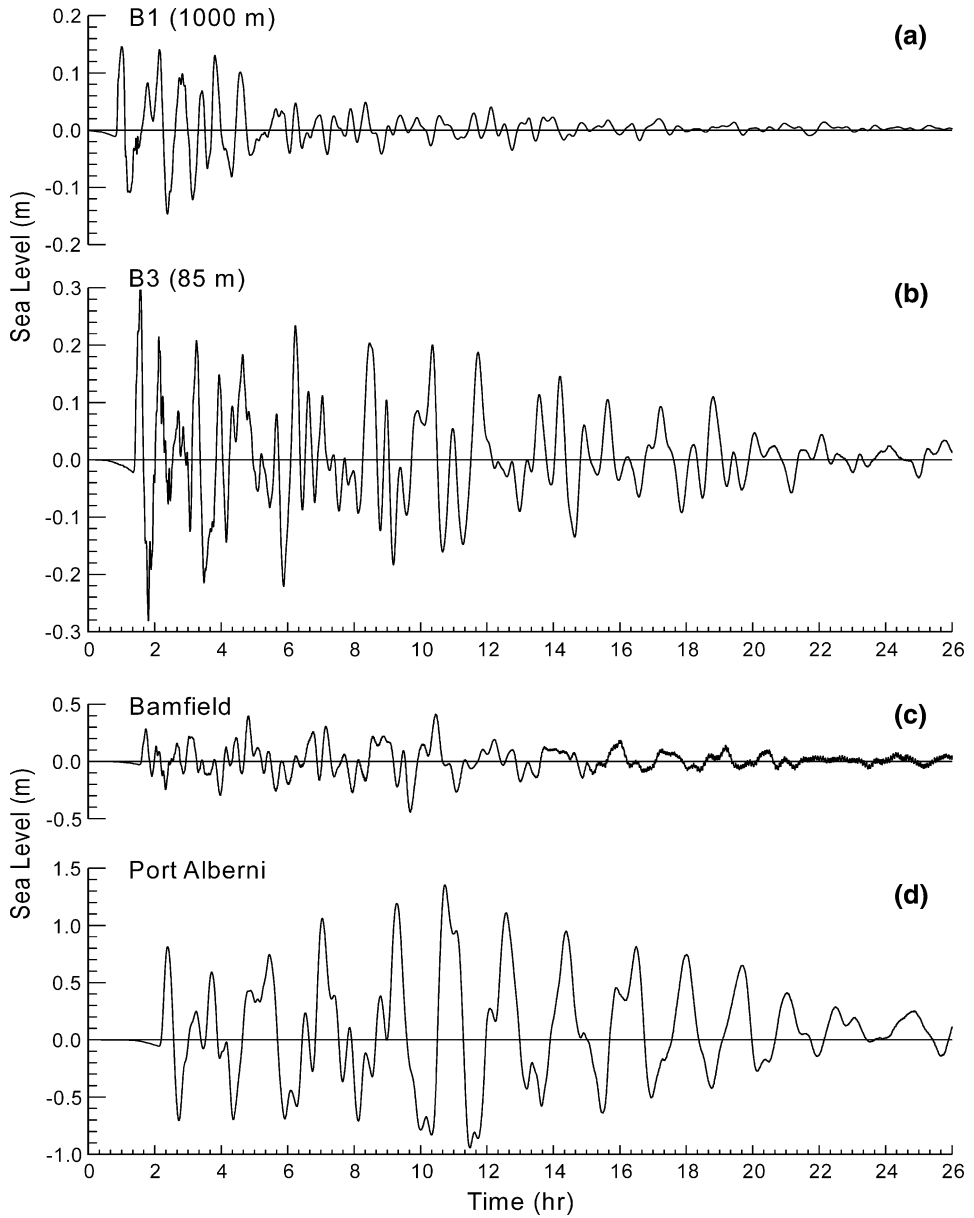
Figure 11
Model B simulated tsunami wave records at four locations: (a) at deep (1000 m) B1 site off Barkley Sound, (b) at B3 site on the continental shelf (85 m) near the entrance to Barkley Sound, (c) near Bamfield and (d) at Port Alberni. Locations of these sites are shown in Figure 1.

Figures 11a-d show time history of sea levels at four select locations: at a deep ocean (1000 m) station off Barkley Sound (B1 in Fig. 1a), at 85-m depth on the continental shelf off Barkley Sound (B3 in Fig. 1a), and at coastal locations near Bamfield and at Port Alberni. The offshore waves (Fig. 11a) decay rather quickly, after about 6 hours, while the waves on the shelf (Fig. 11b), near Bamfield (Fig. 11c) and in Alberni Inlet (Fig. 11d) have considerably longer decay periods. It is notable that the maximum sea level near Port Alberni is about 1.5 m and occurs in this model not during the 1st or the 2nd wave, but during the 6th wave (Fig. 11d), more than 10 hours after the earthquake! If we compare the maximum in Port Alberni to that in deep (1000 m) water, we obtain a maximum amplification factor for this model of about 10. However, by the time (at 10:40) the maximum sea level is reached in Port Alberni (Fig. 11d), amplitude of the waves offshore decays to less than 0.04 m (Fig. 11a).

Maps of the maximum sea level and of the maximum water speed in Barkley Sound and Alberni Inlet during the 26-hr model integration are presented in Fig. 12. The maximum simulated water level of 1.62 m is near Port Alberni (Fig. 12a), though not exactly where the time series shown in Figure 11d was recorded (which explains the
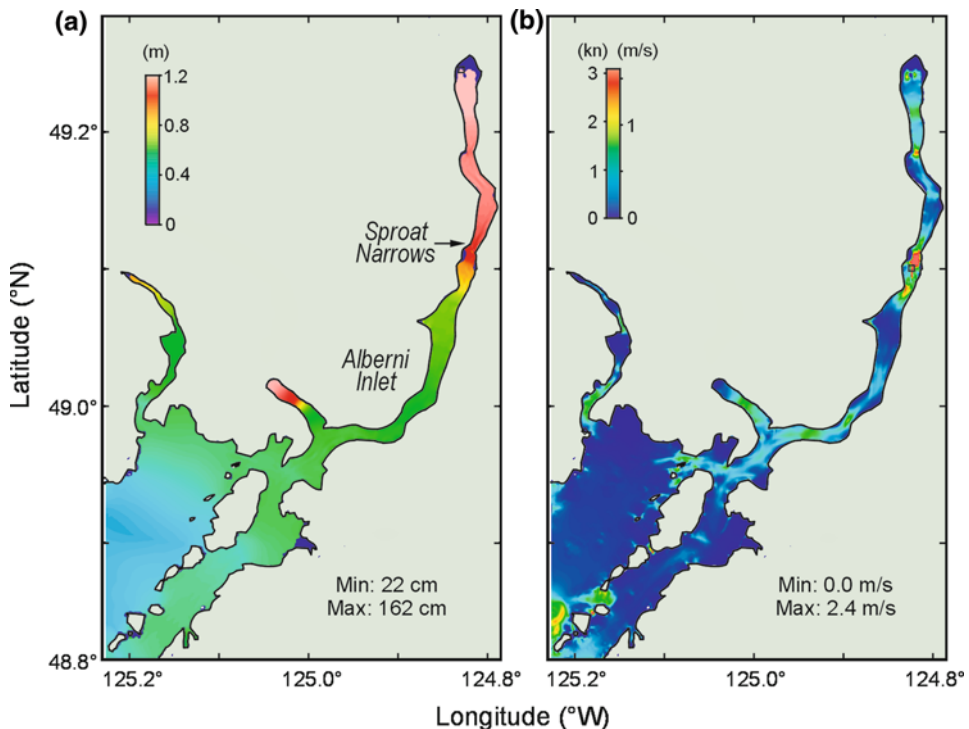
Figure 12
Maps of the model B computed maxima of (a) sea level and (b) water speed in Barkley Sound and Alberni Inlet. The maximum sea level of 1.62 m was near Port Alberni, while the maximum speed of 2.4 m s^{-1} occured in Sproat Narrows.

different maxima in the two figures). The maximum water speed of 2.4 m s^{-1} (5 knots) occurs in the relatively shallow (20–30 m) Sproat Narrows at 49.1°N (Fig. 12b). As was explained in the previous two sections, this channel splits Alberni Inlet into two parts, thus affecting the characteristic modes of the system, which are also apparent in the plot of maximum sea level (Fig. 12a).

The time series of the model B output (Fig. 11) are only 26-hr long and the tsunami wave signals are far from stationary. It is therefore not as straightforward to interpret this model spectrum (Fig. 13), as compared to the higher-quality spectra obtained from long-term observations, or from the much longer integration of the model A, discussed in the previous sections. Nevertheless, the model B spectral peaks compare well to the observed, both for Bamfield (Fig. 13a) and for Port Alberni (Fig. 13b). As was the case for the model A, the main 110-min peak in the model B Port Alberni spectrum is higher than the observed peak, with other peaks appearing as well (67 and 27-min peaks for Bamfield and 47 and 27-min peaks for Port Alberni). The somewhat different peak frequencies can at least in part be attributed to smaller signal to noise ratios and less spectral resolution in the shorter and nonstationary time series from the model B.
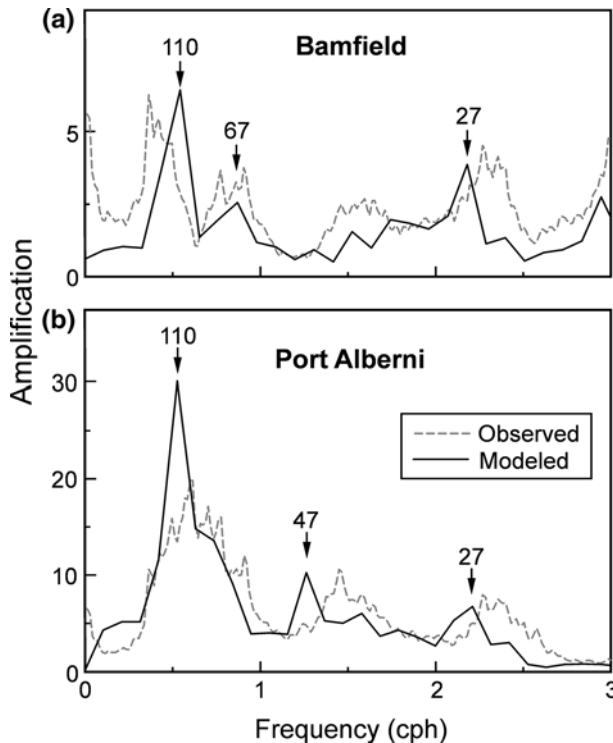
Figure 13
Observed and the model B simulated amplification factor as a function of frequency: (a) at Bamfield and (b) at Port Alberni.

6. Summary and Conclusions

In this work, we have investigated the resonant characteristics and amplification of gravity waves for the tsunami frequency band in Barkley Sound and Alberni Inlet, located on the west coast of Vancouver Island. We analyzed available sea-level observations of two remote tsunamis and of background wave noise, as well as the output from two numerical models for this system. The first model (A) was forced at its open boundary with a stationary autoregressive signal that is similar to the observed background noise. The second model (B) used an initial condition of sea-level deformation from a plausible *short-south* scenario of a Cascadia Subduction Zone earthquake off northern California, producing transient tsunami waves which decay with time.

Analyses of the observations, especially the analyses of background signals from digital tide gauges in Bamfield and Port Alberni, as well as the analysis of spectra from the AR-forced model reveal characteristic features of the frequency response of the system and help to verify the numerical models. For frequencies less than ~ 0.3 cph, spectra from these two tide gauges look almost similar. However, for frequencies higher than ~ 0.3 cph (which include the tsunami frequency band), the two spectra differ significantly, showing wave transformation, modal resonance and amplification in this basin.

Comparison between the observed Port Alberni and Bamfield spectra and their cross-spectra produced very useful results regarding amplification and characteristic modes of the system. We were able to calculate an observed amplification function relative to incoming open-ocean waves, while using an assumption of universal spectra in the ocean. However, data analysis provides results only for specific tide gauge locations (at Port Alberni and Bamfield). It was therefore very informative to use the AR-forced numerical model A, allowing us to study the characteristic modes of the coupled Alberni Inlet–Barkley Sound system and migration of the nodal lines of these modes spanning a wide frequency range over the complete area.

Both the observations and the model A results show that the main features of the frequency response of this area are related to the coupled oscillations in the Barkley Sound-Alberni Inlet system. Because this system has a large length to width ratio, it has a marked quarter-wave resonance, with its fundamental mode ($n = 0$) nodal line located near the open ocean boundary (the entrance to Barkley Sound) at a frequency of about 0.53 cph. The Q-factor of such resonance is related to this ratio. At these frequencies, the system is transparent, i.e., the waves pass freely through its major channels. This also leads to amplification due to the narrowing of the wave path from about 25 km in Barkley Sound entrance to 1–2 km in Alberni Inlet. These two mechanisms combine together to yield a high amplification coefficient over the wide frequency range of 0.4–0.9 cph.

The model A results also show that at the fundamental mode ($n = 0$) frequency of ~ 0.53 cph (period of 112 min), the nodal line of the system is located on the continental shelf near the entrance to Barkley Sound, which is relatively distant from the Alberni Inlet itself (Fig. 1). This is a strong resonant mode, with its amplification factor reaching $A = 12$ at this frequency.

The second prominent amplification peak at 1.4 cph (43 min) is associated with the $n = 2$ mode, while the $n = 1$ mode at about 1.1 cph (54 min) shows only weak amplification. The 43-min mode is directly related to its node being located near Sproat Narrows. The higher frequency modes are not as strong. They are connected with specific smaller-scale features of the inlet system (like Sproat Narrows) and cannot be classified from the point of view of the complete system. Their role in wave transformation is less important, as local amplification at these high frequencies is generally small.

The results from the second model (B) of tsunami waves due to a *short-south* scenario of the Cascadia Subduction Zone earthquake off northern California show spectral characteristics and amplification that are similar to those from model A, or from observed background sea-level data. The nonstationary nature of the model B waves, due to its transient forcing, make direct comparison with the observations or with the model A somewhat inconclusive. However, the model B spectral peaks are at about the same frequencies as in the observed spectra, while its amplification ratios are comparable with those of the model A and the observations. The model B results also show that the maximum tsunami current speeds are in Sproat Narrows, which divides the inlet into two parts, with the largest tsunami waves occurring in the upper Alberni Inlet, especially in the area of Port Alberni.

Acknowledgements

References

ANDERSON, P. S. and GOW, G. A. (2004), *Tsunamis and Coastal Communities in British Columbia: An Assessment of the B.C. Tsunami Warning System and Related Risk Reduction Practices*. 75+xii pp. (Public Safety and Emergency Preparedness Canada, Ottawa, 2004).
CHERNIAWSKY, J. Y., TITOV, V. V., WANG, K., and LI, J. -Y (2007), *Numerical simulations of tsunami waves and currents for southern Vancouver Island from a Cascadia megathrust earthquake*. Pure Appl. Geophys. *164*, 465–492.

CLAGUE, J.J. (2001), *Tsunamis*. In *A Synthesis of Geological Hazards in Canada* (ed. G.R. Brooks) Geol. Surv. Canada, Bull. *548*, 27–42.

CLAGUE, J.J., MUNRO, A., and MURTY, T.S. (2003), *Tsunami hazard and risk in Canada*, Natural Hazards *28* (2–3), 407–434.

DJUMAGALIEV, V.A., RABINOVICH, A.B., and FINE, I.V. (1994), *Theoretical and experimental estimation of transfer peculiarities of the Malokurilsk Bay coast, the Island of Shikotan*, Atmos. Oceanic Phys. *30*(5), 680–686.

DUNBAR, D., LeBLOND, P., and MURTY T.S. (1991), *Evaluation of tsunami amplitudes for the Pacific coast of Canada*. Prog. Oceanogr. *26*, 115–177.

EMERY, W.J. and THOMSON, R.E., *Data Analysis Methods in Physical Oceanography*, 2nd and Revised Edition, (Elsevier, Amsterdam) 2001 638 pp.

FILLOUX, J.H., LUTHER, D.S., and CHAVE, A.D., *Update on seafloor pressure and electric field observations from the north-central and northeastern Pacific*. In *Tidal Hydrodynamics*, (ed. B.B. Parker) pp. 617–639, (J. Wiley, New York 1991).

HEBENSTREIT, G.T. and MURTY, T.S. (1989), *Tsunami amplitudes from local earthquakes in the Pacific Northwest Region of North America. Part 1: The outer coast*, Marine Geodesy *13*, 101–146.

HENRY, R.F. and MURTY, T.S. (1972), *Resonance periods of multi-branched inlets with tsunami amplification*, Dep. Environ. Mar. Sci. Div., MS Rep. 28, 47–79.

HENRY, R.F. and MURTY, T.S. (1995), *Tsunami amplification due to resonance in Alberni Inlet: Normal modes*. In *Tsunami: Progress in Prediction, Disaster Prevention and Warning* (eds. Y. Tsushiya and N. Shuto), pp. 117–128, (Kluwer, Dordrecht, 1995).

IMAMURA, F. (1996), *Review of tsunami simulation with a finite difference method*. In *Long Wave Runup Models* (eds. H. Yeh, P. Liu, and C. Synolakis), pp. 25–42 (World Scientific Publishing, Hackensack, N.J, 1996).

KOWALIK, Z. and MURTY, T.S. (1993), *Numerical simulation of two-dimensional tsunami runup*, Marine Geodesy *16*, 87–100.

KULIKOV, E.A., RABINOVICH, A.B., SPIRIN, A.I., POOLE, S.L., and SOLOVIEV, S.L. (1983), *Measurement of tsunamis in the open ocean*, Marine Geodesy *6*(3–4), 311–329.

LANDER, J.F. (1996), Tsunamis affecting Alaska, 1737–1996. USDC/NOAA, Boulder, CO, USA, 195 pp.

MILLER, G.R. (1972), *Relative spectra of tsunamis*, Hawaii Inst. Geophys, HIG-72-8, 7 pp.

MURTY, T. S. and BOILARD, L. (1970), *The tsunami in Alberni Inlet caused by the Alaska earthquake of March, 1964*. In *Tsunami in the Pacific Ocean* (ed. W.M. Adams) pp. 165–187 (East West Center Press, Honolulu, HI, 1970).

MURTY, T. S. (1992), *Tsunami threat to the British Columbia coast*. In *Geotechnique and Natural Hazards*, pp. 81–89 (BiTech. Publ., Vancouver, 1992).

MYERS, E.P. and BAPTISTA, A.M. (2001), *Analysis of factors influencing simulations of the 1993 Hokkaido Nansei-Oki and 1964 Alaska tsunamis,* Natural Hazards *23*(1), 1–28.

RABINOVICH, A.B. (1997), *Spectral analysis of tsunami waves: Separation of source and topography effects*, J. Geophys. Res. *102 (C6)*, 12,663–12,676.

RABINOVICH, A.B., MONSERRAT, S., and FINE, I.V. (1999), *Numerical modeling of extreme seiche oscillations in the region of the Balearic Islands*, Oceanology *39*(1), 16–24.

RABINOVICH, A.B. and STEPHENSON, F.E. (2004), *Longwave measurements for the coast of British Columbia and improvements to the tsunami warning capability*, Natural Hazards *32*(3), 313–343.

RABINOVICH, A.B., THOMSON, R.E., and STEPHENSON, F.E. (2006), *The Sumatra Tsunami of 26 December 2004 as observed in the North Pacific and North Atlantic Oceans*, Surveys in Geophysics *27*, 647–677.

RABINOVICH, A.B. (2008), *Seiches and harbour oscillations*. In *Handbook of Coastal and Ocean Engineering* (ed. Y.C. Kim) (World Scientific, Singapore) (in press).

SATAKE, K. (1995), *Linear and nonlinear computations of the 1992 Nicaragua earthquake tsunami*, Pure Appl. Geophys. 144, 455–470.

SATAKE, K., Wang, K., and Atwater, B.F. (2003), *Fault slip and seismic moment of the 1700 Cascadia earthquake inferred from Japanese tsunami descriptions*, J. Geophys. Res. 108(B11), doi:10.1029/2003JB002521.

SPAETH, M.G. and BERKMAN, S.C. (1967), *The tsunami of March 28, 1964, as recorded at tide stations*, ESSA Technical report C&GS *33*. 86 pp.

STEPHENSON, F., RABINOVICH, A.B., SOLOVIEVA, O.N., KULIKOV, E.A., and YAKOVENKO, O.I. (2007), *Catalogue of Tsunamis, British Columbia, Canada: 1700–2007*, Preprint, P.P. Shirshov Institute of Oceanology, Moscow, Russia, 133 pp.

STEPHENSON, F. and RABINOVICH, A.B. (2009), *Tsunamis on the Pacific Coast of Canada recorded during 1994–2007*, Pure Appl. Geophys. submitted.

TITOV, V. V. and SYNOLAKIS, C. E. (1993), *A numerical study of wave runup of the September 2, 1992 Nicaraguan tsunami,* Proc. IUGG/IOC Inter. Tsunami Symposium (Wakayama, Japan, 1993) pp. 627–635.

TITOV, V.V. and SYNOLAKIS, C.E. (1997), *Extreme inundation flows during the Hokkaido–Nansei–Oki tsunami*, Geophys. Res. Lett. *24*(11), 1315–1318.

VILIBIĆ, I., MONSERRAT, S., RABINOVICH, A.B., and MIHANOVIĆ, H. (2008), *Numerical modelling of the destructive meteotsunami of 15 June 2006 on the coast of the Balearic Islands*, Pure Appl. Geophys. doi 10.1007/s00024-008-0426-5.

WANG, K., WELLS, R., MAZZOTTI, S., HYNDMAN, R.D., and SAGIYA, T. (2003), *A revised dislocation model of interseismic deformation of the Cascadia subduction zone*, J. Geophys. Res. *108*(B1), doi:10.1029/2001JB001227.

WHITE, W.R.H. (1966), *The Alaska Earthquake – Its effect in Canada*, Can. Geogr. J., 210–219.

WHITMORE, P.M. (1993), *Expected tsunami amplitudes and currents along the North American coast for Cascadia Subduction Zone earthquakes*, Natural Hazards *8*(1), 59–73.

WIGEN, S.O., *Historical studies of tsunamis at Tofino*, Canada. in *Tsunamis – Their Science and Engineering* (ed. K. Iida and T. Kawasaki,) (Terra Sci. Publ. Comp., Tokyo, Japan (1983)). pp. 105–119.

WIGEN, S. O. and WHITE, W. R. H. (1964), *Tsunami of March 27–29, 1964, west coast of Canada*, Unpublished manuscript, 6 pp. (Department of Mines and Technical Surveys, Ottawa, 1964).

To access this journal online:
www.birkhauser.ch/pageoph

Evaluating Tsunami Hazard in the Northwestern Indian Ocean

Mohammad Heidarzadeh,[1] Moharram D. Pirooz,[1] Nasser H. Zaker,[2] and
Costas E. Synolakis[3]

Abstract—We evaluate here the tsunami hazard in the northwestern Indian Ocean. The maximum regional earthquake calculated from seismic hazard analysis, was used as the characteristic earthquake for our tsunami hazard assessment. This earthquake, with a moment magnitude of M_w 8.3 and a return period of about 1000 years, was moved along the Makran subduction zone (MSZ) and its possible tsunami wave height along various coasts was calculated via numerical simulation. Both seismic hazard analysis and numerical modeling of the tsunami were validated using historical observations of the Makran earthquake and tsunami of the 1945. Results showed that the possible tsunami may reach a maximum height of 9.6 m in the region. The distribution of tsunami wave height along various coasts is presented. We recommend the development of a tsunami warning system in the region, and emphasize the value of education as a measure to mitigate the death toll of a possible tsunami in this region.

Key words: Northwestern Indian Ocean, Makran subduction zone (MSZ), deterministic tsunami hazard assessment (DTHA), maximum regional earthquake, near-field effects, numerical modeling.

1. Introduction

The great Sumatra–Andaman tsunami of 2004 has awakened the attention of the scientific community to tsunami hazard in the Indian Ocean basin (Okal and Synolakis, 2008). This mega-tsunami was fresh evidence that lack of tsunami hazard understanding in any tsunami-prone coastline can have serious consequences. According to Clague *et al*. (2003), tsunami hazard is normally evaluated by the maximum wave runup, which can be measured as either the elevation reached by the water, or the horizontal distance the wave floods inland. Throughout this paper, the term *tsunami hazard* is considered as referring the vertical runup.

Different methods have been employed by researchers to assess tsunami hazards in various tsunamigenic zones around the world including: (1) analysis of historical tsunami

---
[1] School of Civil Engineering, College of Engineering, University of Tehran, Tehran, Iran.
E-mail: heidarz@ut.ac.ir
[2] Graduate Faculty of Environment, University of Tehran, Tehran, Iran.
[3] Department of Civil Engineering, University of Southern California, Los Angeles, CA 90089-2531, U.S.A.

(e.g., DOMINEY-HOWES *et al.*, 2007), (2) deterministic modeling (e.g., OKAL and SYNOLAKIS, 2008), and (3) probabilistic modeling (e.g., RIKITAKE and AIDA, 1988).

Compilation and analysis of historical data of tsunamis is of primary importance for tsunami hazard assessment. The compiled data yield important information about the return period of tsunamis, the different types of potential tsunamis in the region, the possible tsunami wave heights, and the most vulnerable coastlines to the impact of tsunamis (DOMINEY-HOWES *et al.*, 2007). Such catalogs have been developed for many tsunami-prone coastlines around the world such as Italy (e.g., TINTI and MARAMAI, 1999), Japan (e.g., ABE, 1985), the Mediterranean (e.g., AMBRASEYS, 1962), U.S.A. (e.g., LANDER *et al.*, 1993), and other regions.

When data of historical tsunamis for a particular site are insufficient, tsunami hazard can be calculated using a deterministic method. This method is based on adopting characteristic scenarios considering the largest event known to have hit the area of interest and to simulate this event through numerical modeling (GEIST and PARSONS, 2006). This technique has been used to assess tsunami hazards in some vulnerable coastlines (e.g., OKAL *et al.*, 2006a; TINTI and ARMIGLIATO, 2003).

The probabilistic method is based on the idea underlying seismic hazard assessment (LIN and TUNG, 1982). This method uses a combination of probability analysis for offshore earthquake occurrence and numerical modeling of tsunamis to determine the probability of having a tsunami whose maximum water elevation exceeds a certain value at a coastal site. The method has been employed by some authors (e.g., RIKITAKE and AIDA, 1988).

In this study, we aim at evaluating the tsunami hazard in the Makran subduction zone (MSZ) in the northwestern Indian Ocean (Fig. 1) using a deterministic method. As shown, the MSZ is formed by the northward subduction of the Arabian plate beneath the Eurasian one. This zone extends east from the Strait of Hormoz in Iran to near Karachi in Pakistan with a length of about 1000 km. This region is prone to large subduction tsunamigenic earthquakes from the MSZ. The last tsunami in the region occurred on November 28, 1945, and was produced by an M_w 8.1 earthquake claiming more than 4000 lives (HECK, 1947).

HEIDARZADEH *et al.* (2008a, 2008b) studied historical tsunamis in the MSZ and presented a preliminary estimation of tsunami hazard for this region. HEIDARZADEH *et al.* (2008b) moved a 1945-type earthquake along the MSZ and calculated the maximum positive tsunami wave height along the various coasts in the region. Although their work is of importance for the Makran region whose tsunami hazard had not been studied before, it is believed that more studies should be performed on the seismicity of the region to more accurately estimate its tsunami hazard. In fact, this study is the continuation of the preliminary work performed by HEIDARZADEH *et al.* (2008a, 2008b) on the Makran tsunami hazard assessment to provide a better understanding of the level of tsunami threat faced in this region.

For regions like Makran where the historical record of tsunamis and earthquakes is both short and insufficient, a more accurate tsunami hazard assessment can be performed
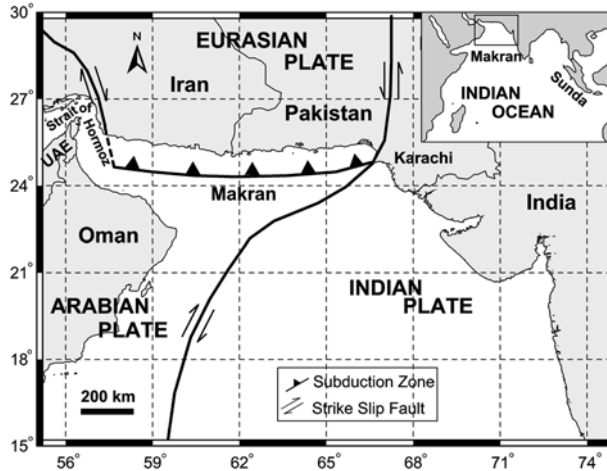
Figure 1
Location map and tectonic setting of the Makran Subduction Zone (MSZ). The inset shows the MSZ compared
to the entire Indian Ocean region.

by application of probabilistic seismic hazard analysis to calculate the maximum regional earthquake, followed by the application of sophisticated hydrodynamic models to calculate possible tsunami wave heights. In this context, we calculated here the maximum magnitude of earthquakes in the MSZ using probabilistic seismic hazard analysis. Subsequently, it was used as the tsunami source in the present deterministic method. Six tsunami scenarios along the MSZ were considered and for each scenario numerical modeling of the tsunami was performed. Also, we discuss the magnitude of the worst possible earthquake in this region and its possible tsunami. The results presented here may assist in developing tsunami preparedness strategies in the northwestern Indian Ocean where the tsunami hazard has been inadequately understood.

2. *Probabilistic Seismic Hazard Analysis and Validation*

The motivations for performing probabilistic tsunami hazard assessment are to calculate the maximum regional magnitude of earthquake in the region, which will then be used as the tsunami source in the next section, and also to estimate the return period of large earthquakes in the region.

The area surveyed for assessing the seismicity comprised a rectangle limited between 23° to 28°N, and 57° to 70°E. A variety of sources was used to compile an earthquake catalog for the MSZ which can be classified as belonging to one of two categories: Historical (non-instrumental) or modern (instrumental). All data concerning events prior to 1900 are of historical type. Modern data consist of hypocenters and instrumentally recorded arrival times from worldwide stations that are reported in various catalogs,
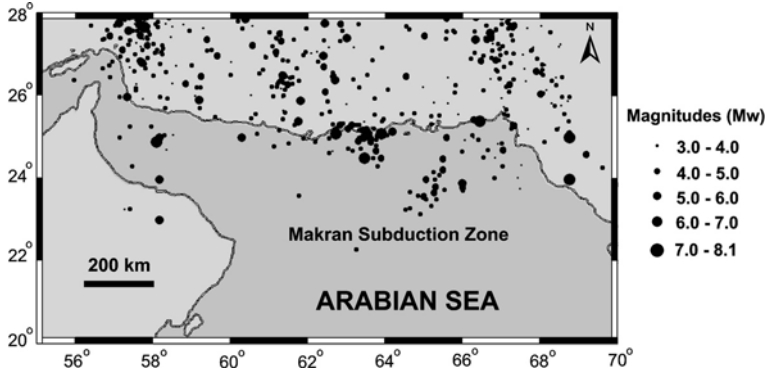
Figure 2
The epicenters and magnitudes of earthquakes in the Makran region.

books and journals. The epicenters and magnitudes of the compiled earthquakes are shown in Figure 2. The maximum observed earthquake in the region is the event of November 28, 1945 with a moment magnitude of 8.1.

The assessment of the recurrence parameters for the MSZ was performed by making use of the procedure developed by KIJKO and SELLEVOLL (1992). Also, the method developed by KIJKO (2004) was employed to calculate the maximum regional earthquake magnitude. Here, we divided the catalog of Makran earthquakes into four parts. The first part contains historical large events (non-instrumental events). The other three parts were complete catalogs including instrumental data each having certain threshold magnitude and standard deviation. The results of seismic hazard assessment for the MSZ are shown in Figure 3. Estimates of the earthquake return periods in the MSZ are shown in Figure 3a. Also, Figure 3b presents the probability of earthquakes with certain magnitudes in the next 1, 50, 100 and 1000 years. For example, based on the results shown in Figure 3, the return period of an M_w 8.1 earthquake is about 250 years in the MSZ, and the probability of having such an earthquake in the next 50 years is about 17.5% in this region. Figure 3 shows that the maximum regional earthquake magnitude in the MSZ is about 8.3 which will be used as the tsunami source in the following sections. The return period of this earthquake is about 1000 years, and the probability of having such an earthquake in the next 50 years is about 5%.

To validate the results of the seismic hazard analysis, we compared our results with previous estimates of the return period of large earthquakes in the MSZ. BYRNE *et al.* (1992) believed that, if all of the plate motion between Eurasia and Arabia occurred during earthquakes like the 1945 event (M_w 8.1), such events would be expected to repeat about every 175 to 300 years in the eastern Makran. By calculating the average uplift rate along the Makran coast, PAGE *et al.* (1979) estimated that the recurrence of a 1945-type earthquake along the MSZ is approximately 125 to 250 years. Our results presented in Figure 3a suggest a return period of about 250 years for a 1945-type earthquake (M_w 8.1), which is in agreement with the previous estimates made of PAGE *et al.* (1979) and BYRNE *et al.* (1992).
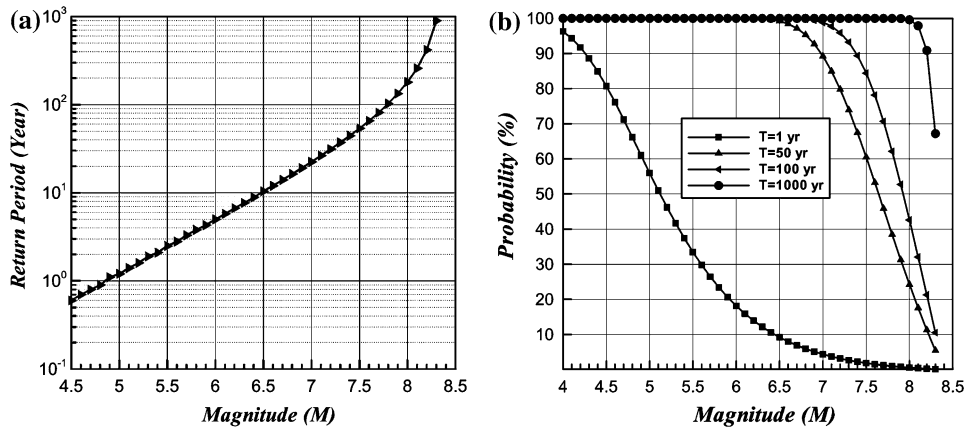
Figure 3
Estimation of earthquake return periods in the MSZ (a), and the probability of earthquakes with certain
magnitudes in the next 1, 50, 100 and 100 years (b).

3. Tsunami Modeling and Verification

The Makran earthquake and tsunami of 1945, which was the only instrumentally recorded tsunami in the northwestern Indian Ocean, was used for validation of our tsunami modeling. Some authors (e.g., AMBRASEYS and MELVILLE, 1982; PAGE *et al.*, 1979) reported that the ocean floor experienced about 2 m of uplift due to this earthquake. The data of the Makran 1945 tsunami wave heights on the coastlines are rather poor and no tide gauge data are available. However, there are some limited data pertaining to tsunami wave heights on some Makran coasts. AMBRASEYS and MELVILLE (1982) reported that the tsunami wave height was approximately 4–5 m in Pasni, about 1.5 m in Karachi, and 2 m in Mumbai. Also, they reported that the tsunami caused extensive flooding of low-lying areas along the Iranian coastline, but no details were presented. PENDSE (1946) reported:

> *"Karachi, which is at a distance of about 276 miles from the epicenter, experienced waves affecting the harbor at 5–30 AM, 7 AM, 7–50 AM and 8–15 AM. The last one was the largest and its height was estimated to be 4.5 ft above normal."*

Other authors reported 12–15 m wave height at Pasni due to the 1945 tsunami (e.g., BERNINGHAUSEN, 1966). HEIDARZADEH *et al*. (2008a) presented evidence that the Makran tsunami of 1945 was associated with other phenomena such as landslides and attributed the large runup of 12–15 m to it. Based on their detailed runup modeling, HEIDARZADEH *et al*. (2008a) concluded that the tectonic source of the 1945 tsunami was capable of producing 4–5 m runup in the near-field (i.e., Pasni), as reported by AMBRASEYS and MELVILLE (1982). Some authors (e.g., AMBRASEYS and MELVILLE, 1982; BILHAM *et al*., 2007) reported that the largest tsunami wave (i.e., wave of 12–15 high) arrived at Pasni about 1.5–2 hours after the earthquake, which supports HEIDARZADEH *et al*.'s (2008a) interpretation of it as belonging to another phenomenon like a submarine landslide.

Table 1

Seismic parameters of the Makran tsunami of 1945 and the maximum regional earthquake (M_w 8.3) used in this study.

Name of event	Dip (°)	Slip (°)	Strike (°)	Depth (km)	Length (km)	Width (km)	Slip (m)	Moment (N m)[a]	Uplift (m)
Maximum Regional Earthquake (M_w 8.3)	7	89	270	27	200[b]	80[b]	8.5[b]	4.08×10^{21}	2.8
1945 Makran Earthquake (M_w 8.1)	7	89	246	27	130	70	6.6	1.80×10^{21}	2.0

[a] The rigidity of the earth is about 3.0×10^{10} N/m² in the Makran region; after BAYER *et al.* (2006).
[b] Estimated using empirical relations of WELLS and COPPERSMITH (1994) and calibrated using the data of the Makran earthquake of 1945.

Here, the algorithm of MANSINHA and SMYLIE (1971) was used to calculate the seafloor deformation due to the earthquake. This algorithm calculates the ground deformation using input seismic parameters that include the strike, dip, and slip angles, the amount of slip, the dimensions of the rupture area (length and width), and the earthquake depth (SYNOLAKIS, 2003). The seismic parameters estimated in the study by BYRNE *et al.* (1992) and calibrated by HEIDARZADEH *et al.* (2008b), were used for tsunami generation modeling which were: 246°, 7°, 89°, 6.6 m, 130 km, 70 km, and 27 km, respectively (Table 1). The maximum calculated uplift using these seismic parameters was about 2 m which was in agreement with the actual observed uplift during the 1945 event.

The numerical model TUNAMI-N2 was used for simulation of propagation and coastal amplification of long waves. The model was originally authored by Nobuo Shuto and Fumihiko Imamura of the Disaster Control Research Center in Tohoku University (Japan) through the Tsunami Inundation Modeling Exchange (TIME) program (GOTO *et al.*, 1997). TUNAMI-N2 is one of the key tools for developing studies for propagation and coastal amplification of tsunamis in relation to different initial conditions (YALCINER *et al.*, 2002). Also, a similar methodology is used in the numerical model MOST (Method of Splitting Tsunami) developed by TITOV and SYNOLAKIS (1998). TUNAMI-N2 and MOST are the only two existing nonlinear shallow water codes, validated with laboratory and field data (YEH et al., 1996).

In this study, we applied bathymetry data provided through the GEBCO (General Bathymetric Chart of the Oceans) digital atlas (IOC *et al.*, 2003). The total number of grid points in the computational domain was 369852, which was 833 × 444 points. The time step was selected as 3.0 s to satisfy the stability condition. The duration time of wave propagation was 4 h in our simulations. Figure 4 presents the results of the numerical modeling of tsunami for the Makran earthquake of 1945. As shown, the distribution of the tsunami wave height along various Makran coasts reproduces most features of the historical observations during this event. Our numerical model successfully reproduces the wave height of about 4–5 m at Pasni as well as 1.5 m in Karachi. The modeling results showed that the largest wave arrives in Karachi about
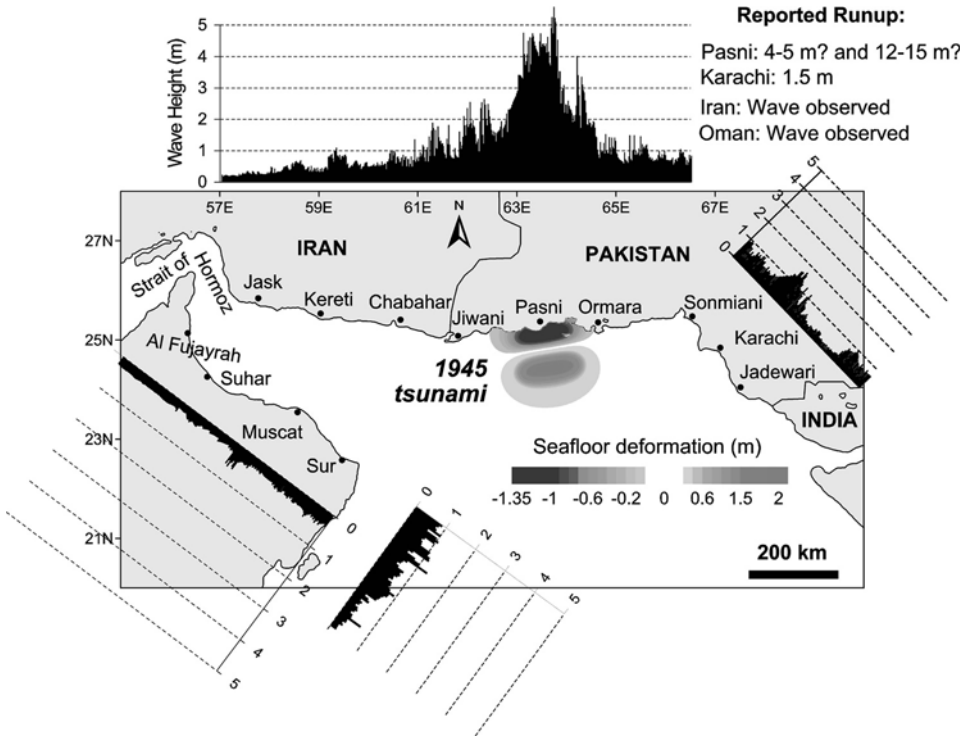
Figure 4

Distribution of the maximum positive tsunami wave heights along the Arabian Sea coasts due to the Makran tsunami of 1945 (after HEIDARZADEH *et al*., 2008b).

120 min after the earthquake, which is in approximate agreement with the historical reports. In addition, Figure 4 shows that the simulated wave heights at the southern coasts of Iran and northern coasts of Oman are less than 1 m, thus it is reasonable since there is scant information regarding the effects of the Makran tsunami of 1945 on these coasts. Also, this is consistent with the results of OKAL *et al*. (2006b) who attempted to find eyewitnesses of the 1945 tsunami in Oman, but found none, although OKAL (2008, personal communication) found one eyewitness who reported 3 m runup in Sur.

4. *Tsunami Scenarios*

The maximum regional earthquake magnitude (M_w 8.3) in the MSZ, estimated in the Section 2, was used for tsunami hazard assessment. Empirical relations proposed by WELLS and COPPERSMITH (1994) were employed to relate the moment magnitude of the earthquake (M_w 8.3) to the fault parameters (rupture length, rupture width and fault displacement). Other seismic parameters were the same as those of the 1945 event (Table 1). However, we used a strike angle of 270° for our source scenarios as the MSZ is
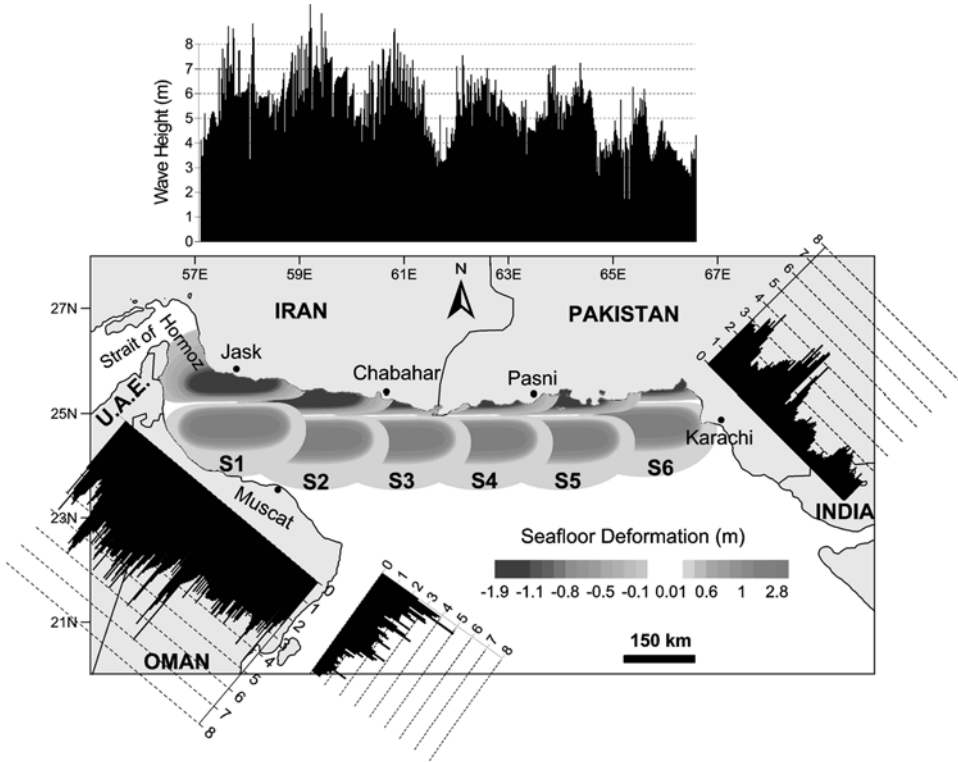
Figure 5

Results of simulations for six tsunami scenarios showing the distribution of maximum positive tsunami wave heights along various coasts.

nearly straight. We note that the predictions made by Wells and Coppersmith's (1994) relations were not directly used here, but we calibrated them using the actual seismic parameters of the Makran earthquake of 1945. As shown in Table 1, the maximum regional earthquake (M_w 8.3) features a seismic moment of about 4.08×10^{21} N m (4.08×10^{28} dyne × cm).

As the entire length of the MSZ is about 1000 km and since every M_w 8.3 earthquake is capable of rupturing about 200 km of the plate boundary, we considered 6 tsunami scenarios with a 25 km overlap between adjacent scenarios (Fig. 5).

5. Results of Deterministic Modeling

The results of tsunami modeling for all of the tsunami scenarios are presented in Figure 5. Also, Figure 6 presents the maximum wave height of the scenario tsunamis as they travel across the Arabian Sea for the case of S4 (Fig. 6a) and S5 (Fig. 6b) along with
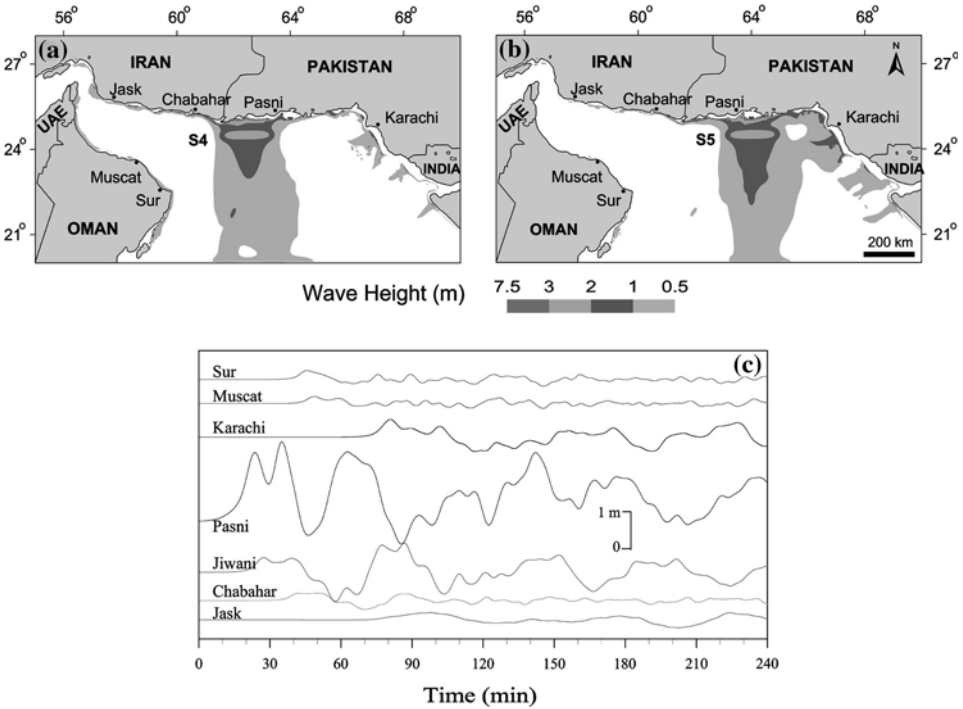
Figure 6

Maximum wave height of the scenario-tsunami as it travels across the Arabian Sea for the case of scenarios S4 (a) and S5 (b), along with the time histories of tsunamis in selected coastlines for the case of S5 scenario (c).

the time histories of the tsunami waves in selected offshore gauges for the case of scenario S5 (Fig. 6c).

Based on Figure 5, the maximum calculated tsunami wave height was about 9.6 m which was due to scenario S2 along the southern coast of Iran. Results showed that, by moving the maximum regional earthquake (M_w 8.3) along the MSZ, the tsunami will reach a height of 4–9.6 m along the southern coasts of Iran and Pakistan, 3–7 m along the northern coast of Oman, 1–5 m along the southern coast of Oman, and 1–4.4 m along the eastern coast of Makran. In their preliminary estimation of the tsunami hazard associated with the MSZ, HEIDARZADEH et al. (2008b) concluded that the southern coasts of Iran and Pakistan will experience the largest wave heights and thus are the coasts with the highest hazard in the northwestern Indian Ocean. However, our results based on the current more comprehensive study, revealed that the northern coast of Oman has hazard as high as the southern coasts of Iran and Pakistan.

Figures 6a,b show that most of the tsunami's energy travels perpendicular to the strike of the fault segment which is evident from the theory of directivity (BEN-MENAHEM and ROSENMAN, 1972). HEIDARZADEH et al. (2008b) showed that tsunamis

originating from the middle and eastern part of the MSZ due to a 1945-type earthquake (M_w 8.1), have minor effects on the Omani and Emirian coasts. Our results, based on an M_w 8.3 earthquake as the tsunami source, support their conclusion, since the maximum wave heights generated by the S4 and S5 scenarios were less than 1 m on the Omani and Emirian coasts (Figs. 6a,b). Therefore, we may conclude that the directivity of tsunami is an important factor when dealing with the tsunami hazard in the northwestern Indian Ocean. HEIDARZADEH *et al.* (2008b) reported up to 2 m of tsunami wave height along the Emirian coast due to a 1945-type earthquake. Our simulations showed a wave height of up to 5 m along this coast. Hence, we repeat the statement made by HEIDARZADEH *et al.* (2008b) that the tsunami hazard of the Emirian coast cannot be neglected.

According to Figure 6c, the tsunami for case S5 will reach the nearest coast (e.g., Jiwani and Pasni) within about 15 min. However, the tsunami travel times to more distant coasts are longer, e.g., about 45 min for the Omani coast, 35 min for Chabahar, and 75 min for Karachi and Jask. Regarding such a short travel time, we believe that the only warning available will be the ground shaking for the nearest coast to the tsunami source, and it is unlikely that a local tsunami warning system could be effective in warning the nearest coast, e.g., Jiwani and Pasni in this case. However, such a system can be used to warn (or to sound an 'all clear' for, which is also an important function of a warning system) the coasts located far to the east, west, or south of the rupture zone, e.g., Jask, Muscat, and Karachi in this case. Therefore, we recommend the development of a tsunami warning system in the northwestern Indian Ocean.

We emphasize that public education is a must. According to SYNOLAKIS and BERNARD (2006), in an era of global citizenship, more comprehensive educational efforts on tsunami hazard mitigation are necessary worldwide. SYNOLAKIS and KONG (2006) reported that simply educating the local populations and training emergency managers in countries at risk in the Indian Ocean region is not enough. In any coastline vulnerable to a tsunami attack, it is important that everyone can identify the precursors of a tsunami attack and knows to evacuate to high ground or inland as quickly as possible, or, if necessary, how to more safely vertically evacuate to well-built structures that are likely to survive (SYNOLAKIS and KONG, 2006). SYNOLAKIS and OKAL (2005) reported that the 1999 Vanuatu tsunami was a milestone in tsunami hazard assessment, showing the value of education as a mitigating factor of the death toll during near-field tsunamis. However, we note that the public must be informed clearly about the level of an expected tsunami threat and about areas at risk.

6. Discussion

The present tsunami hazard assessment was performed by considering the maximum regional earthquake (M_w 8.3) as the tsunami source whose return period is about

1000 years. However, we believe that this earthquake does not represent the worst possible earthquake in the MSZ. Following the 2004 Indian Ocean tsunami and taking into account the lessons learned from this mega-tsunami, OKAL (2007) proposed that the maximum earthquake size expected from a subduction zone depends on the length over which a fault system extends continuously along a convergent plate boundary. This continuous segment is about 500 km for the MSZ as the segmentation of this subduction zone was confirmed by BYRNE *et al.* (1992). By applying the empirical relations of WELLS and COPPERSMITH (1994), the corresponding earthquake magnitude will be about 8.6 in moment magnitude scale. It is evident that such an earthquake and consequent tsunami will be a very rare event, having a far longer return period than that of the maximum regional earthquake (M_w 8.3).

As discussed by HEIDARZADEH *et al.* (2008b), we note that TUNAMI-N2 treats the coastline as a vertical wall, and hence flooding was not permitted in our simulations. In other words, runup calculations were not performed, however the maximum positive tsunami heights along the coast were calculated which provide a reasonable approximation of the runup heights (TINTI *et al.*, 2006; YALCINER *et al.*, 2002). Therefore, it is possible that our results (Fig. 5) underestimate or overestimate the runup heights in some areas where the actual beach topography may have a pronounced influence on the hydrodynamics of tsunami runup.

7. *Conclusions*

To more accurately evaluate tsunami hazard in the northwestern Indian Ocean, a series of tsunamis each resulting from the maximum regional earthquake (M_w 8.3) were simulated. The main findings are:

(1) Based on the results of seismic hazard analysis, the maximum regional earthquake magnitude in the MSZ is M_w 8.3 with a return period of about 1000 years.
(2) The maximum calculated tsunami wave height was about 9.6 m which was obtained along the southern coast of Iran.
(3) The tsunami will reach a height of 4–9.6 m along the southern coasts of Iran and Pakistan, 3–7 m along the northern coast of Oman, 1–5 m along the southern coast of Oman, and 1–4.4 m along the eastern coast of Makran.
(4) As was previously reported by HEIDARZADEH *et al.* (2008b), our results showed that the tsunami hazard of the Emirian coast cannot be neglected.
(5) Our results confirmed HEIDARZADEH *et al.*'s (2008b) conclusion that tsunamis originating from the middle and eastern part of the MSZ have minor effects on the Omani and Emirian coasts.
(6) We recommend the development of a tsunami warning system in the northwestern Indian Ocean.

(7) We emphasize the value of education as an essential measure for mitigating the possible death toll from tsunamis in the northwestern Indian Ocean.

Acknowledgments

REFERENCES

ABE, K. (1985), *Quantification of major earthquake tsunamis of the Japan Sea*, Phys. Earth Planet. Inter. *38*, 214–223.

AMBRASEYS, N. N. (1962), *Data for the investigation of the seismic sea waves in the eastern Mediterranean*, B. Seismol. Soc. Am. *52*, 895–913.

AMBRASEYS, N.N. and MELVILLE, C.P., *A History of Persian Earthquakes* (Cambridge University Press, Britain 1982).

BAYER, R., CHERY, J., TATAR, M., VERNANT, Ph., ABBASSI, M., MASSON, F., NILFOROUSHAN, F., DOERFLINGER, E., REGARD, V., and BELLIER, O. (2006), *Active deformation in Zagros–Makran transition zone inferred from GPS measurements*, Geophys. J. Int. *165*, 373–381.

BEN-MENAHEM, A. and ROSENMAN, M. (1972), *Amplitude patterns of tsunami waves from submarine earthquakes*, J. Geophys. Res. *77*, 3097–3128.

BERNINGHAUSEN, W.H. (1966), *Tsunamis and seismic seiches reported from regions adjacent to the Indian Ocean*, B. Seismol. Soc. Am. *56* (1), 69–74.

BILHAM, R., LODI, S., HOUGH, S., BUKHARY, S., MURTAZA-KHAN, A., and RAFEEQI, S. F. A. (2007), *Seismic hazard in Karachi, Pakistan: Uncertain Past, Uncertain Future*, Seismol. Res. Lett. *78* (6), 601–613.

BYRNE, D.E., SYKES, L.R., and DAVIS, D. M. (1992), *Great thrust earthquakes and aseismic slip along the plate boundary of the Makran subduction zone*, J. Geophys. Res. *97* (B1), 449–478.

CLAGUE, J.J., MUNRO, A., and MURTY, T. (2003), *Tsunami hazard and risk in Canada*, Natural Hazards *28*, 433–461.

DOMINEY-HOWES, D., CUMMINS, P., and BURBIDGE, D. (2007), *Historic records of teletsunami in the Indian Ocean and insights from numerical modeling*, Natural Hazards *42* (1), 1–17.

GEIST, E.L. and PARSONS, T. (2006), *Probabilistic analysis of tsunami hazards*, Natural Hazards *37*, 277–314.

GOTO, C., OGAWA, Y., SHUTO, N., and IMAMURA, F. (1997), *Numerical method of tsunami simulation with the Leap-Frog Scheme (IUGG/IOC Time Project)*, IOC Manual, UNESCO, No. 35.

HECK, N.H. (1947), *List of seismic sea waves*, B. Seismol. Soc. Am. *37*(4), 269–286.

HEIDARZADEH, M., PIROOZ, M. D., ZAKER, N. H., YALCINER, A. C., MOKHTARI, M., and ESMAEILY, A. (2008a), *Historical tsunami in the Makran subduction zone off the southern coasts of Iran and Pakistan and results of numerical modeling*, Ocean Eng. *35* (8–9), 774–786.

HEIDARZADEH, M., PIROOZ, M. D., ZAKER, N. H., and YALCINER, A. C. (2008b), *Preliminary estimation of the tsunami hazards associated with the Makran subduction zone at the northwestern Indian Ocean*, Natural Hazards, doi: 10.1007/s11069-008-9259-x.

IOC, IHO, and BODC (2003), *Centenary edition of the GEBCO digital atlas*, published on CD-ROM on behalf of the Intergovernmental Oceanographic Commission and the International Hydrographic Organization as part of the general bathymetric chart of the oceans, British Oceanographic Data Centre, Liverpool.

KIJKO, A. (2004), *Estimation of the maximum earthquake magnitude m_{max}*, Pure Appl. Geophys. *161*, 1655–1681.

KIJKO, A. and SELLEVOLL, M.A. (1992), *Estimation of earthquake hazard parameters from incomplete data files. Part II: Incorporation of magnitude heterogeneity*, B. Seismol. Soc. Am. *82* (1), 120–134.

LANDER J. F., LOCKRIDGE, P. A., and KOZUCH, M. J. (1993), *Tsunamis Affecting the West Coast of the United States, 1806–1996*, National Geophysical Data Center, Boulder, Colorado, 242 pp.

LIN, I. C. and TUNG, C. C. (1982), *A preliminary investigation of tsunami hazard*, B. Seismol. Soc. Am. *72* (6), 2323–2337.

MANSINHA, L. and SMYLIE, D. E. (1971), *The displacement field of inclined faults*, B. Seismol. Soc. Am. *6*, 1433–1440.

OKAL, E.A. (2007), *Seismic records of the 2004 Sumatra and other tsunamis: A quantitative study*, Pure Appl. Geophys. *164*, 325–353.

OKAL, E. A. and SYNOLAKIS, C. E. (2008), *Far-field tsunami hazard from mega-thrust earthquakes in the Indian Ocean*, Geophys. J. Int. *172* (3), 995–1015.

OKAL, E. A., BORRERO, J. C., and SYNOLAKIS, C. E. (2006a), *Evaluation of tsunami risk from regional earthquakes at Pisco, Peru*, B. Seismol. Soc. Am. *96* (5), 1634–1648.

OKAL, E.A., FRITZ, H.M., RAAD, E.P., SYNOLAKIS, C.E., AL-SHIJBI, Y., and AL-SAIFI, M. (2006b), *Oman field survey after the December 2004 Indian Ocean tsunami*, Earthq. Spectra 22 (S3), S203–S218.

PAGE, W. D., ALT, J. N., CLUFF, L. S., and Plafker, G. (1979), *Evidence for the recurrence of large-magnitude earthquakes along the Makran Coast of Iran and Pakistan*, Tectonophysics *52*, 533–547.

PENDSE, C. G. (1946), *The Mekran earthquake of the 28th November 1945*, India Meteorol. Depart. Sci. Notes *10* (125), 141–145.

RIKITAKE, T. and AIDA, I. (1988), *Tsunami hazard probability in Japan*, B. Seismol. Soc. Am. *78* (3), 1268–1278.

SYNOLAKIS, C.E., *Tsunami and Seiche*, In *Earthquake Engineering Handbook*, (W. F Chen. and C. Scawthorn, eds.), Chapter 9, 1–90 (CRC Press 2003).

SYNOLAKIS, C.E. and OKAL, E.A. (2005), *1992–2002: Perspective on a decade of post-tsunami surveys*. In *Tsunami* (K. Satake, ed.), Advances in Natural and Technological Hazards Research *23*, 1–30.

SYNOLAKIS, C. E. and KONG, L. (2006), *Runup measurements of the December 2004 Indian Ocean tsunami*, Earthquake Spectra 22 (S3), S67–S91.

SYNOLAKIS, C. E. and BERNARD, E. N. (2006), *Tsunami science before and beyond Boxing Day 2004*, Phil. Trans. R. Soc. A *364*, 2231–2265.

TINTI, S. and MARAMAI, A. (1999), *Large tsunamis and tsunami hazard from the new Italian Tsunami Catalog*, Phys. Chem. Earth A *24* (2), 151–156.

TINTI, S. and ARMIGLIATO, A. (2003), *The use of scenarios to evaluate the tsunami impact in southern Italy*, Mar. Geol. *199*, 221–243.

TINTI, S., ARMIGLIATO, A., MANUCCI, A., PAGNONI, G., ZANIBONI, F., YALCINER, A.C., and ALTINOK, Y. (2006), *The generating mechanisms of the August 17, 1999 Izmit Bay (Turkey) tsunami: Regional (tectonic) and local (mass instabilities) causes*, Mar. Geol. *225*, 311–330.

TITOV, V.V. and SYNOLAKIS, C. E. (1998), *Numerical modeling of tidal wave runup*, J. Wtrwy. Port. Cost. Eng. B*124*, 157–171.

WELLS, D. L. and COPPERSMITH, K. J. (1994), *New empirical relationships among magnitude, rupture length, rupture width, rupture area, and surface displacement*, B. Seismol. Soc. Am. *84* (4), 974–1002.

YALCINER, A. C., ALPAR, B., ALTINOK, Y., OZBAY, I., and IMAMURA, F. (2002), *Tsunamis in the Sea of Marmara, historical documents for the past, models for the future*, Mar. Geol. *190*, 445–463.

YEH, H., LIU, P., and SYNOLAKIS, C.E., *Long Wave Runup Models* (World Scientific Publication Company, London 1996), 403 pp.

To access this journal online:
www.birkhauser.ch/pageoph

A Probabilistic Tsunami Hazard Assessment for Western Australia

DAVID BURBIDGE,[1] PHIL R. CUMMINS,[1] RICHARD MLECZKO,[1] and HONG KIE THIO[2]

Abstract—The occurrence of the Indian Ocean Tsunami on 26 December, 2004 has raised concern about the difficulty in determining appropriate tsunami mitigation measures in Australia, due to the lack of information on the tsunami threat. A first step in the development of such measures is a tsunami hazard assessment, which gives an indication of which areas of coastline are most likely to experience tsunamis, and how likely such events are. Here we present the results of a probabilistic tsunami hazard assessment for Western Australia (WA). Compared to other parts of Australia, the WA coastline experiences a relatively high frequency of tsunami occurrence. This hazard is due to earthquakes along the Sunda Arc, south of Indonesia. Our work shows that large earthquakes offshore of Java and Sumba are likely to be a greater threat to WA than those offshore of Sumatra or elsewhere in Indonesia. A magnitude 9 earthquake offshore of the Indonesian islands of Java or Sumba has the potential to significantly impact a large part of the West Australian coastline. The level of hazard varies along the coast, but is highest along the coast from Carnarvon to Dampier. Tsunamis generated by other sources (e.g., large intra-plate events, volcanoes, landslides and asteroids) were not considered in this study.

Key words: Tsunami, probabilistic hazard assessment, Western Australia, earthquake recurrence, Sunda Arc, subduction zone.

1. Introduction

Western Australia appears to experience larger tsunamis with a higher frequency of occurrence than other parts of Australia, primarily due to its proximity to the zone of tectonic activity known as the Sunda Arc, which skirts the southern edge of the Indonesian archipelago. In addition to the Indian Ocean Tsunami of 2004, four tsunami events have affected the coast of Western Australia with runup (maximum inundation height above sea level reached by the tsunami) of 2 meters or more (Fig. 1), with the maximum recorded runup of 9 meters originating from the July 2006 Java earthquake. Although tsunamis have as yet caused no confirmed fatalities in Australia, dozens of bathers on some WA beaches were dragged out to sea (and subsequently rescued by boat) during the 2004 Indian Ocean Tsunami, and campers at Steep point (the purple bar in Fig. 1) were lucky to escape with their lives following the tsunami caused by the 2006 Java earthquake (*The Western Australian*, 19 July, 2006).

---

[1] Geoscience Australia, GPO Box 378, Canberra, ACT 2601, Australia. E-mail: phil.cummins@ga.gov.au
[2] URS Corporation, 566 El Dorado Street, Pasadena, CA, U.S.A.

Assessing just how often and where significant tsunami runup might occur, however, is a difficult problem that would require either an extensive catalogue of historical tsunami inundation events, or sophisticated numerical modelling of the shoaling and inundation that occurs when a tsunami reaches the shoreline. The former does not exist for Western Australia, since there is little or no historical record prior to the 1800s. To the best of the authors' knowledge there has not previously been a probabilistic tsunami hazard assessment specifically for WA, although some preliminary assessments based on limited historic data or a restricted set of numerical models have been completed (RYNN and DAVIDSON, 1999; BURBIDGE and CUMMINS, 2007). Here we present the first probabilistic tsunami hazard assessment for WA expressed in terms of an offshore tsunami amplitude which has a given probability of being exceeded per year. Offshore is defined here to be a water depth of 50 m or greater. Because the modelling of tsunami at this depth or greater is considerably simpler and is less sensitive to shallow bathymetry, thousands of potential sources of tsunami can be simulated, and the results combined into an aggregate 'offshore tsunami hazard map' that should provide some indication of which broad areas of the Western Australian coast are susceptible to tsunami impacts. These areas can then be taken as the focus of subsequent work using more detailed inundation modelling.

The tsunami hazard assessment described here was commissioned by the Fire and Emergency Services Authority of Western Australia (FESA) to cover the coastline of Western Australia. The coastline at which tsunami hazard has been assessed is therefore that of continental Australia west of 130°E longitude. Although results for other coastlines may appear in some figures, the hazard assessment presented here may not be valid for these coastlines (e.g., local tsunami may not have been adequately considered for Christmas Island or Indonesia). The sources considered to have a significant tsunami impact on the coastline of Western Australia are those in the Indian Ocean — in particular the Sunda Arc, east of 90°E longitude and west of 135°E longitude (Fig. 2).

The only type of tsunami source considered in this study are subduction zone earthquakes generated along the Sunda Arc, because they are by far the most frequent source of tsunamis that affect the coast of Western Australia. Three quarters of the world's tsunamis are caused by earthquakes (GUSIAKOV, 2005), and of the 18 historical Indian Ocean-wide tsunami events, only one was not caused by an earthquake (DOMINEY-HOWES *et al.*, 2006). The other sources of tsunamis are:

Volcanic eruptions. The 1883 eruption of Krakatau is the only known major volcanic eruption that has triggered a tsunami which has affected Western Australia. The Krakatau eruption caused a moderate (1–2 m runup) tsunami which was observed all along the WA coast (see Fig. 1). The recurrence time for major eruptions at Krakatau is thought to be 21,000 years (BEAUREGARD, 2001). The potential for other volcanoes in the region generating a tsunami large enough to contribute to the tsunami hazard off WA is unclear.

Asteroid/meteorite impacts. These are a concern for any coastal community, with estimates of return times of 11,000 and 30,000 years for a (respectively) 2 m and a 5 m maximum amplitude offshore tsunami impacting Perth (WARD and ASPHAUG, 2000). More
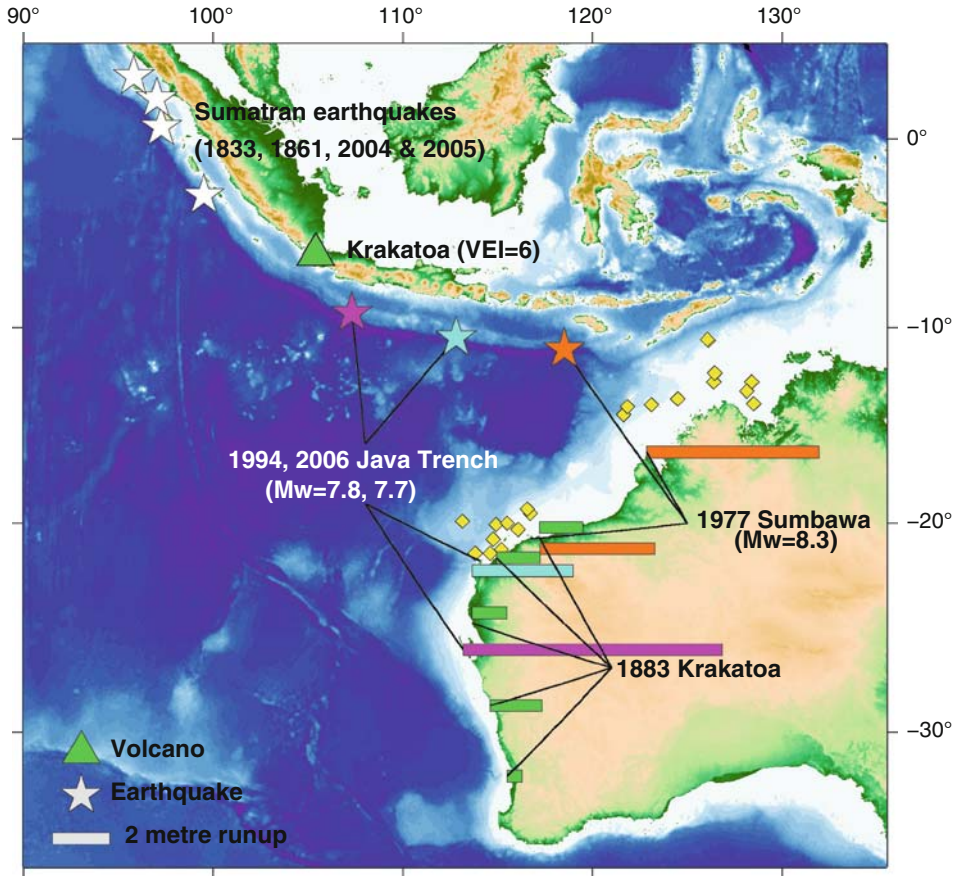
Figure 1

WA Tsunami runup observations and the corresponding tsunamigenic events, with events color-coded to match the runup observations. The basemap shows the bathymetry off the West Australian Coast. M_w is the moment magnitude, while VEI is the Volcanic Explosivity Index, with 6 for Krakatoa being one of the largest in recorded history. There are no recorded observations in Australia of the tsunami events of 1833 and 1861. The length of the columns increases with the height of the observed runup (the scale of the columns is shown in the bottom left hand corner of the figure).

recent work, however, suggests that both the rates and tsunami impacts of the 200–300 m meteors that dominate this hazard source are grossly overestimated (BLAND and ARTEMIEVA, 2003; MELOSH, 2003; KORYCANSKY and LYNETT, 2005)—although CHESLEY and WARD (2006) still consider the higher rates and impacts plausible.

Submarine landslides. Submarine landslides near the coast have the potential to produce large, local tsunamis. While there is evidence of large, potentially tsunami-generating submarine slope failures off Australia's eastern coast (JENKINS and KEENE, 1992), the sparsity of data along the western coast precludes any definitive statement
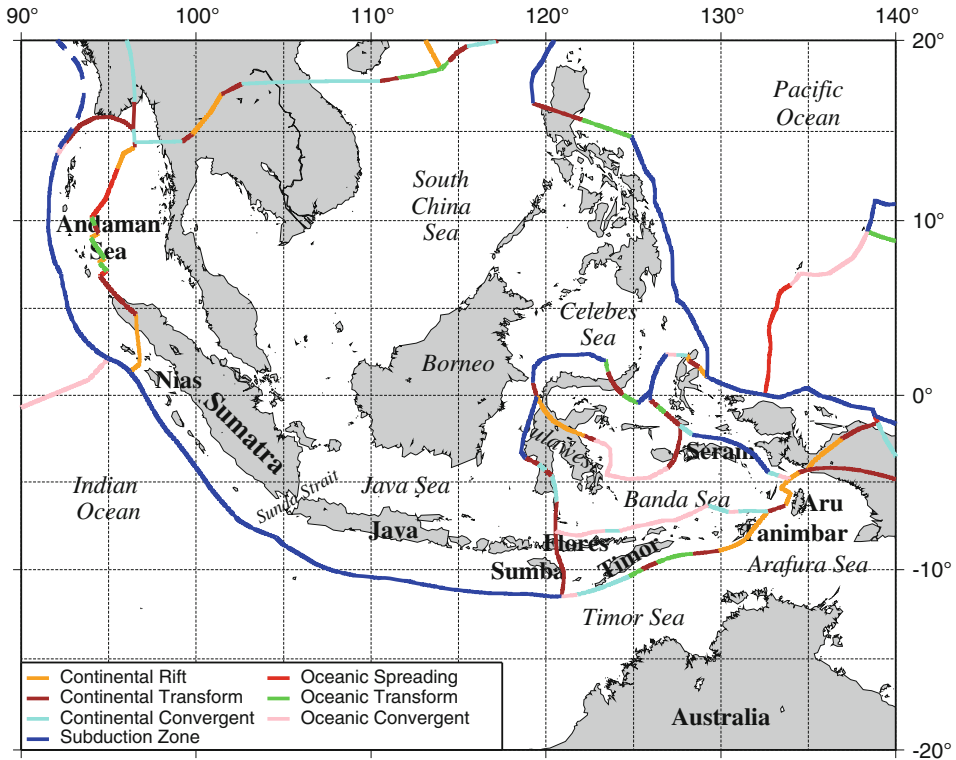
Figure 2

A map of major faults and islands in Indonesia discussed in this study, from BIRD (2003). The northward extension of the Andaman suduction zone (dashed blue line) is from ACHARYYA (1998). In the text we refer to plate boundaries by the name of the nearest island (shown in bold type).

about the frequency of submarine slope failures. It is also thought that ocean-wide tsunamis can be produced by massive failure of a volcanic edifice (WARD and DAY, 2001). Although an argument could be made for possible edifice collapse at Heard/McDonald Island, there is no information on the likelihood of such an event occurring.

While there is some evidence that suggests 'megatsunami', possibly generated by the non-earthquake sources described above, may have impacted Western Australia during the past millennium (NOTT and BRYANT, 2003), the evidence is not conclusive. In any case, what we do know of the above non-earthquake sources of tsunamis suggests the recurrence times of such events will be 10,000 years or more.

In this study, we will only quantitatively estimating the tsunami hazard to WA from tsunamis generated by earthquakes along the Sunda Arc. Not including the other non-Sunda Arc sources like landslides has the effect of underestimating the total tsunami hazard. The magnitude of this effect is difficult to estimate because of the large uncertainty in the frequency of many of these non-Sunda Arc zone sources. However, we

feel that they have the potential to be significant to the hazard for return periods of 10,000 years or longer. Therefore, all hazard maps shown in this paper are for return periods of 2000 years or less, where we feel that tsunamis generated by earthquakes along the Sunda Arc are probably the dominant source of the hazard to WA.

2. *Sunda Arc Earthquake Sources of Tsunami*

In this study we consider the most likely source of tsunamis, earthquakes in the Sunda Arc from the Andaman Islands in the west to Aru in the east (Fig. 2). Although CUMMINS (2007) has suggested that the earthquake potential for the Sunda Arc extends further northward along the coast of Myanmar, as indicated by the dashed line in Figure 2, tsunamis generated by earthquakes along this extension have not been considered here, because they do not direct significant energy towards WA. We also consider tsunamis from the Flores thrust fault to the north of Timor and the Seram subduction zone. In the following sections we discuss the three main regions of the Sunda Arc subduction zone that could produce tsunamis that could affect WA: Sumatra, Java, and Sumba. Unless otherwise specified, we use the moment magnitude values from the Global CMT project (http://www.globalcmt.org/) in this section. However, we acknowledge that various other researchers may give other estimates which can differ by up to about 0.3 units from the USGS value for specific events by using other methods to calculate the magnitude.

The northern most section (called here the Andaman section) was the site of the M_w 9.3 (STEIN and OKAL, 2007) 2004 Andaman earthquake. While this event created the huge Boxing Day tsunami in the northern Indian Ocean, its effects along the WA coast were comparatively small. We consider the Andaman section to be the entire subduction zone from 13°N to the Island of Nias. The Sumatran section lies offshore the Island of Sumatra between the triple junction and the Sunda Strait. The Java section is the subduction zone directly to the south of the Island of Java between the Sunda Strait and approximately 113°E. The Sumba section continues to the east until the subduction zone ends just to the west of the Island of Timor. In the hazard assessments we also include several of the plate boundaries surrounding the Banda Sea; namely: Timor, Tanimbar, Aru, Flores and Seram. Finally, we also discuss the diffuse seismicity between the Indian and Australian plates to the northwest and west of WA.

The purpose of this section is to define the range of sources used in the tsunami hazard map. The discussion of seismicity in the various segments of the Sunda Arc presented here will allow us to establish the combinations of source mechanisms and maximum magnitudes to be used in the logic tree that will serve as the source specification for our hazard map, as described in, e.g., GEIST and PARSONS (2006). Details of this logic tree are presented in Table 1. The dip values for the subduction zones were found by averaging the 0–50 km dip angles of CRUCIANI *et al.* (2005). The maximum seismogenic depth was found by matching the maximum depth of the sub-faults to observed seismicity along each fault. The other columns in Table 1 are determined in the following sections.

Table 1

Geometry and physical properties of the fault segments used in the probabilistic tsunami hazard assessment

Segment Name	Maximum Magnitude (M_w)	Dip (deg)	Maximum Seismogenic Depth (km)	Number p.a.$\geq$ M_w7.0	Slip-rate (mm/yr)
Andaman Megathrust	9.3/9.5[1]	14	50	0.043	
Sumatra Megathrust	9.3/9.5[1]	15	50	0.075	
Java Megathrust	8.5/9.0/9.3/9.5[2]	16	60	0.093	
Sumba Megathrust[3]	8.5/9.0/9.3/9.5[2]	14	60	0.075	
Sumba Normal[3]	8.5/9.0[1]	55	47	0.075	
West Timor Thrust	7.5/8.0[1]	20	17		23.0
East Timor Strike-Slip	7.5/8.0[1]	73	48		17.3
Tamibar Normal	7.5/8.0[1]	55	41		41.0
Wetar-Flores Thrust	8.0/8.5[1]	20	17		34.5
South Aru Strike-Slip	7.5	73	48		47.8
Aru Normal	7.5	55	41		41.0
South Seram Thrust	7.5	20	17		75.7
Seram Megathrust	8.5/9.1[1]	14	30	0.031	
West Seram Thrust	7.5	20	17		64.9

[1] Two models with these maximum magnitudes are considered for this fault segment, each weighted with a 50% chance of being correct.

[2] Four models with these maximum magnitudes are considered for this fault segment, each weighted with a 25% chance of being correct.

[3] Two models are considered for the Sumba section of the Sunda Arc, one with only a megathrust and another with both a megathrust and a normal fault; each model is weighted with a 50% chance of being correct.

2.1. Sumatra-Andaman

Historically most of the larger earthquakes offshore Sumatra appear to be shallow-dipping thrust fault events on the megathrust, as were the 26 December, 2004 M_w 9.3 Andaman earthquake and the 28 March, 2005 M_w 8.6 Nias earthquake, and more recent events in September 2007 (Fig. 3). Great (i.e., larger than magnitude 8.0) thrust earthquakes have also occurred in historic times, prior to the events of 2004 and 2005. NEWCOMB and McCANN (1987) document the occurrence of three major tsunamigenic earthquakes in 1797, 1833 and 1861. More recent analyses of coral microatolls (ZACHARIASEN *et al.*, 1999, and NATAWIDJAJA *et al.*, 2006) have shown that these events likely ranged from magnitude 8.5 to 8.7.

Since 1976, a much smaller number of normal faulting events have occurred to the west of the trench on the outer rise (Fig. 3). This type of earthquake appears to occur much less frequently than the megathrust events, and their magnitudes appear to be considerably smaller (rarely greater than M_w = 7). We therefore discount such events as contributing significantly to the tsunami hazard in Western Australia.

Between the trench and the coast, some strike-slip earthquakes have occurred off Sumatra since 1976. These are thought to be a combination of events on the Mentawai and the Great Sumatran faults. Motion on these faults appears to reflect strain partition of the oblique subduction (BURBIDGE and BRAUN, 1998) in the Sumatra section of the Sunda
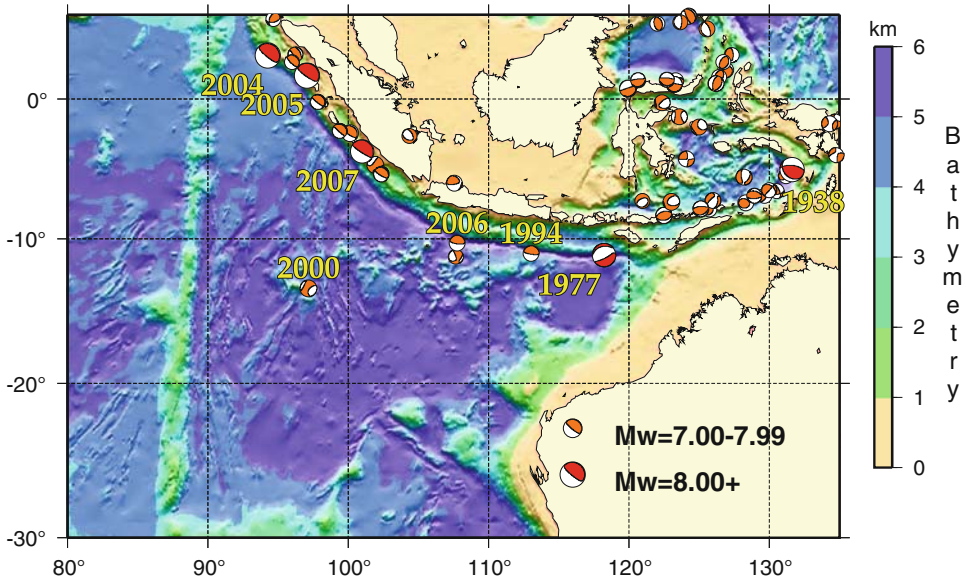
Figure 3

Earthquake focal mechanisms of all the earthquakes in the Global CMT catalogue for the eastern Indian Ocean region since 1976 with $M_w \geq 7.0$ and depth less than 100 km, as well as the mechanism of OKAL and REYMOND (2003) for the 1938 earthquake. The background shows the bathymetry from the ETOPO2 elevation model. Earthquakes discussed in the text have their years indicated.

Arc. The Great Sumatran fault will not produce any tsunami since it is entirely onshore, so it is not included in the tsunami hazard analysis. The Mentawai fault might generate a tsunami, however because it is a strike-slip fault the amount of uplift is likely to be quite small even for a large earthquake. The Mentawai fault is therefore not included in the probabilistic tsunami hazard analysis because it probably has a small maximum magnitude, a low rate of earthquake occurrence, and the earthquakes that do occur are unlikely to generate large tsunamis.

For the reasons described above, only megathrust earthquakes are considered to contribute to the tsunami hazard in WA for the Sumatra-Andaman section of the Sunda Arc. While the maximum magnitude may be only as large as the largest historical event ($M_w = 9.3$, STEIN and OKAL, 2007), the wide megathrust seismogenic zone demonstrated by 2004 and later earthquakes suggests that even larger events may be possible. We therefore consider two branches to the logic tree for this section of the Sunda Arc, one with maximum magnitude of 9.3 and the other with maximum magnitude of 9.5.

2.2. Java

Like the Sumatra section, most of the larger earthquakes offshore Java appear to have been megathrust events. The two largest ones (the M_w 7.8 1994 and M_w 7.7 2006 Java events, see Fig. 3) are both considerably smaller and occurred closer to the trench than the

largest Sumatra events in the same period. Both of these events created significant tsunamis along the WA coast (Fig. 1). The 2006 event created the largest confirmed tsunami runup in Australian history at Steep Point (approximately 9 m, purple bar in Fig. 1). These events also created a damaging tsunami in Java and killed hundreds of people. Both of these events are examples of "tsunami earthquakes" which produce larger tsunamis than expected for their earthquake magnitude. Historical reports (NEWCOMB and MCCANN, 1987) indicate that earthquakes in 1875 and 1859 were large, causing more shaking to Java than recent events, but it is hard to estimate exactly how large any earthquakes may have been before the widespread use of seismographs (i.e., anything before the twentieth century). Other historical earthquakes in 1840, 1859 and 1921 affected an extent of coast similar to the more recent earthquakes and shook Java to a similar level.

While there is now no question that earthquakes of magnitude 9 and greater occur in the western Sunda Arc off northern and central Sumatra, the maximum magnitude of earthquakes occurring in the eastern Sunda Arc off Java is unknown. On the one hand, there are arguments that, because the Australian plate being pushed beneath Java is relatively old, the cooler temperature of the interplate contact will lead to a narrow seismogenic zone, hence smaller earthquakes can be expected off Java (RUFF and KANAMORI, 1980; HYNDMAN and WANG, 1993; OLESKEVICH *et al.*, 1999). This argument is supported by the apparent lack of a wide zone of interplate coupling suggested by geodetic measurements (BOCK *et al.*, 2003). Cooler temperatures would also lead to higher densities, lower buoyancy and potentially weaker coupling which may also influence the maximum magnitude and/or rate of seismic moment release. On the other hand, other studies suggest there is little dependence of subduction zone seismicity (rate or maximum magnitude) on plate age (BIRD and KAGAN, 2004; NISHENKO, 1991; PACHECO *et al.*, 1993), in which case there is no basis for inferring that magnitude 9 earthquakes cannot occur off Java. WELLS *et al.* (2003) have argued that the presence of sedimentary basins between the trench and the coast (the forearc of the subduction zone) correlates with regions of increased megathrust earthquake slip, and since Java and Sumatra both have well developed forearc basins (see, e.g., the seismic reflection profiles of KOPP, 2002), it might be argued that both can host very large earthquakes. Finally, another school of thought suggests that large earthquakes occur when some of the incoming sediment is subducted into a channel between overriding and subducting plates (RUFF and KANAMORI, 1980; RUFF 1989). According to LASKE and MASTERS' (1997) global sediment thickness map, there is a thickness of several kilometers of sediment along the Java trench and even more for southern Sumatra, arguing again for a high maximum magnitude for megathurst earthquakes off Java.

In summary, the age of the plate argues against large earthquakes off Java, but the sediment subduction, rapid convergence and presence of forearc basins argues for it. It should be noted that none of these indications can definitively prove that large earthquakes can or can not occur at a particular subduction zone. In our opinion, the possibility of a large earthquake occurring off Java cannot be ruled out, and we therefore consider a wide range of possible maximum magnitudes for megathrust earthquakes off

Java: 8.5, similar to the largest historical events, but also 9.0, 9.3 and 9.5 (Table 1) to account for the possibility that much larger events occur but are not reflected in the historical record.

2.3. Sumba

To the east of Java there is a major change in the mode of seismicity seen along the Sunda Arc. There have been several major (above magnitude 6.0) normal faulting earthquakes along this section of the Arc. There has also been a host of smaller normal faulting earthquakes right along the trench from Timor to about 113°E. This is a highly unusual pattern of earthquakes for a subduction zone since they are usually dominated by shallow dipping thrust fault earthquakes rather than normal faulting earthquakes. The largest earthquake in this normal faulting sequence was the M_w 8.3 Sumba 1977 event (Fig. 3) which caused a significant tsunami along the northwest coast region of Australia to the south (Fig. 1). This event was located to the south of the trench and had an extensive series of aftershocks, most of which also had normal faulting mechanisms (SPENCE, 1986). The 1977 Sumba event was the largest earthquake to have occurred anywhere along the Arc from the Andaman Sea to Timor during the twentieth century.

The extensive normal faulting along this section of the Sunda Arc suggests that a major change in stress occurs between 113°E and Timor. This could be due to the relatively old (and thus dense) crust subducting along this section of the Arc. The plate itself may be breaking off along a major normal fault at the trench (SPENCE, 1986). This would have the effect of decoupling the megathrust and is consistent with the small number of earthquakes between the trench and the coast. Although there are some earthquakes with a shallow-dipping focal mechanism beneath the Island of Sumba itself (which is consistent with an active megathrust) these are fairly small and quite rare.

In the hazard model, we have two branches to the logic tree representing two different fault models for this section of the Sunda Arc. One has a normal fault extending from 113.5°E to Timor and the other is a shallow-dipping megathrust along the same section of Arc (see Table 1 for details).

2.4. Banda Sea

The tectonic history of the eastern Sunda Arc around the Banda Sea has been the subject of many decades of debate. It has been described by some as one of the most complicated tectonic regions on Earth. The Java trench becomes much more shallow south of Timor. From here to Aru it is known as the Timor Trough. There is no evidence of any large (greater than magnitude 6.0) earthquakes to the south of Timor, though some smaller earthquakes have occurred there. They occur on steeply dipping fault planes, are fairly small, and have only occurred south of West Timor. Most of the major earthquakes in this area have occurred to the north of Timor along the Flores and Wetar thrusts (the pink boundary in Fig. 2 running from east to west and lying just to the north of Timor).

The faults associated with these events are also quite steeply dipping. In between the Flores and Wetar thrusts and the Timor Trough, there is a complicated mixture of earthquake types with no clear dominant mechanism.

To the east, near the Islands of Tanimbar and Aru (Fig. 2), there has been only one major event since 1976 (a M_w 6.9 event in 1988). The events in this region have extensional focal mechanisms. To the north of the Island of Seram we again see shallow-dipping thrust earthquakes between the trench and under the island itself, just like those off the southern coasts of Java and Sumatra. This suggests that a southward-dipping active subduction zone exists in this area beneath the island.

An analysis of GPS measurements by BOCK *et al.* (2003) has shown that the convergence rate between the Australian Plate and the islands of the Sunda Arc immediately to its north decreases dramatically east of Sumba. The convergence rate between the Australian Plate and Timor is low, while the islands further to the north (e.g., Sulawesi) are moving much faster towards Australia than Timor is. This suggests that most of the relative convergence is being accommodated to the north of Timor along the Wetar and Flores thrust faults. The GPS data also indicate that the area around Aru and Tanimbar is extensional since it is moving away from the Australian plate.

In our opinion, the most likely explanation for all these observations is that subduction ceased between Timor and Aru when the Australian plate started to collide with Timor (between 2 million and 10 million years ago). Timor consists of lighter continental crust and so will resist subduction. Most of the convergent motion is now being taken up by the Wetar and Flores thrust faults to the north of Timor. The area to the east near Aru appears to be now undergoing rifting, probably also because of the Timor-Australia collision. The Seram area appears to be the only active subduction zone left in the Banda Sea area.

There is no consensus on the nature of the tectonics in the Banda Sea itself. Some argue that the area is convergent (BIRD, 2003); others argue that it is mostly strike-slip (MCCAFFREY, 1988). The latter is more consistent with the recent focal mechanisms; however they are quite complex and subject to multiple interpretations. The largest earthquake in the Banda Sea itself was the 1938 event (Fig. 3). This event has been estimated to have a magnitude of about M_w 8.6 with a thrust mechanism and to be approximately 60 km deep (OKAL and REYMOND, 2003). It created only a relatively small tsunami for an earthquake of this size, which appears to have caused damage local to the source but did not produce a significant impact in Australia. We believe that any earthquake with a plausible magnitude produced in the central to northern Banda Sea could well produce a local, damaging tsunami in the Banda Sea region. However, any tsunami generated here would be very unlikely to reach Western Australia with a damaging height due to the number of islands between the Banda Sea and Australia.

Due to the great uncertainties and the low likelihood of a hazardous tsunami from the central to north Banda Sea reaching Western Australia, the central Banda Sea itself is not included as a source for the WA tsunami hazard maps. However, the Seram subduction zone, the Timor-Australian plate boundary and the Flores and Wetar thrusts are all

included as earthquake sources in the probabilistic tsunami hazard map, as indicated in Table 1.

2.5. Central Indian Ocean

In June 2000 an M_w 7.9 event occurred about 150 km to the southeast of the Cocos (Keeling) Islands in the middle of the Indian Ocean (the isolated focal mechanism in Fig. 3). Analysis of the event indicates that the earthquake started as a strike-slip event but then may have triggered a simultaneous earthquake on another fault (a compound rupture). The second fault has variously been argued to be another strike-slip fault or a thrust fault (ABERCROMBIE et al., 2003). This earthquake was typical, if large, example of the earthquakes that occur right across the Indian Ocean. Events in this region tend to be a mix of thrust and strike-slip earthquakes. The central Indian Ocean is one of the most seismically active ocean basins, however, its level of activity is still considerably less than the Sunda Arc.

The central Indian Ocean region is currently thought to be a diffuse plate margin separating the Indian and Australian plates (BIRD, 2003). Australia and India are approaching each other by less than 8 mm/yr (BIRD, 2003). Unlike other oceanic plate margins this convergence is being accommodated over a region, which is at least 25 degrees in longitude and 15 degrees in latitude. One transect of the region counted 134 active faults over a distance of 2100 km (CHAMOT-ROOKE et al., 1993). The deformation in this region appears to be accommodated by a complex mix of:

- strike-slip earthquakes along pre-existing transforms formed at the Australian-Antarctic spreading center;
- pre-existing normal faults formed at the spreading center and reactivated as reverse faults; and
- recently formed thrust faults scattered throughout the Indian Ocean.

Since the convergence is spread over so many small faults, the individual slip rate on any fault is probably less than 0.1 mm/yr. Cumulatively this adds up to the still very small ~ 8 mm/yr of relative convergence between the Indian and Australian plates.

There are far too many faults in this area to consider in a probabilistic tsunami hazard assessment using unit sources (like the one done for this study). One would have to use an areal source, similar to the method used in seismic hazard studies in other intra-plate regions, since there is also no known fault map for the area. The slip rates are probably low, so it is quite likely that the effect on the hazard maps to follow will be very small. However, it is worth keeping in mind that there is a small, but non-zero, chance of a major earthquake (up to at least magnitude 8) occurring anywhere in the Indian Ocean. If they are large enough and located close enough to the coast, they may produce a hazardous tsunami. The return periods for a hazardous tsunamigenic events is likely to be very long for any particular fault.

Given the high maximum magnitude and the frequent earthquakes, by far the most likely source of tsunamigenic earthquakes that could affect WA is the Sunda Arc subduction zone off Sumatra and Java. However, it should be remembered that it is still possible (albeit very unlikely) to get tsunamigenic events from earthquakes which could be located anywhere in the Indian Ocean. Such events could potentially be included in a future study of tsunami hazard in this region using area-based sources.

3. Tsunami Hazard Analysis Method

The goal of hazard assessment is to estimate how likely hazardous events are and how large their effects might be. There are two approaches used for hazard assessment: A scenario or deterministic approach that usually focuses on a maximum credible event and historical experience, and a probabilistic approach that considers a broad range of potential events and their likelihoods. In the case of tsunami, the former is normally used for developing inundation maps and evacuation procedures. Because they contain little or no information about likelihood, however, scenario-based methods are of limited usefulness for broader policy and planning decisions. We therefore consider a probabilistic approach here.

Probabilistic Tsunami Hazard Analysis (PTHA, see, e.g., Liu *et al.* 2007; Geist and Parsons, 2006; Ward and Asphaug, 2000; Rikitake and Aida, 1988) was rarely considered until recently—i.e., since the occurrence of the 2004 Indian Ocean Tsunami. PTHA is based on Probabilistic Seismic Hazard Analysis (PSHA, see Cornell, 1968; McGuire, 1976), which is widely used for insurance, planning and design purposes. PSHA considers the probability that some measure of earthquake ground motion, such as Peak Ground Acceleration, may be exceeded at a location of interest. The implementation of PTHA used here, which was described by Thio *et al.* (2008), instead considers the probability that a tsunami wave height will be exceeded immediately offshore at a location of interest. Like almost all implementations of PSHA, the theoretical development of PTHA begins with the assumption that events causing a tsunami exceeding some height follow a time-independent Poisson process (see, e.g., page 128 of Kramer, 1996). Under this assumption, the probability of at least one event occurring in t years that has an offshore tsunami height h greater than h_{crit} at the location of interest i is:

$$P^i(h \geq h_{crit}) = 1 - \exp(-\phi^i(h_{crit})t), \tag{1}$$

where $\phi^i(h_{crit})$ is the annual mean number of events per year that will cause an offshore tsunami height exceeding h_{crit} at the location of interest i. $\phi^i(h_{crit})$ is also known as the *annual frequency of exceedence*. The reciprocal of $\phi^i(h_{crit})$ is known as the 'return period', $\tau^i(h_{crit}) = 1/\phi^i(h_{crit})$. $\phi^i(h_{crit})$ is calculated as the sum over all source zones of the mean number of earthquakes resulting in tsunamis satisfying $h > h_{crit}$ at the location of interest:

$$\phi^i(h_{crit}) = \sum_j N_j(M \geq M^i_{crit}).$$ (2)

Here N_j ($M \geq M^i_{crit}$) is the annual number of earthquakes that occur in source zone j, whose magnitude exceeds M^i_{crit}, which is the magnitude of an earthquake that produces a tsunami whose offshore height is h_{crit} at location i. M^i_{crit} here will be determined by numerically modelling tsunamis from various magnitude earthquakes to the coast. The calculation of the functional form of N_j ($M \geq M^i_{crit}$) can be based on the historic occurrence of subduction zone earthquakes and/or a relationship between the frequency and magnitude of earthquakes, such as the well-known Gutenburg-Richter law. This is considered in more detail in the next section.

3.1. Earthquake Frequency

The simplest way to estimate N_j ($M \geq M^i_{crit}$) for earthquakes or tsunamis is from the frequency at which the event has occurred historically. Unfortunately this method is rarely possible for large earthquakes because they happen so infrequently. Before the 2004 Andaman earthquake, no event greater than magnitude 8 was known to have occurred on this fault, so the above method would give a value for $N_{\text{Andaman}}(M \geq 8.0)$ of zero before 2004, a serious underestimate. The last time an event of this size or larger occurred along this part of the subduction zone may have been long before historical records began. Records of seismicity are rarely long enough to estimate earthquake frequency reliably with this empirical method.

Our alternative method for estimating N_j ($M \geq M^i_{crit}$) for the Sunda Arc subduction zones segments proceeds as follows:

1. Obtain the most comprehensive global catalogue of earthquakes;
2. Determine which events were generated at subduction zones and remove the rest;
3. Work out for this catalogue how many subduction zone earthquakes per annum occur globally above a given magnitude;
4. Find the best recurrence model which fits this data (e.g., the tapered Gutenburg-Richter model). This now gives us the global annual frequency of a subduction zone earthquake N_G ($M \geq M_x$) for any magnitude M_x;
5. Determine the annual frequency of earthquakes above magnitude M_x, $N_j^{sub}(M \geq M_x)$, for subduction zone j. We use the following equation to do this:

$$N_j^{sub}(M \geq M_x) = N_G(M \geq M_x) \frac{v_j L_j}{\sum_i (v_i L_i)},$$ (3)

where v_j is the rate of convergence of subduction zone j and L_j is its length. The sum in the denominator is taken over all subduction zones in the world large enough to host an earthquake of size M_x or greater. The minimum length of the subduction zone required to

host an event of size M_x is assumed to be $L_{MIN} = M_x/\alpha$, where $\alpha = 2.0 \times 10^{-2}$ km^{-1} from SCHOLTZ (2002). This is quite a conservative minimum and is well below the observed length of historic events above magnitude 7 (the minimum magnitude considered here).

6. Determine the fraction of earthquakes for a given subduction zone that is likely to be on the megathrust (as opposed to some other fault in the subduction zone area like the Great Sumatran fault). When the angle of convergence is low the strain is partitioned between strike-slip faults landward of the outer-arc high and slip on the megathrust. Using the formula of BURBIDGE and BRAUN (1998) we can calculate this angle for each subduction zone (assumed to be about 16 degrees for all the megathrust faults used here). For subduction zones with this obliquity angle or less (partitioned subduction zones) we assume that the annual frequency of an earthquake on the megathrust can be found by:

$$N_j(M \geq M_x) = N_j^{sub}(M \geq M_x) \frac{v_j^{con}}{\sqrt{(v_j^{con})^2 + (v_j^{lat})^2}}, \qquad (4)$$

where v^{con} is the convergent component perpendicular to the fault and the lateral component is v^{lat}. For all other (non-partitioned) subduction zones $N_j(M \geq M_x)$ is assumed to be the same as $N_j^{sub}(M \geq M_x)$.

For steps 1–3 we used the results of BIRD and KAGAN (2004). In this paper they classified earthquakes from the PACHECO and SYKES (1992) catalogue according to the nearest plate margin to the earthquake which is appropriate for that earthquake's focal mechanism. They found that all earthquakes across the globe could be approximated by fitting the tapered Gutenburg-Richter (G-R) relationship. The (non-tapered) G-R relationship states that the number of events with magnitude greater than M_x obeys the following relationship:

$$\log[N_G(M \geq M_x)] = a - b \times M_x, \qquad (5)$$

where a and b are two constant numbers. They found that b is always close to 1.0 for small earthquakes, despite the different geological settings. However, for large earthquakes the earthquakes became exponentially less common. So they use a tapered G-R relationship to better fit all earthquakes, large or small. The tapered relationship is given by:

$$N_G(m \geq m_x) = \left(\frac{m_x}{m_t}\right)^{-\beta} \exp\left(\frac{m_t - m_x}{m_C}\right), \qquad (6)$$

where $\beta = 2/3b$, m is the seismic moment, m_t is the seismic moment threshold of the catalogue (i.e., the minimum seismic moment that can be reliably determined) and m_C is the "corner" seismic moment. The seismic moment is related to the magnitude by (PURCARU and BERCKHEMER, 1978):

$$\log m = 1.5M + 9.1. \tag{7}$$

The corner moment (m_C) roughly corresponds to the magnitude at which the G-R relationship began to taper significantly. It is related to the corner magnitude, M_C, by equation (7).

Bird and Kagan (2004) found that the main difference between earthquakes in different geological settings were with their estimates of a and M_C for each setting. In the case of subduction zone earthquakes, Bird and Kagan (2004) argued that there is no statistically significant justification for subdividing the subduction zone setting into smaller subsets (e.g., subduction zones subducting old crust versus subduction zones subducting new crust). The only effect they noticed was that a increases with the rate of subduction (i.e., how fast the plates were moving closer together). The faster the plates converge the more earthquakes above a certain magnitude occur, hence a is larger. For subduction zones they found that M_C was equal to 9.58. The 90% confidence interval for this estimate of M_C had a lower limit of 9.18, but had an unbounded upper limit because of the lack of earthquakes with these high magnitudes in the historic record.

From Bird and Kagan's (2004) data we can calculate their estimate of a for all subduction zones lumped together (based on the Pacheco catalogue and the maximum probability method described in Bird and Kagan (2004)). According to their catalogue, on average 0.5 events greater than M_w 8.0 happen per year somewhere on one of the world's subduction zones. For a Poisson process, this means that the probability of an event greater than M_w 7.5 ocurring somewhere on the globe per year is about 38%.

However, while this is a good estimate of a global frequency of occurrence, we really need an estimate for the specific subduction zones in this study: Sumatra, Java, Sumba and Seram. To calculate this we use equation (3). This equation was chosen in order to partition N_G ($M \geq M_x$) into different subduction zones according to the area being subducted per annum on the subduction zone (vL). Essentially, this implies that earthquakes of a given magnitude are more likely to occur somewhere on a large, fast-moving subduction zone than on a small and/or slowly converging subduction zone. This is motivated by the observation that earthquakes more frequently occur (have a higher a) on faster moving subduction zones than small ones because the rate at which the faults are loaded to failure is faster on rapidly converging subduction zones than on slowly moving subduction zones (Bird and Kagan, 2004). We believe it is also reasonable to assume that an earthquake is more likely to occur on a longer subduction zone than a smaller one because there are simply more places for an earthquake to happen on a large fault than a small one. The accumulation of tectonic moment on the large fault would be much more rapid, and thus the release of seismic moment can be expected to be more rapid too (Kagan, 2002). The frequency of a very large earthquake occurring on a subduction zone with length less than L_{MIN} is zero because the fault is simply too small to host such a large event. Note that splitting up the global seismicity in this way implicitly assumes that the coupling on any given subduction zone is not significantly different from the global average for seismic coupling along megathrusts.

The length and velocity of every subduction zone in the world was calculated using Bird's (2003) digitized plate model. Sections of subduction zones within "orogenic zones" are considered to be distinct from those not within orogenic zones. This splits zones such as the Sunda Arc into two (because Sumatra is within an orogenic zone but Java and Sumba are not). Triple junctions also act to segment subduction zones (i.e., they act like a rupture barrier so that earthquakes on one side cannot propagate to the other). Finally, the Sumba and Java sections were also split into two because of the major change in focal mechanisms that occur there.

When the angle between the fault and the direction of convergence is smaller than a critical angle, the strain is partitioned between strike-slip faults landward of the fault and the megathrust. The strike-slip faults take all the lateral motion, while the thrust fault takes up the convergent component of the motion. Using an argument based on work minimization (Burbidge and Braun, 1998), one can show that the only megathrust fault considered in this study that will be strain partitioned is Sumatra. This is consistent with the fact that only Sumatra has large strike-slip faults between the trench and the coast. Since some of the deformation will be occurring on faults other than the megathrust, this will reduce the frequency of events on the much more tsunamigenic megathrust fault. To represent this we reduce the frequency of all partitioned subduction zones by using equation (4).

Figure 4 shows the return period (the inverse of the annual frequency of exceedence) vs. magnitude for the global subduction zone earthquake catalogue and for six specific subduction zone segments: Java, Sumatra, Sumba, Seram, Nankai (off Japan) and Southern Chile. Our method implies that an event of any given magnitude and year is much more likely on the Java zone, since it is fast and long, and much less likely on Seram, since it is shorter and slower. The Sumba section of the Sunda Arc ends up having much the same frequency of occurrence as the Sumatra section. However, it is important to remember that the Sumba section may or may not be seismically coupled (see discussion in Section 2.3). Since the Sumba section is shorter than the Sumatra section it has a lower maximum magnitude than Sumatra. Events around M_w 9.5 are only possible on long subduction zones like Sumatra, South Chile and Java because of the large area required for a great earthquake of this size. The curves for individual subduction zones flatten at high magnitudes because the tapering of global frequency of earthquakes is almost exactly cancelled by the reduced number of faults big enough to host large earthquakes (the number of large faults decreases exponentially above a certain size, nearly cancelling the exponential taper in equation (6)). This means for the PTHA calculations to follow, we will assume a linear GR relationship up until a given value maximum magnitude. The maximum magnitude chosen depends on fault length and earthquake history along that particular fault.

Nankai and Chile curves are shown in Figure 4 because they have two of the longest catalogues of seismicity anywhere on the globe. The return periods estimated from these catalogues (Scholtz, 2002, for Nankai, and the Servicio Sismologico Universidad de Chile's website for South Chile) are also shown in Figure 4. There have been 11
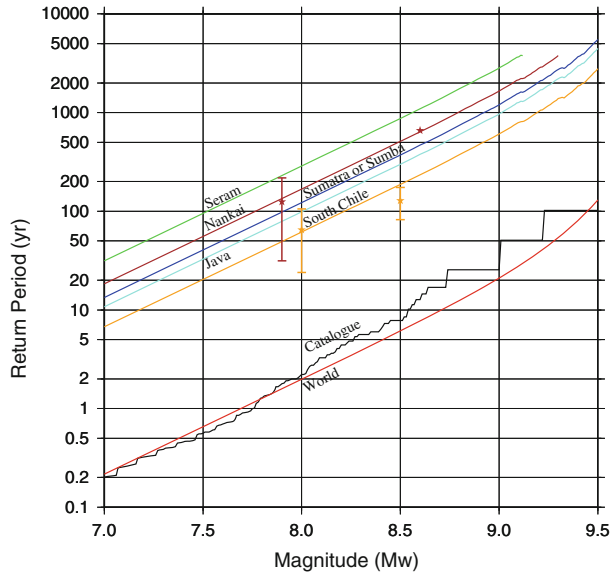
Figure 4

Subduction zone earthquake return period as a function of magnitude. The black line is an empirical model based directly on the maximum probability subset of the Pacheco catalogue (BIRD and KAGAN, 2004). The red line is based on the BIRD and KAGAN's (2004) best fit to these data using the tapered Gutenburg-Richter model. The other lines are the mean return periods for some of the other subduction zones. The zones shown are: Java (cyan), Sumatra (blue), Nankai (brown), Seram (green) and South Chile (orange). The curve for Sumba overlaps Sumatra but has a lower maximum magnitude. The stars with the error bars show the estimated return times from the catalogue by Servicio Sismologico Universidad de Chile and the history of Nankai seismicity described by SCHOLTZ (2002).

events greater than 8.0 on the Nankai subduction zone in the last 1500 years (SCHOLTZ, 2002). Using the historical method this catalogue gives a return period (mean spacing between events of M ≥ 8.0) of 124 ± 93 years. This is statistically indistinguishable from the value calculated with our method (131 years). Similarly the spacing between the two events of magnitude 8.6 or greater (661 years) is very close to our predicted value (640 years).

There is also an extensive seismic catalogue for the southern Chilean subduction zone (the location of the magnitude 9.5 event in 1960). According to the Servicio Sismologico Universidad de Chile's website there have been 7 events greater than 8.0 since 1570. This gives a return period of 65 ± 41 years which compares well with the calculated return period of 61 years. The return period for 8.5 or greater events has been observed to be 128 ± 46 years; our model estimates this to 187 years, again quite close (and still within two standard deviations of the observation). Since the Nankai and Chile subduction zones fit this method quite well, this gives us some confidence that the method we are using here to calculate the return periods is reliable.

The return periods for magnitude 8.0 or greater events for Java, Sumatra, Sumba, Andaman and Seram subduction zones are (respectively) 98 years, 121 years, 122 years, 212 years and 287 years. According to our method, large events occur more frequently on the Java and Sumatra sections of the Sunda Arc than the others studied in this paper. The Sumba megathrust (if coupled) has a similar rate to the Sumatra megathrust. Note that this method does not take into consideration any change in the rate due to the other factors mentioned in the introduction (e.g., sediment, plate age or presence of forearc basins). While these may be linked to the frequency of exceedance, there is currently no way of quantitatively estimating their effect on the earthquake frequency or maximum magnitude. Since this method fits the observations for Nankai and Chile so well, these features may not even be necessary to predict subduction zone earthquake reoccurrence to the accuracy of the historical observations. So for the purposes of this study we will use the values shown in Figure 4 for the subduction zones of interest.

Note that the rates here are for the total seismic release for the subduction zone faults and thus would be comprised of both mainshocks and aftershocks for earthquakes smaller than approximately M_w 7. Thus the observed rate of M_w 7 or smaller events cannot be accurately estimated, even though their return times are less than the instrumental catalogue length, since the number of aftershocks over the last thirty years depends on the number of great (M_w 8+) events over that period. The current rate of M_w 6 and above for Sumatra, for example, is somewhat higher than a direct extrapolation of the curve shown in Figure 4 would suggest, but this is to be expected since the modern catalogue includes a great earthquake and numerous aftershocks above magnitude 6. Thus the instrumental rate of M_w 6 and above over the last few decades may not representative of the long-term rates.

The best value for the maximum magnitude used in the PTHA calculations is highly uncertain, as discussed in Section 2. One can assume that the maximum magnitude is simply a function of length (using SCHOLTZ's, 2002, formula) or we can assume that it is the largest earthquake known for the area. The length restriction limits the Seram subduction zone to a maximum magnitude of approximately 9.1. The Java, Sumatra and Andaman subduction are all long enough to host events up to (and even beyond) magnitude 9.5 (the size of the 1960 Chilean earthquake).

4. Hazard Assessment Results

By combining the information summarized above, we can use the PTHA method to produce a synthetic catalogue of hypothetical earthquakes which includes an estimate of their frequency. The maximum height of the resulting tsunami is then calculated by breaking each fault comprising the tsunamigenic source zones of the Sunda Arc into an array of unit sources. We then numerically model the amount of vertical deformation expected from 1 m of slip on each unit source using WANG *et al.*'s (2005) crustal

Table 2

Crustal properties of the linear elastic crustal layers used to calculate the vertical component of the sea-floor deformation for each unit source

Layer Depth beneath surface (km)	Compressional wave speed (km/s)	Shear wave speed (km/s)	Density (kg/m^3)
0–1	4.5	2.4	2,700
1–13	5.6	3.3	2,700
13–30	6.2	3.7	2,900
30+	7.9	4.6	3,300

deformation model. The crustal model uses three layers above a vertical half space. The parameters of each layer and the halfspace are shown in Table 2.

We then use the vertical component of the crustal deformation as the initial condition for a staggered grid finite-difference numerical model to propagate each tsunami to the coast. The model solves the linear shallow water wave equations over a 2 minute bathymetry grid. The bathymetry data used is a combination of global bathymetry model, DBDB2 V2 (2004) and a downsampled version of Geoscience Australia's 250 m bathymetry model for Australia.

The results of these computations are stored in a rapidly accessible library of unit source 'Green's functions' (i.e., the solution to a differential equation for a point source forcing term). Any one of the tsunami used for the calculation of $\phi^i(h_{crit})$ can then be simulated by appropriately scaling and summing the results for the combination of unit sources that most closely represents the actual earthquake to be simulated. (Note that this type of source decomposition is mathematically valid only for the *linear* shallow water simulations used in this study—e.g., they would not be valid for *non-linear* inundation simulations). For this study, over 5000 earthquakes were simulated in this manner using about 500 unit sources, each corresponding to a 50 km × 50 km subfault. The subfaults were spaced evenly along the strike and down the dip of each fault.

At the end of this process, we now have a maximum tsunami amplitude estimate for each hypothetical earthquake. Since we also have an estimate of the frequency of the earthquake, we can then calculate the wave height which has the required probability of being exceeded (i.e., the tsunami hazard) for points along the WA coast. Below we consider three ways of visualising the hazard: hazard curves, hazard maps, and deaggregated hazard.

4.1. Hazard Curves and Uncertainty

While the goal of any hazard assessment is to give a best estimate of likelihood and impact, it is also important to address the issue of how uncertain these estimates may be. All of the parameters summarized in Table 1 are known with only limited precision, so they all contribute to the uncertainty in this hazard assessment. Other parameters, such as

Figure 5   ▶

Some hazard curves for points off the coast of WA and Java. All the points are in water close to 50 m deep. The *x* axis shows the return period, and the *y* axis shows the wave height exceedances. The blue, cyan, orange and red curves are four models with different estimates of the maximum magnitude earthquake possible on the Java subduction zone (8.5, 9.0, 9.3 and 9.5, respectively). The red curve is usually the "worst case" scenario since it assumes the largest maximum magnitude. The green and black curves are two different models of the Sumba subduction zone. The black curve assumes that the megathrust fault is completely uncoupled and the green one assumes that it is completely coupled to the subducting plate. The thick purple line is our preferred model which is a weighted mean of all the other curves on these figures.

the elasticity of the crust which controls the sea-floor deformation and therefore the size of the initial wave, also contributes to the uncertainty in the final hazard assessment. However, at least for the longer return periods, we believe that two of the largest sources of uncertainty are our poor knowledge of (a) the maximum magnitude of the largest earthquake along the Java section of the trench (M_{max}^{J}) and (b) the presence or absence of a normal fault along the Sumba section of the Sunda Arc. Figure 5 shows some hazard curves (i.e., exceedance height of offshore tsunami as a function of return period) for selected locations off the coast of WA and one for a location on the south coast of Java (near the town of Cilacap). The preferred model is the purple curve in Figure 5. For the preferred model we have given an equal weighting to the $M_{max}^{J} = 8.5$ (blue), 9.0 (cyan), 9.3 (orange) and 9.5 (red) models in the logic tree (i.e., they each have a 25% chance of being correct) and the two Sumba models (i.e., both the normal only (black) and megathrust only (green) fault models have a 50% chance of being correct). Over 5,100 events were included in the preferred (evenly weighted) model, one for each branch of the logic tree. For most locations the preferred model (the purple curve) has a similar hazard curve to the $M_{max}^{J} = 9.0$ model (the cyan curve). Note that this is the "deepwater" wave height at depths of around 50 m. At depths shallower than this the wave shoals significantly and runups could be several times the values shown here. The exact runup amplification factor will vary significantly along the coast depending on the details of the local bathymetry.

The spread in the hazard estimates for the longer return periods shown in Figure 5 gives some idea of the effect of model uncertainty on our hazard estimates. For small return periods the different models do not tend to have much effect on the hazard. At the longer return periods the uncertainty in M_{max}^{J} has a considerable impact on the hazard for locations along the Java coast (like Cilacap) and locations south of about Exmouth (e.g., offshore Fremantle). For locations along the northwest shelf, the model chosen for the Sumba section can also have a significant impact on the wave heights. If only the normal fault is active (the black curve), the hazard is much lower than if only the megathrust is active (the green curve) or if they have a 50/50 chance of being active (the cyan curve). Constraining the wave heights at the longer return periods is always going to be quite uncertain because our historic catalogues do not go back far enough to constrain the maximum magnitudes or (in the case of Sumba) even the type of earthquake we can expect at the zone.
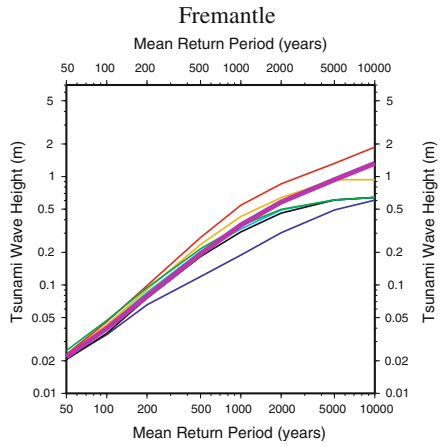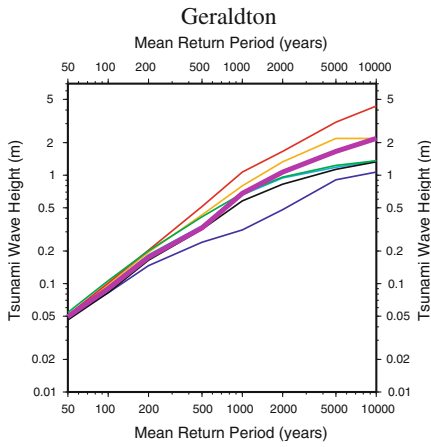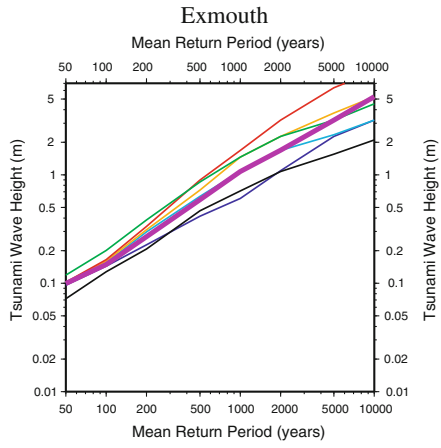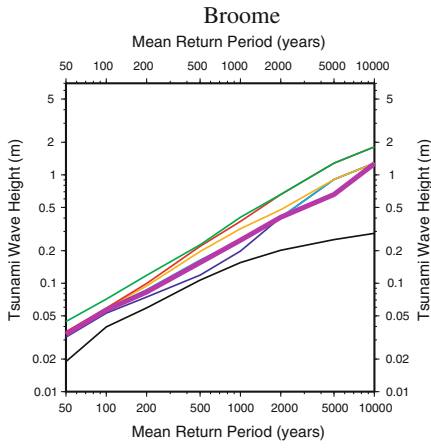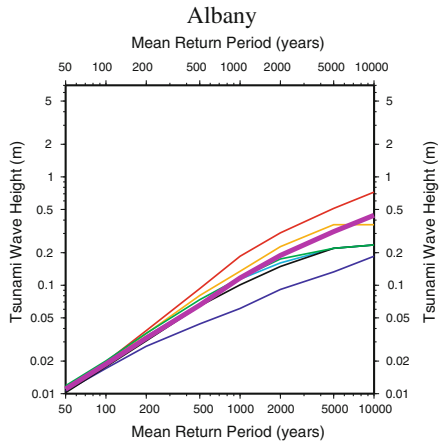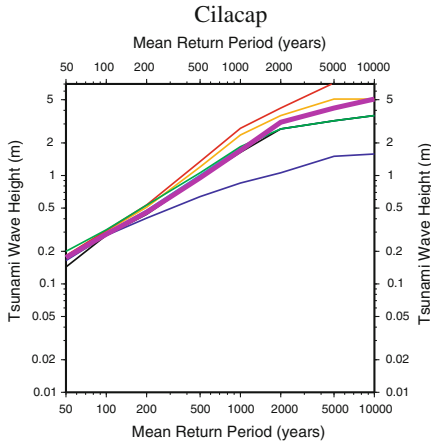
There are other sources of uncertainty which we were not able to include since we needed to keep the number of branches of the logic tree to reasonable values (5,100 branches in this case). For example there is the uncertainty due to errors in the bathymetry, uncertain crustal properties (e.g., elastic parameters) and fault geometry (e.g., dip, rupture area, rupture width, etc). We also assume uniform slip and use the linear shallow water wave equation to solve the propagation of the tsunami. Non-uniform slip is likely to be more important closer to the source (GEIST, 2002), but can also be important in the far field, particularly if islands are in the rupture zone of the earthquake. Nonlinear effects on the wave propagation (such as dispersion) may also become important (HORILLO *et al.*, 2006). All these uncertainties, could in principle, be included in a probabilistic hazard analysis by adding more branches to the appropriate logic trees. However, in practice this is limited by the computational resources available to do the PTHA. Future PTHA are likely to cover a wider range of possibilities than can be considered here, but Figure 5 should give at least some indication of the likely effect of some of the uncertainty for at least M_{max}.

4.2. Hazard Maps

Figure 6 shows the maximum wave heights for different return periods for points interpolated to the 50 m contour off the coast of WA for the preferred model (the purple curve in Figure 5).

The maximum wave heights increase very rapidly with return period. For return periods approaching 2000 years it is very likely that at least one major earthquake (above magnitude 8.5) will occur somewhere along the Java-Sumba sections of the Sunda Arc and create a significant wave. These large waves could inundate a large section of the coast within a few hours, greatly complicating emergency response.

For any given return period, the hazard is largest for WA in the Shark Bay to Exmouth region. The continental shelf tends to reflect energy away from the northwest coast so its hazard tends to be smaller to the northeast of Exmouth. The hazard south of Shark Bay is much lower since it is not in the direct path of any tsunami generated along the Sunda Arc. The hazard along the south coast of WA is very small from tsunami generated by Sunda Arc subduction zone earthquakes since this area of the coast is protected by the Australian landmass.

4.3. Deaggregated Tsunami Hazard

The above results present the variation of offshore tsunami exceedance heights as a function of return period and location along the WA coast. These are based on an aggregate of many different tsunami generated in different parts of the Sunda Arc. These exceedance heights are, therefore, not associated with any particular earthquake or any particular part of the Arc. As discussed above, risk analyses and inundation maps require that inundation modelling be conducted at locations of interest, but these numerical
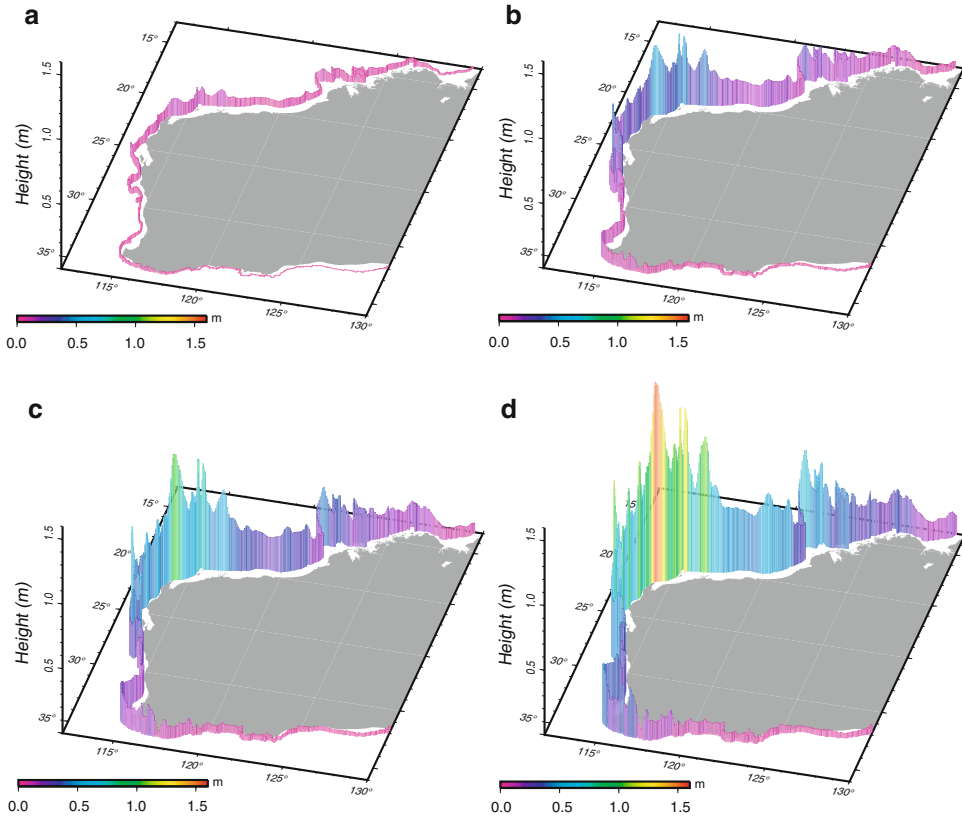
Figure 6

Maximum wave heights along the WA coast (interpolated to the 50 m depth contour) with mean return period of (a) 100 years, (b) 500 years, (c) 1000 years and (d) 2000 years.

computations can only be realistically performed on a per-event basis. Some objective decision must be made then, about which earthquake or set of earthquakes should be used for inundation modelling at a particular location.

The decision of which scenario(s) to simulate for a particular location of interest is complicated by the fact that tsunami propagation is very sensitive to bathymetry, so that it is difficult to tell which part of a coastline will be most affected by a tsunami excited by a given source. This is illustrated in Figure 7a, where the pattern of energy radiated by the 17 July, 2006 Java earthquake is shown. As has been the case for most historical tsunami in WA, most parts of the coast did not experience a significant tsunami during this event, but the combined influence of deep ocean and near-shore bathymetry resulted in pronounced focussing of tsunami energy at a few very limited stretches of coastline. In this case, such focussing lead to a 9 m tsunami runup at Steep Point (purple bar in Fig. 1), the highest ever measured in Australia.
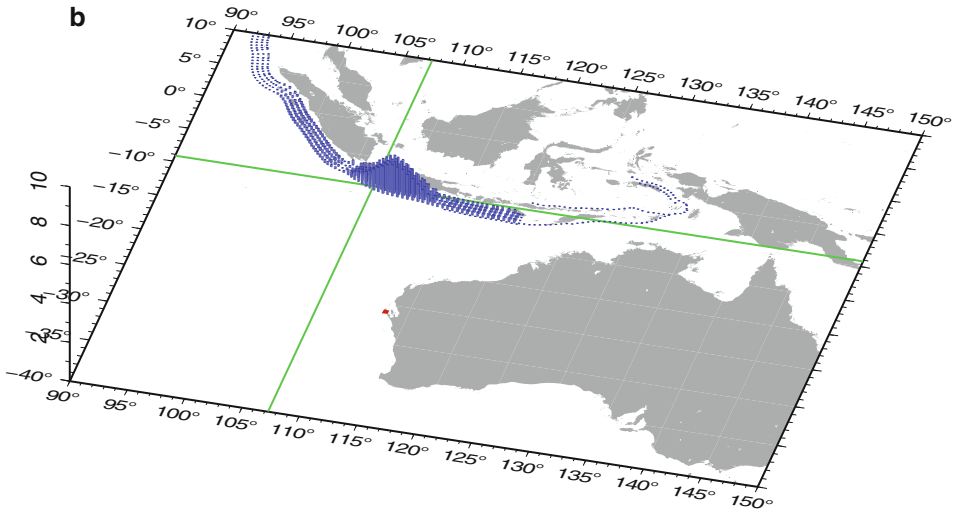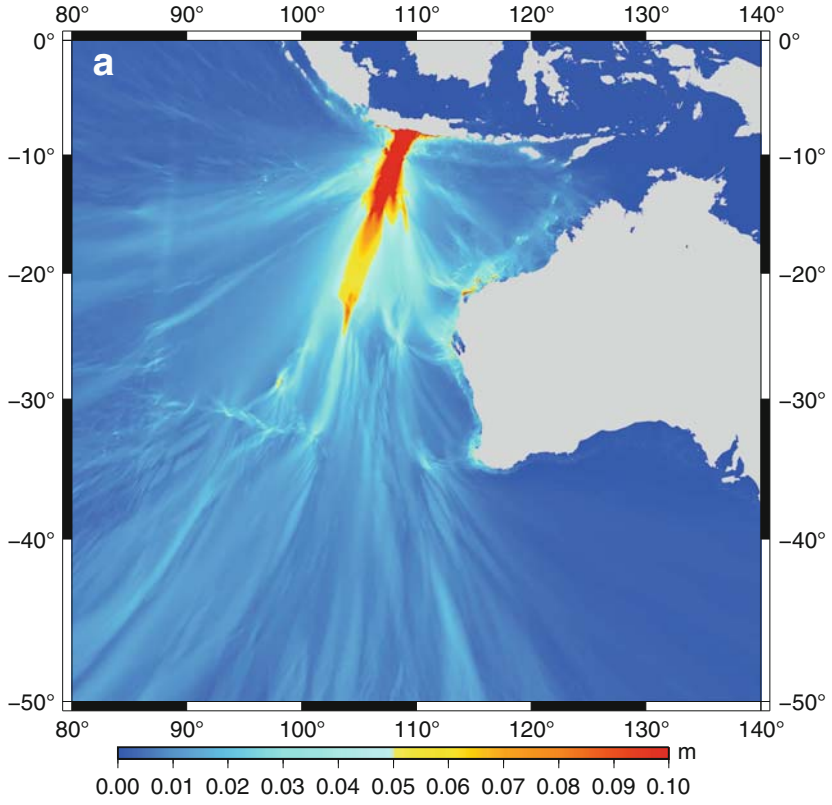
◀   Figure 7
(a) Maximum tsunami amplitude in the Indian Ocean calculated for the 17th July, 2006 Java earthquake, which
resulted in a 9-m tsunami runup at Steep Point, WA; (b) Tsunami hazard deaggregation for Steep Point WA,
showing the tsunami hazard at Steep Point is dominated by earthquakes near the epicenter of the 2006 Java
earthquake (indicated by green crosshairs). The height of the column shows the percentage of the probability
that comes from each unit source for the location of the red dot (Steep Point).

Geographic deaggregation of probabilistic hazard is used in PSHA (e.g., HARMSEN
and FRANKEL, 2001) for the determination of the location of the most probable source
contributing to the hazard at a particular site. This technique is used here to determine
the source locations along the Sunda Arc which make the largest contribution to the
hazard at a particular site of interest, for a given offshore tsunami exceedance height.
Once a particular section of the Sunda Arc has been identified as making the dominant
contribution to the hazard at a site of interest, then one or more scenarios appropriate to
that section of the arc can be used for inundation modelling. This idea is illustrated in
Figure 7b, where the deaggregation for Steep Point (red dot in the fig.) is shown for an
exceedance height of 0.5 m. The deaggregation shows that the 2006 Java earthquake
occurred precisely where we would expect the dominant contribution to tsunami hazard
at Steep Point to originate. If we had been concerned about tsunami impacts at this site,
even prior to the occurrence of the 2006 event, the deaggregation would have suggested
that inundation modelling be performed for a scenario similar to that event. Such
modelling should have established that these events can lead to high runup at Steep
Point, knowledge which may have been useful had it been available at the time of the
tsunami.

Deaggregated tsunami hazard for an exceedance height of 0.5 m is shown in
Figure 8 for Christmas Island and a selection of three sites along the WA coast:
Broome, Exmouth, Freemantle. These show that the bulk of the hazard at this wave
height for communities in the northern part of WA comes from the eastern Sunda Arc
off Sumba (Fig. 8a). For communities further to the south, the most important region
becomes first Java (Fig. 8b) and then to some extent Sumatra (Fig. 8c) becomes
increasingly important. However, for most locations Java is the single most important
section of the Sunda Arc. This is due to both Java being predicted to be quite active and
offshore bathymetry which tends to focus the tsunami towards the coast (Fig. 7a). The
Java section only becomes roughly as important as the Sumatra section for the WA
coast south of Fremantle (Fig. 8c). The hazard faced by Christmas Island, just to the
south of Indonesia, is naturally dominated by the subfaults immediately to the north of
the island, off Java (Fig. 8d).

5. Conclusion

We have completed a probabilistic tsunami hazard assessment for WA for
earthquakes generated by subduction zone earthquakes. The results of this assessment
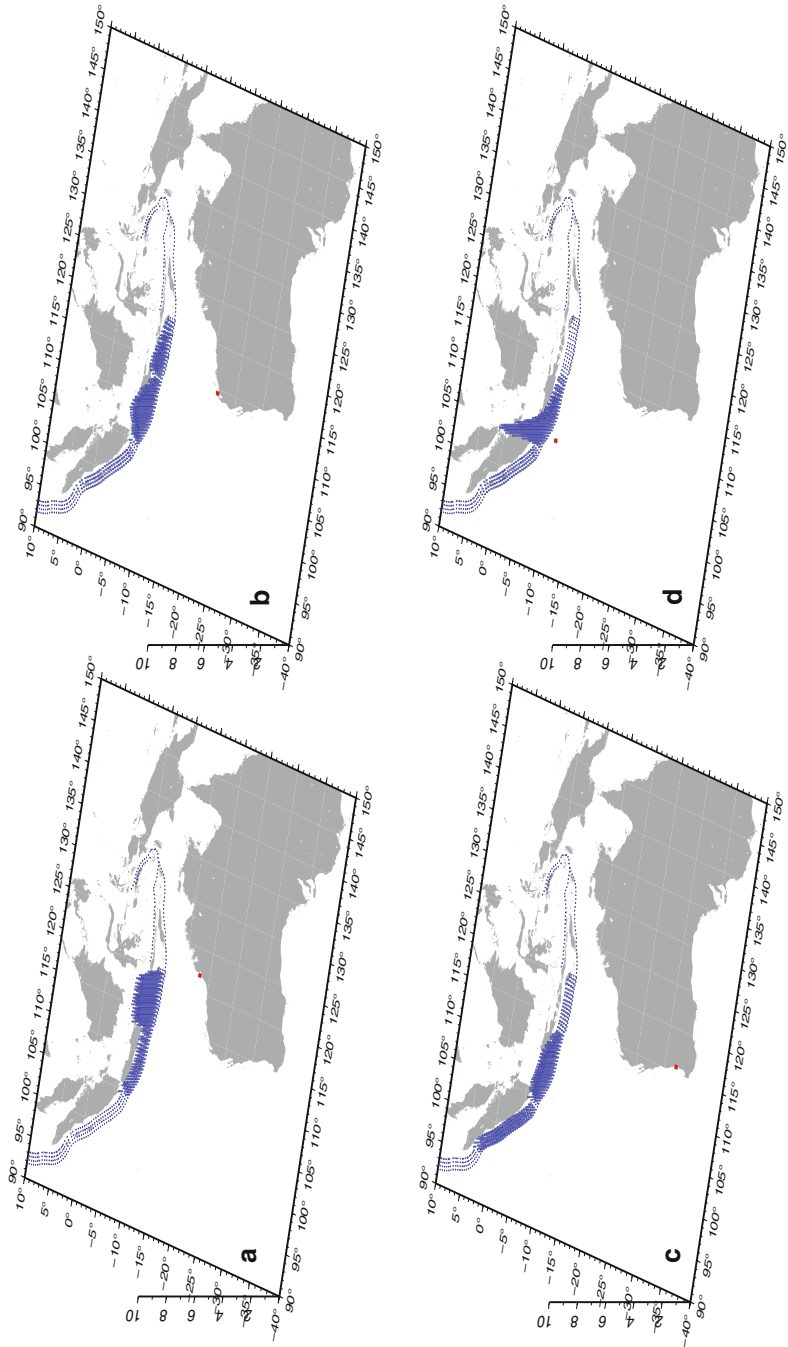
◀   Figure 8
Tsunami hazard deaggregations calculated for a tsunami exceedence height of 0.5 m, for: (a) Broome;
(b) Exmouth; (c) Freemantle, and; (d) Christmas Island. The height of the column shows the percentage of the
probability that comes from each unit source for the location of the red dot.

show that the area offshore Exmouth consistently has the highest hazard (at 50 m water
depth) for any location along the WA coast, and that the hazard is moderate to high
offshore the region roughly between Shark Bay and Dampier, and is moderate offshore
the region between Dampier and Broome. The hazard is much lower further to the
south of Shark Bay, and is very low along the south coast of WA. The hazard
assessment reported here gives an indication of which areas of the WA coastline are
most likely to experience tsunamis, and how likely such events are. The central to
southern part of the west coast is most likely to be affected by the Java segment of
the Sunda Arc, while the northeastern part of the west coast is mostly affected by the
Sumba section of the arc. Bathymetric focussing seems to generate large waves in the
Exmouth area.

    From the perspective of constraining the hazard, one of the urgent priorities
identified by this report is the development of a better understanding of the maximum
size of earthquakes which could occur off Java and Sumba. There have been no
historical events of magnitude 9.0 in this area, but if they occur they will likely
generate tsunami heights on the WA coast considerably larger than what has been
experienced historically. However, accurately estimating slip rates and seismic coupling
for subduction zones is a very difficult scientific problem and is likely to remain so for
some time.

REFERENCES

ABERCROMBIE, R. E., ANTOLIK, M., and EKSTROM, G. (2003), *The June M_w 7.9 earthquake south of
    Sumatra: Deformation in the India-Australia Plate*, J. Geophys. Res. *108*, B1, 2018, doi:10.1029/
    2001JB000674.

ACHARYYA, S. K. (1998), *Break-up of the greater Indo-Australian continent and accretion of blocks framing south and east Asia*, J. Geodynamic *26*, 149–170.

BEAUREGARD, J. O. (2001), *Explosive rhyodacitic volcanism: The evolution and frequency of pre-1883 eruptions at Krakatau volcano, Indonesia*, Ph.d. Thesis, University of Rhode Island, 358 pp.

BIRD, P. (2003). *An updated digital model of plate boundaries*, Geochem. Geophys. Geosys., *4*, 1027, doi:10.1029/2001GC000252.

BIRD, P. and KAGAN, Y. Y. (2004), *Plate-tectonic analysis of shallow seismicity: Apparent boundary width, beta, corner magnitude, coupled lithosphere thickness, and coupling in seven tectonic settings,* Bull. Seism. Soc. Am. *94*, 2380–2399.

BLAND, P. A. and ARTEMIEVA, N. A. (2003), *Efficient disruption of small asteroids in Earth's atmosphere*, Nature *424*, 288–290.

BOCK, Y., PRAWIRODIRDJO, L., GENRICH, J. F., STEVENS, C. W., McCAFFREY, R., SUBARYA, C., PUNTODEWO, S. S. O., and CALAIS, E. (2003), *Crustal motion in Indonesia from Global Positioning System measurements*, J. Geophys. Res. *108*, 2367.

BURBIDGE, D. R. and BRAUN, J. (1998), *Analogue models of obliquely convergent continental plate boundaries*, J. Geophys. Res. *103*, B7, 15,221–15,237.

BURBIDGE, D. and CUMMINS, P. (2007), *Assessing the hazard to western Australia from tsunami generated by earthquakes along the Sunda Arc*, Natural Hazards *43*(3), 319–331.

CHAMOT-ROOKE, N., JESTIN, F., DE VOOGD, B. and PHEDRE WORKING GROUP (1993), *Intraplate shortening in the central Indian Ocean determined from a 2100-km-long north-south deep seismic reflection profile*, Geology *21*, 1043–1046.

CHESLEY, S. R. and WARD, S. N. (2006), *A Quantitative assessment of the human and economic hazard from Impact-generated Tsunami*, Natural Hazards *38*, 355–374.

CORNELL, C.A. (1968), *Engineering seismic risk analysis*, Bull. Seismol. Soc. Am. *58*, 1583–1606.

CRUCIANI, C., CARMINATI, E., and DOGLIONI, C. (2005), *Slab dip vs. lithosphere age: No direct function*, Earth Planet. Sci. Lett. *238*, 298–310.

CUMMINS, P. R. (2007), *The potential for giant tsunamigenic earthquakes in the northern Bay of Bengal*, Nature. *229*, 75–78.

DOMINEY-HOWES, D., CUMMINS, P., and BURBIDGE, D. (2006), *Historic records of teletsunami in the Indian Ocean and insights from numerical modelling*, Natural Hazards Doi: 10.1007/s11069-006-9042-9.

GEIST, E. L. (2002), *Complex earthquake rupture and local tsunamis*, J. Geophys. Res. *107*, 5, 2–1.

GEIST, E. L. and PARSONS, T. (2006), *Probabilistic analysis of tsunami hazards*, Natural Hazards *37*, 277–314.

GUSIAKOV, V. K. (2005), *Integrated tsunami database for the world ocean*, version 5.15, Tsunami Laboratory, ICMMG SD RAS, Novosibirsk, Russia.

HYNDMAN, R. D. and WANG, K. (1993), *Thermal constraints on the zone of major thrust earthquake failure: The Cascadia subduction zone*, J. Geophys. Res. *98*, 2039–2060.

HARMSEN, S. C. and FRANKEL, A. D. (2001), *Geographic deaggregation of seismic hazard in the Untied States*, Bull. Seismol. Soc. Am. *91*, 13–26.

HORRILLO, J., KOWALIK, Z. and SHIGIHARA, Y. (2006), *Wave dispersion study in the Indian Ocean-Tsunami of December 26, 2004*, Marine Geodesy *29*, 149–166.

JENKINS, C. J. and KEENE, J. B. (1992), *Submarine slope failures of the southeast Australian continental slope: A thinly sedimented margin*, Deep-Sea Research *39*, 121–136.

KAGAN, Y. Y. (2002), *Seismic moment distribution revisited: II. Moment conservation principle*, Geophys. J. Int. *149*, 731–754.

KOPP, H. (2002), *BSR occurrence along the Sunda margin: Evidence from seismic data*, Earth Planet. Sci. Lett. *197*, 225–235.

KORYCANSKY, D. G. and LYNETT, P. J. (2005), *Offshore breaking of impact tsunami: The Van Dorn effect revisited*, Geophys. Res. Lett. *32*, 1–4.

KRAMER, S. L., *Geotechnical Earthquake Engineering* (Prentice Hall, New Jersey, 1996).

LASKE, G. and MASTERS, G. (1997), *A Global Digital Map of Sediment Thickness*, EOS Trans. AGU *78*, F483.

LIU, Y., SANTOS, A., WANG, S. M., SHI, Y., LIU, H., and YUEN, D. A. (2007), *Tsunami hazards along Chinese coast from potential earthquakes in South China Sea*, Phys. Earth Planet. Int. *163*, 233–244.

McCaffrey, R. (1988), *Active tectonics of the eastern Sunda and Banda Arcs*, J. Geophys. Res. *93*, B12, 15,163–15,182.

McGuire, R. K. (1976), *FORTRAN computer program for seismic risk analysis*, U. S. Geolog. Survey Open File Report 76–67, pp. 90.

Melosh, H. J. (2003), *Impact-generated tsunamis: An over-rated hazard.* Lunar Planet. Sci. Conf. *34*, Abstract 2013.

Natawidjaja, D. H., Sieh, K., Chlieh, M., Galetzka, J., Suwargadi, B. W., Cheng, H., Edwards, R. L., Avouac, J.-P., and Ward, S. N. (2006), *Source parameters of the great Sumatran megathrust earthquakes of 1797 and 1833 inferred from coral microatolls*, J. Geophys. Res. *111*, doi:10.1029/2005JB004025.

Newcomb, K. R. and McCann, W. R. (1987), *Seismic history and seismotectonics of the Sunda Arc*, J. Geophys. Res. *92*, 421–439.

Nishenko, S. P. (1991), *Circum-Pacific seismic potential: 1989–1999*, Pure Appl. Geophys. *135*, 169–259.

Nott, J. and Bryant, E. (2003), *Extreme marine inundations (tsunamis?) of coastal western Australia*, J. Geology *111*, 691–706.

Okal, E. A. and Reymond, D. (2003), *The mechanism of great Banda Sea earthquake of 1 February 1938: applying the method of preliminary determination of focal mechanism to a historical event*, Earth and Planet. Sci. Lett. *216*, 1–15.

Oleskevich, D. A., Hyndman, R. D., and Wang, K. (1999), *The up-dip and down-dip limits to great subduction zone earthquakes: Thermal and structural models of Cascadia, South Alaska, SW Japan, and Chile*, J. Geophys. Res *104*, 14,965–14,991.

Pacheco, J. F. and Sykes, L. R. (1992), *Seismic moment catalog of large, shallow earthquakes, 1900–1989*, Bull. Seismol. Soc. Am. *82*, 1306–1349.

Pacheco, J. F., Sykes, L. R., and Scholz, C. H. (1993), *Nature of seismic coupling along simple plate boundaries of the subduction type*, J. Geophys. Res. *98*, 14133–14159.

Purcaru, G. and Berckhemer, H. (1978), *A magnitude scale for very large earthquakes*, Tectonophys. *49*, 189–198.

Rikitake, T. and Aida, I. (1988), *Tsunami hazard probability in Japan*, Bull. Seismol. Soc. Amer. *78*, 1268–1278.

Ruff, L. (1989), *Do trench sediments affect great earthquake occurrence in subduction zones?* Pure Appl. Geophys. *129*, 263–282.

Ruff, L. and Kanamori, H. (1980), *Seismicity and the subduction process*, Phys. Earth Planet. Int. *23*, 240–252.

Rynn, J. and Davidson, J. (1999), *Contemporary assessment of tsunami risk and implications for early warning for Australia and its Island Territories*, Sci. Tsunami Hazard *17*(2), 107–125.

Scholtz, C. H., *The Mechanics of Earthquakes and Faulting, Second Edition* (Cambridge Univeristy Press, UK, 2002).

Spence, W. (1986), *The 1977 Sumba earthquake series: Evidence for slab pull force acting at a subduction zone*, J. Geophys. Res. *91*, 7225–7240.

Stein, S. and Okal, E. (2007), *Ultralong Period Seismic Study of the December 2004 Indian Ocean Earthquake and Implications for Regional Tectonics and the Subduction Process*, Bull. Seismol. Soc. Am. *97*, S279–S295.

Thio, H. K., Somerville, P., and Inchinose, G. (2008), *Probabilistic analysis of strong ground motion and tsunami hazards in southeast Asia*, J. Earthquakes and Tsunami, *1*, 119–137.

Tsutsumi, A., Shimamoto, T., Kawamoto, E., and Logan, J. M. (2000), *Nearshore flow velocity of Southwest Hokkaido earthquake tsunami*, J. Waterway, Port, Coastal, and Ocean Engineering, *126*, 136–143.

Wang, R., Martin, F. L., and Roth, F. (2006), *Computation of deformation induced by earthquakes in a multi-layered crust – FORTRAN programs*, EDGRN EDCMP, Comp. and Geosc. *29*, 195–207 (inc. erratum).

Ward, S. N. and Asphaug, E. (2000), *Asteroid impact tsunami: A probabilistic hazard assessment*, Icarus *145*, 64–78.

Ward, S. N. and Day, S. (2001), *Cumbre Vieja volcano — potential collapse and tsunami at La Palma, Canary Islands*, Geophys. Res. Lett. *28*, 3397–3400.

Wells, R. E., Blakely, R. J., Sugiyama, Y., Scholl, D. W., and Dinterman, P. A. (2003), *Basin-centered asperities in great subduction zone earthquakes: A link between slip, subsidence and subduction erosion?* J. Geophys. Res. *108*, 2507, doi:10.1029/2002JB002072.

ZACHARIASEN, M., SIEH, K., TAYLOR, F. W., EDWARDS, R. L., and HANTORO, W. S. (1999), *Submergence and uplift associated with the giant 1833 Sumatran subduction earthquake: Evidence from coral microatolls*, J. Geophys. Res. *104*, 895–919.

To access this journal online:
www.birkhauser.ch/pageoph

Tsunami Probability in the Caribbean Region

Tom Parsons[1] and Eric L. Geist[1]

Abstract—We calculated tsunami runup probability (in excess of 0.5 m) at coastal sites throughout the Caribbean region. We applied a Poissonian probability model because of the variety of uncorrelated tsunami sources in the region. Coastlines were discretized into 20 km by 20 km cells, and the mean tsunami runup rate was determined for each cell. The remarkable ∼500-year empirical record compiled by O'Loughlin and Lander (2003) was used to calculate an empirical tsunami probability map, the first of three constructed for this study. However, it is unclear whether the 500-year record is complete, so we conducted a seismic moment-balance exercise using a finite-element model of the Caribbean-North American plate boundaries and the earthquake catalog, and found that moment could be balanced if the seismic coupling coefficient is $c = 0.32$. Modeled moment release was therefore used to generate synthetic earthquake sequences to calculate 50 tsunami runup scenarios for 500-year periods. We made a second probability map from numerically-calculated runup rates in each cell. Differences between the first two probability maps based on empirical and numerical-modeled rates suggest that each captured different aspects of tsunami generation; the empirical model may be deficient in primary plate-boundary events, whereas numerical model rates lack backarc fault and landslide sources. We thus prepared a third probability map using Bayesian likelihood functions derived from the empirical and numerical rate models and their attendant uncertainty to weight a range of rates at each 20 km by 20 km coastal cell. Our best-estimate map gives a range of 30-year runup probability from 0–30% regionally.

Key words: Tsunami, Caribbean, hazard, earthquake.

1. Introduction

On Sunday, August 4, 1946, a $M = 8.1$ earthquake struck off the northeastern shore of the Dominican Republic that caused extensive damage and loss of life. Luis Miura, a United Press correspondent, described the subsequent tsunami at Ciudad Trujillo: "With a swelling roar it rolled up the bay and smashed against the towns. Dwellings and shops were swept away by the waves. Slabs of walls and roofs were hurled inland from the shore." The tsunami is thought to have killed 1790 people at Matancitas who went to collect fish from the exposed shore when the sea receded after the earthquake; the water returned as a 2.4 m wave that encroached nearly 1 km inland (O'Loughlin and Lander, 2003). Significant runups were recorded at Puerto Rico as well as many other sites on Hispaniola; in this paper we define significant tsunami runup to be in excess of 0.5 m. At least 10 significant tsunamis have been documented in the northern Caribbean since 1498,

---

[1] U.S. Geological Survey, Menlo Park, CA, U.S.A.

six of which are known to have resulted in loss of life. Previous tsunamis destroyed Port Royal, Jamaica, killing an estimated 2000 people in 1692, killed at least 10 Jamaicans on the island's south coast in 1780, and damaged the north coast of Hispaniola and the Virgin Islands in 1842. Population increases mean that now, 35.5 million people in the northern Caribbean region are at risk from tsunami inundation (GRINDLAY *et al.*, 2005).

In this paper we attempt to map out spatial variations in the probability of hazardous Caribbean tsunamis by using the lengthy historic record in combination with numerical modeling techniques. We first calculate purely empirical probabilities using the observed record. We then investigate whether the ∼500-yr historical record is likely to be complete by comparing the observed and expected regional seismic moment as calculated with a finite-element model of Caribbean plate subduction. We then use the modeled slip-rate distribution in combination with tsunami generation and hydrodynamic models for individual earthquakes to calculate multiple synthetic tsunami catalogs. We lastly produce a probability map of the region where tsunami probabilities calculated from the long-term synthetic catalog are combined with the empirical model using a Bayesian method.

2. *Historical Tsunami Catalog*

2.1. *Empirical Runup Frequencies*

A motivating factor in making a probabilistic tsunami hazard assessment for the Caribbean region is the remarkable written record that has its first observation dating back to 1498. We identify 116 individual observations of tsunami runups in excess of 0.5 m in Table 1 that were used to establish empirical estimates of Caribbean tsunami frequency. To calculate empirical tsunami frequency, we gridded the Caribbean region into 20 km by 20 km cells, and summed the number of runup observations ($\geq$0.5 m) in each cell (Fig. 1). The rate within a cell is simply the number of observed events divided by the total observation time. We use the total catalog duration for observation time so that the open intervals can be included.

The empirical tsunami record shows evidence for highest activity in the northern Caribbean region, especially the islands of Hispaniola, Puerto Rico, and the Virgin Islands in the Greater Antilles, and the northern end of the Lesser Antilles along the Caribbean subduction zone (Fig. 1). There is little to no record for much of Cuba and the South American coastline west of Venezuela having been affected in the past 500 yrs, which could be a reporting issue. Although, this pattern of tsunami activity is mirrored by the distribution of large earthquakes (Fig. 2), which would likely be felt regionally.

A key question is to what extent the observed spatial distribution of runups is related to the distribution of earthquake sources vs. areas that might be sheltered from high-amplitude tsunamis by benefit of location (areas protected by other islands that lie in principal propagation paths for example). A further important question regarding the empirical catalog is whether 500 years is long enough to represent the full hazard. For

Table 1

Database of Caribbean tsunami observations with runup ≥ 0.5 m sources: (NOAA online database; O'LOUGHLIN and LANDER, 2003). Runup values are estimates in most cases. Inundation refers to maximum approximate distance water was observed inland from tidal zone.

Tsunami Source					Runup Location		Runup Measurements	
Year	Mo.	Day	Country	Name	Lat.	Lon.	Max water height (m)	Max inundation (m)
1530	9	1	Venezuela	Cumana	10.483	−64.2	6	-
1530	9	1	Venezuela	Isla Cubagua	10.817	−64.183	6	-
1530	9	1	Venezuela	Paria	10.627	−62.167	7.3	-
1692	6	7	Jamaica	Port Royal	17.917	−76.867	1.8	-
1755	11	1	Antigua and Barbuda	Antigua Island	17.12	−61.78	3.7	-
1755	11	1	Barbados	Carlisle Bay	13.083	−59.617	1.5	-
1755	11	1	Cuba	Santiago de Cuba	20	−75.817	-	-
1755	11	1	Dominica	Portsmouth	15.567	−61.45	3.7	-
1755	11	1	Dominican republic	Samana Bay	19.217	−69.317	3.7	-
1755	11	1	Martinique	Martinique	14.667	−61	1.8	-
1755	11	1	Netherlands Antilles	Saba Island	17.633	−63.1	7.6	-
1755	11	1	Saint Martin	Saint Martin Harbor	18.083	−63.083	4.5	-
1755	11	1	Saint Vincent	Lesser Antilles	12	−62	4.5	-
1755	11	18	Saint Martin	Saint Martin Harbor	18.083	−63.083	-	-
1761	3	31	Barbados	Barbados	13.167	−59.533	1.2	-
1780	10	3	Jamaica	Savanna la Mar	18.217	−78.133	3.2	-
1798	2	22	Costa Rica	Barra de Matina	10.005	83.055	0.5	-
1822	5	7	Costa Rica	Barra de Matina	10.005	83.055	0.5	-
1842	5	7	Dominican Republic	Santo Domingo	18.47	−69.95	2	-
1842	5	7	Haiti	(north coast)	19.8	−70.683	2	-
1842	5	7	Haiti	Ile de la Tortue	20.04	−72.75	2	-
1842	5	7	Haiti	Port-de-Paix	19.933	−72.867	4.6	-
1842	5	7	USA Territory	Saint John	17.766	−64.748	3.1	-
1843	2	8	Antigua and Barbuda	Antigua	17.12	−61.85	1.2	-
1853	7	15	Venezuela	Puerto Sucre	10.464	−64.194	5	-
1856	8	9	Honduras	Omoa	15.75	−88.167	5	-
1867	11	18	Antigua and Barbuda	Antigua: St. Johns	17.193	−62.416	2.4	-
1867	11	18	Antigua and Barbuda	West coast	17.717	−61.817	1.4	-
1867	11	18	British Virgin Islands	Peter's Island	18.367	−64.633	1.2	-
1867	11	18	British Virgin Islands	Road Town	18.414	−64.616	1.5	9
1867	11	18	Dominica	Rupert's Bay	15.5	−61.333	3	-
1867	11	18	Grenada	Charlotte Town	12.167	−61.733	3	-
1867	11	18	Grenada	Saint George's	12.015	−61.778	1.5	-
1867	11	18	Guadeloupe	Basse Terre	16	−61.717	1	-
1867	11	18	Guadeloupe	Deshaies	16.317	−61.783	10	-
1867	11	18	Guadeloupe	I'les des Saintes	15.867	−61.617	1	-
1867	11	18	Guadeloupe	Sainte-Rose	16.333	−61.7	10	-
1867	11	18	Saint Lucia	Layon	13.883	−60.967	0.9	-
1867	11	18	Saint Vincent	Bequia island	13.28	−61.25	1.8	146
1867	11	18	St. Thomas	Charlotte Amalie	18.367	−64.933	2.4–4.3	-

Table 1

contd.

Tsunami Source					Runup Location		Runup Measurements	
							Max water height (m)	Max inundation (m)
Year	Mo.	Day	Country	Name	Lat.	Lon.		
1867	11	18	St. Thomas	St. Thomas Harbor	18.367	−64.933	9.1–18.3	-
1867	11	18	St. Thomas	West Gregerie Channel	18.328	−64.955	9	-
1867	11	18	St. Thomas	Little Saba	18.341	−64.982	12	-
1867	11	18	St. Thomas	Water Island	18.323	−64.952	7	-
1867	11	18	St. Thomas	Hassel Island	18.3	−64.96	4.9	-
1867	11	18	St. Thomas	Prince Rupert's Ledge	18.33	−64.926	7	-
1867	11	18	St. Croix	Christiansted and Frederiksted	17.756	−64.799	7.6–9	-
1867	11	18	USA Territory	Puerto Rico: Arroyo	17.983	−66.05	6.1	40
1867	11	18	USA Territory	Puerto Rico: Bahia de San Juan	18.45	−66.117	0.9	-
1867	11	18	USA Territory	Puerto Rico: Fajardo	18.34	65.66	6.1	-
1867	11	18	USA Territory	Puerto Rico: Salinas	17.975	−66.29	6.1	-
1867	11	18	USA Territory	Puerto Rico: Vieques	18.15	−65.45	6.1	-
1867	11	18	USA Territory	Puerto Rico: Culebra	18.305	−65.3	6.1	-
1867	11	18	USA Territory	Puerto Rico: Yabucoa	18.033	−65.883	1.37	-
1867	11	18	USA Territory	Charlotte amalie	18.367	−64.933	6	-
1867	11	18	USA Territory	Frederiksted	17.717	−64.883	7.6	76
1867	11	18	USA Territory	Hassel Island	18.3	−64.96	4.9	-
1867	11	18	USA Territory	Saint Croix	17.75	−64.75	7	-
1868	3	17	Saint Vincent	Bequia Island	13	−61.25	0.9	21
1868	3	17	USA Territory	Puerto Rico: Arroyo	17.983	−66.05	1.5	-
1868	3	17	USA Territory	Charlotte Amalie	18.367	−64.933	0.6	-
1882	9	7	Panama	San Blas Archipelago	9.533	−78.917	3	-
1900	10	29	Venezuela	Puerto Tuy	10.333	−65.917	10	-
1902	8	30	Martinique	Fort de France	14.6	−61.083	1	-
1906	1	31	Panama	Naos Is.	8.917	−79.533	0.7	-
1907	1	14	Jamaica	Annotto Bay	18.267	−76.767	2.2	9
1907	1	14	Jamaica	Buff Bay	18.233	−76.667	2.5	-
1907	1	14	Jamaica	Hope Bay	18.2	−76.567	2.5	-
1907	1	14	Jamaica	Kingston Harbor	17.967	−76.8	2.5	-
1907	1	14	Jamaica	Ocho Rios	18.4	−77.1	2.5	-
1907	1	14	Jamaica	Orange Bay	18.367	−78.317	2.5	-
1907	1	14	Jamaica	Port Antonio	18.167	−76.45	2.5	-
1907	1	14	Jamaica	Port Maria	18.367	−76.9	2.4	-
1907	1	14	Jamaica	Saint Ann's Bay	18.433	−77.2	2.5	-
1907	1	14	Jamaica	Sheerness Bay	18.317	−76.8	2.5	-
1916	4	25	Panama	Isla Col–n	9.385	−82.265	0.5	-
1916	4	25	Panama	Bocas del Toro	9.333	−82.55	0.6	-
1916	4	25	Panama	Careening Cay	9.333	−81.75	1.3	-
1918	10	11	British Virgin Islands	Tortola Island	18.667	−64.65	0.7	-
1918	10	11	Dominican Republic	Rio Ozama	18.47	−69.95	0.7	-

Table 1

contd.

Tsunami Source					Runup Location		Runup Measurements	
							Max water height (m)	Max inundation (m)
Year	Mo.	Day	Country	Name	Lat.	Lon.		
1918	10	11	USA Territory	Puerto Rico: Aguadilla	18.45	−67.133	3.7	-
1918	10	11	USA Territory	Puerto Rico: Arecibo	18.448	−66.733	0.6	-
1918	10	11	USA Territory	Puerto Rico: Bahia de Boqueron	18.463	−66.084	1.1	-
1918	10	11	USA Territory	Puerto Rico: Caja de Muertos	17.867	−66.533	1.5	15
1918	10	11	USA Territory	Puerto Rico: Cayo Cardona	17.959	−66.365	0.75	-
1918	10	11	USA Territory	Puerto Rico: Guanica	17.983	−66.917	0.5	-
1918	10	11	USA Territory	Puerto Rico: Isabela	18.5	−67.033	2	-
1918	10	11	USA Territory	Puerto Rico: Isla Mona	18.08	−67.9	4	-
1918	10	11	USA Territory	Puerto Rico: Mayaguez	18.217	−67.15	1.5	-
1918	10	11	USA Territory	Puerto Rico: Punta Agujereada	18.51	−67.167	6.1	-
1918	10	11	USA Territory	Puerto Rico: Punta Borinquen	18.484	−67.169	4.5	100
1918	10	11	USA Territory	Puerto Rico: Punta Higuero	18.367	-67.267	5.5	-
1918	10	11	USA Territory	Puerto Rico: Rio Culebrinas	18.4	−67.183	4	-
1918	10	11	USA Territory	Puerto Rico: Rio Grande de Loiza	18.45	−65.883	1	-
1918	10	11	USA Territory	Saint Thomas: Krum Bay	18.329	−64.961	1.2	-
1931	10	1	Cuba	Playa Panchita	22.95	−80.417	1	-
1946	8	4	Dominican Republic	Northern coast	19.7	−70.5	4.6	-
1946	8	4	Dominican Republic	Nagua	19.417	−69.817	5	-
1946	8	4	Dominican Republic	Rio Boba	19.467	−69.867	5	-
1946	8	4	USA Territory	Puerto Rico: San Juan	18.483	−66.133	0.66	-
1946	8	8	USA Territory	Puerto Rico: San Juan	18.483	−66.133	0.6	-
1953	5	31	Dominican Republic	Puerto Plata	19.8	−70.683	0.06	-
1969	12	25	Barbados	Barbados	13.167	−59.533	0.46	-
1976	2	4	Honduras	Puerto Cortes	15.833	−87.917	0.45	-
1969	12	25	Dominica	Dominica	15.5	−61.3	0.12	-
1985	3	16	Guadeloupe	Basse Terre	16	−61.717	0.12	-
1989	11	1	USA Territory	Puerto Rico: Cabo Rojo	18.083	−67.15	0.1	-
1991	4	22	Costa Rica	R'o Mo'n	9.73	−82.84	3	-
1991	4	22	Costa Rica	Puerto Viejo	10.5	−83.5	2	-
1991	4	22	Panama	Coco Solo	9.37	−79.881	0.76	-
1991	4	22	Panama	Isla de Carenero	9.33	−82.33	2–3	-
1991	4	22	Panama	Portobelo	9.55	−79.617	0.6	-
1997	12	26	Montserrat	Old Road Bay	16.737	−62.236	3	80

Table 1

contd.

Tsunami Source					Runup Location		Runup Measurements	
							Max water height (m)	Max inundation (m)
Year	Mo.	Day	Country	Name	Lat.	Lon.		
2003	7	12	Guadeloupe	Deshaies	16.317	−61.783	1	25
2003	7	12	Guadeloupe	Vieux Habitants	16.05	−61.75	0.6	-
2003	7	12	Montserrat	Farm Bay	16.737	−67.153	4	-

example, it is evident that the southern part of the Caribbean subduction zone in the Lesser Antilles has produced fewer earthquakes and tsunamis during the past 500 years than has the northern part (Figs. 1, 2). This might reflect genuine differences in the seismic production of the zone, or the southern part of the subduction zone might represent a seismic gap waiting to be filled. We address these issues in detail in Sections 4 and 5. In the next section, we pursue calculation of empirical tsunami probabilities under the assumption that the catalog observations are complete and representative.

3. Monte Carlo Estimation of Rate-Model Uncertainty

Tsunamis affect broad areas as they propagate away from their sources, and a region as complex as the Caribbean has widely distributed tsunamigenic sources. Since tsunamis resulting from multiple seismic sources operating at different recurrence intervals can affect a given coast, the best probability model is one that is time-independent, such as a Poisson process built around an exponential distribution (e.g., GEIST and PARSONS, 2006; 2008). We thus used observed tsunami runups to calculate rate parameters (λ) in the exponential probability density distribution as

$$f(t) = \lambda e^{-\lambda t}, \quad \text{for } t > 0, \tag{1}$$

which when integrated over a given duration gives a time-independent cumulative probability.

Estimation of the event rate λ (inverse of the recurrence interval) for a small number of observations is subject to considerable uncertainty. Further, since the observation period begins at an arbitrary time, and we have no knowledge of what happened before 1498, we wish to treat the first open interval properly. To accomplish both objectives, we rely on Monte Carlo modeling of the tsunami runup frequencies (PARSONS, 2008).

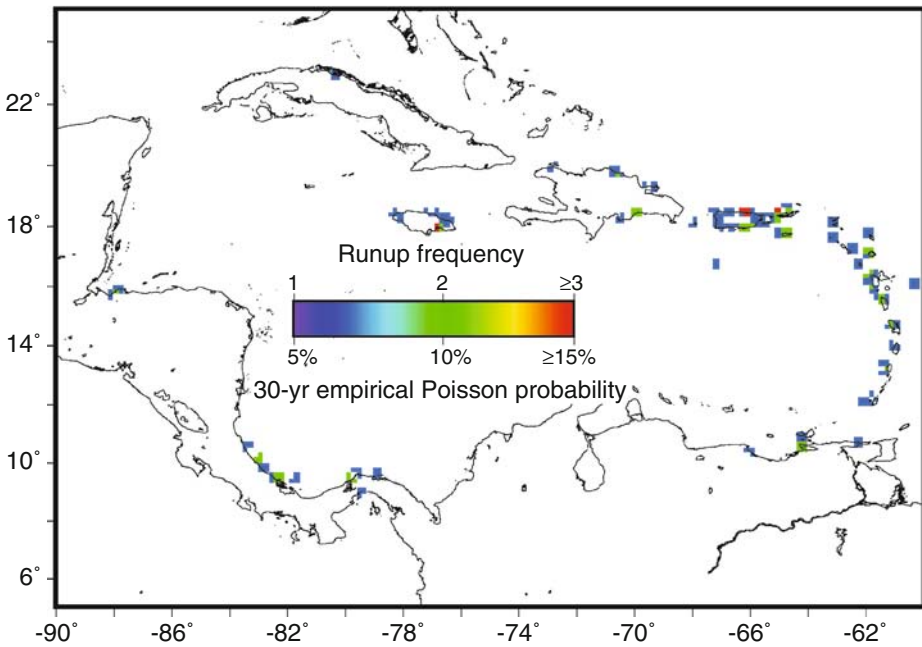Figure 1   ▶

Top shows individual runup observations as noted in Table 1. Circle size represents runup in m. Bottom panel shows summed number of runup observations per 20 km by 20 km cell and the corresponding empirical Poisson probability.

Tsunami runup observations
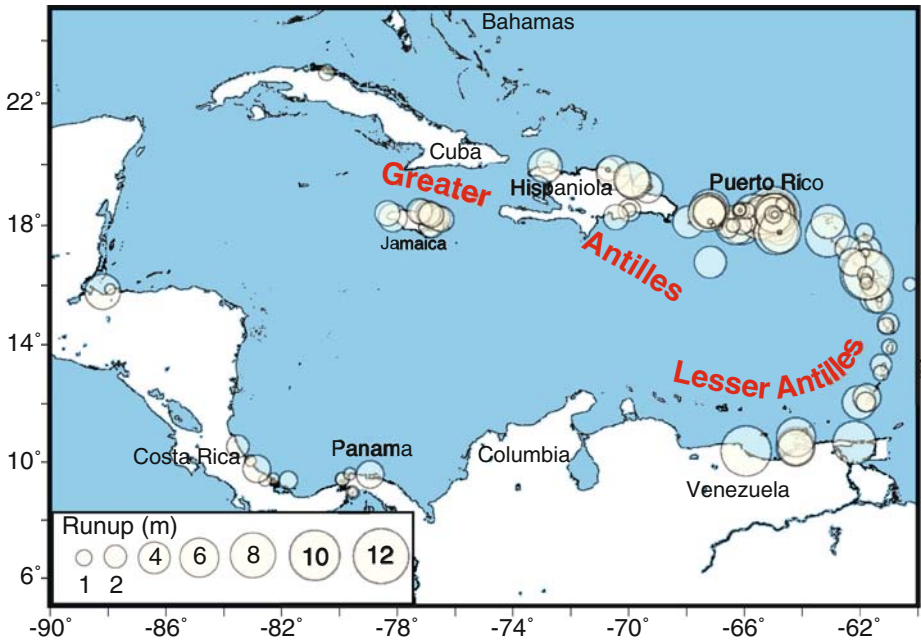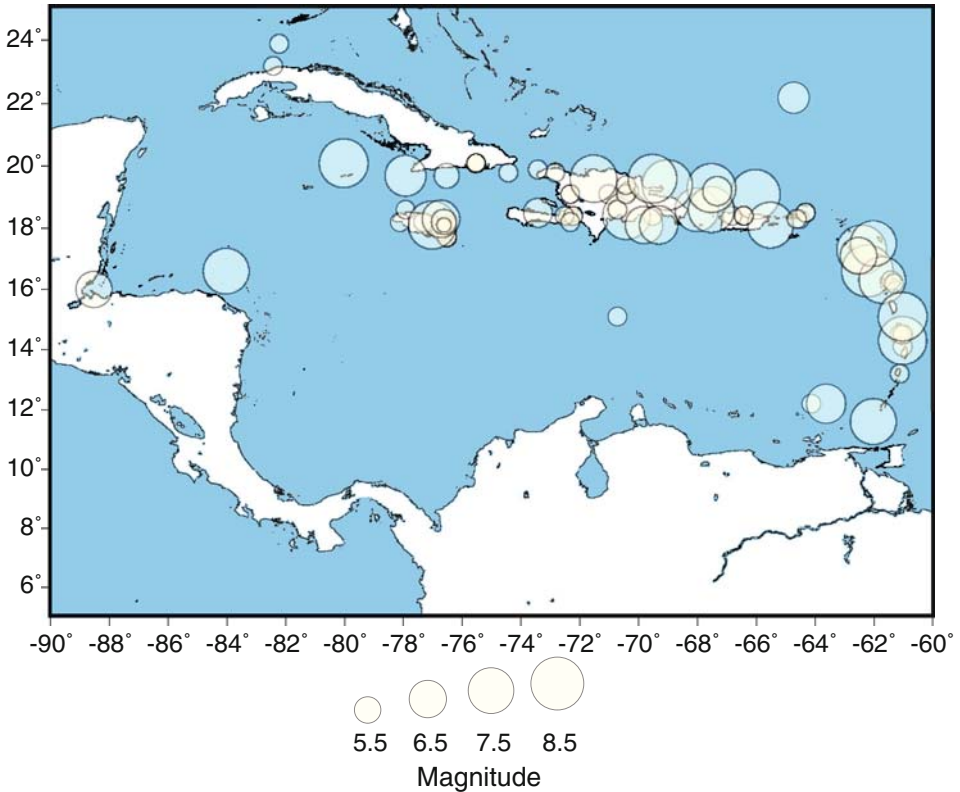

Tsunami frequency in 20 km by 20 km cell

Figure 2

500-yr catalog of large (M ≥ 5) earthquakes in the Caribbean region. Locations of older events are approximations based on historical accounts. The completeness threshold varies with time, and is likely ∼ M = 7 before the 20th century. Sources: SHEPHERD, 1993; NEIC, Significant Worldwide Earthquakes (NOAA).

Here it is assumed that if an exponential distribution is used to calculate tsunami probability, then the best way to estimate the range of possible rate parameters that fit the observations is to find those that most commonly reproduce observed tsunami frequencies. The first step was construction of a series of distributions that covered all reasonable rates (1/10 to 1/3000 yrs^{-1}). Rates were randomly drawn 100,000 times from each series and assembled into tsunami event sequences. These Monte Carlo sequences began with events given freedom to happen any time before 1498. The extra events were not counted into the frequencies, but did establish starting points for Monte Carlo sequences. This was needed because it is expected that tsunamis occurred prior to 1498, but we have no knowledge of them other than that. In this way we avoided the arbitrary starting time having undue influence on rate estimation.

Each event sequence that matched the observed frequencies was tallied. A distribution of matches to the observed record was produced (Fig. 3), and the mode
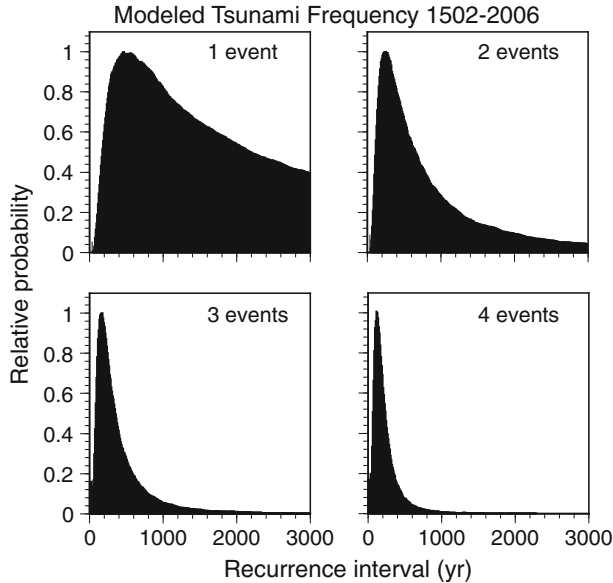
Figure 3

Normalized histograms of the Monte Carlo sequences that matched the indicated event frequencies over 500-year intervals. Ranges of exponential rate parameters are shown (expressed as the inverse, which is recurrence interval) that can match observed frequencies of Caribbean tsunami runups (≥ 0.5 m), which range from 1 to 4 events in ~ 500 yrs.

(most frequent value), median, or mean of that distribution can be taken to represent the rate parameter. This approach also simultaneously estimates uncertainty in the rate parameter resulting from small sampling, and the influence of the open intervals. The Monte Carlo techniques we used are discussed in detail by PARSONS (2008) in relation to paleoseismic earthquake observations.

4. Poisson Probability of Tsunami Occurrence from Empirical Analysis

In the Poisson model, probability depends on the rate parameter (discussed in Section 2) and the duration (Δt) of the interval of interest. Probability is given by

$$P(\Delta t) = 1 - e^{-\lambda \Delta t}. \tag{2}$$

Probability calculation from the rates shown in Figure 3 then is straightforward using Equation (2). Results are shown in Figures 1 and 4. As can be seen from Figure 4, there is considerable spread in probability that results from the spread of possible rates (Fig. 3) consistent with the observed number of runups ≥ 0.5 m in the 20 km by 20 km cells. Mean 30-year probability for sites with one event over the observation period is 4%, for cells with two events the mean is 7%, for three events the mean is 12%, and for four
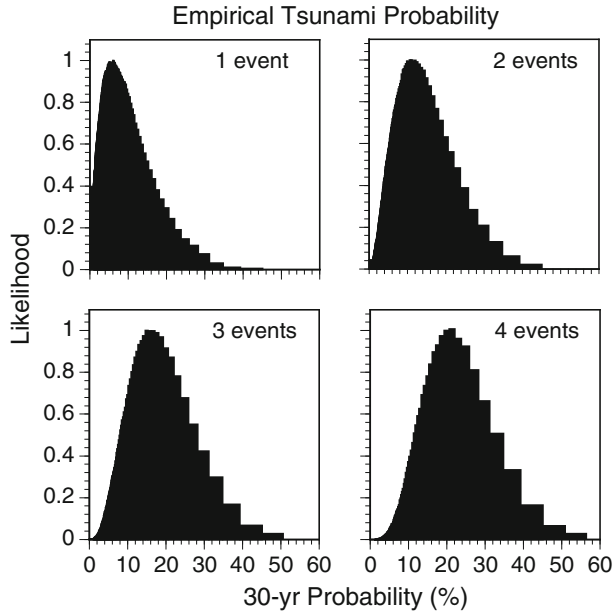
Figure 4

Normalized histograms indicating the likelihood of a given 30-yr Poisson probability resulting from the rate parameters shown in Figure 3, for 20 km by 20 km cells with observations of 1 to 4 events in ∼500 yrs. Means and confidence intervals are given in Table 2.

events the mean is 17%. Using empirical rates under a time-independent Poisson model thus causes the hazard estimate to be greatest where runups were most frequently observed in the past, and assumes that future events will most likely happen where past ones have. In contrast, a time-dependent, renewal, or seismic gap model might place the greatest hazard near submerged faults where little activity has been observed in the recent past.

Given the wide range of credible probability results shown in Figure 4, it is difficult to know what single value might best represent tsunami hazard. The mean value is an obvious choice, although the distributions of possible probability values are not symmetrical (e.g., Gaussian). Thus it is perhaps more useful to think of the hazard in terms of confidence bounds. For example if the empirical model is assumed to be valid, then we can state with 95% confidence that a site that experienced four tsunamis with runup in excess of 0.5 m since 1498 has a 3% to 42% probability of another such event in the next 30 yrs (Table 2).

A central question surrounding exclusive use of empirical tsunami runup rates for future hazard calculations is how complete the empirical record is, and how representative the past ∼500-yr-period has been. Examination of Table 1 shows a much higher frequency of observation in the 19th century as compared with the previous centuries, implying that increased population density increased the number of

Table 2

30-year probabilities of tsunami runup (≥0.5 m) in the 20 km by 20 km cells shown in Figure 1, which contain observations from 1 to 4 past events. 95% and 67% confidence intervals on the probability values as well as means (PARSONS, 2008) are given.

30-Year Poisson probability from empirical rates

Confidence bound	1 Event	2 Events	3 Events	4 Events
97.5%	14%	23%	32%	42%
83.5%	6%	11%	18%	26%
Mean	4%	7%	12%	17%
16.5%	1%	2%	4%	8%
2.5%	1%	1%	2%	3%

observations. Additionally, since the Caribbean catalog is dominated by local-earthquake generated tsunamis, we want to know whether the 500-yr earthquake catalog has released all the expected seismic moment, or whether there needs to be more large earthquakes to satisfy a moment deficit. In the next section we discuss calculation of expected moment and comparison with the moment expressed in the seismic catalog.

5. Is the 500-year Tsunami Catalog Representative? Expected vs. Expressed Seismic Moment in the Caribbean Region

5.1. Model Development

To calculate the expected seismic moment rate in the Caribbean region, we developed a 3-D finite-element model of long-term fault slip (Fig. 5). The purpose was to displace the Caribbean plate relative to North America to simulate slip along the primary plate boundaries. The model tracked the amount of expected slip, which was used to calculate seismic moment accumulation, assuming all of the slip in the seismogenic zone is released during earthquakes. The results gave a sum of total moment that we used to compare with observed seismic moment, as well as a spatial distribution of expected moment. The nature of the problem made a 3-D approach necessary because: (1) Caribbean plate motion is rotational relative to North America, (2) the model involves permanent deformation because lithosphere is variably consumed along the subduction front, and (3) the calculated relative slip rates and rakes are used to generate synthetic tsunamigenic earthquake events.

The model consisted of two blocks that represented the lithosphere on either side of the Caribbean plate boundary with the North American plate. To define the plate boundary geometry, we used surface traces of the primary strike-slip boundary and subduction front (MANN *et al.*, 2007). We extended the strike-slip boundary on the northwestern edge of the Caribbean plate vertically through the crust. We defined the subduction-zone shape from
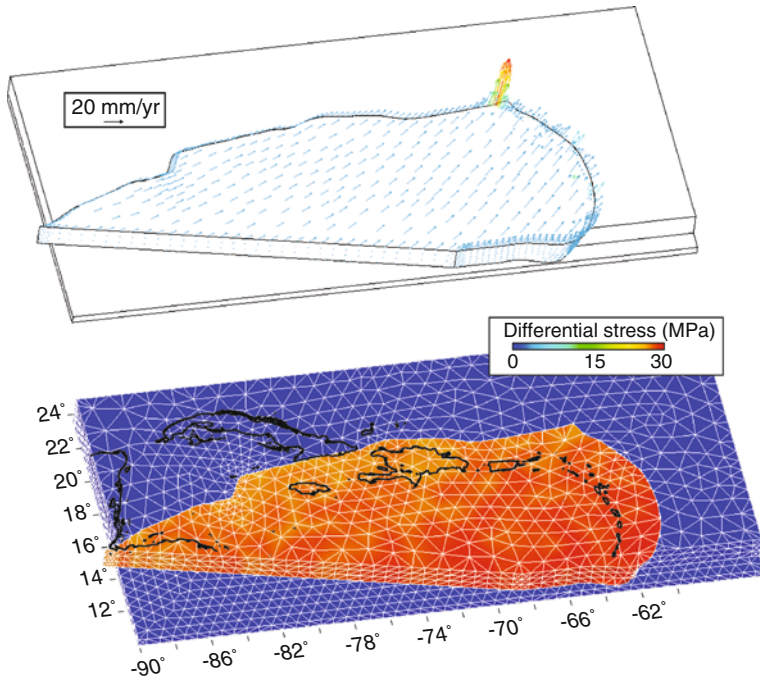
Figure 5

Finite-element model of the submerged parts of the Caribbean-North American plate boundaries. Strike-slip boundary to the northwest is vertical, while the subduction zone is variably dipping according to CRUCIANI *et al.* (2005). The top figure shows displacement vectors, and the color shading on the Caribbean plate below displays small variations in differential stress resulting from displacement.

the database of CRUCIANI *et al.* (2005), who used seismic tomography and earthquake hypocenters to constrain subducted slab geometries. We interpolated the transition from strike-slip into subduction smoothly as shown in Figures 5 and 6. The model Caribbean plate was displaced relative to the North American plate according to the Caribbean-North American "hybrid" rotation pole (latitude = 64.9°N, longitude = 250.5°E, ω = 0.214°/Myr) of DEMETS *et al.* (2000), based in part on GPS measurements reported by DIXON *et al.* (1998).

Volumes were meshed by first estimating element edge lengths for all defining lines. The element edge lengths on these lines were then refined for curvature and proximity of faults in the geometry. The mesh was thus finest where volumes changed shape the most, and in regions of greatest complexity. The model was composed of 24,509 elastic tetrahedral elements defined by 36,412 nodes with an average node spacing of 50 km. Elements were defined by 10 nodes, each having three degrees of freedom (translations in the nodal x, y, and z directions).

Our Caribbean finite-element model had two major contact zones, representing subduction of the North American plate beneath the Caribbean, and transition into strike-
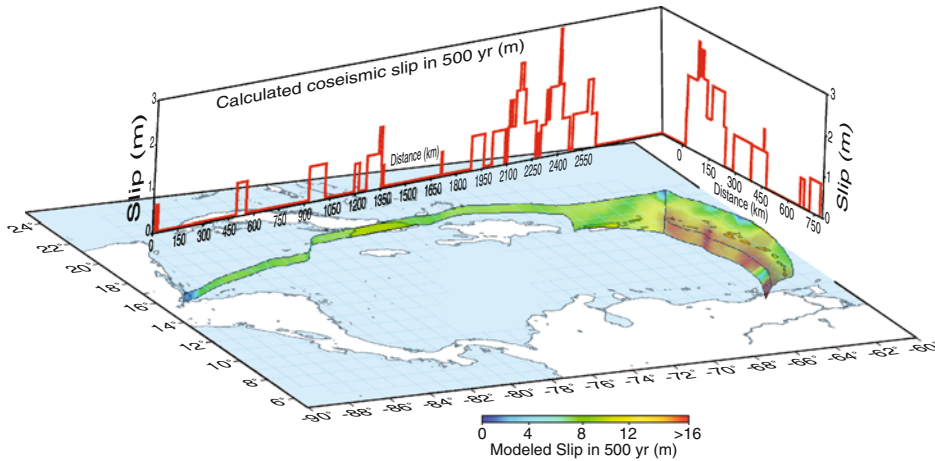
Figure 6
Distribution of slip rate on the submerged Caribbean plate boundary for a 500-yr simulation period (color shading). Approximate seismic slip compiled from the catalog in Figure 2 is shown for comparison (red graph). Slip was derived from reported magnitudes using regressions of WELLS and COPPERSMITH (1994).

slip motion along the northern Caribbean plate to the northwest (Fig. 5). These faults were deformable, and were constructed from contact elements obeying the Coulomb failure stress (*CF*) relation

$$CF \equiv \bar{\tau}_f + \mu\sigma_n, \tag{3}$$

where $\bar{\tau}_f$ is shear stress acting on a fault surface, μ is the friction coefficient, and σ_n is the component of stress acting normal to a fault surface. Contact elements had zero thickness and were welded to the sides of tetrahedral elements. We assigned a low friction coefficient ($\mu = 0.2$) to the subduction and strike-slip interfaces (e.g., CATTIN *et al.*, 1997; RUFF, 2002; KOPF and BROWN, 2003).

We loaded our model by decomposing the Caribbean plate rotation into E-W and N-S vectors at each model node within the Caribbean plate. These combined motions resulted in a ~18–20 mm/yr of relative plate motion depending on the plate-boundary orientation. The Caribbean block was constrained not to sink along its base, but could slip freely, simulating the asthenosphere-lithosphere boundary. Rather than subducting the North American plate beneath the Caribbean in the model, we caused the Caribbean plate to override North America, which generates the equivalent moment accumulation, but is a much simpler model because no subduction channel was required. We ran the model for a 10,000-year simulation to ensure steady-state slip along the plate boundaries and extracted 500-yr periods for comparison with observed seismic moment release. Total slip divided by 500 years gave the long-term slip rate distribution.

6. Comparison between Expected and Observed Seismic Moment

Our model of Caribbean-North American plate interaction enabled calculation of expected slip rate distribution ($\dot{u}$) on the interplate megathrust and strike-slip zones, which was used to calculate the tectonic moment rate ($\dot{m}_t$) distribution, as $\dot{m}_t = \mu A \dot{u}$, where A is fault area and μ is the shear modulus (where $\mu = 3 \cdot 10^{11}$ dyne-cm^{-2}) (Fig. 6).

We calculated the total tectonic moment for a 505-year period (duration of seismic catalog AD1502-2006) to be $7.42 \cdot 10^{29}$ dyne-cm on the surface shown in Figure 6. The expressed seismic moment sum from the earthquake catalog shown in Figure 2 is $2.39 \cdot 10^{29}$ dyne-cm. Thus the ratio of expressed seismic to expected tectonic moment release (coupling coefficient) is $c = 0.32$. We note that KAGAN (2002a; 2002b) arrived at a similar low coupling coefficient for the Caribbean region using modern catalog data, and a simpler plate boundary model. One of two conclusions can be drawn from this result: (1) The seismic coupling coefficient around the Caribbean plate is low, or (2) there is a large temporal seismic gap waiting to be expressed.

If we were to accept the low seismic coupling estimate for the Caribbean region, then we could further conclude that the tsunami runup probabilities we calculated from the empirical rates represent a valid forecast. However, if the 500-yr observation period is deficient, then we require an alternative runup rate model. We pursue such a model in Section 7, where the slip rates derived from the finite-element model are discretized into earthquake events, some of which are tsunamigenic (i.e., result in ≥ 0.5 m runups). We then applied a hydrodynamic model to assess runup potential throughout the Caribbean region.

7. Numerical Models of Expected Tsunami Frequency

If we know the slip rate along the Caribbean plate boundaries, we can calculate the expected rate of earthquakes greater than a certain magnitude using a Gutenberg-Richter magnitude-frequency distribution. Some percentage of these events is expected to cause observable tsunamis. Tsunami runups for a given earthquake can be approximated using standard generation and hydrodynamic models; multiple realizations can give an estimate of the likely range in frequencies at any coastal location in the model (e.g., GEIST and PARSONS, 2006). Given the very real possibility that the past 500-yr observations are incomplete, we describe the development of an alternative tsunami rate model below, which is based on the modeled slip-rate distribution from Section 4 and the assumption of complete seismic coupling along the Caribbean plate boundary.

7.1. General Probabilistic Framework

To develop synthetic tsunami catalogs, we used a general aggregation equation for determining the rate (λ) at which tsunamis will exceed a certain runup (R_0) at a coastal location as

$$\lambda(R > R_0) = \sum_{\text{type}=i} \sum_{\text{zone}=j} v_{ij} \int P(R > R_0|\psi_{ij}) f_\psi(\psi_{ij}) \, d\psi, \qquad (4)$$

where the index i refers to the type of tsunami source (e.g., $i = 1$ earthquakes, $i = 2$ landslides, etc.), index j the zone which that source occurs in (according to some particular zonation scheme), v_{ij} the mean rate for source (i,j), ψ_{ij} the tsunami source parameters for source (i, j), f_ψ the probability distribution for tsunami source parameters, and $P(R > R_0|\psi_{ij})$ is the probability that runup will exceed R_0 at the coastal location for a given source parameter (GEIST and PARSONS, 2006; GEIST *et al.*, 2008). For this study, we only considered earthquake-generated tsunamis scaled according to the seismic moment m, where moment magnitude M is related to seismic moment according to $M = (2/3)(\log m-9.05)$ (HANKS and KANAMORI, 1979). Equation (4) therefore is reduced to

$$\lambda(R > R_0) = \sum_{\text{zone}=j} v_j \int_{m_t}^{\infty} P(R > R_0|m_j) f_j(m) \, dm. \qquad (5)$$

Propagation distance was included in the term $P(R > R_0|m_j)$ since this term is computed by numerical propagation models described below. The term $f_j(m)$ is the frequency-moment distribution for earthquakes in zone j. We used the tapered Gutenberg-Richter (G-R) distribution in which the complementary cumulative (survivor) distribution $F_j(m)$ is given by (KAGAN, 2002a; KAGAN and JACKSON, 2000)

$$F_j(m) = (m_t/m)^\beta \exp\left(\frac{m_t - m}{m_c}\right), \quad m \geq m_t, \qquad (6)$$

where β is the shape parameter for the distribution, m_t is the threshold moment, and m_c is the corner moment that controls the tail of the distribution.

7.2. Seismic Zonation

The northern boundary of the Caribbean plate was divided into 7 zones in which the rate calculations were aggregated. The first two zones represented the eastern and western parts of the Cayman transform fault, separated by the Cayman spreading center (LEROY *et al.*, 2000). The remaining zones represented the Greater Antilles (zones 3 through 5) and Lesser Antilles (zones 6 and 7) subduction zones. For each zone, the frequency-moment distribution parameters were set equal to the parameters determined from the global study of BIRD and KAGAN (2004) according to their tectonic setting: i.e., zones 1 and 2, $\beta = 0.64$ and M_c=8.14 for slow oceanic transform faults and zones 3 through 7, $\beta = 0.64$ and M_c=9.58 for subduction zones. See BIRD and KAGAN (2004) regarding uncertainty estimates associated with these values.

The source rate parameter for each zone (v_j) was defined as the activity rate for earthquakes of $m \geq m_t$ and is related to the seismic moment rate $(\dot{m}_s)$ as described by KAGAN (2002b):

$$v(m) = \frac{(1 - \beta)\dot{m}_s}{m^\beta m_c^{1-\beta} \Gamma(2 - \beta) e^{m/m_c}}, \qquad (7)$$

where Γ is the gamma function. The "tectonic" moment rate $(\dot{m}_t)$ is given by $\dot{m}_t = \mu A \dot{u}$, where μ is the shear modulus, A is the area of the seismogenic part of the fault zone, and $\dot{u}$ is the long-term slip rate along the fault determined from the finite-element modeling described in Section 5. $\dot{m}_s$ and $\dot{m}_t$ are related by a seismic coupling parameter $(0 \leq c \leq 1)$: $\dot{m}_s = c\dot{m}_t$. For a fault that has no aseismic slip at seismogenic depths, $c = 1$. Since the empirical catalog already provides a low-coupling rate estimate, we assumed that $c = 1$ in determining the maximum activity rate of earthquakes for each zone from the tectonic rate.

To calculate $\dot{m}_t$ for each zone, the long-term slip rate $(\dot{u})$ from the finite-element modeling was averaged over seismogenic depths. Fault lengths (L) were taken from the surface traces of the faults. For the oceanic transform faults, the fault width at seismogenic depths is taken from BIRD and KAGAN (2004), whereas for the subduction faults, the fault width was taken from ten BRINK and LIN (2004). A constant shear modulus of 30 GPa was assumed for each zone.

7.3. Monte Carlo Implementation

We implemented Equation (5) using a Monte Carlo-type procedure in which a synthetic earthquake catalog of fixed duration was prepared from random samples of the distribution defined by Equations (6) and (7). Two different Monte Carlo analyses were conducted: (1) Tsunami results were aggregated from 310 M ≥ 7 earthquakes representing a single catalog of duration 4,442 years and (2) tsunami results were aggregated from 50 separate earthquake catalogs of duration 500 years each (approximately the duration of the observed earthquake catalog). The number of earthquakes sampled from the tapered G-R distribution (Equation (8)) varied for each source zone, depending on $\dot{m}_t$. For a given time period τ, the expected number of earthquakes of moment $m \geq m_t$ was derived from (7) (cf., McCAFFREY, 1994):

$$N(m > m_t) = \frac{(1 - \beta)\dot{m}_t \tau}{m_t^\beta m_c^{1-\beta} \Gamma(2 - \beta) e^{m_t/m_c}}. \qquad (8)$$

The location of each earthquake was randomly varied within each source zone according to a uniform distribution.

Other source parameters were scaled with respect to seismic moment according to global scaling relationships. For subduction zones, the fault length scaling relationship was taken from the LAY *et al.* (1982) catalog of subduction zone earthquake source

parameters, updated to include more recent earthquakes (GEIST, 2002). For the oceanic transform fault, the WELLS and COPPERSMITH (1994) scaling relationship was used. Fault width was assumed to be half the fault length (GELLER, 1976), with a maximum fault width constrained by the dimensions of the seismogenic zone. Each earthquake had a stochastic slip distribution that conformed to a k^{-2} slip spectrum (HERRERO and BERNARD, 1994; TSAI, 1997) with average slip scaled to seismic moment based on the global subduction zone earthquake catalog.

For each earthquake, vertical and horizontal coseismic seafloor displacements are the initial conditions for tsunami modeling (TANIOKA and SATAKE, 1996). We calculated these displacements using OKADA's (1985) analytic functions that are applicable for an elastic half-space. A finite rise-time of 20 s was applied uniformly along the rupture zone, with no preferred rupture propagation direction. We modeled the propagation of the tsunami wavefield using a finite-difference approximation to the linear long-wave equations (AIDA, 1969; SATAKE, 2002). A 2-arc-minute bathymetric grid (SMITH and SANDWELL, 1997) was used with an 8 s time step that satisfied the Courant-Friedrichs-Lewy stability criterion for the Caribbean region. A reflection boundary condition was imposed at the 250 m isobath, whereas a radiation boundary condition was imposed along the open-ocean boundaries of the model (REID and BODINE, 1968). Runup (R_0) was approximated from the coarse grid model for use in Equation (4) by finding the nearest model grid point to the coastline and then multiplying the peak offshore tsunami amplitude by a factor of 3 that roughly accounts for shoaling amplification and the runup process itself (SATAKE, 1995, 2002; SHUTO, 1991). For the first experiment (single 4,442-year synthetic catalog), the exceedance probability was calculated for 3 runup threshold values: 0.5 m, 1.0 m, and 2.0 m (Fig. 7). For the second experiment (fifty 500-year catalogs), the exceedance probability was calculated using a 0.5 m runup threshold for each of the 50 synthetic catalogs.

It is likely that runup varies considerably within the scale of our cell size. Significant focusing of tsunami waves from nearshore bathymetric variation can greatly amplify tsunami runup as exemplified in high resolution runup models (e.g., TITOV and SYNOLAKIS, 1997; MATSUYAMA et al., 1999), such that the runup thresholds we use in our coarse-grid model are low-estimate values. Furthermore, in coastal low-lying regions, inundation from low runup regions can cover a large area, as exemplified by the 1 km inundation distance from the 2.5 m runup at Matanzas, Dominican Republic, in 1946.

We found that the fifty 500-year catalogs captured more variability in spatial runup distribution than did the 4442-year catalog. This resulted from the multiple catalogs having more variety of earthquake locations since a few very large events can dominate the distribution of moment, and consequently regional tsunami runup distribution, due to the Gutenberg-Richter constraint. We thus used the set of fifty 500-year catalogs to determine mean rates and uncertainties in the probability calculations that follow.
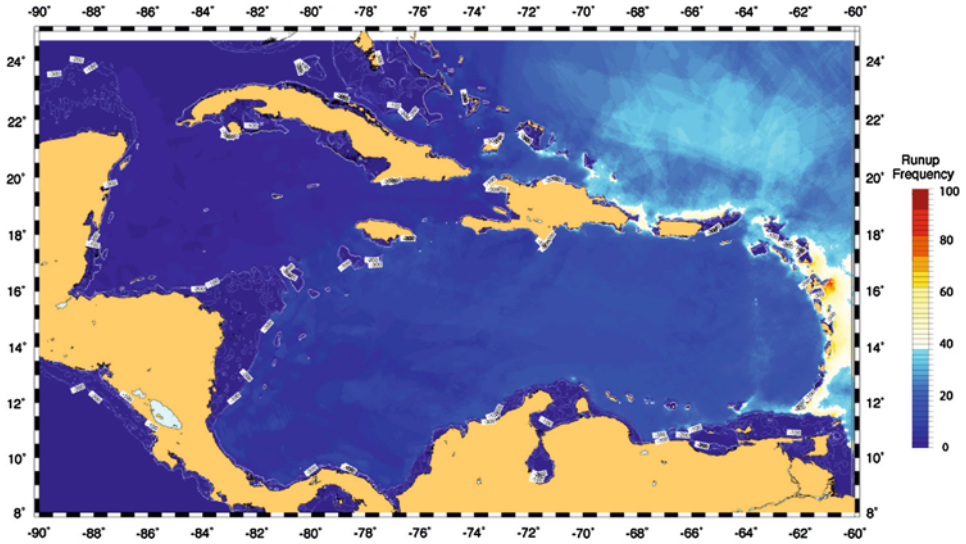
Figure 7

Example calculation of expected runup (≥ 0.5 m) frequency over a 4442-yr period calculated from the expected seismic moment rate shown in Figure 6.

8. Poisson Probability of Tsunami Occurrence from Numerical Modeling

8.1. Probability Mapping

Numerical models of expected tsunami frequency gave us an alternative estimate of the rate of $R_0 \geq 0.5$-m runup throughout the Caribbean region (Fig. 7). We calculated Poisson probabilities from these rates in the same manner as was used for the empirical observations, and the results are shown in Figure 8. We used the mean frequency in Equation (2) at each 20 km by 20 km coastal cell from the 50 Monte Carlo runs described in Section 7.

Results from mapping probability from modeled tsunami rates show highest probability (~ 20–30% in 30 years) along the Lesser Antilles. The Greater Antilles also show significant runup probability in the 10–20% range, particularly in Puerto Rico and eastern Hispaniola. The majority of sites around the Caribbean region show low probability, which is evident in Figure 8. The overall distribution of values shows that the vast majority of 20 km by 20 km cells have 0–5% probability in 30 years (Fig. 9).

One concern with the probability results from the numerical model is that we used a simplified version of the plate boundary, which might have the effect of maximizing hazard along the subduction front, and omitting events emanating from accommodating intra-plate faults, particularly in the intra- and backarc regions of the Greater Antilles and the convergence zone north of Panama and South America (e.g., AUDEMARD and AUDEMARD, 2002), that were not in our model. In Section 10, we investigate ways of
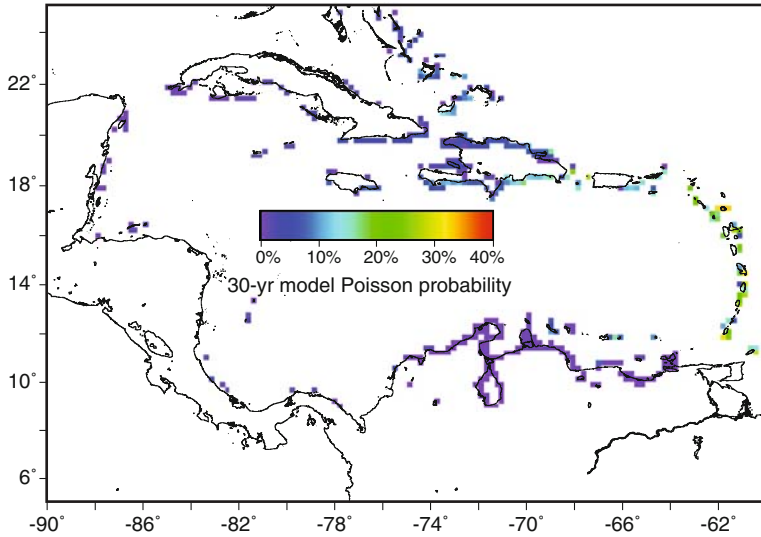
Figure 8
Mapping of 30-year Poisson probability calculations made from numerical modeling of tsunami runup rates.
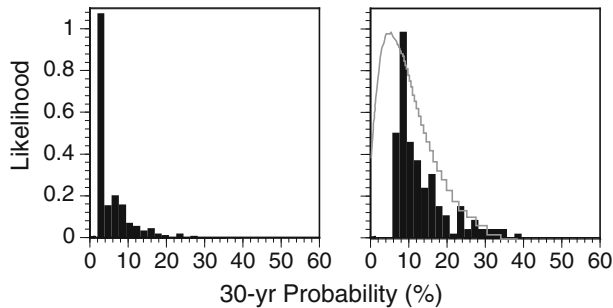

Figure 9
Histograms of 30-year runup (≥ 0.5 m) probability for all Caribbean coastlines modeled. The left panel shows results mapped in Figure 8; the vast majority of 20 km by 20 km cells have less than 5% probability. The right panel shows the distribution of values greater than 5%. The gray line gives an example shape from the empirical tsunami probability distributions shown in Figure 4 for comparison.

combining the numerically modeled rates with the empirical rates to account for the sources not included in the numerical models, but first we compare results from the two methods below.

9. Comparison of Empirically-Derived Probability with Model-Derived Values

One of the key reasons for undertaking the numerical modeling exercise for tsunami runup frequency was to determine if there were low-probability events associated with

plate boundary earthquakes not present in the empirical record, and if the spatial frequency patterns were similar, or greatly different. The probability map shown in Figure 8 indicates many regions with low probability that were not evident in the empirical mapping shown in Figure 1, including the coasts of Venezuela, Columbia, Cuba, and the Bahamas. These regions show 30-year probabilities of less than 5%, which loosely translates into rates fewer than 1 in 500 years, which may explain why the empirical map has virtually no observations from these regions (Fig. 1). These regions where the numerical-modeling results augment the empirical are straightforward to combine in an overall mapping, since there is no overlap. Where the two methods overlap and potentially conflict will require a relative weighting process for combination.

To assess similarities and differences between the empirical and numerically modeled results, we made two maps with the same probability thresholds (5–15%; Fig. 10). Perhaps the most obvious difference between the two models where they have overlapping results is along the Lesser Antilles, where modeled probabilities are nearly uniformly higher than empirical. This is a result of the numerical model having 100% seismic coupling vs. the observed seismic release being $\sim 30\%$ of the expected moment release. The model-derived probabilities are also higher than empirical along southern Hispaniola (Fig. 10).

There are places where probabilities derived from the empirical rate observations are higher than the numerical models predict. In particular this is seen at Puerto Rico, Jamaica, Costa Rica, and Panama. In these instances it is likely that the empirical model has captured localized tsunami events that were caused by landslides and/or accommodating faults associated with the plate boundary that were not specifically included in the numerical model sources. Many of the secondary earthquake sources not included have very slow and uncertain slip rates, making implementation into a numerical model difficult.

10. Combination of Empirical and Modeled tsunami Runup Rates through a Bayesian Process with Likelihood Functions

As with any probabilistic forecast, we were confronted with considerable uncertainty from many sources. Key sources of epistemic uncertainty included: (1) Expected tsunami runup rates, (2) tsunami sources not explicitly known or included in the model, (3) seismic coupling coefficient of the Caribbean plate boundary zones, and (4) degree of completeness in the empirical tsunami catalog. To encompass these uncertainties into our probability estimates, we created a Bayesian framework to build tsunami runup rate estimates within 20 km by 20 km cells that contain coastlines throughout the Caribbean region. The key advantage of our approach is that the model results end up being weighted by their attendant uncertainties.

We combined model and empirical rates which addressed the above-listed uncertainties as follows. (1) Runup-rate uncertainty: Monte Carlo rate-model fits to the
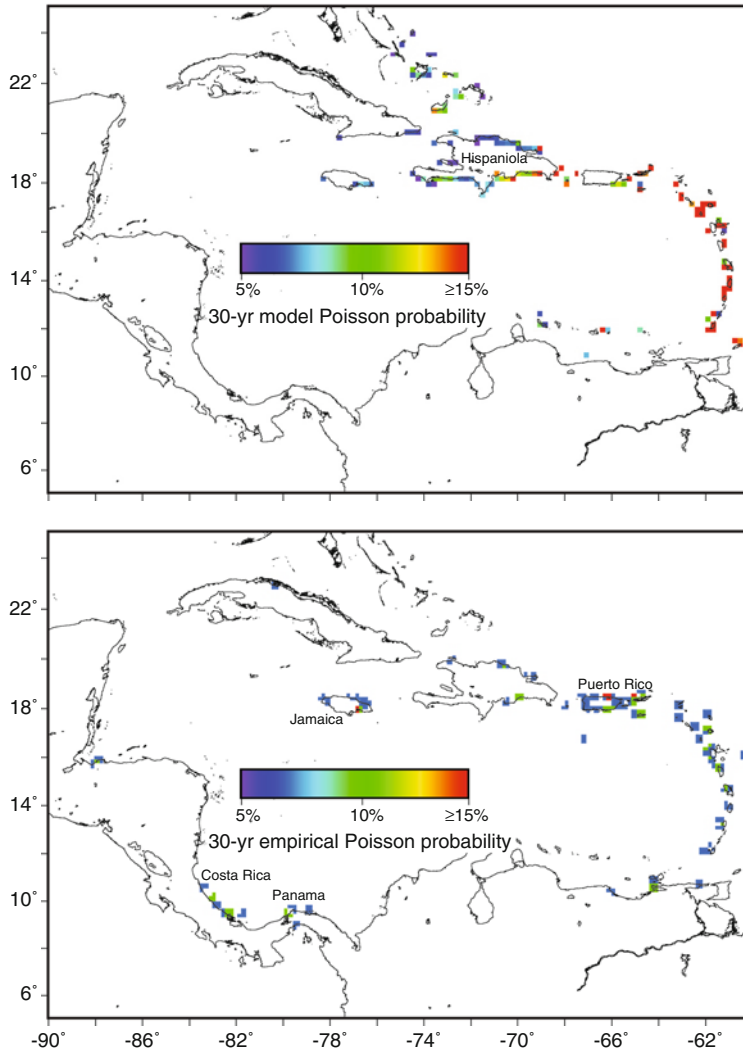
Figure 10
Comparison between (top) model-derived 30-year Poisson probability of tsunami runups (≥ 0.5 m) and (bottom) empirically derived values. See text for discussion.

empirical rates as shown in Figure 3 along with results from 50 numerical model runs provided arrays of possible runup rate values at each cell. (2) Unknown/unaccounted-for tsunami sources: Inclusion of the empirical rates added sources not accounted for in the numerical model (most-affected areas can be seen by comparing the panels of Fig. 10); our forecast may suffer from incomplete knowledge if events not covered by our numerical models have also not occurred in the empirical catalog over the past 500 years.

(3) Seismic coupling: The empirical model implies low seismic coupling of 0.32, whereas the numerical models have coupling coefficients of 1.0. (4) Completeness: We accounted for low-rate plate-boundary events potentially not seen in the empirical catalog with the 50 numerical model runs.

As described in more detail below, we combined our model-derived runup rates with empirical rates according to the following set of logic-tree branches: In cells where there were no empirical values, the numerical model-derived rates were given full weight. Conversely, empirical rates were given full weight where numerical model rates were zero. Lastly, where there were empirical and model rate estimates within the same cells, we used Bayesian likelihood functions to weight the two models. Distributions shown in Figure 3 give the relative probability of different rates for a Poisson model that could have caused the empirical observations. Similarly, results from the 50 numerical model runs produced relative probability (Fig. 11) of different rates in each model cell.

To rank different rate models for each cell where more than one estimate existed, we made a likelihood calculation to weight the models. In the simplest binomial case likelihood is defined as proportional to the probability of obtaining results A given a fixed hypothesis H resulting from a set of fixed data. If A_1 and A_2 are two possible mutually exclusive results, then

$$P(A_1 \ or \ A_2 | H) = P(A_1 | H) + P(A_2 | H), \tag{9}$$

and likelihood is thus

$$L(H|A) = kP(A|H), \tag{10}$$

where k is an arbitrary constant.

The results from likelihood functions were used to obtain the final weights using Bayes' rule (Equation (11)), where the posterior distribution is proportional to the likelihood function multiplied by the prior. For our study, we used a uniform (noninformative) prior such that there was equal probability of all rates in each coastal 20 km by 20 km cell. Further, since we update the prior twice, once for the empirical result, and again for the numerical result, the same result is achieved by simply multiplying the two likelihood functions. Thus the likelihood of a given rate λ where there were empirical estimates (e1) and numerical-modeled estimates (e2) is

$$L(\lambda|e1, e2) = k[p_1(e1|\lambda)][p_2(e2|\lambda)], \tag{11}$$

where $p(e1|\lambda)$ is the probability of rate λ based on the Monte Carlo fits shown in Figure 3, and $p(e2|\lambda)$ is the probability of rate λ from the 50 numerical model runs. The constant k is used for normalizing the weights so that they add to 1.

We used likelihood functions to weight rate models over a range from 0 to 10 events in the 500-yr observation period. We considered rates between 0 and 10 events in 500 years for all cells, assuming no further prior information. Final rates were found by weighted means of the posterior rates. To summarize the process, where model and
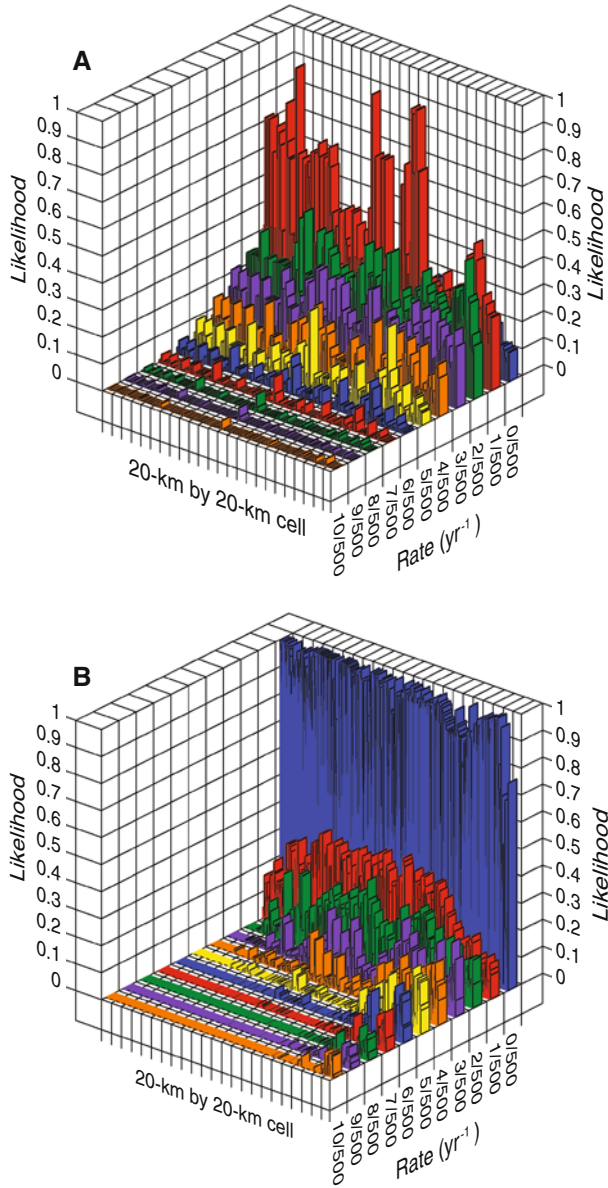
Figure 11
(a) Normalized histogram (likelihood) of tsunami runup ($R_0 \geq 0.5$ m) rates in 214 20-km by 20-km cells defined using likelihood functions from empirical rates (Fig. 3) and from 50 numerical modeling simulations. (b) Normalized histogram of runup rates from numerical modeling in 685 cells where there were no empirical observations. Mean values from these distributions were used in the best-estimate probability calculations mapped in Figure 12.
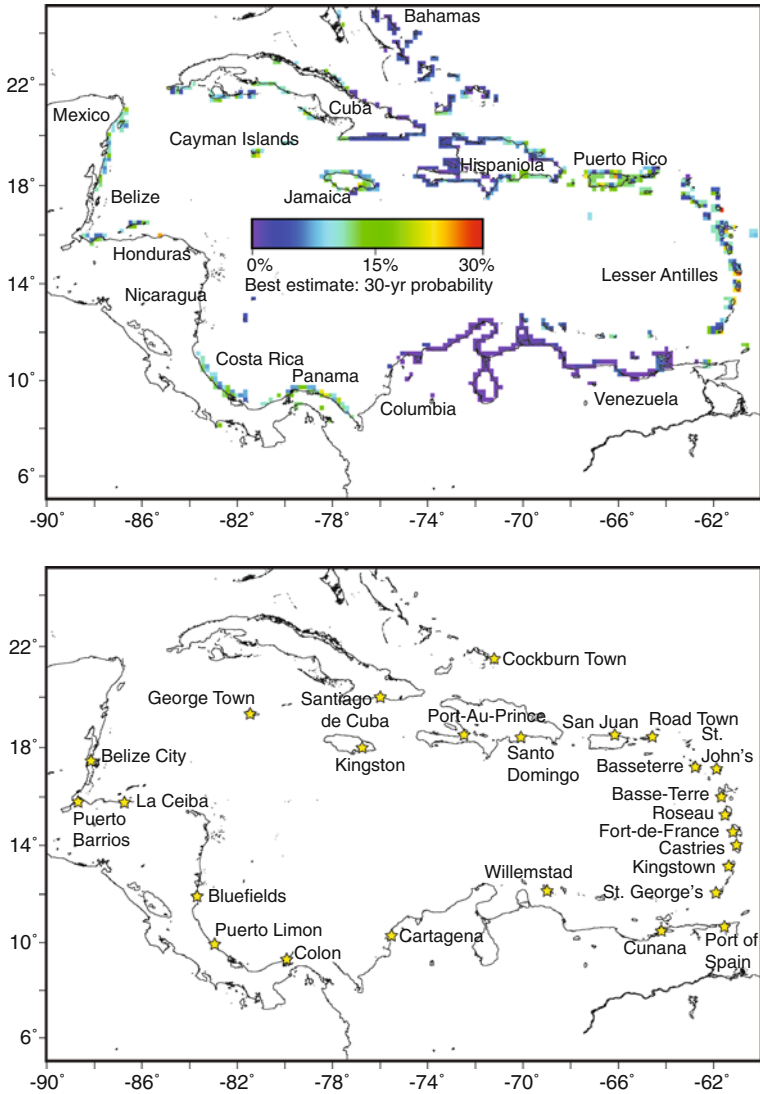
Figure 12

30-year tsunami runup (r ≥ 0.5 m) probability in 20 km by 20 km cells at coastal sites in the Caribbean region made from combined rate estimates from empirical and numerical models. Lower panel shows locations of cities listed in Table 3.

empirical values were both absent for a given rate, the posterior distribution was zeroed. When one model provided rates, its likelihood function was used to update the priors, and when both empirical and numerical rate estimates were available, likelihood was developed through combination and renormalization using Equation (11), which was then used to update the priors.

Table 3

30-year probability of tsunami runup in excess of 0.5 m in cells that contain population concentrations in 20 km by 20 km cells for representative Caribbean countries and territories. Population given as a relative measure of risk throughout the region. Values were calculated as uniform over cell areas, and are not intended to convey any detail at selected cities, but are presented for comparison purposes. Dashes indicate negligible calculated probability.

Country	Nearest coastal city in 20 km × 20 km cell	Latitude	Longitude	Population	30-yr probability r ≥ 0.5 m (%)
Antigua and Barbuda	St. John's	17.1167°	−61.8500°	24,226	5.74
Belize	Belize City	17.4847°	−88.1833°	70,800	-
Cayman Islands	George Town	19.3034°	−81.3863°	20,626	10.79
Columbia	Cartagena	10.4000°	−75.5000°	895,400	0.08
Costa Rica	Puerto Limon	10.000°	−83.0300°	78,909	8.32
Cuba	Santiago de Cuba	20.0198°	−75.8139°	494,337	2.31
Dominica	Roseau	15.3000°	−61.3833°	14,847	11.94
Dominican Republic	Santo Domingo	18.5000°	−69.9833°	913,540	17.56
France, Guadeloupe	Basse-Terre	16.2480°	−61.5430°	44,864	11.79
France, Martinique	Fort-de-France	14.5833°	−61.0667°	94,049	5.33
Grenada	St. George's	12.0500°	−61.7500°	7,500	2.48
Guatemala	Puerto Barrios	15.7308°	−88.5833°	40,900	-
Haiti	Port-Au-Prince	18.5333°	−72.3333°	1,277,000	0.01
Honduras	La Ceiba	15.7667°	−86.8333°	250,000	-
Jamaica	Kingston	17.9833°	−76.8000°	660,000	21.95
Netherlands Antilles	Willemstad	12.1167°	−68.9333°	125,000	7.04
Nicaragua	Bluefields	12.0000°	−83.7500°	45,547	-
Panama	Colon	9.3333°	−79.9000°	204,000	17.56
St. Kitts and Nevis	Basseterre	17.3000°	−62.7333°	15,500	6.95
St. Lucia	Castries	14.0167°	−60.9833°	10,634	5.52
St. Vincent and the Grenadines	Kingstown	13.1667°	−61.2333°	25,307	11.32
Trinidad and Tobogo	Port of Spain	10.6667°	−61.5167°	49,031	-
Turks and Caicos	Cockburn Town	21.4590°	−71.1390°	5,567	3.57
UK, Virgin Islands	Road Town	18.4333°	−64.5000°	9,400	13.85
USA, Puerto Rico	San Juan	18.4500°	−66.0667°	434,374	22.24
USA, Virgin Islands	Charlotte Amalie	18.3500°	−64.9500°	18,914	17.56
Venezuela	Cunana	10.4564°	−64.1675°	305,000	6.27

11. Probability Results from the Rate Model

We calculated a best-estimate set of 30-year tsunami runup probability ($R_0 \geq 0.5$ m) values for the 20 km by 20 km coastal cells throughout the Caribbean region (Fig. 12). Generally, the highest probabilities (typically 10–20% in 30 years for runup $R_0 \geq 0.5$ m) we calculated were for the eastern Lesser Antilles, including the Islands of Antigua, Barbuda, Dominica, Guadeloupe, Martinique, Greneda, St. Kitts, Nevis, St. Lucia, St. Vincent, and the Grenadines (Fig. 12, Table 3). Additionally, relatively higher hazard was calculated for the easternmost Greater Antilles including the Virgin Islands, Puerto Rico, and eastern Hispaniola. These sites were elevated primarily because of their proximity to the Caribbean-North American subduction plate boundary. However, we

also forecasted relatively high hazard from the Cayman transform boundary at Jamaica, driven primarily by empirical rate estimates. The empirical rate model also significantly effected for Costa Rica and Panama, likely caused by events along the north Panama convergence zone in addition to basin-wide tsunamis, for which we calculated relatively high probabilities (Fig. 12).

For reference, we give the calculated 30-year probability of tsunami runup ($r \geq 0.5$ m) in cells that contain population concentrations in 20 km by 20 km cells for representative Caribbean countries and territories in Table 3. Probabilities do not take into account the relative vulnerability of the populations at different sites related to specifics of coastal topography and very near-shore bathymetry. Thus maps and tables presented here might best be applied as sources of relative hazard, subject to corrections related to local site variations

12. Conclusions

Combination of a ~ 500-year period of tsunami runup observations with numerical modeling enabled us to make a coarsely-sampled (20 km by 20 km) tsunami hazard map of the Caribbean region. The primary source of uncertainty is the degree of completeness that a 500-year catalog represents. We found that we cannot quantify this uncertainty without knowledge of the seismic coupling coefficient of the Caribbean-North American plate boundary zones. We thus used likelihood functions to weight an empirical tsunami runup rate estimate that suggested a very low seismic coupling coefficient of $c = 0.32$ against numerical models of tsunami runup that assumed full coupling ($c = 1$). Combining empirical and modeled rates made up for some of the deficiencies in each approach; the empirical catalog is likely not a complete record of all possible interplate tsunami sources, whereas the numerical model did not account for accommodating intra-plate faults and/or landslide sources that appear likely causes of tsunamis in the empirical record.

REFERENCES

AIDA, I. (1969), *Numerical experiments for the tsunami propagation–The 1964 Niigata tsunami and the 1968 Tokachi-Oki tsunami*, Bull. Earthq. Res. Insti. *47*, 673–700.

AUDEMARD, F. E. and AUDEMARD, F. A. (2002), *Structure of the Mérida Andes, Venezuela: Relations with the South America-Caribbean geodynamic interaction*, Tectonophysics *345*, 299–327.

BIRD, P. and KAGAN, Y. Y. (2004), *Plate-tectonic analysis of shallow seismicity: Apparent boundary width, beta-value, corner magnitude, coupled lithosphere thickness, and coupling in 7 tectonic settings*, Bull. Seismol. Soc. Am. *94*, 2380–2399.

CATTIN, R., LYON-CAEN, H., and CHÉRY, J. (1997), *Quantification of interplate coupling in subduction zones and forearc topography*, Geophys. Res. Lett. *24*, 1563–1566.

CRUCIANI, C., CARMINATI, E., and DOGLIONI, C. (2005), *Slab dip vs. lithosphere age: No direct function*, Earth Planet. Sci. Lett. *238*, 298–310.

DEMETS, C., JANSMA, P. E., MATTIOLI, G. S., DIXON, T. H., FARINA, F., BILHAM, R., CALAIS, E., and MANN, P. (2000), *GPS geodetic constraints on Caribbean-North American plate motion*, Geophys. Res. Lett. *27*, 437–440.

DIXON, T. H., FARINA, F., DEMETS, C., JANSMA, P., MANN, P., and CALAIS, E. (1998), *Relative motion between the Caribbean and North American plates and related boundary zone deformation from a decade of GPS observations,* J. Geophys. Res. *103*, 15157–15182.

GEIST, E. L. (2002), *Complex earthquake rupture and local tsunamis*, J. Geophy. Res. *107*, doi:10.1029/2000JB000139.

GEIST, E. L. and PARSONS, T. (2006), *Probabilistic analysis of tsunami hazards*, Natural Hazards *37*, 277–314.

GEIST, E. L. and PARSONS, T. (2008), *Distribution of tsunami inter-event times*, Geophys. Res. Lett. *35*, doi:10.1029/2007GL032690.

GEIST, E. L., PARSONS, T., TEN BRINK, U. S., and LEE, H. J., *Tsunami Probability*. In *The Sea* (eds. Bernard, E. N. and Robinson, A. R.) (Harvard University Press, Cambridge, Massachusetts (2008)), in press.

GELLER, R. J. (1976), *Scaling relations for earthquake source parameters and magnitudes*, Bull. Seismol. Soc. Am. *66*, 1501–1523.

GRINDLAY, N. R., HEARNE, M., and MANN, P. (2005), *High risk of tsunami in the northern Caribbean*, EOS Trans. *86*, 121–132.

HANKS, T. C. and KANAMORI, H. (1979), *A moment magnitude scale,* J. Geophys. Res. *84*, 2348–2350.

HERRERO, A. and BERNARD, P. (1994), *A kinematic self-similar rupture process for earthquakes*, Bull. Seismol. Soc. Am. *84*, 1216–1228.

KAGAN, Y. Y. (2002a), *Seismic moment distribution revisited: I, Statistical Results*, Geophys. J. Int. *148*, 520–541.

KAGAN, Y. Y. (2002b), *Seismic moment distribution revisited: II, Moment conservation principle*, Geophys. J. Int. *149*, 731–754.

KAGAN, Y. Y, and Jackson, D. D. (2000), *Probabilistic forecasting of earthquakes*, Geophys. J. Int. *143*, 438–453.

KOPF A., and BROWN, K. M. (2003), *Friction experiments on saturated sediments and their implications for the stress state of the Nankai and Barbados subduction thrusts*, Marine Geology *202*, 193–210.

LAY, T., KANAMORI, H., and RUFF, L. J. (1982), *The asperity model and the nature of large subduction zone earthquakes*, Earthq. Predict. Res. *1*, 3–71.

LEROY, S., MAUFFRET, A., PATRIAT, P., and MERCIER DE LÉPINAY, B. (2000), *An alternative interpretation of the Cayman trough evolution from a reidentification of magnetic anomalies*, Geophys. J. Int. *141*, 539–557.

MANN, P., ROGERS, R., and GAHAGAN, L., *Overview of plate tectonic history and its unresolved tectonic problems*. In *Central America: Geology, Resources, and Hazards* vol. 1 (eds. Bundschuh, J. and Alvarado, G.) (Taylor and Francis/Balkema, Leiden, The Netherlands 2007), pp. 201–237.

MATSUYAMA, M., WALSH, J. P., and YEH, H. (1999), *The effect of bathymetry on tsunami characteristics at Sissano Lagoon, Papua New Guinea*, Geophys. Res. Lett. *26*, 3513–3516.

MCCAFFREY, R. (1994), *Dependence of earthquake size distributions on convergence rates at subduction zones*, Geophys. Res. Lett. *21*, 2327–2330.

OKADA, Y. (1985), *Surface deformation due to shear and tensile faults in a half-space*, Bull. Seismol. Soc. Am. *75*, 1135–1154.

O'LOUGHLIN, K. F. and LANDER, J. F., *Caribbean Tsuanmis: A 500-Year History from 1498–1998* (Kluwer Academic Publishers, Dordrecht, The Netherlands (2003)).

PARSONS, T. (2008), *Monte Carlo method for determining earthquake recurrence parameters from short paleoseismic catalogs: Example calculations for California*, J. Geophys. Res. *112*, doi:10.1029/2007JB004998.

REID, R. O. and BODINE, B. R. (1968), *Numerical model for storm surges in Galveston Bay*, J. Waterways and Harbors Div., A.C.E. *94*, 33–57.

RUFF, L. J. , *State of stress within the Earth*. In *International Handbook of Earthquake and Engineering Seismology*, 81A (eds. Lee, W. H. K., Kanimori, H., Jennings, P. C., and Kisslinger, C.) (Academic Press, Amsterdam 2002) pp. 539–557.

SATAKE, K. (1995), *Linear and nonlinear computations of the 1992 Nicaragua earthquake tsunami*, Pure Appli. Geophys., *144*, 455–470.

SATAKE, K., *Tsunamis*. In *International Handbook of Earthquake and Engineering Seismology*, 81A (eds. Lee, W. H. K., Kanimori, H., Jennings, P. C., and Kisslinger, C.) (Academic Press, Amsterdam 2002) pp. 437–451.

SHEPHERD, J.B., *Seismic hazard in the eastern Caribbean*. In *The Practice of Earthquake Hazard Assessment* (ed. McGuire, R.K.) (IASPEI, Denver (1993)) pp. 51–55.

SHUTO, N. (1991), *Numerical simulation of tsunamis–Its present and near future*, Natural Hazards *4*, 171–191.

SMITH, W. H. F. and SANDWELL, D. T. (1997), *Global seafloor topography from satellite altimetry and ship depth soundings*, Science *277*, 1957–1962.

TANIOKA, Y. and SATAKE, K. (1996), *Tsunami generation by horizontal displacement of ocean bottom*, Geophys. Res. Lett. *23*, 861–865.

tEN BRINK, U. S. and LIN, J. (2004), *Stress interaction between subduction earthquakes and forearc strike-slip faults: Modeling and application to the northern Caribbean plate boundary*, J. Geophys. Res. *109*, doi:12310.11029/12004JB003031.

TITOV, V. V. and SYNOLAKIS, C. E. (1997), *Extreme inundation flows during the Hokkaido-Nansei-Oki tsunami*, Geophys. Res. Lett. *24*, 1315–1318.

TSAI, C. P. (1997), *Slip, stress drop and ground motion of earthquakes: A view from the perspective of fractional Brownian motion*, Pure Appli. Geophys. *149*, 689–706.

WELLS, D. L., and COPPERSMITH, K. J. (1994), *New empirical relationships among magnitude, rupture length, rupture width, rupture area, and surface displacement*, Bull. Seismol. Soc. Am. *84*, 974–1002.

To access this journal online:
www.birkhauser.ch/pageoph

Pure and Applied Geophysics

Scenarios of Earthquake-Generated Tsunamis for the Italian Coast of the Adriatic Sea

Mara Monica Tiberti,[1] Stefano Lorito,[1] Roberto Basili,[1] Vanja Kastelic,[1,2] Alessio Piatanesi,[1] and Gianluca Valensise[1]

Abstract—We calculated the expected impact on the Italian coast of the Adriatic Sea of a large set of tsunamis resulting from potential earthquakes generated by major fault zones. Our approach merges updated knowledge on the regional tectonics and scenario-like calculations of expected tsunami impact.

We selected six elongated potential source zones. For each of them we determined a Maximum Credible Earthquake and the associated Typical Fault, described by its size, geometry and kinematics. We then let the Typical Fault float along strike of its parent source zone and simulated all tsunamis it could generate. Simulations are based on the solution of the nonlinear shallow water equations through a finite-difference technique. For each run we calculated the wavefields at specified simulation times and the maximum water height field (above mean sea level), then generated travel-time maps and maximum water height profiles along the target coastline. Maxima were also classified in a three-level code of expected tsunami threat.

We found that the southern portion of Apulia facing Albania and the Gargano promontory are especially prone to the tsunami threat. We also found that some bathymetric features are crucial in determining the focalization-defocalization of tsunami energy. We suggest that our results be taken into account in the design of early-warning strategies.

Key words: Tsunamis, Adriatic Sea, seismotectonics, active faulting, seismic hazard, tsunami hazard.

1. Introduction

The Adriatic Sea is an elongated basin stretching NW-SE in the central Mediterranean Sea (Fig. 1). It has been struck several times by tsunamis (e.g., Ambraseys, 1962; Caputo and Faita, 1984; Papazachos and Dimitriu, 1991; Soloviev et al., 2000; Maramai et al., 2007; Tinti et al., 2007; see also Paulatto et al., 2007 for a complete review), most often along the coasts of the Gargano promontory (De Martini et al., 2003; Tinti et al., 2004). The northwestern portion of the Adriatic basin is also the most vulnerable because of its large low-topography coastal area extending for over 150 km. This area also hosts the city of Venice, that is particularly vulnerable to sea-level rise. From the regional

[1] Istituto Nazionale di Geofisica e Vulcanologia, Sezione di Sismologia e Tettonofisica, Via di Vigna Murata 605, 00143 Rome, Italy. E-mail: tiberti@ingv.it
[2] Faculty of Natural Sciences and Engineering, Department of Geology, University of Ljubljana, Aškerčeva 12, 1000 Ljubljana, Slovenia.
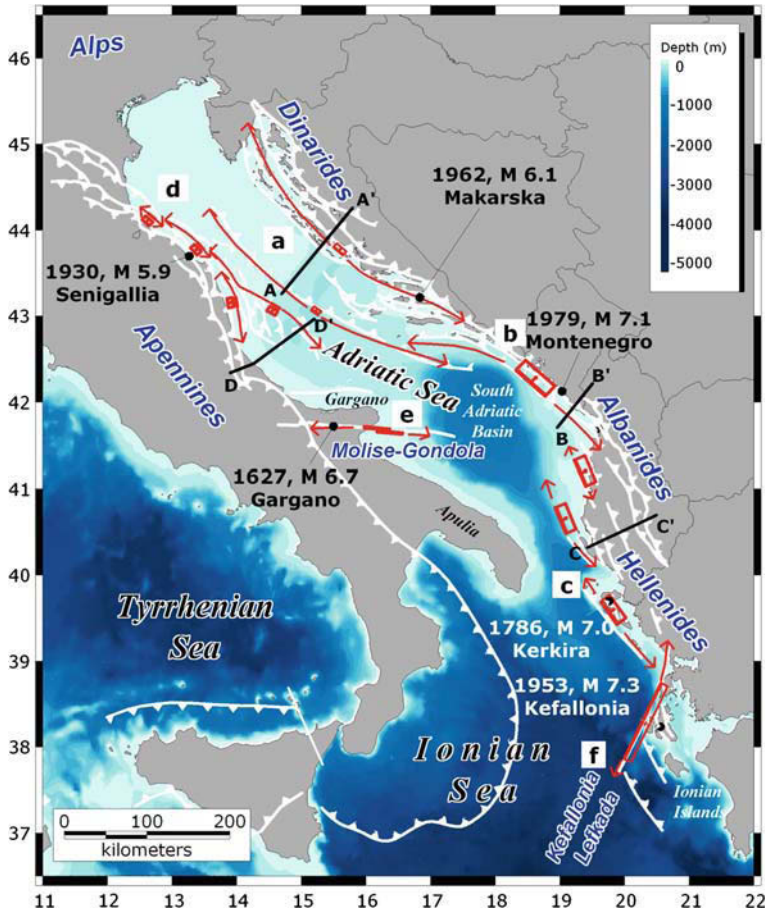
Figure 1

Tectonic sketch map of the Adriatic basin. The double-headed arrow indicates the floating path of the Typical Faults (see Table 1 for their parameters). a) Coastal and Offshore Croatia; b) Montenegro; c) Albania - Northern Greece; d) Northern Apennines; e) Apulia; f) Kefallonia-Lefkada. Selected major earthquakes discussed in the paper are indicated. The traces of the cross sections in Figure 2 are also shown.

tectonics standpoint, the Adriatic Sea falls in the middle of the Adria plate that is being pushed by Africa northward against stable Europe. Overall, the Adria is affected by active compression and overridden by thrust belts on all sides.

The purpose of this work was to assess systematically the potential threat posed by earthquake–generated tsunamis on the Italian coastline of the Adriatic Sea, following the approach proposed by LORITO *et al.* (2008). To this end, we first compiled a database of potentially-tsunamigenic earthquake faults, then used them as input in the preparation of scenarios of maximum water height (above mean sea level) based on numerical simulations of tsunami propagation. Potential tsunami sources were selected from the seismogenic sources listed in version 3.0.4 of the Database of Individual Seismogenic

Sources (DISS WORKING GROUP, 2007; BASILI *et al.*, 2008), adapted to the modeling needs and integrated with additional data, particularly for the eastern side of the basin.

Our scenarios supply at-glance information of the expected tsunami impact onto the target coastline and can be progressively updated as knowledge of earthquake source advances. As such, our approach can be easily converted into an application program for disaster prevention from which results can be handed out to a variety of stakeholders, such as civil protection agencies or land-use planners. Similar approaches have been independently developed, for example, for Australia and New Zealand by BURBIDGE and CUMMINS (2007) and POWER *et al.* (2007), respectively. Using a different approach, PAULATTO *et al.* (2007) studied the tsunami potential of the Adriatic Sea seismic sources adopting two fault locations for each selected source zone.

The results of our work include the determination of the maximum water height along 2100 km of the Adriatic Italian coastline calculated for six source zones located inside or very close to the Adriatic Sea. These results were compared with the threat posed by tsunamis generated in the Hellenic Arc source zone (LORITO *et al.*, 2008), i.e., the source of the largest tsunamis generated outside the basin with the capability to strike our target coastline. All profiles of maximum water heights are given in aggregated form together with averages and standard deviations. Maxima were also classified in a three-level code of expected tsunami threat. Finally, we explored the role of specific bathymetric features in controlling the focalization-defocalization of tsunami energy.

2. Method

To assess the potential threat posed by earthquake-generated tsunamis in the Adriatic Sea we adopted the method developed by LORITO *et al.* (2008). We systematically carried out a number of simulations for all source zones that can possibly affect the target coastlines. A Source Zone (SZ) includes an active tectonic structure at regional scale that is made up of a number of individual fault segments, each one capable of releasing a significant earthquake. For each SZ we identified a Maximum Credible Earthquake (MCE) and an associated Typical Fault (TF). We let the TF float along the entire SZ and computed a tsunami scenario at regular intervals. To assess the MCE for each SZ we selected the largest earthquake that has ever occurred in that zone and for which there exists, or is possible to obtain, a reliable magnitude estimation. The TF is defined by parameters that must comply with both the seismological properties of the MCE and the tectonic properties of its parent SZ. To estimate them we largely relied on published data, and particularly on those made available in the DISS database (DISS WORKING GROUP, 2007; BASILI *et al.*, 2008). Strike, dip and rake were slightly adjusted as needed to account for the internal geometric variations of the SZ at each position of the TF. The amount of slip was derived from the seismic moment of the MCE, using the formulations by KANAMORI and BRODSKY (2004). Steps were taken at one or half fault length to guarantee a sufficient spatial sampling of the tsunamigenic structure. At each new position the TF was made to release its MCE by

uniform slip over the entire fault plane. The initial seawater elevation associated with the earthquakes generated by the floating TF was assumed equal to the coseismic vertical displacement of the sea bottom computed according to OKADA's (1985, 1992) formula. Rupture was assumed to be instantaneous, and the initial velocity field was assumed to be identically zero. For the numerical modeling of the tsunami propagation we used the nonlinear shallow water equations that were solved numerically by means of a finite - difference method on a staggered grid (MADER, 2001). We set the boundary conditions as pure wave reflection at the solid boundary, by setting to zero the velocity component perpendicular to the coastline. Full wave transmission was set at the open boundary (open sea). The sea-floor topography was taken from the ETOPO2 bathymetric data set (SMITH and SANDWELL, 1997), that we oversampled at 0.5 arcmin to achieve a sufficient sampling of the wave features. We fixed a minimum depth of 10 meters, then modified all shallower bathymetry accordingly. Our simulation domain is 9° to 23° longitude E, and 30° to 46° latitude N.

We performed a distinct numerical experiment for each fault position in each SZ for a total of 129 runs. From each simulation we extracted the maximum water height above sea - level (HMAX) profiles along the Adriatic coasts of Italy. The HMAX was calculated at the points adjacent to the coastline, that is at a fixed water depth of 10 meters. The HMAX values along the target coastline were then grouped according to the causative source zone. For each group we then calculated the absolute maximum, the average, and the standard deviation of the HMAX values. Finally, we set three HMAX thresholds at 0.05, 0.5, and 1.0 m and coded the different levels of threat as *marine*, *land* and *severe land threat*, respectively. ALLEN and GREENSLADE (2008) pointed out that the practical use of the threat levels requires considerable caution because the local effects of a tsunami can be precisely described only through fine-scale inundation models. In addition to being computationally very demanding, this approach is not feasible because inundation models rely on fine-scale bathymetry data that are currently not available for the entire coast under investigation (see also LORITO *et al.*, 2008). Nevertheless the HMAX represents an average coastal level that is certainly appropriate for comparing risk levels and for tsunami preparedness, provided that a *caveat* is included specifying that the wave height can be locally higher.

3. Tsunamigenic Source Zones in the Adriatic Sea

The Adriatic Sea is mostly surrounded by active fold-and-thrust belts and strike-slip faults (Fig. 1). Frequent earthquakes occur along these well-known fault zones, most of which run close to the coastlines or in the open sea and are thus potential sources for tsunamis. The largest earthquakes (M > 7) occurred near the eastern margin of the central Adriatic Sea, along the Montenegro portion of the Dinaride-Albanide chain, and at the southern end of the basin near the Ionian Islands along the Kefallonia-Lefkada right-lateral shear zone. Most of the remaining structures exhibit a potential for earthquakes of magnitude $6 \leq M \leq 7$, thereby holding a significant tsunamigenic potential.

This section describes the local tectonic setting of the six selected Source Zones grouped into four major tectonic domains. The reasoning followed to define the Typical Fault (TF) of each zone will also be illustrated.

3.1. Dinarides, Albanides and Hellenides

A contractional belt longer than 1,000 km runs along the eastern margin of the Adriatic Sea from the southern Alps, to the north, to the Kefallonia-Lefkada Fault, to the south (Fig. 1). This fold-and-thrust belt is usually split into three different domains named Dinarides, Albanides and Hellenides, respectively from north to south, that started forming as a consequence of the subduction of Adria under the European plate. Adria acts as an indenter pushing northward into stable Europe (e.g., ALJINOVIĆ et al., 1990; PRELOGOVIĆ et al., 1995; HERAK, 1999). GPS data document compressional strain across the chain at a rate of about 30 nanostrain/yr (HOLLENSTEIN et al., 2003; SERPELLONI et al., 2005). Stronger earthquakes mostly concentrate in the Albanides and Hellenides. The outer portion of these chains is partly located offshore and characterized by numerous thrust fronts that all seem to be currently active. Available focal mechanisms indicate predominant SW-NE shortening (PAPAZACHOS et al., 1999); reverse faulting earthquakes dominate (VANNUCCI et al., 2004; PONDRELLI et al., 2006).

Croatia. The Dinarides is a wide NW-SE fold-and-thrust belt stretching from southwestern Slovenia to Croatia along the Adriatic coast (Fig. 1). The Dinaric accretionary prism is dominated by NW-SE trending, NE dipping thrust faults (MAMUZIĆ, 1975; IVANOVIĆ et al., 1976; HERAK, 1991, 1999) whose geometry is well imaged in seismic profiles and constrained by gravity surveys (Fig. 2a; SKOKO et al., 1987; ALJINOVIĆ et al., 1990; LAWRENCE et al., 1995; PRELOGOVIĆ et al., 1995). In the southern and central parts of the Dinarides the active thrust front lies offshore and is blind along most of its length (TARI-KOVAČIĆ and MRINJEK, 1994; HERAK et al., 2005). The amount of shortening and the hanging-wall displacement increase towards the NE, where the faults become surface-breaking (KUK et al., 2000; HERAK et al., 2005). Moving towards the NW, fault planes become steeper and exhibit more oblique to dextral strike-slip kinematics (PRELOGOVIĆ et al., 1995).

GPS studies show a shortening rate across the central Dinarides of few a millimeters per year (BATTAGLIA et al., 2004; GRENERCZY et al., 2005). Earthquake focal mechanisms manifest thrusting on NE-dipping faults at shallow to medium depth in the Dinarides and oblique to dextral-strike slip motion on steeper NE-dipping planes in the northern Adriatic (HERAK et al., 1995; IVANČIĆ et al., 2006). The average orientation of compression in the Dinaric region is N-S, varying from N15° to N340° (HERAK et al., 1995; PRELOGOVIĆ et al., 1999, 2003), also consistent with GPS data. BENNETT et al. (2007) used regional GPS data to model a N77°W oriented thrust fault that accommodates the modern stress field in the southern Dinarides.
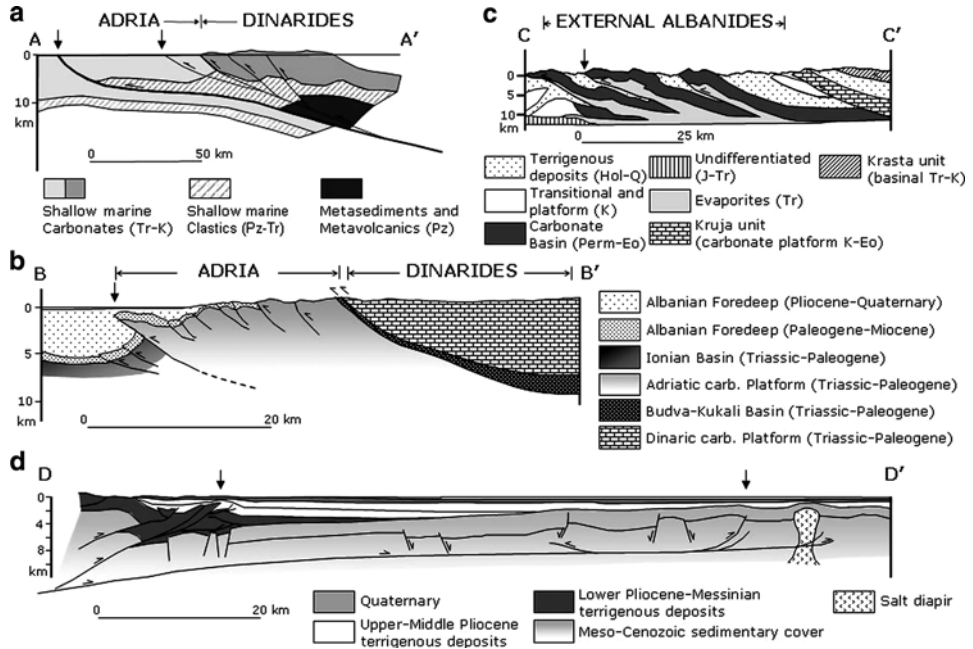
Figure 2

Cross sections of the main thrust structures. Vertical arrows indicate the position of the active fronts selected for the modeling (see Fig. 1). a) Dinarides: Data taken from Tari-Kovačić and Mrinjek (1994); Tari (2002) and Ivančić *et al.* (2006); b) Montenegro: Data taken from Dragašević (1983) and Picha (2002); c) Northern Albania offshore: Section modified after Graham Wall *et al.* (2006); d) Northern Apennines: Section redrawn after Scrocca *et al.* (2007).

Based on the geometry, kinematics, and spatial distribution of individual faults and on data pertaining to the associated instrumental and historical earthquakes, we have chosen to split the Dinarides into two source zones. One running close to the coast of mainland Croatia (Fig. 1); the other located offshore almost in the middle of the Adriatic Sea (Fig. 1).

The geometry and depth of the typical fault of the Coastal Croatia SZ (Table 1) were taken from published seismic profiles and analyses of instrumental earthquakes. From south to north, the strike of the typical fault varies by nearly 40° from NW-SE to NNW-SSE; in its turn, the rake varies from almost pure thrusting to dextral oblique thrusting. The strongest earthquake generated by the Dinaric coastal source zone is the M_L 6.1, 11 January, 1962 Makarska earthquake that was also followed by a tsunami (Herak *et al.*, 2001). Other earthquakes associated with this source zone are the 2 July, 1898, $I_0 =$ IX, Split; 29 December, 1942, M_L 6.0, Imotski (Kuk *et al.*, 2000); and 5 September, 1996, M_L 6.0, Ston (Markušić *et al.*, 1998). As the 1962 earthquake is the largest known event associated with this source zone, we chose M_W 6.1 as the magnitude of its MCE.

The Offshore Croatia SZ (Table 1) comprises a blind thrust faulting system. The strike of the typical fault changes from N320° to N290° from south to north whereas the rake changes from pure thrusting to oblique slip. The largest event recorded in the past 20 years

Table 1

Summary of parameters of the Typical Faults shown in Figure 1. L: fault length; W: fault down-dip width; D: depth of top edge of fault below sea level. MCE: Maximum Credible Earthquake for the given fault

	Source Zone	L (km)	W (km)	D (km)	Slip (m)	Strike (deg)	Dip (deg)	Rake (deg)	MCE (M_W)
a	Coastal Croatia	16	7	1	0.6	312	40	110	6.1
	Offshore Croatia	11	6.6	2	0.6	305	45	80	6.0
b	Montenegro	50	20	1	2.5	312	35	82	7.2
c	Albania-N Greece	36.2	16	1	2.0	337	35	96	7.0
d	Northern Apennines	12	8	2.5	0.6	140	30	90	6.1
e	Apulia	34	15	1	0.9	275	80	173	6.7
f	Kefallonia-Lefkada	110	18	3	2.0	27	60	162	7.3

is the 29 March 2003, M_W 5.6 earthquake, located near the island of Jabuka (HERAK *et al.*, 2005). Instrumental and historical catalogues locate the 30 November, 1934, M_L 5.6 event in the northwestern part of this source zone; KUK *et al.* (2000) also place in the same epicentral region a disastrous event in 361 AD. Even if known earthquakes do not exceed M 5.6, we adopted the value of M_W 6.0 for the MCE because reports of the 361 AD earthquake hint at a larger magnitude than that of the more recent instrumental event.

Montenegro. This portion of the chain runs NW-SE parallel to the coast just offshore of Montenegro and is narrower than its own northern and southern prolongations (Fig. 1). It comprises fewer major structures than the rest of the chain, however, these structures are bigger and more tightly imbricated. The outermost thrust front lies about 20 km off the coast (Fig. 2c; e.g., DRAGASEVIC, 1983; PICHA, 2002).

The area is currently characterized by moderate shallow instrumental earthquakes, however, a number of strong events ($M_W \geq 7.0$) are listed in the historical catalogue compiled by PAPAZACHOS and PAPAZACHOU (1997). The largest well-known earthquake (M_W 7.1) occurred on 15 April, 1979 off the coast of southern Montenegro (CONSOLE and FAVALI, 1981), and was probably generated by the most external thrust (BENETATOS and KIRATZI, 2006). It also generated a tsunami (e.g., BEDOSTI and CAPUTO, 1986; see also PAULATTO *et al.*, 2007 and references therein). Most earthquakes in this zone, including the 1979 event, exhibit reverse focal mechanisms with NW-SE fault planes (VANNUCCI *et al.*, 2004; BENETATOS and KIRATZI, 2006; PONDRELLI *et al.*, 2006), overall suggesting compression with P-axes oriented roughly N230° (PAPAZACHOS *et al.*, 1999). The average strike and rake from focal mechanisms are consistent with plate motion vectors derived from GPS data and with the orientation of thrust fronts.

We placed the Montenegro SZ (Table 1) on the main and most external of the thrust fronts, which has the largest potential of generating tsunamis and is thought to be responsible for the 1979 earthquake. As for the MCE, we adopted M_W 7.2 based on the maximum magnitude assessment given by ALIAJ *et al.* (2004) for the Lezha-Ulqini area, which includes the majority of the Montenegro SZ. We derived strike, dip, and rake from focal mechanisms and from the average geometry of the thrust faults as revealed by seismic reflection profiles.

Albania — Northern Greece. In the southern Adriatic Sea, the submerged edge of the Apulia platform acts as an indenter in the European plate. Here continental collision creates a series of NW-SE thrusts fronts involving the Apulian platform itself (Fig. 1), occasionally interrupted by NE-SW strike-slip faults. Seismic profiles image the sole-thrust at about 10 km depth (Fig. 2b; e.g.: ARGNANI *et al.*, 1996; SULSTAROVA *et al.*, 2000; BALLAURI *et al.*, 2002; FINETTI and DEL BEN, 2005; ALIAJ, 2006; GRAHAM WALL *et al.*, 2006).

The Albania offshore is characterized by shallow instrumental seismicity with many $4 < M < 5$ earthquakes (DUNI *et al.*, 2003), although numerous larger events (up to M_W 6.8) are reported by historical catalogues (e.g., PAPAZACHOS and PAPAZACHOU, 1997). The offshore area of northern Greece is also characterized by shallow seismicity, nonetheless events in the magnitude range of 6 to 7 are frequent. The largest known event took place near Kerkira Island on 5 February, 1786 and had an estimated M_W 7.0. Another large earthquake (M_W 6.8) is thought to have occurred near Kerkira on 20 February, 1743 (PAPAZACHOS and PAPAZACHOU, 1997; see also GUIDOBONI *et al.*, 2007 for a complete review). Most earthquakes exhibit reverse focal mechanisms over NW-SE planes both in Albania and northern Greece (VANNUCCI *et al.*, 2004; PONDRELLI *et al.*, 2006). Subhorizontal compression with P axes from focal mechanisms trending 230–240° dominates the area (PAPAZACHOS *et al.*, 1999); the average strike and rake from focal mechanisms are consistent with plate motion vectors derived from GPS data and with the orientation of thrust fronts.

We identified the Albania - Northern Greece SZ (Table 1) as made of three segments that cover the set of thrust fronts with the highest potential for tsunami generation (Fig. 1). As for the MCE, we adopted the 1786 Kerkira Island event. A M_W 7.0 is also the maximum expected magnitude estimated by ALIAJ *et al.* (2004) for this area. Similarly to the Montenegro SZ, we derived strike, dip, and rake from focal mechanisms and from the average geometry of the thrust faults as detected on seismic reflection profiles.

3.2. *Northern Apennines*

The Apennines is a fold and thrust belt running all along the Italian peninsula. The northern Apennines orogenic wedge grew and migrated throughout the Neogene as a response to the NE-ward roll-back of a retreating slab at the western edge of the Adria plate (e.g., ROYDEN *et al.*, 1987 DOGLIONI, 1991). The most external thrust structures are known from seismic exploration data and are located offshore beneath a cover of Early Pliocene to Quaternary synorogenic deposits (Figs. 1 and 2d; CASERO *et al.*, 1990; DEL BEN, 2002; FRANCIOSI and VIGNOLO, 2002; SCROCCA *et al.*, 2007).

The shortening rate across the thrust belt during the whole orogenic process is estimated at ~ 2.9 mm/yr (BASILI and BARBA, 2007, and references therein). Because of the limited number of permanent stations available, GPS data on strain rates for this area are scarce and not yet reliable; however they do indicate shortening at a few mm/yr across the northern Adriatic (ZERBINI *et al.*, 2006). In addition, geomorphic evidence for

active growth above individual blind thrusts running along the coast has provided a slip rate of 0.24–0.36 mm/yr (VANNOLI et al., 2004). Available focal solutions show NE-SW compression at shallow depth, consistent with the geometry of the thrusts detected in seismic profiles (PICCININI et al., 2006; LAVECCHIA et al., 2007; MELETTI et al., 2008).

We identified a long portion of the coastal and offshore thrusts as the Northern Apennines SZ (Table 1). The largest known event occurred on 30 October, 1930 on the coast close to Senigallia and had an estimated magnitude of M_W 5.9. This event was followed by a small tsunami (BOSCHI et al., 2000). However, the 1930 earthquake is probably not the largest to have ever occurred in the area, as geological and geomorphic data from an area about 30 km to the NW indicate the presence of a fault whose size is compatible with earthquakes up to M_W 6.1 (DISS WORKING GROUP, 2007). Although there is no known historical earthquake associated with this fault, we sized the TF of this source zone on the basis of geological evidence, as this represents the worst case scenario. The eastern boundary of the source zone follows the pattern of the domain that according to SCROCCA (2006) has been affected by contractional deformation during the Late Quaternary.

3.3. Apulia

The southern part of the Apulian foreland is characterized by a number of right-lateral E-W striking shear zones (Fig. 1). These tectonic structures extend westward below the outer edge of the Apennines orogenic wedge and eastward into the Adriatic Sea. Most of them probably started forming during the Mesozoic under a different tectonic setting as left-lateral kinematics is documented by structures with a long deformation history, but according to the majority of workers their most recent reactivation is dominantly right-lateral (ARGNANI et al., 1993; BOSELLINI et al., 1993; CHILOVI et al., 2000; DI BUCCI and MAZZOLI, 2003; VALENSISE et al, 2004). The northernmost shear zone, known as Tremiti Line, is thought to represent the effect at shallow crustal depths of a lithospheric tear in the Adria microplate (DOGLIONI et al., 1994). A few kilometers to the south of the Tremiti Line, the Molise-Gondola shear zone, which includes the Mattinata fault, shows evidence of recent dextral strike-slip activity in the offshore area (DI BUCCI et al., 2007; RIDENTE et al., 2008).

The present-day stress field of this source zone exhibits NE-SW compression that appears to be a direct result of the Africa-Europe convergence (e.g., NOQUET and CALAIS, 2004; SERPELLONI et al., 2007). Focal mechanisms mostly consist of dextral strike-slip faulting on subvertical planes at depths of 10–25 km (PONDRELLI et al., 2004; VANNUCCI et al., 2004; MILANO et al., 2005; DEL GAUDIO et al., 2007). The western portion of the Molise-Gondola shear zone is responsible for the 31 October and 1 November, 2002, M_W 5.7 Molise earthquakes (VALENSISE et al., 2004; CHIARABBA et al., 2005). Historical and instrumental seismicity data suggest the presence of similar shear zones both to the north and to the south of the Molise-Gondola (FRACASSI and VALENSISE, 2007; MELETTI et al., 2008).

The largest known earthquake of the Apulian foreland is the 30 July, 1627, M_W 6.7 Gargano event (GRUPPO DI LAVORO CPTI, 2004). It was followed by a tsunami that severely affected the northern coast of the Gargano Promontory (TINTI and PIATANESI, 1996; BOSCHI *et al.*, 2000; TINTI and ARMIGLIATO, 2003), where geological evidence for recurrent tsunamis is found in coastal deposits (DE MARTINI *et al.*, 2003). We have chosen the Molise-Gondola shear zone as a sample structure for the whole set of E-W faults that affect this region because it is the best documented structure, especially in the offshore, and adopted it as the Apulia SZ (Table 1). The size of the 1627 earthquake was adopted as its MCE; its causative source from the DISS WORKING GROUP (2007) was taken as typical fault for this shear zone.

3.4. *Kefallonia-Lefkada*

The Kefallonia-Lefkada fault marks the boundary between the NNE-directed subduction of the Africa oceanic lithosphere beneath the Aegean continental lithosphere to the south and the continental collision between the Adriatic and European plates to the north (Fig. 1). South of the Kefallonia-Lefkada alignment the rate of convergence between the African and Aegean plates is ∼4–5 cm/yr and observed GPS velocities are the fastest of the entire Mediterranean basin (KAHLE *et al.*, 2000; MCCLUSKY *et al.*, 2000), whereas north of it they decrease rapidly. As a result, inferred strain rates vary from more than 100–200 nanostrain/yr in the Hellenic Arc to about 30 nanostrain/yr in the Hellenides chain (KAHLE *et al.*, 2000; HOLLENSTEIN *et al.*, 2003). The Kefallonia-Lefkada fault thus accommodates a deformation of at least 100 nanostrain/yr (KAHLE *et al.*, 1998; HOLLENSTEIN *et al.*, 2006). GPS data also indicate right-lateral relative motion across the shear zone at ∼4 cm/yr, even if earthquakes account for only about 50% of that value (KAHLE *et al.*, 1996).

The Kefallonia-Lefkada fault is one of the most seismically active areas in the Mediterranean and is largely characterized by strike-slip earthquakes (PAPAZACHOS *et al.*, 1998; VANNUCCI *et al.*, 2004). In 1983 a M_W 7.0 earthquake with a transpressional mechanism occurred on the southern portion of the zone (PAPAZACHOS and PAPAZACHOU, 1997; LOUVARI *et al.*, 1999). The largest known event in this area is the 12 August, 1953, M_W 7.3 Kefallonia earthquake that caused ∼0.5 m of vertical displacement testified by raised shorelines (PIRAZZOLI *et al.*, 1994; STIROS *et al.*, 1994). LOUVARI *et al.* (1999) associate this earthquake with the southern segment of the Kefallonia-Lefkada strike-slip fault.

We identified as the Kefallonia-Lefkada SZ (Table 1) the entire fault and adopted the size of the 1953 event (M_W 7.3) as the MCE, consistent with the maximum magnitude reported for the Kefallonia zone by PAPAIOANNOU and PAPAZACHOS (2000). We constrained the depth of this SZ based on the hypocentral distributions from various workers (up to 20 km). Strike, dip and rake were also based on data from various workers who analyzed the instrumental seismicity (PAPAZACHOS *et al.*, 1998; LOUVARI *et al.*, 1999); its kinematics is consistent with the GPS velocity field by COCARD *et al.* (1999).

4. Modeling Results

We analyzed the tsunami impact expected on the Adriatic coasts of Italy as a result of earthquakes generated in each of six independent SZs. All tsunamis generated by a single SZ were grouped together. The corresponding HMAXs expected along the Adriatic coastline of Italy are shown as profiles of their maximum, average and average plus one standard deviation, respectively (Fig. 3). Abscissa values are distances along the coastline and increase from south to north from an arbitrarily chosen starting point (Fig. 4); since the true length of coastlines depends on the yardstick used, these are not intended to be accurate distances but rather a practical way to map the HMAXs values along the coastline. We also emphasized the threat level by color coding the background of each diagram. The use of such color codes is quite a common practice and a similar approach is routinely adopted for tsunami warnings and advisory by the Japan Meteorological Agency (http://www.jma.go.jp/en/tsunami/). We decided to adopt a three-color code: yellow for *marine threat*, corresponding to 0.05 m < HMAX < 0.5 m; orange for *land threat*, corresponding to 0.5 m < HMAX < 1 m; red for *severe land threat*, corresponding to HMAX > 1 m. This choice is coherent with the approach followed by ALLEN and GREENSLADE (2007), who proposed a three-level stratified warning method and set a threshold of 0.5 m between *marine* and *land threat* based on WHITMORE (2003).

4.1. Croatia, Montenegro, Albania, and Northern Greece

Our calculations show that the Croatia SZs pose a rather low threat to a ∼700 km-long stretch of the Adriatic coast of Italy from the northern edge of the Gargano promontory to north of Ancona (Fig. 3a). Here the level of maximum HMAXs (black line) enters the yellow zone by 0.1 m at the most, hence exceeding the lower threshold of the *marine threat* level. Conversely the average HMAX (blue line) always lies below this level. The difference between the maximum and average values is almost one order of magnitude at some locations, and the standard deviation is relatively high (green line). This may be the evidence that, depending on the relative position of the fault with respect to the coast, the tsunamis following each single earthquake generated by the floating fault have mainly local effects. It is also likely that the main contribution to the maximum values is brought by the source zone facing the coasts of Italy, whereas tsunamis generated in the Coastal Croatia SZ are shielded by the Dalmatian Islands (Figs. 1 and 4).

The Montenegro SZ revealed a tsunamigenic potential beyond the attention level, i.e., over the lower bound of *marine threat*, almost everywhere on the Adriatic coast of Italy (Fig. 3b), and consistently inside the *marine threat* band from about the 150 km position in Apulia to just north of Ancona. *Land threat* (orange background) is to be taken into account for a ∼550 km-long stretch running along the Apulian coast from the 200-km position to north of the Gargano promontory. The Gargano itself is exposed to a *severe*
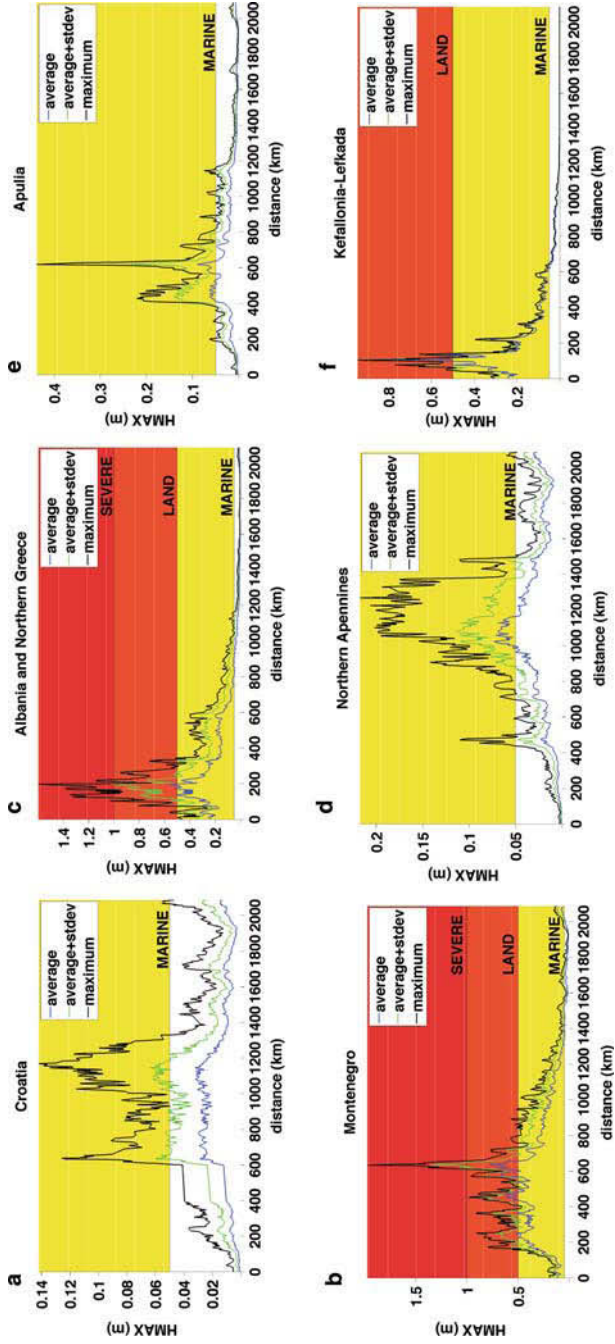
Figure 3

Diagram of tsunami impact along the Italian coastlines of the Adriatic Sea following earthquakes generated by the a) Croatia SZ, b) Montenegro SZ, c) Albania-Northern Greece SZ, d) Northern Apennines SZ, e) Apulia SZ, and f) Kefallonia-Lefkada SZ. The profiles show maximum (black), average (blue) and average plus one standard deviation (green) of the HMAXs (maximum water height above the mean sea level) aggregated for each SZ. Horizontal scales are distances in kilometers: see Figure 4 for locating the diagram relative to the coastline. Vertical scales are water heights in meters. Yellow, orange and red in the background show the *marine*, *land* and *severe land threat* levels respectively (see text).

land threat level, as shown in Figure 3b, where the peak of the maximum values (black line) is almost two meters high, thereby largely entering the red code zone.

The Albania-Northern Greece SZ (Fig. 3c) poses a threat comparable to that of Montenegro. The *marine threat* level is reached on the entire coast stretch from Apulia up
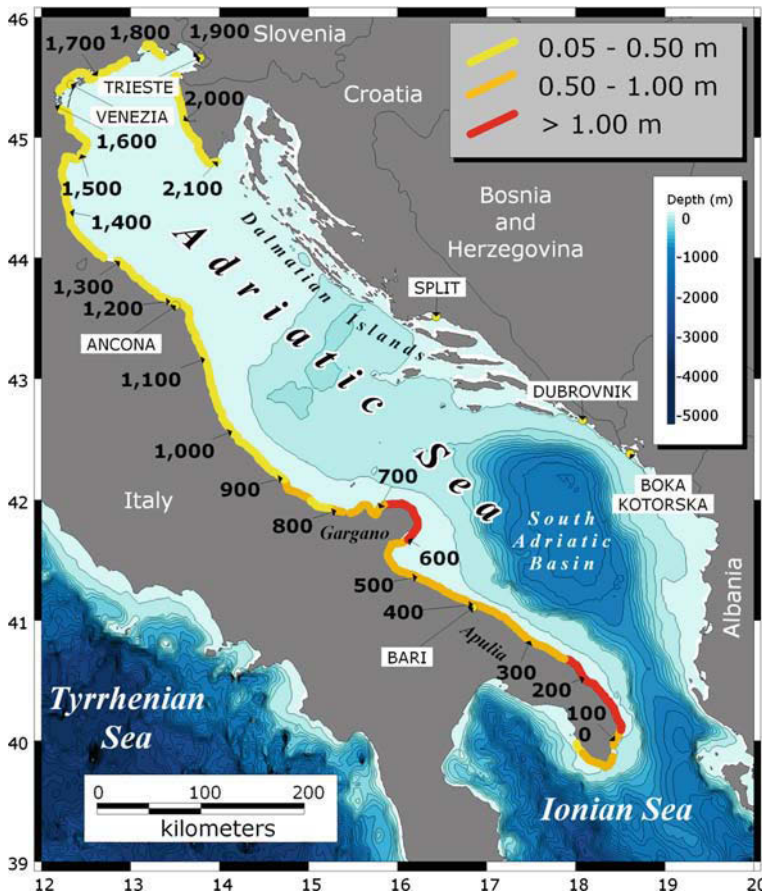

Figure 4

Combined threat levels posed by all SZs considered in this study (except for the Hellenic Arc), color-coded as in Figure 3, and progressive distance (in km) along the target coastlines used for displaying the modeling results. This map is intended for use in conjunction with Figures 3, 6 and 7.
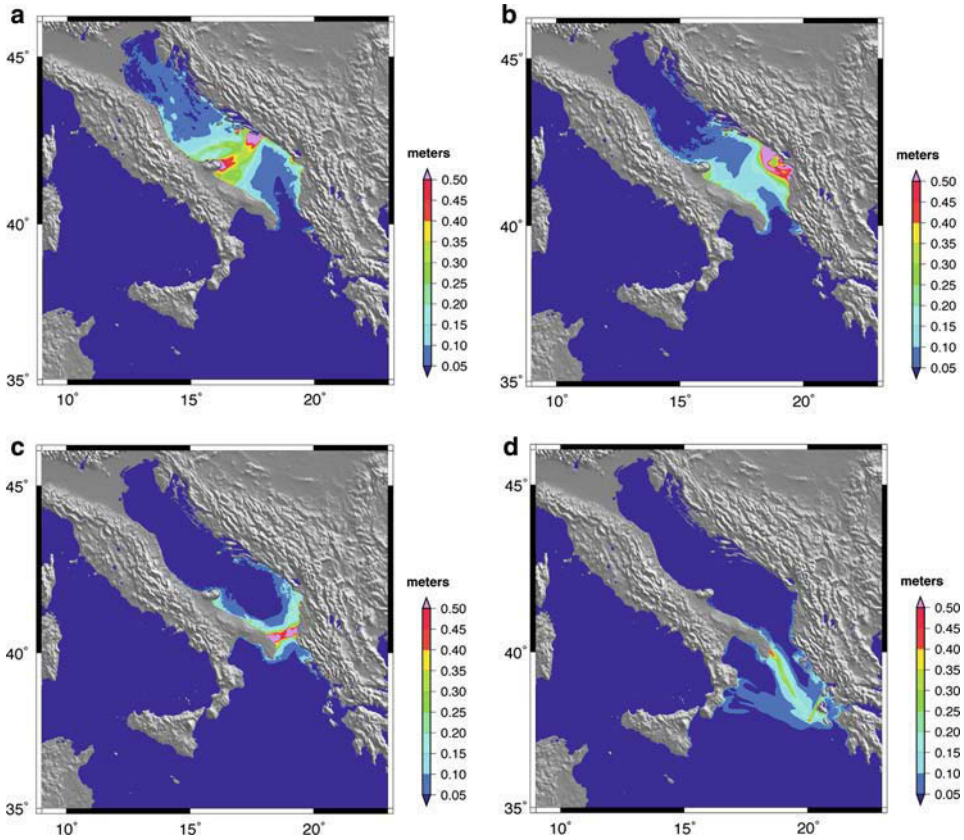
Figure 5

Map of the maximum water height above the mean sea level in the simulation domain, for some selected fault positions in two different SZ: a) and b) are generated by two faults in the Montenegro SZ; c) is generated by a fault in the Albania-Northern Greece SZ; d) is generated by a fault in the Kefallonia-Lefkada SZ.

to around Ancona, however the southern part of Apulia is exposed to *land* and even *severe land threat* involving a ~50 km-long stretch where the highest peak of maximum HMAX may exceed 1.5 m.

It is worth analyzing jointly the results we obtained for Montenegro and Albania as they revealed a peculiar bathymetry-induced propagation effect due to the presence of the relatively deep South Adriatic Basin (Fig. 1). Figures 5a-c show HMAX maps for the entire calculation domain. Figures 5a and 5b show the propagation of the tsunamis generated by two earthquakes on the Montenegro SZ, whereas Figure 5c shows a tsunami generated by the Albania-Northern Greece SZ. The case of Figure 5b shows that the basin acts as a convex lens deflecting most of the propagating wave energy back to the Montenegro coast, thus limiting the height of the tsunami wave reaching the Apulian coast. This effect is predicted for faults located in the southernmost portion of the Montenegro SZ. Conversely, when the source fault is placed to the north of the South

Adriatic Basin (Fig. 5a), tsunami energy is focused towards the Gargano promontory at the basin edge. This is why the height of the narrow peak of the maximum values at ∼650 km in Figure 3b is almost three times larger than the corresponding average value, and it is abundantly in the *severe land threat* band, whereas the threat to the adjacent coast to the south is only at the *land threat* level, with an average of less than half of the tsunami wave height. At the southern end of the basin, the Albania-Northern Greece SZ again exceeds 1.0 m (Fig. 5c), and poses a *severe land threat* to Apulia. In this case, the proximity of the sources to the target coasts causes the maximum to be about three times the average HMAX values (Fig. 3c), meaning that the tsunami may be locally higher along the stretch of coast directly facing the source. This *severe land threat* peak is slightly broader than that of the Montenegro SZ case, reflecting the fact that more than one source contributes to it as the fault floats.

4.2. Northern Apennines

The Northern Apennines SZ generally poses a low threat that can only locally be slightly higher but is always comparable to that of the Croatia offshore SZ. The affected portion of the Adriatic coasts of Italy is restricted to a ∼750-km-long stretch from the northern side of the Gargano promontory to the south of the Po River delta (Fig. 3d). The level of maximum HMAXs (black line) attains the *marine threat* zone from ∼1050 to ∼1400 km. Similarly to the Croatia SZ, the average (blue line) is significantly lower than the maximum HMAX. Near-field effects of the coastal sources again dominate, the main contribution to the maximum being brought by faults facing the coasts of Italy, whereas faults running farther offshore contribute relatively less (Fig. 1). The peak at ∼450 km could result from a focalization effect at the northern edge of the deeper South Adriatic Basin, as illustrated earlier for the Montenegro case.

4.3. Apulia

The typical fault floating along the Apulia SZ generates a series of tsunamis that may pose a *marine threat* (Fig. 3e) along a stretch of coast extending from Bari (at 400 km) northward for ∼500 km. Further north the lower *marine threat* threshold is exceeded only at scattered locations. Around the ∼500 km position there seem to be only near-field effects, as revealed by the difference between maximum and average values. The highest peak is almost 0.5 m, just below the lower threshold of *land threat*, and occurs at ∼640 km.

4.4. Kefallonia-Lefkada

The maximum HMAXs profile of the Kefallonia-Lefkada SZ (Fig. 3f) features a quite narrow peak that starts in the *marine threat* band and then rises into the *land threat* band in the 40–140 km interval. Maximum height is ∼0.9 m, almost at the lower threshold of

the *severe land* threat band. The maxima curve then drops again while remaining in the *marine threat* band as far as a point at 640 km. North of the Gargano promontory the coast is free from serious threats. Conversely, the peak that almost reaches the *severe land threat* level is due to a bathymetric effect (Fig. 5d). The shelf extending to the southeast of Apulia (Fig. 1) acts as a wave-guide for tsunami propagation. It focuses the energy in a relatively narrow band thereby enhancing the wave height that reaches the southernmost tip of Apulia. This is the well-understood continuous refraction and amplification phenomenon seen during the global propagation of the 26 December, 2004 Sumatra-Andaman tsunami—just to mention a recent example — when the wave reached the Mid-Atlantic Ridge, which in turn efficiently transmitted the wave energy (THOMSON *et al.*, 2007). Another example of a similar phenomenon is the unexpectedly major damage suffered by the Crescent City harbor, California, on occasion of the 15 November, 2006 Kuril Islands earthquake (M_W 8.3) and tsunami. The damage was caused by a secondary wave that was reflected by a sea-mount and focused by the Mendocino escarpment, and that arrived at Crescent City two hours after the main wave (KOWALIK *et al.*, 2008). Thus, despite the slight vertical sea-floor displacement expected due to the strike-slip style of the causative fault, the Kefallonia-Lefkada SZ poses a significant threat to the coasts of Italy, which may be further increased by bathymetric amplification.

5. *Discussion*

We investigated the potential effects on the Italian coasts of the Adriatic Sea for all the earthquake source zones that are known to be capable of generating tsunamis. To this end we used an approach that combines a detailed knowledge of the tectonic setting of the source zones with the evaluation of the tsunami impact onto the target coastline. This was done by introducing the concept of a typical fault that is sized after the maximum credible earthquake of the area and is let floating along its parent source zone.

Similar approaches for other tsunami-prone areas in the world are those of BURBIDGE and CUMMINS (2007) and POWER *et al.* (2007). The first explored the effects on the western coast of Australia for tsunamis generated by faults in three different positions along the Sunda Arc with two possible earthquake magnitudes (M_W 8.5 and 9.0). The second analyzed the impact on New Zealand's coasts of tsunamis generated in the South America subduction zone, exploring a range of possible earthquake magnitudes and obtaining results expressed in probabilistic terms.

By displaying the aggregated HMAX values throughout target coastlines our method allows an easy comparison between the effects of different source zones and shows the relative level of tsunami threat for different stretches of the coast. The results of our modeling could also serve as input data for detailed studies of local effects, provided that finer bathymetry data are available. The purpose of our work is to provide an estimation of HMAX for an earthquake occurring at any position along a known source zone rather

than just for a specific past earthquake. Historical tsunamis of the Adriatic Sea were recently reviewed by PAULATTO et al. (2007), who also carried out simulations for a set of earthquakes in six potential source zones. Their approach, however, substantially differs from ours as the earthquake sets are defined considering three magnitude values and three depth values at two locations, inland and offshore, for each source zone; the results are then shown in terms of maximum water height and arrival time at selected localities.

Our predictions can be compared with limited historical accounts of tsunamis that occurred around the Adriatic basin:

- according to GUIDOBONI and TINTI (1988), the tsunami that followed the 1627 Gargano earthquake caused sea withdrawal of about 3 km at the mouth of the Fortore River (northern side of Gargano) and an estimated runup of 2–3 m in the town of Manfredonia (southern side of Gargano);
- according to contemporary newspapers, an anomalous high tide was observed in the Ancona harbor after the 1930 Senigallia earthquake. An American steamship broke its moorings and struck the docks. A tsunami intensity of 4 is attributed to this event in the Italian Tsunami Catalogue (BOSCHI et al., 2000; MARAMAI et al., 2007; TINTI et al., 2007);
- according to SOLOVIEV et al. (2000), no tsunami followed the 1953 Kefallonia earthquake, even if a previous publication, based on press reports, indicated the flooding of the port of Vathi (Lefkada Island). In any case, flooding of the port was ascribed to a local landslide and was hence not a direct effect of seafloor displacement;
- a minor disturbance was recorded at the tide gauge of Split following the 1962 Makarska earthquake (HERAK et al., 2001);
- although PAPAZACHOS and PAPAZACHOU (1997) report that after the 1979 Montenegro earthquake a ship sank and several houses on the waterfront were eradicated, at Boka Kotorska (Montenegro) the tide gauges recorded a sea wave of just 6 cm. Other disturbances were noted at the tide gauges of Dubrovnik and Bari (BEDOSTI and CAPUTO, 1986; SOLOVIEV et al., 2000).

For the Kefallonia, Makarska and Montenegro tsunamis our results show HMAX values greater than those reckoned by interpreting available historical data, in agreement with our aim at representing worst-case scenarios. The tsunamis following the Senigallia and Gargano earthquakes need further discussion. The Senigallia tsunami produced significant effects only in the harbor of Ancona. Even if an instrumental measure of tsunami effects in the harbor of Ancona does not exist, we cannot rule out that our simulation underestimates the wave height inside the harbor. This may be due to poor resolution of the bathymetry model at the harbor scale, and/or to local amplifications and resonance phenomena that are common in quasi-closed basins (e.g., KOWALIK et al., 2008). The Gargano tsunami is a case that, despite several studies, still presents unresolved issues. A major inconsistency exists between the macroseismic field, that suggests an inland source, and the tsunami effects, that cannot be satisfactorily reproduced either by inland or offshore sources (TINTI and PIATANESI, 1996; TINTI and
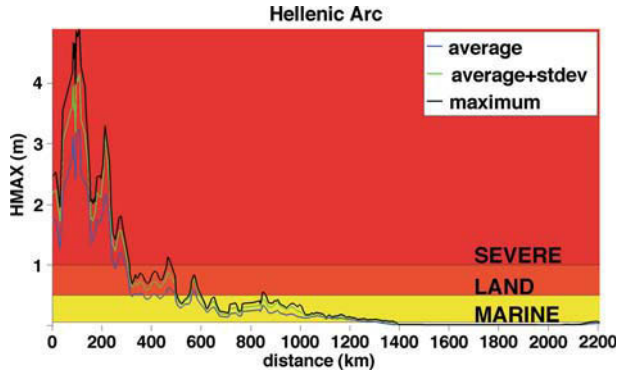
Figure 6

Diagram of tsunami impact along the Italian coastlines of the Adriatic Sea: Aggregated HMAXs (maximum water height above the mean sea level) from the Hellenic Arc SZ. Line colors and threat levels in the background as in Figure 3.
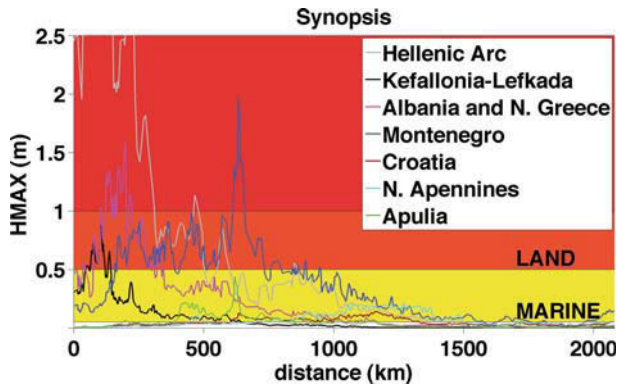

Figure 7

Synoptic diagram of tsunami impact shown as aggregated HMAXs maximum for each source zone. Black: Kefallonia-Lefkada; magenta: Albania-Northern Greece; blue: Montenegro; brown: Croatia; cyan: Northern Apennines; green: Apulia. The maximum HMAXs produced by the Hellenic Arc SZ is shown in gray. Threat levels in the background as in Figure 3, water heights are above the mean sea level.

ARMIGLIATO, 2003). For this tsunamigenic source we estimated a maximum wave of about 0.5 m, comparable to the results of TINTI and PIATANESI (1996). One could invoke a contribution by a secondary source (e.g., a submarine landslide), but this option falls outside the scope of our work.

To fully explore the significance of our results in terms of tsunami threat to the Italian coasts of the Adriatic Sea we used the results obtained by LORITO *et al*. (2008) for the Hellenic Arc SZ as a term of comparison. Their HMAXs (Fig. 6) show that the Hellenic Arc SZ poses a *severe land threat* to southern Apulia; the threat drops progressively northward to the level of *land threat* first, then to *marine threat* north of the Gargano

promontory, and finally to nearly no threat north of Ancona. Remarkably, even the propagation of tsunamis from the Hellenic Arc SZ into the Adriatic Sea is strongly influenced by the two bathymetric effects illustrated in the previous section. The first is the focalization along the ridge that conveys energy towards the southernmost tip of Apulia - resulting in a peak of more than 4 m in the HMAX profile (Fig. 6) - similar to that which was illustrated for the Kefallonia-Lefkada SZ. The second is the shielding effect of the northern Adriatic by the South Adriatic Basin. This results in a deflection of most of the wave energy towards the coast of the southern Adriatic Sea and a consequent increased dissipation. Recall that a similar shielding effect has already been discussed for the Albania - Northern Greece and Montenegro SZs.

Figure 7 summarizes the HMAXs associated with all six SZs considered in this study. Although most of the sources generate waves well beyond the level of attention of the *marine threat* band, we found that only three SZs enter the *land threat* band. The first is the Kefallonia-Lefkada SZ (black line) which, despite its limited size and strike-slip style, poses a significant threat for a short reach of the coast due to the bathymetric focalization. The two most threatening SZs are the Albania-Northern Greece (magenta) and Montenegro (blue) SZs, which generate water heights that locally exceed the *severe land threat* level. The threat posed by the Albania-Northern Greece SZ, however, is always lower than that posed by the Hellenic Arc (gray line) at the same coastal positions. Nevertheless, tsunami waves from the Albania-Northern Greece SZ reach the Italian coast in less than 30 minutes (Fig. 8a), whereas waves from the Hellenic Arc take 50 to 90 minutes (LORITO *et al*., 2008), depending on the exact position of the fault source. This means that the time available to issue a warning or take countermeasures is much shorter in the case of the Albania-Northern Greece SZ. The threat posed by the Montenegro SZ exceeds that of the Hellenic Arc for a significant coastline length and the HMAX peak at ∼640 km is the highest of all Adriatic source zones (Fig. 7). However, the propagation of tsunamis from the Montenegro SZ to the coasts of Italy takes more than 50 minutes (Fig. 8b), comparable with the minimum time needed for propagation from the Hellenic Arc.

The combination of expected HMAX values and propagation times will become especially useful in the design of early-warning systems if integrated with analyses of the Euro-Mediterranean seismic network performance (e.g., OLIVIERI and SCOGNAMIGLIO, 2007) for different tsunamigenic source zones.

6. Conclusions

Following the approach proposed by LORITO *et al*. (2008) we defined a maximum credible earthquake and an associated typical fault for each of six source zones potentially threatening the Adriatic coasts of Italy with sizable tsunamis. For each of the zones we let a pre-defined typical fault float along the entire source zone and computed a tsunami scenario at regular intervals. We then aggregated the maximum water heights
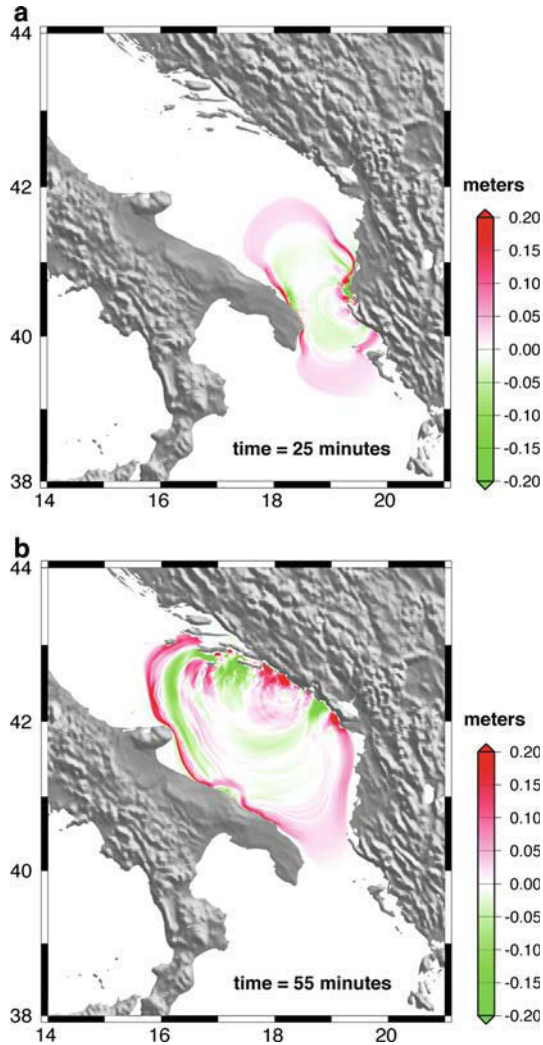
Figure 8
Snapshots of the tsunami wave height for two selected faults: a) in the Albania–Northern Greece SZ; b) in the Montenegro SZ.

above the mean sea level of each source zone and performed calculations of their maxima, averages and standard deviations along the target Adriatic Sea coasts of Italy. We finally coded the resulting tsunami threat for three different levels defined as: *marine*, *land* and *severe land*, shown in yellow, orange and red, respectively.

We determined that the southern part of Apulia facing Albania and the Gargano promontory are the portions of the Adriatic coasts facing the largest tsunami threat (Fig. 4). We also found that some bathymetric features are crucial in determining the

focalization-defocalization of tsunami energy. Despite its expected strike-slip faulting style, the Kefallonia-Lefkada source poses a significant threat for the southernmost tip of Apulia due to energy focalization along a bathymetric ridge. A further significant result is that the northern part of the Adriatic coast, where the cities of Venice and Trieste are located, is generally safer than the southern part. Only the region south of the Po Delta may suffer from tsunamis, also due to its intrinsic vulnerability to flooding resulting from the extremely flat topography.

We also compared the threat posed by the investigated sources to that associated with earthquake sources in the Hellenic Arc. We found that the latter is potentially more destructive than the former, although the effects of small local sources can outpace those of the Hellenic Arc sources at specific locations. This is partly due to bathymetric effects, which can either reduce or enhance the threat posed by sources falling at specific locations.

We believe our results can be a valuable guidance for designing early warning systems, assessing risk and planning land-use for the coasts of southern Italy.

REFERENCES

ALIAJ, S., *The Albanian orogen: Convergence zone between Eurasia and the Adria microplate*. In *The Adria Microplate: GPS Geodesy, Tectonics and Hazards* (eds. Pinter N. *et al.*) (Springer, Netherlands 2006) pp. 133–149.

ALIAJ, S., ADAMS, J., HALCHUK, S., SULSTAROVA, E., PEÇI, V., and MUÇO, B. (2004), *Probabilistic seismic hazard maps for Albania*, 13th World Conference on Earthquake Engineering, Vancouver, B.C., Canada, August 1–6, Paper No. 2469.

ALJINOVIĆ, B., PRELOGOVIĆ, E., and SKOKO, D. *Tectonic processes on the contact of the Adriatic Platform and the Dinarides in the area of the Northern Dalmatia*, Conf. on Mechanics of Jointed and Faulted Rock, Inst. of Mech/Tech. Univ. of Vienna, Proc. (A. A. Balkema, Rotterdam/Brookfield, 1990) pp 179–182.

ALLEN, S. C. R. and GREENSLADE, D. J. M. (2007), *Developing tsunami warnings from numerical model output*, Natural Hazards *46*, 35–52, doi: 10.1007/s11069-007-9180-8.

AMBRASEYS, N. N. (1962), *Data for the investigation of seismic sea waves in the Eastern Mediterranean*, Bull. Seismol. Soc. Am. *52*, 895–913.

ARGNANI, A., FAVALI, P., FRUGONI, F., GASPERINI, M., LIGI, M., MARANI, M., MATIETTI, G., and MELE, G. (1993), *Foreland deformational pattern in the Southern Adriatic*, Ann. Geofis. *36*, 229–247.

ARGNANI, A., BONAZZI, C., EVANGELISTI, D., FAVALI, P., FRUGONI, F., GASPERINI, M., LIGI, M., MARANI, M., and MELE, G. (1996), *Tettonica dell'Adriatico Meridionale*, Mem. Soc. Geol. It. 51, 227–237.

BALLAURI, A., BEGA, Z., MEEHAN, P., GAMBINI, R., and KLAMMER, W. (2002), *Exploring in structurally complex thrust belt: Southwest Albania Case*, AAPG Hedberg Conference, May 14–18, 2002, Palermo-Mondello (Sicily, Italy).

BASILI, R., and BARBA, S. (2007), *Migration and shortening rates in the northern Apennines, Italy: Implications for seismic hazard*, Terra Nova *19*, 462–468, doi: 10.1111/j.1365-3121.2007.00772.x.

BASILI, R., VALENSISE, G., VANNOLI, P., BURRATO, P., FRACASSI, U., MARIANO, S., TIBERTI, M. M., and BOSCHI, E. (2008), *The Database of Individual Seismogenic Sources (DISS), version 3: Summarizing 20 years of research on Italy's earthquake geology*, Tectonophysics *453*, 20–43, doi:10.1016/j.tecto.2007.04.014.

BATTAGLIA, M., MURRAY, M. H., SERPELLONI, E., and BÜRGMANN, R. (2004), *The Adriatic region: An independent microplate within the Africa-Eurasia collision zone*, Geophys. Res. Lett. *31*, L09605, doi:10.1029/2004GL019723.

BEDOSTI, B. and CAPUTO, M. (1986), *Primo aggiornamento del catalogo dei maremoti delle coste italiane*, Atti della Accademia Nazionale dei Lincei, Rendiconti Classe Scienze Fisiche, Matematiche, Naturali s.VIII *80*, 570–584.

BENETATOS, C. and KIRATZI, A. (2006), *Finite-fault slip models for the 15 April 1979 (M_w 7.1) Montenegro earthquake and its strongest aftershock of 24 May 1979 (M_w 6.2)*, Tectonophysics *421*, 129–143.

BENNETT, R.A., HREINSDÓTTIR, S., BUBLE, G., BAŠIĆ, T., BAČIĆ, Ž., MARIANOVIĆ, M., CASALE, G., GENDASZEK, A., and COWAN, D. (2007), *Eocene to present subduction of southern Adria mantle litosphere beneath the Dinarides*, Geology *36*, 3–6, doi: 10.1130/G24136A.1.

BOSCHI, E., GUIDOBONI, E., FERRARI, G., MARIOTTI, D., VALENSISE, G., and GASPERINI, P. (eds.) (2000), *Catalogue of strong italian earthquakes from 461 B.C. to 1997*, Ann. Geofis. *43*, with CD-Rom, 259 pp.

BOSELLINI, A., NERI, C., and LUCIANI, V. (1993), *Platform margin collapses and sequence stratigraphic organization of carbonate slopes: Cretaceous-Eocene, Gargano Promontory*, Terra Nova 5, 282–297.

BURBIDGE, D. and CUMMINS, P. (2007), *Assessing the threat to Western Australia from tsunami generated by earthquakes along the Sunda Arc*, Natural. Hazards *43*, 319–331, doi:10.1007/s11069-007-9116-3.

CAPUTO, M., and FAITA, G. (1984), *Primo catalogo dei maremoti delle coste italiane*, Atti Accademia Nazionale dei Lincei, Memorie Classe Scienze Fisiche, Matematiche, Naturali s. VIII *17*, 213–356.

CASERO, P., RIGAMONTI, A., and IOCCA, M. (1990), *Paleogeographic relationships during Cretaceous between the Northern Adriatic area and the Eastern Southern Alps*, Mem. Soc. Geol. It. *45*, 807–814.

CHIARABBA, C., DE GORI, P., CHIARALUCE, L., BORDONI, P., CATTANEO, M., DE MARTIN, M., FREPOLI, A., MICHELINI, A., MONACHESI, A., MORETTI, M., AUGLIERA, G.P., D'ALEMA, E., FRAPICCINI, M., GASSI, A., MARZORATI, S., DI BARTOLOMEO, P., GENTILE, S., COVONI, A., LOVISA, L., ROMANELLI, M., FERRETTI, G., PASTA, M., SPALLAROSSA, D., and ZUMINO, E. (2005), *Mainshocks and aftershocks of the 2002 Molise seismic sequence, southern Italy*, J. Seismol. *9*, 487–494.

CHILOVI, C., DE FEYTER, A. J., and POMPUCCI, A. (2000), *Wrench zone reactivation in the Adriatic Block: the example of the Mattinata Fault System (SE Italy)*, Boll. Soc. Geol. It. *119*, 3–8.

COCARD, M., KAHLE, H.-G., PETER, Y., GEIGER, A., VEIS, G., FELEKIS, S., PARADISSIS, D., and BILLIRIS, H. (1999), *New constraints on the rapid crustal motion of the Aegean region: Recent results inferred from GPS measurements (1993–1998) across the West Hellenic Arc*, Greece, Earth Planet. Sci. Lett. *172*, 39–47.

CONSOLE, R., and FAVALI, P. (1981), *Study of the Montenegro earthquake sequence (March–July 1979)*, Bull. Seismol. Soc. Am. *71*, 1,233–1,248.

DEL BEN, A. (2002), *Interpretation of the CROP M-16 seismic section in the Central Adriatic Sea*, Mem. Soc. Geol. It. *57*, 327–333.

DEL GAUDIO, V., PIERRI, P., FREPOLI, A., CALCAGNILE, G., VENISTI, N., and CIMINI, G.B. (2007), *A critical revision of the seismicity of Northern Apulia (Adriatic microplate—Southern Italy) and implications for the identification of seismogenic structures*, Tectonophysics *436*, 9–35.

DE MARTINI, P. M., BURRATO, P., PANTOSTI, D., MARAMAI, A., GRAZIANI, L., and ABRAMSON, H. (2003), *Identification of tsunami deposits and liquefaction features in the Gargano area (Italy): Paleoseismological implication*, Ann. Geophys.-Italy *46*, 883–902.

DI BUCCI, D. and MAZZOLI, S. (2003), *The October-November 2002 Molise seismic sequence (Southern Italy): An expression of Adria intraplate deformation*, J. Geol. Soc. London *160*, 503–506.

DI BUCCI, D., RAVAGLIA, A., SENO, S., TOSCANI, G., FRACASSI, U., and VALENSISE, G. (2007), *Modes of fault reactivation from analogue modeling experiments: Implications for the seismotectonics of the Southern Adriatic foreland (Italy)*, Quater. Internat. *171–172*, 2–13.

DISS WORKING GROUP (2007), *Database of Individual Seismogenic Sources (DISS), Version 3.0.4: A Compilation of Potential Sources for Earthquakes Larger than M 5.5 in Italy and Surrounding Areas*, http://diss.rm.ingv.it/diss.

DOGLIONI, C. (1991), *A proposal for the kinematics modelling of the W-dipping subductions-possible application to the Tyrrhenian-Apennines system*, Terra Nova *3*, 423–434.

DOGLIONI, C., MONGELLI, F., and PIERI, P. (1994), *The Puglia uplift (SE Italy): An anomaly in the foreland of the Apenninic subduction due to buckling of a thick continental lithosphere*, Tectonics *13*, 1309–1321.

DRAGAŠEVIĆ, T. (1983), *Oil geologic exploration in the Montenegro offshore in Yugoslavia*, Nafta *7–8*, 397–404.

DUNI, L., KUKA N., and DUSHI, E. (2003), *Monitoring of seismicity in Albania, CSEM Newsletter n. 20, September 2003*, 13–16, www.emsc-csem.org.

FINETTI, I.R., and DEL BEN, A., *Crustal tectono-stratigraphic setting of the Adriatic Sea from new CROP seismic data. In CROP, Deep Seismic Exploration of the Mediterranean Region* (ed. Finetti I R.) (Elsevier, 2005) pp. 519–547.

FRACASSI, U. and VALENSISE, G. (2007), *Unveiling the sources of the catastrophic 1456 multiple earthquake: Hints to an unexplored tectonic mechanism in Southern Italy*, Bull. Seismol. Soc. Am. *97*, 3, 725–748, doi:10.1785/0120050250.

FRANCIOSI, R. and VIGNOLO, A. (2002), *Northern Adriatic foreland—A promising setting for the southalpine mid-triassic petroleum system*, EAGE 64th Conference & Exhibition—Florence, Italy, 27–30 May, 2002.

GRAHAM WALL, B.R., GIRBACEA, R., MESONJESI, A., and AYDIN, A. (2006), *Evolution of fracture and fault-controlled fluid pathways in carbonates of the Albanides fold-thrust belt*, Am. Ass. Petroleum Geologists Bull. *90*, 1227–1249, doi:10.1306/03280304014.

GRENERCZY, G., SELLA, G., STEIN, S., and KENYERES, A. (2005), *Tectonic implications of the GPS velocity field in the northern Adriatic region*, Geophys. Res. Lett. *32*, L16311, doi:10.1029/2005GL022947.

GRUPPO DI LAVORO CPTI (2004), *Catalogo Parametrico dei Terremoti Italiani, versione 2004 (CPTI04)*. INGV, Bologna (also available at: http://emidius.mi.ingv.it/CPTI04/).

GUIDOBONI, E., FERRARI, G., MARIOTTI, D., COMASTRI, A., TARABUSI, G., and VALENSISE, G. (2007), *CFTI4Med, Catalogue of Strong Earthquakes in Italy (461 B.C.-1997) and Mediterranean Area (760 B.C.–1500)*, INGV-SGA, available at http://storing.ingv.it/cfti4med/.

GUIDOBONI, E. and TINTI, S. (1988), *A review of the historical 1627 tsunami in southern Adriatic*, Sci. Tsunami Hazards *6*, 11–16.

HERAK, M.J. (1991), *Dinarides. Mobilistic view of the genesis and structure*, Acta Geologica *21*, 35–117.

HERAK, M.J. (1999), *Tectonic interrelation of the Dinarides and the Southern Alps*, Geologica Croatica *52*, 83–98.

HERAK, M., HERAK, D., and MARKUŠIĆ, S. (1995), *Fault plane solutions for earthquakes (1956–1995) in Croatia and neighbouring regions*, Geofizika *12*, 43–56.

HERAK, D., HERAK, M., PRELOGOVIĆ, E., MARKUŠIĆ, S., and MARKULIN, Ž. (2005), *Jabuka Island (Central Adriatic Sea) earthquakes of 2003*, Tectonophysics *398*, 167–180.

HERAK, M., ORLIĆ, M., and KUNOVEC-VARGA, M. (2001), *Did the Makarska earthquake of 1962 generate a tsunami in the central Adriatic arcipelago*? J. of Geodyn. *31*, 71–86.

HOLLENSTEIN, C., KAHLE, H.-G., and GEIGER, A., *Plate tectonic framework and GPS-derived strain-rate field within the boundary zones of the Eurasian and African plates. In The Adria Microplate: GPS Geodesy, Tectonics and Hazards* (eds. Pinter N. *et al.*) (Springer, Netherlands 2006) pp. 35–50.

HOLLENSTEIN, Ch., KAHLE, H.-G., GEIGER, A., JENNY, S., GOES, S., and GIARDINI, D. (2003), *New GPS constraints on the Africa-Eurasia plate boundary zone in southern Italy*, Geophys. Res. Lett. *30*, 1935, doi:10.1029/2003GL017554.

IVANOVIĆ, A., SAKAČ, K., MARKOVIĆ, S., SOKAČ, B., ŠUŠNJAR, M., NIKLER, L., and ŠUŠNJARA, A. (1976), *Osnovna geološka karta SFRJ, list Obredovac, 1:100000*, Inst. geol. istraž., Zagreb (1967), Savezni geol. zavod, Beograd.

IVANČIĆ, I., HERAK, D., MARKUŠIĆ, S., SOVIĆ, I., and HERAK, M. (2006), *Seismicity of Croatia in the period 2002–2005*, Geofizika *23*, 87–103.

KAHLE, H.-G., COCARD, M., PETER, Y,. GEIGER, A., REILINGER, R., BARKA, A., and VEIS, G. (2000), *GPS-derived strain rate field within the boundary zones of the Eurasian, African and Arabian Plates*, J. Geophys. Res. *105*(B10), 23,353–23,370, doi: 10.1029/2000JB900238.

KAHLE, H.-G., MÜLLER, M.V., and VEIS, G. (1996), *Trajectories of crustal deformation of Western Greece from GPS observations 1989–1994*, Geophys. Res. Lett. *23*, 677–680.

KAHLE, H-G., STRAUB, C., REILINGER, R., McCLUSKY, S., KING, R., HURST, K., VEIS, G., KASTENS, K., and CROSS, P. (1998), *The strain rate field in the eastern Mediterranean region, estimated by repeated GPS measurements*, Tectonophysics *294*, 237–252.

KANAMORI, H., and BRODSKY, E. E. (2004), *The physics of earthquakes*, Rep. Prog. Phys. *67*, 1429- 1496.

KOWALIK, Z., HORRILLO, J., KNIGHT, W., and LOGAN, T. (2008), *Kuril Islands tsunami of November 2006: 1. Impact at Crescent City by distant scattering*, J. Geophys. Res. *113*, C01020, doi:10.1029/2007JC004402.

KUK, V., PRELOGOVIĆ, E., and DRAGIČEVIĆ, I. (2000), *Seismotectonically Active Zones in the Dinarides*, Geologica Croatica *53*, 295–303.

LAVECCHIA, G., DE NARDIS, R., VISINI, F., FERRARINI, F., and BARBANO, M.S. (2007), *Seismogenic evidence of ongoing compression in eastern-central Italy and mainland Sicily: A comparison*, Boll. Soc. Geol. Ital. (Ital. J. Geosci.) *126*, 209–222.

LAWRENCE, S.R., TARI-KOVAČIĆ, V., and GJUKIĆ, B. (1995), *Geological evolution model of the Dinarides*, Nafta *46*, 103–113.

LORITO, S., TIBERTI, M. M., BASILI, R., PIATANESI, A., and VALENSISE, G. (2008), *Earthquake-generated tsunamis in the Mediterranean Sea: Scenarios of potential threats to Southern Italy*, J. Geophys. Res. *113*, B01301, doi:10.1029/2007JB004943.

LOUVARI, E., KIRATZI, A.A., and PAPAZACHOS, B.C. (1999), *The Cefalonia Transform Fault and its extension to western Lefkada Island (Greece)*, Tectonophysics *308*, 223–236.

MADER, C. L., *Numerical modeling of water waves*, Los Alamos series in *Basic and Applied Sciences* (CRC Press, Boca Raton, Florida, 2001), 206 pp.

MAMUZIĆ, P. (1975), *Osnovna geološka karta SFRJ, list Šibenik, 1:100000*, Inst. geol. istraž., Zagreb (1966), Savezni geol. zavod, Beograd.

MARAMAI, A., GRAZIANI, L., and TINTI, S. (2007), *Investigation on tsunami effects in the central Adriatic Sea during the last century – A contribution*, Nat. Hazards Earth Syst. Sci. *7*, 15–19.

MARKUŠIĆ, S., HERAK, D., IVANČIĆ, I., and SOVIĆ, I. (1998), *Seismicity of Croatia in the period 1993–1996 and the Ston-Slano earthquake of 1996*, Geofizika *15*, 83–101.

McCLUSKY, S., BALASSANIAN, S., BARKA, A., DEMIR, C., ERGINTAV, S., GEORGIEV, I., GURKAN, O., HAMBURGER, M., HURST, K., KAHLE, H., KASTENS, K., KEKELIDZE, G., KING, R., KOTZEV, V., LENK, O., MAHMOUD, S., MISHIN, A., NADARIYA, M., OUZOUNIS, A., PARADISSIS, D., PETER, Y., PRILEPIN, M., REILINGER, R., SANLI, I., SEEGER, H., TEALEB, A., TOKSÖZ, M. N., and VEIS, G. (2000), *Global Positioning System constraints on plate kinematics and dynamics in the eastern Mediterranean and Caucasus*, J. Geophys. Res. *105* (B3), 5695–5719, 10.1029/1999JB900351.

MELETTI, C., GALADINI, F., VALENSISE, G., STUCCHI, M., BASILI, R., BARBA, S., VANNUCCI, G., and BOSCHI, E. (2008), *The ZS9 seismic source model for the seismic hazard assessment of the Italian territory*, Tectonophysics *450*, 85–108.

MILANO, G., DI GIOVAMBATTISTA, R., and VENTURA, G. (2005), *Seismic constraints on the present-day kinematics of the Gargano foreland, Italy, at the transition zone between the southern and northern Apennine belts*, Geoph. Res. Lett. *32*, L24308, doi:10.1029/2005GL024604.

NOCQUET, J.-M. and CALAIS, E. (2004), *Geodetic measurements of crustal deformation in the Western Mediterranean and Europe*, Pure Appl. Geophys. *161*, 661–681, doi:10.1007/s00024-003-2468-z.

OKADA, Y. (1985), *Surface deformation due to shear and tensile faults in a half-space*, Bull. Seismol. Soc. Am. *75*, 1135–1154.

OKADA, Y. (1992), *Internal deformation due to shear and tensile faults in a half-space*, Bull. Seismol. Soc. Am. *82*, 1018–1040.

OLIVIERI, M. and SCOGNAMIGLIO, L. (2007), *Toward a Euro Mediterranean tsunami warning system: The case of the February 12, 2007, Ml = 6.1 earthquake*, Geophys. Res. Lett. *34*, L24309, doi:10.1029/2007GL031364.

PAPAIOANNOU, Ch. A. and PAPAZACHOS, B.C. (2000), *Time-independent and time-dependent seismic hazard in Greece based on seismogenic sources*, B. Seismol. Soc. Am. *90*, 1, 22–33.

PAPAZACHOS, B. C. and DIMITRIU, P. P. (1991), *Tsunamis in and near Greece and their relation to the earthquake focal mechanisms*, Natural Hazards *4*, 161–170.

PAPAZACHOS, B., and PAPAZACHOU, C., *The earthquakes of Greece (Ziti, Thessaloniki, Greece, 1997)*.

PAPAZACHOS, B.C., PAPADIMITRIOU, E.E., KIRATZI, A.A., PAPAZACHOS, C.B., and LOUVARI, E.K. (1998), *Fault plane solutions in the Aegean Sea and the sourrounding area and their tectonic implications*, Boll. Geof. Teor. Appl. *39*, 199–218.

PAPAZACHOS, B. C., PAPAIOANNOU, C. A., PAPAZACHOS, C. B., and SAVVAIDIS, A. S. (1999), *Rupture zones in the Aegean region*, Tectonophysics *308*, 205–221.

PAULATTO, M., PINAT, T., and ROMANELLI, F. (2007), *Tsunami hazard scenarios in the Adriatic Sea domain*, Natural. Hazards Earth Syst. Sci. *7*, 309–325.

PICCININI, D., CHIARABBA, C., AUGLIERA, P., and MONGHIDORO EARTHQUAKE GROUP (M.E.G.) (2006), *Compression along the northern Apennines? Evidence from the Mw 5.3 Monghidoro earthquake*, Terra Nova *18*, 89–94, doi: 10.1111/j.1365-3121.2005.00667.x.

PICHA, F.J. (2002), *Late orogenic strike-slip faulting and escape tectonics in frontal Dinarides-Hellenides, Croatia, Yugoslavia, Albania, and Greece*, Am. Ass. Petroleum Geologists Bull., *86*, 1659–1671.

PIRAZZOLI, P.A., STIROS, S. C., LABOREL, J., LABOREL-DEGUEN, F., ARNOLD, M., PAPAGEORGIOU, S., and MORHANGE, C. (1994), *Late-Holocene shoreline changes related to palaeoseismic events in the Ionian Islands, Greece*, The Holocene *4*, 397–405.

PONDRELLI, S., PIROMALLO, C., and SERPELLONI, E. (2004), *Convergence vs. Retreat in Southern Tyrrhenian Sea: Insights from kinematics*, Geophys. Res. Lett. *31*, L06611, doi:10.1029/2003GL019223.

PONDRELLI, S., SALIMBENI, S., EKSTRÖM, G., MORELLI, A., GASPERINI, P., and VANNUCCI, G. (2006), *The Italian CMT dataset from 1977 to the present*, Phys. Earth Planet. Int. *159*, 286–303.

POWER, W., DOWNES, G., and STIRLING, M. (2007), *Estimation of Tsunami Hazard in New Zealand due to South American Earthquakes*, Pure Appl. Geophys. *164*, 547–564, doi:10.1007/s00024-006-0166-3.

PRELOGOVIĆ, E., ALJINOVIĆ, B., and BAHUN, S. (1995), *New data on structural relationships in the North Dalmatian area*, Geologica Croatica *48*, 167–176.

PRELOGOVIĆ, E., KUK, V., BULJAN, R., TOMLJENOVIĆ, B., and SKOKO, D. (1999), *Recent tectonic movements and earthquakes in Croatia*, Proc. Second International Symposium, *Geodynamics of Alps-Adria Area by means of Terrestrial and Satellite Methods*, Dubrovnik, 255–262.

PRELOGOVIĆ, E., PRIBIČEVIĆ, B., IVKOVIĆ, Ž., DRAGIČEVIĆ, I., BULJAN, R., and TOMLJENOVIĆ, B. (2003), *Recent structural fabric of the Dinarides and tectonically active zones important for petroleum-geological exploration in Croatia*, Nafta *55*, 155–161.

RIDENTE, D., FRACASSI, U., DI BUCCI, D., TRINCARDI, F., and VALENSISE, G. (2008), *Middle Pleistocene to Holocene activity of the Gondola Fault Zone (Southern Adriatic Foreland): deformation of a regional shear zone and seismotectonic implications*, Tectonophysics *453*, 110–121, doi:10.1016/j.tecto.2007.05.009.

ROYDEN, L., PATACCA, E., and SCANDONE, P. (1987), *Segmentation and configuration of subducted lithosphere in Italy: An important control on thrust-belt and foredeep-basin evolution*, Geology *15*, 714–717.

SCROCCA, D. (2006), *Thrust front segmentation induced by differential slab retreat in the Apennines (Italy)*, Terra Nova *18*, 154–161.

SCROCCA, D., CARMINATI, E., DOGLIONI, C. and MARCANTONI, D., *Slab retreat and active shortening along the centralnorthern Apennines*. In *Thrust Belts and Foreland Basins: From Fold Kinematics to Hydrocarbon Systems* (eds. Lacombe O., Lave' J., Roure F., and Verges J.,) (Frontiers in Earth Sciences, Springer-Verlag, Berlin Heidelberg, Germany 2007) pp. 471–487.

SERPELLONI, E., VANNUCCI, G., PONDRELLI, S., ARGNANI, A., CASULA, G., ANZIDEI, M., BALDI, P., and GASPERINI, P. (2007), *Kinematics of the Western Africa-Eurasia plate boundary from focal mechanisms and GPS data*, Geophys. J. Int. *169*, 1180–1200, doi: 10.1111/j.1365-246X.2007.03367.x.

SERPELLONI, E., ANZIDEI, M., BALDI, P., CASULA, G., and GALVANI, A. (2005), *Crustal velocity and strain-rate fields in Italy and surrounding regions: New results from the analysis of permanent and non-permanent GPS networks*, Geophys. J. Int. *161*, 861–880, doi: 10.1111/j.1365-246X.2005.02618.x.

Skoko, D., Prelogović, E., and Aljinović, B. (1987), *Geological structure of the Earth's crust above the Moho discontinuity in Yugoslavia*, Geophys. J. Roy. Astron. Soc. *89*, 379–382.

Smith, W. H. F. and Sandwell, D. T. (1997), *Global sea-floor topography from satellite altimetry and ship depth soundings*, Science *277*, 1956–1962.

Soloviev, S. L., Solovieva, O. N., Go, C. N., Kim, K. S., and Shchetnikov, N. A., *Tsunamis in the Mediterranean Sea 2000 B.C.– 2000 A.D., Advances in Natural and Technological Hazard Research* (Kluwer Academic Publishers, 2000).

Stiros, S.C., Pirazzoli, P.A., Laborel, J., and Laborel-Deguen, F. (1994), *The 1953 earthquake in Cephalonia (Western Hellenic Arc): coastal uplift and halotectonic faulting*, Geophys. J. Int. *117*, 834–849.

Sulstarova, E., Peçi, V., and Shuteriqi, P. (2000), *Vlora-Elbasani-Dibra (Albania) transversal fault zone and its seismic activity*, J. Seismol. *4*, 117–131.

Tari, V. (2002), *Evolution of the northern and western Dinarides: A tectonostratigraphic approach*, EGU Stephan Mueller Special Publication Series *1*, 223–236.

Tari Kovačić, V. and Mrinjek, E. (1994), *The Role of Paleogene clastics in the tectonic interpretation of northern Dalmatia (Southern Croatia)*, Geologica Croatica *47*, 127–138.

Thomson, R. E., Rabinovich, A. B., and Krassovski, M. V. (2007), *Double jeopardy: concurrent arrival of the 2004 Sumatra tsunami and storm-generated waves on the Atlantic coast of the United States and Canada*, Geophys. Res. Lett. *34*, L15607, doi:10.1029/2007GL030685.

Tinti, S. and Armigliato, A. (2003), *The use of scenarios to evaluate the tsunami impact in southern Italy*, Marine Geology *199*, 221–243.

Tinti, S. and Piatanesi, A. (1996), *Numerical simulations of the tsunami induced by the 1627 earthquake affecting Gargano, Southern Italy*, J. Geodyn. *21*, 141–160.

Tinti, S., Maramai, A., and Graziani, L. (2004), *The new catalogue of Italian tsunamis*, Natural Hazards *33*, 439–465.

Tinti, S., Maramai, A., and Graziani, L. (2007), *The Italian Tsunami Catalogue (ITC), Version 2*, http://web1.ingv.it:8080/portale_ingv/servizi-e-risorse/cartella-banche-dati/catalogo-tsunami/catalogo-degli-tsu-nami-italiani.

Valensise, G., Pantosti, D., and Basili, R. (2004), *Seismology and tectonic setting of the 2002 Molise, Italy, earthquake*, Earthquake Spectra *20*, S1, 23–37.

Vannoli, P., Basili, R., and Valensise, G. (2004), *New geomorphic evidence for anticlinal growth driven by blind-thrust faulting along the northern Marche coastal belt (central Italy)*, J. Seismol. Spec. *8*, 297–312.

Vannucci, G., Pondrelli, S., Argnani, A., Morelli, A., Gasperini, P., and Boschi, E. (2004), *An atlas of Mediterranean seismicity*, Annals of Geophys. Suppl. to vol. *47*, 247–306.

Whitmore, P.M. (2003), *Tsunami amplitude prediction during events: A test based on previous tsunamis*, Sci. Tsunami Haz. *21*, 135–143.

Zerbini, S, Matonti, F., and Doglioni, C. (2006), *Crustal movements in northeastern Italy from permanent GPS stations*, Europ. Geosci. Union 2006, Geophys. Res. Abstracts *8*, 06257.

To access this journal online:
www.birkhauser.ch/pageoph

Stromboli Island (Italy): Scenarios of Tsunamis Generated by Submarine Landslides

STEFANO TINTI, FILIPPO ZANIBONI, GIANLUCA PAGNONI, and ANNA MANUCCI

Abstract—Stromboli is an Italian volcanic island known for its persistent state of activity, which leads to frequent mass failures and consequently to frequent tsunamis ranging from large (and rare) catastrophic events involving the entire southern Tyrrhenian Sea to smaller events with, however, extremely strong local impact. Most of tsunamigenic landslides occur in the Sciara del Fuoco (SdF) zone, which is a deep scar in the NW flank of the volcano, that was produced by a Holocene massive flank collapse and that is the accumulation area of all the eruptive ejecta from the craters. Shallow-water bathymetric surveys around the island help one to identify submarine canyons and detachment scars giving evidence of mass instabilities and failures that may have produced and might produce tsunamis. The main purpose of this paper is to call attention to tsunami sources in Stromboli that are located outside the SdF area. Further, we do not touch on tsunami scenarios associated with gigantic sector collapses that have repeat times in the order of several thousands of years, but rather concentrate on intermediate size tsunamis, such as the ones that occurred in December 2002. Though we cannot omit tsunamis from the zone of the SdF, the main emphasis is on the elaboration of preliminary scenarios for three more possible source areas around Stromboli, namely Punta Lena Sud, Forgia Vecchia and Strombolicchio, with the aim of purposeful contributing to the evaluation of the hazard associated with such events and to increase the knowledge of potential threats affecting Stromboli and the nearby islands of the Aeolian archipelago.

The simulations show that tsunami sources outside of the SdF can produce disastrous effects. As a consequence, we recommend that the monitoring system that is presently operating in Stromboli and that is focussed on the SdF source area be extended in order to cover even the other sources. Moreover, a synoptic analysis of the results from all the considered tsunami scenarios leads to a very interesting relation between the tsunami total energy and the landslide potential energy, that could be used as a very effective tool to evaluate the expected tsunami size from estimates of the landslide size.

Key words: Landslide-induced tsunamis, Stromboli, tsunami scenarios.

1. Introduction

The island of Stromboli, located in the SE Tyrrhenian Sea (Fig. 1), is characterized by a well-known persistent volcanic activity, which results in frequent paroxysmal events (ROSI *et al.*, 2000). Its morphology reflects the sequence of catastrophic events that

Sector of Geophysics, Department of Physics, University of Bologna, viale Carlo Berti-Pichat, 8, Bologna, Italy. E-mail: filippo.zaniboni@unibo.it
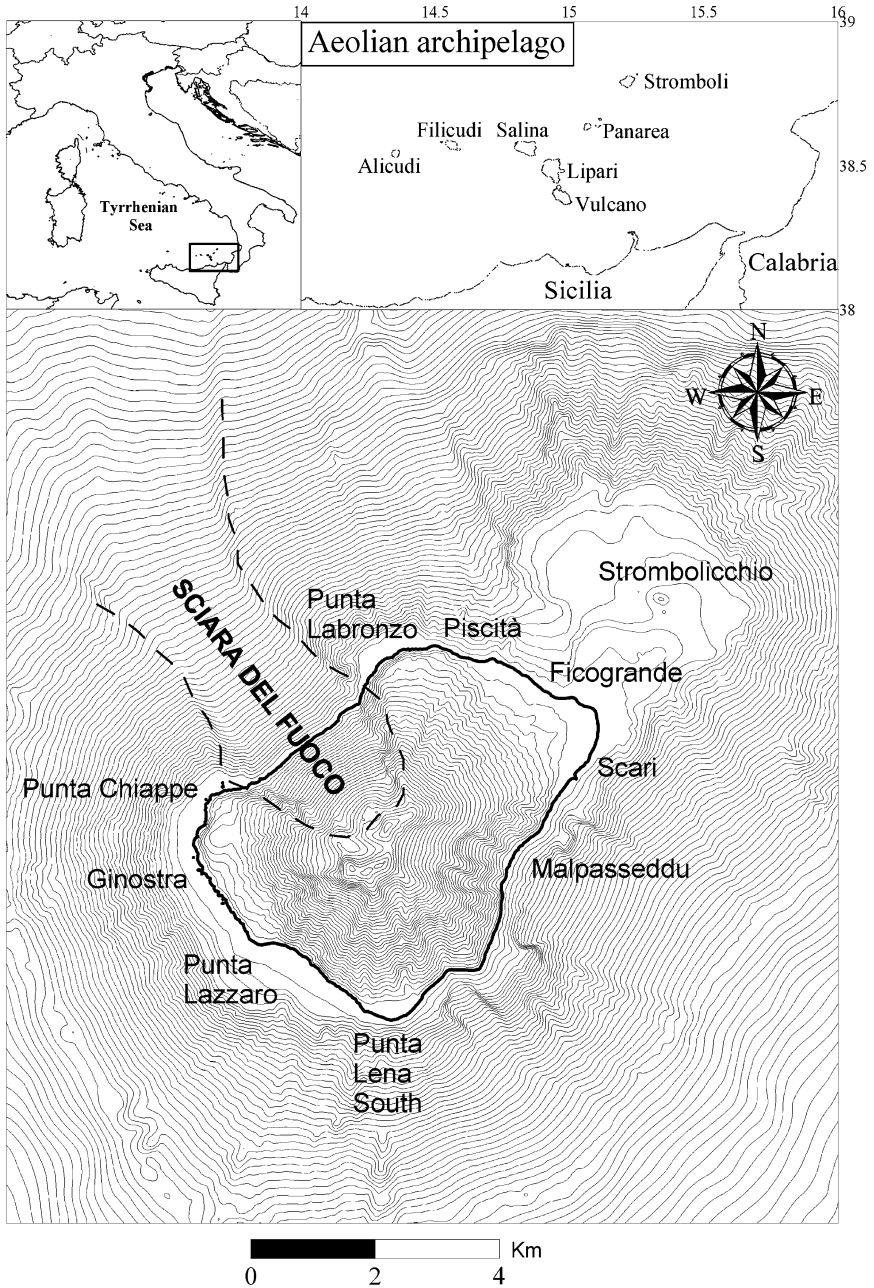
Figure 1
Topobathymetric map of Stromboli, the northernmost island of the Aeolian archipelago, in the southeast Tyrrhenian Sea. Some of the most relevant toponyms quoted in the paper are reported. The most relevant feature is the Sciara del Fuoco scar. Notice also numerous small canyons throughout the coast.

marked the history of the island in the last 100 Ka, the last of which is the Holocene collapse that formed the Sciara del Fuoco (SdF) scar on the northwestern flank of the volcano (KOKELAAR and ROMAGNOLI, 1995; TIBALDI, 2001).

A mass with a volume of approximately 1 km^3, partly submerged and partly subaerial, slid into the sea, very probably provoking a huge tsunami (TINTI et al., 2000, 2003), and definitely changing the shape of the island. From that event, most material ejected from the craters accumulates in this zone, and is driven to the sea through this big canyon, around 2-km wide, with vertical walls up to 200–300 m high. The scar starts just under the craters and continues underwater for more than 10 km. The concomitance of different factors, such as the continuous accumulation of material, the steep slopes characterizing the SdF (exceeding 40° in the upper part) and the ground shaking due to intense seismic activity and thick intrusion, contributes to frequent mass failures, that especially in periods of paroxysmal crises can reach rather large volumes and give origin to tsunamis (APUANI et al., 2005a, b).

The recent history of the island counts many sliding events that generated tsunamis, as reported in the Italian tsunami catalogue (see Table 1 for the events of the last 100 years, and also TINTI et al., 2004, and MARAMAI et al., 2005a).

As can be seen from Table 1, most of the reported tsunamis have been generated by events occurring in the SdF, such as the two most recent tsunamigenic landslides of December 30, 2002. In this case, the tsunami waves affected all the coasts of the island with runup reaching 10 meters, and fortunately without casualties due to the occurrence in a non-tourist season period. Surveys carried out after the tsunami showed that the first slide was submarine and the second one was subaerial, with total volume around 2–3·10^7 m^3 (CHIOCCI et al., 2003).

Examining Table 1 one also learns that events generated outside the SdF did occur in the past, as reported by eyewitnesses. For example, the 1944 double tsunami involved sliding along the SdF incline, but also a hot avalanche entering the sea on the opposite flank of the volcano in the Forgia Vecchia region. Further, the 1954 case was probably due to a submarine landslide detaching on the southeast side of Stromboli with effects on the eastern coast.

In this work we adopt a scenario approach (TINTI and ARMIGLIATO, 2003; TINTI et al., 2006a; ARMIGLIATO, 2006) to explore the effects of tsunami sources that are not located in the SdF zone and that we refer to as "extra-SdF" sources, namely Punta Lena Sud, Forgia Vecchia and Strombolicchio (see Fig. 3). These areas have been identified by considering jointly morpho-bathymetric data and data on historical events. In our strategy, first we define the sliding mass, then we perform numerical simulations of the landslide motion and thirdly we compute the consequent tsunami, with the aim of examining the tsunami propagation pattern and of inferring the tsunami impact on the coasts of Stromboli and of the other Aeolian islands. The purpose is to quantify the hazard and to identify the coastal segments that are most exposed to the tsunami attacks. In the following, for the sake of completeness, we will first illustrate synthetically the numerical models we use in the paper, and then provide a description of the SdF 2002 double tsunami. However, since

Table 1

Tsunamis which occurred in Stromboli in the last 100 years, modified after MARAMAI et al. (2005a).

Year	Month	Day	Cause (*)	Intensity (Ambraseys scale)	Short Description
1916	7	3	Speculated submarine landslide in the Sciara del Fuoco	2	Sea retreat and flooding of the beach called Spiaggia Longa in northern Stromboli
1919	5	22	Speculated submarine landslide in the Sciara del Fuoco	3	In Stromboli, sea retreat by 200 m and flooding of the beach. Boats carried inland in the vineyards by more than 300 m.
1930	9	11	Double event: One caused by an observed hot avalanche at Piscità and one by a speculated submarine landslide	2 [1] 4 [2]	A hot avalanche raised water waves that scalded and killed one man in the Eolo's grotto (northern Stromboli). Landslide-induced tsunami: Sea retreat by 100 m followed by flooding of the beach of Sopra Lena by 200 m (NE Stromboli). One man killed on the beach of San Vincenzo (NE Stromboli) by 2.5-m-high waves. On the Calabrian coast, wave of 2–3 m observed.
1944	8	20	Double event: One caused by a speculated mass failure concomitant with an observed lava flow at Sciara del Fuoco, and one caused by an observed hot avalanche at Forgia Vecchia	2 [3] 4 [4]	Big waves in the Sciara del Fuoco area. Big waves in the East coast of Stromboli. One house destroyed. Beach full of fish.
1954	2	2	Speculated submarine landslide in SE coast	3	Initial sea retreat followed by water waves in E Stromboli. Boats carried inland.
2002	12	30	Double event: one caused by a submarine slide, the other by a subaerial slide in the Northern part of the Sciara del Fuoco	5	Heavy damages in Stromboli, especially in Piscità, Ficogrande, Punta Lena Nord and Scari. Measured runup heights up to 10.9 m at Spiaggia Longa, exceeding 10 m at Piscità and Ficogrande, exceeding 4 m at Scari. Damage in Panarea. Seen in other Aeolian islands, at Ustica, and on the Tyrrhenian coasts of Sicily, Calabria and Campania.

* All tsunamis of Stromboli occurred during periods of major eruptions.
1. Intensity of the tsunami due to the hot avalanche at Piscità.
2. Intensity of the tsunami observed in Sopra Lena and in San Vincenzo.
3. Intensity of the tsunami observed in the Sciara del Fuoco.
4. Intensity of the tsunami observed in Forgia Vecchia.

this case has been the object of numerous published studies (see e.g., TINTI *et al*., 2005a, b), we shall treat it here very briefly, and then we will move to scenarios centered on the extra-SdF sources.

2. Numerical Simulations

The simulations of landslide tsunami events are performed by means of a set of numerical codes that have been developed by the University of Bologna and have been reported in various works (TINTI *et al*., 2005a, 2006c). To compute the motion of the sliding masses, we developed the codes UBO-BLOCK1 and UBO-BLOCK2, implementing a Lagrangian block model: the mass is split into several constant-volume blocks that can change shape but cannot separate or penetrate each other. The first basic difference between these two codes is that the former deals with a 1-D chain of blocks, while the latter handles a 2-D matrix of blocks. The acceleration of the *k*-th block is split according to the equation:

$$a_{i,k} = G_{i,k} + R_{i,k} + F_{i,k}. \tag{1}$$

At the *i*-th time step, for the center of mass (CoM) of the block *k*, we compute the acceleration as the sum of the gravitational term $G_{i,k}$ (accounting for gravity, buoyancy and basal friction), the resistance term $R_{i,k}$, deriving from the interaction between the block and the environmental fluid (this term vanishes for subaerial motion) and the block-block interaction term $F_{i,k}$, regulating the pushes between adjacent blocks. The simulation is stopped when the mass reaches the end of the computational domain or when the velocity goes below a predefined threshold (TINTI *et al*., 1997).

The second main difference between UBO-BLOCK1 and UBO-BLOCK2 is that in the first code the CoM of all blocks run on the same trajectory that has to be predefined (usually the trajectory is a curve built following the maximum gradient of the bathymetric slope or it is deduced from observational data, when available). Therefore all forces acting on a given block are projected along the common trajectory line. The data input for this code therefore will be the sliding surface, the sliding mass, the trajectory of the CoMs and the lateral boundaries, determining the lateral spreading of the mass during the motion (for further details on UBO-BLOCK1, see TINTI *et al*., 1997). On the other hand, the code UBO-BLOCK2 treats landslides that can be discretized as an irregular matrix of blocks. Each block moves along its own trajectory, that is dynamically determined by the model, with the limitation, however, that blocks keep invariant their topological relationships within the matrix.

For the sake of correctness, it is of value to point out that the code UBO-BLOCK1 can be considered a 1.5-D model rather than a pure 1-D model, since also the transversal (i.e., in direction orthogonal to the CoM trajectory) distribution of the landslide mass plays a role. The code assumes that the transversal cross section has a given parabola-like shape, with thickness vanishing on the lateral boundaries and highest on the CoM

trajectory line. Further, the code accommodates the cross-section area in order to keep constant the total volume of each block and of the total landslide (see TINTI *et al.*, 1997 for further details). Notice that the lateral extension of the landslide influences the landslide dynamics since it affects the resistance drag force exerted by the environmental fluid (sea water) on the sliding mass.

In the following study the simulations of the SdF case were carried out by using the UBO-BLOCK2, while all the scenarios of extra-SdF sources were examined by making use of code UBO-BLOCK1. We chose to adopt the 1-D approach for these cases because it is computationally simpler, and therefore more adequate for a preliminary analysis, but also because that algorithm allowed us to control better the mass elongation and spreading during the motion.

The simulation of the generated tsunami is performed here by using a finite-element scheme UBO-TSUFE: The computational domain is covered by an irregular mesh of triangles, whose sizes are proportional to the square of the local sea depth. On this grid, the Navier-Stokes equations are solved, in the nonlinear shallow water approximation (2) including bottom friction:

$$\partial_t \eta = \partial_t h_s - \nabla \cdot [(h + \eta)\vec{v}]$$
$$\partial_t \vec{v} = -g\nabla\eta - (\vec{v} \cdot \nabla\vec{v}) - \frac{gn^2}{(h + \eta)^{4/3}}\vec{v}|\vec{v}|. \tag{2}$$

Here η is the sea-water elevation above still level, h the local sea depth and $\vec{v}$ is the depth-averaged horizontal velocity vector. The term $\partial_t h_s$ corresponds to the forcing provided by the sliding mass, and represents the link between the landslide and the tsunami simulation code. The boundary conditions are of pure transmission on the open sea boundary, while the interaction with the coast is regulated by a reflection coefficient, allowing also a partial absorption of the tsunami energy (TINTI *et al.*, 1994). Further, the bottom friction is accounted for through the Manning's expression in which n is the dimensional roughness coefficient, that usually is assumed between 0.01–0.03 s m$^{-1/3}$ offshore, while it has larger values in the inundation zone, depending on local ground conditions (see SHIGIHARA *et al.*, 2006). Since we do not compute tsunami flooding in this paper through the code UBO-TSUFE, but we use a static domain with vertical reflecting walls at coastal boundaries, we adopt here the standard offshore coefficient values for n.

The output of the landslide simulation provides the instantaneous changes of the sea floor caused by the moving mass, which is converted into the sea-surface forcing $\partial_t h_s$ through a filter depending on the local sea depth. Since the landslide model and the tsunami model use different space grids, mapping from the Lagrangian model space to the triangular elements grid is the task of an *ad hoc* interpolation code called UBO-TSUIMP, that can be considered as the interface between the landslide and the tsunami models.

3. December 30, 2002 Tsunamis

The last months of 2002 were characterized by a period of increasing activity of Stromboli: the crisis reached its apex at the end of the year, when a series of landslides detached from the northern side of the SdF slope, for a total estimated volume of 2–$3 \cdot 10^7$ m^3 (Chiocci *et al.*, 2003). Two main failure events were recognized. The first one was submarine, with a volume of approximately $15 \cdot 10^6$ m^3, and detached underwater just near the coastline. After about seven minutes another mass, around 4 10^6 m^3, fell into the sea from the subaerial part of the SdF, just above the previous body, and this was interpreted as the retrogression of the first failure process. These motions generated two distinct tsunamis that hit the coasts of the entire island, with maximum runup values exceeding 10 m, and maximum inundation distance greater than 100 m in the most flattened coastal zone. Fortunately, despite the violence of the tsunami waves, no casualties resulted, since beaches and low-land coastal belts were unpopulated due to the winter season (Tinti *et al.*, 2005b, 2006b; Maramai *et al.*, 2005b).

As anticipated above, the landslides were studied by using the code UBO-BLOCK2, while to compute the resulting tsunamis use was made of the tsunami propagation code UBO-TSUFE. According to our calculations, the submarine slide (the first one) soon reached a speed greater than 40 m/s, followed by a slow deceleration phase when it moved in deeper waters on a lower gradient slope. On the other hand, the subaerial slide (the second one) attained a peak velocity of more than 60 m/s, and experienced an abrupt deceleration when it reached the sea. The computed tsunamis differ, only slightly from each other, though the first is slightly larger than the second. Waves are huge in the generation zone (the SdF coasts), reaching several tens of meters.

Figure 2 shows the computed maximum and minimum water elevations on the northeastern coast of Stromboli, the most inhabited of the island. In this area the tsunami reached at least 5 meters height, with maxima around 20 meters. Further, the graph shows the observed runup (black triangles) and the computed maximum elevations along the coast of Stromboli in the case of the first landslide (see also Tinti *et al.*, 2006c, case 1B). Notice that, though in principle the post-event observations refer to the cumulative effects of both tsunamis, the observed runups should be mainly attributed to the first tsunami since, according to the reports of some eyewitnesses (and also to our simulations), the second tsunami was generally weaker. Interestingly, notwithstanding that, as already mentioned in Section 2, the tsunami model UBO-TSUFE does not use a moving boundary domain and hence does not specifically compute the shoreline displacement and the consequent runup heights, nonetheless the comparison between the observations (runup heights) and the outcome of the model (i.e., the maximum sea-level elevations at the coastal nodes) is very satisfactory.

These cases can be considered as intermediate-scale events since they do not involve particularly huge masses. They were very important since they called attention to the tsunami impact on Stromboli and stimulated research and studies on tsunami generation
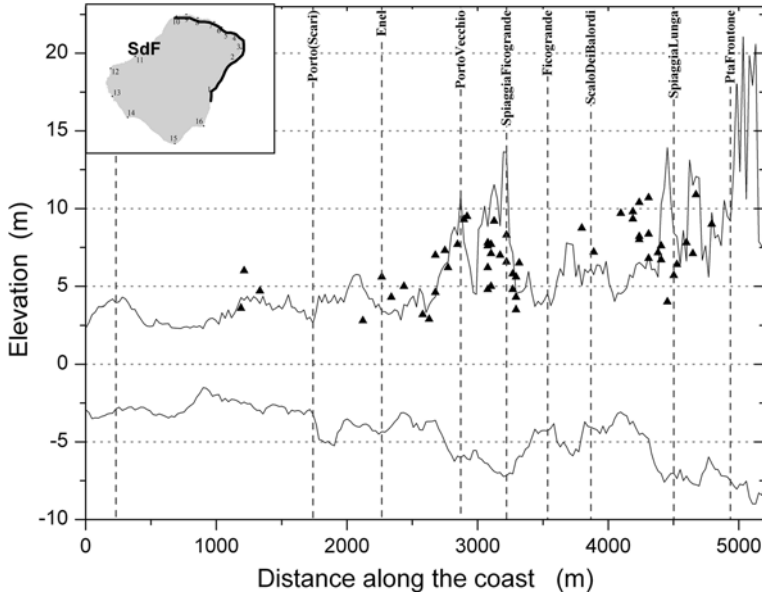
Figure 2

December 30, 2002 tsunami (see Tɪɴᴛɪ *et al*., 2006c, case 1B). Computed maximum and minimum water elevations along the northeastern coast of Stromboli, that is the most densely inhabited, compared with the observed runup heights (black triangles). The "distance along the coast" is measured starting from Malpasseddu.

and propagation in the Aeolian archipelago. In particular, the study of these two tsunamis revealed some features we also found to be relevant for the extra-SdF sources:

— Stromboli steep slopes, that are typical of a volcanic environment, cause high acceleration and velocity of the sliding mass and in turn large tsunamigenic impulses;
— tsunami wave energy does radiate outward from Stromboli, but also tends to be trapped near Stromboli, which is typical of wave propagation around steep-slope islands;
— the northeastern coast of Stromboli, the most densely populated especially during the summer season, is characterized by pocket beaches, beaches and generally by flat topography prone to tsunami inundation.

4. *Extra-SdF Landslide Simulations*

As indicated by the tsunami catalogue, most tsunamigenic sliding events occur along the SdF zone, both in the subaerial and in its submerged part. For this reason the zone is carefully and continuously monitored. In this work, however, we investigate the
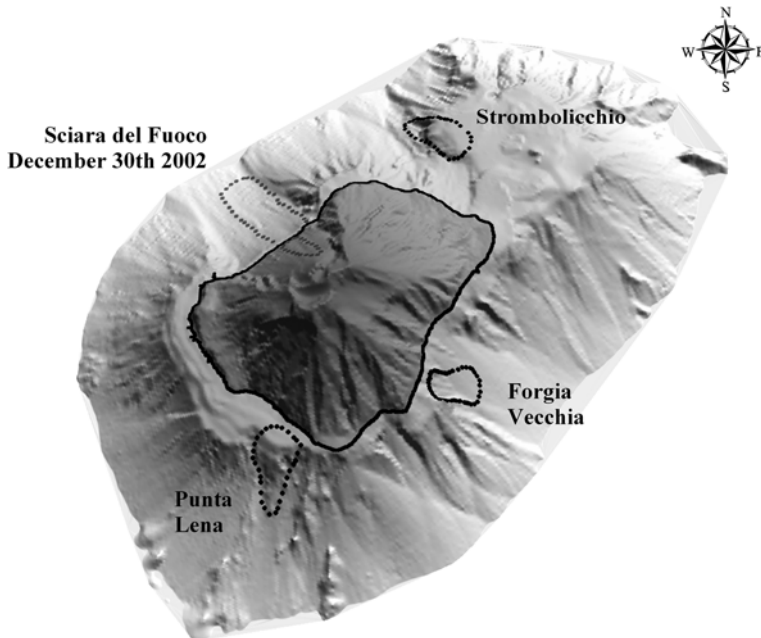
Figure 3

Source areas (dotted lines) of the tsunamigenic landslides considered in this paper: Sciara del Fuoco, Punta Lena, Forgia Vecchia and Strombolicchio. As regards the Sciara del Fuoco area, both the submarine slide and the subaerial slide (respectively case 1B and case 2 in TINTI *et al.*, 2006c) are represented. The emerged zone of Stromboli is dark-grey and delimited by a solid black line.

propagation pattern and the coastal impact of tsunamis generated by events occurring in other zones of the island, out of the SdF.

Figure 3 shows a three-dimensional reconstruction of the volcanic edifice. It is evident that along its flanks one can find many scars and canyons throughout the island, starting also from rather shallow depth. Based on some of the events reported in the tsunami catalogue (Table 1), we set up tsunami scenarios for three extra-SdF source areas (see Fig. 3), partly recalling historical occurrences. We stress that we are not carrying out reconstructions of real landslides, but that, following a typical scenario approach, we consider reasonably hypothetical submarine sliding bodies with volumes of the same order of magnitude (10^7 m^3) as the SdF submarine slide, which is compatible with the known local morphology. The first scenario, in the Punta Lena Sud source area, may recall the 1954 event. The second source area, in the section of the eastern coast called Forgia Vecchia, was the theater of the 1944 tsunami. Further, for the sake of completeness, we also consider a third source area we locate in correspondence of quite clear incisions that are found on the northwestern margin of the volcanic platform of Strombolicchio that extends north of Stromboli.

For each one of these cases we performed numerical simulations, using the code UBO-BLOCK1, the interface module UBO-TSUIMP, and the finite-element tsunami code UBO-TSUFE.

4.1. *The Punta Lena Sud Landslide Scenario*

The first case we consider recalls the 1954 event. According to Table 1, the cause was a speculated submarine slide occurring on the SE coast, provoking an initial water withdrawal on the eastern coast of the island, and a successive sea perturbation also carrying some boasts inland. As can be seen in Figure 4, we considered a sliding mass detaching close to the coastline (around 20 m depth), about 1 km long and 0.5 km wide, with a mean thickness around 30 m, and a point of maximum thickness of approximately 100 m located toward the coast: all this results in a $15 \cdot 10^6$ m^3 volume. In Figure 4 the predefined trajectory of the CoM of the blocks and the lateral boundaries of the sliding surface are also shown.

The landslide simulation is performed with 0.25 second time step, and is stopped after about 300 s when the mass, moving southward and at the end slightly eastward, reaches the end of the computational domain. Here the slide has a length of about 3 km and an average thickness of no more than 5–6 meters, due to the widening and longitudinal elongation of the mass. At the simulation stop time, the average speed of the landslide is around 12 m/s, still relevant. However, at this point in time the tsunamigenic potential of the mass is almost negligible since it moves at a depth of 1400 m, more than 5 km from the coast. As far as the landslide model parameters are concerned, we adopted a bottom friction coefficient of 0.02 and a density of 2650 kg/m^3, analogous with values that have already been adopted for simulations of underwater sliding masses in the SdF.

4.2. *The Forgia Vecchia Landslide Scenario*

The second source area is located along the eastern coast, near Malpasseddu (see Fig. 5), accidentally in the place where one of the two tsunamis of 1944 originated. Indeed, we know that a hot avalanche was the cause of water waves. Here we consider a scenario of an ordinary submarine landslide generating a tsunami.

Again we assume a submarine mass detaching near the coast (in this case from about 80 m depth), about 800 m long and 500 m wide, with a volume of 13.2 millions m^3 and a mean thickness of around 35 m. The simulations shows for the sliding mass a run-out of more than 5 km, SE directed. When calculations are stopped (after 187 s), the body has a residual speed of 17 m/s. With reference to this, the same remarks given for the Punta Lena Sud case can be repeated here. Mass spreading is less conspicuous here, with a mean final thickness of more than 10 meters. The model parameters (time step, friction
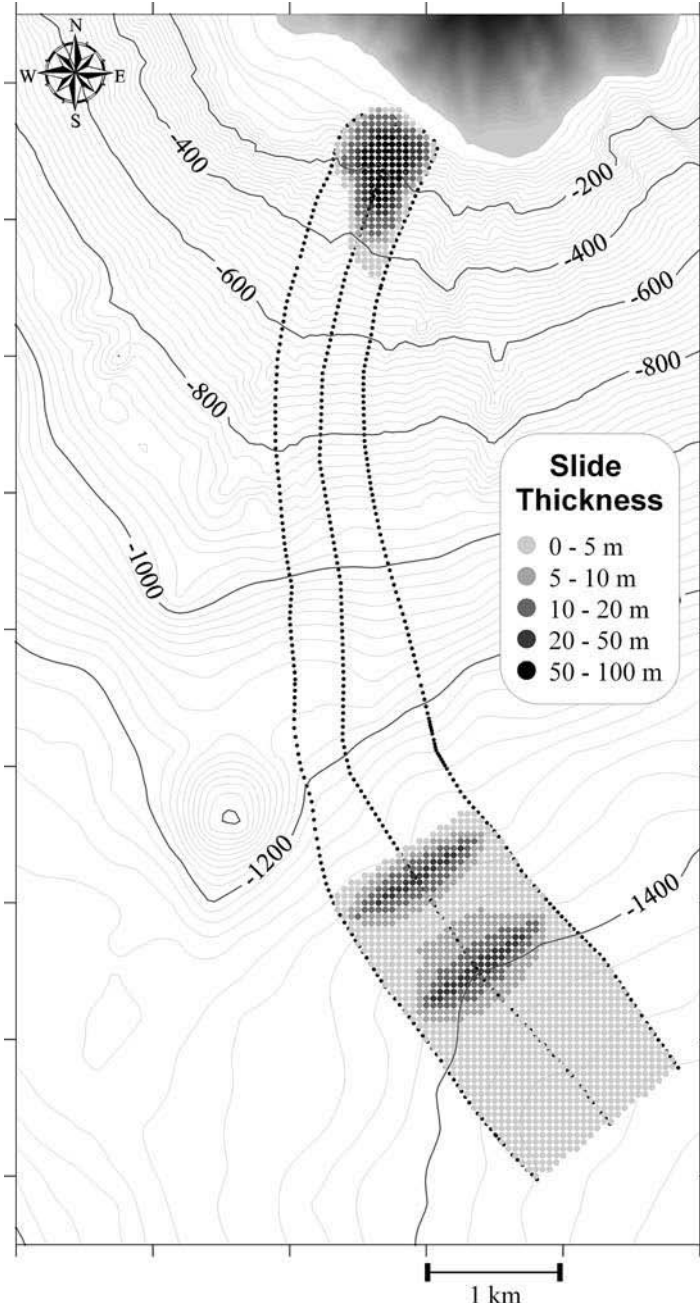
Figure 4
Scenario of the Punta Lena source area. Predefined CoM trajectory (central) and lateral boundaries of the basal sliding surface (dotted lines). Assumed initial and computed final mass distribution of the slide is given in grey scale. Consider that the final slide position is not the final position of the mass deposit, since the model calculations are stopped when the mass reaches a depth of roundly 1400 m and its tsunamigenic potential becomes negligible.
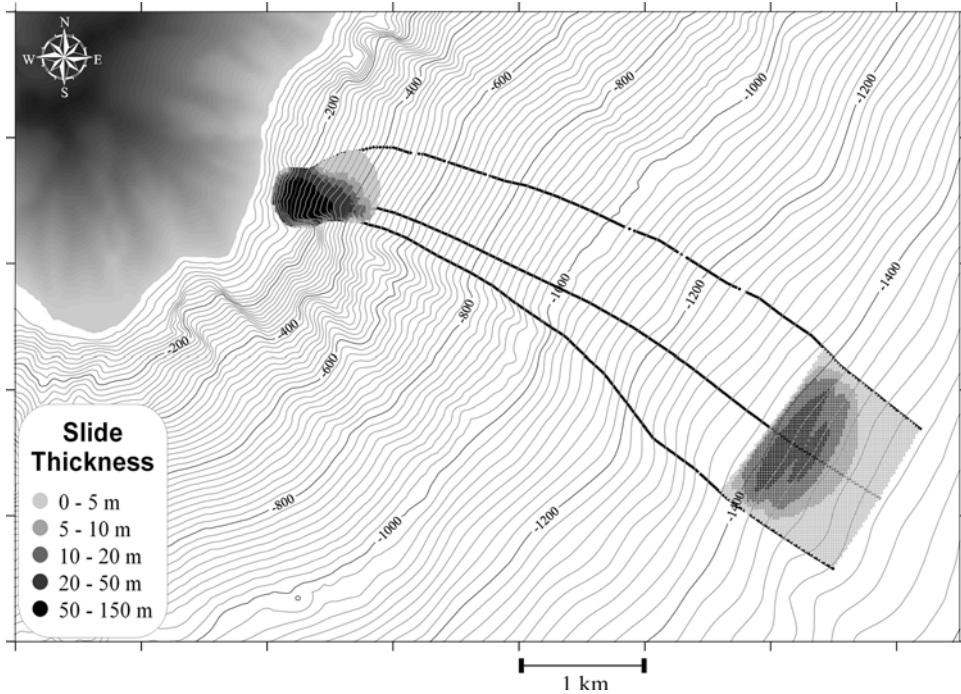
Figure 5
Scenario of the Forgia Vecchia source zone. See the caption of Figure 4.

coefficient, density) are the same as those for the previous case of the Punta Lena scenario.

4.3. The Strombolicchio Landslide Scenario

The last scenario sliding mass has been modelled in the source area located to the north of Stromboli; that is in front of the coastal segment that is the most populated in summer time.

We choose a body detaching from the Strombolicchio plane (Fig. 6), i.e., a shallow-water zone, that may be seen as the continuation of the upper part of the volcanic edifice mainly developed in NE-SW direction. The mass, moving to the NW has a volume of $9.6 \cdot 10^6$ m^3, detaching 1 km away from the coast at a local depth of 150–200 m. The simulation, performed with 0.25 s time step and the friction coefficient of 0.2, is stopped after about 188 s, when the mass has the residual velocity of more than 20 m/s, 7 km from the initial position. In this case the mass elongates (from 1 km to about 3 km) and widens (from 0.5 to 1.5 km), and hence the average thickness decreases considerably (from about 20 m to less than 3 m).
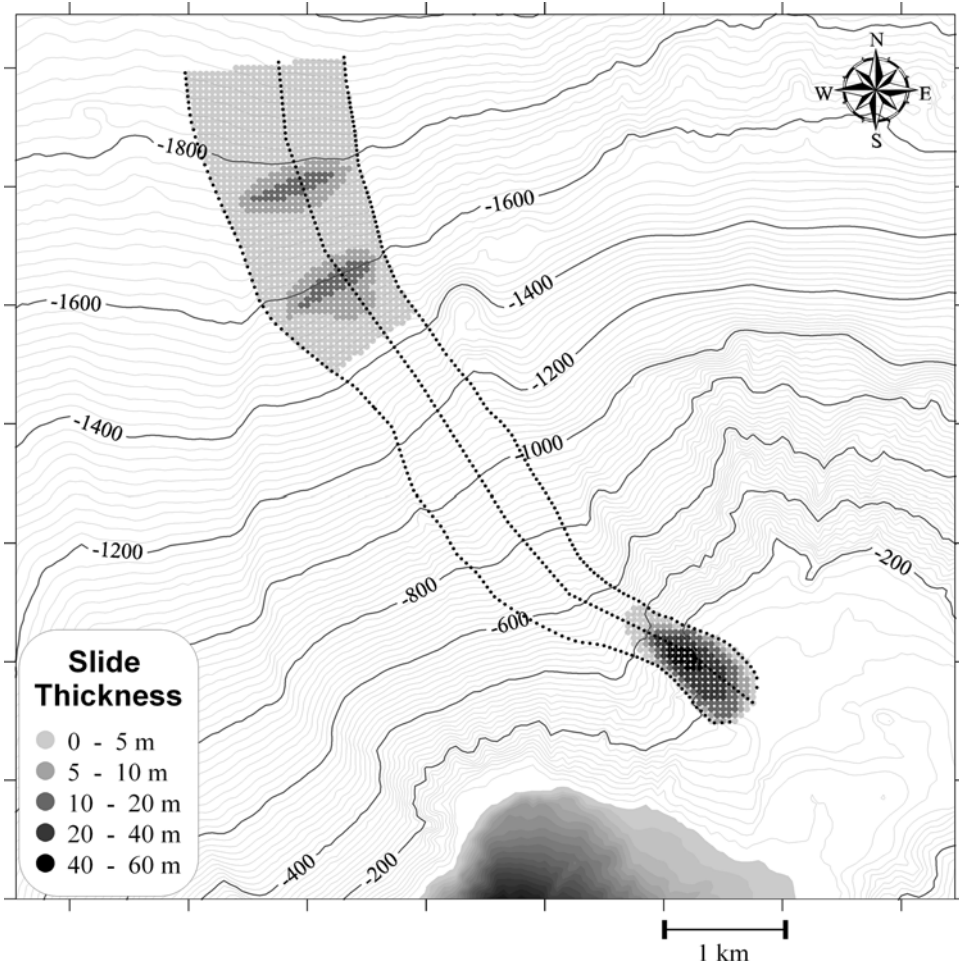
Figure 6
Scenario of the Strombolicchio source area. See the caption of Figure 4. The final computational sea depth is approximately 1800 m for this case. Observe that the slide mass spreads over a large area, with its length increased by a factor of 3 and maximum thickness decreased to values between 10 and 20 m.

4.4. Slide Velocities and Froude Numbers

Graphs on Figure 7 show the velocities of the three extra-SdF scenario landslides compared to the results obtained for the December 2002 submarine slide down the SdF zone slope. Generally, we can see curves with common features: a strong initial acceleration followed by a long phase of slow deceleration, due to the fact that at the beginning the masses reside in steeper slopes, typical of volcanic environments, sliding rapidly in the lower angle zone, where they slow down. We notice that the peak velocities
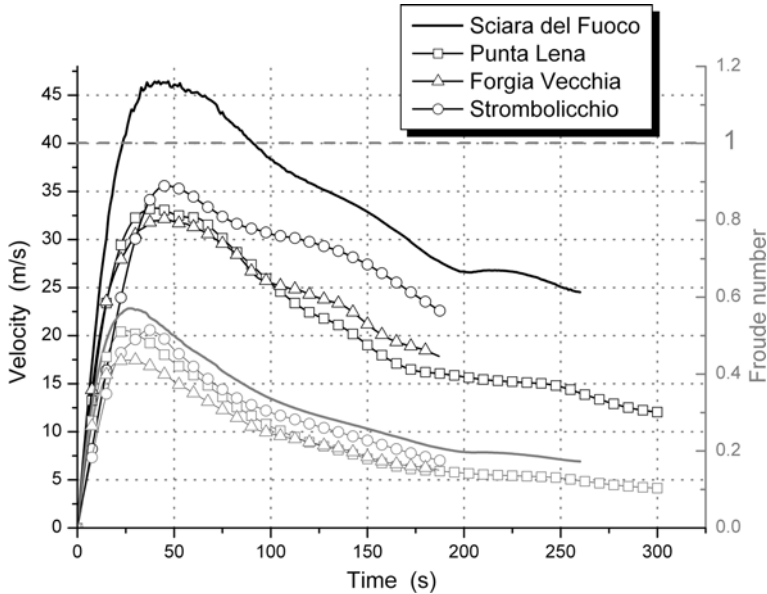
Figure 7

Velocities (four upper curves) and Froude numbers (four lower curves) for the landslide scenarios considered in this paper (namely the scenarios with source areas given in Figs. 4–6) plotted together with the Sciara del Fuoco landslide scenario (case 1B in TINTI *et al.*, 2006c). The slide velocity is computed as the average of the velocities of the individual blocks forming the slide. The dashed horizontal line marks the critical value, i.e., 1, of the Froude number.

of the extra-SdF cases are indeed significant, though slightly lower, between 32 and 35 m/s, than the 45 m/s of the SdF case.

The Froude number is a parameter reflecting the landslide capability to generate a tsunami: it is calculated as the ratio between the horizontal velocity of the slide and the phase velocity of the tsunami wave (i.e., $\sqrt{g \cdot h}$, where g is the gravitational acceleration and h is local sea depth). When this ratio is close to one, the mass and the generated wave move coupled-wise, meaning that the slide movement continues to "feed" the wave, and to provide energy. The graph shows that the most tsunamigenic phase for all cases starts after 25–30 seconds from the landslide initiation, when the Froude number reaches peak values of 0.4–0.5 (slightly more for the SdF case). After some 100 seconds, the velocities decrease, the masses move in deeper waters and the Froude numbers reduce consistently, falling below 0.3.

5. *Tsunami Propagation around the Stromboli Coasts*

The tsunami propagation and impact on the coasts are simulated through the code UBO-TSUFE over a finite-element mesh formed by triangles, smaller in shallow-

water in the near-shore zone, and larger offshore. The main optimum criterion for the mesh building algorithm is the uniformity of the crossing time for the tsunami wave for the triangular elements of the grid. In Figure 8 the computed maximum and minimum elevations along the coast of Stromboli are given for the three extra-SdF scenarios.

We observe that the Strombolicchio landslide gives rise to the weakest tsunami and does not produce significant waves on the coast: only between Scari (node 3) and Punta Labronzo (node 10), i.e. on the northeastern coast in front of the source, 1 m signal may be seen in the graph.

The Punta Lena Sud case produces the strongest tsunami, with very significant waves near the source zone exceeding 80 m between Punta Lazzaro and Punta Lena Sud (nodes 14 and 15, respectively), travelling in both directions along the Stromboli coast. On the eastern coast a 20 m maximum elevation is computed almost everywhere, while on the northern coast, which is protected by the cape of Punta Lena Nord (between nodes 3 and 4), the elevation reduces to 7–8 m, still remaining considerably high. Also Punta Chiappe (node 12) is seen to have some shielding effects on the western coast, that is affected by peaks reaching 8–10 m.

The Forgia Vecchia case gives rise to a very significant tsunami, especially near the source zone, on the eastern coast, with peaks up to 80 meters, and an average height approaching 20 m throughout the shore. Our results for both the Punta Lena Sud and the Forgia Vecchia tsunamis are quite similar on this segment of coast. However, if one
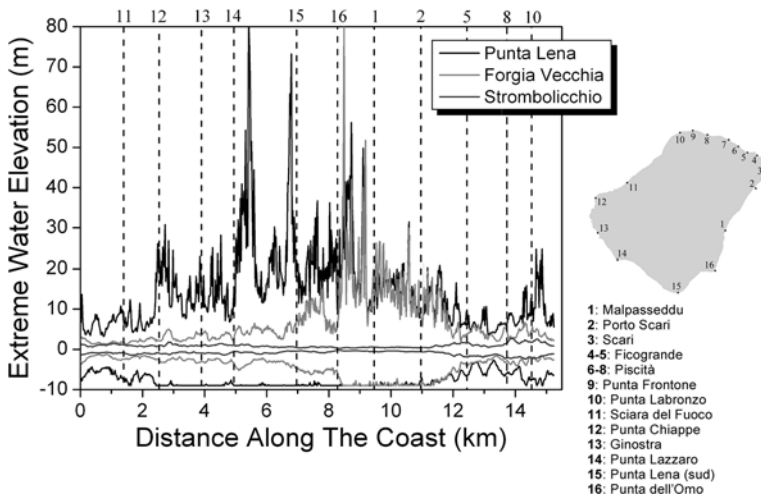

Figure 8

Computed maximum and minimum tsunami elevations along the entire coast of Stromboli for the three extra-SdF source areas. The "distance along the coast" is measured anticlockwise starting from an origin that is located in the SdF area between points 10 and 11, that are named here Punta Labronzo and Sciara del Fuoco. Dashed vertical lines mark the position along the coast of the locations listed on the right side.
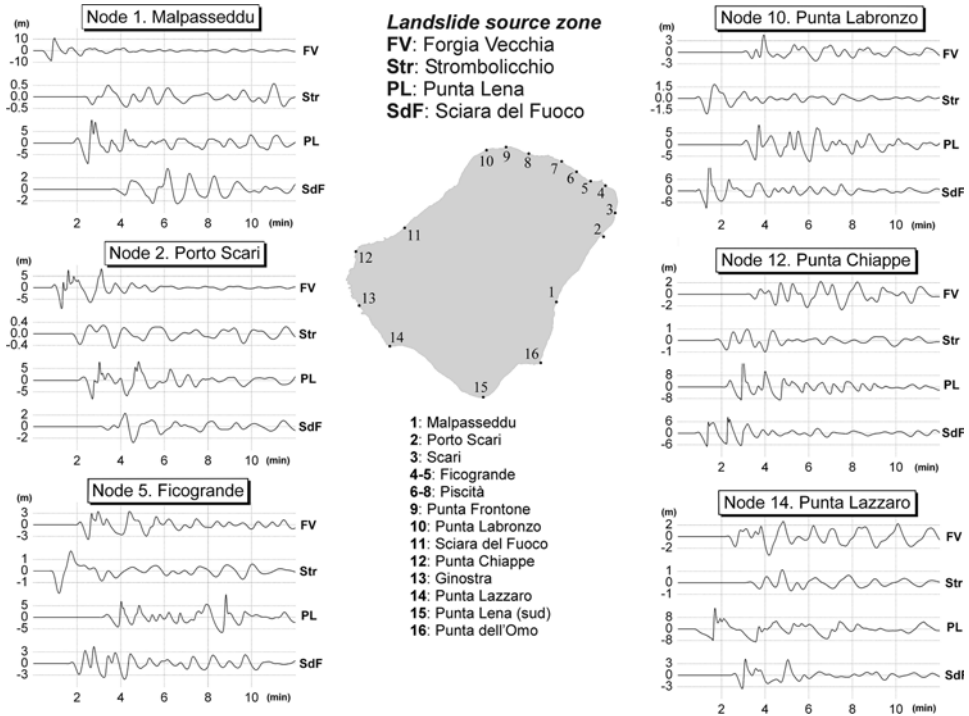
Figure 9

Comparison of tsunami waveforms computed at six different coastal nodes for the 4 cases treated in the paper. Notice that in most places the first predominant signal is negative, corresponding to a sea withdrawal.

moves to the south (clockwise in the graph), after Punta Lena Sud (node 15), one sees that the southern and western coasts are affected by 2–3 m elevation waves, which is much less than the Punta Lena Sud case.

Figure 9, reporting computed tsunami waveforms in some selected coastal nodes, presents other interesting and significant information. Starting from node 1, Malpasseddu, we can notice that on the eastern coast the highest signal is given by the Forgia Vecchia source, placed just in front of it, with 10 m waves. Also Punta Lena Sud gives significant signals, more than 5 meters, while the Strombolicchio tsunami is here absolutely negligible. The SdF case affects this area with 2 m waves, with a significant delay in time (4 minutes) due to the fact that the source area is on the opposite side of the island. One further significant feature for all cases is that the first signal is negative, corresponding to a sea withdrawal followed by a strong peak. The tsunami still continues to affect the sea at the end of the computed tide gauge records. It is also important to note that the dominant period of the tsunami is around 60–90 seconds, which is clearly different from (much shorter than) typical periods of earthquake generated tsunamis (ARMIGLIATO *et al.*, 2006). Moving to Scari (node 2), we

can see similar features, apart from the attenuation of the effects of the Forgia Vecchia tsunami.

The time history computed for node 5, corresponding to Ficogrande beach, one of the most active tourist zones of Stromboli, shows relevant effects as concerns the Strombolicchio case, around 1 m of withdrawal and positive signal. The tsunami originating from Punta Lena Sud reaches this area after the other three cases, and its maximum signal occurs six minutes after the first arrival. The Forgia Vecchia and the SdF cases show similar behavior, both in the maxima and in the first arrivals. Even here the dominant tsunami period is around 60–90 seconds.

In Punta Labronzo (node 10) the SdF tsunami is the first to arrive and has the predominant extreme elevations. Also the Strombolicchio case shows here its maxima, 1.5 m. The first arrival manifesting as a withdrawal is persistent, confirming that this is a typical feature of the submarine landslide tsunamis.

At Punta Chiappe (node 12), the largest signals come from the SdF case, with more than 6 m wave, but also decidedly significant is the Punta Lena Sud slide tsunami, causing here more than 8 m wave. Contrastingly, the Forgia Vecchia case has its minimum effects here, around 2 m, while Strombolicchio gives the lowest, though not negligible, signal (around 1 m). Again the most noticeable features are the initial sea withdrawal and the 60–90 second tsunami period. We conclude the travel around the coasts at Punta Lazzaro (node 14), in the middle of the southern coast of Stromboli: here the Punta Lena case gives the most significant waves, more than 8 m.

6. Tsunami Propagation around Stromboli and Panarea

Generally Stromboli landslide tsunamis also impact the other islands of the Aeolian archipelago, to the extent of the Sicily and Calabria coasts. This was true, for example for the December 2002 SdF tsunami, that was observed in Lipari, Vulcano, etc., and that was strong enough to produce damage in Panarea, an island 20 km SW of Stromboli, where the tsunami front arrived within 5 minutes after the landslide initiation (TINTI *et al.*, 2005b). Further, we recall that here was obtained the only instrumental record of these tsunamis, showing 1 m amplitude sea-level oscillations, though the sampling rate of the sensor (5 minutes) was unsuitable to correctly reproduce the tsunami waveforms. Surveying Table 1, we can see also that the 1930 tsunami provoked 2–3 m waves in Calabria. From the hazard assessment point of view, it is therefore important to evaluate the effects of the Stromboli tsunamis not only on the Stromboli coasts but also on all the coasts of the South Tyrrhenian Sea, where one can find several coastal towns, industrial plants, commercial and transport infrastructures, and touristic industry facilities.

In this work we present results focussed on the intermediate field, that is over a computational domain comprehending Stromboli and the nearest island of Panarea. In Figure 10 the propagation of the tsunami generated by the Punta Lena case is depicted.
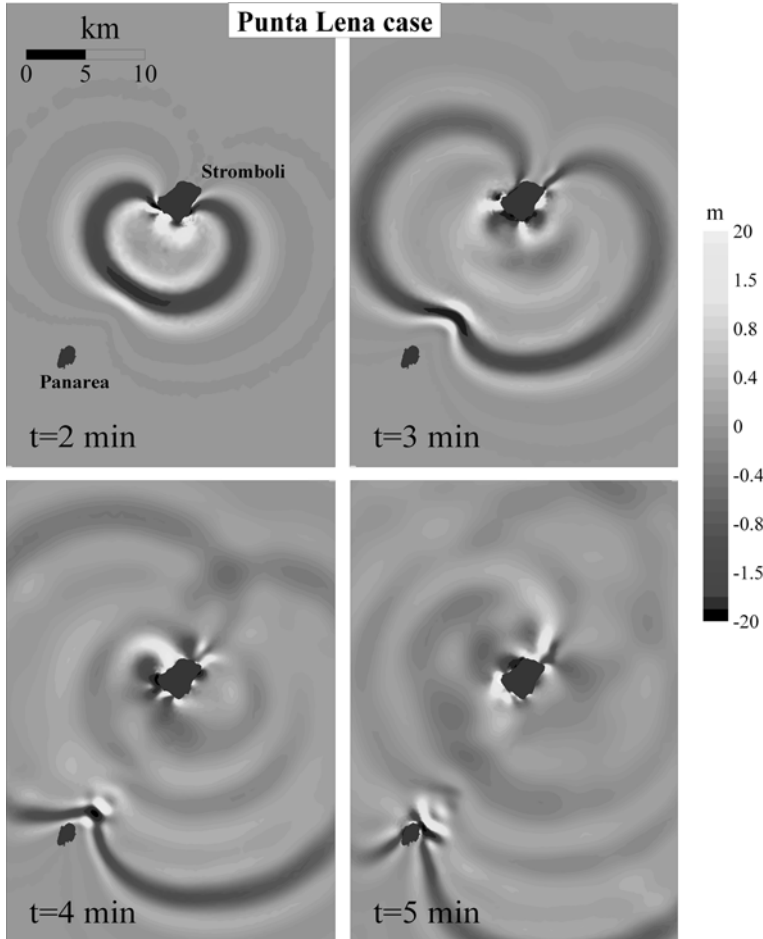
Figure 10
Propagation of the tsunami generated by the Punta Lena landslide shown at different times over a computational domain also including the Panarea Island, about 20 km SW of Stromboli. Notice the initial radial symmetry of the tsunami front, broken after 3 minutes by bathymetric effects when it is approaching Panarea. The tsunami strikes the entire Stromboli coast in less than 4 minutes, and affects Panarea in about 5 minutes.

We choose this one both because it is the strongest tsunami of the considered extra-SdF sources, and owing to the position of the source with respect to the Panarea Island. The tsunami propagation towards Panarea is, in the other two cases, partly weakened by the Stromboli Island. From the snapshots of Figure 10 we can perceive the strong negative leading signal travelling around Stromboli. After 2 minutes the tsunami strikes the eastern coast of the island and starts to strike the western coast. After only 4 minutes the two negative fronts converge on the northern coast of Stromboli. As to the SW-ward propagation towards Panarea, the wave front begins to deform, as the result of
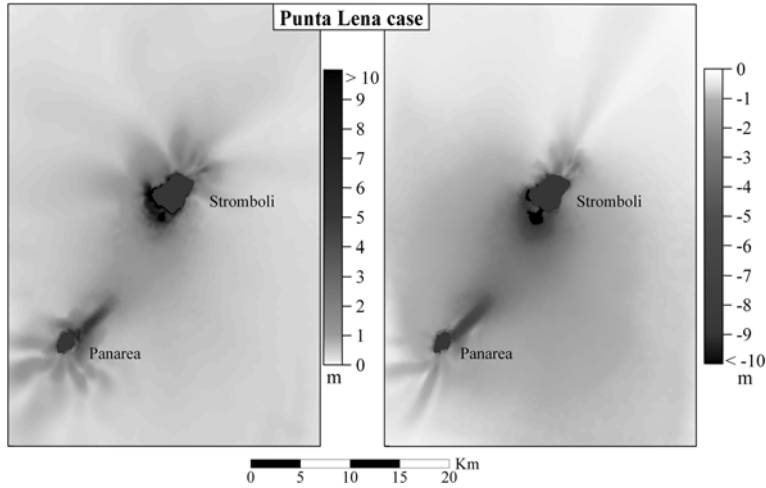
Figure 11
Maximum and minimum water elevation fields for the Punta Lena tsunami case. Observe the lobe patterns around the two islands and the beam from Stromboli to Panarea, showing the strong directivity effects of the tsunami fronts, depending on the local bathymetry.

bathymetric irregularities. After 4 minutes Panarea is affected by the tsunami, with wave heights reaching 6 m just in front of the slide trajectory, as can be seen in Figure 11, representing the maximum and minimum elevations on the computational field. Around Stromboli one can observe the formation of a train of waves, which is a typical expression of tsunami energy trapping along the coasts.

Figure 11 is also interesting because it shows clearly that the tsunami energy does not radiate isotropically away from the source area, but it travels along paths or beams with strong directivity effects. Therefore maximum and minimum tsunami elevation graphs can be used to identify at a glance the coastal segments that are mostly affected by tsunamis from a given source, and can be seen as a first-step aid for tsunami hazard assessment. In this respect, Figure 11 indicates that the Punta Lena Sud tsunami has a preferential propagation towards the NE cape of Panarea. The other maxima that can be seen around Stromboli are the effect of local wave trapping and amplification.

7. Landslide Potential Energy and Tsunami Total Energy

An interesting issue to evaluate the tsunami generation capability of a given source area can be the search for a correlation between a quantity related to the landslide, i.e., its potential energy, and the energy transferred by the landslide to the water, i.e., the tsunami total energy. To do this, we performed several simulations starting from the four cases
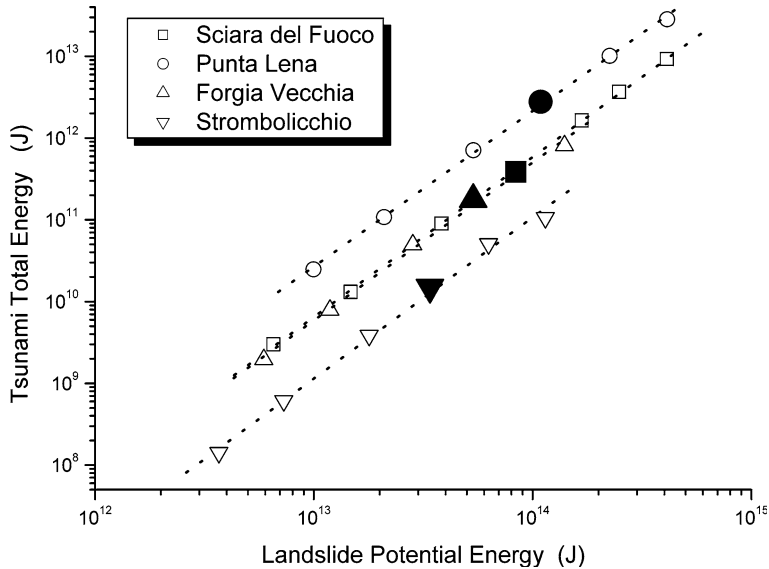
Figure 12

Bi-logarithmic graph correlating the landslide potential energy to the tsunami total energy for the four tsunamigenic source areas considered in the paper. Note the remarkable alignment of all cases over parallel straight lines. Solid symbols denote the four scenarios treated in the paper.

considered above and for each of them we changed the initial mass thickness and computed the consequent tsunami.

For our purposes, the total energy of the tsunami is defined as the sum of the instantaneous kinetic and potential energies corrected by the addition of the energy dissipated through bottom friction. This implies the computation of space integrals extended over the entire ocean domain, that, in our finite-element numerical code are computed by calculating the integrals in each triangular element, and then by summing the contribution of all elements. Indeed, since the computational domain is finite, we take into account the tsunami energy fluxes across the open-sea boundaries, and add this contribution to the total internal energy.

It is known that the tsunami energy budget changes with time. In case of a landslide-induced tsunami, it starts initially from zero and, after an initial growth, usually it reaches a peak value, followed by a slight decrease. Subsequently, after the landslide comes to a rest and can no longer impart energy to the ocean, it stabilizes at a constant value (see TINTI and BORTOLUCCI, 2000; TINTI *et al.*, 2001). In our interpretation, the ocean energy growth in the initial stage is that which one expects since the moving landslide body is expected to communicate energy to the water. This occurs since the slide-mass impulses and the ocean waves tend to be in phase. The following tsunami energy fall is not trivial to explain, since it means that the sliding body unexpectedly subtracts energy to the ocean

waves. Indeed, this happens commonly because the impulses of the landslide and the tsunami front sooner or later go out of phase, with the landslide becoming considerably slower than the tsunami. In fact, the tsunami energy decreases because the slide mass imparts positive impulses in regions of tsunami troughs and negative impulses in regions of tsunami crests, with the total result of decreasing the total tsunami amplitude. As stated, the successive constant energy value means that the interaction between the landslide and the water has ceased.

The landslide potential energy is computed as the difference between the potential energy of the landslide body in its initial position and its potential energy in the instant when the tsunami reaches the maximum value. Physically, the slide potential energy is defined as the integral of the density times the gravity acceleration extended over the body volume. In the block-based landslide code UBO-BLOCK1 and UBO-BLOCK2, the computation of the landslide potential energy simplifies to the sum over all the blocks of the product $m \cdot g \Delta h$, with g representing the gravity acceleration and m the constant mass of the block. Coherently, Δh is the difference between the initial altitude of the CoM of the block slide and its altitude in the instant of the maximum tsunami total energy.

The graph reported in Figure 12 is obtained by plotting in a bi-logarithmic scale the peak tsunami total energy (in Joule) vs. the landslide potential energy (in Joule) computed according to the definitions given above.

In order to build the plot, for each source area we varied the basic landslide scenario discussed in the previous sections by changing the initial thickness of the body (which results in a consequent change of the potential energy) and by computing the corresponding tsunami. One can see that increasing the landslide potential energy leads to an increase in the tsunami total energy, which is not surprising. Especially interesting is that for a given source area, the tsunami and the landslide energies seem to be linked by a linear relationship in the log-log plot. And even more interestingly, taking a look at Table 2, where the parameters A and B of the linear fit are reported, one observes that the slope of the straight line (the dimensionless parameter B) has values very close to 2 for all the cases. One can conclude that to an increase of the slide potential energy by one order of magnitude, the total tsunami energy correspondingly increases by two orders of magnitude. We notice further that the different cases are characterized by parallel lines,

Table 2

Parameters of the linear fit $Log(y) = A + B \, Log(x)$ between the landslide potential energy (x) and the tsunami total energy (y), both expressed in J (see Fig. 12).

	A	B
SdF	-15.6 ± 0.2	1.96 ± 0.01
PL	-14.3 ± 0.4	1.90 ± 0.03
FV	-15.3 ± 0.9	1.92 ± 0.07
ST	-16.6 ± 0.9	1.97 ± 0.07

shifted vertically: it seems that the parameter *A* of the linear fit discriminates between the sources; depending on the position around the island, a slide can be more or less efficient in generating a tsunami. The SdF and the Forgia Vecchia source areas have similar behavior, which stresses once more a manner of axial symmetry between the slides occurring on the opposite sides of the volcanic edifice that is aligned along the SW-NE axis.

We remark that the above interesting curves link together spatial integrated quantities, namely quantities defined by integrals extended over the entire domain, and that they do not pose constraints on local quantities, such as, for example, the maximum wave elevation or the maximum water velocity. In other terms, a landslide in the SdF region with higher potential energy than a landslide in the Forgia Vecchia source area may give rise to a smaller tsunami peak elevation without contradicting the above law. With this caution in mind, we emphasize that these relationships can be used as a practical expedite tool to make estimates of the tsunami size. If one identifies in a given source area a potentially unstable body and is able to make rough estimates of its volume and run-out distances, which is an exercise that pertains to the regular practice of many marine geologists and volcanologists, one comes to some evaluation of the potential energy of the sliding mass, and then, by using the above relationships, one can also make inferences regarding the total energy of the tsunami.

8. Conclusions

The Island of Stromboli, in the SE Tyrrhenian Sea, is characterized by a strong and persistent volcanic activity, manifesting in continuous ejection of material from its craters. This material accumulates along the SdF, a sizeable scar on the NW flank of the volcanic edifice that formed about 5 Ka ago and is characterized by a steep unstable slope. Hence, as can be seen also from tsunami catalogues, sliding events generating tsunamis are frequent, justifying the continuous and rigorous monitoring of the area. A typical example of episodes of failure along the SdF is the two landslides of December 30, 2002, with about 20–30 millions cubic meters of total volume, generating destructive waves, up to 10 m high, battering all the coasts of Stromboli.

In this work we have investigated the effects on the coasts of Stromboli and on the near Island of Panarea of possible landslides located in other positions of the Stromboli submerged edifice, we named extra-SdF source areas. We selected these areas, namely Punta Lena Sud, Forgia Vecchia and Strombolicchio, based on occurrences included in the tsunami catalogue and on the morphobathymetric analysis of the near-shore sea floor. We have considered reference scenarios of possible submarine landslides with the same size as the December 30, 2002 landslides.

The simulations showed clearly that extra-SdF events also can produce significant waves. The Punta Lena Sud source area, the southernmost one, has the most extended

effects, since it produces a tsunami pounding the northern coasts with waves reaching 6 m, the other coasts with 20 m waves and near the source coast with a wave reaching even 80 m. Also the Forgia Vecchia case produces significant effects, although more limited to the eastern coast. Instead, the Strombolicchio source, although it is characterized by a Froude number comparable with the other cases, is probably too distant from the coast of Stromboli to produce significant effects, apart from the northern coast near Punta Labronzo, where more than a 1 m wave is generated. For all cases, the tsunami impacts all the island coasts within about four minutes, manifests as an initial sea withdrawal that is followed by a train of crests and troughs, and the first signal is not always the strongest one. The dominant tsunami period is around 60–90 seconds.

The study of the propagation in the intermediate field, involving the close Island of Panarea, is limited in this paper to the Punta Lena Sud case, and indicates that after 5 minutes the coasts of the island, 20 km from Stromboli, can be affected by significant waves, more than 5 m high. The maximum and minimum water elevation maps of Figure 11 show that there is a preferential direction of tsunami propagation, channelling the tsunami energy from Stromboli towards Panarea, which facilitates our understanding of which zones in Panarea and Stromboli can be the most affected by destructive waves.

Ultimately, we put in relation the landslide potential energy with the tsunami total energy. We explored a set of several cases by varying the initial thickness of the slide with respect to the basic reference scenario in all source areas, which implies a consequent change of the potential energy, and then we ran the simulation of the correspondent tsunamis. We have found that in a bi-logarithmic graph there is a strong linear correlation between the two quantities. If we increase the potential energy by one order of magnitude, we obtain two orders of magnitude growth in the tsunami total energy. This is true for all the SdF and extra-SdF cases considered here, since all fitting curves share the same slope B. Further, the curves differ by the intercept parameter A, which seems to be discriminant of the source area. The found relationship can be exploited as a useful tool to make a rough estimate of the expected tsunami energy (and therefore size) from estimates of potential energy of unstable bodies.

A final remark regards the monitoring system that is today installed in Stromboli and that was mainly implemented following the tsunamigenic 2002 crisis that continued until the initial months of 2003. The system is chiefly focussed on the SdF, which is considered the most prone to instability. Our work proves that tsunamis generated in other areas of Stromboli can be as disastrous as the 2002 tsunamis, and since we know from the tsunami catalogue that other areas have been active in the past, this should suggest the extension of the monitoring activity to cover these additional areas, which could be more effective if use is made also of adequate offshore monitoring techniques.

REFERENCES

APUANI, T., CORAZZATO, C., CANCELLI, A., and TIBALDI, A. (2005a), *Stability of a collapsing volcano (Stromboli, Italy): Limit equilibrium analysis and numerical modelling*, J. Volcan. Geoth. Res. *144*, 191–210.

APUANI, T., CORAZZATO, C., CANCELLI, A., and TIBALDI, A. (2005b), *Physical and mechanical properties of rock masses at Stromboli: A data set for volcano instability evaluation*, Bull. Eng. Geology and Environ. *64*, 419–431.

ARMIGLIATO, A., GALLAZZI, S., MANUCCI, A., PAGNONI, G., TONINI, R., ZANIBONI, F., and TINTI, S. (2006), *Generation, propagation and impact of scenario tsunamis in the Corinth Gulf (Greece)*, Europ. Conf. Earthq. Eng. Seismol. 2006, Geneva (Switzerland), 3–8 September 2006.

CHIOCCI, F. L., BOSMAN, A., ROMAGNOLI, C., TOMMASI, P., and DE ALTERIIS, G. (2003), *The December 2002 Sciara del Fuoco (Stromboli Island) submarine landslide: A first characterisation*, EGS-AGU-EUG Joint Assembly, Nice, France, April 2003, Geophys. Res. Abst., vol. 5, CDROM Version.

KOKELAAR, P., and ROMAGNOLI, C. (1995), *Sector collapse, sedimentation and clast population evolution at an active island-arc volcano: Stromboli, Italy*, Bull. Volcanol. *57*, 240–262.

MARAMAI, A., GRAZIANI, L., and TINTI, S. (2005a), *Tsunami in the Aeolian Islands (southern Italy): A review*, Marine Geology *215*, 11–21.

MARAMAI, A., GRAZIANI, L., ALESSIO, G., BURRATO, P., COLINI, L., CUCCI, L., NAPPI, R., NARDI, A., and VILARDO, G. (2005b), *Near- and farfield survey report of the 30 December 2002 Stromboli (Southern Italy) tsunami*, Marine Geology *215*, 93–106.

ROSI, M., BERTAGNINI, A., and LANDI, P. (2000), *Onset of the persistent activity at Stromboli volcano*, Bull. Volcanol. *62*, 294–300.

SHIGIHARA, Y., GOTO, D., IMAMURA, F., KITAMURA, Y., MATSUBARA, T., TAKAOKA, K., and BAN, K. (2006), *Hydraulic and numerical study on the generation of a subaqueous landslide-induced tsunami along the coast*, Natural Hazards *39*, 159–177.

TIBALDI, A. (2001), *Multiple sector collapses at Stromboli volcano, Italy: How they work*, Bull. Volcanol. *63*, 112–125.

TINTI, S., GAVAGNI, I., and PIATANESI, A. (1994), *A finite-element numerical approach for modelling tsunamis*, Annals of Geophys. *37*, 1009–1026.

TINTI, S., BORTOLUCCI, E., and VANNINI, C. (1997), *A block-based theoretical model suited to gravitational sliding*, Natural Hazards *16*, 1–28.

TINTI, S., and BORTOLUCCI, E. (2000), *Energy of water waves induced by submarine landslides*, Pure Appl. Geophys. *157*, 281–318.

TINTI, S., BORTOLUCCI, E., and ROMAGNOLI, C. (2000), *Computer simulations of tsunamis due to flank collapse at Stromboli, Italy*, J. Volcanol. Geoth. Res. *96*, 103–128.

TINTI, S., BORTOLUCCI, E., and CHIAVETTIERI, C. (2001), *Tsunami excitation by submarine slides in shallow-water approximation*, Pure Appl. Geophys. *158*, 759–797.

TINTI, S., and ARMIGLIATO, A. (2003), *The use of scenarios to evaluate the tsunami impact in Southern Italy*, Marine Geology *199*, 221–243.

TINTI, S., PAGNONI G., ZANIBONI F., and BORTOLUCCI, E. (2003), *Tsunami generation in Stromboli Island and impact on the southeast Tyrrhenian coasts*, Natural Hazards Earth Sys. Sci. *3*, 1–11.

TINTI, S., MARAMAI, A., and GRAZIANI, L. (2004), *The new catalogue of Italian tsunamis*, Natural Hazards *33*, 439–465.

TINTI, S., ARMIGLIATO, A., MANUCCI, A., PAGNONI, G., and ZANIBONI, F. (2005a), *Landslides and tsunamis of 30th December, 2002 at Stromboli, Italy: Numerical simulations*, Bollettino di Geofisica Teorica ed Applicata *46*, 2–3, 153–168.

TINTI, S., MANUCCI, A., PAGNONI, G., ARMIGLIATO, A., and ZANIBONI, F. (2005b), *The 30th December 2002 landslide-induced tsunami in Stromboli: Sequence of the events reconstructed from the eyewitness accounts*, Natural Hazards Earth Sys. Sci. *5*, 763–775.

TINTI, S., ARMIGLIATO, A., PAGNONI, G., and ZANIBONI, F. (2006a), *Scenarios of giant tsunamis of tectonic origin in the Mediterranean*, ISET J. Earthq. Technol. *42*, 4, 171–188.

TINTI, S., MARAMAI, A., ARMIGLIATO, A., GRAZIANI, L., MANUCCI, A., PAGNONI, G., and ZANIBONI, F. (2006b), *Observations of physical effects from tsunamis of December 30, 2002 at Stromboli volcano*, Italy. Bull. Volcanol. *68*, 450–461.

TINTI, S., PAGNONI, G., and ZANIBONI, F. (2006c), *The landslides and tsunamis of 30th December 2002 in Stromboli analysed through numerical simulations*, Bull. Volcanol. *68*, 462–479.

To access this journal online:
www.birkhauser.ch/pageoph

Pure and Applied Geophysics

Numerical Modelling of the Destructive Meteotsunami of 15 June, 2006 on the Coast of the Balearic Islands

Ivica Vilibić,[1] Sebastià Monserrat,[2,3] Alexander Rabinovich,[4,5] and Hrvoje Mihanović[6]

Abstract—A destructive tsunami-like event (locally known as "rissaga" waves) occurring on 15 June, 2006 in Ciutadella Harbour (Menorca, Balearic Islands) is reproduced by a numerical model forced by a travelling atmospheric disturbance. The disturbance is reconstructed from microbarograph measurements, being the only available instrumental data at the time of the event. The model is verified based on two weaker 1997 events, which were recorded by a number of bottom pressure recorders operating at that time on the Menorca shelf, in Ciutadella Inlet and adjacent Platja Gran Inlet. Both 1997 events are numerically simulated and good agreement is achieved with observations in time, frequency (including eigenfrequencies of the affected inlets) and wave heights. Subsequently the same model is applied to simulate the 2006 event. The vigorous currents with speeds up to 400 cm/s are found to occur specifically at those areas of the harbour where the most severe damage and sinking of boats had been reported. Maximum simulated sea-level heights of 2.5 m were about one half of those reported by eyewitnesses. This difference is apparently caused by quality and spatial resolution of bathymetry data. However, in general, the model is capable of reproducing the event fairly well and can probably be used for future assessment and mitigation activities on the coasts of the Balearic Islands.

Key words: Rissaga, numerical modelling, atmosphere-ocean coupling, Proudman resonance, harbour oscillations, meteotsunami, Balearic Islands, Ciutadella Harbour.

1. Introduction

On 15 June 2006 at 20:50 local time (18:50 UTC) Ciutadella Harbour, located on the west coast of Menorca Island (Balearic Islands, Western Mediterranean), was affected by a destructive flood event. A sudden first negative (ebb) wave of more than 4 metres,

[1] Institute of Oceanography and Fisheries, Šetalište I. Meštrovića 63, 21000 Split, Croatia.
[2] IMEDEA (UIB-CSIC), Institut Mediterrani d'Estudis Avançats, C/ Miquel Marquès 21, 07190 Esporles, Mallorca, Balearic Islands, Spain.
[3] Universitat de les Illes Balears, Departament de Física, Palma de Mallorca, Balearic Islands, E-07122, Spain.
[4] Department of Fisheries and Oceans, Institute of Ocean Sciences, 9860 West Saanich Road, Sidney, B.C. V8L 4B2, Canada.
[5] Russian Academy of Sciences, P.P. Shirshov Institute of Oceanology, 36 Nakhimovsky Prosp., Moscow 117997, Russia.
[6] Hydrographic Institute of the Republic of Croatia, Zrinsko Frankopanska 161, 21000 Split, Croatia.

reported by local witnesses, caused the catastrophic drying of a significant part of the harbour. As a result, most of the boats in the harbour broke free from their moorings on the harbour walls and were dragged by the current when the water re-entered the harbour only a few minutes later. More than 35 boats were sunk and about 100 were severely damaged (Fig. 1), with the total economic loss estimated to be in the order of several tens of millions of euros. This tsunami-like event was not produced by any reported earthquake in the Mediterranean but was presumably associated with an abrupt atmospheric pressure jump passing over the Balearic Islands (MONSERRAT *et al.*, 2006; JANSÀ *et al.*, 2007).

Significant short-period seiche oscillations regularly occur in many bays and harbours of the Catalan and Valencian coasts of the Iberian Peninsula, and on the coast of the Balearic Islands. The phenomenon is known as "*rissaga*" (a local Catalan word that means 'drying', similar to a Spanish word "*resaca*"). The rissaga waves in Ciutadella Harbour are particularly high and occur more frequently than in any other location (RAMIS and JANSÀ, 1983; TINTORÉ *et al.*, 1988; MONSERRAT *et al.*, 1991a, 1991b, 1998, 2006; GOMIS *et al.*, 1993; GARCIES *et al.*, 1996; RABINOVICH and MONSERRAT, 1996, 1998).

Ciutadella Inlet is a natural elongated inlet about 1 km long, 100 m wide and 5 m deep; the harbour is located at the head of the inlet (Fig. 2). The fundamental period of the inlet (Helmholtz mode) is approximately 10.5–10.6 min (RABINOVICH and MONSER-RAT, 1996; RABINOVICH *et al.*, 1999; VIDAL *et al.*, 2000; LIU *et al.*, 2003). Due to the specific geometry of Ciutadella Inlet, it has a large Q-factor, which results in significant resonant amplification of longwave oscillations arriving from the open sea. Seiche oscillations of duration ranging from a few hours to several days and wave heights exceeding 0.5 m recur in Ciutadella every summer. However, rissaga events producing wave heights exceeding 2 m, with destructive consequences for the harbour, usually take place once in 5–6 years and positively catastrophic rissagas with wave heights more than 3–4 m once in 15–20 years. In particular, during the rissaga of 21 June 1984, about 300 boats were destroyed or extensively damaged (JANSÀ, 1986; RABINOVICH and MONSERRAT, 1996). The rissaga of 15 June, 2006 was the most dramatic event since that time, when 4–5 m waves were reported in the harbour (MONSERRAT *et al.*, 2006).

Similar destructive tsunami-like longwaves, apparently unrelated to seismic activity, regularly occur at several other regions of the World Ocean (cf. MONSERRAT *et al.*, 2006; RABINOVICH, 2008). Extremely strong seiche oscillations, locally known as "*abiki*" waves, are repeatedly observed in Nagasaki Bay, Japan (cf. HIBIYA and KAJIURA, 1982). Comparable devastating oscillations on the coast of Sicily are called "*marrubbio*" ("*marrobbio*") (DEFANT, 1961; CANDELA *et al.*, 1999). Other places with frequent extreme seiches are, for example, Longkou Harbour, China (WANG *et al.*, 1987), the Port of Rotterdam, Netherlands (DE JONG *et al.*, 2003; DE JONG and BATTJES, 2004) and the Port of Trieste, Italy (DEFANT, 1961). These waves are analogous to ordinary tsunami waves and can affect coasts in the same damaging way, although they are related to atmospheric forcing and not to seismic activity or submarine landslides. DEFANT (1961), RABINOVICH

Figure 1
A sequence of photographs (from top to bottom) taken during the 15 June, 2006 rissaga event in Ciutadella Harbour (Menorca Island, Spain).
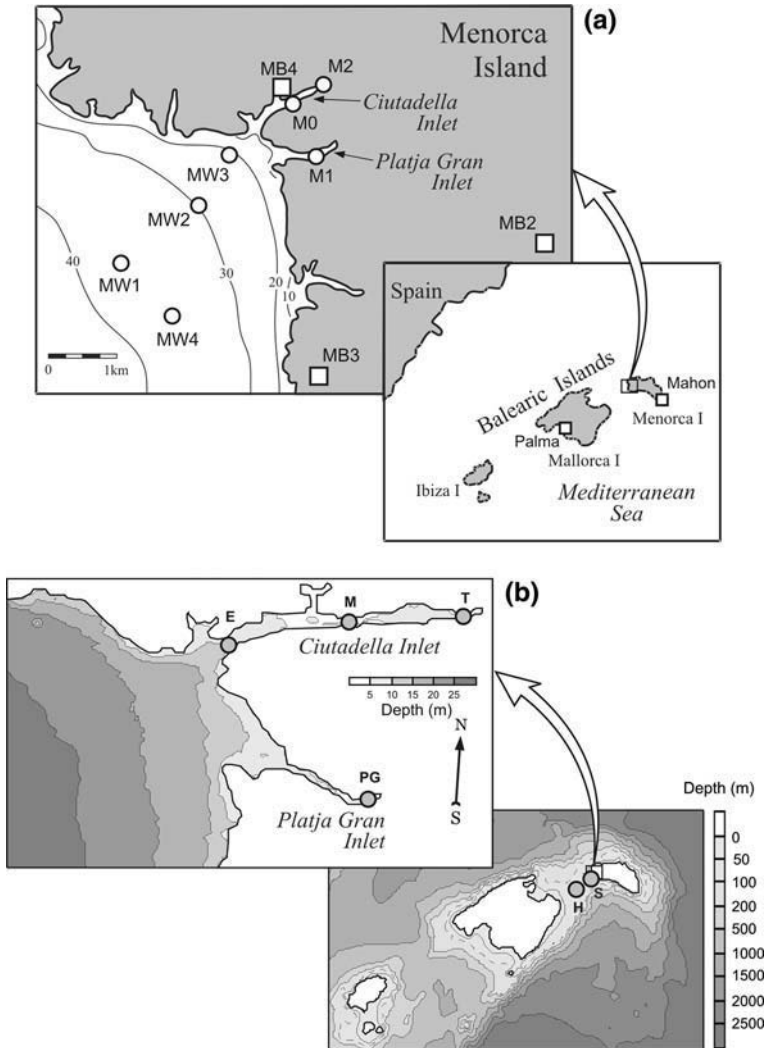
Figure 2
(a) A map of the Balearic Islands, with an inset showing Ciutadella and Platja Gran inlets and the LAST-97 instrument positions. (b) The "external" (Balearic Islands) and "internal" (Ciutadella Inlet) computational domains with the position of select grid points used in the analyses.

and MONSERRAT (1996) and MONSERRAT *et al*. (2006) suggested using the term *'meteorological tsunamis'* (*'meteotsunami'*) for this type of waves.

Atmospheric disturbances, producing meteotsunamis, may have different origins: dynamic instability, orographic influence, frontal passages, gales, squalls, storms, tornados, atmospheric convection cells, and atmospheric gravity waves (cf. MONSERRAT *et al*., 1991a, 1991b, 2006; RABINOVICH, 2008). Travelling air pressure disturbances have

been considered as the common generator of meteotsunamis; yet, DE JONG and BATTJES (2004) introduced travelling surface wind fluctuations as the source of the Rotterdam harbour meteotsunamis. However, even during the strongest events, the atmospheric pressure oscillations at the meteotsunami time scales (from a few minutes to a few hours) reach only 2–6 hPa, corresponding to only a 2–6 cm change in sea level. Consequently, these atmospheric fluctuations may produce significant sea-level response only when resonance occurs between the ocean and the atmosphere. During the resonance process, the atmospheric disturbance propagating above the ocean surface generates significant long ocean waves by continuously pumping additional energy into these waves (RABINOVICH, 1993, 2008). The most common type of resonance is the *Proudman resonance* (PROUDMAN, 1929), when $U = c$, i.e., the atmospheric disturbance speed (U) is equal to the longwave speed of ocean waves $c = \sqrt{gh}$, where g is the gravitational acceleration and h is the local depth. Energetic ocean waves arriving at the entrance of a semi-closed coastal basin (bay, inlet, or harbour) can induce hazardous oscillations in the basin due to harbour resonance if the arriving waves have frequencies matching the eigenfrequencies of the basin.

One of the regions where meteorological tsunamis regularly occur is the Eastern Adriatic Sea. During the catastrophic flood in June 1978 in Vela Luka Bay (Korčula Island, Croatia) the oscillations attained wave heights of about 6 m (HODŽIĆ, 1979/1980; ORLIĆ, 1980). A similarly destructive event also took place in June 2003 in Stari Grad Bay (Hvar Island) and Mali Ston Bay (Dalmatian Coast of Croatia). As was shown by ORLIĆ (1980) for the 1978 event and by VILIBIĆ et al. (2004) for the 2003 event, these events were produced by the combination of the open-sea Proudman resonance and local harbour resonances.

VILIBIĆ et al. (2004) constructed an efficient numerical model that could properly reproduce the extreme sea-level oscillations and currents in Stari Grad and Mali Ston Bays for the 2003 event. The observational data from a number of microbarographs were used to determine the direction of propagation, wave speed and the shape of the atmospheric disturbance responsible for this devastating event; subsequently this information was employed as an input for the constructed model. Further development and improvement of the model, done by VILIBIĆ et al. (2005) and VILIBIĆ (2008), enabled the authors to examine specific resonant effects and to bring to light the physical mechanism of such catastrophic events observed in this region.

The main purpose of the present study is to apply a similar model for the region of the Balearic Islands, and particularly for Ciutadella Harbour, to numerically simulate and to explain the catastrophic rissaga event of 15 June 2006. Unfortunately, there were no available observational sea-level data during this event; the only data that we had were the air pressure records from two microbarographs (JANSÀ et al., 2007). For this reason, to verify and to fit the model we used the data of the LAST–97 hydrophysical experiment (summer 1997) when numerous bottom pressure gauges were deployed on the shelf of Menorca Island, in Ciutadella Inlet and in adjacent Platja Gran Inlet (Figure 2a) and several significant but non-destructive rissaga were recorded (MONSERRAT et al., 1998; LIU

et al., 2003). Thereafter the verified model is used for the 15 June 2006 event employing the atmospheric pressure records as the input.

This paper is organized in the following way. Section 2 describes the numerical model, recalls the LAST-97 experiment and presents certain findings from this and other previous experiments. Section 3 demonstrates the capacity of the numerical model to reproduce the 1997 rissaga events. Section 4 comprises the modelling of the 2006 rissaga and reveals the destructive potential of the sea level and currents in Ciutadella Inlet associated with this event. A summary, discussion and conclusions are presented in Section 5.

2. *Material and Methods*

The Balearic Islands (Fig. 2) are situated on a large plateau separated from the mainland by a deep channel and bordered by a steep slope on the southeastern side. A broad shelf, 50 to 100 m deep, with a SW-NE orientation, is located between Mallorca and Menorca Islands. Apparently, this particular shelf promotes the generation of intense long ocean waves by travelling atmospheric disturbances. Zooming to the Ciutadella region, we can see a decrease in depth at the entrance of the outer bay; such a configuration is conducive to the enlargement of the arriving longwave (including tsunami waves) by the topographically – induced constraints. Finally, Ciutadella Inlet, in which the largest rissaga waves have been reported (see MONSERRAT *et al.*, 2006, and references therein), is a shallow, narrow and long bay with a large amplification factor ($Q \approx 10$) (RABINOVICH *et al.*, 1999).

2.1. *Numerical Model*

Ocean waves in the region of the Balearic Islands (Fig. 2b) forced by travelling atmospheric disturbances were numerically simulated by a 2-D nonlinear shallow-water model. The model is based on the momentum equations containing the air pressure forcing term and the continuity equation:

$$\frac{\partial u}{\partial t} + u\frac{\partial u}{\partial x} + v\frac{\partial u}{\partial y} - fv = -g\frac{\partial \zeta}{\partial x} - \frac{gu(u^2 + v^2)^{1/2}}{C^2(h + \zeta)} - \frac{1}{\rho}\frac{\partial P}{\partial x}; \tag{1}$$

$$\frac{\partial v}{\partial t} + u\frac{\partial v}{\partial x} + v\frac{\partial v}{\partial y} + fu = -g\frac{\partial \zeta}{\partial y} - \frac{gv(u^2 + v^2)^{1/2}}{C^2(h + \zeta)} - \frac{1}{\rho}\frac{\partial P}{\partial y}; \tag{2}$$

$$\frac{\partial \zeta}{\partial t} + \frac{\partial}{\partial x}[(h + \zeta)u] + \frac{\partial}{\partial y}[(h + \zeta)v] = 0, \tag{3}$$

where t is time, u and v are the vertically averaged velocity components in the x and y directions, g is the acceleration of gravity, ζ is the sea-level elevation, h is the undisturbed water depth, f is the Coriolis parameter, ρ is the water density, P is the air pressure, and C is the Chezy's friction coefficient (cf. CUNHA and ROSMAN, 2005):

$$C = 18 \log(0.37h/z_0), \tag{4}$$

where z_0 is the roughness scale. An explicit leapfrog scheme (cf. IMAMURA, 1996) is used to solve equations (1)–(3).

The large-scale (coarse) model domain (Fig. 2b) encompasses the entire area of the Balearic Islands; the corresponding grid was taken from the GEBCO bathymetry database (available from http://www.ngdc.noaa.gov/mgg/gebco). This grid has 1' resolution, i.e., 1.45 km×1.85 km (for longitude and latitude), the size of the computational domain was 241×121 grid cells. According to a numerical stability criterion, the time step was taken to be $\Delta t = 4$ s and the bottom roughness scale z_0 was set to 0.001 m; a radiation condition was used at all open boundaries. A nested grid with 10 m horizontal spatial resolution was used for Ciutadella Inlet and neighbouring Platja Gran Inlet (Fig. 2b); the incoming waves at the lateral boundaries were taken as the output of the coarse model.

The model was forced by a moving air-pressure disturbance that was introduced into the model in the following way: (1) speed and direction of the moving air-pressure disturbance were set to be constant over the whole domain with the values estimated by the Pressure Gradient Method (PGM in the following, see details in Appendix), (2) the time interval elapsed from the passage of the air-pressure front above each grid point was calculated, and (3) the air-pressure data were interpolated linearly in time at each grid point by using the observed values (from MB4 station, see Fig. 2a) shifted in time according to the determined time interval. The model was tested and verified based on the 1997 rissaga events (recorded during the LAST-97 experiment) and then, with the same parameters, it was applied to the 15 June 2006 event.

2.2. LAST-97 Experiment and Observed Properties of Rissaga Waves

In summer 1997, as part of the LAST-97 experiment, seven high-quality bottom pressure recorders (BPR) were deployed in the region of Ciutadella: Four instruments (MW1, MW2, MW3, and MW4) on the shelf of Menorca Island at depths of 20 to 35 m, two (M0 and M2) directly in Ciutadella Inlet (in the middle and at the head of the inlet), and one (M1) in Platja Gran Inlet (Fig. 2a) (MONSERRAT *et al.*, 1998). Also, a triangular array of three precise microbarographs (MB2, MB3 and MB4) was deployed on the coast of Menorca (Fig. 2a). The BPRs and microbarographs had sampling intervals of 1 min and 30 s, respectively. The main purpose of the LAST-97 experiment was the examination of the physical mechanism responsible for the rissaga generation.

The experimental period was rich in events; there were no destructive meteotsunamis during this period, however several rissaga events were recorded by numerous of instruments. Three of the most energetic events were: (1) 7–11 June 1997 (with maximum trough-to-crest height of about 115 cm); (2) 1–4 July 1997 (125 cm); and (3) 23–25 July 1997 (125 cm). These three events were thoroughly examined by MONSERRAT *et al.* (1998), VIDAL *et al.* (2000), and LIU *et al.* (2003). Without detailing the corresponding findings, we would like to call attention to certain important features of the observed rissaga waves:

(1) All events were associated with significant atmospheric disturbances (pressure jumps or trains of atmospheric gravity waves).

(2) These atmospheric disturbances propagated approximately in the same direction - from SW to NE (i.e., along the southeastern coast of Mallorca Island: see Fig. 2a) and with similar speeds of 25 to 28 m/s (which are close to the longwave speed for the southeastern shelf of Mallorca: $c = \sqrt{gh} \approx 27\text{m/s}$).

(3) The estimated transfer functions $T(\omega)$, where ω is the angular frequency, between atmospheric pressure and generated open-sea longwaves were similar for all three cases, thus the transfer function obtained for one event (Rissaga 2) could be successfully used to predict detailed spectral properties of other events (Rissagas 1 and 3).

(4) The observed periods of rissaga waves in Ciutadella and Platja Gran inlets were 10.5 and 5.5 min, respectively, i.e., they were precisely related to the periods of the fundamental (Helmholtz) modes in these inlets.

These findings are in good agreement with previous results conveying that rissaga waves in Ciutadella Inlet are the fundamental eigen oscillations of this specific inlet externally forced by atmospheric disturbances, and that the main characteristics of these disturbances (direction and phase speed) during various observed rissaga events are very much alike (MONSERRAT *et al.*, 1991a, 1991b; MONSERRAT and THORPE, 1992; GARCIES, 1996; RABINOVICH and MONSERRAT, 1996).

The source of the large-pressure atmospheric disturbances (gravity waves) is related to a particular synoptic condition, when a warm air mass from the Sahara flows into the Balearic Islands, at near-surface levels, just below a strong middle-level SW jet (MONSERRAT *et al.*, 1991b). These synoptic situations are normally observed during the summer; that is why all known rissaga events have occurred between June and September (MONSERRAT *et al.*, 1991a; RABINOVICH and MONSERRAT, 1996). The most favourable conditions for strong rissagas are those when atmospheric waves propagate northeastwards over the Balearic shelf with velocities of 22 to 30 m/s. In that case, long ocean waves are resonantly generated on the Mallorca shelf (due to the Proudman resonance); propagating over the shelf they arrive at the southwestern Menorca coast and strike the bays and inlets located there, of which the most exposed is Ciutadella Inlet. According to MONSERRAT and THORPE (1992) and RABINOVICH *et al.* (1999), the largest amplification in the inlet is associated with the waves approaching from 225°.

3. Verification of the Model

For verification of the numerical model we used data from the LAST-97 experiment. Because of some technical problems and the different times of the instrument deployments, various rissaga events were recorded by different numbers of instruments.

We selected and numerically simulated two specific events: (1) 7–9 June (R1 event), and (2) 22–25 July (R3 event), which were measured by a number of instruments: The propagating atmospheric disturbances which caused these rissaga events were recorded by all three microbarographs (MB1, MB2, and MB3); while the sea-level oscillations were recorded by both gauges in Ciutadella Inlet (M0 and M2) and by several gauges on the shelf. Unfortunately, the BPR in Platja Gran Inlet (M1) was deployed in the middle of July 1997, so it only worked during the second event.

Maximum observed trough-to-crest wave heights at four sites are shown in Table 1. As could be expected, the strongest oscillations were recorded inside the inlets, at the M2 site at the head of Ciutadella Inlet (140.5 cm for R1 and 155.4 cm for R3 events) and at the M1 site in Platja Gran Inlet (156.0 cm for R3). These rissaga waves were likely associated with intense short-period atmospheric disturbances traveling over the region of the Balearic Islands on 8 June and 23 July 1997. Figure 3 shows the microbarograph records for both events. According to the records, the corresponding pressure jumps were of about 3.5 and 4.5 hPa, respectively (Fig. 3). The records from the three microbarographs look similar, although there are clear time shifts that enable us to estimate the speed (U) and direction (φ) of the respective air-pressure disturbances. The PGM (see Appendix for details) estimates for the periods of the most intense oscillations were: $U =$ 23 m/s, $\varphi = 259°$ for R1 and $U = 25$ m/s, $\varphi = 235°$ for R3.

According to these results, the major atmospheric disturbance, responsible for the generation of the R1 event of 8 June 1997, arrived from WSW. The rissaga began abruptly (as typical tsunami waves) at about 02:50 UTC; strong oscillations (with wave heights more than 40 cm at site M0) lasted for about 8 hours (Fig. 4). In comparison with the shelf (site MW4), the arriving waves were amplified 2.4 times in the middle of Ciutadella Inlet (M0) and more than 3 times at the head of the inlet (M2).

The R3 event was more energetic and long lasting than the R1 event. The strongest seiche oscillations in Ciutadella and Platja Gran inlets were associated with a 4.5 hPa pressure jump that occurred at about 16:20 UTC on 23 July 1997 (Fig. 3b). As was indicated by HIBIYA and KAJIURA (1982) and RABINOVICH and MONSERRAT (1998), large temporal and spatial atmospheric pressure gradients are the key factor conducive to the generation of strong meteotsunamis. The calculated parameters of the atmospheric

Table 1

Observed and numerically modelled maximum trough-to-crest wave heights (in cm) during rissaga events of 8 June and 23 July, 1997

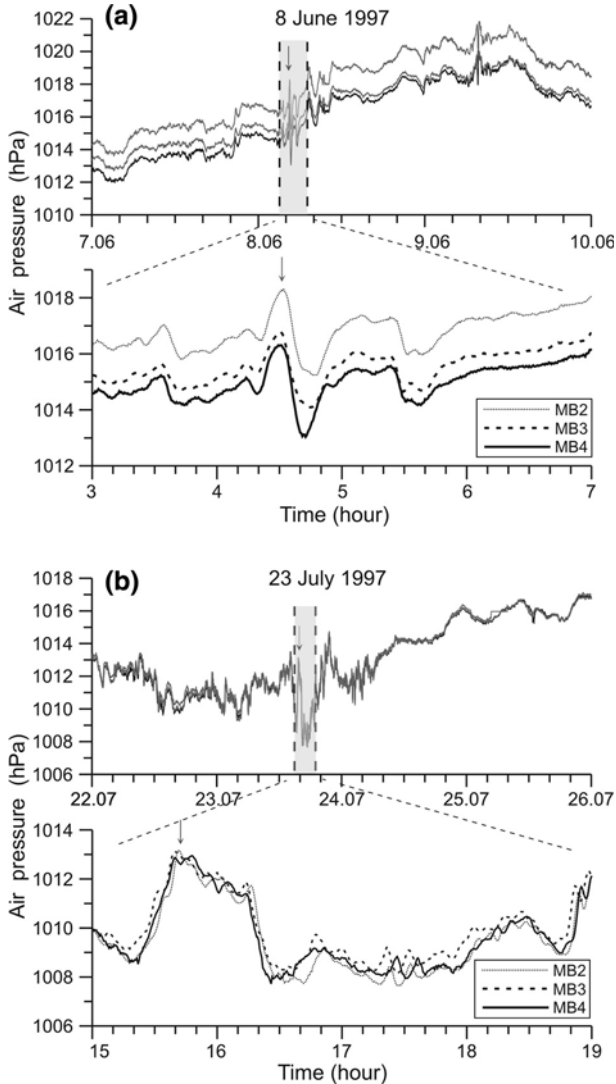| Station, location	8 June 1997 (R1)		23 July 1997 (R3)	
	Observed	Modelled	Observed	Modelled
MW4 (shelf)	44.5	45.9	51.8	51.8
M1 (Platja Gran)	-	60.6	156.0	102.9
M0 (Ciutadella-center)	105.5	99.2	123.4	144.6
M2 (Ciutadella-head)	140.5	128.7	155.4	194.9

Figure 3

Atmospheric pressure records from MB2, MB3 and MB4 microbarographs during (a) R1 rissaga event of 7–9 June 1997 and (b) R3 rissaga event of 22–25 July, 1997. Bottom panels show zoomed 4-hour segments of the respective records. The arrows indicate the main pressure jumps.

disturbance for the R3 event ($U = 25$ m/s, $\varphi = 235°$) are more favourable for the generation of significant rissaga than those of the R1 event because the direction was closer to $225°$, which was previously found to be the direction of maximum amplification (RABINOVICH *et al.*, 1999). The ratios between the inlet and the shelf maximum wave heights (M0/MW4, M2/MW4) were 2.4 and 3.0, respectively, i.e., the inlet amplifications
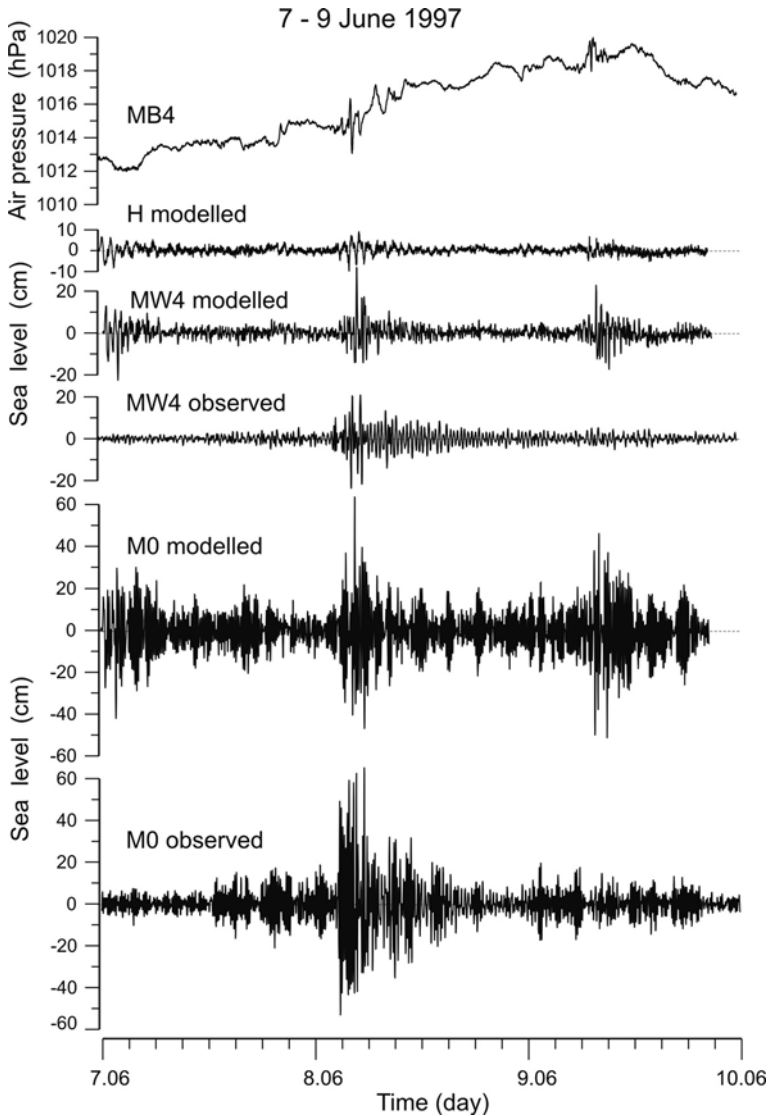
Figure 4
Simulated and observed sea-level records at particular sites during the R1 rissaga event of 7–9 June, 1997 and simultaneous MB4 atmospheric pressure record. The observed records at MW4 and M0 sites are high-pass filtered with a cut-off period of 150 min.

were approximately the same as for the R1 event. This result is quite important: it indicates that the extreme rissaga events in Ciutadella Inlet are more related to stronger waves arriving at the shelf of Menorca Island than to some anomalous amplification of the waves inside the inlet during the events.

The estimated parameters of the atmospheric disturbances were used for numerical modelling of the R1 and R3 meteotsunami events. The spatial fields of sea levels and currents were computed for the shelf of the Balearic Islands, and Ciutadella and Platja Gran inlets. Time variations of sea-level elevations and currents were simulated for particular grid points: T, M, PG, S (roughly corresponding to stations M2, M0, M1 and MW4, respectively), E (located at the entrance of Ciutadella Inlet) and H (on the shelf between Mallorca and Menorca Islands) (Fig. 2b). The speed and direction of atmospheric waves were presumed to be constant during the entire computational period (three days – 7–9 June 1997 – for R1 and four days – 22–25 July 1997 – for R3). The comparative (observed and simulated) results are presented in Table 1 and shown in Figures 4 and 5.

In general, the model reproduces well the oscillations on the shelf for both the R1 and R3 events. Maximum computed wave heights for site MW4 almost coincide with the observed values (Table 1). For oscillations inside Ciutadella Inlet (M0 and M2) the model slightly underestimates (by 6–8%) the observed heights for the R1 event and overestimates (by 17–25%) the heights for the R3 event. These differences are apparently related to frequency properties of the computed input signal and respective spectrum of the arriving waves (i.e., to the energy at near-resonant frequencies for Ciutadella Inlet). The most probable reason for the differences between computed and observed records for Platja Gran (R3 event) is the insufficient resolution of the bathymetry for this small inlet.

An interesting result of the numerical modelling is the "false" computed oscillations on 9 June 1997, i.e., the oscillations that were obtained based on the numerical simulations but were absent in the observations (Fig. 4). This numerical result was driven by the air pressure disturbance of 9 June recorded by MB4 and other microbarographs (Fig. 3). The fact that the 9 June disturbance did not produced noticeable oscillations in Ciutadella Inlet and in other bays and inlets of the Balearic Islands indicates that the entire system is very selective (cf. RABINOVICH and MONSERRAT, 1998; MONSERRAT *et al.*, 2006). The resonant generation conditions that induced the rissaga of 8 June 1997 (which for the present model were supposed to be uniform during the whole event) did not apparently work on 9 June. This interesting issue is beyond of the scope of the present study but will be carefully examined.

To determine the spectral properties of the rissaga waves and to compare these properties for observed and numerically simulated records, we applied a spectral analysis procedure similar to that described by EMERY and THOMSON (2003) (see also RABINOVICH *et al.*, 1999; LIU *et al.*, 2003). To improve the spectral estimates, we used a Kaiser-Bessel (KB) window with half-window overlaps prior to the fast Fourier transform. The length of the KB-window was chosen to be 256 min, yielding 62 and 84 degrees of freedom per spectral estimate for the R1 (3-day segment) and R3 (4-day segment) events, respectively. The results of this analysis at the four sites (M0, M1, M2, and MW4) are presented in Figures 6 and 7.

The most important results of this analysis are: (1) That the numerical model properly reproduces the main spectral properties of the examined region (which are known from
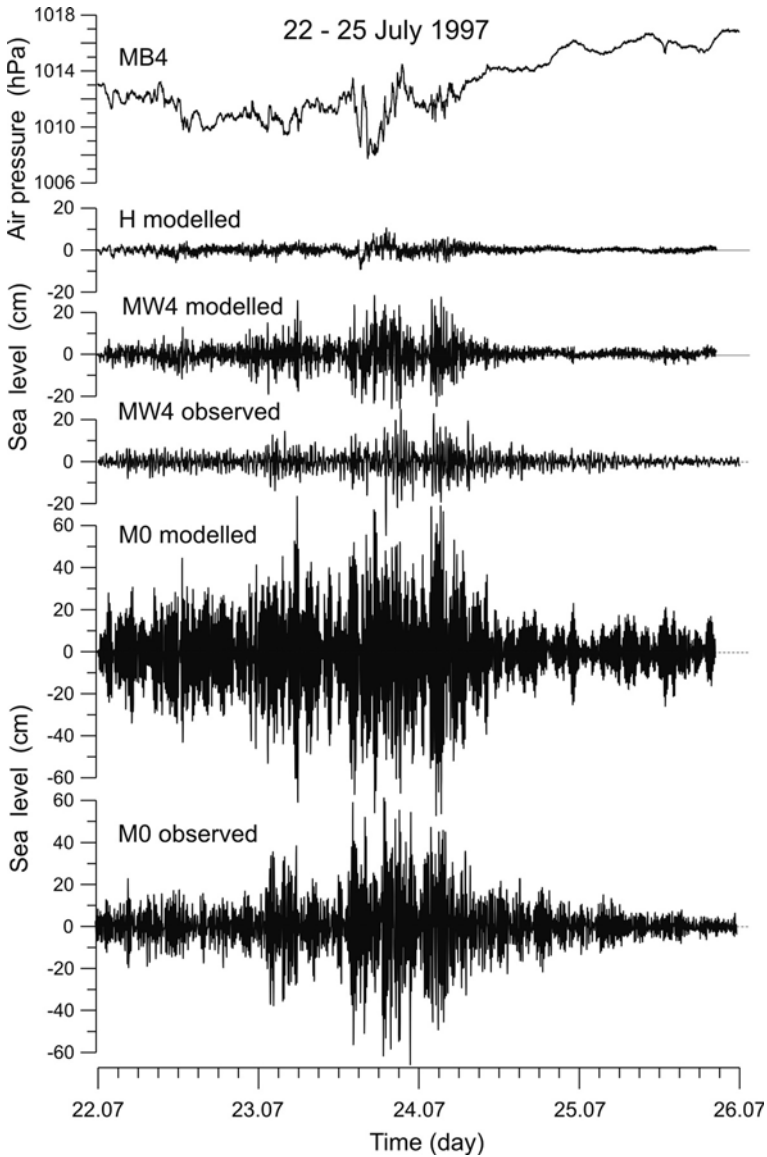
Figure 5
The same as in Figure 4 but for the R3 rissaga event of 22–25 July, 1997.

previous studies, cf. GARCIES *et al.*, 1996; MONSERRAT *et al.*, 1998; RABINOVICH *et al.*, 1999; LIU *et al.*, 2003; MARCOS *et al.*, 2004) and (2) that for both the R1 and R3 events there is a good agreement between the results of numerical modelling and observations. In particular, the computed period of 11.1 min for the fundamental (Helmholtz) mode in Ciutadella Inlet is very close to the observed period of this mode (10.5–10.6 min) at sites
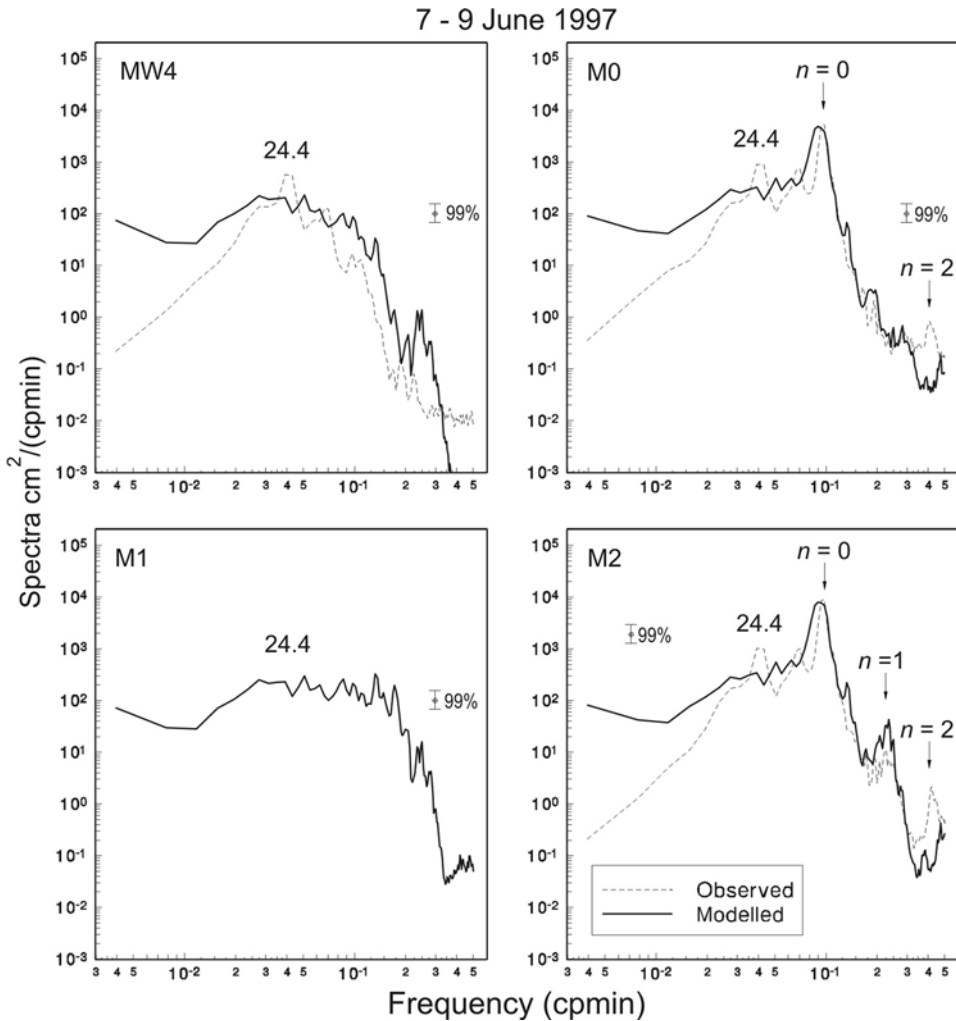
Figure 6
Computed spectra of observed (high-pass filtered) and modelled sea-level records during the R1 rissaga event of 7–9 June, 1997 for four sites: MW4 (Menorca shelf), M0 (middle of Ciutadella Inlet), M1 (Platja Gran Inlet) and M2 (head of Ciutadella Inlet). Periods (in min) of the main spectral peaks and eigen inlet frequencies are indicated.

M0 and M2. The first inlet mode with a period of 4.4 min has a nodal line which is located close to the position of the M0 site; thus neither computed nor observed spectra at this site have the respective spectral peak, however such a peak is clearly seen in the spectra at the M2 site (Figs. 6 and 7). The fundamental period of Platja Gran Inlet of approximately 5.5 min and the shelf period of 24.4 min are also reproduced in the computed spectra, although less clearly, apparently because of the insufficient resolution of the bathymetry for Platja Gran Inlet and the shelf/slope of the Balearic Islands.
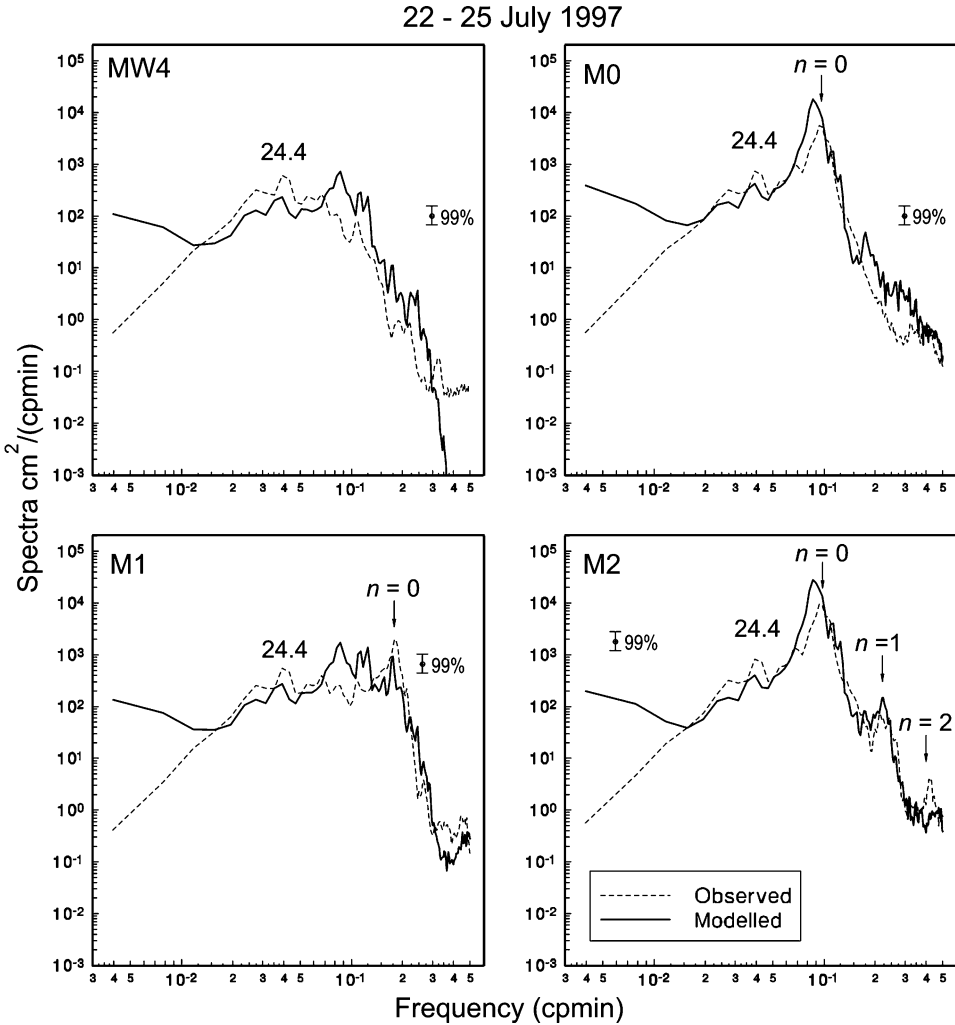
Figure 7
The same as in Figure 4 but for the R3 rissaga event of 22–25 July, 1997.

Not only is there similarity of the fine frequency structure of the computed and observed spectra, but also the general shape of the spectra and the energy level (the energy decay of the observed spectra at the low frequencies is due to the 3-hour high-pass filtering). We would like to emphasize that the atmospheric pressure was the only forcing factor that we used in our model. Thus, such good agreement (Figs. 6 and 7) indicates that other external factors influencing sea level and producing seiches (in particular, wind, internal waves or infragravity waves, generated by nonlinear interaction of wind waves, cf. RABINOVICH, 2008) are of secondary importance for this region and play an inconspicious role in formation of the rissaga phenomenon.

There is one small but important difference in the computed and observed spectra on the shelf (at site MW4) for the R3 event. Specifically, in the frequency band 0.07–0.15 cpm (i.e., at periods of 14 to 7 min) the computed spectrum noticeably exceeds the observed spectrum (Fig. 7). The fundamental period of Ciutadella Inlet is particularly sensitive to this frequency band. Thus, the extra simulated energy at the near-resonance frequencies on the shelf caused a stronger response of the inlet to the arriving waves (see in Figure 7 computed and observed spectra at M0 and M2 for the R3 event), resulting in the difference between the simulated and observed oscillations in Ciutadella Inlet (Fig. 5). In contrast, for the R1 event the computed and observed spectra on the shelf (MW4) for the near-resonant frequency band were similar (Fig. 6); consequently, the computed and observed seiches in the inlet were also similar (Fig. 4). A worthy open question for future study is to ascertain the reason of this near-resonant energy excess (in comparison with observations) in the oscillations on the shelf of Menorca Island.

In general, we can conclude that the model is capable of reproducing both the generation of the meteotsunami waves and their amplification within Ciutadella Inlet, and is applicable to a meteotsunami event, such as the catastrophic event that occurred on 15 June 2006.

4. Numerical Simulation of the 2006 Event

As indicated in the early analyses by MONSERRAT *et al.* (2006) and JANSÀ *et al.* (2007), the rissaga of 15 June 2006 was an extraordinary event, sinking and damaging several tens of boats and resulting in a cost of more than 30 million Euro. According to eyewitness reports, the peak sea-level range was 4–5 m, driving exceptionally strong currents which sank many boats. The atmospheric pressure dramatically increased in Palma de Mallorca for $\Delta P_a \approx 7$ hPa in only half an hour, and more impressively, the last 5 hPa occurred in less than $\Delta t = 10$ min (Fig. 8). This impressive pressure jump was associated with a squall line and was accompanied by strong (20–25 m/s) wind gusts. The pressure jump travelled in direction from SW to NE, first being recorded at Palma de Mallorca and then about 77 min later at Mahon (Menorca Island). By using the data collected at these two high-resolution stations (Palma and Mahon; locations of the stations are shown in Fig. 2a) and from the analysis of all available data (JANSÀ *et al.*, 2007), the speed of the disturbance has been estimated to be about 25 m/s, while the incoming direction was roughly 225°, being the most favourable direction for generation of strong seiches in the inlets of the western Menorca coast (RABINOVICH *et al.*, 1999).

For this reason, we chose the speed of $U = 25$ m/s and the incoming direction of $\varphi = 225°$ and extrapolated the 15 June atmospheric pressure time series recorded at Mahon over the entire model domain. The results were somewhat different from those for the R1 and R3 events, as the temporal and spatial air pressure gradients were much stronger and encompassed only a single stepwise disturbance (shown in the upper panel in Fig. 8). The ocean responded violently, generating strong eigenoscillations inside both
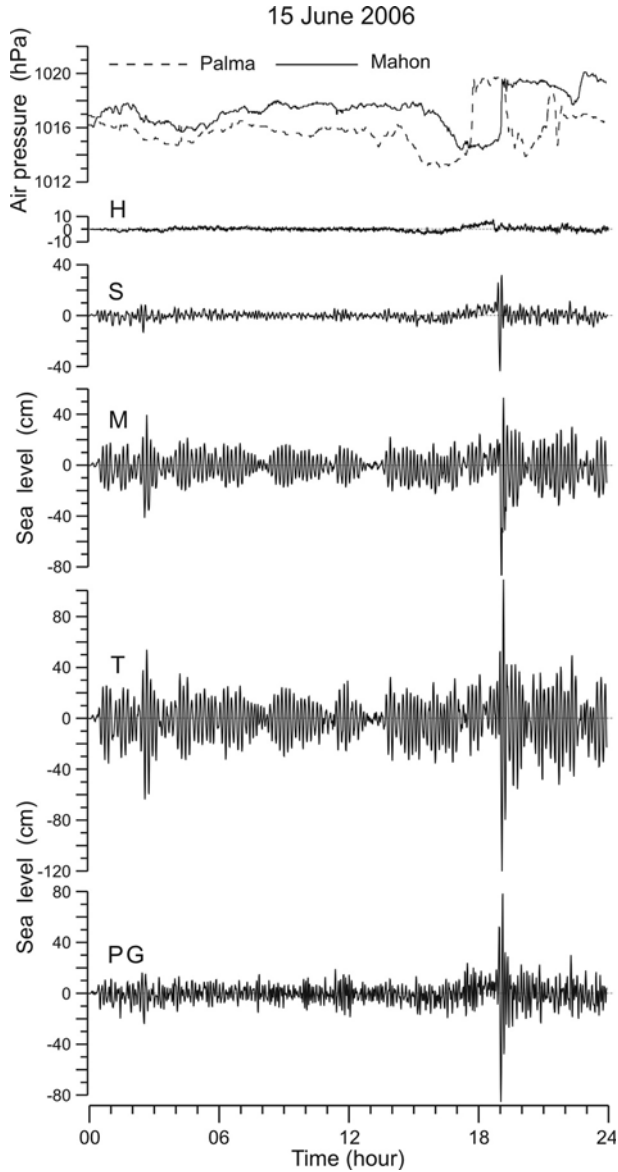
Figure 8
Observed microbarograph atmospheric pressure records at Palma (Mallorca Island) and Mahon (Menorca Island) and simulated sea-level records at sites H, S, M, T and PG during the rissaga event of 15 June, 2006.

Ciutadella and Platja Gran inlets (Fig. 8). The oscillations at the middle of the shelf between Mallorca and Menorca Islands (see H grid point) were not pronounced, with the amplitude of only a few centimetres (Figs. 8, 9a); however, the wave height of the resonantly-generated ocean waves grew rapidly with the waves approaching the Menorca

coastline. The wave height reached 80 cm at grid point S just before striking Ciutadella Inlet, being approximately double that of the oscillations recorded during the R1 and R3 events (Figs. 4 and 5). Such rapid amplification of ocean waves propagating along the Balearic shelf is apparently attributed to the extremely strong air pressure gradients, which resulted in efficient manifestation of the Proudman resonance over the limited generation area (VILIBIĆ, 2008). HIBIYA and KAJIURA (1982) derived a simple expression for the resonantly amplified (due to the Proudman resonance) open-ocean waves propagated across the East China Sea to explain the catastrophic meteotsunami ("abiki" waves) in Nagasaki Bay (Japan) of 31 March 1979:

$$\Delta\zeta = \frac{\Delta\bar{\zeta}}{L_1}\frac{x_f}{2}, \tag{5}$$

where $x_f = Ut$ is the distance travelled by the pressure jump during time t, L_1 is the length of the leading pressure increase, $\Delta\bar{\zeta} = -\Delta P_a/\rho g$ is the static inverted barometer sea-level variation and ρ is the water density. Assuming that $\Delta P_a = 5$ hPa, $\Delta\bar{\zeta} \approx -5$cm, $L_1 = U\Delta t = 25$ m/s×600 s = 15 km and $x_f \approx 90$ km (corresponding to $t \approx 1$ hour, which is the approximate time for the pressure jump to travel from Palma to the vicinity of Ciutadella Inlet), we obtain $\Delta\zeta \approx 15$ cm.

According to (5), the resonant amplification of open-ocean waves is inversely proportional to L_1, whereby the faster the change in atmospheric pressure (i.e., the more abrupt the pressure jump), the stronger is the amplification of the generated waves (HIBIYA and KAJIURA, 1982; MONSERRAT *et al.*, 2006). The fine structure of the pressure gradient at Mahon (fortunately we had the pressure measurements every 30 s) indicates even larger pressure gradients: $\Delta P_a/\Delta t \approx 1$ hPa/1 min that produces $\Delta\zeta \approx 30$ cm off the Menorca coast, in good agreement with our modelling results. Additional topographical amplification occurs on the shallower inner shelf (3–5 km wide) off the entrance of Ciutadella Inlet. The modelled amplitude at S grid point is $\Delta\zeta \approx 80$ cm (Figs. 8, 9a, b). A similar effect was found by HIBIYA and KAJIURA (1982) for the vicinity of Nagasaki Bay: Between the outer shelf and the mouth of Nagasaki Bay the arriving waves were amplified by a factor of 2.4 due to the combined effects of topographic funnelling, partial reflection and shoaling.

Due to the harbour resonance, the incoming waves are then amplified within the inlet, reaching the trough-to-crest wave height of about 230 cm at grid point T (Figs. 8 and 9b). Further on, the inlet becomes shallower than the wave amplitude; consequently the ebb flow produces a complete drying of the inner part of Ciutadella Harbour. Nonlinearity effects become more important in the inlet, as an asymmetry of the major rissaga wave may be seen when zooming at the series at grid points M and T (Fig. 8; that was not the case in R1 and R3 rissagas). Figure 10 gives the scenario and quantitative analysis of the modelling results for Ciutadella Inlet. Simultaneously, strong rissaga oscillations occurred also in Platja Gran Inlet, with a maximum wave height of about 170 cm at the head of the inlet.

The main damage and destruction during this meteotsunami event were related not to the abrupt sea-level changes, but to the vigorous currents (clearly seen in Fig. 1). Modelled currents at the entrance (E), in the middle (M) and at the head (T) of Ciutadella Inlet are shown in Figure 11; the spatial distribution of maximum currents in Ciutadella and Platja Gran inlets are presented in Figure 9c. The strongest currents were observed in the middle of Ciutadella Inlet close to grid point M (see photos in Fig. 1), while near the entrance (E) and at the head (T) the currents were substantially weaker (Fig. 9c). The ebb current of 250 cm/s (according to our computations) at about 19:05 broke the boats from their moorings and dragged them along the inlet, however the real damage and sinking of boats were caused by the flood current which occurred a few minutes later. Maximum computed flood currents were more than 400 cm/s in the narrow "neck" in the central part of Ciutadella Inlet (Figs. 9c and 11). For comparison, destructive currents in Mali Ston Bay (Eastern Adriatic), which caused substantial damage to shellfish farms and displaced bottom protective moorings weighting a thousand kilograms during the Adriatic meteotsunami of 27 June 2003, only reached 150 cm/s (VILIBIĆ et al., 2004), i.e., approximately three times smaller.

5. Discussion and Conclusions

Previous empirical studies of rissaga waves in Ciutadella Inlet clearly indicated that this phenomenon has a resonant nature and is associated with very specific directions and speeds of atmospheric disturbances propagating over the Balearic Islands (cf. MONSERRAT et al., 1991a, 1991b, 1998; GOMIS et al., 1993; GARCIES et al. 1996; RABINOVICH and MONSERRAT, 1998). To better examine the physical mechanism of this effect and to investigate the sensitivity of the model to the atmospheric parameters, we conducted several numerical experiments and estimated maximum sea-level heights as a function of speed and direction of atmospheric disturbances. For this purpose we used the same 2006 Mahon air pressure series used in the calculations for Figures 8, 9 and 11 but with disturbance speeds of 20 to 35 m/s and incoming directions of 210° to 260°. The results of these computations for sites S, T and PG are shown in Figure 12. The largest response for the shelf (S grid point) was found to be around 28 m/s and 240°; atmospheric waves with this specific speed and direction create strong oscillations in the vicinity of Ciutadella Inlet. The strongest seiches in Ciutadella Inlet (T grid point) are generated by atmospheric waves of 27 m/s and 230° and in Platja Gran Inlet (PG grid point) by waves of 25 cm/s and 228°. An interesting issue which is seen in the plots in Figure 12 is that the favourable speed for the Proudman resonance increases with an increase of wave direction (and *vice versa)*. This effect is caused by greater depths (and respective ocean longwave speeds) at the northern parts (80–120 m) of the Balearic shelf than on the southern parts (60–80 m).

The results of these computations are in good agreement with those by MARCOS et al. (2003) who tested for the constant wave direction of 225° the Ciutadella Inlet response to the atmospheric waves travelling with speeds of 15, 20,..., 50 m/s and found that the

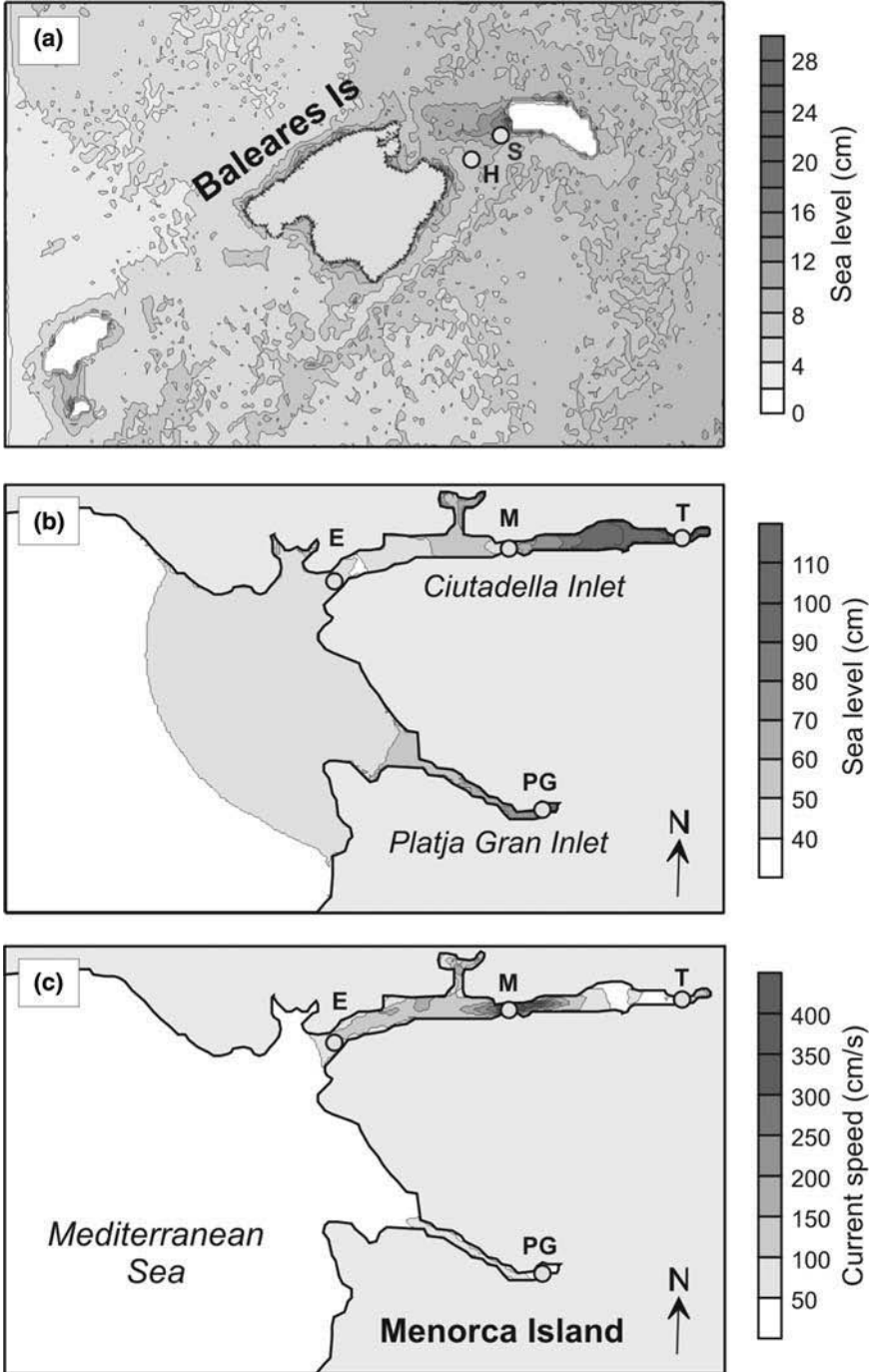◄   Figure 9
Simulated sea levels and currents for the rissaga of 15 June, 2006. (a) Maximum sea levels modelled for the
external domain (shelf of the Balearic Islands); (b) maximum sea levels and (c) maximum currents modelled for
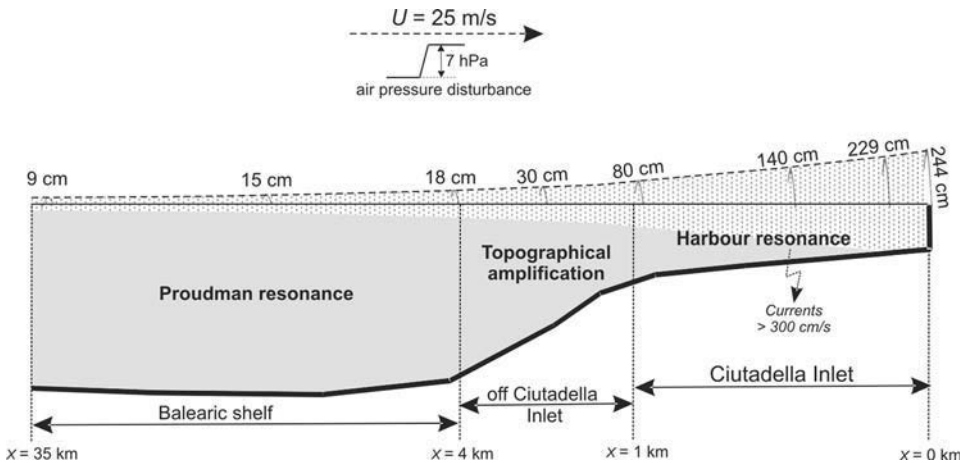the internal domain (Ciutadella and Platja Gran Inlets).

Figure 10
A sketch illustrating the physical mechanisms responsible for the formation of the destructive rissaga on 15
June, 2006 in Ciutadella Harbour (Menorca Island).

largest seiches in the inlet are produced by disturbances with the speed of 25 m/s, close to
our estimate of 27 m/s. Because during the 2006 event there were only two working
microbarographs, the model parameters $U = 25$ m/s and $\varphi = 225°$, which were selected
based on the data from these microbarographs and general synoptic estimates (cf. JANSÀ
et al., 2007) and used for the simulation of the 2006 rissaga (Figs. 8–11), should be
considered as very approximate. If we use $U = 27$ m/s and $\varphi = 230°$, the computed wave
heights will be roughly 7% larger and 260 cm at the head of Ciutadella Inlet.

In any case, the calculated maximum wave heights in the harbour were approximately
one half of those reported by eyewitnesses. The most probable reason of this
disagreement is the insufficient accuracy and spatial resolution of the bathymetry, both
in the outer region (off the Balearic Islands) and inner region of Ciutadella and Platja
Gran inlets. A better model bathymetry has to be used in future, possibly also through a
double- or multiple-nesting procedure; the smoothing of the inner bathymetry is also
important to minimize the bias arising from both the nesting procedure and from the
improper inclusion of topographical features into the model.

Despite the disagreement between the 2006 observed and simulated wave heights,
multitude useful results were obtained through the numerical modelling of the 1997 and
2006 events. Numerical models clearly indicated that extreme rissaga events are related
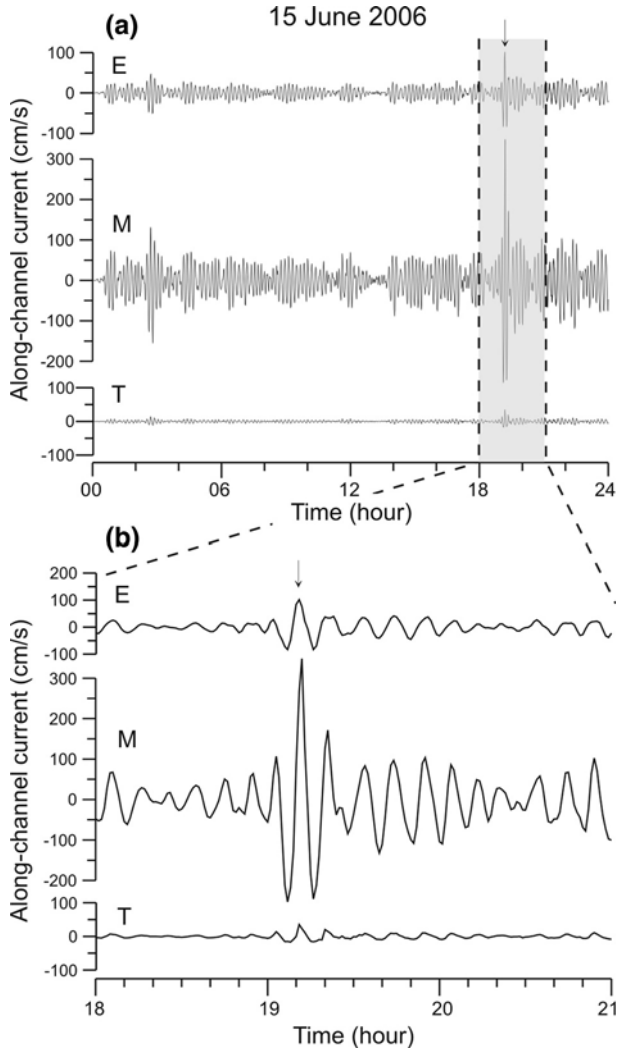only to particular atmospheric wave speeds and directions, with the strongest oscillations

Figure 11

(a) Simulated along-channel currents at sites E, M and T in Ciutadella Inlet for the rissaga of 15 June, 2006; (b) zoomed 3-hour segment of the records shown in (a). The arrows indicate the maximum flood current.

in Ciutadella Inlet associated with $U = 27$ m/s and $\varphi = 230°$. The models also properly reproduced the timing of the events, including times of the observed maximum wave heights and currents. Based on the model results, we could demonstrate that the destruction of boats in the middle of Ciutadella Inlet and huge economic losses were related to very strong (> 4 m/s) currents affecting this part of the inlet. Last but not least, through the modelling of the phenomenon at its source region (i.e. at the southeastern shelf of the Balearic Islands), we achieved a coherent picture of the formation, propagation and amplification of destructive rissagas for the western Menorca coast.
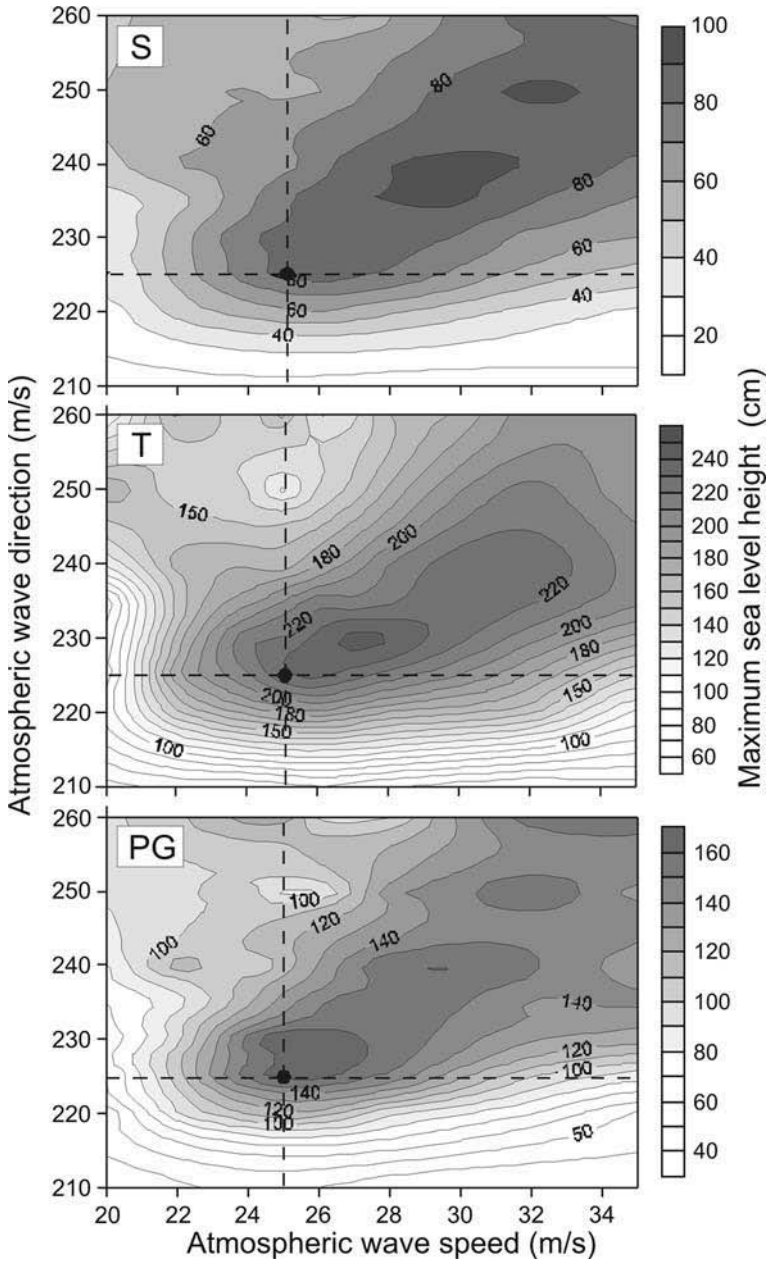
Figure 12
Maximum sea-level height at sites S, T and PG modelled for various atmospheric disturbance speeds (20–35 m/s)
and directions (210–260°). The dashed lines indicate speed and direction of 25 m/s and 225°, respectively, which
were used for numerical modelling of the rissaga event of 15 June, 2006.

As was pointed out by JANSÀ *et al.* (2007), the Meteorological Centre of the Instituto Nacional de Meteorologia (Palma de Mallorca, Baleares, Spain) has been forecasting potential rissaga events since 1984. Typically, "rissaga warnings" are issued when the specific synoptic condition is expected: (1) Low level Mediterranean air with weak surface depression; (2) warmer African air blowing around 850 hPa isobaric; (3) an inversion layer separating (1) and (2); (4) an instable layer between the African air and colder upper air. The June 2006 "rissaga warning" was issued the day before the event. However, one day anticipation of a potential rissaga event strongly diminishes the effectiveness of the forecast, especially if no updates are provided. The results of the present study indicate that this approach, based on pre-modelling studies and numerical simulation prototype rissaga events, can be efficiently used in a future Balearic meteotsunami warning system, in particular, to become an element of the Northeastern Atlantic, the Mediterranean and Connected Seas Tsunami Warning System (NEAMTWS). The atmospheric jump of 15 June 2006 was recorded at Palma de Mallorca about one hour before it arrived at Menorca and catastrophic sea-level oscillations and destructive currents occurred in Ciutadella Harbour. Thus, if a timely and reliable forecast were to be done based on this information and fast modelling estimates, it could significantly reduce the actual economical losses.

Appendix. Pressure Gradient Method (PGM)

We used a simple method to estimate the speed U and direction φ of travelling atmospheric waves based on observations on a triangle of microbarographs with coordinates: $(0, 0)$, (x_2, y_2) and (x_3, y_3) (Fig. 13). We assumed that: (i) the disturbance does not change during its travel over the domain, and (ii) the disturbance has a constant speed and direction. A simple plane geometry yields to the following expressions:

$$\tan \varphi = a = \frac{t_3 y_2 - t_2 y_3}{t_3 x_2 - t_2 x_3}, \tag{A1}$$

$$U = \frac{1}{t_2} \frac{y_2 - a x_2}{\sqrt{1 + a^2}} = \frac{1}{t_3} \frac{y_3 - a x_3}{\sqrt{1 + a^2}}, \tag{A2}$$

where t_2 and t_3 are the time lags between stations 2 and 3 and station 1. If the wavelength (period) of the atmospheric waves is considerebly larger than the distance between the instruments, then these time lags can be estimated from the following formula (see Fig. 13):

$$\Delta t = \frac{\Delta p}{\partial p / \partial t}, \tag{A3}$$

where Δt and Δp are the time and pressure differences between two stations and $\partial p/\partial t$ is the local air pressure derivation (Fig. 13) averaged for two stations. As it follows from (A3), time lags t_2 and t_3 may be estimated as
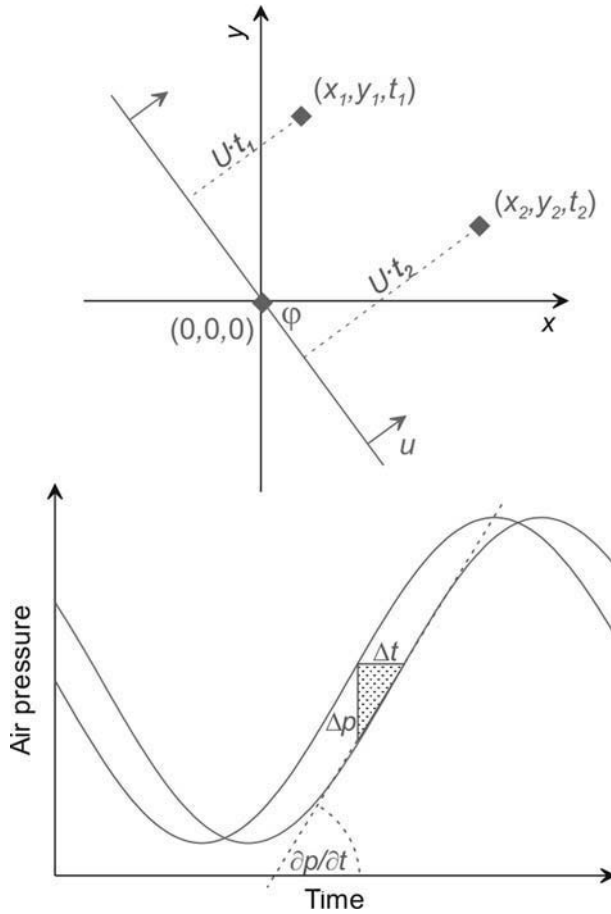
Figure 13
The upper panel illustrates the detection of the atmospheric disturbance speed (U) and direction (φ) by using a triangle of microbarographs recording atmospheric pressure $P_i(t)$ at fixed points (x_i, y_i). The lower panel visualizes the relation (A3) used for computation of time t between two microbarographs by the Pressure Gradient Method.

$$t_2 = \frac{2(p_2 - p_1)}{(\partial p_1/\partial t + \partial p_2/\partial t)}, \tag{A4a}$$

$$t_3 = \frac{2(p_3 - p_1)}{(\partial p_1/\partial t + \partial p_3/\partial t)}. \tag{A4b}$$

The equations (A1), (A2) and (A4) determine the speed U and direction φ of the propagating atmospheric disturbance. This method was applied for the pronounced air-pressure disturbances during the meteotsunami events R1 and R3, which are shown in Figures 3–5.

Acknowledgements

REFERENCES

CANDELA, J., MAZZOLA, S., SAMMARI, C., LIMEBURNER, R., LOZANO, C.J., PATTI, B., and BONNANO, A., (1999), *The "Mad Sea" phenomenon in the Strait of Sicily*, J. Phys. Oceanogr. *29*, 2210–2231.

CUNHA, C.L.N. and ROSMAN, P.C.C. (2005), *A semi-implicit finite element model for natural water bodies*, Water Res. *39*, 2034–2047.

DEFANT, A. *Physical Oceanography*, vol. 2, (Pergamon Press, Oxford, UK, 1961), 598 pp.

DE JONG, M.P.C., HOLTHUIJSEN, L.H. and BATTJES, J.A. (2003), *Generation of seiches by cold fronts over the southern North Sea*, J. Geophys. Res. *108*(C4), 3117, doi:10.1029/ 2002JC001422.

DE JONG, M.P.C. and BATTJES, J.A. (2004), *Low-frequency sea waves generated by atmospheric convection cells*, J. Geophys. Res. *109*, C01011, doi:10.1029/ 2003JC001931

EMERY, W.J. and THOMSON, R.E. *Data Analysis Methods in Physical Oceanography*, second and revised edition, (Elsevier, New York, 2003) 638 pp.

GARCIES, M., GOMIS, D., and MONSERRAT, S (1996), *Pressure-forced seiches of large amplitude in inlets of the Balearic Islands. Part II: Observational study*, J. Geophys. Res. *101*(C3), 6453–6467.

GOMIS, D., MONSERRAT, S., and TINTORÉ, J. (1993), *Pressure-forced seiches of large amplitude in inlets of the Balearic Islands*, J. Geophys. Res. *98*, 14 437–14 445.

HIBIYA, T. and KAJIURA, K. (1982), *Origin of 'Abiki' phenomenon (kind of seiches) in Nagasaki Bay*, J. Oceanogr. Soc. Japan *38*, 172–182.

HODŽIĆ, M. (1979/1980), *Occurrences of exceptional sea-level oscillations in the Vela Luka Bay (in Croatian)*, Priroda *68*(2–3), 52–53.

IMAMURA, F. *Review of tsunami simulation with finite difference method. In Long-Wave Runup Models* (eds. H. Yeh, P. Liu, and C. Synolakis), (World Scientific, Singapore 1996), pp. 25–42.

JANSÀ, A. (1986), *Respuesta marina a perturbaciones mesometeorológicas: la 'rissaga' de 21 de junio de 1984 en Ciutadella (Menorca) (in Spanish)*, Revista Meteorologia, junior, 5–29.

JANSÀ, A., MONSERRAT, S., and GOMIS, D. (2007), *The rissaga of 15 June 2006 in Ciutadella (Menorca), a meteorological tsunami*, Advan. Geosci., *12*, 1–4.

LIU, P.L.-F., MONSERRAT, S., MARCOS, M., and RABINOVICH, A.B. (2003), *Coupling between two inlets: Observation and modeling*, J. Geophys. Res. *108*(C3), 3069, doi:10.1029/ 2002JC001478.

MARCOS, M., MONSERRAT, S., MEDINA, V., and VIDAL., C., *Influence of the atmospheric wave velocity in the coastal amplification of meteotsunamis. In Submarine Landslides and Tsunamis* (eds. A.C. Yalçiner, E.N. Pelinovsky, C.E. Synolakis, and E. Okal, E.), (Kluwer Acad. Publ., Dordrecht 2003), pp. 247–253.

MONSERRAT, S. and THORPE, A. J. (1992), *Gravity-wave observations using an array of microbarographs in the Balearic Islands*, Quart. J. Roy. Met. Soc. *118*, 259–282.

MONSERRAT, S., IBBERSON, A., and THORPE, A.J. (1991a), *Atmospheric gravity waves and the "rissaga" phenomenon*, Quart. J. Roy. Met. Soc. *117*, 553–570.

MONSERRAT, S., RAMIS, C., and THORPE, A.J. (1991b), *Large-amplitude pressure oscillations in the Western Mediterranean*, Geophys. Res. Lett. *18*, 183–186.

MONSERRAT, S., RABINOVICH, A.B., and CASAS, B. (1998), *On the reconstruction of the transfer function for atmospherically generated seiches*, Geophys. Res. Lett. *25*(12), 2197–2200.

MONSERRAT, S., VILIBIĆ, I., and RABINOVICH, A.B. (2006), *Meteotsunamis: Atmospherically induced destructive ocean waves in the tsunami frequency band*, Natural Hazards Earth Syst. Sci. *6*, 1035–1051.

ORLIĆ, M. (1980), *About a possible occurrence of the Proudman resonance in the Adriatic*, Thalassia Jugoslavica *16*(1), 79–88.

PROUDMAN, J. (1929), *The effects on the sea of changes in atmospheric pressure*, Geophys. Suppl. Mon. Notices R. Astr. Soc. *2*(4), 197–209.

RABINOVICH, A.B. *Long Ocean Gravity Waves: Trapping, Resonance, and Leaking* (in Russian), (Gidrometeoizdat, St. Petersburg 1993), 325 pp.

RABINOVICH, A.B. *Seiches and harbour oscillations*. In: *Handbook of Coastal and Ocean Engineering* (ed. Y.C. Kim) (World Scientific, Singapore 2008) (in press).

RABINOVICH, A.B. and MONSERRAT, S. (1996), *Meteorological tsunamis near the Balearic and Kuril Islands: Descriptive and statistical analysis*, Natural Hazards *13*(1), 55–90.

RABINOVICH, A.B. and MONSERRAT, S. (1998), *Generation of meteorological tsunamis (large amplitude seiches) near the Balearic and Kuril Islands*, Natural Hazards *18*(1), 27–55.

RABINOVICH, A.B., MONSERRAT, S., and FINE, I.V. (1999), *Numerical modeling of extreme seiche oscillations in the region of the Balearic Islands*, Oceanology *39*(1), 16–24.

RAMIS, C. and JANSÀ, A. (1983), *Condiciones meteorológicas simultáneas a la aparición de oscilaciones del nivel del mar de amplitud extraordinaria en el Mediterráneo occidental* (in Spanish), Revista Geofísica *39*, 35–42.

TINTORÉ, J., GOMIS, D., ALONSO, S., and WANG, D.P. (1988), *A theoretical study of large sea-level oscillations in the Western Mediterranean*, J. Geophys. Res. *93*, 10 797–10 803.

VIDAL, C., MEDINA, R., MONSERRAT, S., and MARTÍN, F.L. (2000), *Harbor resonance induced by pressure-forced surface waves*, 27th Intern. Conf. Coastal Eng., Sydney, 3615–3628.

VILIBIĆ, I. (2008), *Numerical simulation of the Proudman resonance*, Cont. Shelf Res. *28*, 574–581.

VILIBIĆ, I., DOMIJAN, N., ORLIĆ, M., LEDER, N., and PASARIĆ, M. (2004), *Resonant coupling of a travelling air-pressure disturbance with the east Adriatic coastal waters*, J. Geophys. Res. *109*, C10001, doi:10.1029/2004JC002279.

VILIBIĆ, I., DOMIJAN, N., and ČUPIĆ, S. (2005), *Wind versus air pressure seiche triggering in the Middle Adriatic coastal waters*, J. Mar. Syst. *57*, 189–200.

WANG, X., LI, K., YU, Z., and WU, J. (1987), *Statistical characteristics of seiches in Longkou Harbour*, J. Phys. Oceanogr. *17*, 1963–1966.

To access this journal online:
www.birkhauser.ch/pageoph

Pure and Applied Geophysics

Validation and Verification of Tsunami Numerical Models

C. E. Synolakis,[1] E. N. Bernard,[2] V. V. Titov,[3] U. Kânoğlu,[4] and F. I. González[2]

Abstract—In the aftermath of the 26 December, 2004 tsunami, several quantitative predictions of inundation for historic events were presented at international meetings differing substantially from the corresponding well-established paleotsunami measurements. These significant differences attracted press attention, reducing the credibility of all inundation modeling efforts. Without exception, the predictions were made using models that had not been benchmarked. Since an increasing number of nations are now developing tsunami mitigation plans, it is essential that all numerical models used in emergency planning be subjected to validation—the process of ensuring that the model accurately solves the parent equations of motion—and verification—the process of ensuring that the model represents geophysical reality. Here, we discuss analytical, laboratory, and field benchmark tests with which tsunami numerical models can be validated and verified. This is a continuous process; even *proven* models must be subjected to additional testing as new knowledge and data are acquired. To date, only a few existing numerical models have met current standards, and these models remain the only choice for use for real-world forecasts, whether short-term or long-term. Short-term forecasts involve data assimilation to improve forecast system robustness and this requires additional benchmarks, also discussed here. This painstaking process may appear onerous, but it is the only defensible methodology when human lives are at stake. Model standards and procedures as described here have been adopted for implementation in the U.S. tsunami forecasting system under development by the National Oceanic and Atmospheric Administration, they are being adopted by the Nuclear Regulatory Commission of the U.S. and by the appropriate subcommittees of the Intergovernmental Oceanographic Commission of UNESCO.

Key words: Tsunami, benchmarked tsunami numerical models, validated and verified tsunami numerical models.

1. Introduction

Following the Indian Ocean tsunami of 26 December, 2004, there has been substantial interest in developing tsunami mitigation plans for tsunami prone regions worldwide (Synolakis and Bernard, 2006). While UNESCO has been attempting to coordinate capacity building in tsunami hazards reduction around the world, several national agencies have been making exceptional progress towards being tsunami-ready.

[1] Viterbi School of Engineering, University of Southern California, Los Angeles, CA 90089, USA.
[2] NOAA/Pacific Marine Environmental Laboratory, Seattle, WA 98115, USA.
[3] NOAA/Pacific Marine Environmental Laboratory, Seattle, WA 98115, USA and Joint Institute for the Study of the Atmosphere and Ocean (JISAO), University of Washington, Seattle, WA 98195, USA.
[4] Department of Engineering Sciences, Middle East Technical University, 06531 Ankara, Turkey.

The National Oceanic and Atmospheric Administration (NOAA) is the federal agency charged with mitigating tsunami hazards in the United States. Tsunami models are prominent in two components of the NOAA strategy: Short-term forecast products in support of Tsunami Warning Centers (TWCs) operated by the National Weather Service and long-term forecast products such as inundation maps for hazard assessment and planning by Member States of the National Tsunami Hazard Mitigation Program (NTHMP). The NTHMP was formed through a directive of the U.S. Senate Appropriations Committee in 1994 to develop a plan for a tsunami warning system that reduces the risk to coastal residents. After the Indian Ocean tsunami, the U.S. expanded the role of NTHMP to serve as the organizational framework to implement the recommendations of the NATIONAL SCIENCE and TECHNOLOGY COUNCIL (2005).

One of the recommendations was to "Develop standardized and coordinated tsunami hazard and risk assessments for all coastal regions of the U.S. and its territories." Standards for modeling tools do not currently exist, yet an increased number of states either are developing or will need to develop tsunami mitigation plans. There is risk that forecast products may be produced with older or untested methodologies. This is a worldwide problem, as the Intergovernmental Oceanographic Commission (IOC) of UNESCO has found out in its efforts to help member nations develop tsunami hazard maps. Unrealistic estimates can be costly both in terms of lives lost, or in unnecessary evacuations that sometimes put lives at risk and reduce the credibility of the world system. Standards are urgently needed to ensure a minimum level of quality and reliability for real-time forecasting and inundation mapping products. Further, unrealistic estimates can lead to panic. Examples include the 30 m runup estimates for Cascadia tsunamis (THE SEATTLE TIMES, 2005; NEW SCIENTIST, 2005; ASSOCIATED PRESS, 2005) and large runup estimates for islands in the Eastern Mediterranean in 2007 (ETHNOS, 2007); in both instances, an inordinate effort took place to restore common sense.

In the past ten years, the process of model validation and verification has shown that coastal effects of tsunamis can be described by a set of depth-averaged hydrostatic equations of motion, also known as the shallow-water wave (SW) equations. Comparisons with both large-scale laboratory data and field data have demonstrated a compelling and not always expected capability to describe complex evolution phenomena, and to estimate the maximum runup and inundation, over wide ranges of tsunami waves. In the current state of knowledge, the main uncertainty arises from the ambiguities of the initial condition, assuming the solution methodology solves the equations of motion satisfactorily. The increasing deployment of Deep-ocean Assessment and Reporting of Tsunamis (DART) buoys—tsunameters or tsunamographs—that monitor tsunami evolution in the deep ocean, allows for real-time updates of the characteristics of the source and thus leads to better definition of the initial conditions, at least for tectonic tsunamis (SATAKE *et al.*, 2007). Realistic initial data as input in benchmarked computational tools lead to focused and reliable forecasts.

While equation solvers of higher-than-the-SW approximations of the parent Navier–Stokes equations now exist, they are presently too computationally intensive for

inundation mapping or operational forecasting, and are generally used for free-surface flows of very limited geographical extent. These models remain largely unvalidated over wide ranges of tsunami events and in fact many of them work only in one propagation direction. Yet, the rapid development of packaged numerical modeling tools facilitates their application by untrained users.

In the next section, we discuss model evaluation with state-of-the-art benchmark tests for validating and verifying computational tools for predicting the coastal effect of tsunamis. Then, we recommend standards and guidelines for operational codes used for inundation mapping and tsunami forecasting.

2. Model Evaluation Standards

Tsunami models have evolved in the last two decades through careful and explicit validation/verification by comparing their predictions with benchmark analytical solutions, laboratory experiments, and field measurements. While there is in principle no assurance that a numerical code that has performed well in all benchmark tests will always produce realistic inundation predictions, validated/verified codes largely reduce the level of uncertainty in their results to the uncertainty in the geophysical initial conditions. Furthermore, when coupled with real-time free-field tsunami measurements from tsunameters, validated/verified codes are the only choice for realistic forecasting of inundation.

Here we develop recommendations for national agencies approval of modeling tools, their further development, and their transfer to operations. These steps can be classified into four categories: basic hydrodynamic considerations, benchmarking, scientific evaluations, and operational evaluations.

2.1. Basic Hydrodynamic Considerations

Mass conservation: While the equation of conservation of mass is solved in all numerical computations of water-wave motions, cumulative numerical approximations can sometimes produce results that violate the principle. This is particularly true when the model employs friction factors or smoothing to stabilize inundation computations. For a closed domain within reflective boundaries, conservation of mass can be checked by calculating the water volume at the beginning and end of the computation, derived upon integration of the disturbed water surface $\eta(x, y, t)$ over the entire solution domain up to the maximum extend of inundation. The integral of the entire flow depth $h(x, y, t)$, where $h(x, y, t) = \eta(x, y, t) + d(x, y, t)$ and $d(x, y, t)$ is the undisturbed water depth, should not be used; typically, $\eta \ll d$ offshore, and integrating h will tend to mask errors. For a domain with open or absorbing boundaries, the net volume flux across each such boundary must be considered in the estimate of total displaced volume. Numerical errors in such computations can be highly additive, and mass invariably might not be conserved in long numerical

computations. Nonetheless, the initial total displaced volume should agree with the displaced volume at the end of the computation within a prespecified margin of error. If the difference is not acceptable, then the code numerics must be examined for errors or inadequacies, and/or the grid must be readjusted. Improvements can usually be achieved with a few changes in grid size(s) and time step. Obviously the process must be shown to converge to increasingly smaller mass losses.

Convergence: Extreme runup/rundown locations are optimally suited for checking convergence of the numerical code used to a certain asymptotic limit, presumably the actual solution of the equations solved. A graph needs to be prepared presenting the variation of the calculated runup/rundown (ordinate) with the step size (abscissa). As the step size is reduced, the numerical predictions should be seen to converge to a certain value, with further reductions in step size not appreciably changing the results. One excellent example is given in PEDERSEN (2008).

2.2. Benchmark Solutions

Benchmarking of numerical models can be classified into analytical, laboratory, and field benchmarking. Some of the benchmarks we will describe here have been used in the 1995 and 2004 Long-Wave Runup Models Workshops in Friday Harbor, Washington (YEH *et al.*, 1996) and Catalina, California (LIU *et al.*, 2008), respectively. More detailed descriptions of these benchmarks are given in SYNOLAKIS *et al.* (2007).

2.2.1 Analytical benchmarking. The real usefulness of analytical calculation is its identification of the dependence of desired results (such as runup) on the problem parameters (such as offshore wave height, beach slope, depth variation). Numerical solutions will invariably produce more accurate specific predictions, but will rarely provide useful information about the problem scaling, unless numerical computations are repeated *ad nauseam*. Comparisons with exact solutions can identify systematic errors and are thus useful in validating the complex numerical methods used in realistic applications.

Here, we present analytical solutions to certain common 1+1 (one directional and time) propagation problems. The results are derived for idealized initial waveforms often used in tsunami engineering to describe the leading wave of a tsunami. Generalization to more realistic spectral distributions of geophysical tsunamis is trivial, given that results are shown in closed-form integrals.

It is important to note that validation should always take place with non-periodic waves. During runup, individual monochromatic waves reflect with slope-dependent phase shifts (SYNOLAKIS, 1986). Whereas a particular code may model a periodic wave well, it may not model superposition equally well. This was a problem of earlier SW computations that did not account for reflection. While their predictions for the Carrier–Greenspan (CARRIER and GREENSPAN, 1958) sinusoids appeared satisfactory, they exhibited significant errors when modeling solitary waves or N-waves.
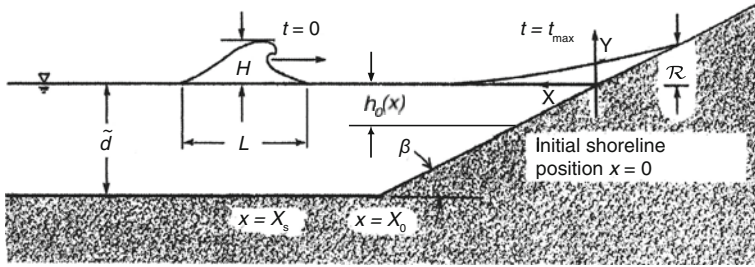
Figure 1
Definition sketch for a canonical consideration.

Linear solutions on a simple beach: We consider a solitary and N-wave propagation first over the constant-depth region then sloping beach—canonical problem (Fig. 1). The topography is described by $h_0(x) = x \tan\beta$ when $x \le X_0$ and $h_0(x) = 1$ when $x \ge X_0$ where $X_0 = \cot\beta$. The origin of the coordinate system is at the initial position of the shoreline and x increases seaward. Even though dimensionless variables are not preferred in numerical calculations and engineering practice, in analytical solutions they have distinct advantages as everything scales simply with an offshore characteristic depth or a characteristic length. Here dimensionless variables are introduced as: $x = \tilde{x}/\tilde{d}$, $(h, \eta, h_0, \mathcal{R}) = (\tilde{h}, \tilde{\eta}, \tilde{h}_0, \tilde{\mathcal{R}})/\tilde{d}$, $u = \tilde{u}/\sqrt{\tilde{g}\tilde{d}}$, and $t = \tilde{t}/\sqrt{\tilde{d}/\tilde{g}}$ provided the depth $\tilde{d}$ of the constant-depth region is chosen as the characteristic scale. Quantities with tilde are dimensional and η is the amplitude, u is the depth-averaged horizontal velocity, h_0 is the undisturbed water depth, and $\tilde{g}$ is the gravitational acceleration.

Consider a tsunami evolution problem described by the $1 + 1$ nonlinear shallow-water wave (NSW) equations:

$$h_t + (u\,h)_x = 0, \quad u_t + uu_x + \eta_x = 0, \tag{1}$$

with $h(x, t) = \eta(x, t) + h_0(x)$. Neglecting nonlinear terms, through elementary manipulations, (1) reduces to an equation $\eta_{tt} - (\eta_x\,h_0)_x = 0$ known as the linear shallow-water wave (LSW) equation. SYNOLAKIS (1986, 1987) matched the linear theory solution at the constant-depth region with the linear solution over the sloping beach as derived by KELLER and KELLER (1964) to determine the solution for the wave height $\eta(x, t)$ over the sloping beach,

$$\eta(x,t) = 2 \int\limits_{-\infty}^{+\infty} \Phi(\omega) \frac{J_0(2\omega\sqrt{xX_0})e^{-i\omega(X_0+t)}}{J_0(2X_0\omega) - iJ_1(2X_0\omega)} \, d\omega. \tag{2}$$

Here, $\Phi(\omega)$ is the spectrum of the incoming wave offshore. This solution is only valid when $0 \le x \le X_0$; LSW equation does not reduce to Bessel's equation when $x < 0$. Notice that the integral (2) can be evaluated with standard numerical methods; however, the advantage of this form is that it allows calculation of the solution for many physically

realistic tsunami waveforms simply by using the $\Phi(\omega)$ of the incoming wave in (2), hopefully known at some offshore location.

Solitary wave evolution and runup: An initial solitary wave centered offshore at $x = X_s$ has the surface profile, $\eta(x, t = 0) = H \operatorname{sech}^2 \gamma(x - X_s)$ where $\gamma = \sqrt{3H/4}$ and H is the dimensionless wave height, i.e., $H = \widetilde{H}/\widetilde{d}$. Upon substituting its spectrum in equation (2), SYNOLAKIS (1991) showed that the maximum local value of the wave amplitude $\eta_{\max}$ is given explicitly by $\eta_{\max}/H = (X_0/x)^{1/4} = (1/h_0)^{1/4}$, an amplitude variation usually referred to as *Green's law*. The region over which this amplitude variation applies is the region of gradual shoaling; the region of rapid shoaling is often identified with the Boussinesq result, i.e., $\eta_{\max} \sim h_0$. The fact that both evolution laws may coexist was first identified by SHUTO (1973). SYNOLAKIS and SKJELBREIA (1993) also present results which show that Green's law type evolution is valid over a wide range of slopes and for finite-amplitude waves at least in the region of gradual shoaling.

In the LSW theory, the shoreline does not move beyond $x = 0$. The maximum value of $R(t) = \eta(0, t)$ is the maximum runup $\mathcal{R}$, arguably the most important parameter in the long-wave runup problem, and it is the maximum vertical excursion of the shoreline. The result (2) can be readily applied to derive the maximum runup of a solitary wave climbing up a sloping beach. Per SYNOLAKIS (1986), the integral (2) with the solitary wave spectrum $\Phi(\omega)$ can be reduced into a Laurent series using contour integration. The series can be simplified further by using the asymptotic form for large arguments of the modified Bessel functions, making it possible to obtain its extremum, leading to the following expression for the maximum runup $\mathcal{R}$:

$$\mathcal{R} = 2.831 \sqrt{\cot\beta}\, H^{5/4}. \tag{3}$$

This result is formally correct when $\sqrt{H} \gg 0.288 \tan\beta$, the assumption implied when using the asymptotic form of the Bessel functions. The asymptotic result (3) is valid for waves that do not break during runup. Equation (3) was derived by SYNOLAKIS (1986) and has since been referred to as *the runup law* and shown in Figure 2. As will be apparent in later sections, this methodology is quite powerful to find the maximum runup and it allows calculation of the runup of other waveforms such as N-waves, not to mention the runup of waves evolving over piecewise-linear bathymetries.

N-wave runup: Most tsunami eyewitness accounts suggest that tsunamis are N-wave like, i.e., they are dipolar, which means they appear as a combination of a depression and an elevation wave, and frequently as a series of N-waves, sometimes known as double N-waves. Until the late 1990s, the solitary wave model was used exclusively to evaluate the runup of tsunamis. Even though it was suspected that the leading tsunami wave might be a depression wave (MEI, 1983), before 1992, these waves were believed to be hydrodynamically unstable; the crest was assumed to quickly overtake the trough. The N-wave model was motivated by observations from a series of nearshore-triggered tsunamis starting in 1992 (TADEPALLI and SYNOLAKIS, 1994; SYNOLAKIS and OKAL, 2005), all of which produced tsunami waves which caused nearby shorelines to first recede before advancing. The most
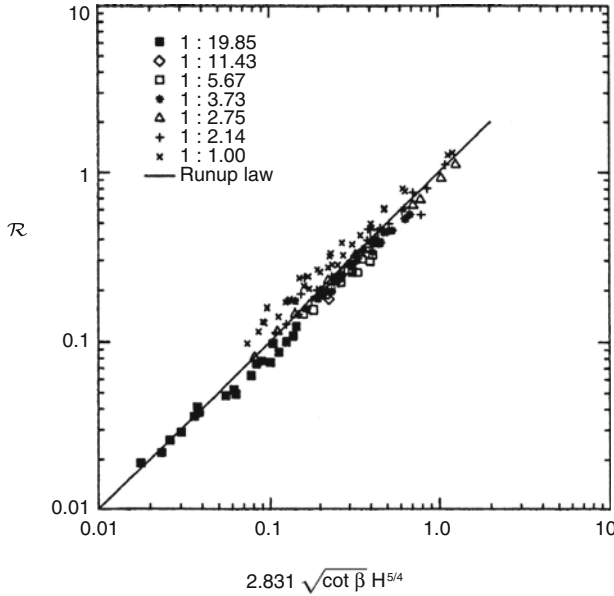
$\mathcal{R}$

Figure 2

Laboratory data for maximum runup of nonbreaking waves climbing up different beach slopes: 1:19.85 (Synolakis, 1986); 1:11.43, 1:5.67, 1:3.73, 1:2.14, and 1:1.00 (Hall and Watts, 1953); 1:2.75 (Pedersen and Gjevik, 1983). The solid line represents the runup law (3).

spectacular account was during the 9 October, 1995 Manzanillo, Mexico earthquake. Minutes after the earthquake, one eyewitness saw the shoreline retreat beyond a rock outcrop which was normally submerged in over 4 m depth and at a distance of about 400 m from the shoreline (Borrero et al., 1997), suggesting a leading-depression N-wave (LDN). Before the megatsunami of 26 December, 2004, this had been the only photographic evidence of LDN. Recall that the megatsunami manifested itself first with a rapid withdrawal in most locales east of the rupture zone, and as a leading-elevation N-wave (LEN) west of it (Synolakis and Kong, 2006).

To reflect the fact that tsunamigenic faulting in subduction zones is associated with both vertical uplift and subsidence of the sea bottom, Tadepalli and Synolakis (1994, 1996) conjectured that all tsunami waves at generation have an N-wave or dipole shape. Tadepalli and Synolakis (1996) proposed a general function as a unified model for both nearshore and farfield tsunamis as generalized N-waves, i.e., a wave propagates with the trough first is referred to as an LDN and the crest arrives first is referred to as an LEN. For a special class of N-waves with elevation and depression waves of the same height H, referred to as isosceles N-waves, $\eta(x,0) = \mathcal{H}\,\text{sech}^2[\gamma(x-X_N)]\tanh[\gamma(x-X_N)]$ with $\mathcal{H} = \frac{3\sqrt{3}H}{2}$ and $\gamma = \frac{3}{2}\sqrt{\sqrt{\frac{3}{4}H}}$, using contour integration and the same asymptotic approximation methodology as used in the solitary wave results, Tadepalli and Synolakis (1994) showed that

$$\mathcal{R}_{\mathrm{LEN}} = 3.86\sqrt{\cot\beta}\ H^{5/4}. \tag{4}$$

Because of the symmetry of the profile, this is also the minimum rundown of an isosceles LDN. TADEPALLI and SYNOLAKIS (1994) also showed that the normalized maximum runup of nonbreaking isosceles LEN is smaller than the runup of isosceles LDN, and that both are higher than the runup of a solitary wave with the same wave height. The latter became known as *the N-wave effect* (Fig. 3).

Nonlinear solutions on a simple beach: Calculation of the nonlinear evolution of a wave over a sloping beach is theoretically and numerically challenging due to the moving boundary singularity. Yet, it is important to have a good estimate of the shoreline velocity and associated runup/rundown motion, since they are crucial for the planning of coastal flooding and of coastal structures. To solve the nonlinear set (1) for the single sloping beach case, $h_0(x) = x$ (Fig. 4), CARRIER and GREENSPAN (1958) used the characteristic length $\widetilde{l}$ as a scaling parameter and introduced the dimensionless variables as: $x = \widetilde{x}/\widetilde{l}$, $(h, \eta, h_0, \mathcal{R}) = (\widetilde{h}, \widetilde{\eta}, \widetilde{h}_0, \widetilde{\mathcal{R}})/(\widetilde{l}\tan\beta)$, $u = \widetilde{u}/\sqrt{\widetilde{g}\widetilde{l}\tan\beta}$, and $t = \widetilde{t}/\sqrt{\widetilde{l}/(\widetilde{g}\tan\beta)}$. CARRIER and GREENSPAN (1958) defined a hodograph transformation known as Carrier–Greenspan transformation
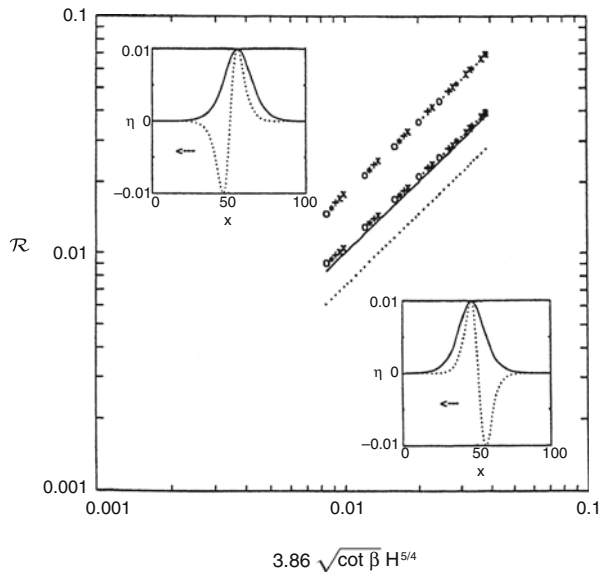

Figure 3

Maximum runup of isosceles N-waves and solitary wave. The top and lower set of points are results for the maximum runup of leading-depression and -elevation isosceles N-waves, respectively. The dotted line represents the runup of solitary wave (3). The upper and lower insets compare a solitary wave profile to a leading-depression and -elevation isosceles N-waves, respectively. After TADEPALLI and SYNOLAKIS (1994).
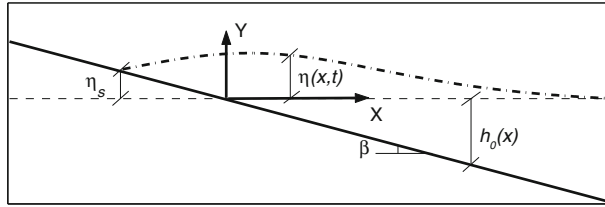
Figure 4
Definition sketch for an initial value problem.

$$x = \frac{\sigma^2}{16} - \eta, \quad t = u - \frac{\lambda}{2}, \quad \eta = \frac{\psi_\lambda}{4} - \frac{u^2}{2}, \quad u = \frac{\psi_\sigma}{\sigma}, \tag{5}$$

thus reducing the NSW equations to a single second-order linear equation:

$$(\sigma\psi_\sigma)_\sigma - \sigma\psi_{\lambda\lambda} = 0. \tag{6}$$

Here $\psi(\sigma, \lambda)$ is a Carrier–Greenspan potential. Notice the conservation of difficulty. Instead of having to solve the coupled nonlinear set (1), one now has to solve a linear equation (6), however the transformation equations (5) which relate the transformed variables to the physical variables are nonlinear, coupled, and implicit. Yet, a redeeming feature is that in the hodograph plane, i.e., in the (σ, λ)-space, the instantaneous shoreline is always at $\sigma = 0$. This allows for direct analytical solutions without the complications of the moving shoreline boundary.

In general, it is quite difficult to specify boundary or initial data for the nonlinear problem in the physical (x, t)-space coordinates without making restrictive assumptions; a boundary condition requires specification of $(X_0, \forall t)$ while an initial condition requires specification at $(\forall x, t_0)$. Even when boundary or initial conditions are available in the (x, t)-space, the process of deriving the equivalent conditions in the (σ, λ)-space is not trivial. These difficulties have restricted the use of Carrier–Greenspan transformation, and this is why they are discussed here again, in an attempt to demystify them.

Boundary value problem (BVP) for the constant depth/beach topography: Using the solution (2) of the equivalent linear problem, at the seaward boundary of the beach, i.e., at $x = X_0 = \cot\beta$ corresponding to $\sigma = \sigma_0 = 4$ based on characteristic depth scale, SYNOLAKIS (1986, 1987) was able to show that the Carrier–Greenspan potential is given by

$$\psi_b(\sigma, \lambda) = -\frac{16i}{X_0} \int_{-\infty}^{+\infty} \frac{\Phi(\kappa)}{\kappa} \frac{J_0(\sigma\kappa X_0/2) e^{-i\kappa X_0\left(1-\frac{\lambda}{2}\right)}}{J_0(2\kappa X_0) - iJ_1(2\kappa X_0)} \, d\kappa. \tag{7}$$

Note that the hodograph transformation includes $\cot\beta$ as coefficient because the scaling used in SYNOLAKIS (1986, 1987), i.e., $x = \cot\beta\left(\frac{\sigma^2}{16} - \eta\right)$ and $t = \cot\beta\left(u - \frac{\lambda}{2}\right)$. Then the amplitude $\eta(x, t)$ can be calculated directly from equation (5), so comparisons with numerical simulations for any given $\Phi(\kappa)$ is possible and straightforward. One example of the application of the BVP solution of SYNOLAKIS (1986, 1987) is given in Figure 5.
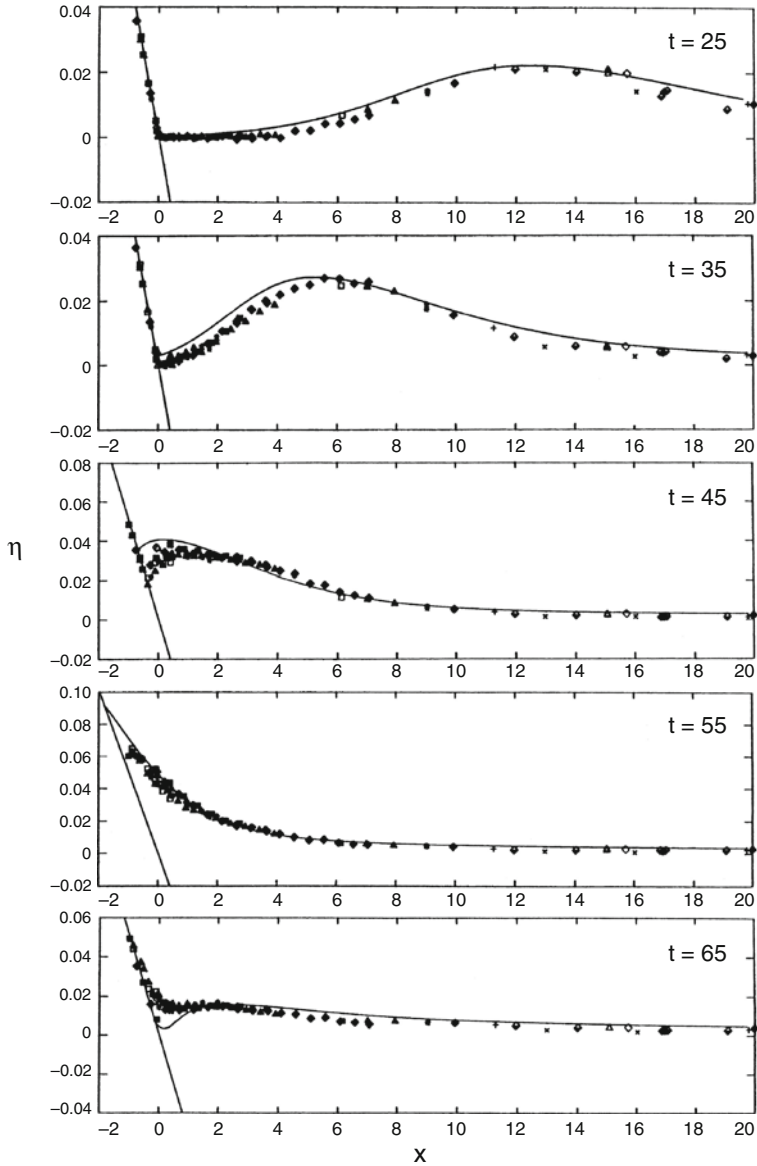
Figure 5
Time evolution of a $\tilde{H}/\tilde{d} = 0.0185$ solitary wave up a 1:19.85 beach (Fig. 1). While the markers show different realizations of the same experiment, the solid lines show boundary value problem solution of the nonlinear shallow-water wave equations. Refer to SYNOLAKIS (1986, 1987) for details.

Initial value problem (IVP) for a sloping beach: For the initial condition where $\Psi(\sigma) = u_\lambda(\sigma, 0) = 4\eta_\sigma(\sigma, 0)/\sigma$, CARRIER and GREENSPAN (1958) presented the following potential in the transform space,

$$\psi_i(\sigma, \lambda) = -\int_0^\infty \int_0^\infty \frac{1}{\omega} \xi^2 \Psi(\xi) J_0(\omega\sigma) J_1(\omega\xi) \sin(\omega\lambda) \, d\omega d\xi. \tag{8}$$

Note that a characteristic length scale is used to define dimensionless variables. KÂNOĞLU (2004) proposed that the difficulty of deriving an initial condition in the (σ, λ)-space is overcome by simply using the linearized form of the hodograph transformation for a spatial variable in the definition of initial condition. Once an IVP is specified in the (x, t)-space as $\eta(x, 0)$, the linearized hodograph transformation $x \cong \frac{\sigma^2}{16}$ is used directly to define the initial waveform in the (σ, λ)-space, $\eta\left(\frac{\sigma^2}{16}, 0\right)$. Thus $\Psi(\sigma) = 4\eta_\sigma\left(\frac{\sigma^2}{16}, 0\right)/\sigma$ is found, and $\psi_i(\sigma, \lambda)$ follows directly through a simple integration.

Once $\psi_i(\sigma, \lambda)$ is known, one can investigate any realistic initial waveform such as Gaussian and N-wave shapes as employed in CARRIER *et al.* (2003). While KÂNOĞLU (2004) does not consider waves with initial velocities, later, KÂNOĞLU and SYNOLAKIS (2006) solved a more general initial condition, i.e., initial wave with velocity.

Since it is important for coastal planning, simple expressions for shoreline runup/ rundown motion and velocity are useful. Considering that the shoreline corresponds to $\sigma = 0$ in the (σ, λ)-space, the runup/rundown motion can be evaluated. Here, note that the mathematical singularity of the $u = \psi_\sigma/\sigma$, i.e., $J_1(\omega\sigma)/\sigma$, at the shoreline ($\sigma = 0$) is removed with the consideration of the $\lim_{\sigma \to 0}[J_1(\omega\sigma)/\sigma] = \frac{\omega}{2}$ (SYNOLAKIS, 1986; KÂNOĞLU, 2004). An example is provided in Figure 6 for IVP (KÂNOĞLU, 2004).

Solitary wave on a composite beach: 1+1 models that perform well with the single beach analytical solutions must still be tested with the composite beach geometry, for which an analytical solution exists, with solitary waves as inputs. Most topographies of engineering interest can be approximated by piecewise-linear segments allowing the use of LSW equation to determine approximate analytical results for the wave runup in closed form. In principle, fairly complex bathymetries can be represented through a combination of positively/negatively sloping and constant-depth segments. Solutions of the LSW equation at each segment can be matched analytically at the transition points between the
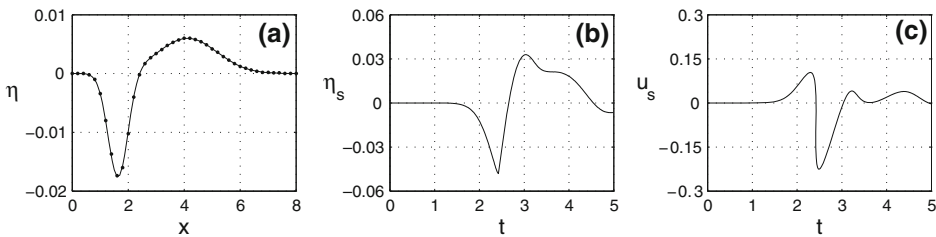

Figure 6

Initial value problem solution of the nonlinear shallow-water wave equations. (a) The leading-depression initial waveform presented by CARRIER *et al.* (2003), $\eta(x, 0) = H_1 \exp\left(-c_1(x - x_1)^2\right) - H_2 \exp\left(-c_2(x - x_2)^2\right)$ with $H_1 = 0.006$, $c_1 = 0.4444$, $x_1 = 4.1209$, $H_2 = 0.018$, $c_2 = 4.0$, and $x_2 = 1.6384$ (solid line) compared with the one resulting from approximation (dots), using the linearized form of the transformation for the spatial variable, (b) shoreline position, and (c) shoreline velocity. After KÂNOĞLU (2004).
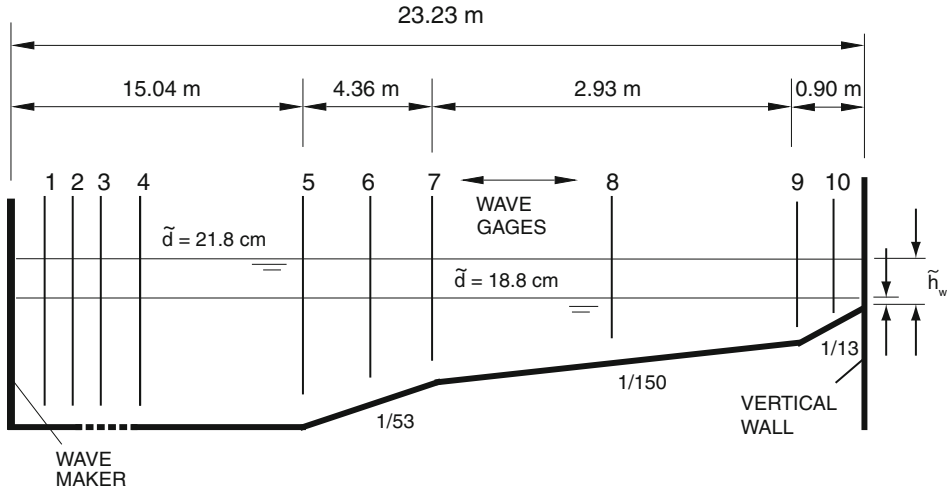
Figure 7

Definition sketch for the Revere Beach topography. $h_w = \widetilde{h}_w/\widetilde{d}$ is the water depth at the foot of the seawall, i.e., there were $\widetilde{h}_w = 1.7$ cm and 4.7 cm depths at the seawall when $\widetilde{d} = 18.8$ cm and 21.8 cm, respectively. Not to scale.

segments, and then the overall amplification factor and reflected waves can be determined, analytically. As an example, KÂNOĞLU and SYNOLAKIS (1998) considered three sloping segments and a vertical wall at the shoreline, as in Revere Beach in Massachusetts (Fig. 7). They were able to show that the maximum runup of solitary waves with maximum wave height H can be calculated analytically and is given by the runup law,

$$\mathcal{R} = 2h_w^{-1/4}H. \tag{9}$$

The runup law above suggests that the maximum runup only depends on the depth at the seawall h_w fronting the beach, and it does not depend on any of the three slopes in front of the seawall. Laboratory data exist for this topography and the runup law (9) predicts the nonbreaking data surprisingly well (Fig. 8). The laboratory data are discussed briefly in section 2.2.2 and in greater detail in YEH *et al.* (1996), KÂNOĞLU (1998), and KÂNOĞLU and SYNOLAKIS (1998).

Subaerial landslide on a simple beach: Inundation computations are exceedingly difficult when the beach is deforming during a subaerial landslide. LIU *et al.* (2003) considered tsunami generation by a moving slide on a uniformly sloping beach, using the forced LSW equation of TUCK and HWANG (1972), and were able to derive an exact solution. Let $\widetilde{\delta}$ and $\widetilde{L}$ be the maximum vertical thickness of the sliding mass and its horizontal length respectively, and $\mu = \widetilde{\delta}/\widetilde{L}$. Tilde representing dimensional quantities, LIU *et al.* (2003) normalized the forced LSW equation with $(\eta, h_0, \mathcal{R}) = (\widetilde{\eta}, \widetilde{h}_0, \widetilde{\mathcal{R}})/\widetilde{\delta}$, $x = \widetilde{x}/\widetilde{L}$, and $t = \widetilde{t}/\left(\sqrt{\widetilde{\delta}/\widetilde{g}}/\mu\right)$, i.e., $\eta_{tt} - (\tan\beta/\mu)(\eta_x x)_x = h_{0,tt}$ where $h_0(x,\,t)$ is the time-dependent
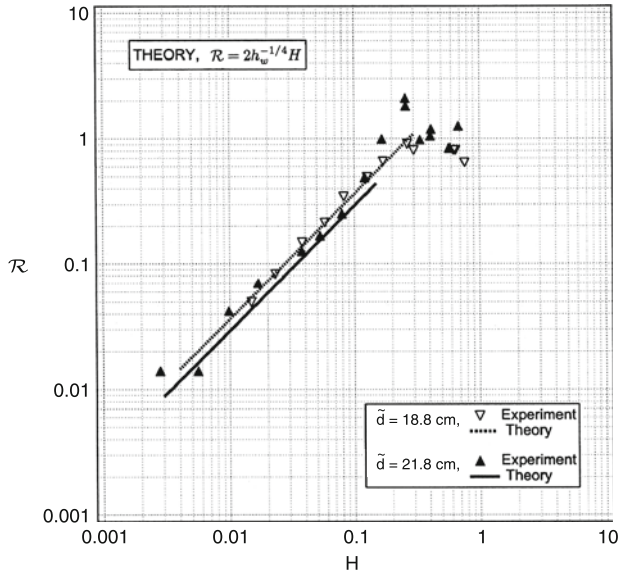
Figure 8

Comparison of the maximum runup values for the linear analytical solution (9) and the laboratory results for two different depths, i.e., $\tilde{d} = 18.8$ cm and 21.8 cm. h_w is the nondimensional depth at the toe of the seawall, and it varies with $\tilde{d}$. After KÂNOĞLU and SYNOLAKIS (1998).

perturbation of the sea floor with respect to the uniformly sloping beach. The focus in their analysis is on thin slides where $\mu = \tilde{\delta}/\tilde{L} \ll 1$.

Consider a translating Gaussian-shaped mass, initially at the shoreline, given by $h_0(x,\ t) = \exp[-(\xi - t)^2]$ with $\xi = 2\sqrt{\mu x/\tan\beta}$. Once in motion, the mass moves at constant acceleration. The free surface wave height is given by

$$\eta(\xi, t) = \int_0^\infty J_0(\rho\xi)\rho\left[a(\rho)\cos(\rho t) + \frac{1}{\rho}b(\rho)\sin(\rho t)\right]d\rho + \frac{1}{3}(h_0 - \xi\, h_{0,\xi}), \qquad (10)$$

where $a(\rho)$ and $b(\rho)$ can be determined by the initial conditions, i.e., unperturbed water surface and zero velocity initially. Details can be found in LIU *et al*. (2003), nevertheless it is clear that once the seafloor motion is specified, the wave height can be calculated explicitly. Figure 9 shows one example of the solution. Comparisons of the maximum runup estimates of this solution with a nonlinear numerical computation are shown in Figure 10, as an example of the validation process.

2.2.2 Laboratory benchmarking. Long before the availability of numerical codes, physical models at small scale had been used to visualize wave phenomena in the laboratory and then predictions were scaled to the prototype. Even today, when designing harbors, laboratory experiments—scale model tests—are used to confirm different flow details and validate the numerical model used in the analysis.
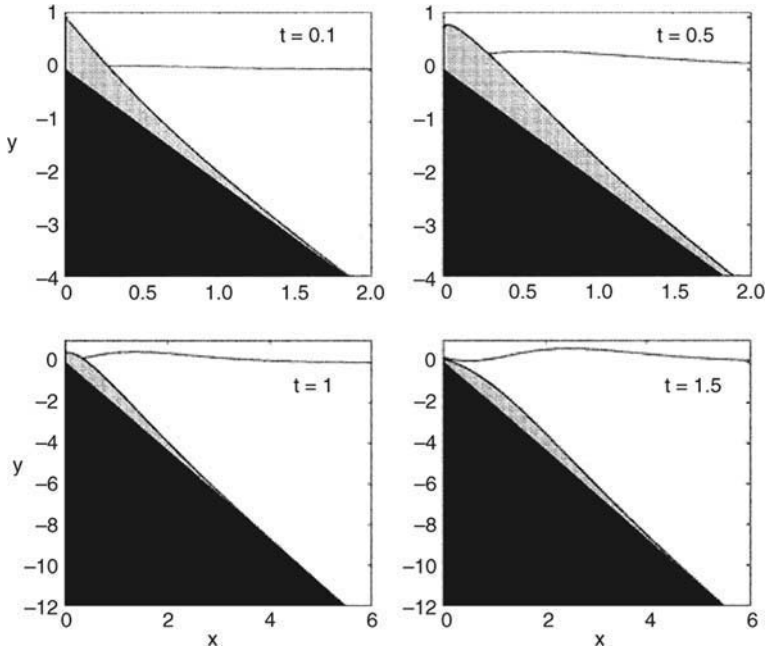
Figure 9

Spatial snapshots of the analytical solution at four different times for a beach slope, $\beta = 5°$, and landslide aspect ratio, $\mu = 0.05$ ($\tan\beta/\mu = 1.75$). The slide mass is indicated by the light shaded area, the solid beach slope by the black region, and η by the solid line (LIU *et al.*, 2003).
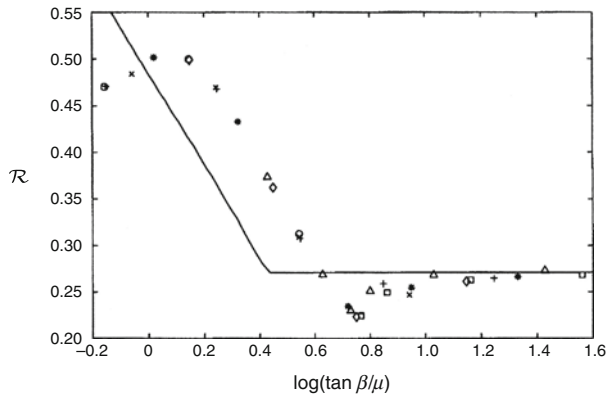

Figure 10

Maximum runup as a function of $\log(\tan\beta/\mu)$. The analytical solutions are shown by the solid line, and the various symbols are from nonlinear shallow-water wave simulations of LIU *et al.* (2003), corresponding to different slopes ranging from 2° to 20°.

Numerical codes developed in the last decade that consistently produce predictions in excellent agreement with measurements from small-scale laboratory experiments have been shown to also model geophysical-scale tsunamis well. For example, a numerical code that adequately models the inundation observed in a 1-m-deep laboratory model is also expected to compute the inundation in a 1-km-deep geophysical basin, as the grid sizes are adjusted accordingly and in relationship to the scale of the problem. While scale laboratory models, in general, do not have bottom friction characteristics similar to real ocean floors or sandy beaches, this has proven not to be a severe limitation for validation of numerical models. It is a problem when the laboratory results are used for designing prototype structures by themselves and without the benefit of numerical models. For example, sediment transport cannot be extrapolated from the laboratory to geophysical scales because the dynamics of sand grain motions do not scale proportionally to the geometric scales of the model, and it is otherwise impossible to achieve dynamic similarity.

The results from five laboratory experiments are described as laboratory benchmarking: Solitary wave experiments on a 1:19.85 sloping beach (SYNOLAKIS, 1986, 1987), on a composite beach (KÂNOĞLU, 1998; KÂNOĞLU and SYNOLAKIS, 1998), and on a conical island (BRIGGS *et al.*, 1995; LIU *et al.*, 1995; KÂNOĞLU, 1998; KÂNOĞLU and SYNOLAKIS, 1998); tsunami runup onto a complex three-dimensional beach (TAKAHASHI, 1996); and tsunami generation and runup due to a three-dimensional landslide (LIU *et al.*, 2005).

For the solitary wave experiments, the initial location, X_s in the analysis changes with different wave heights; solitary waves of different heights have different effective *wavelengths*. A measure of the *wavelength* of a solitary wave is the distance between the point x_f on the front and the point x_t on the tail where the local height is 1% of the maximum, i.e., $\eta(x_f, t = 0) = \eta(x_t, t = 0) = (\widetilde{H}/\widetilde{d})/100$. The distance X_s is at an offshore location where only 5% of the solitary wave is already over the beach, so that scaling can work. Therefore, in the laboratory experiments initial wave heights are identified at a point $X_s = X_0 + (1/\gamma) \operatorname{arccosh}\sqrt{20}$ with $\gamma = \sqrt{3(\widetilde{H}/\widetilde{d})/4}$. In the laboratory, even idealized solitary waveforms dissipate. If the wave height is measured far offshore and used as an initial condition for non-dissipative numerical models, the comparisons will be less meaningful, as the solitary wave will slightly change as it propagates towards the beach in the laboratory. By keeping the same relative offshore distance for defining the initial condition, meaningful comparisons are assured.

Solitary wave on a simple beach: Given that a small number of 2+1 wave basin laboratory measurements exists, 1+1 versions of the 2+1 numerical models should be first tested with 1+1 directional laboratory models. The solitary wave experiments on the canonical model should be used first (SYNOLAKIS, 1987). In this set of experiments, the 36.60-m-long, 0.38-m-wide, and 0.61-m-deep California Institute of Technology, Pasadena, California wave tank was used with water at varying depths. The tank is described by HAMMACK (1972), GORING (1978), and SYNOLAKIS (1986). A ramp with a slope of 1:19.85 was installed at one end of the tank to model the bathymetry of the

canonical problem of a constant-depth region adjoining a sloping beach. The toe of the ramp was 14.95 m distant from the rest position of the piston used to generate waves.

A total exceeding 40 experiments with solitary waves running up the sloping beach was performed, with depths ranging from 6.25–38.32 cm. Solitary waves are uniquely defined by their maximum height $\widetilde{H}$ to depth $\widetilde{d}$ ratio and the depth, i.e., $\widetilde{H}/\widetilde{d}$ and $\widetilde{d}$ are sufficient to specify the wave. $\widetilde{H}/\widetilde{d}$ ranged from 0.021 to 0.626. Breaking occurs when $\widetilde{H}/\widetilde{d} > 0.045$, for this particular beach.

This set of laboratory data has been used extensively for code validation: Refer to SYNOLAKIS (1987), ZELT (1991), TITOV and SYNOLAKIS (1995; 1997; 1998), TITOV and GONZÁLEZ (1997), GRILLI *et al.* (1997), LI and RAICHLEN (2000; 2001; 2002). In particular, the data sets for the $\widetilde{H}/\widetilde{d} = 0.0185$ (Fig. 5) nonbreaking and $\widetilde{H}/\widetilde{d} = 0.3$ (Fig. 11) breaking solitary waves seem the most often used and most appropriate for code validation.

Solitary wave on a composite beach: 1+1 models that perform well with the solitary wave on simple beach experiments must still be tested with the Revere Beach composite beach geometry. Revere Beach is located approximately 6 miles northeast of Boston in the City of Revere, Massachusetts. To address beach erosion and severe flooding problems, a physical model was constructed at the Coastal Engineering Laboratory of the U.S. Army Corps of Engineers, Vicksburg, Mississippi facility, earlier known as Coastal Engineering Research Center. The model beach consists of three piecewise-linear slopes of 1:53, 1:150, and 1:13 from seaward to shoreward with a vertical wall at the shoreline (Fig. 7). In the laboratory, to evaluate the overtopping of the seawall, the wavemaker was located at 23.22 m and tests were done at two depths, 18.8 cm and 21.8 cm.

In the experiments, solitary waves of different heights $\widetilde{H}/\widetilde{d}$ were generated at the location X_s for the reason explained. In terms of specific measurements, time histories of the water surface elevations exist at the locations X_s, midway in each sloping segment, and at the transition points. One example of the time histories of water surface elevations is given in Figure 12 and compared with the analytical solution of KÂNOĞLU and SYNOLAKIS (1998). A comparison of numerical results with a laboratory case near the breaking limit offshore will ensure that the code remains stable, even for extreme waves. The runup variation for solitary waves striking the vertical wall was also determined. The maximum runup values on the vertical wall were measured visually and are presented in Figure 8 for the whole experimental parameter range.

Solitary wave on a conical island: 2+1 dimensional calculations should be tested with the conical island geometry. Motivated by the catastrophe in Babi Island, Indonesia (YEH *et al.*, 1994), during the 1992 Flores Island tsunami, large-scale laboratory experiments were performed at the Coastal Engineering Research Center, Vicksburg, Mississippi, in a 30-m-wide, 25-m-long, and 60-cm-deep wave basin (Fig. 13). An initial solitary wave-like profile was created in the basin by a Directional Spectral Wave Generator (DSWG) located at $\widetilde{x} = 12.96$ m from the center of the island. The particular 27.42-m-long DSWG consisted of sixty 46 cm × 76 cm individual paddles, each driven independently. Allowing generation of waves with different crest lengths.
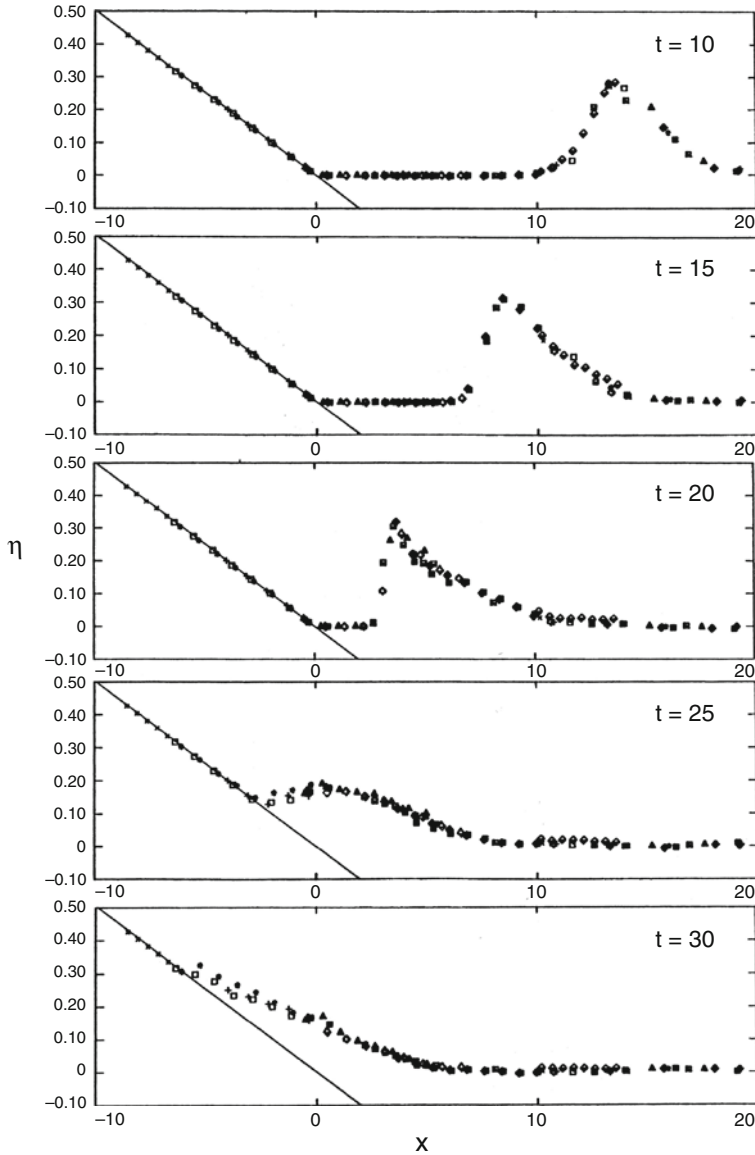
Figure 11

Time evolution of a $\tilde{H}/\tilde{d} = 0.30$ solitary wave up a 1:19.85 beach (Fig. 1). The markers show different realizations of the same experiment of SYNOLAKIS (1986). Refer to SYNOLAKIS (1986; 1987) for details.

In the physical model, a 62.5-cm-high, 7.2-m toe-diameter, and 2.2-m crest-diameter circular island with a 1:4 slope was located in the basin. Experiments were conducted at 32 cm and 42 cm water depths. Each experiment was repeated at least twice. The wavemaker trajectories were recorded to allow the assignment of the same boundary
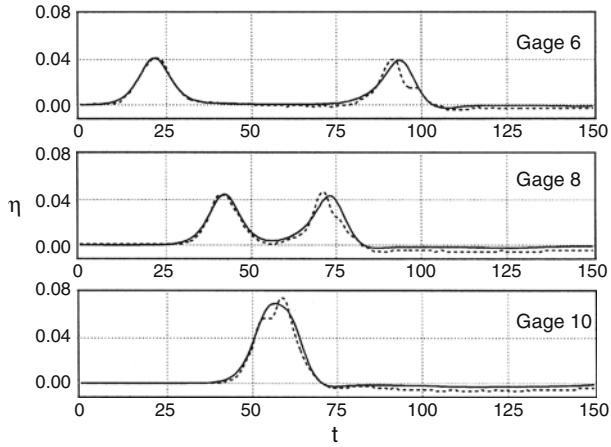
Figure 12
Comparison of the time histories of the free surface elevations midway in each sloping segment for the analytical solution (solid line) of KÂNOĞLU and SYNOLAKIS (1998) and the laboratory data (dotted line) for a $\tilde{H}/\tilde{d} = 0.038$, $\tilde{d} = 21.8$ cm, solitary wave. Refer to KÂNOĞLU and SYNOLAKIS (1998) for details.
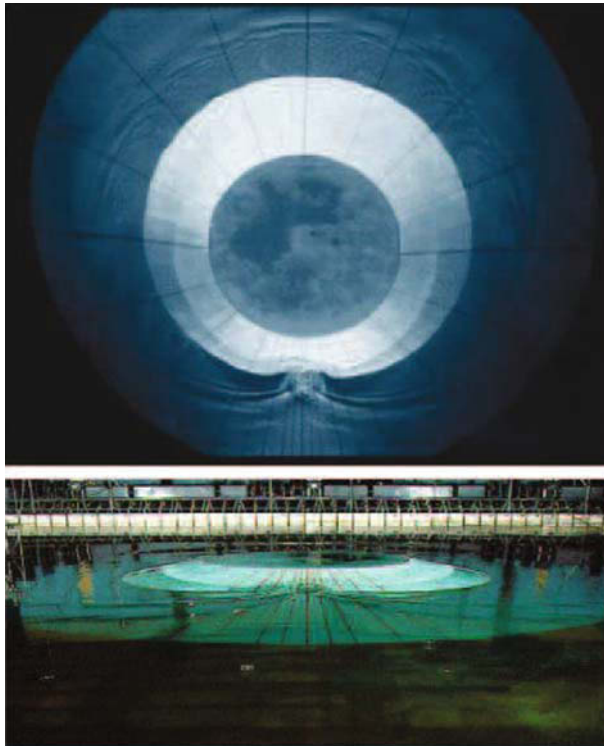

Figure 13
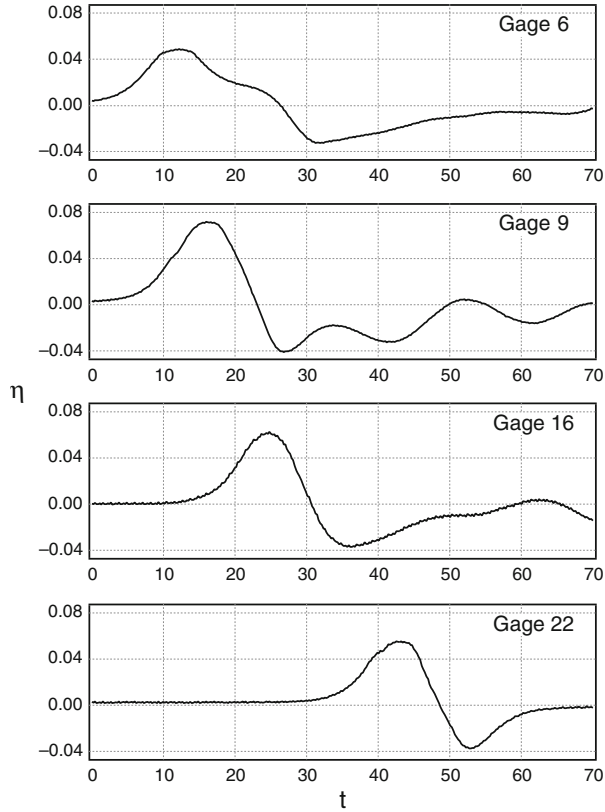Views of the conical island (top) and the basin (bottom). After KÂNOĞLU and SYNOLAKIS (1998).

Figure 14

Laboratory data for the time histories of surface elevation for a $\tilde{H}/\tilde{d} = 0.045$, $\tilde{d} = 32$ cm, solitary wave at four gages. Gage 6 is located at the toe of the conical island on the 0° radial line, i.e., incoming wave direction. Gages 9, 16, and 22 are the gages closest to the shoreline on the 0°, 90°, and 180° radial lines respectively. Refer to LIU *et al.* (1995) and KÂNOĞLU and SYNOLAKIS (1998) for experimental details.

motion in numerical computations. Water-surface time histories were measured with 27 wave gages located around the perimeter of the island. One example is provided here and time histories of the surface elevation around the circular island are given at four locations (Fig. 14). Maximum runup heights around the perimeter of the island were measured at 24 locations (Fig. 15). Any numerical computation of two-dimensional runup should stably model two wave fronts that split in front of the island and collide behind it.

The conical island experiments provided runup observations for validating numerical models and supplemented comparisons with analytical results (KÂNOĞLU and SYNOLAKIS, 1998). The experiments are described in greater detail in LIU *et al.*, 1995; BRIGGS *et al.*, 1995; KÂNOĞLU, 1998; KÂNOĞLU and SYNOLAKIS, 1998.

Complex three-dimensional runup on a cove; Monai Valley: 2+1 numerical computations should also be benchmarked with the laboratory model of Monai Valley,
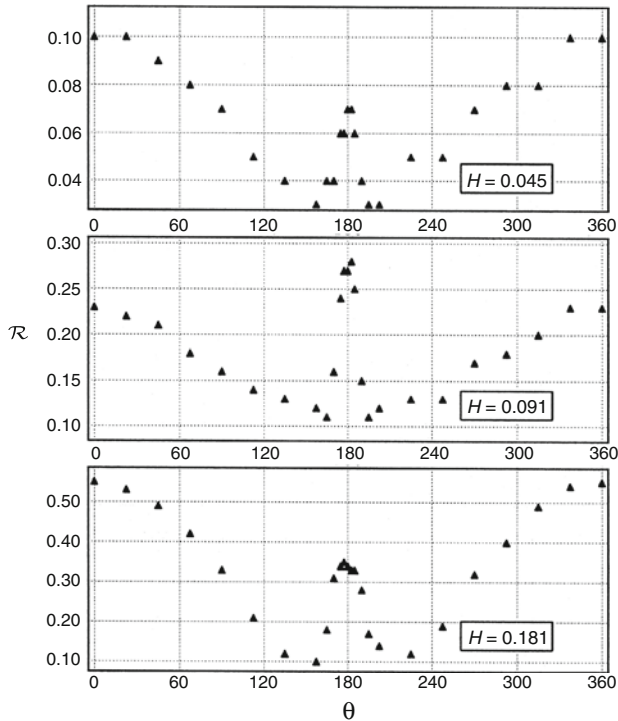
Figure 15
Maximum runup heights from the laboratory data for three solitary waves $\tilde{H}/\tilde{d} = 0.045$, 0.091, and 0.181, $\tilde{d} = 32$ cm.

Okushiri Island, Japan. The Hokkaido–Nansei–Oki (HNO) tsunami of 1993 struck Okushiri resulting in 30 m extreme runup heights and currents of the order of 10–18 m/sec, (HOKKAIDO TSUNAMI SURVEY GROUP, 1993). The extreme tsunami runup mark was discovered at the tip of a very narrow gulley within a small cove at Monai. High resolution seafloor bathymetry existed before the event and, when coupled with bathymetric surveys following it, allowed meaningful characterization of the seafloor deformation that triggered the tsunami.

A 1/400 laboratory model closely resembles the actual bathymetry and topography of Monai Valley and was constructed in a 205-m-long, 6-m-deep, and 3.5-m-wide tank at the Central Research Institute for Electric Power Industry (CRIEPI) in Abiko, Japan (Fig. 16a). The incident wave from offshore was an LDN with a −2.5 cm leading-depression and a 1.6 cm crest following it (Fig. 16b). The vertical sidewalls were totally reflective. Waves were measured at 13 locations, as shown in Figure 16c for one location. Comparing model output for this benchmark with the laboratory data shows how well a given code performs in a rapid sequence of withdrawal and runup.

Three-dimensional landslide: Landslide wave generation remains the frontier of numerical modeling, particularly for subaerial slides. The latter not only involves the
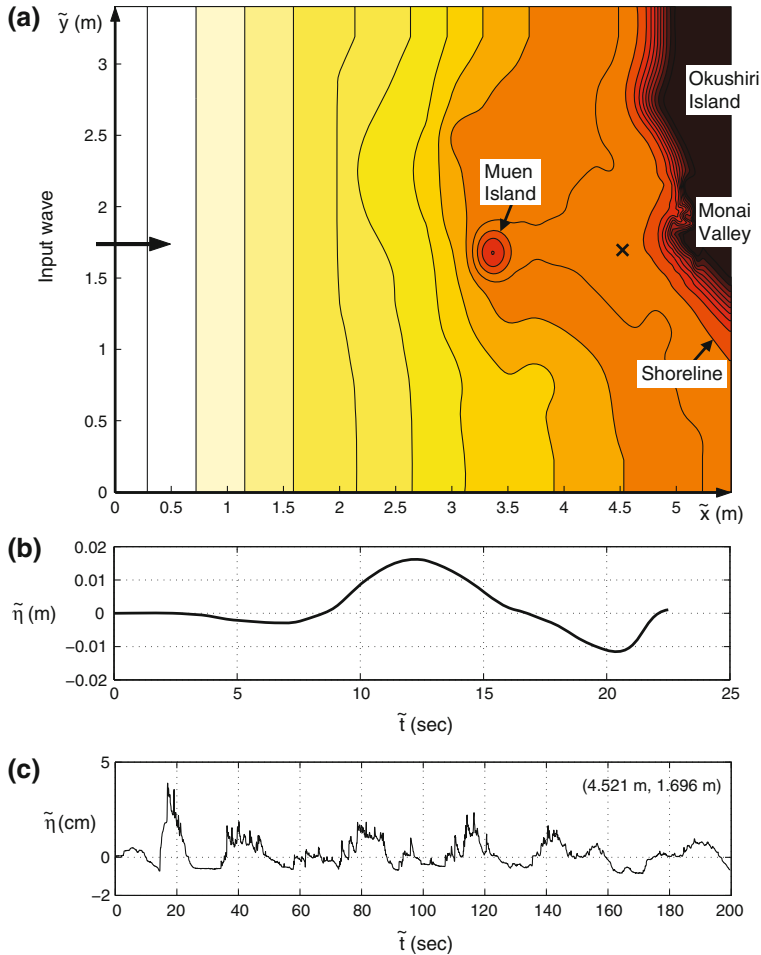
Figure 16
(a) Bathymetric and topographic profile for the Monai Valley experimental setup. Light to dark shading shows deep to shallow depth. Not to scale. (b) Input wave profile. (c) Time series of surface elevation at (4.521 m, 1.696 m).

rapid change of the seafloor, but also the impact with the still water surface. Numerical codes that will be used to model subaerial-landslide triggered tsunamis need to be tested against three-dimensional landslide benchmarks.

Large-scale experiments have been conducted in a wave tank with a 104-m-long, 3.7-m-wide, and 4.6-m-deep wave channel with a plane slope (1:2) located at one end of the tank; part of the experimental setup is shown in Figure 17, after RAICHLEN and SYNOLAKIS (2003). A solid wedge was used to model the landslide. The triangular face had a horizontal length of 91 cm, a vertical face with a height of 45.5 cm, and a width of 61 cm (Fig. 17). The horizontal surface of the wedge was initially positioned either a short
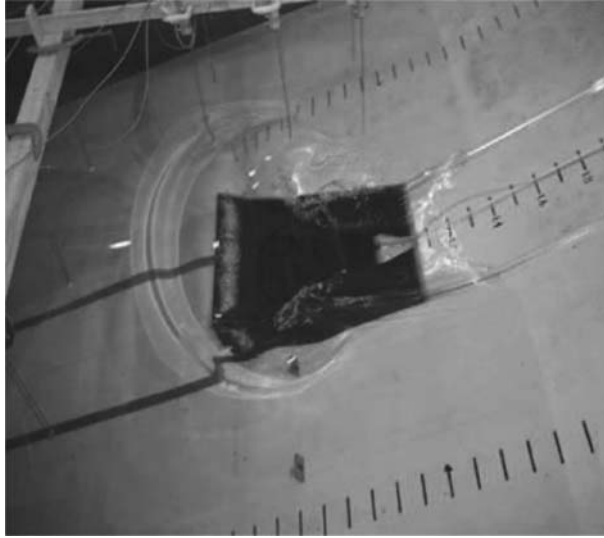
Figure 17
A picture of part of the experimental setup. After RAICHLEN and SYNOLAKIS (2003).
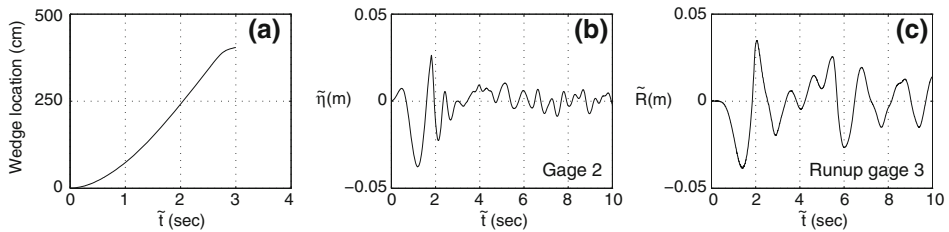

Figure 18
(a) Time histories of the block motion, (b) time histories of the surface elevation, and (c) runup measurements
for the submerged case with $\Delta = -0.1$ m. Gage 2 and runup gage 3 are located approximately one wedge-width
away from the center cross-section, i.e., 0.635 m and 0.61 m, respectively. While gage 2 is located 1.245 m
away from the shoreline, the runup gage 3 is located at the shoreline. Refer to LIU *et al.* (2005) for details.

distance above or below the still water level to reproduce a subaerial or submarine
landslide. The block was released from rest, abruptly moving downslope under gravity,
rolling on specially designed wheels (with low friction bearings) riding on aluminum
strips with shallow grooves inset into the slope. The wedge was instrumented with an
accelerometer to measure the acceleration-time history and a position indicator to
independently determine the velocity and position time histories which can be used for
numerical modeling (Fig. 18).

A sufficient number of wave gages were used to determine the seaward propagating
waves, the waves propagating to either side of the wedge, and for the submerged case, the

water surface-time history over the wedge. In addition, the time history of the runup on the slope was accurately measured. Time histories of the surface elevations and runup measurements for the case with submergence $\Delta = -0.1$ m are presented in Figure 18. A total of more than 50 experiments with moving wedges, hemispheres, and paralleliped bodies were conducted, and the wedge experiments were used as benchmark tests in the 2004 Catalina Island, Los Angeles, California workshop (LIU *et al*., 2008). Details and more experimental results can be found in RAICHLEN and SYNOLAKIS (2003) and LIU *et al*. (2005).

2.2.3 Field data benchmarking. Verification of any model in a real-world setting is essential, after all computations are presumed to model geophysical reality, especially for operational models. Benchmark testing is a necessary but not a sufficient condition. The main challenge of testing a model against real-world geophysical data is to overcome the uncertainties inherent in the definition of the tsunami source. While the source of the wave is deterministic in the controlled setting of the laboratory experiment and can usually be reproduced with precision in computations, the initialization of the numerical computation of a prototype tsunami is not as well constrained. It has not been uncommon for modelers to introduce ad hoc amplification factors in standard source solutions a la OKADA (1985) to obtain better agreement between their runup predictions and observations. Clearly such comparisons are circuitous, and fortunately with the further deployment of DART buoys—tsunamographs—they will be obsolete. For tsunamis, deep-ocean measurements (BERNARD *et al*., 2006) are the most unambiguous data quantifying the source of a tsunami. One example of tsunami source quantification through deep-ocean measurements is given in WEI *et al*. (2008).

No DART buoys—tsunameters—existed in the Indian Ocean at the time of the megatsunami, since DART buoys then had only been deployed in the Pacific Ocean. Satellite altimetry measurements of the Indian Ocean tsunami provide insufficient quality and coverage to constrain the tsunami source. Hydrodynamic inversion remains an ill-posed problem and criteria for its regularization are lacking. Hence, the 2004 event is not as yet one of the better operational benchmarks in terms of forecasting inundation, given the still raging debate as to the details of the seafloor deformation.

Deep-ocean measurements allow for more defensible inversions, since they are not affected by local coastal effects. Several events have been recorded by both deep-ocean and coastal gages in the Pacific and allow reasonably constrained comparison with models. The expanded DART system array will be providing more tsunami measurements for future events, expanding the library of well-constrained propagation scenarios for model verification. NOAA's National Geophysical Data Center (http://www.ngdc.noaa.gov/hazard/tsu.shtml), NOAA's Tsunami Warning Centers (http://www.prh.noaa.gov/ptwc/ and http://wcatwc.arh.noaa.gov/), and NOAA's Center for Tsunami Research (http://nctr.pmel.noaa.gov/) websites provide updated information on the latest tsunami data. Here, we first present field data for the 1993 HNO tsunami then
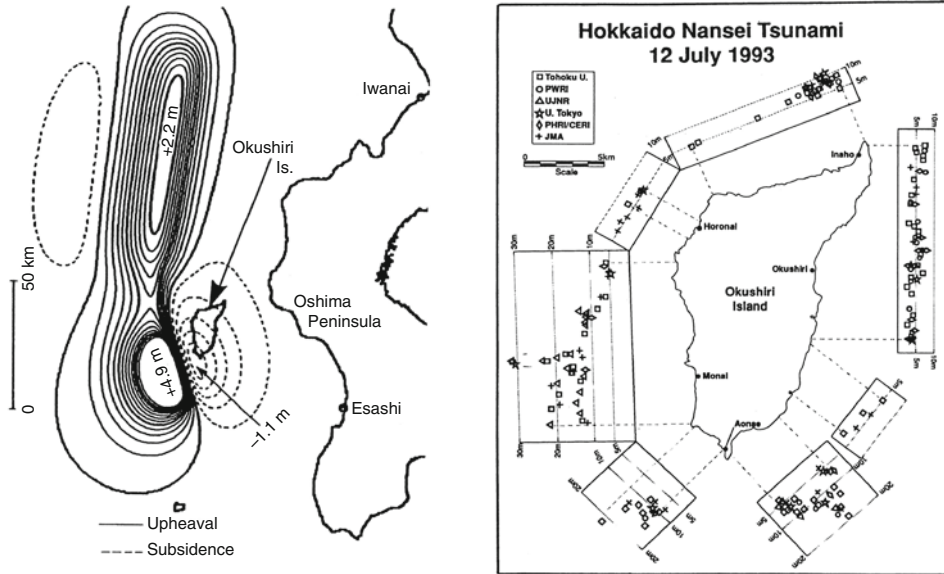
Figure 19

(Left inset) Fault plane constructed by the Disaster Control Research Center, Japan. (Right inset) Maximum runup measurements around Okushiri Island. Refer to TAKAHASHI (1996) for details.

present the data used for the first real-time model forecast test as an example of data which might be used for model verification.

Okushiri Island: 2+1 numerical computations should be tested with the field runup measurements from the HNO tsunami around Okushiri, Japan. The bathymetry data set and the initial condition formulated a benchmark problem for the 2nd International Long-Wave Runup Models Workshop and are thoroughly explained in TAKAHASHI (1996). The magnitude $M_s = 7.8$ HNO earthquake occurred on 12 July, 1993 with a depth of 37 km hypocenter located off the southwestern coast of Hokkaido. There are several field observations which need to be explained by numerical modeling. First, the computation should estimate the wave arrival at Aonae 5 min after the earthquake. The numerical model should generate two waves at Aonae approximately 10 min apart; with the first wave arriving from the west and the second from the east. In addition, the tide gage records as presented in TAKAHASHI (1996) need to be estimated. Maximum runup predictions should then be compared with the measurements (Fig. 19). The runup high at Hamatsumae, east of Aonae needs to be illustrated, as the locale is sheltered against the direct attack of the tsunami by Aonae point.

The Rat Islands tsunami: For operational codes, benchmark testing should invert the tsunameter signal of the 17 November, 2003 Rat Islands tsunami to improve the initial estimate of sea-surface displacement derived from a seismic deformation model. It should then use the results as input to a Hilo, Hawaii inundation model to hindcast the tide gage
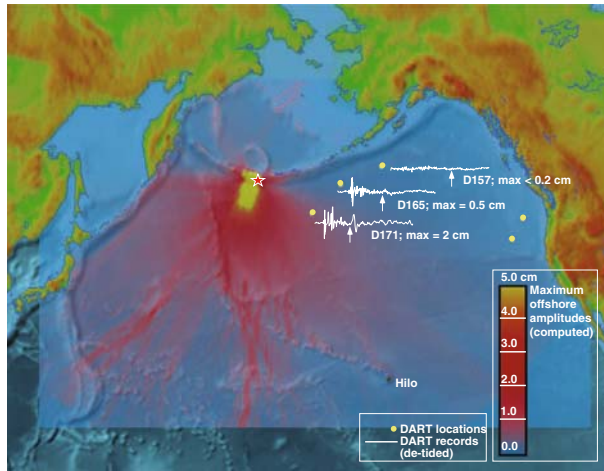
Figure 20

Propagation of the 17 November, 2003 Rat Islands tsunami. Star indicates epicenter location of the earthquake. Yellow dots are locations of DART buoys. White lines near the DART locations show recorded tsunami signal (detided) at corresponding tsunameter, arrows indicate tsunami arrival on the recordings. Filled colors show example of computed maximum tsunami amplitudes of a model propagation scenario.

record observed during the tsunami at Hilo. This is the most difficult but most realistic test for any operational model, for it involves a forecast (now hindcast) and needs to be done much faster than real time.

The magnitude $M_w = 7.8$ parent earthquake was located near Rat Islands, Alaska. This tsunami was detected by three tsunameters located along the Aleutian Trench and was also recorded at many coastal locations (Titov *et al.*, 2005). The combined use of tsunami propagation and inundation models is required for simulation of tsunami dynamics from generation to inundation. The test requires matching the propagation model data with the DART recording to constrain the tsunami source model (Fig. 20). If a finite-difference method on a structured grid is used, several nested numerical grids would allow *telescoping* from a coarse-resolution propagation model into a high-resolution inundation model with a model grid of at least 50 m resolution. If an unstructured grid method is used, a single grid may include enough resolution near the coast. The data-constrained propagation model should drive a high-resolution inundation model of Hilo Harbor. The inundation model being tested should reproduce the tide gage record at Hilo (Fig. 21). Since this benchmarking is required for the forecasting models, it is essential to model four hours of Hilo Harbor tsunami dynamics in 10 min of computational time.

2.3. *Scientific Evaluation*

Peer-review documentation: Any model used for inundation mappings or operational forecasts must be published in peer-reviewed scientific journals. One or more of these
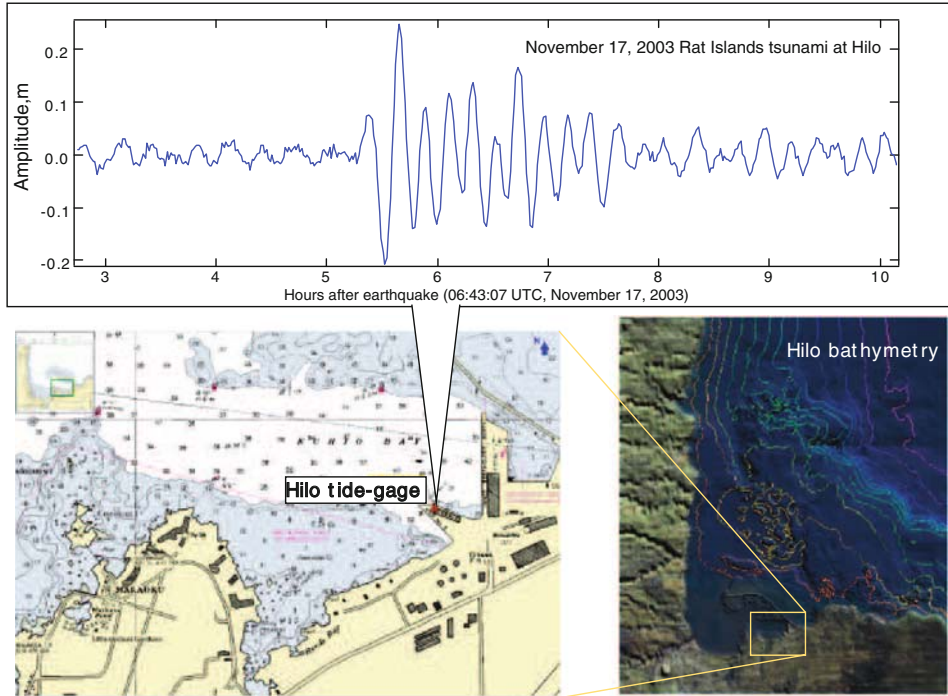
Figure 21
Location of Hilo tide gage and the recording of the 17 November, 2003 Rat Islands tsunami.

publications should include either the benchmark comparisons described here or their equivalents. However, it must be stressed that a single comparison is not sufficient.

Formal scientific evaluation: To identify best available practices and set standards based on these practices, a formal evaluation process of individual models needs to be established. This process may include solicitation of additional reviews of the model's veracity by experts.

2.4. *Operational Evaluation*

To ensure consistency in interpretation, the same model(s) should be used to produce inundation map and operational forecast products. If a tsunami inundation model is under consideration to generate operational forecast products, then an additional evaluation should be conducted to determine the suitability of the model for operational applications. This evaluation should be conducted in a test-bed environment consisting of research and operational parts, in order to assess a number of model features that bear on important operational factors, such as special implementation hardware/software issues, ease of use, computation time, etc. In particular, the operational evaluation of

candidate models for real-time forecasting and inundation mapping should include the following steps:

Step 1—*Meet operational forecasting and inundation mapping requirements and objectives*: Operational requirements include: Basic forecasting and inundation computation; analysis and visualization tools; integration with operations (vs. separate, stand-alone applications); basic data assimilation techniques; computational resources needed to meet milestones; etc. If a candidate model does not meet specified forecasting or inundation mapping requirements and objectives, it should be rejected at this point.

Step 2—*Meet modular development requirements*: Various pieces of the forecast model must be developed in parallel, based on the overall objectives defined in step 1.

Step 3—*Meet test bed and model standards*: In this step, the candidate model is tested against operational standards, with special attention given to its ability to simulate previous major tsunamis with the required speed and accuracy. Based on these test results, forecast model development may return to step 2, proceed, or the candidate model may be rejected for operational use.

Step 4—*Meet operational testing requirements*: The candidate model is integrated into the operational setting for testing. Potential sources are defined and the model is tested in a forecasting mode on an operational platform. Graphical interfaces are developed and forecast models are applied to a few cases to test operational integration and important individual factors such as speed, accuracy, and reliability (see section 3). Operational testing and feedback is provided by the TWCs at this point, and adjustments are made as necessary.

Step 5—*Implement operationally*: The model is fully integrated into the operational setting and procedures.

3. Criteria for Evaluating Operational Forecasting and Inundation Mapping Models

Given the accumulated experience in the tsunami community in the past 50 years, it is now possible to describe the requirements for an ideal tsunami model. Given an earthquake fault mechanism and tsunameter data, the ideal model should satisfactorily predict tsunami inundation at-risk coastlines in a sufficiently short time. Sufficiently short is defined as any time interval between the initiation of the tsunami and the calculation of the inundation forecast that allows for evacuation of the target communities. For example, the State of Hawaii needs about three hours for a complete and orderly evacuation. An ideal model would accurately forecast inundation at least three hours before the tsunami impact is expected anywhere in Hawaii.

3.1. Model Computational Time Constraints

Computational speed standards for inundation mapping and real-time forecasting are different. Inundation mapping can safely be conducted over months. An effective

short-term forecast must be produced faster than real-time. It should be available a few minutes before the tsunami strikes the nearest community, to allow sirens to trigger the evacuation of beach and coastal residents and give emergency personnel time to mobilize resources and prepare for search and rescue. Furthermore, a forecast must correctly predict the duration of the series of waves that comprise the tsunami event, to identify when it will be safe for search and rescue operations to begin without endangering the lives of responders. Tsunamis often became trapped in closed bays or on the continental shelf, resulting in sea-level oscillations that may persist for several hours. During the 1993 HNO tsunami, bay oscillation at Aonae trapped the tsunami for over 30 min, and a large portion of Aonae remained submerged for much of this time. The Crescent City, California harbor oscillated for several hours following the 15 November, 2006 tsunami (USLU *et al.*, 2007).

3.2. *Model Accuracy Constraints*

The accuracy of any given model depends on how well the computational procedure represents the correct solution of the parent equations of motion. When exact solutions exist (as, for example, for certain cases of the LSW and NSW equations), the determination of the accuracy of a solution algorithm is straightforward, i.e., through comparisons of the numerical results with the analytical predictions. Determining maximum runup numerically within 5% of the analytical solution is now possible with a handful of models.

For most bathymetries of geophysical interest, analytical solutions do not exist, and it is unlikely that they will ever be determined, due to the complexity of the physical terrain. However, a few laboratory models at smaller scale than the prototype exist. The Catalina Island, Los Angeles, 2004 model validation workshop of the National Science Foundation identified a handful of models that could predict the laboratory measurements within 10%. While greater compliance with measurements is hoped for in the next decade, 10% accuracy with respect to laboratory experiments is achievable now and should be considered a standard. In addition, for operational forecast models, propagation accuracy of 10% and an error in estimating arrival times for farfield events of 3 min, both are now possible (TITOV *et al.*, 2005).

An associated accuracy constraint is grid resolution. This depends on the complexity of the shoreline. On a fairly plane, wide, and very long beach such as those of Southern California, a 100-m-grid resolution may be sufficient. The smallest offshore and onshore features likely to affect tsunami impact on a coastal community should be reflected in the numerical grids. If a community is fronted by a sand spit of width 100 m, at least four grid points are needed to provide accurate resolution of the flow over the spit.

We emphasize again that laboratory and analytical benchmarks are necessary but not sufficient conditions for confidence for extrapolation of the methodology at geophysical scales. One example is wave-breaking. While a numerical model may realistically approximate the solution of the Navier–Stokes equations at laboratory scales, it may not do

so at large scales. Calculating the evolution of breaking waves involves calculating turbulent shear terms and invoking turbulence closure constraints which are scale-dependent. Therefore a reliability constraint needs to be applied, and this is discussed next.

3.3. Model Reliability and Reality Constraints

Model reliability refers to how well a given model predicts inundation consistently and realistically at geophysical scales. Linear theory may predict wave evolution consistently, but not always realistically. For example, linear theory predicts that the height of shoaling waves will grow continuously; in reality, however, waves will eventually break, if they exceed threshold height-to-depth and height-to-wavelength ratios.

Reliability is a crucial issue. Several widely-used numerical models include *ad hoc* friction factors. These factors were not developed to model the physical manifestation of frictional dissipation but to stabilize what is by its very nature a marginally stable computation. It is therefore not possible to know *a priori* how well a model that has been fairly successful in a small number of cases performs in general. For example, a model developed and calibrated to provide stable computations along steep coastlines for which inundation distances are less than 200 m may not perform equally well when forecasting inundation penetration of more than 3 km inland, as in the case of Banda Aceh during the 26 December, 2004 Boxing Day tsunami.

Clearly, any numerical model must be tested over a variety of scales from the laboratory to prototype to ensure both reliability and realism. Ideally, inundation models should be continuously tested with every new set of laboratory data or tsunami field data that becomes available. This will also allow for their further improvement.

4. Conclusions

State-of-the-art inundation codes in use today have evolved through a painstaking process of careful validation and verification. Operational forecast models based on these codes have been developed through extensive additional verification with measurements from real tsunamis. Mining this experience, procedures for approval and application of numerical models for operational uses are proposed as: establishment of standards for model validation and verification; scientific evaluation of individual models; operational evaluation of individual models; development of operational applications for forecasting; and procedures for transfer of technology to operations. Only through parallel testing of models under identical conditions, as when there is a tsunami emergency and an operational forecast is performed, can the community determine the relative merits of different computational formulations, an important step to further improvements in speed, accuracy, and reliability.

NOAA has adopted the standards and procedures discussed here for the development and evaluation of operational models for the Pacific and the West Coast/Alaska TWCs

(Synolakis *et al.*, 2007; http://nctr.pmel.noaa.gov/benchmark/). In addition to NOAA, UNESCO's Intergovernmental Coordination Group (ICG) for the Indian Ocean Tsunami Warning and Mitigation System (ICG/IOTWS) adapted a similar document based on Synolakis *et al.* (2007) during its fourth session at Mombasa, Kenya on 28 February–2 March, 2007 with additional field benchmarking for Sumatra, 26 December, 2004; Nias, 28 March, 2005; Tonga, 3 May, 2006; and Java, 17 July, 2006 events. Also, again UNESCOs ICG for the Northeastern Atlantic, the Mediterranean and Connected Seas Tsunami Early Warning and Mitigation System (ICG/NEAMTWS) is considering adoption of a similar document as well.

It is again emphasized that model testing must be a continuous process. Operational products produced in real time during an actual event must be thoroughly reviewed, and the operational models must be systematically tested in hindcast mode after each tsunami strike. The results must be documented and reported to the community in order to develop and implement improvement through the identification and resolution of any serious problems or inadequacies of the models and/or products. While this process may appear onerous, it does reflect our current state of scientific knowledge. This process is thus the only defensible methodology when human lives are at stake.

Acknowledgements

References

Associated Press (2005), *New analysis boosts potential tsunami threat*, December 7, 2005. http://www.kgw.com/sharedcontent/APStories/stories/D8EBN7NO7.html.

Bernard, E.N., Mofjeld, H.O., Titov, V., Synolakis, C.E., and González, F.I. (2006), *Tsunami: Scientific frontiers, mitigation, forecasting, and policy implications*, Philos. T. R. Soc. A *364*, 1989–2007.

Borerro, J., Ortiz, M., Titov, V.V., and Synolakis, C.E. (1997), *Field survey of Mexican tsunami*, EOS Trans. Amer. Geophys. Un. *78*(8), 85, 87–88 (Cover article).

Briggs, M.J., Synolakis, C.E., Harkins, G.S., and Green, D. (1995), *Laboratory experiments of tsunami runup on a circular island*, Pure Appl. Geophys. *144*, 569–593.

Carrier, G.F. and Greenspan, H.P. (1958), *Water waves of finite amplitude on a sloping beach*, J. Fluid Mech. *17*, 97–110.

Carrier, G.F., Wu, T.T., and Yeh, H. (2003), *Tsunami runup and drawdown on a sloping beach*, J. Fluid Mech. *475*, 79–99.

ETHNOS (2007), *Predictions for earthquakes and tsunamis*, http://www.ethnos.gr/article.asp?catid=11386&subid=2&pubid=139228.

GORING, D.G. (1978), *Tsunamis—the propagation of long waves onto a shelf*, W.M. Keck Laboratory of Hydraulics and Water Resources, California Institute of Technology, Pasadena, California. Report No. KH-R-38.

GRILLI, S.T., SVENDEN, I.A., and SUBRAYAMA, R. (1997), *Breaking criterion and characteristics of solitary waves on a slope*, J. Waterw. Port Coast. Ocean Eng. *123*(2), 102–112.

HALL, J.V. and WATTS, J.W. (1953), *Laboratory investigation of the vertical rise of solitary waves on impermeable slopes*, Tech. Memo. 33, Beach Erosion Board, U.S. Army Corps of Engineers, 14 pp.

HAMMACK, J.L. (1972), *Tsunamis—A model for their generation and propagation*, W.M. Keck Laboratory of Hydraulics and Water Resources, California Institute of Technology, Pasadena, California, Report No. KH-R-28.

HOKKAIDO TSUNAMI SURVEY GROUP (1993), *Tsunami devastates Japanese coastal region*, EOS Trans. Amer. Geophys. Un. *74*(37), 417 and 432.

KÂNOĞLU, U. (1998), *The runup of long waves around piecewise linear bathymetries*, Ph.D. Thesis, University of Southern California, Los Angeles, California, 90089–2531, 273 pp.

KÂNOĞLU, U. (2004), *Nonlinear evolution and runup–rundown of long waves over a sloping beach*, J. Fluid Mech. *513*, 363–372.

KÂNOĞLU, U. and SYNOLAKIS, C.E. (1998), *Long wave runup on piecewise linear topographies* J. Fluid Mech. *374*, 1–28.

KÂNOĞLU, U. and SYNOLAKIS, C. (2006), *Initial value problem solution of nonlinear shallow water-wave equations*, Phys. Rev. Lett. *97*, 148501.

KELLER, J.B. and KELLER, H.B. (1964), *Water wave runup on a beach*, ONR Research Report NONR-3828(00), Department of the Navy, Washington DC, 40 pp.

LI, Y. and RAICHLEN, F. (2000), *Energy balance model for breaking solitary wave runup*, J. Waterw. Port Coast. Ocean Eng. *129*(2), 47–49.

LI, Y. and RAICHLEN, F. (2001), *Solitary wave runup on plane slopes*, J. Waterw. Port Coast. Ocean Eng. *127*(1), 33–44.

LI, Y. and RAICHLEN, F. (2002), *Non-breaking and breaking solitary runup*, J. Fluid Mech. *456*, 295–318.

LIU, P.L.-F., CHO, Y.-S., BRIGGS, M.J., KÂNOĞLU, U., and SYNOLAKIS, C.E. (1995), *Runup of solitary waves on a circular island*, J. Fluid Mech. *320*, 259–285.

LIU, P.L.-F., LYNETT, P., and SYNOLAKIS, C.E. (2003), *Analytical solutions for forced long waves on a sloping beach*, J. Fluid Mech. *478*, 101–109.

LIU, P.L.-F., WU, T.-R., RAICHLEN, F., SYNOLAKIS, C.E., and Borrero, J. (2005), *Runup and rundown generated by three-dimensional sliding masses*, J. Fluid Mech. *536*, 107–144.

LIU, P.L.-F., YEH, H., and SYNOLAKIS, C. (eds.), *Advanced Numerical Models for Simulating Tsunami Waves and Runup*, In *Advances in Coastal and Ocean Engineering 10* (World Scientific, Singapore 2008).

MEI, C. C., *The Applied Dynamics of Ocean Surface Waves* (Wiley, New York, NY 1983).

NATIONAL SCIENCE and TECHNOLOGY COUNCIL (2005), *Tsunami Risk Reduction for the United States: A Framework for Action*, A joint report of the subcommittee on Disaster Reduction and the United States Group on Earth Observations, 30 pp.

NEW SCIENTIST (2005), *Heaving seabed triggered Asian tsunami*, December 10, 2005. http://seattle-times.nwsource.com/html/localnews/2002668973_tsunami07m.html.

OKADA, Y. (1985), *Surface deformation due to shear and tensile faults in a half-space*, Bull. Seismol. Soc. Am. *75*, 1135–1154.

PEDERSEN, G., *A Lagrangian model applied to runup problems*. In *Advanced Numerical Models for Simulating Tsunami Waves and Runup* (eds. Liu, P.L.-F., Yeh, H., and SYNOLAKIS, C.), In *Advances in Coastal and Ocean Engineering 10* (World Scientific, Singapore 2008).

PEDERSEN, G. and GJEVIK, B. (1983), *Runup of solitary waves*, J. Fluid Mech. *135*, 283–299.

RAICHLEN, F. and SYNOLAKIS, C.E. (2003), *Runup from three- dimensional sliding masses*, Proc. *Long Waves Symposium*, Thessaloniki, Greece (eds. M. Briggs, and Ch. Koutitas), pp. 247–256.

SATAKE, K., OKAL, E.A. and BORRERO, J.C. (2007), *Tsunami and its hazard in the Indian and Pacific Oceans: Introduction*, Pure Appl. Geophys. *164*(2-3), 249-259.

SHUTO, N. (1973), *Shoaling and deformation of nonlinear waves*, Coastal Eng. Japan *16*, 1–12.

SYNOLAKIS, C.E. (1986), *The Runup of Long Waves*, Ph.D. Thesis, California Institute of Technology, Pasadena, California, 91125, 228 pp.

Synolakis, C.E. (1987), *The runup of solitary waves*, J. Fluid Mech. *185*, 523–545.

Synolakis, C.E. (1991), *Green law and the evolution of solitary waves*, Phys. Fluids A-Fluid Dynamics *3*, 490-491.

Synolakis, C.E. and Skjelbreia, J.E. (1993), *Evolution of maximum amplitude of solitary waves on plane beaches*, J. Waterw. Port Coast. Ocean Eng. *119*(3) 323–342.

Synolakis, C.E. and Okal, E.A. (2005), *1992–2002: Perspective on a decade of post-tsunami surveys*, Adv. Nat. Technol. Hazards *23*, 1-30.

Synolakis, C.E. and Bernard, E.N. (2006), *Tsunami science before and after Boxing Day 2004*, Phil. Trans. R. Soc. A *364*(1845), 2231–2265.

Synolakis, C.E. and Kong, L. (2006), *Runup measurements of the December 2004 Indian Ocean Tsunami*, Earthq. Spectra *22* (Suppl. 3), S67-S91.

Synolakis, C.E., Bernard, E.N., Titov, V.V., Kânoğlu, U., and González, F. (2007), Standards, criteria, and procedures for NOAA evaluation of tsunami numerical models. NOAA OAR Special Report, Contribution No 3053, NOAA/OAR/PMEL, Seattle, Washington, 55 pp.

Tadepalli, S. and Synolakis, C.E. (1994), T*he runup of N-waves on sloping beaches*, Proc. R. Soc. Lond. A. *445*, 99–112.

Tadepalli, S. and Synolakis, C.E. (1996), *Model for the leading waves of tsunamis*, Phys. Rev. Lett. *77*(10), 2141–2144.

Takahashi, T., *Benchmark problem 4; the 1993 Okushiri tsunami—Data, conditions and phenomena*. In *Long-Wave Runup Models* (eds. Yeh, H., Liu, P.L.-F., and Synolakis, C.E.) (World Scientific Publishing, Singapore 1996) pp 384–403.

The Seattle Times (2005), *Tsunami expers forecast raises a flag*, December 7, 2005, http://seattle-times.nwsource.com/html/localnews/2002668973_tsunami07m.html.

Titov, V.V. and Synolakis, C.E. (1995), *Modeling of breaking and nonbreaking long-wave evolution and runup using VTCS-2*, J. Waterw. Port Ocean Coast. Eng. *121*(6), 308–316.

Titov, V.V. and González, F.I. (1997), *Implementation and testing of the method of splitting tsunami (MOST)*, NOAA Technical Memorandum ERL-PMEL-112, PB98-122773, Pacific Marine Environmental Laboratory, Seattle, Washington, 11 pp.

Titov, V.V. and Synolakis, C.E. (1997), E*xtreme inundation flows during the Hokkaido–Nansei–Oki tsunami*, Geophys. Res. Lett. *24*(11), 1315–1318.

Titov, V.V. and Synolakis, C.E. (1998), *Numerical modeling of tidal wave runup*, J. Waterw. Port Ocean Coast. Eng. *124*(4), 157–171.

Titov, V.V., González, F.I., Bernard, E.N., Eble, M.C., Mofjeld, H.O., Newman, J.C., and Venturato, A.J. (2005), *Real-time tsunami forecasting: Challenges and solutions* Nature Hazard *35*(1), 41–58.

Tuck, E.O. and Hwang, L.S. (1972), *Long-wave generation on a sloping beach*, J. Fluid Mech. *51*, 449–461.

Uslu, B., Borrero, J.C., Dengler, L.A., and Synolakis, C.E. (2007), *Tsunami inundation at Crescent City, California generated by earthquakes along the Cascadia Subduction Zone*, Geophys. Res. Lett. *34*, L20601.

Wei, Y., Bernard, E.N., Tang, L., Weiss, R., Titov, V.V., Moore, C., Spillane, M., Hopkins, M., and Kânoğlu, U. (2008), *Real-time experimental forecast of the Peruvian tsunami of August 2007 for U.S. coastlines*, Geophys. Res. Lett *35*, L04609.

Yeh, H., Liu, P.L.-F., Briggs, M., and Synolakis, C.E. (1994), *Tsunami catastrophe in Babi Island*, Nature *372*, 6503–6508.

Yeh, H., Liu, P.L.-F., and Synolakis, C.E. (eds.), *Long-Wave Runup Models* (World Scientific Publishing, Singapore 1996).

Zelt, J.A. (1991), *The runup of breaking and nonbreaking solitary waves*, Coastal Eng. *125*, 205–246.

To access this journal online:
www.birkhauser.ch/pageoph

▌Pure and Applied Geophysics

An Efficient and Robust Tsunami Model on Unstructured Grids. Part I: Inundation Benchmarks

Yinglong J. Zhang[1] and António M. Baptista[1]

Abstract—A modern multi-purpose baroclinic circulation model (SELFE) has been recently extended to include the ability to simulate tsunami propagation and inundation. The core model is based on the 3-D nonlinear shallow-water wave (NSW) equations, which are solved on unstructured grids, using the finite-element method. A semi-implicit method is used to solve all equations to enhance numerical stability, thus bypassing the most stringent CFL restriction on the time step. Further aided algorithmically by an Eulerian-Lagrangian solution of the advection terms in the momentum equation and by a simple yet effective inundation algorithm, SELFE is very efficient and robust in both quasi-2-D (with two vertical layers) and 3-D modes. A quasi-2-D version of the model is being used to update and expand the characterization of tsunami hazards along the Oregon coast. As a part of a rigorous testing procedure that includes multiple types of coastal problems, we present in this paper a quantitative assessment of performance of the quasi-2-D SELFE for two challenging open benchmark problems proposed in the 3rd International Workshop on Long-wave Runup Models. Satisfactory results are obtained for both problems.

Key words: Tsunami inundation, cross-scale modeling, finite elements, semi-implicit model, Eulerian-Lagrangian Method.

1. Introduction

The Indian Ocean mega-tsunami of 2004 dramatically reinforced the importance of tsunami hazard assessment and mitigation, and challenged all involved communities to re-evaluate their strategies for a holistic analysis of risk.

In the United States, the State of Oregon has been pro-active in tsunami hazard assessment and mitigation since the early 1990s, when, in the wake of the Nicaragua and Okushiri tsunamis of 1992 and 1993, and prompted by newly found evidence of a tsunamogenic Cascadia Subduction Zone, the Oregon Department of Geology and Mineral Industries (DOGAMI) developed a state-wide tsunami hazard map (Priest, 1995). That work has been refined over the years through a series of local studies, leading progressively to highly detailed community-specific inundation maps that help coastal

[1] Science and Technology Center for Coastal Margin Observation and Prediction, Oregon Health & Science University, 20000 NW Walker Road, Beaverton, OR 97006, U.S.A. E-mail: yinglong@stccmop.org
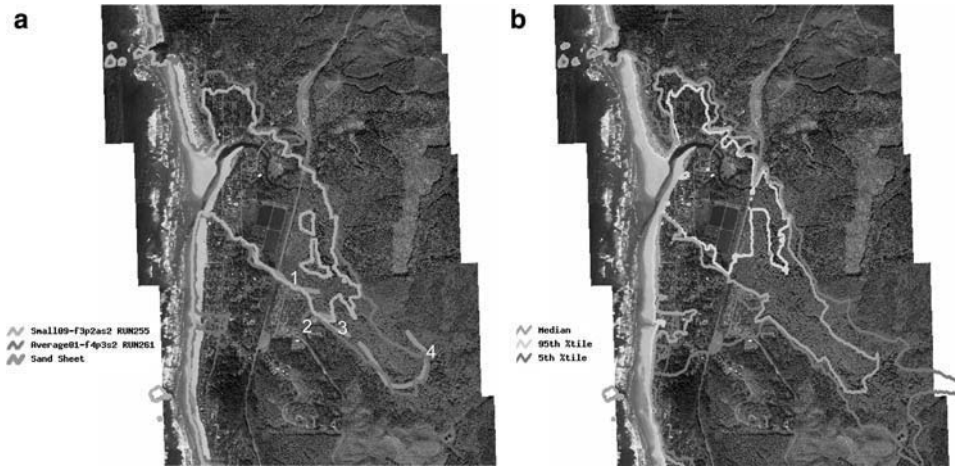
Figure 1

(a) Paleo-tsunamis on Cannon Beach, Oregon. The four sand sheets were collected by Dr. Rob Witter of DOGAMI and indicate the minimum extent of inundation due to past tsunami events. Sheets 1 and 2 are attributed to small events, and sheets 3 and 4 to average to large events. Also shown are the maximum inundation extent calculated using the model for typically small and average tsunami events on inferred paleo-landscapes around Cannon Beach. (b) Quasi-probabilistic inundation map for Cannon Beach, based on the results for 25 scenarios (8 cases each for average, large and largest events, plus 1 case for small events).

planners increase community preparedness, in part through education and raised awareness supported by evacuation maps and well-marked evacuation routes. Also, bridges have been upgraded based on perceived risk, and new critical infrastructure (such as hospitals and schools) has been located so as to minimize risk.

Recent tsunami studies in Oregon have been conducted with a multi-disciplinary approach that (a) attempts to characterize the underwater earthquake source based on best-available geological and seismic evidence, including but not limited to analyses of turbidite data (GOLDFINGER et al., 2003) and sand tsunami deposits contained in cored samples (WITTER et al., 2003; Fig. 1a); and (b) embraces a probabilistic concept of risk (Fig. 1b). A similar multi-disciplinary approach towards the probabilistic tsunami hazard analysis was also conducted at Seaside, Oregon by the TSUNAMI PILOT STUDY WORKING GROUP (2006). The combination of (a) and (b) entails hundreds of tsunami simulations, which could not be realistically accomplished by the numerical hydrodynamic model (ADCIRC; LUETTICH et al., 1991) that we have used over the past ten years to study the propagation and coastal inundation of Cascadia Subduction Zone (CSZ) tsunamis.

This led us to evaluate the potential of two very efficient 3-D circulation models (ELCIRC, ZHANG et al., 2004; and SELFE, ZHANG and BAPTISTA, 2008), developed in recent years to sustain advanced modeling within ocean observatories (BAPTISTA, 2006), as reference models for our tsunami studies. This is the first of a series of papers that report on the extension of these models to tsunami simulations. Our focus in this article is on inundation modeling, and in particular on benchmarking one of the models (SELFE)

against analytical and laboratory tests. We will report elsewhere on the results of the validation of the models against field data in the well documented 1993 Hokkaido-Nansei-Oki tsunami (MYERS and BAPTISTA, 1995; SHIMAMATO *et al.*, 1995), and on applications to Cascadia Subduction Zone tsunamis. As general cross-scale ocean models, SELFE and ELCIRC have also been cross-applied to a range of coastal margin processes, including characterization of 3-D estuarine and plume circulation, in which context they have been extensively validated against field data (BAPTISTA *et al.*, 2005; ZHANG and BAPTISTA, 2008).

The paper is organized as follows. After this introduction, we place the development of SELFE in context of the state-of-the-art in hydrodynamic modeling of tsunamis (Section 2). We then summarize the main SELFE physical and numerical formulations, including the new inundation algorithm (Section 3). Results from benchmarking SELFE with two challenging initial- and boundary-value problems are presented in Section 4. Conclusions and road maps for future work are presented in Section 5.

2. SELFE in Context of the State-of-the-Art of Tsunami Modeling

Over the past two decades tremendous progress has been made in numerical modeling of tsunamis, from its generation (source model) to propagation through the open ocean to final inundation on dry land (propagation and inundation model). Uncertainties exist in all stages of simulation, with arguably the largest occurring in the initial stage: The characterization of the earthquake/landslide source of the tsunami (WANG and HE, 1999; SYNOLAKIS and BERNARD, 2006). However, reducing errors in the propagation and inundation of the tsunami wave remains an important challenge, not only because of the need to improve the characterization/comparison of impacts for defined sources, but also to improve the ability to characterize sources post-event via inversion of sea-level data (arguably not a well posed problem without better propagation/inundation models; see SYNOLAKIS and BERNARD, 2006; WEI *et al.*, 2008).

Increasingly sophisticated methods have been proposed to tackle the high nonlinearity and supercritical flow as found in the propagation and, in particular, inundation processes. These models usually solve shallow-water wave equations (either linear (LSW) or nonlinear (NSW), in which the wave dispersion is neglected), or Boussinesq or Euler equations which incorporate dispersion effects, in 1-D, 2-D or 3-D. Smoothed Particle Hydrodynamics (SPH) also showed promise recently (DIAS and DUTYKH, 2007). Most popular models of the current generation are so-called "2 + 1" models (i.e., depth-averaged in space plus time evolution) based on the NSW equations. Among others, TITOV and SYNOLAKIS (1995) demonstrated that except in the wave-breaking region, the NSW formulation was able to accurately predict long wave runup. On the other hand, the NSW formulation may not be appropriate for dispersive waves as found in trans-oceanic and in many landslide-generated tsunamis (LIU *et al.*, 2005), for which a Boussinesq or Euler formulation may be necessary. BURWELL *et al.* (2007) presented an approach to use numerical dispersion to mimic physical dispersion.

With few exceptions, most current numerical tsunami models use the finite-difference method on structured rectangular grids (TITOV and SYNOLAKIS, 1995; LYNETT et al., 2002; YALCINER et al., 2002). A recent notable exception to finite differences was introduced by GEORGE and LEVEQUE (2006) and LEVEQUE and GEORGE (2007), who used a Godunov-type finite-volume method for enforcing conservation properties and obtained excellent results for some benchmark problems. In addition, they also proposed an adaptive mesh refinement strategy. However, the flux limiter used is one-dimensional in nature and its extension to the transverse direction is still problematic.

More than the use of finite differences, the general preference for structured grids is somewhat surprising. Indeed, the complex geometry and bathymetry/topography of coastlines are often responsible for many intriguing localized inundation patterns (e.g., the large runup in a narrow valley in the Okushiri Island in the 1993 Hokkaido-Nansei-Oki tsunami, see SHIMAMATO et al. (1995); Nicaragua tsunami, see BAPTISTA et al., 1993). The natural ability of structured grids to accurately resolve these important features is limited, and therefore various grid nesting or adapting approaches have been proposed to address localized refinement (VENTURATO et al., 2007; GEORGE and LEVEQUE, 2006). The proper imposition of boundary conditions at the interfaces between grids of various resolutions remains a challenging issue (VENTURATO et al., 2007).

By contrast, unstructured grids have the inherent ability to resolve complex geometry and bathymetry/topography. Yet, relatively few such models have been used on a sustained basis for practical tsunami propagation and inundation studies. An exception is ADCIRC (LUETTICH et al., 1991), a model that we adapted to tsunamis in the mid-1990s (MYERS and BAPTISTA, 1995, 1997, 2001; MYERS, 1998; MYERS et al., 1999). Originally written as a general circulation model, and based on the solution of the Generalized Wave-continuity equation (GWCE; LYNCH and WERNER, 1991) by finite elements on unstructured grids, ADCIRC has — in an interesting contrast between closely related fields — been extensively used in inundation studies for storm surges and hurricanes (WESTERINK et al., 2004).

Our experiences with ADCIRC as a tsunami propagation and inundation model were mixed. While the model was transformative in extensively mapping tsunami inundation in the Oregon coast (PRIEST, 1995; PRIEST et al., 1995, 1997a, 1997b, 1998, 1999a, 1999b, 2000, 2002, 2003; PRIEST and BAPTISTA 2000), some numerical limitations became apparent. Issues related to volume/mass conservation and to parasitic oscillations, due to the use of GWCE in lieu of the primitive momentum equations,[1] were particularly of concern. Also, numerical stability constraints forced very small time steps to be used, resulting in computational inefficiency. Finally, the inundation algorithm could lead to serious instabilities during the inundation in benchmark problems as described in the review paper by SYNOLAKIS and BERNARD (2006).

---

[1] Recently there has been some progress in incorporating the Discontinuous Galerkin Finite-Element method in ADCIRC in order to use the primitive equations; see KUBATKO et al. (2006). However, the efficiency problem remains an issue.

The recent development of a new generation of very efficient 3-D unstructured grid circulation models (such as UnTRIM, CASULLI and WALTERS, 2000; ELCIRC, ZHANG et al., 2004; SELFE, ZHANG and BAPTISTA, 2008; and FVCOM, CHEN et al., 2003), whose performance in realistic simulations of estuarine and coastal dynamics rivals or surpasses ADCIRC, has created the opportunity to revisit options available for unstructured grid modeling of tsunamis. The main goal of the present work is to introduce a tsunami propagation and inundation version of SELFE. Based on the finite-element solution of the primitive NSW equations, SELFE is hydrostatic, and hence is not currently suited for problems in which wave dispersion effects are important. Yet, the physics of SELFE is essentially the same as in MOST, a reference model used by NOAA in tsunami simulations worldwide and originally developed by TITOV and SYNOLAKIS (1995).

SELFE uses semi-implicit time stepping and treats the advection with an Eulerian-Lagrangian method (ELM; BAPTISTA, 1987), and therefore most stringent stability conditions (e.g., CFL) are bypassed, resulting in greater efficiency. The matrices in the model are all positive definite and symmetric, and very efficient solvers like the Conjugate Gradient (CG) method can be used with fast convergence guaranteed. The well-conditioning of the matrices and a simple yet effective inundation algorithm lead to great robustness of the model; only minimal instabilities are encountered near the wetting and drying interface, even without bottom friction and viscosity. Compared to ADCIRC, the new model is considerably more efficient, conserves volume and mass well, and suffers little from the parasitic oscillations. Therefore the model is well suited for realistic applications, including forecasting.

Since the original model was 3-D, and incorporates baroclinicity as well as realistic tidal and atmospheric forcings, the new tsunami model can simulate these effects in a straightforward fashion.[2] The importance of nonlinear interactions between tides and tsunami waves has been demonstrated in MYERS (1998). Three-dimensional effects are also important in landslide-generated tsunamis (LIU et al., 2005). However, better physical formulations (e.g., dispersion effects, small-scale turbulence etc.) may be needed in order to take full advantage of the 3-D model. These formulations will be considered in the future model.

3. Physical and Numerical Formulation of SELFE

The equations SELFE solves are the 3-D nonlinear shallow-water wave (NSW) equations, transport equations for salt and heat, and turbulence closure. Since only the barotropic model is used in this paper, the transport and turbulence closure equations are not included in this paper; however, we note that these are existing capabilities of the model. The equations used in the tsunami model are then:

---

[2] 3D tsunami simulations are inevitably expensive, but with the judicious use of unstructured grid and a parallel code that became available recently, the current model is able to do such simulations.

$$\nabla \cdot \mathbf{u} + \frac{\partial w}{\partial z} = 0 \tag{1}$$

$$\frac{\partial (\eta - b)}{\partial t} + \nabla \cdot \int_{-h}^{\eta} \mathbf{u} dz = 0 \tag{2}$$

$$\frac{D\mathbf{u}}{Dt} = \mathbf{f} - g\nabla\eta + \frac{\partial}{\partial z}\left(v\frac{\partial \mathbf{u}}{\partial z}\right);$$

$$\mathbf{f} = -f\mathbf{k} \times \mathbf{u} + \alpha g \nabla \hat{\psi} - \frac{1}{\rho_0}\nabla p_A - \frac{g}{\rho_0}\int_z^{\eta}\nabla\rho\, d\zeta + \nabla \cdot (\mu\nabla\mathbf{u}) \tag{3}$$

where

(x,y)	horizontal Cartesian coordinates, in $[m]$
z	vertical coordinate, positive upward, in $[m]$
∇	$\left(\frac{\partial}{\partial x}, \frac{\partial}{\partial y}\right)$
t	time $[s]$
$\eta(x, y, t)$	free-surface elevation, in $[m]$
$b(x,y,t)$	seabed displacement in $[m]$ (positive for uplift)
$h(x, y)$	bathymetric depth, in $[m]$
$\mathbf{u}(x, y, z, t)$	horizontal velocity, with Cartesian components (u,v), in $[ms^{-1}]$
w	vertical velocity, in $[ms^{-1}]$
f	Coriolis factor, in $[s^{-1}]$
g	acceleration of gravity, in $[ms^{-2}]$
$\hat{\psi}(\phi, \lambda)$	earth-tidal potential, in $[m]$
α	effective earth-elasticity factor
$\rho(\mathbf{x}, t)$	water density; by default, reference value ρ_0 is set as 1025 kgm^{-3}
$p_A(x, y, t)$	atmospheric pressure at the free surface, in $[Nm^{-2}]$
v	vertical eddy viscosity, in $[m^2\ s^{-1}]$
μ	horizontal eddy viscosity, in $[m^2\ s^{-1}]$

Comparing these equation to those in ZHANG and BAPTISTA (2008), the only difference is in Equation (2), where the bed deformation is included, and therefore the current model is capable of simulating the initial seabed movement during the earthquake. This is important because in real tsunamis the initial acceleration is very large despite the initial velocities being small, and therefore strictly speaking, an elevation field that mirrors the bed deformation with zero velocity everywhere is not the right initial condition (DUTYKH et al., 2006; KANOGLU and SYNOLAKIS, 2006). All equations have appropriate initial and boundary conditions.

Since a detailed description of the numerical formulation is given in ZHANG and BAPTISTA (2008), only a brief summary is given here. The horizontal domain is discretized into a series

of triangular elements (unstructured grid technique), and the vertical dimension is divided into layers. A semi-implicit finite-element method is used to solve the coupled continuity and momentum Equations (2) and (3); a key step is to decouple the two equations through the bottom boundary layer. The advection in Equation (3) is treated with ELM, which is explicit but unconditionally stable (BAPTISTA, 1987). A finite-volume method is used to solve the continuity Equation (1). The resulting matrices are all symmetric and positive-definite if a mild restriction is placed on the water depth (ZHANG and BAPTISTA, 2008), and therefore the numerical scheme is very efficient and robust. If the horizontal viscosity is not used, there is no stability constraint in the current model and large time steps could be used; however, a smaller time step is necessary to ensure accuracy because of the relatively short period for tsunami waves (WALTERS, 2005) and the highly nonlinear inundation process.

As regards the tsunami simulation, we found that one of the most critically important issues is related to the inundation algorithm. The wetting and drying process can be treated in a relatively straightforward fashion based on the water depths in SELFE (ZHANG and BAPTISTA, 2008). The challenges of the inundation algorithm and the solution thereof will be detailed in the following subsection.

3.1. Inundation Algorithm

The inundation process as found in typical tsunamis is a highly complex and nonlinear moving-boundary problem, and some processes such as overland flow, scoured sediments and wave breaking have not been fully understood. However, for practical estimates of inundation extent and maximum wave runups, TITOV and SYNOLAKIS (1995) showed that NSW formalism gives remarkably good results. From a numerical viewpoint, while a moving/adaptive grid is conceptually more efficient in capturing the moving shoreline (e.g., HUBBARD and DODD (2002) proposed a hierarchical Cartesian Adaptive Mesh Refinement (AMR) algorithm that largely bypassed the need for tracking the shoreline), it does pose some robustness issues as the flow is supercritical near the wetting and drying interface (VENTURATO et al., 2007). Therefore we use fixed meshes, and in doing so preclude partial wetting and drying in an element. This drawback is remedied by using high resolution near the wetting and drying interfaces, which is made possible by judicious use of an unstructured grid.

The inundation algorithm used in SELFE is intuitive and relatively straightforward. At the beginning of each time step, the interfaces (or shorelines) between wet and dry regions are computed. Then at the end of that time step, each node on the interfaces is examined in turn to determine if the interface there needs to be advanced or retreated. The interfaces are then updated and the process is repeated until new interfaces are found. The procedure is summarized as follows:

1. Compute wet/dry interfaces (Γ^n) at time step n (Fig. 2a);
2. At the end of time step $n + 1$, go through and examine all interfacial nodes on Γ^n.
   If a node (say, A) is surrounded by wet elements (with all nodes being wet-based on

newly computed elevations), the local interface line is advanced into the dry region, and the velocity at the center of the dry side is calculated as the average of the adjacent sides (Fig. 2b). If one or more elements surrounding a node (say, B) are dry (based on newly computed elevations), the local interface line is retreated towards the wet region;

3. Update interface lines based on the results from step 2, and iterate until the final interface lines at the step $n + 1$ (Γ^{n+1}) are found (Fig. 2c);
4. Go through all nodes on Γ^{n+1}, and do constant extrapolation of the elevations into the dry region (e.g., elevation(A'') = elevation(A')) if the total volume flux from the adjacent sides on the interface is into the dry region (Fig. 2d).

Note that step 4 is similar to the extrapolation procedure in TITOV and SYNOLAKIS (1995), and is an effective way to smooth numerical instabilities commonly found near the interfaces; otherwise the large elevation gradients near the interfaces would lead to unrealistically large velocity.

4. Benchmarks

As expounded in SYNOLAKIS and BERNARD (2006) and SYNOLAKIS et al. (2007), inundation models need to be carefully benchmarked against three types of data: analytical solutions, laboratory data, and field measurements. Due to the enormous uncertainties in most real-case tsunamis, the comparisons with known analytical solutions and laboratory data are critically important to gain confidence in the numerical model. Therefore in this paper, we present the results for the first two benchmark tests published by the 3rd International Workshop on Long-wave Runup Models (IWLRM, LIU et al., 2008; http://www.cee.cornell.edu/longwave/index.cfm?page=benchmark&problem=1). The evaluation of model performance in real tsunami applications (1993 Hokkaido-Nansei-Oki, 1964 Alaska, and historical tsunamis caused by Cascadia Subduction Zone earthquakes, etc.) is left to future publications.

4.1. Wave Runup on a Uniform Plane Beach

The first problem has a simple setup, with a uniformly sloping beach and no variation in the lateral direction, and therefore is a 2-D problem in the vertical plane. The only forcing is the initial displacement of the free surface that resembles a typical N-wave, with a leading-depression wave followed by an elevation wave, as found in most tsunamis (Fig. 3). The initial-value-problem (IVP) technique introduced by CARRIER et al. (2003), and later improved by KÂNOGLU (2004), provides a nonlinear analytical solution, which can be downloaded from the IWLRM website. IVPs are particularly challenging for numerical models as the inherent numerical dissipation in a model will become quite apparent due to the lack of continuous supply of energy into the domain as found in
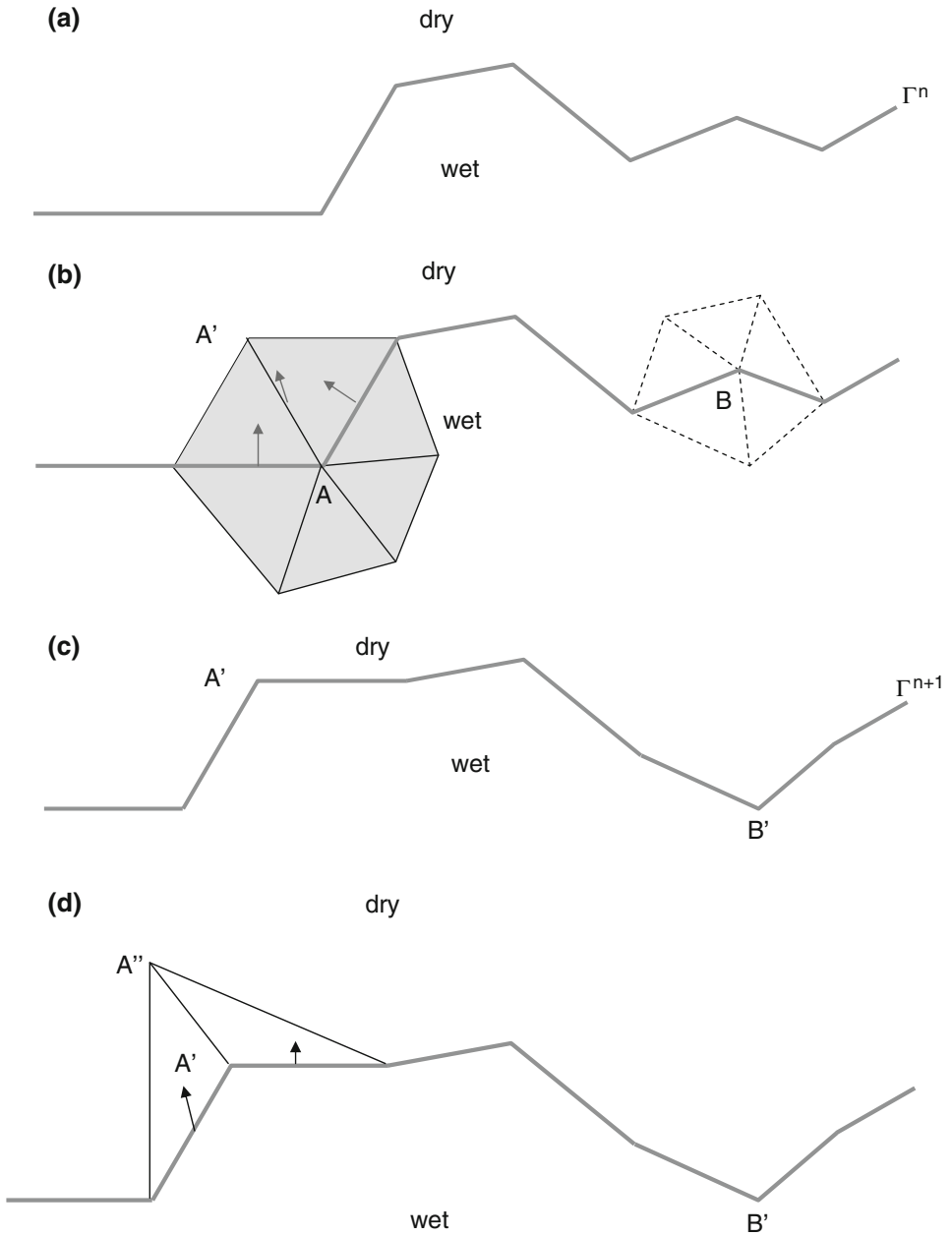
Figure 2

The inundation algorithm in SELFE. (a) Initial wet/dry interface at step n; (b) evaluate wet/dry status for interfacial nodes based on new elevations at step $n + 1$; (c) update the wet/dry interface, and iterate between (b) and (c); (d) final extrapolation of elevations along the final interface.
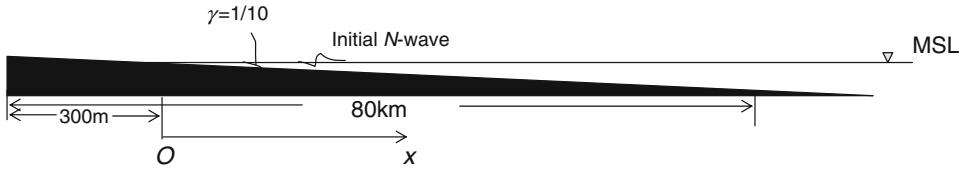
Figure 3

Definition sketch of the plane beach runup test. Depth in the domain is $x/10$.

boundary-value problems; in other words, the energy loss due to excessive numerical dissipation would lead to poor results in IVPs.

The initial shoreline is at $x = 0$ (Fig. 3), and the domain is about 80 km long, with the region between $x = -300$ m to $x = 0$ being initially dry. The large domain was chosen to minimize the reflection from the right boundary, where a radiation boundary condition was imposed. Various grid resolutions, ranging from 40 m to 2.5 m, were tested, but only uniform grids (by splitting each rectangle into 2 triangles) were used for simplicity and to facilitate the convergence study (see below). In other words, we did not take full advantage of using an efficient variable-resolution unstructured grid in this study. Two vertical layers were used in the vertical direction, and therefore essentially a 2-D depth-averaged model was used. The time step was fixed at 0.1 s. Although a much larger time step can be used without comprising numerical stability, a small time step was chosen for accurate simulation of the inundation process.[3] The implicitness factor was set to be 1 (i.e., fully implicit). Bottom friction and viscosity were all neglected in order to be consistent with the analytical solution. The run was carried out for a total of 600 sec, but most comparisons were done for the first 300 sec. All runs shown in this paper were carried out on an AMD Opteron 2.2 GHz processor. With $\Delta x = \Delta y = 5$ m and a grid with 176011 nodes, the 600 sec-run took 16 hours CPU time.

The initial amplitude of the N-wave is about 12 m, which translates to a very large extent of inundation (over 36 m in the vertical and 400 m in the horizontal excursion of the shoreline; Fig. 4), and supercritical flow near the shoreline (Fig. 5). The comparison of instantaneous surface elevations and velocity in the x direction at three time instances ($t = 160$, 175, and 220 sec) is presented in Figure 4. The 2nd and 3rd time instances roughly correspond to maximum drawdown and runup. The model results for elevation are excellent for all stages of the wave, with an error of 4.7% for the predicted maximum runup, which is within the error limit proposed in SYNOLAKIS et al. (2007). Larger errors in the velocity are observed, especially near the shoreline; probably due to numerical dissipation, the model seems to have lost some energy in that region.

The comparison of shoreline position and velocity is shown in Figure 5. The average and maximum errors in the predicted shoreline position are 10 m and 40 m, respectively.

---

[3] For real applications, a variable time step approach is usually used; the model is run with a larger time step (e.g., 5–10 s) until the first wave hits the coastline and then the time step is reduced to capture the inundation.
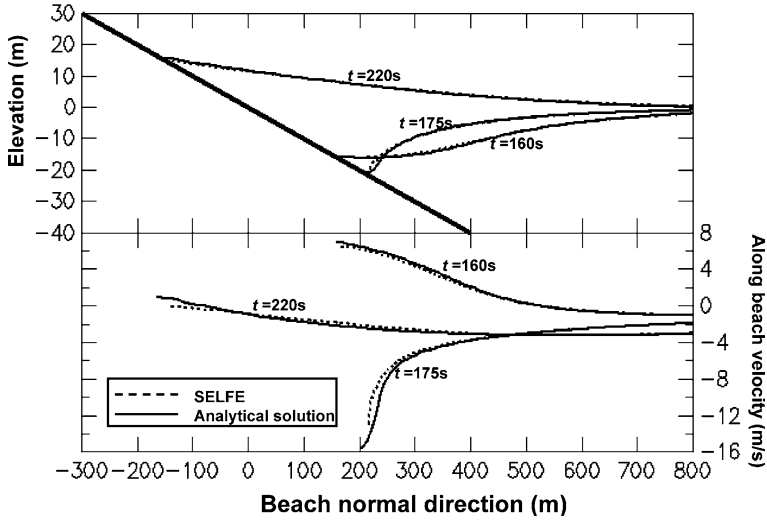
Figure 4
Comparison of instantaneous free surface (top panel) and velocity (bottom panel) along the plane beach at three time instances. The thick black line in the top panel indicates the bottom position.

Again, larger errors are observed in the shoreline velocity during both drawdown and runup stages, although the general trend is captured. A small amount of numerical instability can be seen near the shoreline (Fig. 5b), although it did not appear to affect the solution elsewhere.

Because extrapolation is used in the model, the convergence property of the model must be tested. We chose the error metrics to be the Root-Mean-Square (RMS) errors for the shoreline position and velocity as presented in Figure 5, and studied them as the grid resolution was varied. As indicated in ZHANG and BAPTISTA (2008), the Courant number is increased as the grid size is decreased, and by virtue of ELM, convergence is expected. This is indeed confirmed in Figure 6.

Volume and energy conservation is an important issue in tsunami applications (MYERS, 1998), which has caused serious problems in our application of ADCIRC. The total energy in the domain (at a particular time step) is:

$$E(t) = E_p + E_k, \tag{4}$$

Where the potential and kinetic energies are given by:

$$E_p = \frac{\rho g}{4} \int \eta^2 \, dA,$$

$$E_k = \frac{\rho g}{2} \int \left(|\mathbf{u}|^2 + w^2 \right) dV. \tag{5}$$

Assuming that the outgoing wave travels at a speed of $\sqrt{gh}$, the energy flux across the right-hand boundary per unit length in the y direction and during each time step is then
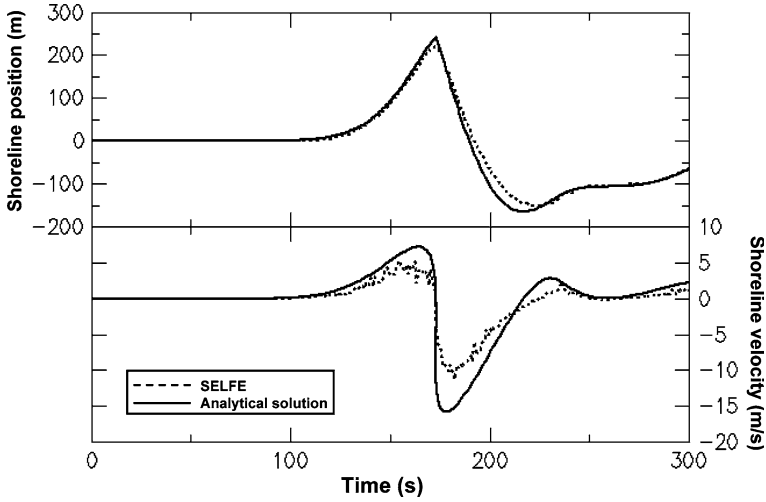
Figure 5
Comparison of time histories of shoreline position (top panel) and velocity at shoreline (bottom panel).
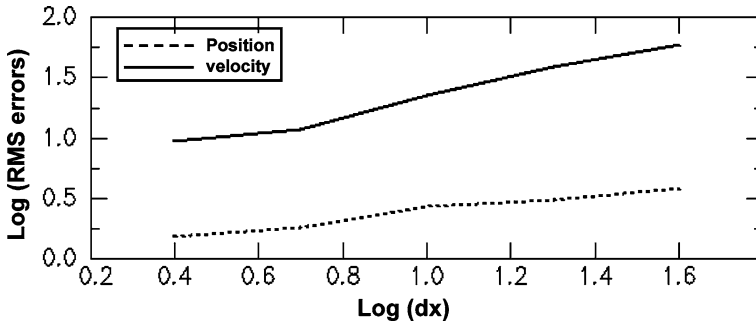
Figure 6
RMS errors in the predicted shoreline position and velocity as a function of grid size used, to show the convergence of the inundation algorithm. Log-log plot is used and the RMS error for the position is in m and that for the velocity is in m/s.

$$E_b = \frac{\rho \Delta t}{2} \left(g\eta^2 + h|\mathbf{u}|^2 \right), \qquad (6)$$

and the loss due to friction is:

$$E_f = \rho \Delta t \int C_D |\mathbf{u}|^3 dA, \qquad (7)$$

where C_D is the friction coefficient. Since no bottom friction was used in this test, $E_f = 0$. An energy budget can then be constructed from Equations (4–7).
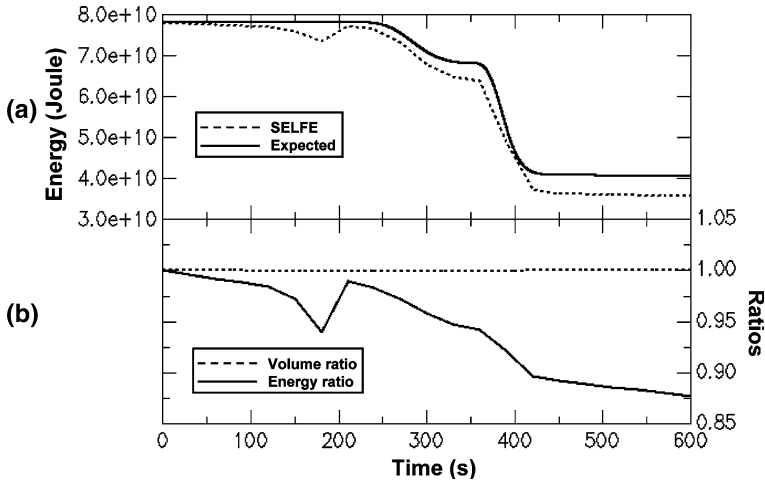
Figure 7

Energy and volume conservation in the plane beach test. (a) Time history of expected (analytical) and numerical total mechanical energies, accounting for the energy loss through the right open boundary. (b) Time history of volume ratio between expected and predicted volumes (both account for volume loss through the open boundary), and energy ratio between the energies shown in (a). The increase of the energy ratio around $t = 200$ s coincides with the inundation stage where extrapolation is used.

Starting from the potential energy in the initial *N*-wave, the time history of "expected" total energy can be calculated from the budget presented above. This is then compared with the actual amount of total energy in the model results in Figure 7. In addition, Figure 7b also shows the errors in volume conservation (a volume budget can be constructed by taking into account the water that leaves the domain during each time step). The volume conservation errors remain very small (<0.01%) throughout the entire simulation, which is in sharp contrast to the early ADCIRC results (unpublished). The actual energy is always smaller than the "expected" value, indicating a net loss. The temporary increase in energy during the runup stage (from $t = 180$ to 210 sec) is most likely due to the extrapolation used, which has added energy back to the system. The total energy loss at the end of 10 min is about 12.5%, which is a considerably better result than those from the ADCIRC runs (unpublished).

4.2. Wave Runup on a Complex 3-D Beach

The 1993 Hokkaido-Nansei-Oki tsunami serves as one of the best benchmark tests for inundation models because of the detailed bathymetric surveys before and after the event, and excellent field measurements. The earthquake occurred just west of Okushiri Island, and caused extensive damage along the Hokkaido coastline, however, the largest runup (up to 32 m) was observed at a narrow valley (Tsuji) within a small cove near Monai on the west coast of Okushiri Island (SHIMAMATO *et al.*, 1995).
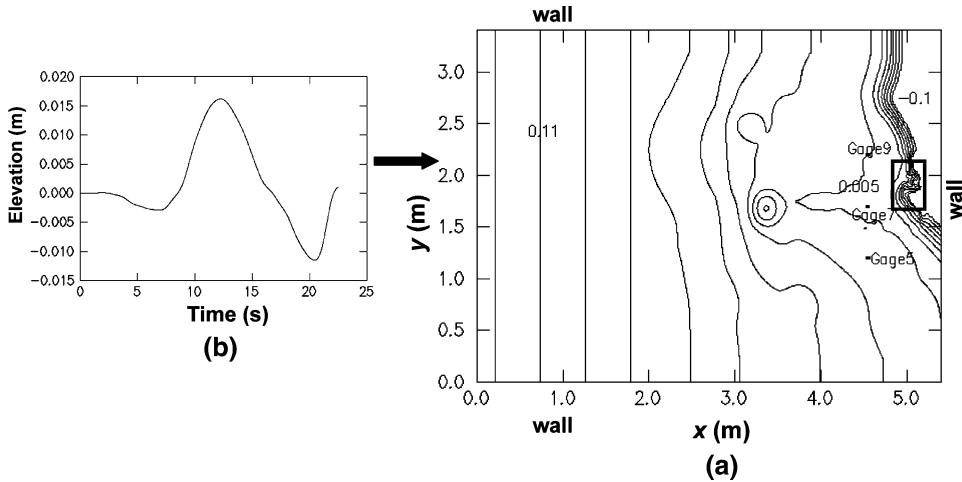
Figure 8

(a) Top view of the wave tank used in the laboratory test for the 1993 Okushiri tsunami. The increment between isolines is 0.015 m. The box indicates the approximate location of Tsuji valley where the largest runup was observed. Also shown are the locations of the three gages (5, 7, and 9) that measure the elevations. (b) The incoming N-wave profile.

In this section, we concentrate on the 1:400 scale laboratory experiment for this event, performed at Central Research Institute for Electric Power Industry (CRIEPI) in Abiko, Japan. The main theme of the experiment was to reproduce the largest runup around Monai, using a large-scale tank of 205 m long, 6 m deep, and 3.4 m wide (Fig. 8).

Figure 8 shows the set-up of the laboratory experiment and bathymetry and topography in the tank. It can be seen that the coastline is very complex especially near the Tsuji valley. The sidewalls at $y = 0$, and 3.5 m and $x = 5.49$ m are reflective. The incident N-wave from offshore, at the water depth $h = 13.5$ cm comes in from the left-hand side ($x = 0$). Therefore this is a boundary-value problem instead of an initial-value problem as in Section 4.1. The temporal variation of water surface elevation at three gages (Fig. 8) as well as animations of shoreline positions captured by three cameras are given on the IWLRM website. The maximum runups along the coast calculated from the MOST model (TITOV and SYNOLAKIS, 1998) were also given in CHAWLA et al. (2007). Therefore we will compare SELFE results with the laboratory measurements at the three gages as well as the results presented in CHAWLA et al. (2007).

The model grid resolution is $\Delta x = \Delta y = 1.4$ cm (with each rectangle split into two triangles), roughly the same as the internal fine grid used in CHAWLA et al. (2007); again, we did not use a more efficient variable resolution unstructured grid for simplicity. As a result, the horizontal grid has 95892 nodes and 190512 elements. A time step of $\Delta t = 0.01$ sec, as in CHAWLA et al. (2007), was used. Similar to Section 4.1, the implicitness factor was set to be 1, bottom friction and viscosities were all neglected, and

two vertical layers were used in the vertical direction. The total duration of the run was 22.5 sec, which took 3.75 hours CPU time on the same platform as in Section 4.1.

The comparison of elevations at the three gages between SELFE and lab measurements is depicted in Figure 9; similar comparison can be found in Figure 4 of CHAWLA *et al.* (2007). The results for the first 10 sec are discarded because the model is still being ramped up. The overall agreement is satisfactory; the calculated maximum elevations at the three gages are within 4.6%, 5.1%, 4.6% of measure values, and lag the measured arrival times by 0.2, <0.001, and 0.1 sec, respectively; note the excellent match of arrival time at Gage 7. The results are also comparable to those in CHAWLA *et al.* (2007); the main difference occurs at Gage 9. While the simulated elevation at this gage in CHAWLA *et al.* (2007) was such that the position of the tide gage was dry from $t = 13.5$ to 15 sec, this gage is always submerged under water in our results, although the total water depths are very thin (<0.1 mm) during this period (Fig. 9b). The measured elevation at this gage is larger than those in either model (Fig. 9a).
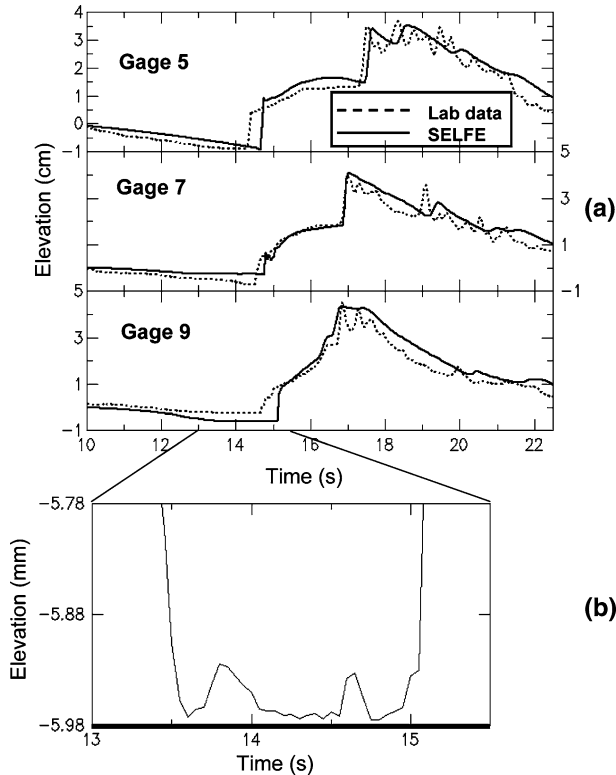

Figure 9
(a) Comparison of surface elevations at the gages shown in Figure 8. (b) Zoom-in of SELFE results at gage 9, where the depth is 5.98 mm (the bottom is indicated as the thick black line), from t = 13 to 15.5 s. Note that the total depth is positive despite being very small (<0.1 mm) between $t = 13.5$ s and 15 s.
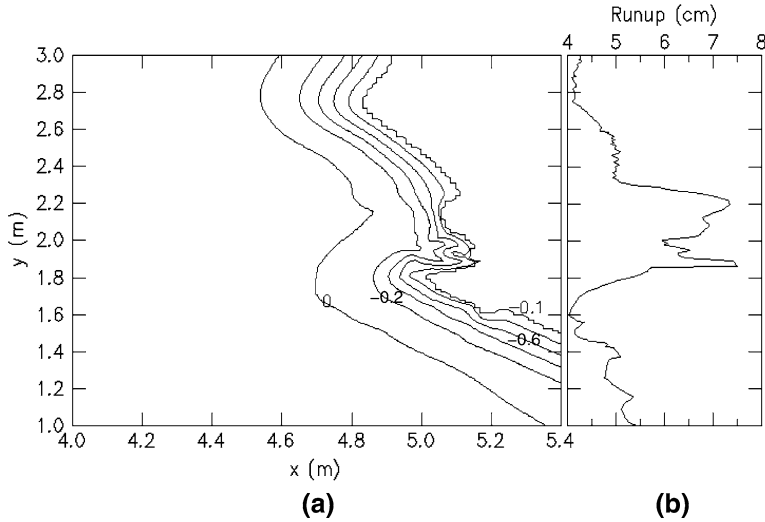
Figure 10
Maximum runup along the coastline. (a) Isobaths in the tank in the increment of 0.2 m; (b) maximum runup along the y-axis.

The calculated maximum wave runup around the Tsuji valley is shown in Figure 10, and can be compared to Figure 5 of CHAWLA et al. (2007). Both models predicted a large runup inside the cove, although the maxima there are different (10 cm for MOST vs. 7.5 cm for SELFE). If a linear scaling is assumed, the projected maximum runups in the cove for the real event are 40 m for MOST and 30 m for SELFE, with the field estimate being about 32 m. It should be emphasized that this simple scaling may not be appropriate as the experiment cannot faithfully reproduce all nonlinear processes that have occurred during the real event. Another peak in the runups north of the cove also appeared in both models, although at slightly different locations. Without actual measurements in this region, it is difficult to compare the two models there.

5. Concluding Remarks

A new tsunami model is proposed, and its ability to address stringent inundation benchmarks demonstrated. SELFE is based on the solution of the NSW equations with a semi-implicit finite-element method on unstructured grids, with Eulerian-Lagrangian treatment of advective terms in the momentum equation. A simple and yet effective inundation algorithm is incorporated in the model. Compared to a reference unstructured-grid tsunami model (ADCIRC), SELFE is computationally efficient, robust, accurate, and has improved volume and energy conservation properties. A parallel (MPI-based) version of the model, which has become available recently, will add to its attractiveness as a computationally efficient tool.

SELFE is in this paper benchmarked against two test problems: An initial-value problem with an analytical solution, and a laboratory experiment inspired by the 1993 Hokkaido-Nansei-Oki tsunami. Satisfactory results are obtained in both cases. We have also applied the SELFE to the 1993 Hokkaido-Nansei-Oki tsunami, with equally satisfactory results, which we will report in Part II. Applications of SELFE to the 1964 Alaska tsunami and to Cascadia Subduction Zone tsunamis are in progress; each application involves both an element of field validation and a re-assessment of the tsunami hazard for Oregon communities.

SELFE is a multi-purpose open source code, available at http://www.ccalmr.ogi.edu/ CORIE/modeling/selfe/. Other applications of SELFE include studies of 3-D circulation in estuaries and plumes, reported elsewhere (ZHANG and BAPTISTA, 2008). The ability of SELFE to address fully 3-D problems effectively opens the opportunity for studies of sediment transport during tsunami events; a perspective that has strong potential value for Cascadia Subduction Zone tsunamis, whose strongest field evidence of inundation resides on sedimentary deposits.

Acknowledgements

REFERENCES

BAPTISTA, A.M. (1987), *Solution of Advection-dominated Transport by Eulerian-Lagrangian Methods Using the Backwards Methods of Characteristics*, Ph.D. Thesis, Massachusetts Institute of Technology (260 pp), Civil Engineering. Cambridge, Massachusetts.

BAPTISTA, A.M. (2006), *CORIE: The first decade of a coastal margin collaborative observatory*, Oceans'06 MTS/IEEE, Boston, MA.

BAPTISTA, A.M., PRIEST, G.R., and MURTY, T.S. (1993), *Field Survey of the 1992 Nicaragua Tsunami*, Marine Geodesy *16*(2), 169–203.

BAPTISTA, A.M., ZHANG, Y.L., CHAWLA, A., ZULAUF, M.A., SEATON, C., MYERS, E.P., KINDLE, J., WILKIN, M., BURLA, M., and TURNER, P.J. (2005), *A cross-scale model for 3D baroclinic circulation in estuary-plume-shelf systems: II. Application to the Columbia River*, Continental Shelf Res. *25*, 935–972.

BURWELL, D., TOLKOVA, E., and CHAWLA, A. (2007), *Diffusion and dispersion characterization of a numerical tsunami model*, Ocean Modelling *19*, 10–30.

CARRIER, G. F., WU, T. T., and YEH, H. (2003), *Tsunami run-up and run-down on a plane beach*, J. Fluid Mech. *475*, 79–99.

CASULLI, V. and WALTERS, R. A. (2000), *An unstructured grid, three-dimensional model based on the shallow water equations*, Int. J. Num. Meth. Fluids *32*, 331–348.

CHAWLA, A., BORRERO, J., and TITOV, V., *Evaluating wave propagation and inundation characterstics of the MOST tsunami model over a complex 3D beach*. In *Advanced Numerical Models for Simulationg Tsunami Waves and Runup* (eds. P. L.-F. Liu, H. Yeh, and C.E. Synolakis), vol. 10, *Advances in Coastal and Ocean Engineering* (World Scientific, 2008).

CHEN, C., H. LIU, H., and BEARDSLEY, R.C. (2003), *An Unstructured Grid, Finite-Volume, Three-Dimensional, Primitive Equations Ocean Model: Application to Coastal Ocean and Estuaries*, J. Atmos. Oceanic Tech. *20*, 159–186.

DIAS, F. and DUTYKH, D., *Dynamics of Tsunami Waves*, (Springer, Netherlands 2007).

DUTYKH, D., DIAS, F., and KERVELLA, Y. (2006), *Linear theory of wave generation by a moving bottom*, C. R. Acad. Sci. Paris, Ser. I, *343*, 499–504.

GEORGE, D. L. and LEVEQUE, R. J. (2006), *Finite volume methods and adaptive refinement for global tsunami propagation and local inundation*, Science of Tsunami Hazards *24*, 319–328.

GOLDFINGER, C., NELSON, C.H., and JOHNSON, J.E. (2003), *Holocene earthquake records from the Cascadia subduction zone and Northern San Andreas fault based on precise dating of offshore turbidites*, Ann. Rev. Earth Planet. Sci. *31*, 555–577.

HUBBARD, M.E. and DODD, N. (2002), *A 2-D numerical model of wave runup and overtopping*, Coastal Eng., *47*, 1–26.

KÂNOGLU, U. (2004), *Nonlinear evolution and runup–rundown of long waves over a sloping beach*, J. Fluid Mech. *513*, 363–372.

KÂNOGLU, U. and SYNOLAKIS, C.E. (2006), *Initial value problem solution of nonlinear shallow water-wave equations*, Phys. Rev. Lett. *97*(14), 148501.

LEVEQUE, R.J. and GEORGE, D.L., *High-resolution finite volume methods for the shallow water equations with bathymetry and dry states*. In *Advanced Numerical Models for Simulationg Tsunami Waves and Runup* (eds. P. L.-F. Liu, H. Yeh and C.E. Synolakis), vol. 10, *Advances in Coastal and Ocean Engineering* (World Scientific 2008).

LIU, L.-F., WU, T.R., RAICHLEN, F., SYNOLAKIS, C.E., and BORRERO, J.C. (2005), *Runup and rundown generated by three-dimensional sliding mass*, J. Fluid Mech. *536*, 107–144.

LIU, P. L.-F., YEH, H., and SYNOLAKIS, C.E. In *Advanced Numerical Models for Simulating Tsunami Waves and Runup* (eds. P. L.-F. Liu, H. Yeh, and C. E. Synolakis), vol. 10, *Advances in Coastal and Ocean Engineering* (World Scientific 2008).

LUETTICH, R.A., WESTERINK, J.J., and SCHEFFNER, N.W. (1991), *ADCIRC: An advanced three-dimensional circulation model for shelves, coasts and estuaries*, Coastal Engin. Res. Ct., U.S. Army Engs. Wtrways. Experiment Station, Vicksburg, MS.

LYNCH, D.R. and WERNER, F.E. (1991), *Three-dimensional hydrodynamics on finite elements. Part II: Non-linear time-stepping model*, J. Num. Meth. in Fluids *12*, 507–533.

LYNETT, P., WU, T.-R., and LIU, P.L.-F. (2002), *Modeling wave runup with depth-integrated equations*, Coastal Engin. *46*(2), 89–107.

MYERS, E.P., BAPTISTA, A. M., and PRIEST, G.R. (1999), *Finite element modeling of potential Cascadia subduction zone tsunamis*, Science of Tsunami Hazards *17*, 3–18.

MYERS, E.P. (1998), *Physical and numerical analysis of long wave modeling for tsunamis and tides*, Environmental Science and Engineering, Beaverton, Oregon, Graduate Institute of Science and Technology, 273 pp.

MYERS, E.P. and BAPTISTA, A.M. (1995), *Finite element modeling of the July 12, 1993 Hokkaido Nansei-Oki tsunami*, Pure Appl. Geophys. *144*(3/4), 769–801.

MYERS, E.P. and BAPTISTA, A.M. (1997), *Finite element solutions of the Hakkaido Nansei-Oki benchmark*. In *Long-Wave Runup Models* (eds. Yeh, H. *et al.*), pp. 272–280.

MYERS, E.P. and BAPTISTA, A.M. (2001), *Analysis of factors influencing simulations of the 1993 Hokkaido Nansei-Oki and 1964 Alaska tsunamis*, Natural Hazards *23*(1), 1–28.

PRIEST, G.R. (1995), *Explanation of mapping methods and use of the tsunami hazard maps of the Oregon coast*, Oregon Department of Geology and Mineral Industries, Open-File Report O–95-67, 95 pp.

PRIEST, G.R., ALLAN, J. C., MYERS, E.P., BAPTISTA, A.M., and KAMPHAUS, R. (2002), *Tsunami hazard map of the Coos Bay Area, Coos County, Oregon*, Oregon Department of Geology and Mineral Industries, Interpretive Map Series IMS-21.

PRIEST, G.R. and BAPTISTA, A.M. (2000), *Digital reissue of tsunami hazard maps of coastal quadrangles originally mandated by Senate Bill 379 (1995)*, Oregon Department of Geology and Mineral Industries, Open-File Report O-00-05, maps in.pdf and GIS formats and text files for Open File Reports O-95-38 and O-95-43 to O-95-67 [maps of the tsunami inundation zone (most probable Cascadia event) for the entire Oregon coast].

PRIEST, G.R., CHAWLA, A., and ALLAN, J.C. (2003), *Tsunami hazard map of the Alsea Bay (Waldport) area, Lincoln County, Oregon*, Oregon Department of Geology and Mineral Industries, Interpretive Map Series IMS-23.

PRIEST, G.R., MYERS, E., BAPTISTA, A.M., ERDAKOS, G., and KAMPHAUS, R. (1999a), *Tsunami hazard map of the Astoria area, Clatsop County, Oregon*, Oregon Department of Geology and Mineral Industries, Interpretive Map Series map IMS-11, scale 1:24,000.

PRIEST, G.R., MYERS, E.P., BAPTISTA, A.M., and KAMPHAUS, R. (1999b), *Tsunami hazard map of the Warrenton area, Clatsop County, Oregon*, Oregon Department of Geology and Mineral Industries, Interpretive Map Series IMS-12, scale 1:24,000.

PRIEST, G.R., MYERS, E.P., BAPTISTA, A.M., and KAMPHAUS, R. (2000), *Tsunami hazard map of the Gold Beach area, Curry County, Oregon*, Oregon Department of Geology and Mineral Industries, Interpretive Map Series IMS-13, scale 1:12,000.

PRIEST, G.R., MYERS, E.P., BAPTISTA, A.M., KAMPHAUS, R., PETERSON, C.D., and DARIENZO. M.E. (1997a), *Tsunami hazard map of the Yaquina Bay area, Lincoln County, Oregon*, Oregon Department of Geology and Mineral Industries: Interpretive Map Series IMS-2, scale 1:12,000.

PRIEST, G. R., MYERS, E.P., BAPTISTA, A.M., KAMPHAUS, R., PETERSON, C.D., and DARIENZO. M.E. (1998), *Tsunami hazard map of the Seaside-Gearhart area, Clatsop County, Oregon*, Oregon Department of Geology and Mineral Industries: Interpretive Map Series IMS-3, scale 1:12,000.

PRIEST, G. R., MYERS, E.P., BAPTISTA, A.M., KAMPHAUS, R., PETERSON, C.D., and DARIENZO. M.E. (1997b), *Cascadia subduction zone tsunamis: hazard mapping at Yaquina Bay, Oregon*, Oregon Department of Geology and Mineral Industries: 144.

PRIEST, G.R., QI, M., BAPTISTA, A.M., KAMPHAUS, R., C.D., and DARIENZO, M.E. (1995), *Tsunami hazard map of the Siletz Bay area, Lincoln County, Oregon*, Oregon Department of Geology and Mineral Industries: GMS-99, scale 1:12,000.

SHIMAMATO, T., TSUTSUMI, A., KAWAMOTO, M., MIYAWAKI, M., and SATO, H. (1995), *Field survey report on tsunami disasters caused by the 1993 Southwest Hokkaido earthquake*, Pure Appl. Geophy. *144*(3/4), 665-692.

SYNOLAKIS, C.E. and BERNARD, E.N. (2006), *Tsunami science before and beyond Boxing Day 2004*, Phil. Trans. R. Soc. A *364*, 2231–2265.

SYNOLAKIS, C.E., BERNARD, E.N., TITOV, V.V., KANOGLU, U., and GONZALEZ, F. (2007), *Standard, criteria, and procedures for NOAA evaluation of tsunami numerical models*, NOAA Technical Memorandum, OAR PMEL–135.

TITOV, V.V. and SYNOLAKIS, C.E. (1995), *Modeling of breaking and non-breaking long-wave evolution and runup using VTCS-2*, J. Waterway, Ports, Coastal and Ocean Engin. *121*(6), 308–316.

TITOV, V.V. and SYNOLAKIS, C.E. (1998), *Numerical modeling of tidal wave runup*, J. Waterway, Ports, Coastal and Ocean Engin. *124*(4), 157–171.

TSUNAMI PILOT STUDY WORKING GROUP (2006), *Seaside, Oregon Tsunami Pilot Study-Modernization of FEMA flood hazard maps*, NOAA OAR Special Report, Contribution No 2975, NOAA/OAR/PMEL, Seattle, WA, 83 pp. +7 appendices.

VENTURATO, A.J., ARCAS, D., and KANOGLU, U. (2007), *Modeling tsunami inundation from a Cascadia Subduction Zone earthquake for Long Beach and Ocean Shores, Washington*, NOAA Technical Memorandum, OAR PMEL-137.

WALTERS, R.A. (2005), *A semi-implicit finite-element model for non-hydrostatic (dispersive) surface waves*, Internat. J. Num. Meth. in Fluids *49*, 721–737.

WANG, K. and HE, J. (1999), *Mechanics of low-stress forearcs: Nankai and Cascadia*, J. Geophys. Res. *104*, 15191–205.

WEI, Y., BERNARD, E.N., TANG, L., WEISS, R., TITOV, V.V., MOORE, C., SPILLANE, M. HOPKINS, M., and KÂNOGLU, U. (2008), *Real-time experimental forecast of the Peruvian tsunami of August 2007 for U.S. coastlines*, Geophys. Res. Lett. *35*, L04609.

WESTERINK, J.J., FEYEN, J.C., ATKINSON, J.H., LUETTICH, R.A., DAWSON, C.N., POWELL, M.P., DUNION, J.P., ROBERTS, H.J., KUBATKO, E.J., and POURTAHERI, H. (2004), *A new generation hurricane storm surge model for southern Louisiana*, http://www.nd.edu/~adcirc/pubs/westerinketal_bams_ref1935b.pdf.

WITTER, R.C., KELSEY, H.M. and HEMPHILL-HALEY, E. (2003), *Great Cascadia earthquakes and tsunamis of the past 6700 years, Coquille River estuary, southern coastal Oregon*, Geolog. Soc. Am. Bull. *115*, 1289–1306.

YALCINER, A.C., ALPAR, B., ALTINOK, Y., OZBAY, I., and IMAMURA, F. (2002), *Tsunami in the Sea of Marmara: historical documents for the past, models for future*, Marine Geology *190*(1–2), 445–463.

ZHANG, Y.-L. and BAPTISTA, A. M. (2008), *SELFE: A semi-implicit Eulerian-Lagrangian finite-element model for cross-scale ocean circulation*, Ocean Modeling *21*(3–4), 71–96.

ZHANG, Y.-L., BAPTISTA, A.M., and MYERS, E.P. (2004), *A cross-scale model for 3D baroclinic circulation in estuary-plume-shelf systems: I. Formulation and skill assessment*, Continental Shelf Res. *24*, 2187–2214.

To access this journal online:
www.birkhauser.ch/pageoph

Runup Characteristics of Symmetrical Solitary Tsunami Waves of "Unknown" Shapes

IRA DIDENKULOVA,[1,2] EFIM PELINOVSKY,[1] and TARMO SOOMERE[2]

Abstract—The problem of tsunami wave runup on a beach is discussed in the framework of the rigorous solutions of the nonlinear shallow-water theory. We present an analysis of the runup characteristics for various shapes of the incoming symmetrical solitary tsunami waves. It will be demonstrated that the extreme (maximal) wave characteristics on a beach (runup and draw-down heights, runup and draw-down velocities and breaking parameter) are weakly dependent on the shape of incident wave if the definition of the "significant" wavelength determined on the 2/3 level of the maximum height is used. The universal analytical expressions for the extreme wave characteristics are derived for the runup of the solitary pulses. They can be directly applicable for tsunami warning because in many cases the shape of the incident tsunami wave is unknown.

Key words: Tsunamis, nonlinear shallow-water theory, long-wave runup.

1. Introduction

The reliable estimation of inundation extent is a key problem of coastal wave dynamics, and in particular for tsunami mitigation. Since the characteristic length of a tsunami wave in the coastal zone is several kilometers, the nonlinear shallow water theory is an appropriate theoretical model to describe the process of tsunami runup on a beach. The problem of the runup of long non-breaking waves on a plane beach is well described mathematically within the framework of a nonlinear shallow water theory. This approach leads to an analytical solution based on the Carrier–Greenspan transform (CARRIER and GREENSPAN, 1958). Various shapes of the periodic incident wavetrains such as the sine wave (KAISTRENKO *et al.*, 1991; MADSEN and FUHRMAN, 2008), cnoidal wave (SYNOLAKIS, 1991) and nonlinear deformed periodic wave (DIDENKULOVA *et al.*, 2006, 2007b) have been analyzed in the literature. The relevant analysis has also been performed for a variety of solitary waves and single pulses such as soliton (PEDERSEN and GJEVIK, 1983; SYNOLAKIS, 1987; KÂNOĞLU, 2004), sine pulse (MAZOVA et al., 1991), Lorentz pulse (PELINOVSKY and MAZOVA, 1992), Gaussian pulse (CARRIER *et al.*, 2003;

KÂNOĞLU and SYNOLAKIS, 2006), *N*-waves (TADEPALLI and SYNOLAKIS, 1994), "character-ized tsunami waves" (Tinti and Tonini, 2005) and the random set of solitons (BROCHINI and GENTILE, 2001). As is often the case in nonlinear problems, reaching an analytical solution is seldom possible. Runup of solitary pulses is, however, often easily implemented experimentally in measuring flumes, and various experimental expressions are available (see MADSEN and FUHRMAN, 2008 for references).

The existing results for the water wavefield are based on various initial conditions (shapes of the incident waves) and are therefore not directly comparable with each other. Sometimes, the shape of the incident wave is unknown, and this situation is typical for tsunamis. To get universal expressions for runup characteristics several parameters can be used. MADSEN and FUHRMAN (2008) suggest expressing the formula for runup height in terms of a surf-similarity. These expressions are applicable for nonbreaking waves on a plane beach and for breaking waves as well. DIDENKULOVA *et al.* (2007a, 2008) parameterize runup expressions using various definitions of the wavelength of nonbreaking wave pulses. In this study we demonstrate that the definition of wavelength on the 2/3 level from a maximal value (as the "significant wavelength" in physical oceanography and ocean engineering) is optimal. In this case formulas for various extreme runup characteristics (runup and draw-down heights and velocities, breaking parameter) are universal and the influence of the initial wave form on extreme runup characteristics is weak. This result is obtained for incident symmetrical solitary waves.

The paper is organized as follows. The analytical theory of long wave runup on a beach in the framework of shallow-water theory is briefly described in section 2. Numerical computations of the tsunami waves far from the beach and on the shoreline, based on spectral Fourier series are presented in Section 3. The parameterization of wave shapes in formulas for the extreme (maximal) wave characteristics on a beach is discussed in section 4. The main results are summarized in section 5.

2. *Analytical Theory of the Long-Wave Runup on a Beach*

The runup of tsunami waves on a beach can be described in the framework of the nonlinear shallow-water equations. If the wave propagates perpendicularly to the isobaths, basic equations are,

$$\frac{\partial \eta}{\partial t} + \frac{\partial}{\partial x}[(h(x) + \eta)u] = 0, \tag{1}$$

$$\frac{\partial u}{\partial t} + u \frac{\partial u}{\partial x} + g \frac{\partial \eta}{\partial x} = 0, \tag{2}$$

where $\eta(x, t)$ is the vertical displacement of the water surface, $u(x, t)$ is the depth-averaged water flow, $h(x)$ – unperturbed water depth, and g is the gravitational acceleration. Analytical solutions of this system are obtained for a plane beach only,
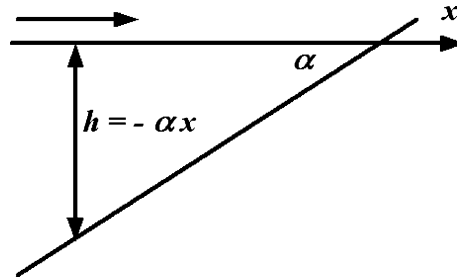
Figure 1
Sketch of the problem.

where the depth $h(x) = -\alpha x$ (Fig. 1). The procedure of the solution is based on the hodograph transformation initially described in the pioneering work of CARRIER-GREENSPAN (1958), and reproduced in different papers cited in section 1.

According to this method all variables can be expressed through the "nonlinear" wave function $\Phi(\sigma, \lambda)$ by means of the hodograph transformation:

$$\eta = \frac{1}{2g}\left(\frac{\partial\Phi}{\partial\lambda} - u^2\right), \tag{3}$$

$$u = \frac{1}{\sigma}\frac{\partial\Phi}{\partial\sigma}, \tag{4}$$

$$t = \frac{1}{\alpha g}\left(\lambda - \frac{1}{\sigma}\frac{\partial\Phi}{\partial\sigma}\right), \tag{5}$$

$$x = \frac{1}{2\alpha g}\left(\frac{\partial\Phi}{\partial\lambda} - u^2 - \frac{\sigma^2}{2}\right), \tag{6}$$

and the wave function, $\Phi(\lambda, \sigma)$ satisfies the cylindrical linear wave equation

$$\frac{\partial^2\Phi}{\partial\lambda^2} - \frac{\partial^2\Phi}{\partial\sigma^2} - \frac{1}{\sigma}\frac{\partial\Phi}{\partial\sigma} = 0. \tag{7}$$

The variables λ and σ denote generalized coordinates. Since

$$\sigma = 2\sqrt{g(-\alpha x + \eta)}, \tag{8}$$

the point $\sigma = 0$ corresponds to the instantaneous position of the shoreline (called moving shoreline in what follows).

It is interesting to note that if we analyze the linear system of shallow-water wave theory

$$\frac{\partial\eta}{\partial t} + \frac{\partial}{\partial x}[(-\alpha x)u] = 0, \tag{9}$$

$$\frac{\partial u}{\partial t} + g \frac{\partial \eta}{\partial x} = 0, \tag{10}$$

the linear version of the hodograph transformation

$$\eta_l = \frac{1}{2g}\left(\frac{\partial \Phi_l}{\partial \lambda_l}\right), \quad u_l = \frac{1}{\sigma_l}\frac{\partial \Phi_l}{\partial \sigma_l}, \quad t = \frac{\lambda_l}{\alpha g}, \quad x = -\frac{\sigma_l^2}{4\alpha g}, \tag{11}$$

transforms (9)–(10) to the wave equation

$$\frac{\partial^2 \Phi_l}{\partial \lambda_l^2} - \frac{\partial^2 \Phi_l}{\partial \sigma_l^2} - \frac{1}{\sigma_l}\frac{\partial \Phi_l}{\partial \sigma_l} = 0, \tag{12}$$

which coincides with the wave equation (7) in the nonlinear problem. However, in this case the point $\sigma_l = 0$ corresponds to the unperturbed shoreline ($x = 0$).

Tsunami waves in the deep ocean have small amplitudes and can be described by the linear theory with very high accuracy. For such an incident wave the boundary conditions for the "nonlinear" (7) and "linear" (12) wave equations coincide, provided they are defined in a far and deep enough area. Consequently, the solutions of the nonlinear and linear problems also coincide in terms of solutions of the wave equation, as the functional forms of its "linear" and "nonlinear" solutions coincide: $\Phi(\sigma, \lambda) \equiv \Phi_l(\sigma_l, \lambda_l)$. Moreover, if the "linear" solution $\Phi_l(\sigma_l, \lambda_l)$ is known, the solution of the nonlinear problem (1)–(2) can be directly found from expressions (3)–(6). In particular, the description of properties of the moving shoreline $\sigma(x, t) = 0$ is straightforward. If the velocity of water particles on the unperturbed shoreline ($x = 0$) is calculated in frames of the linear theory, a real "nonlinear" velocity of the moving shoreline can be expressed in an implicit form (PELINOVSKY and MAZOVA, 1992; DIDENKULOVA *et al.*, 2007b):

$$u(t) = U(\tilde{t}), \quad \text{where } \tilde{t} = t + \frac{u(t)}{\alpha g}. \tag{13}$$

Mathematically the function $U(t)$ in the linear theory is defined as $U(t) = \lim\limits_{\sigma_l \to 0} u_l$.

The described features allow use of a rigorous "two-step" method to calculate the runup characteristics under assumption that the linear theory adequately describes their motion far offshore. Firstly, the wave properties on the unperturbed shoreline ($x = 0$) such as the vertical displacement $R(t)$ or the velocity of wave propagation $U(t)$

$$U(t) = \frac{1}{\alpha}\frac{dR}{dt}, \tag{14}$$

are determined from the linear shallow-water theory. Secondly, the properties of the solution of the nonlinear problem (e.g., the real "nonlinear" speed of the moving shoreline) are found from Equation (13). Finally, the vertical displacement of the water level and position of the shoreline (equivalently, the horizontal extent of the inundation) at any instant of time is

$$r(t) = \eta(t, \sigma = 0) = R\left(t + \frac{u}{\alpha g}\right) - \frac{u^2}{2g}. \tag{15}$$

The important conclusion from Equations (13) and (15) is that the maxima of vertical displacements (equivalently, the runup height or the draw-down depth) and the velocity of the shoreline displacement in the linear and nonlinear theories coincide, as noted by CARRIER and GREENSPAN (1958) and SYNOLAKIS (1987, 1991) and as rigorously demonstrated by PELINOVSKY and MAZOVA (1992).

Another important outcome from Equations (13) and (15) is the simple definition of the conditions for the first breaking of waves on a beach. The temporal derivative of the velocity of the moving shoreline, found from Equation (13), approaches infinity (equivalently, wavebreaking occurs) when

$$Br = \frac{\max(dU/dt)}{\alpha g} = 1. \tag{16}$$

This condition has a simple physical interpretation: The wave breaks if the maximal acceleration of the shoreline $R''\alpha^{-1}$ along the sloping beach exceeds the along-beach gravity component αg. This interpretation is figurative, because formally R'' only presents the vertical acceleration of the shoreline in the linear theory and the "nonlinear" acceleration du/dt (that is not explicitly calculated here) is what actually approached infinity at the moment of breaking.

3. Method for Computing Extreme Runup Characteristics

Following the "two-step" method described above, the linear theory can be used for the computation of extreme characteristics of the tsunami wave runup. An effective method for solving linear partial differential equations is the Fourier method and its generalizations (for instance, the Hankel transformation for cylindrical wave equation). It is convenient to describe the wavefield in terms of its complex (amplitude-phase) spectrum $A(\omega)$ (equivalently, Fourier integral of the associated sea-level variations). The particular bounded solution of the cylindrical wave equation can be represented by the Fourier integral

$$\eta(x, t) = \int\limits_{-\infty}^{+\infty} A(\omega) J_0\left(\frac{2\omega|x|}{\sqrt{gh(x)}}\right) \exp(i\omega t) d\omega, \tag{17}$$

where $J_0(y)$ is the zero-order Bessel function. The spectrum $A(\omega)$ can be found from the spectrum $H(\omega)$ of the incident wave with the use of the asymptotic representation of the wavefield (17) at $x \to -\infty$ as the superposition of the incident η_+ and reflected η_- waves

$$\eta(x \rightarrow -\infty, t) = \eta_+[x, t + \tau(x)] + \eta_-[x, t - \tau(x)]. \tag{18}$$

Here

$$\tau(x) = \frac{2|x|}{\sqrt{gh(x)}} = \int\limits_{-|x|}^{0} \frac{dx}{\sqrt{gh(x)}} \tag{19}$$

is the travel time from a given location x to the unperturbed original shoreline. This measure can also be interpreted as the phase shift of the reflected wave in space.

In the same limit $x \rightarrow -\infty$, Equation (17) gives

$$\eta_\pm(x \rightarrow \infty, t) = \frac{1}{\sqrt{2\pi\tau(x)}} \int\limits_{-\infty}^{+\infty} \frac{A(\omega)}{\sqrt{|\omega|}} \exp\left[i\left(\omega(t \pm \tau(x)) \mp \frac{\pi}{4} \mathrm{sign}(\omega)\right)\right] d\omega. \tag{20}$$

We assume that the incident wave at a fixed point $|x| = L$ (located distantly from the shoreline) is specified by the Fourier integral

$$\eta_+(t) = \int\limits_{-\infty}^{+\infty} H(\omega) \exp(i\omega t) d\omega. \tag{21}$$

Its complex spectrum $H(\omega)$ is easily found in an explicit form in terms of the inverse Fourier transform:

$$H(\omega) = \frac{1}{2\pi} \int\limits_{-\infty}^{+\infty} \eta_+(t) \exp(-i\omega t) dt. \tag{22}$$

We assume now that the point $|x| = L$ is located so remotely from the unperturbed shoreline that decomposition (20) (that formally is correct for $x \rightarrow -\infty$) can be used at this point. Comparison of Equations (20) and (22) then reveals that

$$A(\omega) = \sqrt{2\pi|\omega|\tau(L)} \exp\left[\frac{i\pi}{4} \mathrm{sign}(\omega)\right] H(\omega). \tag{23}$$

The solution in Equation (17) is thus completely determined by the incident wave.

The vertical displacement at the unperturbed shoreline $x = 0$ is a function of the location L

$$R(t) = \sqrt{2\pi\tau(L)} \int\limits_{-\infty}^{+\infty} \sqrt{|\omega|} H(\omega) \exp\left\{i\left(\omega(t - \tau(L)) + \frac{\pi}{4} \mathrm{sign}(\omega)\right)\right\} d\omega. \tag{24}$$

The "linear" horizontal velocity of water particles at this point ($x = 0$) can be found from Equation (14). As was mentioned above, the extreme wave amplitudes (understood as the maximum displacement of water surface) and velocities at the unperturbed

shoreline $x = 0$ in linear theory coincide with the maximum runup (draw-down) heights and velocities in the nonlinear theory. Therefore, we would like to emphasize that solving of nonlinear equations is not necessary if only extreme characteristics of tsunami waves are analyzed.

Integral properties of a wave runup dynamics also can be found from the linear theory. For instance, an integrated vertical displacement of the shoreline ("set-up") is

$$\hat{R} = \int_{-\infty}^{+\infty} R(t)dt = \sqrt{2\pi\tau(L)} \int_{-\infty}^{+\infty} dt \int_{-\infty}^{+\infty} \sqrt{|\omega|} H(\omega) \exp\left\{ i\left(\omega(t - \tau(L)) + \frac{\pi}{4}\text{sign}(\omega)\right)\right\} d\omega$$

$$(25)$$

After changing the order of integration and taking into account the properties of delta-function Equation (25) can be rewritten as

$$\hat{R} = 2\pi\sqrt{2\pi\tau(L)} \int_{-\infty}^{+\infty} \sqrt{|\omega|} H(\omega) \exp[i(\pi/4)\text{sign}(\omega)]\delta(\omega)d\omega. \qquad (26)$$

A physical sense of $H(0)$ is an integrated displacement of the incident wave which is bounded. Since the integrand is a continuous function, the integral in Equation (26) is equal to zero. Therefore, the tsunami runup is always presented as reversal oscillations of the shoreline, and a runup phase changes into a receding phase, the process of which does not depend on the shape of the incident wave.

We consider an incident tsunami wave having pulse shape (for example, a positively defined disturbance — wave of elevation or crest) with amplitude H_0 and duration T_0 at $|x| = L$ propagating onshore. It can be nondimensionalized as

$$\eta(t) = H_0 f(t/T_0), \quad f(\zeta) = \int_{-\infty}^{\infty} B(\Omega) \exp(i\Omega\zeta)d\Omega, \qquad (27)$$

where

$$\zeta = t/T_0, \quad \Omega = \omega T_0, \quad B(\Omega) = \frac{1}{2\pi} \int_{-\infty}^{\infty} f(\zeta) \exp(-i\Omega\zeta)d\zeta. \qquad (28)$$

In this case, formulas for velocity of the moving shoreline (14) and linear acceleration, connected with the breaking parameter of the wave (16), and for the maximal vertical displacement (24), can be presented as

$$R_{\max} = R_0 p_R, \quad p_R = \max\{I\}, \quad I = \int_{-\infty}^{\infty} \sqrt{|\Omega|} B(\Omega) \exp\left[i\left(\Omega\zeta + \frac{\pi}{4}\text{sign}(\Omega)\right)\right]d\Omega, \quad (29)$$

$$U_{\max} = \frac{R_0}{\alpha T_0} p_U, \quad p_U = \max\left\{\frac{dI}{d\zeta}\right\}, \tag{30}$$

$$(dU/dt)_{\max} = \frac{R_0}{\alpha T_0^2} p_{Br}, \quad p_{Br} = \max\left\{\frac{d^2I}{d\zeta^2}\right\}, \tag{31}$$

$$R_0 = \sqrt{\frac{4\pi L}{\lambda_0}} H_0, \quad \lambda_0 = \sqrt{gh_0}\, T_0, \tag{32}$$

where λ_0 is the wavelength and h_0 is the water depth at $|x| = L$.

In many cases the manner of determining the wavelength λ_0 and the duration T_0 of a solitary pulse is not clear. In particular, most of the wave shapes (represented by analytical functions that are continuous in all derivatives) are nonzero everywhere at $-\infty < t < \infty$. There is obvious ambiguity in the definition of their wavelength (or duration) that can be interpreted as their width at any level of elevation, or by the value of an appropriate integral (DIDENKULOVA *et al.*, 2007a, 2008).

A convenient definition of the wavelength is the extension (spatial or temporal) of the wave profile elevation exceeding the 2/3 level of the maximum wave height. This choice is inspired by the definition of the significant wave height and length in physical oceanography and ocean engineering. For symmetric solitary waves, "significant" wave duration and "significant" wavelength are

$$T_s = 2T_0 f^{-1}\left(\frac{2}{3}\right), \quad \lambda_s = \sqrt{gh_0}\, T_s, \tag{33}$$

where f^{-1} is the inverse function of f. Thus the formulas for the maximal displacement, the velocity of the moving shoreline, and the breaking parameter can be expressed as

$$R_{\max} = \mu_R^+ H_0 \sqrt{\frac{L}{\lambda_s}}, \quad U_{\max} = \mu_U^+ \frac{H_0 L}{\lambda_s} \sqrt{\frac{g}{\alpha \lambda_s}}, \quad Br = \mu_{Br} \frac{H_0 L}{\alpha \lambda_s^2} \sqrt{\frac{L}{\lambda_s}}, \tag{34}$$

where coefficients (below called form factors) μ_R^+, μ_U^+ and μ_{Br} depend on the wave form:

$$\mu_R^+ = 2\sqrt{2\pi f^{-1}\left(\frac{2}{3}\right)}\, p_R, \quad \mu_U^+ = 4\sqrt{2\pi\left[f^{-1}\left(\frac{2}{3}\right)\right]^3}\, p_U, \quad \mu_{Br} = 8\sqrt{2\pi\left[f^{-1}\left(\frac{2}{3}\right)\right]^5}\, p_{Br}. \tag{35}$$

The analogous formulas for draw-down height and velocity can be obtained from (34, 35) by replacing $p_R \to \bar{p}_R = \min\{I\}$, $p_U \to \bar{p}_U = \min\{dI/d\zeta\}$ and $p_{Br} \to \bar{p}_{Br} = \min\{d^2I/d\zeta^2\}$ in (29) and (30).

A remarkable property of this choice is that if the solitary wave duration is determined at the 2/3 level of the maximum height (33), the effect of the difference in the wave shapes will be fairly small. The analytical expressions for maximal runup characteristics (runup and draw-down heights, runup and draw-down velocities and

breaking parameter) become universal and depend on the height and duration of the incoming onshore wave only.

4. Results of Calculations

We first consider the runup of incident symmetrical positive waves which have the shape of various "powers" of a sinusoidal pulse

$$f(\zeta) = \cos^n(\pi\zeta), \quad \text{where } n = 2, 3, 4, \ldots \tag{36}$$

which are defined on the segment [–1/2, 1/2]. Their shapes have a certain similarity, however, their wave characteristics, such as mean water displacement, energy and wave duration on various levels, differ considerably (Fig. 2). The functions representing such impulses have different smoothness: their n-th order derivatives are discontinuous at their ends. The case of $n = 1$ is not considered, as the relevant integrals in Equations (29) and (30) do not converge. The runup of sinusoidal pulse for the case of $n = 2$ is presented on Figure 3. Such oscillations are typical for runup of symmetric solitary waves on a beach of constant slope.

Form factors for runup μ_R^+ and draw-down μ_R^- height, runup μ_U^+ and draw-down μ_U^- velocity and breaking parameter μ_{Br}, calculated for all sine power pulses (36) with the use of the definition of the characteristic wave length λ_s (33) at the 2/3 level of the maximum height, are presented in Figure 6 at the end of section 4. Calculating means and root-mean-square deviations results in the values of form factors for the maximum wave runup $\mu_R^+ = 3.61 \cdot (1 \pm 0.02)$ and draw-down $\mu_R^- = 1.78 \cdot (1 \pm 0.28)$ that have a fairly limited variation (Table 1).

Initially, it is significant that the runup height is higher than the draw-down height. This feature is observed for all sets of positive impulses. The form factor for the
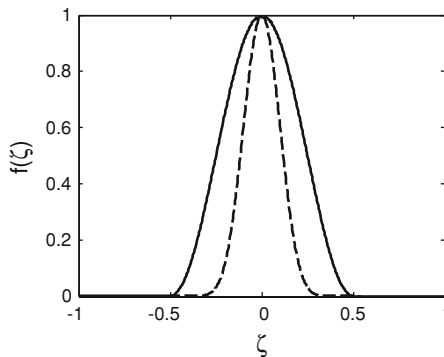

Figure 2
Family of sine power pulses (36): Solid line $n = 2$ and dashed line $n = 10$.

Table 1

Calculated form factors for different wave shapes

μ	Sine power	Soliton power	Lorentz pulse power
μ_R^+	$3.61 \cdot (1 \pm 0.02)$	$3.55 \cdot (1 \pm 0.05)$	$3.53 \cdot (1 \pm 0.08)$
μ_R^-	$1.78 \cdot (1 \pm 0.28)$	$1.56 \cdot (1 \pm 0.28)$	$1.51 \cdot (1 \pm 0.44)$
μ_U^+	$4.65 \cdot (1 \pm 0.30)$	$4.15 \cdot (1 \pm 0.22)$	$4.07 \cdot (1 \pm 0.26)$
μ_U^-	$6.98 \cdot (1 \pm 0.01)$	$6.98 \cdot (1 \pm 0.02)$	$6.99 \cdot (1 \pm 0.04)$
μ_{Br}	$13.37 \cdot (1 \pm 0.10)$	$12.90 \cdot (1 \pm 0.03)$	$12.99 \cdot (1 \pm 0.13)$

maximum wave runup in Equation (35) is almost independent on the power n, demonstrating that the influence of the initial wave shape on the extreme runup characteristics can be made fairly small by an appropriate choice of the characteristic wavelength. The above choice of the (significant) wavelength reduces the variation of the form factor for the sine power pulses to a remarkably small value, about 2%.

The deepest draw-down is more affected by the wave shape: The relevant form factor varies up to 28%. This feature can be explained by the presence of a complex field of motions in the draw-down phase. A positive wave first executes runup and only later draw-down (see Fig. 3). Therefore the runup process is predominantly governed by the incident wave dynamics while the draw-down phenomena occurs under the influence of a set of distributed wave reflections and re-reflections from the slope and consequently it is more sensitive to the wave shape variations.

A similar analysis can be applied to maximum runup and draw-down velocities of the moving shoreline. Calculated form factors for maximum run-up μ_U^+ and draw-down μ_U^- velocities are presented on Figure 7 with triangles. The maximal values for the draw-down velocity are always greater than for the runup velocity for initial unidirectional impulses. The form factor for the draw-down velocity $\mu_U^- = 6.98 \cdot (1 \pm 0.01)$ is almost constant for all values of n (root-mean-square deviation is 1%) whereas the runup velocity $\mu_U^+ = 4.65 \cdot (1 \pm 0.30)$ changes in a wider range ($\pm 30\%$); see Table 1.
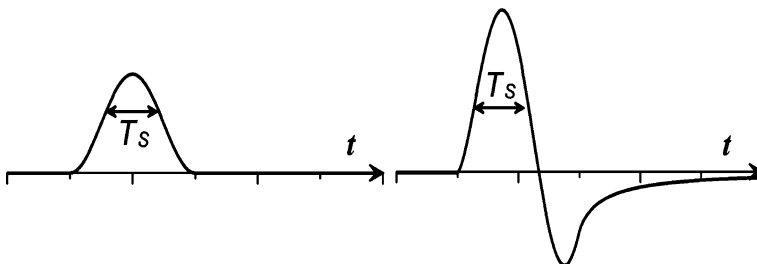

Figure 3

The runup of a symmetric solitary wave on a beach of constant slope. Left panel shows water surface elevation at $x = -L$, right panel shows wave runup on shore. Notice that the duration T_s of the incident wave is defined at $x = -L$ and is not necessarily conserved during the run-up and rundown process.

Variations of the form factor for the breaking parameter are also weak (see Fig. 8, triangles). The case of $n = 2$, corresponding to the discontinuity of the second-order derivative, is excluded since the integral in Equation (31) diverges. The relevant form factors $\mu_{Br} = 13.37 \cdot (1 \pm 0.10)$ can be considered a constant with a reasonable accuracy (Table 1).

Thus, form factors for the most important parameters such as runup height, draw-down velocity, and to some extent for breaking parameters, are universal and do not depend on the particular shape of a sine power impulse. The variations of form factors for draw-down height and runup velocity are more significant (about 30%), however, they also can be neglected for engineering estimates.

As the second example of the proposed approach we consider the family of solitary waves, described by the following expression,

$$f(\zeta) = \sec h^n(4\zeta), \quad n = 1, 2, 3, \ldots \tag{37}$$

These impulses are unlimited in space with exponential decay of the elevation at their ends (see Fig. 4). The case $n = 2$ corresponds to the well-known soliton solution of the Korteweg-de Vries (KdV) equation, which is frequently used as a generic example of shallow water solitary waves.

The runup of the KdV solitons on a constant beach was studied previously by SYNOLAKIS (1987) who presented both experimental and theoretical results. In our notation, the Synolakis formula (SYNOLAKIS, 1987) is

$$\frac{R_{\max}}{H_0} = 2.8312 \sqrt{\frac{L}{h_0}} \left(\frac{H_0}{h_0}\right)^{1/4}. \tag{38}$$

The "significant" wavelength of the soliton is easily calculated from the well-know analytical expression for a soliton in a constant-depth basin
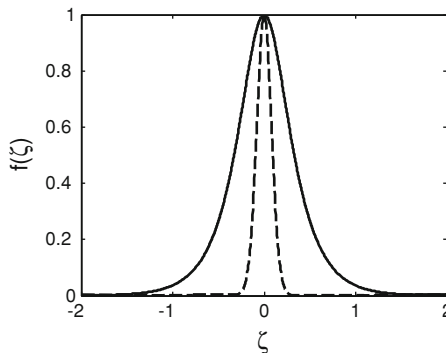

Figure 4
Family of soliton-like impulses (37): Solid line $n = 1$ and dashed line $n = 10$.

$$\eta(x) = H_0 \text{sech}^2 \left(\sqrt{\frac{3H_0}{4h_0}} \frac{x}{h_0} \right) \tag{39}$$

and has the explicit form:

$$\lambda_s = 4 \text{sech}^{-1} \left(\sqrt{\frac{2}{3}} \right) h_0 \sqrt{\frac{h_0}{3H_0}}, \tag{40}$$

where $\text{sech}^{-1}(z)$ is an inverse function of $\text{sech}(z)$. Substituting the expression for H_0/h_0 from (40) into the right-hand side of (38), we obtain

$$\frac{R_{\max}}{H_0} = 3.4913 \sqrt{\frac{L}{\lambda_s}}. \tag{41}$$

Our numerical calculations lead to the same value of the form factor, $\mu_R^+ = 3.4913$ at $n = 2$. This example indicates that the theory of soliton runup on a beach, which leads to a nonlinear relation between the runup height and the soliton amplitude, is consistent with a general theory of the runup of solitary waves on a beach and represents a special case.

The form factors for the maximum height of the wave runup and draw-down for different values of n (Fig. 6) again virtually do not depend on the exponent n. This feature suggests that the proposed approach is not sensitive with respect to the shape of the impulses. The form factors, averaged over the range $n = 1$ - 20 are $\mu_R^+ = 3.55 \cdot (1 \pm 0.05)$ for the runup and $\mu_R^- = 1.56 \cdot (1 \pm 0.28)$ for the draw-down height (Table 1). Notice that these values are close to analogous coefficients for sine power pulses.

Form factors for runup and draw-down velocities and breaking parameters (Figs. 7 and 8) are $\mu_U^+ = 4.15 \cdot (1 \pm 0.22)$, $\mu_U^- = 6.98 \cdot (1 \pm 0.02)$, and $\mu_{Br} = 12.90 \cdot (1 \pm 0.03)$ (Table 1). The variation of these parameters for different values of n for soliton-like impulses is to some extent similar to the analogous dependence for sine power pulses. The largest difference is that the runup velocity form factor for sine-pulses increases with a decrease of the exponent, while the runup velocity form factor for soliton-like impulses decreases with a decrease of the exponent.

Similar results are obtained for solitary ridges of a Lorentz-like shape with algebraic decay (Fig. 5)

$$f(\zeta) = \frac{1}{\left[1 + (4\zeta)^2 \right]^n}, \quad n = 1, 2, 3, \dots \tag{42}$$

The calculated runup and draw-down height form factors for this class of solitary waves (Fig. 6) show some variability in the range of $n = 1 \div 20$. The average values are $\mu_R^+ = 3.53 \cdot (1 \pm 0.08)$ for the runup and $\mu_R^- = 1.51 \cdot (1 \pm 0.44)$ for the draw-down height (Table 1). The variation of μ_R^+ is still very reasonable. The form factors for runup and draw-down velocities and breaking parameter (Figs. 7 and 8) show even smaller
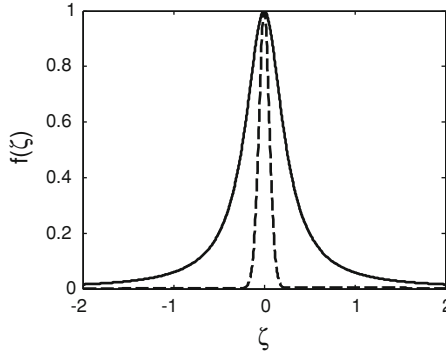
Figure 5
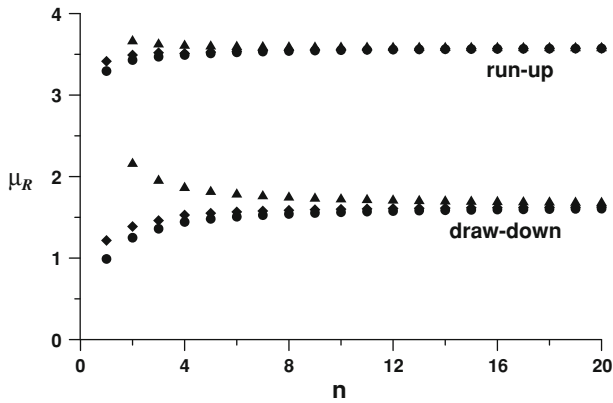Family of Lorentz-like impulses (42): Solid line $n = 1$ and dashed line $n = 10$.

Figure 6
Calculated form factors for the maximum runup μ_R^+ and draw-down μ_R^- height for sine power pulses (triangles), soliton-like (diamonds) and Lorentz-like (circles) impulses.

variation: $\mu_U^+ = 4.07 \cdot (1 \pm 0.26)$, $\mu_U^- = 6.99 \cdot (1 \pm 0.04)$, and $\mu_{Br} = 12.99 \cdot (1 \pm 0.13)$. Their dependence on the exponent n is similar for other families of impulses.

5. Conclusions

The central outcome from the presented study is that the influence of the initial wave form on maximal runup characteristics can be almost removed, or made fairly weak, by means of a proper choice of incident wave characteristics. The properties of the features with the largest variation such as the runup heights, draw-down velocities, and the
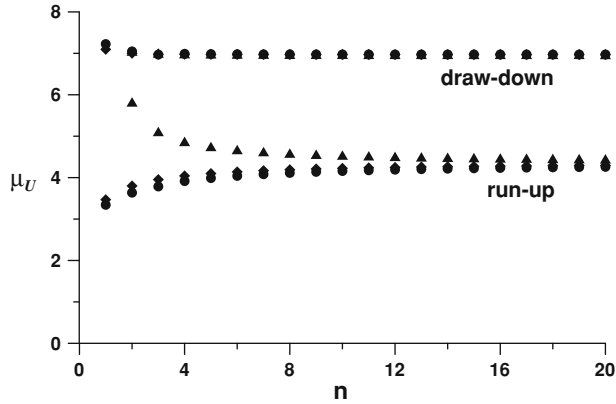
Figure 7

Calculated form factors for the maximum runup μ_U^+ and draw-down μ_U^- velocity for sine power pulses (triangles), soliton-like (diamonds) and Lorentz-like (circles) impulses.
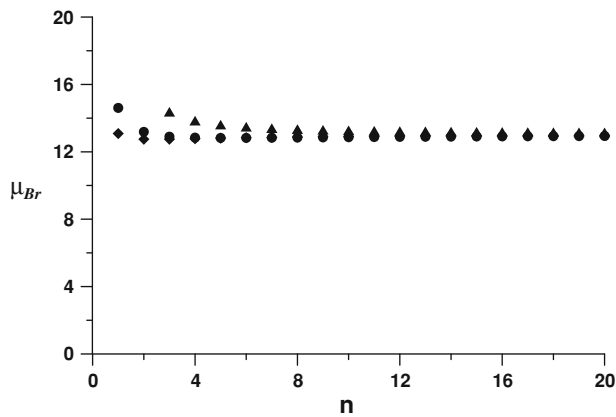

Figure 8

Calculated form factors for the breaking parameter μ_{Br} for sine power pulses (triangles), soliton-like (diamonds) and Lorentz-like (circles) impulses.

breaking parameter are at best described with this approach while the other key properties such as the draw-down depths of runup velocity are reasonably reproduced.

Another key result of the study is that the average values of calculated form factors for all concerned classes of symmetrical positive solitary waves (Table 1, Figs. 6–8) and formulas (34) for the maximum runup and draw-down characteristics of solitary waves virtually do not depend on the form of the incident wave if the wave duration is appropriately defined. This is especially evident with the form factors for the runup height and draw-down velocity, where the variations for all the wave classes in question do not exceed 8%.

This property suggests that the definition of the "significant" wavelength for solitary waves at the 2/3 level of their maximum height is optimal. In this case the following approximate analogues of formulas (34) for the runup and draw-down characteristics of the long waves on a beach are universal:

$$R_{\text{run-up}} = 3.5 H_0 \sqrt{\frac{L}{\lambda_s}}, \quad R_{\text{draw-down}} = 1.5 H_0 \sqrt{\frac{L}{\lambda_s}}, \tag{43}$$

$$U_{\text{run-up}} = 4.5 \frac{H_0 L}{\lambda_s} \sqrt{\frac{g}{\alpha \lambda_s}}, \quad U_{\text{draw-down}} = 7 \frac{H_0 L}{\lambda_s} \sqrt{\frac{g}{\alpha \lambda_s}}, \quad Br = 13 \frac{H_0 L}{\alpha \lambda_s^2} \sqrt{\frac{L}{\lambda_s}}. \tag{44}$$

Expressions (43–44) can be used for estimates of the runup and draw-down characteristics of approaching tsunamis as soon as rough estimates for their heights, significant lengths and periods in the open ocean become available.

Finally, we note that the obtained results hold only for symmetrical solitary waves. If the incident wave is shaped as an *N*-wave, also typical for the tsunami problem (TADEPALLI and SYNOLAKIS, 1994, 1996; TINTI and TONINI, 2005), the magnitude of coefficients in the "runup" formulas will differ from that given in (43)–(44); see for comparison the difference between run-up heights of a soliton and its derivative (SYNOLAKIS, 1987; TADEPALLI and SYNOLAKIS, 1994). If the incident wave is an asymmetrical wave, with different steepness of the front and back slopes, the runup characteristics depend on the front-slope steepness (DIDENKULOVA *et al.*, 2006, 2007b). Therefore, the universal character of runup characteristics can be achieved "inside" each class of incident wave shapes. As a result, estimates of run-up characteristics require knowledge of only a few "robust" parameters of the incident tsunami wave (positive crest or negative trough, *N*-wave or asymmetrical wave) but not a detailed description of the wave shape. This conclusion is important in practice, as it allows prediction of runup characteristics of tsunami waves with "unknown" shapes.

Acknowledgements

REFERENCES

BROCCHINI, M. and GENTILE, R. (2001), *Modelling the run-up of significant wave groups*, Cont. Shelf Res. *21*, 1533–1550.

CARRIER, G.F. and GREENSPAN, H.P. (1958), *Water waves of finite amplitude on a sloping beach*, J. Fluid Mech. *4*, 97–109.

CARRIER, G.F., WU, T.T., and YEH, H. (2003), *Tsunami run-up and draw-down on a plane beach*, J. Fluid Mech. *475*, 79–99.

DIDENKULOVA, I.I., ZAHIBO, N, KURKIN, A.A., LEVIN, B. V., PELINOVSKY, E.N., and SOOMERE, T. (2006), *Run-up of nonlinearly deformed waves on a coast*, Dokl. Earth Sci. *411*, 1241–1243.

DIDENKULOVA, I.I., KURKIN, A.A., and PELINOVSKY, E.N. (2007a), *Run-up of solitary waves on slopes with different profiles*, Izvestiya, Atmos. Oceanic Phys. *43*, 384–390.

DIDENKULOVA, I., PELINOVSKY, E., SOOMERE, T., and ZAHIBO, N. (2007b), *Run-up of nonlinear asymmetric waves on a plane beach*, *Tsunami and Nonlinear Waves* (ed. Kundu, A.) (Springer), pp. 173–188.

DIDENKULOVA, I.I. and PELINOVSKY, E.N. (2008), *Run up of long waves on a beach: the influence of the incident wave form*, Oceanology *48*, 1–6.

KAISTRENKO, V.M., MAZOVA, R.Kh., PELINOVSKY, E.N., and SIMONOV, K.V. (1991), *Analytical theory for tsunami runup on a smooth slope*, Int. J. Tsunami Soc. *9*, 115–127.

KÂNOĞLU, U. (2004), *Nonlinear evolution and run-up-rundown of long waves over a sloping beach*, J. Fluid Mech. *513*, 363–372.

KÂNOĞLU, U., and SYNOLAKIS, C. (2006), *Initial value problem solution of nonlinear shallow water-wave equations*, Phys. Rev. Lett. *97*, 148–501.

MADSEN, P.A., and FUHRMAN, D.R. (2008), *Run-up of tsunamis and long waves in terms of surf-similarity*, Coastal Engin. *55*, 209–223.

MAZOVA, R.Kh., OSIPENKO, N.N., and PELINOVSKY, E.N. (1991), *Solitary wave climbing a beach without breaking*, Rozprawy Hydrotechniczne *54*, 71–80.

PEDERSEN, G. and GJEVIK, B. (1983), *Run-up of solitary waves*, J. Fluid Mech. *142*, 283–299.

PELINOVSKY, E. and MAZOVA, R. (1992), *Exact analytical solutions of nonlinear problems of tsunami wave run-up on slopes with different profiles*, Natural Hazards *6*, 227–249.

SYNOLAKIS, C.E. (1987), *The run-up of solitary waves*, J. Fluid Mech. *185*, 523–545.

SYNOLAKIS, C.E. (1991), *Tsunami run-up on steep slopes: How good linear theory really is*, Natural Hazards *4*, 221–234.

TADEPALLI, S. and SYNOLAKIS, C.E. (1994), *The run-up of N-waves*, Proc. Roy. Soc. London *A445*, 99–112.

TADEPALLI, S. and SYNOLAKIS, C.E. (1996), *Model for the leading waves of tsunamis*, Phys. Rev. Lett. *77*, 2141–2145.

TINTI, S., and TONINI, R. (2005), *Analytical evolution of tsunamis induced by near-shore earthquakes on a constant-slope ocean*, J. Fluid Mech. *535*, 33–64.

To access this journal online:
www.birkhauser.ch/pageoph

© Birkhäuser Verlag, Basel, 2008

▌Pure and Applied Geophysics

A Tsunami Detection and Warning-focused Sea Level Station Metadata Web Service

JOHN J. MARRA,[1] UDAY S. KARI,[1] and STUART A. WEINSTEIN[2]

Abstract—Currently information used to describe sea-level stations (such as location, collection and transmission capabilities, operator identification, etc.) is distributed among databases held by multiple agencies, institutions and organizations. Such information could be used to support detection and warning. However, the Indian Ocean Tsunami of 26 December, 2004 made it clear that such information is not readily accessible, is difficult to use, and is often incomplete. In addressing this issue, agencies within the Pacific region are collaborating to develop a web service to expose station metadata enabling various types of real-time data mining client applications that support decision-making and strategic planning at Tsunami Warning Centers. Because information about sea levels has a broad range of applications, integration of this information in a way that is comprehensive, and enhances its access and use, would have a tremendous impact on lives and livelihoods.

Key words: Tsunami detection, Tsunami warning, XML, service-oriented architecture.

List of acronyms

Acronym	Definition
API	Application Programming Interface
CISESE	Centro de Investigación Científica de Ensenada
CO-OPS	Center for Operational Oceanographic Products and Services
DAPS	Data Acquisition and Processing System
GIS	Geographic Information Systems
GTS	Global Telecommunications System
GUI	Graphic User Interface
HTML	HyperText Markup Language
IDEA	Integrated Data and Environmental Applications
JMA	Japan Meteorological Agency
KML	A file format used to display geographic data in browser such as Google Earth, Google Maps, and Google Maps and is based on the XML standard
NCDC	National Climatic Data Center
NDBC	National Data Buoy Center
NESDIS	National Environmental Satellite Data and Information Service
NOAA	US National Oceanic and Atmospheric Administration
NOS	National Ocean Service

[1] NOAA IDEA Center, East-West Center, 1601 East West Road, Honolulu, Hawaii 96848-1601, U.S.A. E-mail: john.marra@noaa.gov, uday.kari@noaa.gov

[2] NOAA Pacific Tsunami Warning Center, 91-270 Fort Weaver Road, Ewa Beach, Hawaii 96706-2928, U.S.A. Eail: stuart.weinstein@noaa.gov

NTF   Australian National Tidal Facility
NWS   National Weather Service (NWS)
NWSTG   National Weather Service Telecommunications Gateway
OGC   Open Geospatial Consortium
PDC   Pacific Disaster Center
PRIDE   Pacific Region Integrated Data Enterprise
PTWC   Pacific Tsunami Warning Center
SHOA   Servicio Hidrográfico y Oceanográfico de la Armada de Chile
SOAP   Simple Object Access Protocol
SWE   Sensor Web Enablement
TWML   Tsunami Warning Markup Language
UHSLC   University of Hawaii Sea-Level Center
UNESCO   United Nations Educational Scientific and Cultural Organization
WC-ATWC   West Coast and Alaska Tsunami Warning Center
WMO   World Meteorological Organization
XML   Extensible Markup Language

1. Introduction

The Tsunami of 26 December, 2004 exposed a need for sea-level station data to be at the fingertips of warning center personnel and disaster managers. Specifically, in the critical moments after the earthquake was reported, it was unclear to officials if there were any sea-level stations located nearby operating in real-time and, if so, whom to contact to obtain the water level records. In post-disaster hindsight, it became obvious that information about sea-level stations that could be used to support detection and warning (such as location, collection and transmission capabilities, operator identification) are insufficiently known or simply inaccessible.

In 2005, parties interested in enhancing the access and use of sea-level station data united under the US National Oceanic and Atmospheric Administration (NOAA), National Environmental Satellite Data and Information Service (NESDIS), National Climatic Data Center (NCDC), Integrated Data and Environmental Applications (IDEA), and the Center's Pacific Region Integrated Data Enterprise (PRIDE) program. The first order of business was to develop a plain language semantic description of a sea-level station as applicable to tsunami hazards. This semantic description was later formalized into an Extensible Markup Language (XML) schema definition.

Thus a multiyear effort began to develop a distributed metadata system describing sea-level stations, starting with pilot activities in a regional framework and focusing on tsunami detection and warning systems being developed by various agencies. A summary of discussions and concepts related to this effort is described in the United Nations Educational Scientific and Cultural Organization (UNESCO) document IOC/INF-1226 of April, 2006.

This activity has matured to whereby metadata for stations monitored by the Pacific Tsunami Warning Center's (PTWC) "Tide Tool" application are now available for

consumption by XML enabled client applications. Specifically, the service is available in two formats: KML, which can be opened with Google Earth, and XML (http://www.sealevelstations.org/). Through these services users can visually locate sea level stations in an area of interest (such as in immediate proximity of an undersea earthquake) and simply click on station icon to access station metadata, and in some cases the wave and water level records at the station.

During recent years, the data content and sharing issues embodied in this schema have been discussed at various forums. Resultingly various stakeholders have emerged who have different provider and user perspectives (semantic content) and also exchange formats (not limited to just XML). The challenge then, is not only to capture all data requirements, but also to have formal representation that is easily transformed into any specified format (ICG/PTWS, 2006). The latest revision of the sea-level gauge schema (Version 0.3) begins to address this challenge. It encompasses a broader range of provider and user perspectives, such as station operators, warning system managers, disaster managers, and other marine hazard warning systems (such as storm surge and sea-level change monitoring and research). The plain language version of the schema can be found at http://www.sealevelstations.org/docs/schema.pdf. An XML version can be found at http://www.sealevelstations.org/pride/xmlschema/wls.xsd.

Users will be able to create custom client applications to quickly drill-down to detailed information or conduct custom transformations to monitor a real-time event
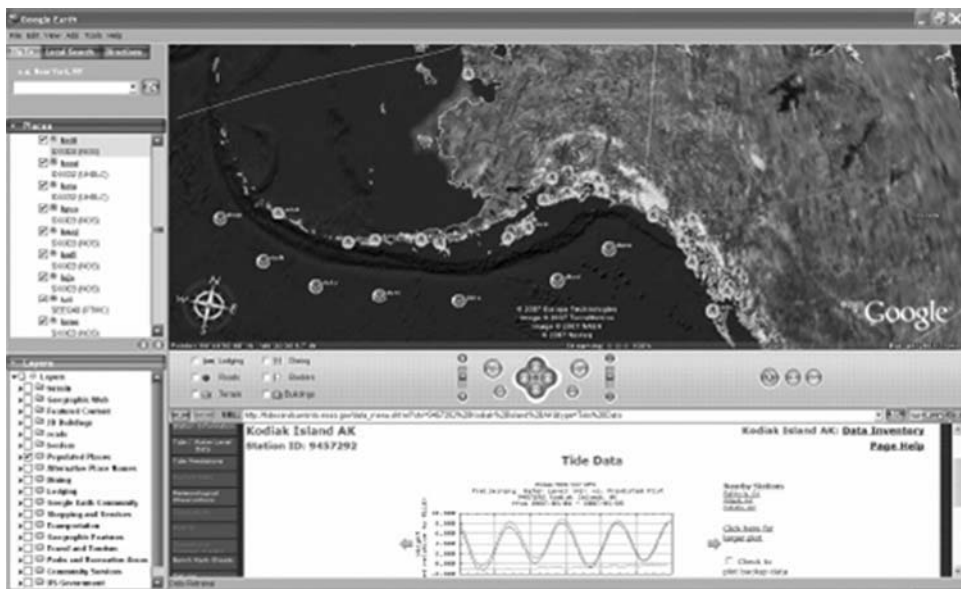

Figure 1
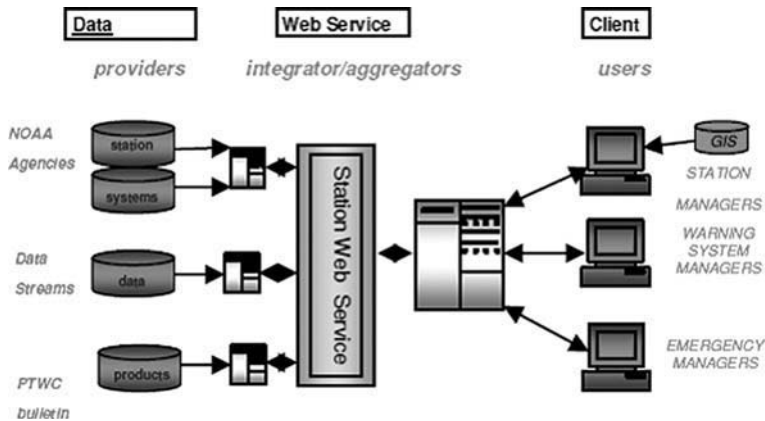Sea-level Station Web Service (enabling Google Earth Desktop Client).

Figure 2
Sea-level Station Web Service Architecture.

using tools like the PTWC TideTool. Some of these transformations can be simple XML-to-XML transformation such as the KML standard supported by a rich client like Google Earth, as shown in Figure 1. Others can support loosely coupled Simple Object Access Protocol (SOAP) web service clients' applications that consume the same service for different purposes.

As shown in Figure 2, the high-level technical motivation was to convert various data *sources* to data *services*. This represents the best hope of integrating various data sets and extending them to seamlessly enable real-time interactions with various clients featuring water level information. The XML schema and application programming interface (API) address key parameters and remote procedures that pertain to tsunami warnings. As long as all the metadata on sea-level stations are exposed in a consistent format, a decision-maker can determine what kind of sea-level stations are deployed out in the ocean and how many of those can be depended on to support tsunami warnings (i.e., meet specific sampling/transmission standards).

The gist of Figure 2 is that data sources can be of various types however, the client side view is intended to be integrated and seamless thanks to the web service. The client could be Geographic Information System (GIS)-based, as shown. Or, it could be a SOAP-based client that extends the published interfaces to mine the web service for data according to the needs of various domains (such as station managers, warning system managers and emergency managers), as shown under user perspectives in Figure 2.

2. The Tide Tool Use Case

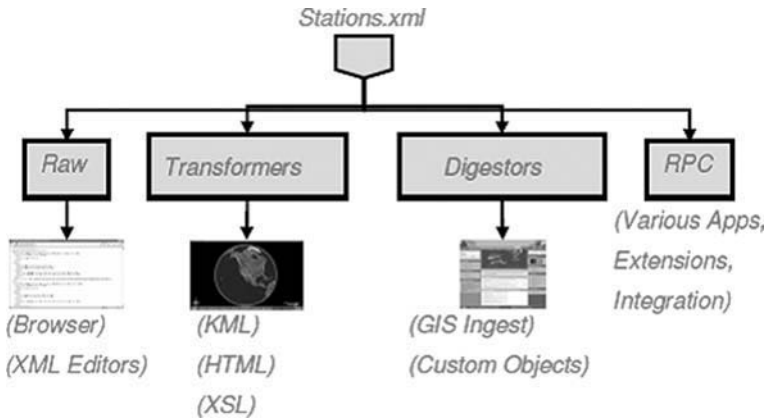As shown in Figure 3, there are four chief methods of consuming the XML station metadata released by the PTWC:

Figure 3
Web Service Consumption Patterns.

- Raw: Various XML aware applications such as web browsers and sophisticated XML editors can be configured to visualize some or all of the station metadata being exposed.
- Transformation: By applying a stylesheet or equivalent programmatic transformations, the raw XML may be transformed into markup languages like KML/HTML to enable specific clients like Google Earth.
- Digest: Fundamentally, the digest pattern involves absorption or conversion into completely different object models or schemas. Typically, these object models are used to populate customized database tables (such as GIS layers).
- Remote Procedure Calls (RPC): Various applications may build on the schema for the stations XML file and feature remote procedures to mine the data referred to by the metadata contained in the file.

Stuart Weinstein developed a Tide Tool as a platform-agnostic tool (Tcl/Tk environment) to process sea-level data at the NOAA PTWC. Sea-level data are transmitted across the Global Telecommunications System (GTS), World Meteorological Organization (WMO) circuit and flows to the PTWC over a dedicated circuit. The data are downloaded into a log file that is changed daily. PTWC's Watertool program reads the log file every 15 seconds to retrieve new data. Watertool has three main parts: A decoder, a graphic user interface (GUI) and a monitor. Graphics are created by the Tcl/Tk programming language. Tcl/Tk is an Open-Source and is an independent platform/ operating system. While Tcl/Tk may be platform-independent, Watertool is a complicated piece of software that is not very transportable. Watertool is an embedded Tcl/Tk application. In an effort to create something transportable and easy to maintain, Dr. Weinstein developed Tide Tool as a pure Tcl/Tk application (WEINSTEIN, 2006). For more information on Tide Tool and to obtain the Tide Tool software contact WEINSTEIN directly at stuart.weinstein@noaa.gov.

In the Pacific Ocean region, sea-level gauges are maintained by various agencies such as the PTWC, West Coast and Alaska Tsunami Warning Center (WC-ATWC), NOAA National Ocean Service (NOS), Center for Operational Oceanographic Products and Services (CO-OPS), and National Weather Service (NWS), National Data Buoy Center (NDBC), Servicio Hidrográfico y Oceanográfico de la Armada de Chile (SHOA), the Australian National Tidal Facility (NTF), Japan Meteorological Agency (JMA), Centro de Investigación Científica de Ensenada (CISESE), and University of Hawaii Sea-Level Center (UHSLC). The data are received by satellite and forwarded to PTWC via the National Weather Service Telecommunications Gateway (NWSTG). The Data Acquisition and Processing System (DAPS) system is used as a backup.

The systems are constantly being upgraded. For instance, while many stations still transmit hourly, West Coast, Hawaii, Puerto Rico, and Alaska NOS gauges have been upgraded to a 6-minute transmission schedule. In any case, the decoding of raw sea-level data is fraught with breakdowns because *several ever-changing data formats are being used*.

2.1. Examples

UHSLC Format – Readable ASCII.
SWIO40 RJTD 250015
:ENB 1 #1M 3908 3908 3910 3909 3911 3909 3912 3910 3913 3913 3917 3917 3917 3917 3915 3918 3914 3917 3912 3913 3913 3913 3912 3913 3911 3908 3908 3905 3909
:ENC 1 #2 3409 3410 3411 3411 3413 3419 3419 3420 3419 3415 3414 3418 3411 3408 3410 3409 3409 3408 3409 3409 3414 3413 3409 3414 3414 3410 3412 3409 3410 3413
:BATTLOAD 0 12.83
:NAME=
Values are sea level in one hundreds of a foot. Newer gauges are metric.

NTC Format - Unreadable Format.
91642 46/// /1205 10296 40080 22200 00287 555 77744 A0102 516'3 60029 6315B
03024 83030 00A07 02548 02901 29631 6B090 24520 2400A 13025 90036 00297
317B1 50240 60310 0A190 26230 38002 96317 B2102 37103 100A2 50266 50330
02973 18B27 02331 02800 A3102 70103 10029 8318B 33022 92026 00A37 02736
03401 29831 8B390 22570 2801A 43027 66028 00299 319B4 50222 50230 0A490
27960 34002 98319 B5102 19202 901A5 50282 20380 02983 19B57 02163 03200
BV289 134S1 41249 C0501 22080 00070 23677 44777=

NOS Format - No Apparent Pattern. SXXX03 KWAL 222359
^^336B73B2174235919″P94440901CdM~[@@v0E~W1A@v@JBA|Ay>AAe5A^<-
VF2@vf@E@″@vC nTWxPBOBSBWB_BeBn 43+0NN 150 W
This example was transmitted from the Port Angeles sea-level station. The "T" near the end is the "tsunami data" flag. What follows is the payload of 6 one-minute samples.

This represents an unpredictable requirement for the Tide Tool to first figure out how the data is encoded and how frequently it is transmitted. In fact, a considerable amount of code in Tide Tool is dedicated to maintaining pace with the changing station metadata from various agencies. With a sea-level station web service that is dedicated to keeping station metadata current, the Tide Tool code base can be stabilized and focused in its area of core competence, which is to conduct data mining and to display water level data.

This demonstrates the potential value of the sea-level station web service to a desktop client application that needs to harvest detailed wave and water level information based on station metadata exposed by the service.

3. Future Directions

To support comprehensive hazards data and product-sharing in Hawaii and the Pacific Ocean region, we envision creating self-describing data services that feature schema and procedures which directly enable custom clients for various domains. At the current status of the development, we consider ourselves to be viewing the tip of an iceberg in terms of what is possible.

Specific actions we plan to take in the near term include:

- Initiate contact with individual sea-level station operators in the Pacific and explore opportunities to stand-up operator-based web services.
- Refine the XML-based tide station metadata schema by following the process that leads to development of the pilot sea-level station metadata web service. Consult with station operators and user community regarding additional elements in the XML schema. Ideally, expand it to include metadata applicable to other marine hazard warning systems (such as storm surges), sea-level change monitoring and research (ICG/PTWS, 2006).
- Facilitate creation and deployment of a web-enabled client-application that harvests and displays sea-level station metadata and other relevant information and that, at a minimum, could be used by tsunami warning system managers.

Over the medium to long-term we will strive to:

- Make web services user-driven. Specifically, create data mining remote procedure calls enabling clients to maintain and harvest data for various purposes.
- Promote the regular use of web services in disaster training, simulation and exercises. Only through regular usage will we be able to work out the defects to a point where the web service enabled clients can be useful in a real event to save lives.
- Explore relevant and emerging standards, such as, the Open Geospatial Consortium (OGC), Sensor Web Enablement (SWE) Framework, Tsunami Warning Markup Language (TWML), etc. that will serve all prospective stakeholders in the community most usefully (i.e., in an extensible, scalable) manner.

- Fully integrate a GIS client like Google Earth with an HTTP enabled desktop client application like PTWC Tide Tool, display tsunami arrival times.
- Continue communication and coordination with interested parties, building upon the discussions described in the UNESCO document IOC/INF-1226 of April 2006.

The development of a sea-level station metadata web service and associated activities described here is part of a broader vision of coastal inundation and erosion data and product development that:

- Effectively integrates observations, research, integrated modeling, forecasting, assessment, information management and education; and
- Involves a true partnership among the providers of information on coastal conditions and the users of that information in government, resource management, community planning, business and science (MARRA *et al.*, 2007).

The desired outcome is that planners, managers, and other decision-makers will have timely access to information that is both accurate and appropriate, and, as such, will afford them the opportunity to plan and respond accordingly. As a result, the resilience and adaptive capacity of coastal communities affected by inundation in all its forms will be enhanced.

REFERENCES

Intergovernmental Coordination Group Pacific Tsunami Warning System (ICG/PTWS) *Message Formats Content*. Working Group 2: Sea Level Measurements, Data Collection and Exchange, Melbourne, Australia, May 1-2, 2006.

International Oceanographic Data and Information Exchange (IODE). *Meeting on the Development of a Sea Level Metadata Web Service Demonstrator Project*. IOC/INF-1226 Intergovernmental Oceanographic Commission (UNESCO), Ostend, Belgium, March 28–29, 2006. Available at http://www.sealevelstations.org/.

KARI, U., MARRA, J., and WEINSTEIN, S. A. *Tsunami-Focused Tide Station Data Sharing Framework*. IN22A-03 Earth and Space Science Informatics Session, AGU Fall Meeting Abstract, San Francisco, California, December 12, 2006.

MARRA, J. J., ALLEN, T., EASTERLING, D., FAUVER, S., KARL, T., LEVINSON, D., MARCY, D., PAYNE, J., PIETRAFESA, L., SHEA, E., and VAUGHAN, L.. *An Integrating Architecture for Coastal Inundation and Erosion Program Planning and Product Development*. Special Issue Marine Technology Society Journal, Spring 2007.

WEINSTEIN, S.A., *Operations, Systems and Procedures Manual*, Working Draft Edition 0.90, Pacific Tsunami Warning Center, Ewa Beach, Hawaii, April 2006. Available on the UNESCO website: ftp://ioc.unesco.org/ITIC/PTWC/ as PTWCOpsManual.doc <ftp://ioc.unesco.org/ITIC/PTWC/PTWCOpsManual.doc> or PTWC-OpsManual_v0.90_12pt.doc. <ftp://ioc.unesco.org/ITIC/PTWC/PTWCOpsManual_v0.90_12pt.doc>.

To access this journal online:
www.birkhauser.ch/pageoph

Long-Term Tsunami Data Archive Supports Tsunami Forecast, Warning, Research, and Mitigation

Paula K. Dunbar,[1] Kelly J. Stroker,[1] Vanita R. Brocko,[2] Jesse D. Varner,[2]
Susan J. McLean,[1] Lisa A. Taylor,[1] Barry W. Eakins,[2] Kelly S. Carignan,[2]
and Robin R. Warnken[1]

Abstract—In response to the 2004 Indian Ocean tsunami, the United States began a careful review and strengthening of its programs aimed at reducing the consequences of tsunamis. Several reports and calls to action were drafted, including the Tsunami Warning and Education Act (Public Law 109–424) signed into law by the President in December 2006. NOAA's National Geophysical Data Center (NGDC) and co-located World Data Center for Geophysics and Marine Geology (WDC-GMG) maintain a national and international tsunami data archive that fulfills part of the P.L. 109-424. The NGDC/WDC-GMG long-term tsunami data archive has expanded from the original global historical event databases and damage photo collection, to include tsunami deposits, coastal water-level data, DART[TM] buoy data, and high-resolution coastal DEMs. These data are used to validate models, provide guidance to warning centers, develop tsunami hazard assessments, and educate the public about the risks from tsunamis. In this paper we discuss current steps and future actions to be taken by NGDC/WDC-GMG to support tsunami hazard mitigation research, to ultimately help save lives and improve the resiliency of coastal communities.

Key words: Tsunami, historical events, data archive, bathymetry, coastal hazard, damage photos, DART[TM], water-level data, DEM.

1. Introduction

The 2004 Indian Ocean tsunami tragically illustrated the fact that although deadly tsunamis are infrequent natural hazards, their impacts can be devastating. Immediately following this event, the United States began a careful review of its programs aimed at reducing the consequences of tsunamis. Several reports and calls to action were drafted, including the United States Tsunami Warning and Education Act (Public Law 109–424) signed into law by the President in December 2006. This law identifies the National Oceanic and Atmospheric Administration (NOAA) as the lead agency responsible for tsunami warnings, research, and mitigation in the United States. Section 4-b-6 of the

---

[1] National Oceanic and Atmospheric Administration (NOAA), National Geophysical Data Center (NGDC), Boulder, CO 80305-3328, U.S.A. E-mail: Paula.Dunbar@noaa.gov

[2] Cooperative Institute for Research in Environmental Sciences (CIRES), University of Colorado, Boulder, CO 80309-0216, U.S.A.

P.L. 109–424 states that NOAA is required to maintain data quality and management systems to support the requirements of the NOAA tsunami program. The current steps and future actions to be taken by NOAA's National Geophysical Data Center (NGDC) and co-located World Data Center for Geophysics and Marine Geology (WDC-GMG) to fulfill the requirements of the P.L. 109–424 and to support tsunami research and coastal resiliency are discussed in this paper.

NGDC is one of three national data centers operated by NOAA's National Environmental Satellite, Data, and Information Service. NGDC's mission is to provide long-term scientific data stewardship for the Nation's geophysical data, ensuring quality, integrity, and accessibility. NGDC hosts the WDC for Geophysics and Marine Geology (consolidation of the WDC for Tsunami, WDC for Solid Earth Geophysics, and WDC for Marine Geology and Geophysics). The World Data Center System is operated by the International Council for Science (ICSU). Since its establishment in 1957, the World Data Center System has held to the mission that data constitute the raw material of scientific understanding. The strategic goal for ICSU in the 2006–2011 period is to facilitate a coordinated global approach to scientific data and information that ensures equitable access to quality data and information for research, education and informed decision-making. The WDC for Geophysics and Marine Geology provides free and open access to natural hazards data and products, data describing the sea floor and subsea floor, and global gravity and magnetic data. NGDC/WDC-GMG (referred to as NGDC/WDC in the remainder of this document) provides data management expertise to the scientific community, including knowledge of data and metadata standards, data transfer standards, data delivery best practices, and data archive. The principal challenge, particularly in regards to the long-term tsunami data archive, is to provide integrated access to the wide variety of tsunami-related data.

2. Tsunami Data at NGDC/WDC

The NGDC/WDC long-term tsunami data archive provides data and derives products essential for tsunami hazard assessment, forecast and warning, inundation modeling, preparedness, mitigation, education, and research. As a result of NOAA's efforts to strengthen its tsunami activities, the long-term tsunami data archive has grown from less than 5 gigabyte in 2004 to more than 2 terabytes in 2007 (http://www.ngdc.noaa.gov/ hazard/tsu.shtml). The types of data archived for tsunami research and operation activities have also expanded in fulfillment of the P.L. 109–424. The archive now consists of:

- global historical tsunami, significant earthquake and significant volcanic eruptions database
- global tsunami deposits and proxies database
- reference database
- damage photos

- coastal water-level data (i.e., digital tide gauge data and marigrams on microfiche)
- bottom pressure recorder (BPR) data as collected by Deep-ocean Assessment and Reporting of Tsunamis (DART[TM]) buoys.

At the request of the U.S. National Tsunami Hazard Mitigation Program (NTHMP) in 2006, NGDC led an effort to identify data collection and management requirements necessary for the NOAA tsunami program. The results of this project were published in the NOAA technical report *Tsunami Data Management Plan* (NOAA, 2008). This report identified a gap in the long-term archive of high-resolution coastal water-level data as measured by tide stations. NGDC/WDC is currently working with several national and international partners to develop this archive. The seismic data archive is maintained by the Integrated Research Institutions for Seismology (IRIS) (http://www.iris.edu).

NGDC/WDC also provides ocean bathymetric data which are necessary for generating tsunami travel-time maps, and is building high-resolution digital elevation models (DEMs) for select U.S. coastal regions from these and other data sets. These combined bathymetric–topographic DEMs are used to support tsunami forecasting and modeling efforts at the NOAA Center for Tsunami Research, Pacific Marine Environmental Laboratory (PMEL).

The tsunami data archive originates from a wide variety of data providers and sources. These include the NOAA Tsunami Warning Centers (TWC), NOAA National Data Buoy Center (NDBC), NOAA National Ocean Service (NOS), IOC/NOAA International Tsunami Information Center (ITIC), PMEL, U.S. Geological Survey (USGS), tsunami catalogs, reconnaissance reports, journal articles, newspaper articles, internet web pages, and email.

NGDC/WDC has been active in the management of some of these data for more than 50 years while other data management efforts are more recent. These data are openly available, either directly on-line (http://www.ngdc.noaa.gov/) or by contacting NGDC/WDC. Each of the data sets described above are covered in more detail in the following sections.

2.1. *Global Historical Databases*

NGDC/WDC maintains global historical tsunami, significant earthquake, and significant volcanic eruptions databases. These data are compilations of instrumental and/or eyewitness accounts. The data are stored in a spatially-enabled relational database system (RDBMS). During the last three years there has been a major, ongoing effort to review and verify the events in these databases. To accomplish this, NGDC/WDC has retrieved over 2,000 of the original source documents. Each event in the database is associated with a list of one or more source documents. In some cases, different sources provide differing information for a particular record. NGDC/WDC records this information in an event comment field. Currently, the data for 50% of the tsunami

sources, 60% of the tsunami runups, 25% of the earthquakes, and 90% of the volcanic eruptions have been verified by checking the original sources.

The historical tsunami database includes information on more than 2,000 tsunami source events since 2,000 B.C. and more than 12,900 locations where tsunamis were observed. The tsunami event table includes the date, time, and location of the source event, type of source (e.g., earthquake, volcano, landslide, explosion, unknown), magnitude of the source, event validity, maximum wave height, tsunami magnitude and intensity, total number of runups, and the total number of fatalities, injuries, houses damaged, dollar damage from the tsunami, and the source event tabulated separately. The tsunami runup table includes arrival times, travel times, distance from the source, maximum inundation distance, type of measurement (e.g., tide gauge, deep ocean gauge, water height), maximum wave height, first motion of the wave, wave period, and the total number of fatalities, injuries, houses damaged, and dollar damage at the specific runup location. The tsunami source events and associated runups are also linked to the available tide gauge, DART^{TM}, and damage photo data. Figure 1 shows an example of some of the types of data available for the 2004 Indian Ocean tsunami and generating earthquake.

A careful review of the validity of each tsunami event is part of the quality control effort. A validity score, based on several factors, is assigned to each event ranging from 0 for erroneous entries, to 4 for definite tsunamis. For example, tsunamis recorded on tide gauges generated by earthquakes recorded on seismographs are assigned a high validity of 4 in the database. Historical events that occurred before the invention of the seismograph or tide gauge must be evaluated differently. If the event caused significant effects such as deaths or damage, was observed in many locations, or was listed in several reliable independent sources, it is also assigned a high validity. Historical tsunami events generated by earthquakes or volcanoes are crosschecked with regional and local earthquake or volcano catalogs. For example, if a tsunami was reported to have been generated by an earthquake, but there are no listings in the earthquake catalogs, the validity is lowered. Whether the tsunami event occurred before or after the invention of seismographs and tide gauges, a high validity of 3 or 4 is considered a confirmed report of a tsunami event, whereas a validity of 0, 1, or 2 is considered an unconfirmed report.

The review effort also involves checking the water height values in the tsunami runup database with the source documents. The database includes a variety of measurement types including tide gauge data, deep ocean gauge data, water marks measured on buildings during reconnaissance trips, and eyewitness accounts. The definition of the water height will vary depending on the type, and each record in the runup database is flagged to indicate the type of measurement. For example, for tide gauges the water height stored in the database is the amplitude, or half of the peak-to-trough measurement. NGDC/WDC has attempted to use the definitions of maximum runup, maximum water level, and inundation defined in the *Report of the International Measurements Workshop* (LANDER and YEH, editors, 1995) and in the introduction of several NGDC/WDC publications such as p. 4–5 of *Tsunamis Affecting Alaska* (LANDER, 1996). Pdf files of these publications are available on the NGDC/WDC website. Unfortunately, it is not

always possible to determine from the source documents if the tide gauge measurement is the amplitude or double-amplitude, or if tidal corrections have been applied. NGDC/WDC has determined the original source document and verified the water height reported for 75% of the tsunami runups.

The significant earthquake table contains information on more than 5,500 destructive earthquakes from 2150 B.C. to the present that meet at least one of the following criteria: Caused fatalities, caused moderate damage (approximately $1 million or more), magnitude 7.5 or greater, Modified Mercalli Intensity X or greater, or the earthquake generated a tsunami. The table includes the date, time, location, magnitude (m_b, M_L, M_s, M_w, etc.), focal depth, intensity, and the total number of fatalities, injuries, houses damaged, and dollar damage for each earthquake. If the earthquake generated a tsunami, it is linked to the tsunami event. In the past, if different sources provided different information for an earthquake event, multiple records for a single event were included in the table. NGDC/WDC is in the process of removing these duplicates by comparing and consolidating records with the same date, time, and epicentral location. Until this work is completed, statistics derived from the significant earthquake table must be carefully analyzed.

The significant volcanic eruptions table contains information for over 400 volcanic eruptions from 4350 B.C. to the present that meet at least one of the following criteria: Caused fatalities, caused moderate damage (approximately $1 million or more), generated a tsunami, or was associated with a major earthquake. The table includes basic data on each volcano such as the volcano name, location, elevation, and type of volcano that are taken from the Smithsonian publication, *Volcanoes of the World* (SIEBERT and SIMKIN, 2002 to the present). The table also includes information on the volcanic explosivity index, and effects such as deaths, injuries, and damage, which are collected from a variety of sources.

The historical record of a hazard provides clues about what might happen in the future. For example, the frequency of tsunami occurrence and maximum wave heights can be determined from the tsunami tables. Therefore, these data are important for hazard assessment. Utilizing the NGDC/WDC tsunami and the USGS earthquake databases, the NGDC/WDC in collaboration with the USGS completed the first hazard assessment for all U.S. coasts. The results were published in the NOAA technical report *U.S. States and Territories National Tsunami Hazard Assessment: Historical Record and Sources for Waves* (DUNBAR and WEAVER, 2008).

2.2. Global Tsunami Deposits and Proxies Database

As discussed above, the tsunami history of an area is important for assessing the hazard. However, instrumental and written records generally span insufficient time to reveal the full range of a region's tsunami hazard. For example, the cycles of uplift and subsidence along the U.S. Pacific Northwest coast (Cascadia) produced the 1700 tsunami observed in Japan (ATWATER *et al.,* 2005), but observations in North America are recorded

only geologically. By adding the component of tsunamis inferred from the geologic record, the new NGDC/WDC Global Tsunami Deposits and Proxies database extends the record of tsunamis backward in time. The sedimentary deposits of tsunamis increasingly complement instrumental and human observations. Many of the data descriptions (37%) are of tsunami deposits in historic time. Studies of these deposits can be verified by historical and instrumental observations. Tsunamis inferred from proxies, such as evidence for coseismic subsidence, are also included to estimate recurrence intervals, but are flagged to highlight the absence of a physical deposit. Although the best methods for identifying tsunami deposits in the geologic record remain under discussion, developing a general picture of where tsunamis have affected coasts, calculating recurrence intervals, and approximating runup height and inundation distance provides a better estimate of a region's true tsunami hazard.

The Global Tsunami Deposits and Proxies database includes descriptions of tsunami deposits for locations all over the world that were extracted from published sources. The first 965 descriptions were extracted by Dr. Barbara Keating and Matt Wanink
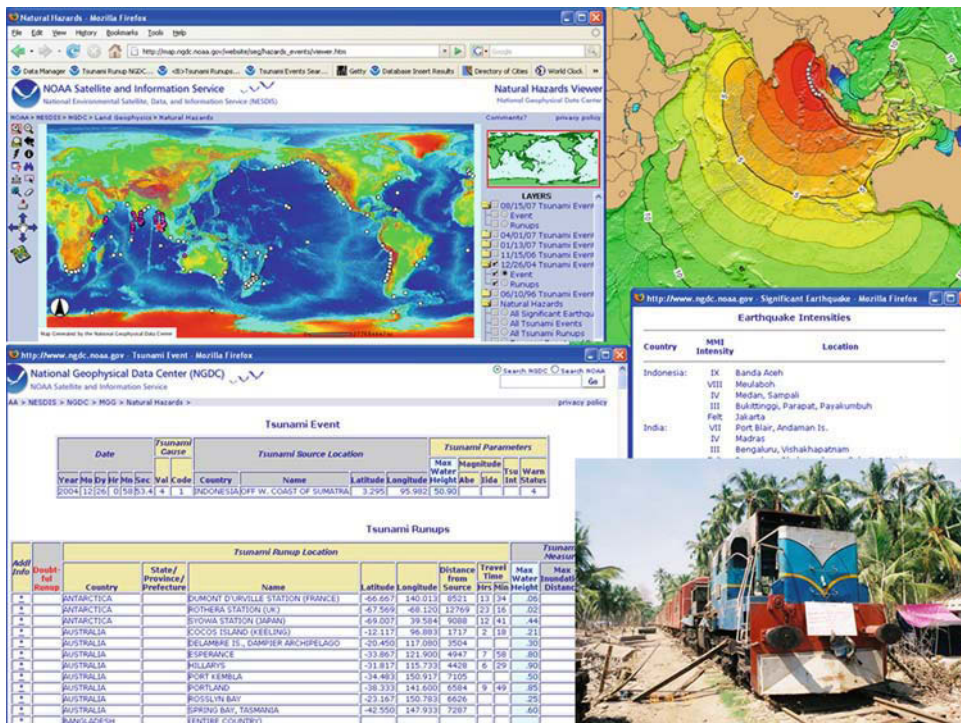

Figure 1
Collection of data available online for the 2004 Indian Ocean earthquake and tsunami, including an interactive map, tsunami travel-time map, listing of runups, listing of earthquake intensities, and a photo showing damage to a train in Sri Lanka.

(University of Hawaii) and provided to NGDC/WDC for development of a searchable database. The basic unit around which the database is built is a unique combination of the location and the evidence description. Since some locations have been described in more than one publication, the database is designed to include multiple descriptions of deposits at a given location. All descriptions, including dissenting ones, are included in the database and all the published information gathered about each deposit are available to users. Rather than assign a validity rank to each description, a publication is identified by type (peer-reviewed journal, thesis, dissertation, newsletter article, email, etc.). Users can restrict searches to publication types they trust or use all the information available. Other criteria refine the search by author, region, age of deposit, and/or sedimentary features. The database also includes photos of the tsunami deposits where available (Fig. 2).

2.3. Reference Database

The development and verification of the NGDC/WDC historical tsunami events and tsunami deposits databases have resulted in a collection of more than 2,000 source documents. These documents include journal articles, reconnaissance reports, catalogs, etc. The citation information for each document is stored in a RDBMS and the references are associated with all the events that are described in that particular document. NGDC/WDC has scanned these documents to PDF format and those documents not
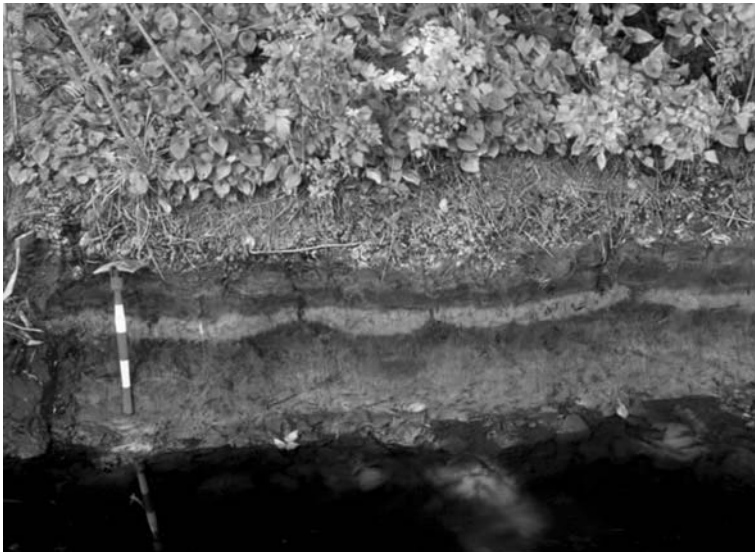

Figure 2
Photo showing tsunami sand layer (light colored) sandwiched between layers of grass (courtesy of Andrew Moore and Bruce Jaffe, USGS).

restricted by copyright are available on request. In addition to the reference citations links from the global historical and tsunami deposits databases, the reference database itself is also searchable online. For example, a user can select a list of all references that include data on tsunamis in the Caribbean or for earthquakes from a particular time period.

2.4. Damage Photos

The NGDC/WDC long-term tsunami data archive includes photographs of damage resulting from specific historical events and of tsunami deposits. These photographs are a permanent record that would otherwise have been erased forever by cleanup and reconstruction projects. They serve as a reminder to both the research scientist and the public that these events occurred, and can possibly recur, and we should be prepared to handle their consequences in the future (Fig. 3). NGDC/WDC first began distributing geologic hazard photos in the 1980s. The collection now includes more than 3,000 images covering tsunamis, earthquakes, volcanic eruptions, landslides, faults, seismic creep, and erosional landforms. The images can be searched, viewed, and downloaded online. For example, users can view the damage caused by the 1906 San Francisco earthquake or search for all occurrences of the word "fault" in the slide captions. The photos are also linked to the associated tsunami, earthquake, or volcanic eruption in the global historical databases.

Figure 3
Damage from the 2004 Indian Ocean tsunami to a home on the shoreline of Velankanni, India, a partially urbanized community with mixed fishing and tourism economy.

2.5. *Coastal Water-Level Data*

Scientists are often interested in high-resolution coastal water-level data, as well as maximum water levels measured at a tide gauge during a tsunami or other extreme water event. As a result, NGDC/WDC is currently expanding the long-term tsunami data archive to include coastal water-level data. NGDC/WDC is developing a process to archive coastal water-level data from NOAA's Center for Operational Oceanographic Products and Services (CO-OPS). Following the 2004 Indian Ocean tsunami, CO-OPS began a system-wide upgrade of its instrumentation to increase the rate of data collection and transmission at all coastal National Water Level Observation Network (NWLON) stations including the Great Lakes, Alaska, Hawaii, the Pacific Ocean Island Territories, Puerto Rico, and the U.S. Virgin Islands. Over 100 upgraded tide stations are currently equipped with new hardware and software to enable collection and dissemination of 1-minute water-level sample data in support of tsunami warning and mitigation efforts. These data are available in near-real time from the CO-OPS website (http://tidesandcurrents.noaa.gov/). NGDC/WDC is also working with the Global Sea Level Observing System (GLOSS) of the IOC and other international partners on a method to retain international coastal water-level data for the long term (Fig. 4).
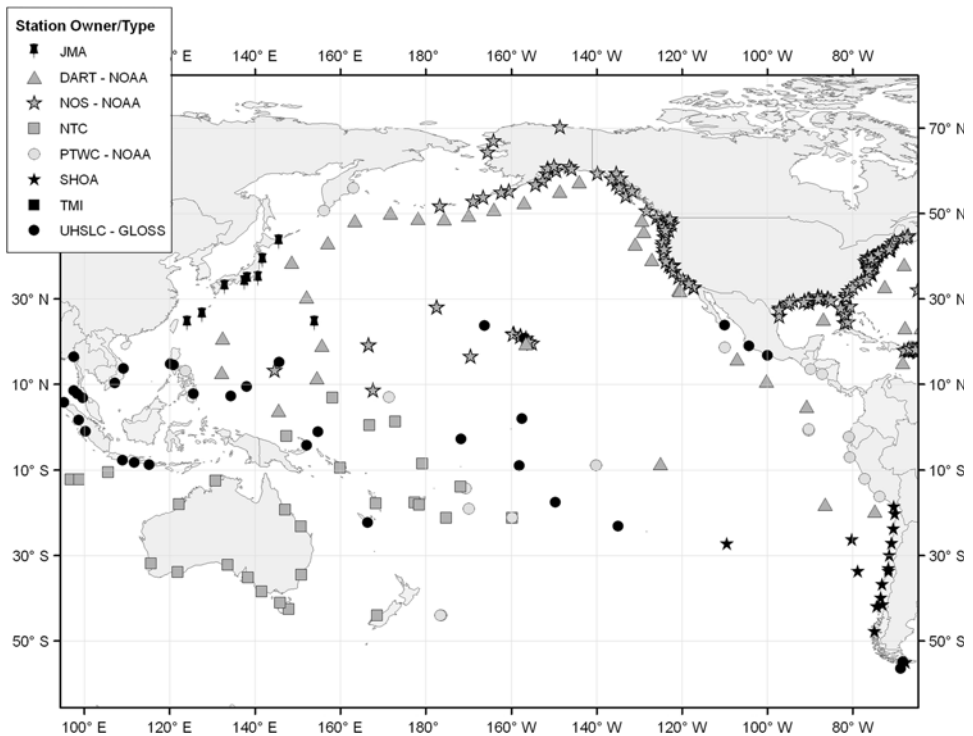

Figure 4
Sea level gauges and networks contributing to the Tsunami Warning System in the Pacific.

In addition to the digital coastal water-level data, NGDC/WDC has microfiche copies of more than 3,000 tide gauge records for tsunami events (marigrams) from 1850 to 1981 from U.S. and international tide stations. Each fiche consists of the recording at a given location for a specific tsunami event. These marigrams are very useful for understanding tsunamis and tsunamigenic earthquakes, particularly for events prior to the installation of the USGS Worldwide Standardized Seismograph Network in 1960. NGDC/WDC is in the process of scanning these microfiche to digital image files. Once this process is completed, the images will be available online.

2.6. Deep-Ocean Assessment and Reporting of Tsunami (DART^{TM}) Data

The DART^{TM} is an ongoing, multi-agency cooperative effort to maintain and improve the capability for the early detection and real-time reporting of tsunamis in the open ocean. DART^{TM} stations are sited to provide *in situ* tsunami detection and water-level observations for NOAA's tsunami forecast, warning, and mitigation responsibilities. Similar to the coastal water-level data, scientists are often interested in the time series data measured by a DART^{TM} station. As a result, in 2005 the NGDC/WDC long-term tsunami data archive was expanded to include these data.

Each DART^{TM} system consists of an anchored seafloor bottom pressure recorder (BPR) acoustically coupled to a moored surface buoy. NDBC acquires and manages all original real-time DART^{TM} data and monitors the hourly messages containing real-time standard 15-minute data. These data, along with real-time event data, are displayed and made available for download in near real-time on the NDBC website (http://www.ndbc.noaa.gov/dart.shtml). An internal tsunami detection algorithm (MOFJELD, 2007) monitors the estimated water level to detect changes in successive 15-second values (tides removed) exceeding a threshold. When the internal detection software identifies an event, the system ceases standard mode reporting and begins event mode transmissions. In event mode, 15-second values are transmitted during the initial few minutes, followed by 1-minute averages.

DART^{TM} BPR packages are deployable for 48 months at depths up to 6,000 meters and are typically on a 24-month service schedule. The recovered BPR contains the high-frequency data (temperature and pressure averaged over 15-second intervals) for the entire bottom-package deployment period. PMEL and NGDC/WDC process the high-frequency data, then add the raw, edited, and processed data to the NGDC/WDC tsunami data archive along with all of the available metadata. The high-resolution, edited BPR data, along with accompanying metadata, are available from NGDC/WDC and can be viewed, plotted, and downloaded. The archive currently includes raw, calibrated, edited, and filtered data from October 1983–May 2003 deployments and raw data from 2002–2006 deployments. The archive also includes tidal harmonic constants for all deployed DART^{TM} buoys, computed by CO-OPS, and event-specific data from those BPR packages that have not yet been recovered. The event-specific data include a map showing which buoys were triggered and the highest resolution data that are available for download.

The data from the buoys include several signals, including tides and earthquake waves. In the open ocean, tsunamis are very small (a few centimeters), but tides can be large (∼1 meter) and earthquake waves can be very large (several meters). Therefore, to see the tsunami, the data need to be filtered to remove signals of tidal or earthquake frequencies. NGDC/WDC is developing an on-line filtering tool.

The original six DART^{TM} buoy operational array, completed in 2001, is on schedule to grow to an operational array of 39 NOAA-operated DART^{TM} buoys in the Pacific and Atlantic Oceans, the Caribbean Sea, and the Gulf of Mexico in 2008 (Fig. 5). There are additional buoys operated by Chile, Indonesia, Thailand, and Australia.

2.7. Digital Elevation Models

Fundamental to coastal hazard assessment, community resiliency, and tsunami forecasting and inundation mapping efforts, is the modeling of tsunami waves as they propagate from their source to the coastal zone. The tsunami modeling requires accurate digital representations of the seafloor and coastal topography as a base layer for the
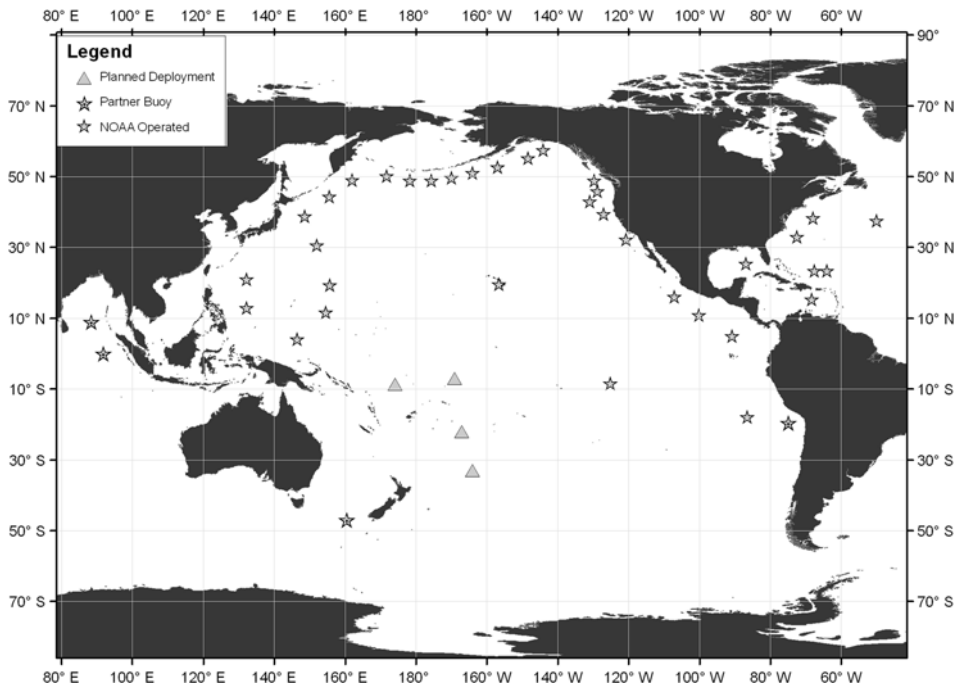

Figure 5
The DART^{TM} buoy operational array expected by the end of 2008.

modeled tsunami to propagate across and flood. NGDC/WDC is the U.S. National archive for bathymetric data (e.g., multibeam sonar and hydrographic surveys) and operates the International Hydrographic Organization (IHO) Data Center for digital bathymetry. Commencing in 2006, NGDC/WDC began building high-resolution digital elevation models (DEMs) for select U.S. coastal communities. These DEMs combine carefully evaluated bathymetric and topographic data into seamless representations of Earth's surface (EAKINS and TAYLOR, submitted).

The coastal inundation DEMs are part of the U.S. tsunami forecast system, Short-term Inundation Forecasting for Tsunamis developed by PMEL for the NOAA TWCs. The DEMs are also used in the Method of Splitting Tsunami model developed by PMEL to simulate tsunami generation, propagation, and inundation. Figure 6 shows a perspective view of the DEM built for Lahaina, Hawaii. To date, NGDC/WDC has built 33 coastal inundation DEMs. The DEMs, metadata, and associated technical reports are available on the NGDC/WDC website, which also identifies communities for which NGDC/WDC will build DEMs in the future.

Bathymetric, topographic, and shoreline data used to compile the DEMs are obtained from various national sources, including NGDC/WDC, NOAA NOS, USGS, U.S. Army Corps of Engineers, Federal Emergency Management Agency, and other federal, state, and local government agencies, academic institutions, and private companies. The DEMs are referenced to the vertical tidal datum of mean high water and horizontal datum of World Geodetic System 1984. Grid spacing for the coastal inundation DEMs range from 1/3 arc-second (∼10 meters) to 3 arc-seconds (∼90 meters).

NGDC/WDC also has other global and regional bathymetric data, such as ETOPO2, a two-minute gridded global relief model for both ocean and land, and the Coastal Relief Model of the contiguous U.S. coastal zone. The ETOPO2 global relief model is used to
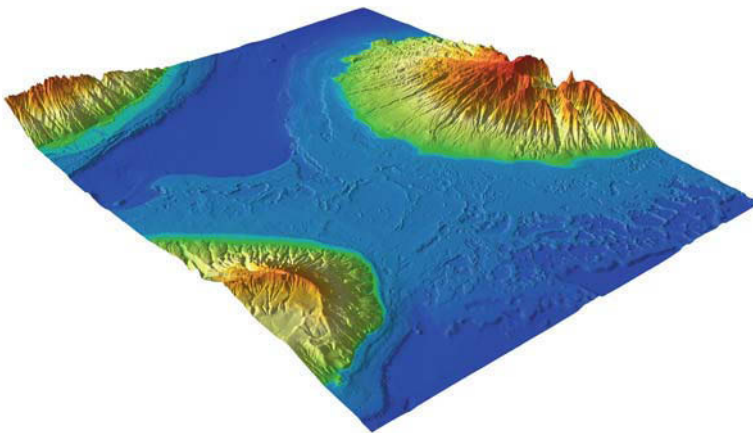

Figure 6
Perspective view of the Lahaina, Hawaii, DEM built by NGDC/WDC.

produce ocean-spanning tsunami travel-time maps. NGDC/WDC has also developed a refined 1-minute ($\sim$2 km at the equator) gridded global relief model.

3. Data Integration and Distribution System

NGDC/WDC is committed to delivering data in a manner that enables integration and supports multiple use and re-use of data. Most of the data in the NGDC/WDC archive is in the public domain and is discoverable on-line at (http://www.ngdc.noaa.gov/). These public domain data may be used without restriction, although users should cite sources of data.

A primary goal of NGDC/WDC is to make the data easily discoverable and integrated (i.e., a user can link from one dataset to related data in another dataset). NGDC/WDC manages and delivers the tsunami data in a RDBMS, facilitating the integration and delivery of these data (Fig. 7). The data can be searched from web forms interfaces by attribute (date, location, magnitude, etc.) and displayed as tables, reports, interactive maps, and imagery. For example, a user might be interested in all of the significant earthquakes in Japan that generated a tsunami. If an earthquake generated a tsunami, the user could directly access related information from the tsunami event table and display a list of locations that were affected by the tsunami, additional comments, references, and photos.

NGDC/WDC has recently integrated the DART^{TM} data with the tsunami runup data. For example, if a DART^{TM} buoy was triggered by a tsunami it will be listed in the tsunami runup database. The time series data can then be accessed directly from the runup database. The same integration and access will also be provided for the coastal water-level and tsunami runup data.

The tsunami data are also accessible via interactive web maps and through the Open Geospatial Consortium (OGC) Web Map Service (WMS) that allows any OGC-enabled client to incorporate a map image of the data. Both services operate off the same RDBMS as the traditional forms. The interactive maps provide integrated web-based GIS access to the tsunami databases as well as additional auxiliary geospatial data. The maps provide access to individual GIS layers of tsunami sources, tsunami runups, significant earthquakes, significant volcanic eruptions, volcano locations, tsunami inundation DEMs, underlying bathymetric data, DART^{TM}, and various spatial reference layers including topography, population density, and political boundaries. The map service also provides links to additional hazards information such as the hazards photos.

The NGDC/WDC website now provides a Keyhole Markup Language (KML) file containing tsunami sources and runups, significant earthquakes and volcanic eruptions. Many applications display KML, including *Google Earth, Google Maps*, NASA *WorldWind*, and ESRI ArcGIS Explorer. The KML file provides basic information on each event (date, magnitude, death, damage) and links to the NGDC database for the full content (Fig. 8).
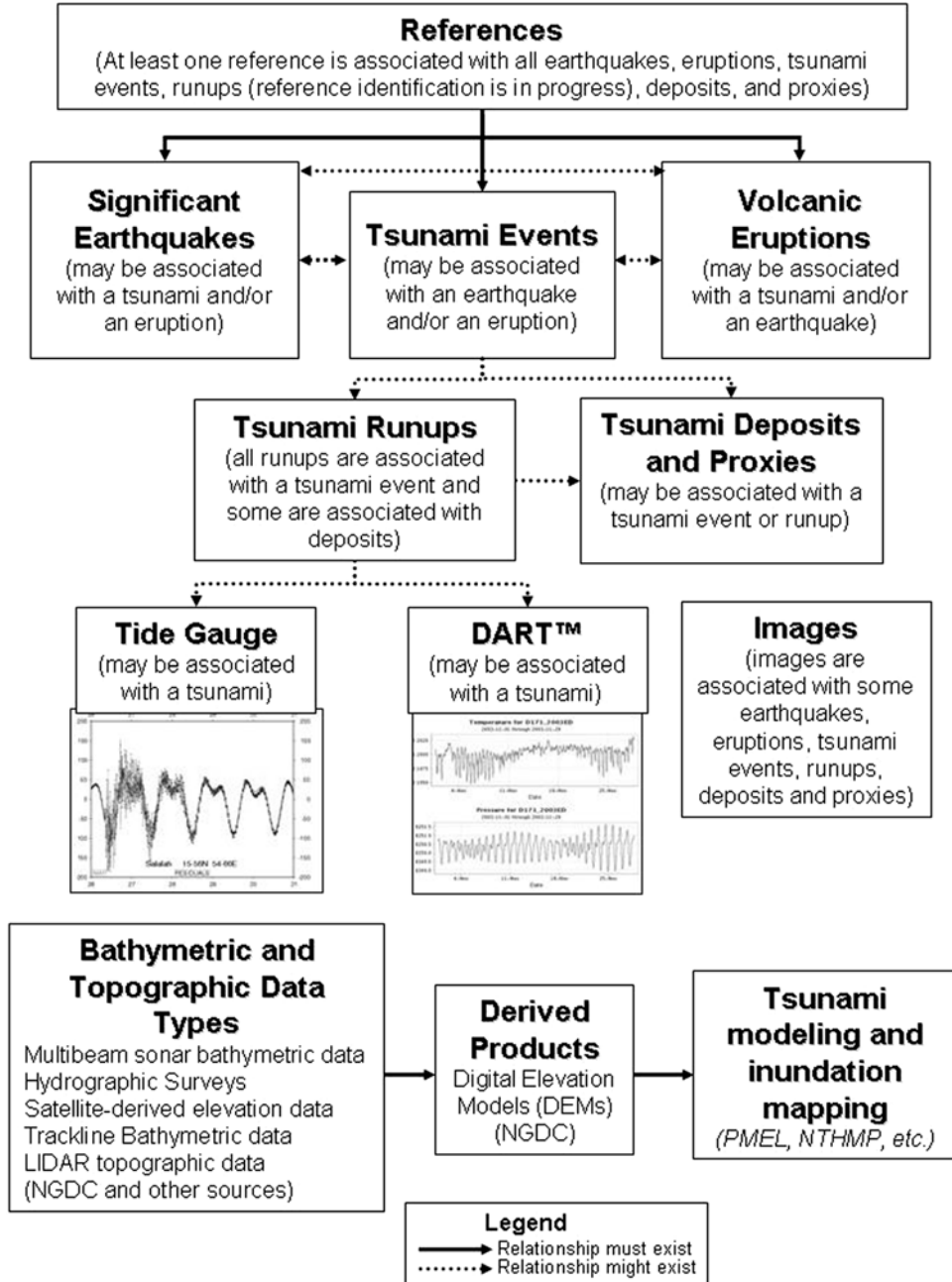
Figure 7
Schematic showing the integration of the NGDC/WDC long-term tsunami data archive.

NGDC/WDC also produces tsunami travel-time maps for several significant tsunami events (Fig. 1, upper right). Users can access these maps and then link to the historical tsunami event and runup databases. The observed tsunami travel times in the database can be compared with the calculated tsunami travel times displayed in the maps.

4. Challenges

NGDC/WDC faces many challenges in archiving and disseminating tsunami data. Some are particular to the tsunami data archive and some are challenges faced by any data center. Greatly increasing volumes of data require tremendous amounts of disk space and tape storage. Making these large data sets quickly and easily discoverable and available to users with varying capabilities to download data is also a challenge. It is important to document the data (i.e., creating metadata) so that scientists 50 years from
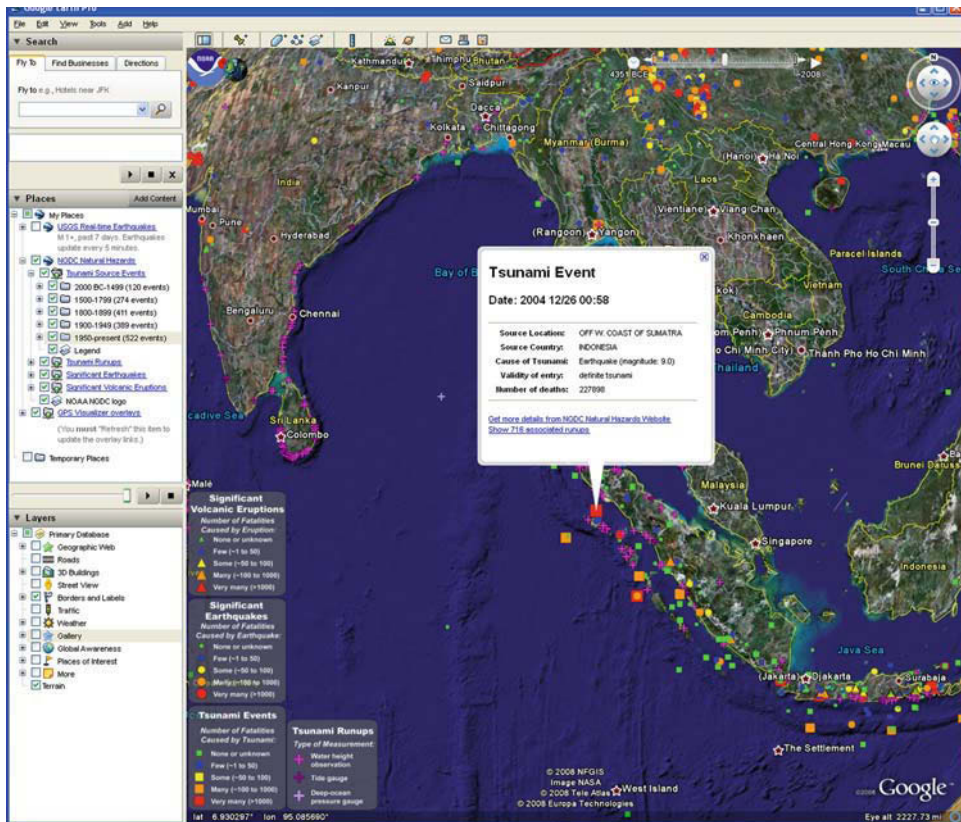

Figure 8
Google-Earth view of the NGDC/WDC global historical databases.

now can understand and use the data. This includes documenting data formats and differences in versions of data. The data center must continually evaluate new technologies as well as data and metadata standards to determine the best way to archive and disseminate data.

Tsunamis present a unique challenge to a data center since they are global and multi-disciplinary in nature. Tsunamis can affect many geographic areas and must be studied on a global basis. Tsunami sources are multi-hazard (earthquake, volcano, landslide, etc.) and understanding tsunami generation, propagation, and runup requires knowledge in many scientific fields including seismology, volcanology, geodesy, and oceanography. These scientific disciplines require many different types of data, often data that a coastal State may consider sensitive. Data types range from point data to time-series, grids, and descriptive data. Often the communities with primary responsibility and expertise in the collection of "tsunami" data are not focused on tsunamis, but rather support a completely different mission. NGDC/WDC strives to work with the various communities to identify and adopt appropriate standards for the description, dissemination, and archive of tsunami data. Working with the IOC and the ITIC, the WDC system encourages coastal States to share tsunami data and information to minimize the loss of life and economic impact of tsunamis on all coastal communities.

5. Conclusion

Since the 2004 Indian Ocean Tsunami, the NGDC/WDC long-term tsunami data archive has expanded from the original global historical event databases and damage photo collection, to now include tsunami deposits, coastal water-level data, DART^{TM} buoy data, and high-resolution coastal DEMs. These data support many aspects of the NOAA Tsunami Program, as well as other national and regional tsunami warning systems. The goal of a tsunami warning system is to provide real-time tsunami predictions for coastal locations while the tsunami is propagating through the open ocean, before the waves have reached the coastlines. These predictions are developed from tsunami propagation and inundation models. The data in the archive are essential input for the development and validation of these models. The data are also important for producing tsunami hazard assessments and educating the public about tsunamis. Therefore, the improvement in the content and access to the tsunami data archive will ultimately help to save lives and improve the resiliency of coastal communities. The data archive will continue to grow as observing networks expand, new data are received, and new partners and data agreements are established. NGDC/WDC is committed to maintaining a high-quality long-term tsunami data archive by carefully reviewing and documenting data sources and types, as well as adhering to accepted data and metadata standards. NGDC/WDC will also continue to search for and evaluate new technologies for data discovery, integration, and dissemination.

REFERENCES

ATWATER, B., SATAKE, K., YOSHIOBU, T., KAZUE, U., and YAMAGUCHI, D.K., *The Orphan Tsunami of 1700—Japanese Clues to a Parent Earthquake in North America*, U.S. Geological Survey Professional Paper 1707 (Reston, Virginia; University of Washington Press, Seattle and London, 2005), 144 pp.

DUNBAR, P.K. and WEAVER, C.S., *U.S. States and Territories National Tsunami Hazard Assessment: Historical Record and Sources for Waves,* National Oceanic and Atmospheric Administration, National Geophysical Data Center Technical Report No. 3 (U.S. Department of Commerce, 2008), 59 pp.

EAKINS, B.W. and TAYLOR, L.A. (2008), *Development of high-resolution coastal digital elevation models for the U.S.: Seamlessly integrating bathymetric and topographic data to support tsunami forecast and modeling efforts*, submitted to Ocean Globe.

LANDER, J., *Tsunamis Affecting Alaska, 1737–1996,* National Geophysical Data Center, Key to Geophysical Records Documentation No. 31, (U.S. Department of Commerce, 1996), 195 pp.

LANDER, J.F. and YEH, H., eds., *Report of the International Tsunami Measurements Workshop* (Estes Park, Colorado, 1995), 102 pp.

MOFJELD, H.O., *Tsunami Detection Algorithm*, retrieved January 2007 from the World Wide Web http://nctr.pmel.noaa.gov/tda_documentation.html.

SIEBERT, L. and SIMKIN, T., *Volcanoes of the World: An Illustrated Catalog of Holocene Volcanoes and their Eruptions* (Smithsonian Institution, Global Volcanism Program Digital Information Series, GVP-3, http://www.volcano.si.edu/world/, 2002 to present).

NATIONAL OCEANIC and ATMOSPHERIC ADMINISTRATION, *Tsunami Data Management Plan: An Initial Report on the Management of Environmental Data Required to Minimize the Impact of Tsunamis in the United States*, National Oceanic and Atmospheric Administration, National Geophysical Data Center Technical Report No. 2 (U.S. Department of Commerce, 2008), 87 pp.

PUBLIC LAW 109–424, *Tsunami Warning and Education Act*, approved December 2006. http://frwebgate.access.gpo.gov/cgi-bin/getdoc.cgi?dbname=109_cong_public_laws&docid=f:publ424.109.pdf, 9 pp.

To access this journal online:
www.birkhauser.ch/pageoph